University of Napoli Federico II

Doctorate in
Structural Engineering, Geotechnics and Seismic Risk
XXXIII CYCLE

EXPERIMENTAL BEHAVIOR, ANALYSIS AND DESIGN OF ENERGY PILES

Gabriella Marone

PhD Coordinator
Prof. Luciano Rosati

Supervisor
Prof. Gianpiero Russo

2020/ 2021

List of Abbreviations

ASTM American Society for Testing and Materials

CFA Continuous Flight Auger

CNTC Negative Temperature Coefficient Chain

DDR Dimensionless Displacement Ratio

DOF Degree Of Freedom

DSR Dimensionless Stress Ratio

DTV Daily Thermal Variations

EBEP End Bearing Energy Pile

EG Energy Geostructure

EP Energy Pile

FC Fully Constrained

FEM Finite Elements Method

FEP Floating Energy Pile

FH Free Head

GEP Geothermal Energy Pile

GHE Ground Heat Exchanger

GS Geothermal System

GSHP Ground Source Heat Pump

H-S Hardening Soil

HTV Hourly Thermal Variations

HVAC Heating Ventilation and Air Conditioning

ILT Ideal Load Test

LE Linear Elastic

LVDT Linear **V**ariable **D**isplacement **T**ransducer

M-C Mohr Coulomb

NP Null Point

NTC Negative Temperature Coefficient

PC Primary Circuit

SF Safety Factor

SG Strain Gauge

THM Thermo Hydro Mechanical

VWG Vibrating Wire Strain Gauge

Table of contents

1 Introduction

1.1 *Geothermal energy and Geo-structures*

One of the major challenges facing the 21st century is the continuous need to mitigate the environmental damage caused by the burning of fossil fuels with the need to move away from the use of non-renewable based energy sources. In the construction sector directives and regulations are increasingly requiring the use of so-called environmentally friendly technologies that allow a limited impact on the environment. Among the various energy sources available, herein the attention is devoted to geothermal energy that is the energy contained as heat in the Earth's interior (Babier, 1997). This natural heat results from the formation of the planet, the radioactive decay of minerals and the solar energy absorbed at subsurface (Laloui and Rotta Loria, 2019). It is contained in huge practically inexhaustible quantities in the earth's crust being one of the most promising decentralized renewable energy. Unlike solar and wind energy, geothermal energy is always available, 365 days a year. Below the shallow subsurface the temperature field remains relatively stable throughout the year ranging from 10 °C to 25 °C depending on the latitude. For most locations around the world the ground temperature is higher than atmosphere temperature during Winter and conversely during Summer allowing the ground heat extraction or energy injection.

The systems that harvest geothermal energy are defined as Geothermal systems. Depending on the exploitation depth of geothermal energy these systems can be classified as Shallow geothermal systems or Deep geothermal system (deeper than 400 m). The former kind of systems are also known as Low Enthalpy systems that deal with temperatures lower than 80 °C. These systems need to be coupled with a heat pump therefore they act at the Ground Heat Exchangers (GHEs) as part of Ground Source Heat Pump (GSHP) Systems.

Shallow geothermal system (GS) can be used to provide heating, cooling and hot water, using underground temperatures less than 25 °C (Laloui and RottaLoria, 2019). Typical geothermal systems are vertical and horizontal geothermal boreholes, geothermal baskets and groundwater capture systems.

When structural members already required for structural need are also used for energy supply the shallow geothermal system is defined as Energy Geo-structure or thermo-active ground structure. This technology is increasingly spreading all around the world because negates the initial drilling cost and the land area required for the installation of traditional boreholes. With respect to other closed loop systems energy geostructures (EGs) are constructed with filling materials that have more favourable thermal properties making advantage in the heat exchange process. The first application of heat exchange via foundation elements was in Austria and Switzerland. Shallow foundation elements like bearing slabs and shallow basement walls were first utilised for energy exchange, and these were quickly followed by bearing piles (mid-1980s), diaphragm walls (mid-1990s) and tunnel (early 2000s). Deep foundations enable a limited use of subsurface and reaching higher depths representing great advantages compared to shallow foundations. When pile foundation couples its primary structural role to exploitation of geothermal energy from the ground for the purpose of space heating and cooling in buildings it is known as Geothermal Energy Pile (GEP) or Energy Pile (EP).

Rotta Loria and Laloui (2019) reported the state of art about the energy geostructure projects (updated to June 2018) showing that the construction of EGs is increasing with predominant application of EPs (Figure 1-1). Piles are the most common type of energy geostructure, their application has expanded but their numbers are still minor compared to the total GSHP installations worldwide (Loveridge et al., 2020). In Figure 1-1 the carbon dioxide savings associated with EGs constructed worldwide is plotted. The dominant amount of carbon dioxide savings is related to EPs applications.

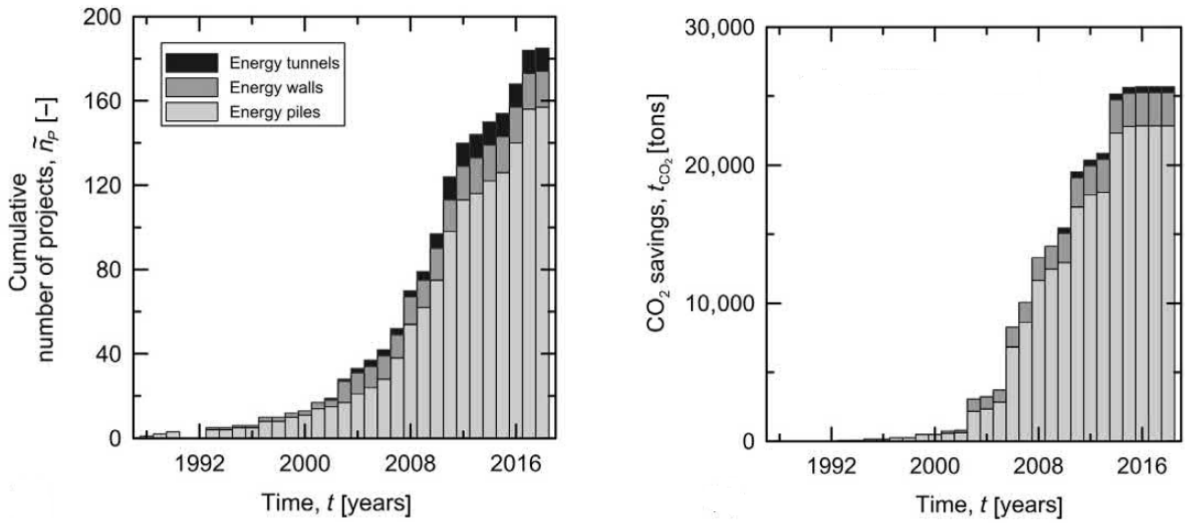

(a) (b)

Figure 1-1:Energy geostructures installed around the world from Laloui and RottaLoria (2019); (a) Energy Geostructures projects and (b) CO_2 savings.

The dual role of these foundations makes their design challenging with respect to traditional piles foundation. When deciding to exploit piles from energy supply additional effects induced by temperature variation on the structures are involved. The behavior of GEP is characterised into two main aspects the thermal performance and the thermomechanical behavior. In this chapter an overview on the former aspect is presented along with the general description of the system.

1.2 *Geothermal Energy Pile (GEP) systems*

A GSHP system primary purpose is exploiting the ground as heat source or heat sink. For cold seasons or climates, the ground is used as heat source i.e., the heat is extracted from the ground and transferred to the superstructure. During hot seasons or for warm climates, the ground is used as heat sink i.e., the heat is injected into the ground and extracted from the superstructure (Figure 1-2).

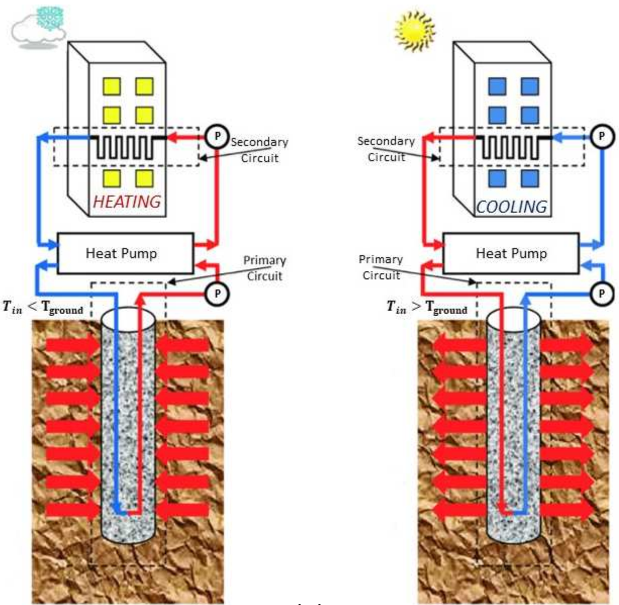

(a) (b)

Figure 1-2: Heat exchange mechanism for GSHP system; (a) Heating of the upper structure (cooling of the pile); (b) Cooling of the upper structure (heating of the pile).

To achieve these purposes the EGs need two circuits. The first is installed inside the pile and is defined as Primary Circuit (PC) because it allows the heat exchange between the pile and surrounding soil. The second circuit named as secondary circuit is closed-pipelines network installed inside the built environment to be cooled or heated. Heat exchange in the built environment is typically achieved through heat exchangers such as radiant heating floors or ceilings, radiators, fan coil units, etc (Laloui and Rotta Loria, 2019). The distribution schemes employed for the secondary circuit are typically the same as conventional systems. Loops can be installed in bridge decks, roads, airport runways for de-icing purposes (Brandl, 2006).

Between primary and secondary circuits heat pumps or reversed heat pumps are employed. These machines do not work when the energy piles or geostructure are in "free heating" or *Geo Cooling* i.e., when the operating modes are targeted without using external energy sources.

The principle behind the heat pumps is that fluids are heated when they are compressed into a smaller volume. For reversed heat pumps fluids become cooler when they are expanded. The heat pump is used to raise the temperature of the heat extracted from the ground to a temperature suitable for space heating (Sani et al., 2019). The working mechanism is comparable to reverse order refrigerator. Evaporator, Condenser, Compressor and Expansion valve are the main four components of a simple heat pump (Figure 1-3).

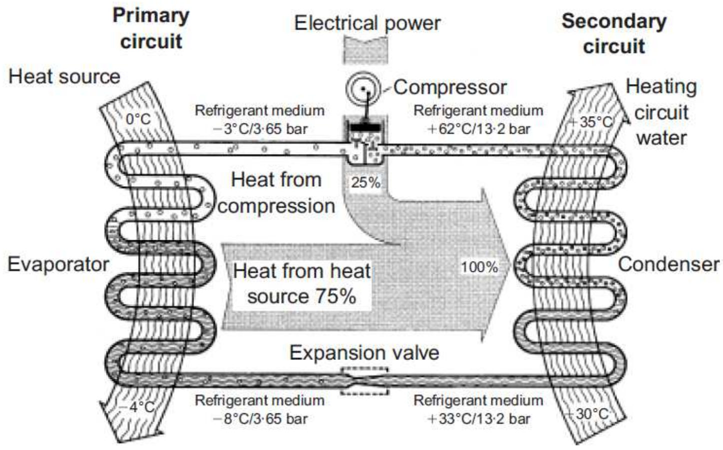

Figure 1-3:Scheme of compression heat pump considering R290 as refrigerant medium as example. Heat exchange from the primary circuit to the refrigerant medium in the evaporator from refrigerant medium to secondary circuit from Brandl (2006).

As showed in Figure 1-3 during the heating operation the heat career medium is pumped and circulated through the Primary circuit. The heat carer fluid absorbs heat from the ground and is fed into the evaporator where a refrigerant fluid (liquid state) is put in contact with the heat carrier fluid. The refrigerant is a special fluid that circulates in closed circuit of the heat pump. With the evaporator the refrigerant fluid absorbs the heat from the heat transfer fluid raising the temperature of the refrigerant. The refrigerant circulated through the compressor that compresses and turns it into a high pressure and temperature fluid. In the compressor, this gas is compressed by using external energy e.g., electrical power. At the condenser, the resulting hot gas transfers its heat to the heat carrier fluid circulating in the secondary circuit to heat the building. The refrigerant cools down at the condenser level and it fed through the expansion valve which lowers its pressure and temperature to its original conditions prior to enter again in the evaporator a new cycle starts. This process is reversed when reversed heat pumps are used for cooling. The required water flow can range from 2-3 m^3/h and power of 4-6 kW up to 60 m^3/h for 300 kW heat pumps (Laloui and Rotta Loria, 2019). The amount of external energy supplied to the heat pump should be kept as low as possible to achieve heat pump efficiency. The measurement of heat pump efficiency is provided by the Coefficient of Performance (COP) defined according to Equation 1-1 (Brandl, 2006).

Equation 1-1: $COP = \frac{Energy\ output\ after\ heat\ pump[kW]}{Energy\ input\ for\ operation\ [kW]}$

For economic reasons, a value of $COP \geq 4$ should be achieved. A heat pump system should be designed to get to a COP value of 4 in heating and 6 in cooling to achieve higher performance at the lowest possible cost (Sani et al., 2019). To have a good efficiency, the usable temperature in the building should not exceed 35-45 °C and the extraction temperature in the pipes should not fall below 0-5°C (Brandl, 2006).

EPs can be classified by pile material and by the way a heat exchange loop is installed. Three main pile types by material are used cast in-situ concrete, prestressed high strength concrete and steel (Fadej et al., 2017). At the present time, a wide range of pile types have been adapted to include the heat exchangers pipes made from high-density polyethylene (HDPE) plastics Polyvinyl-chloride or Polybutylene pipes with diameter ranging between 10-44 mm and wall thickness ranging between 2-4 mm (Sani et al.,2019). Heat exchange loop in the pile can be installed as single U-tube, Bent U-shaped, double U-tube, W-shaped, Spiral or Helix and coaxial tube (Figure 1-4).

Figure 1-4:Pipe configuration types for EPs from Fadej et al. (2017) and Laloui and Rotta Loria (2019).

Because of the difficulties associated with installation the spiral pipe configuration is not commonly employed despite its marked heat transfer potential. The multi-U-shaped pipe configuration is often used for large diameter piles. Careful consideration should be taken to ensure the best pipe shape is chosen to result in effective system performance (Sani et al., 2019). Pipes are fixed along the reinforcing cage or placed within the filling material. Fixing the pipes to the reinforcing cage of energy geostructures can be performed either in a plant or on site. The latter is more common whereby the piping is delivered to site a special working area is addressed to the assembly (Brandl, 2006). At the inflow and outflow of the pipework a locking valve and a manometer are fixed (Brandl, 2006). These instruments allow the pipe circuit to be pressurised within a range of 5-8 bar for integrity check. Pressure testing for 24 hours after concreting is good practice. The pressure in the pipes is again applied before the working phase involving the construction of the superstructure starts (Brandl, 2006). The common issues with each pile type are how to integrate the pipe with minimal impact on the construction process along with how to prevent damage during the installation (Laloui and Di Donna,2013). Continuous flight auger piling and plunging of the heat exchanger with the reinforcement cage into wet pile concrete may affect the final integrity of the plastic absorber pipes. The risk of absorber pipe damage can be lowered by welding the helical reinforcement to the vertical reinforcement bars (Brandl, 2006). The optimum position of the loops is on the inside of the reinforcing cage allowing the full cover for the reinforcement cage. During concreting of the pile, the thermal loops should be filled with water and subjected to nominal pressure in order to prevent the crushing of pipes caused by the fluid concrete (GSHP,2012). The size, position and configuration of the primary circuit is one of the main design choices on which the thermal performance of the pile depends. Brandl (2006) provided approximate data about the energy that can be extracted depending on pile's diameter. For pile foundations with diameter ranging between 0.3–0.5 m the specific heat extraction/injection is about 40–60 W /m. For pile foundations with diameter D ≥ 0.6 m the heat extraction/injection is about 35 W per m^2 earth-contact area.

1.3 *Mechanical response of Energy piles*

In Service condition EPs are subjected to combined thermomechanical load therefore with respect to pile foundations the effect of the additional thermal loadings have to be considered. EP's geotechnical performance must be firstly ensured throughout their working life both in terms of maximum supportable loading and acceptable displacements. A deeper knowledge about their thermo-mechanical behavior would lead the engineers to be more confident with this technology (Di Donna, 2014).

GSHP standard and SIA 2005 suggest 2 °C-50 ° C as range of temperature that can occur during EP's working life. By the circulation of heat exchanger fluid within the PC the pile is heated and cooled in service condition. When the pile is subjected to a temperature increase i.e., the pile is heated up, it tends to expand conversely when the pile is subjected to a temperature decrease i.e., the pile is cooled down, it tends to contract. The pile expansion and or contraction determines additional displacement and strains but also additional axial loads and thermal stresses. The interaction with the surrounding soil blocked part of the thermal strain that the pile would have had if it had been free to elongate or contract ($\varepsilon_{\mathrm{th,free}}$). Therefore, both displacements, strains and stresses and axial loads depend on how the pile interact with the surrounding soil. It should be also remarked that the blocked strain and therefore the additional stresses and axial loading along the pile depend on the fact that the pile is part of a foundation system (e.g., slab and other foundation piles). Therefore, additional thermal stresses and loadings are induced on the pile if the foundation system acts as constraint to the expansion and/or contraction. In contrast to the influence of mechanical loads that cause pile displacements in unique direction (downward) thermal loads involve two pile portions that displace in opposite directions from the so-called null point (NP) of the vertical displacement (Rotta Loria and Laloui, 2018). Accordingly, shaft friction is mobilised in opposite directions at pile's shaft to ensure equilibrium with the surrounding soil. The difficulties of assessing stress and strain in heat exchanger pile lies in the evaluation on the way the thermal strains are restrained by the ground and the supported structure. A priori only in situ strain measurement along the pile while it is heated or cooled would provide an exact quantification of how the thermal strain is blocked (Knellwolf et al., 2011). Currently, thermomechanical schemes based on the results of full scale in situ tests are available for developing preliminary considerations related to more involved situations characterised by irreversible conditions. Rotta Loria and Laloui (2018) provided representative schemes of relevant stress, strain and displacement evolution caused along EPs based on linear thermo-elasticity theory. The more complex observed behavior depends mainly on thermal loading, the level of mechanical stress, the constraint action at pile's ends (head and toe), characteristics of the ground and pile type.

Pile can be classified as *Floating*, *Semi-floating* and *End Bearing* piles. A floating pile is such that almost the entire weight of the building is transferred to the ground through friction along the pile shaft and no or little weight is supported by the base of the pile. A semi-floating pile support the weight of the building both at its base and through friction along its lateral surface. *End Bearing* piles transmit most of the load at the tip. Different pile's response of course occurred depending on this classification.

As described above the magnitude of temperature applied during thermal operation is included between upper and lower boundaries that are corroborated by experimental evidence and design of GSHP systems. Different consideration could be made about the kind and time duration of thermal solicitations to be applied to energy piles. Firstly, the experimental evidence corroborated that the increasing number of thermal cycles induces plastic effects as additional axial forces and displacements. Transient calculation enables to have a good assessment of additional axial forces and displacements and to accounts for the impact of thermal diffusion (Rammal et al., 2017). To analyse the long-term effect of cyclic solicitation methods of analysis such as finite elements methods (FEMs) can be employed to address the investigations. When analyses methods are employed the more common and realistic method to apply thermal solicitation consists of imposing temperature-time functions uniformly along pile's length. In this perspective different type of thermal solicitations can be considered e.g., constant temperature, continuous sinusoidal solicitations, krenel solicitations. The choice of solicitations to be applied concerns also the time scaling: year, day or hours and the option of modelling one or more recovery thermal phases. Rammal et al. (2018) showed that the presence of recovery phase has a negligible impact in terms of the pile mechanical behavior while the application of constant temperature under transient conditions results to be conservative. Further studies should be carried to analyse the influence of the thermal solicitation type on the behavior of single pile (Rammal et al. 2019).

Mechanical loads can be idealised as prescribed force that typically cause stress and strain variations that decreases with depth. In most cases the evolutions with depth of the variations caused by the mechanical loads are more uniform than those caused by thermal loads and are associated with downwards displacements (Rotta Loria and Laloui, 2018). The mechanical loading level can be defined according to the ratio between the applied load at pile's load and the ultimate bearing capacity i.e., Safety Factor (SF). Nguyen et al. (2017) performed laboratory tests on small pile (see chapter 2) founding that the irreversible settlement of the pile head is higher at a higher pile head load. Kalantidou et al. (2012), carrying out small scale tests on single EP in sand (see chapter 2), showed that the pile response appears to be thermo-elastic under thermal cycles when $SF \geq 2.5$, while if the $SF < 2.5$ irreversible piles settlement appears to develop. According to Santamarina et al. (2014) piles with low SF accumulate gradually decreasing strains until reaching a shakedown state.

The mechanical properties of soil such as stiffness and thermal expansion coefficient of course influences EPs response. Some general conclusions about the impact of soil stiffness and thermal expansion coefficient can be summarised on the basis of previous studies. Bodas Freitas et al. (2013), noted that increasing the soil stiffness by a factor of two led to increased axial thermal stress and interface shear stress. Bourne-Webb et al. (2016) carried out a parametric numerical study to examine the impact of the thermal expansion coefficient of soil on pile-soil thermo mechanical interaction. When the ratio between the thermal expansion coefficient of soil to the thermal expansion coefficient of the pile is less than 1 stress change during pile's heating are compressive. When this ratio increases, there is a distinct change in the predicted response with axial stress changes due to heating becoming less compressive and in the case of larger ratios, becoming tensile (Bourne-Webb et al., 2019). A comprehensive parametric study was performed by Oliaei et al. (2018) on various indicator parameters such as pile length and diameter, head-spring, ultimate side shear and toe resistance by means of finite difference method. Side shear and toe resistance result to reducing thermal axial strains. Increasing the diameter of the pile thermal axial strains increases. Effect of considering reduction factor on better prediction Thermal strains along pile for various pile diameter and vice versa by increasing diameter of pile, the thermal strain increases. The effect of increasing toe resistance is more complex with its increase, the small effect is created at the upper sections of the pile. Except for diameter increasing other parameters results to increasing axial thermal compressive stress. This shows that in the case of thermal loads unlike mechanical loads, stiff soils or long piles could lead to more axial stress than what was expected for mechanical loads (Oliaei et al., 2018).

The current European norms and Eurocodes lack recognised rules that suitably consider in the design process the effects of thermal loads associated with geothermal operation (Rotta Loria et al., 2019). Guide in Switzerland (SIA D 0190), standard in UK (GSHP standard, 2012) and one recommendation in France (CFMS-SYNTEC-SOFFONS-FNTP, 2017) have been proposed to guide the EPs design. The recommendations suffer of some lacks as in the case of the GSHP standard they can be applied only to a limited number of situations. The French recommendations account for the effect of thermal loading employing a partial factor for thermal actions that can underestimate the related effects. The phenomena caused by the thermal loads determines effects that are coupled with those of mechanical loadings and that can be comparable to them therefore they should be considered in the EP design. The UK standards suggests that induced stress associated with completely restrained condition may be considered as additional load to be applied at pile toe. This involve a lengthening of energy piles that can be conservative for failure related verifications against mechanical loads, but it is not conservative for deformations related problem under thermomechanical loads (Rotta Loria and Laloui, 2018). Mimouni and Laloui (2013) investigated the impact of temperature variation on the mobilised bearing capacities of geothermal piles. Over-sizing geothermal piles compared to conventional piles can have a negative impact on their serviceability. In general, both strains and stresses can cause two types of problems: achievement of the Ultimate limit states (ULS) or Serviceability Limit states (SLS). Stresses may exceed the acceptable design stress, while large-amplitude strain cycles alter the magnitude and distribution of shaft friction mobilised between the pile and the soil. Additionally, other phenomena occur in the cooling phase (Duphray et al., 2014). With the current state of knowledge, it is quite difficult to state reliably when tension might arise as it will be highly dependent on the particular conditions being considered (Bournewebb et al., 2019).

1.4 *Research Plan and overview of the thesis*

The research program aims to develop activities focused on the application of EP installed in a specific geographic area and particular subsoil conditions. This purpose is developed through numerical analysis and experimental investigations both at laboratory (small scale) and field scale.

Firstly, an insight on the main well documented in situ and small-scale laboratory tests and numerical studies is presented along with a review about the main topics involving the operation of EPs (Chapter 2). Three dimensionless parameters are introduced to summarize the main effects of thermal loadings in terms of thermo-mechanical interaction between pile and soil. An overview of the main numerical studies showed that, with only a few exceptions, thermal stresses are often underestimated. Numerical analyses rarely refer to realistic subsoil conditions and real thermal loadings. Studies where right values of thermal stresses were reproduced are those where soil parameters were calibrated on the basis of full-scale thermal tests (Bourne-Webb et al., 2019). To this aim in Chapter 3 a calculation procedure based on the mechanical calibration of soils parameters is presented. Back analyses of three case-histories from literature allowed the validation of the procedure. Then, the results of short term thermo-mechanical coupled analyses along with a sensitivity analysis provide insight about the effect of different parameters on the mechanical response. Different aspects were investigated e.g., the coupling among the effect of the imposed surface boundary conditions and the pile thermal loadings, different kinds of thermal loading, the influence of the constraint at pile's head and at the pile's tip, and long-term previsions.

In Chapter 4 the design of two laboratory models and the experimental setup are described. Two models were developed: Model A and Model B. The difference between the models is that gravity loads were applied at soil surface in Model B. For each model different kinds of test have been carried out. Mechanical tests to failure were carried out for both models to define the capacity of the pile-soil system. Thermal and thermomechanical short-term tests were carried on Model A while on Model B longer cyclic thermo-mechanical tests were described.

Chapter 5 deals with full scale investigations carried out in Crispano, Napoli (IT). The layout of the test along with the measurement of soil temperature in the shallow zone and the estimation of soil diffusivity are provided along with the results of three short term thermal test. The experimental campaign presented herein is only the starting point of a longer research plan.

References

Amatya, B.L., Soga, K., Bourne-Webb, P.J., Amis, T., Laloui, L., 2012. Thermo-mechanical behavior of energy piles. Geotechnique 62, 503–519. https://doi.org/10.1680/geot.10.P.116

Barbier, E., 1997. Nature and technology of geothermal energy: A review. Renew. Sustain. Energy Rev. 1, 1–69. https://doi.org/10.1016/S1364-0321(97)00001-4

Bourne-Webb, P.J., Amatya, B., Soga, K., Amis, T., Davidson, C., Payne, P., 2009. Energy pile test at lambeth college, London: Geotechnical and thermodynamic aspects of pile response to heat cycles. Geotechnique 59, 237–248. https://doi.org/10.1680/geot.2009.59.3.237

Bourne-Webb, P.J., Bodas Freitas, T.M., Assunção, R.M.F., 2016. Soil-pile thermal interactions in energy foundations. Geotechnique 66, 167–171. https://doi.org/10.1680/jgeot.15.T.017

Bourne-Webb, P.J., Bodas Freitas, T.M., Freitas Assunção, R.M., 2019. A review of pile-soil interactions in isolated, thermally-activated piles. Comput. Geotech. 108, 61–74. https://doi.org/10.1016/j.compgeo.2018.12.008

Brandl, H., 2006. Energy foundations and other thermo-active ground structures. Geotechnique 56, 81–122. https://doi.org/10.1680/geot.2006.56.2.81

CFMS-SYNTEC-SOFFONS-FNTP. Recommandations pour la conception, le dimensionnement et la mise en oeuvre des géostructures thermiques. 2017. p. 120.

Di Donna, A. 2014. Constructive recommendations for optimized and reliable heat exchanger pile systems 249.

Dupray, F., Laloui, L., Kazangba, A., 2014. Numerical analysis of seasonal heat storage in an energy pile foundation. Comput. Geotech. 55, 67–77. https://doi.org/10.1016/j.compgeo.2013.08.004

Fadejev, J., Simson, R., Kurnitski, J., Haghighat, F., 2017. A review on energy piles design, sizing and modelling. Energy 122, 390–407. https://doi.org/10.1016/j.energy.2017.01.097

Freitas, B.T.M., Silva, C.F., Bourne-Webb, P.J., 2013. The response of energy foundations under thermo-mechanical loading. 18th Int. Conf. Soil Mech. Geotech. Eng. Challenges Innov. Geotech. ICSMGE 2013 4, 3347–3350.

Ground Source Heat Pump Association NEC. Thermal pile design, installation & materials standards. Davy Avenue, Knowlhill, Milton Keyenes 2012. p. 86.

Kalantidou, A., Tang, A.M., Pereira, J.M., Hassen, G., 2012. Preliminary study on the mechanical behavior of heat exchanger pile in physical model. Geotechnique 62, 1047–1051. https://doi.org/10.1680/geot.11.T.013

Knellwolf, C., Peron, H., Laloui, L., 2011. Geotechnical Analysis of Heat Exchanger Piles. J. Geotech. Geoenvironmental Eng. 137, 890–902. https://doi.org/10.1061/(asce)gt.1943-5606.0000513

Loveridge, F., McCartney, J.S., Narsilio, G.A., Sanchez, M., 2020. Energy geostructures: A review of analysis approaches, in situ testing and model scale experiments. Geomech. Energy Environ. 22, 100173. https://doi.org/10.1016/j.gete.2019.100173

Mimouni, T., Laloui, L., 2014. Towards a secure basis for the design of geothermal piles. Acta Geotech. 9, 355–366. https://doi.org/10.1007/s11440-013-0245-4

Nguyen, V.T., Tang, A.M., Pereira, J.M., 2017. Long-term thermo-mechanical behavior of energy pile in dry sand. Acta Geotech. 12, 729–737. https://doi.org/10.1007/s11440-017-0539-z

Oliaei, M., Kiani, M.A., Torkaman, M., 2019. Advanced finite difference method for study energy piles behavior in temperature dependent soils. Springer Ser. Geomech. Geoengin. 0, 105–112. https://doi.org/10.1007/978-3-319-99670-7_14

Pasten, C., Santamarina, J.C., 2014. Thermally Induced Long-Term Displacement of Thermoactive Piles. J. Geotech. Geoenvironmental Eng. 140, 06014003. https://doi.org/10.1061/(asce)gt.1943-5606.0001092

Rammal, D., Mroueh, H., Burlon, S., 2018. Impact of thermal solicitations on the design of energy piles. Renew. Sustain. Energy Rev. 92, 111–120. https://doi.org/10.1016/j.rser.2018.04.049

Rotta Loria, A.F., Bocco, M., Garbellini, C., Muttoni, A., Laloui, L., 2020. The role of thermal loads in the performance-based design of energy piles. Geomech. Energy Environ. 21. https://doi.org/10.1016/j.gete.2019.100153

Rotta Loria, A.F., Laloui, L., 2019. Thermo-mechanical schemes for energy piles. Springer Ser. Geomech. Geoengin. 0, 218–225. https://doi.org/10.1007/978-3-319-99670-7_28

Sani, A.K., Singh, R.M., Amis, T., Cavarretta, I., 2019. A review on the performance of geothermal energy pile foundation, its design process and applications. Renew. Sustain. Energy Rev. 106, 54–78. https://doi.org/10.1016/j.rser.2019.02.008

SIA-D0190. Utilisation de la Chaleur du Sol par des Ouvrages de Fondation et de Soutènement en Béton. Guide pour la Conception, la Realisation etla Maintenance. Zurich, Switzerland 2005.

2 Literature Review

2.1 *Energy transfer in geothermal piles and temperature influence on mechanical behavior*

2.1.1 Introduction

EPs embedded in the soil work as heat exchangers extracting or injecting heat from/into the soil using mostly HDPE pipes with circulating fluid. Due to the temperature difference between the heat carrier fluid and the soil a thermal gradient is created and therefore heat transfer mechanisms occur (Faizal et al. 2016).

For cheap GSHP systems with heat exchanger piles, accurate quantification of heat transfer through EPs should be an integral part of the design. Typically, analytical solutions are used to determine the fluid temperature changes for a given thermal demand to estimate the available energy within certain temperature limits (Loveridge et al.,2020). It is important to apply limits to temperature changes to ensure its long-term sustainability. At the lower end of the temperature change it is important to ensure that the quantity of heat extracted is not so great to determine ground freezing. About upper thresholds there are not strict rules but restricting the upper temperature to 40°C- 45 °C maintains good efficiency at the heat pump (Loveridge, 2012). The total usable heat extracted using EPs can be computed referring to Equation 2-1 (Vasilescu, 2019):

Equation 2-1: $Q_{tot} = Q_{in} - Q_{out} m c_{fluid} (T_{inlet} - T_{outlet})$

where: Q_{tot} is the total heat extracted, m is the mass flux density of the heat career fluid, c_{fluid} is the heat capacity of the circulating fluid, $T_{inlet} - T_{outlet}$ is the difference between the inlet and the outlet temperature. The heat capacity is defined as the amount of heat necessary to raise the temperature of a given mass of one degree. Heat capacity can alternatively be defined as the amount of energy stored in a specific mass of a material per unit change in temperature (Brandl, 2006). The heat capacity is calculated as the product of a mass and its specific heat that is the heat capacity per unit mass of a material.

The amount of energy exchanged depends on several factors as initial soil temperature, soil characteristics as moisture content and soil type, groundwater and eventually ground flow (if any), resistances to heat transfer provided by the elements of the whole foundation system.

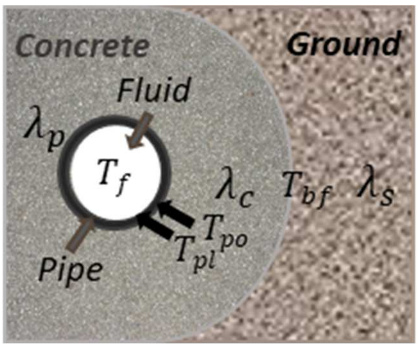

Figure 2-1: Plan of thermal pile components (Fluid, pipe, concrete and ground) involved in the heat transfer process.

The heat transfer mechanism occurs of course from the body with higher temperature to the body with lower temperature. In GS composed by EPs the body characterised by the higher temperature could be pile or soil according to the thermal demand of the upper structure. Therefore, the soil can be used as heat source or heat sink. In both cases the temperature gradient determines the heat flow process until an equilibrium is attained. However, the inlet and outlet temperature of the heat carrier fluid ensures a continuous heat flow process. The heat exchange mechanism in EPs is a complex process that includes all the underground circuits' components of GS.

Involved exchange mechanisms are forced convection of the fluid in the pipes, conduction across the pipe walls, conduction through the concrete of the pile to the ground, conduction in the ground (usually the dominant process) and advection if the groundwater is flowing faster than 0.5-1.0 m/day (Loveridge and Powrie, 2012).

To simplify the thermal problem most approaches separate the temperature change (ΔT_f) into different zones i.e., ground (ΔT_{ground}), pile (ΔT_{pile}), and pipe (ΔT_{pipe}) for which specific solutions are applied and then combined through superposition principle (Loveridge et al.,2020). The change between inlet and outlet temperature of the circulating fluid could be expressed by Equation 2-2:

Equation 2-2: $\Delta T_f = \Delta T_{ground} + \Delta T_{pile} + \Delta T_{pipe}$

The most common analytical techniques assume that the ground temperature is calculated through transient temperature response function (G-function) while ΔT_{pile} and ΔT_{pipe} are evaluated considering instantaneous thermal steady state as described in the following.

Newton's law of cooling describes the convection mechanism where the rate of heat transfer (Q) per unit of area (A) is related to temperature difference (T_{pi}-T_f) between the solid interface (pipe wall) and the fluid (Figure 2-1) and to the convective heat transfer coefficient (h). The heat transfer between the heat carrier fluid in the pipes and the pipes' walls is described by Equation 2-3.

Equation 2-3 : $\frac{Q}{A} = h\left(T_{pi} - T_f\right)$

The heat transfer coefficient, expressed in W/m^2 K, depends on the properties of the carrier fluid, the nature of flow conditions and pipe size. Water is the one of the most efficient heat transfer fluid because of its low viscosity and of the heat transfer characteristics. Due to temperature gradient across EPs and to the possible energy demand from the superstructure, it is possible to operate with fluid's temperatures close to 0 °C, therefore, anti-freeze should be added to the water. Propylene glycol or ethylene glycol can be added to reduce the freezing point of the fluid producing also an increase of viscosity. Ethylene glycol has better thermo-physical properties than glycol, but the latter is often mandatory because of its lower toxicity (Loveridge, 2012). To determine the heat transfer coefficient which controls convective heat flow from fluid to pipe it is necessary to define the flow regime in the pipes. The flow conditions inside the pipe could be classified as laminar flow, where the streamlines of fluid movement are smooth and largely linear, or turbulent flow where the streamlines are chaotic, and the velocity is characterised by high fluctuations (Loveridge, 2012). The intensive mixing of fluids in turbulent flow enhances the capacity of heat transfer compared with laminar flow (Loveridge, 2012). A higher flow rate results in intense turbulent flow and the heat convection between the working fluid and pipe wall is also enhanced in the condition of high flow rate (Park et al. 2018). On the other hand, an excessive fast flow rate does not allow enough contact time for heat exchange between working fluid and pipe wall. Therefore, in terms of thermal performance an excessively fast flow rate is not efficient. A compromise in terms of flow rate of the working fluid is generally fixed at 11-12 l/min (Park et al. 2018).

Assuming constant fluid properties and laminar flow the heat transfer coefficient can be related to the Nusselt number that is the ratio of convective to conductive heat transfer across a boundary. For turbulent flow with fully developed thermal conditions the Nusselt number is not constant and depends on the Reynolds number (relative balance of inertial and viscous forces) and on the Prandtl number (measure of the relative importance of viscous diffusion to thermal diffusion).

The heat transfer pipes are usually formed from HDPE to ensure the needed longevity of the system because it is not possible to apply maintenance to the embedded pipe.

The reciprocal of the heat transfer coefficient multiplied by the unit Area (m^2) is the thermal resistance (for convection):

Equation 2-4: $R_{con} = \frac{1}{hA} = \frac{\Delta T}{|Q|}$

According to Equation 2-3 and Equation 2-4 heat flux depends only on the combination of the geometry and of the thermal properties of the system.

For steady one-dimensional heat conduction, Fourier's law describes the relationship between the heat transfer rate and the temperature profile according to Equation 2-5:

Equation 2-5: $\frac{Q}{A} = -\lambda \frac{\Delta T}{L}$

where λ is the thermal conductivity that is a measure of the heat passing perpendicularly through a unit area of homogeneous material of unit thickness under a temperature difference of one degree. In the SI λ is expressed in W/m °C. The ratio between the thermal conductivity and the heat capacity is defined thermal diffusivity, a, that indicates how quickly a material changes temperature. A high thermal diffusivity indicates that heat transfer through a material will be fast, and the amount of heat storage will be small. On the other hand, materials with low thermal diffusivity respond slowly to an imposed temperature difference. Typical unit for thermal diffusivity is square unit length per unit time (m^2/sec).

The resistance to heat transfer, R, is defined according to Equation 2-6, as follows:

Equation 2-6 : $R = \frac{\Delta T}{|Q|} = \frac{L}{A\lambda}$

Like electrical resistance the component resistances of a geothermal pile may be added to give the overall resistance of the system as showed in Equation 2-7 (Loveridge et al., 2020).

Equation 2-7: $R = R_{pcon} + R_{pcond} + R_c$

where R_{pcon} is referred to the convection while R_{pcond} is the thermal resistance of the pipe wall and R_c is thermal resistance of the material of the pile (concrete) and is also dependent on the cross-section geometry. The heat transfer inside the heat exchange is not simply linear, the previous approach sums up the resistances of the different components (Figure 2-1) neglecting both contact resistances to heat flow and pipe-to-pipe interactions (Loveridge and Powrie, 2013).

Standard approaches to determine the resistance associated with the fluid and the pipe (R_{pcon} and R_{pcond}) are adopted for borehole heat exchangers (BHEs) and used for EPs. R_c is more complex and depends on the geometric positioning of the pipes; therefore, specific methods for thermal piles are required. Thermal resistance of concrete is described in2.1.4.

Thermal resistances of pipe's wall and concrete are expressed in Equation 2-8 and Equation 2-9.

Equation 2-8: $R_{pcond} = \frac{ln\left(\frac{r_{out}}{r_{in}}\right)}{2N\pi\lambda_p}$

Equation 2-9 $R_{pconv} = \frac{1}{2N\Pi r_{in} h_t}$

Where r_{out} and r_{in} are the outer and inner radius of the exchanger pipe, respectively, N is the number of pipes per cross-section, λ_p is the thermal conductivity of the pipes' walls and h_t is the heat transfer coefficient and the expression of R_c is as follows:

Equation 2-10: $R_c = \frac{1}{\lambda_c S_c}$

Where: λ_c is the thermal conductivity of material of the pile and S_c is the shape factor accounting for position and number of pipes in the cross-section of the pile. The shaft factor could be optimized to reduce thermal resistance but accounting for concrete cover and the interaction between hot and cold pipes.

2.1.2 Heat exchange mechanism in the soil

While heat transfer within a heat exchanger is often assumed to be at steady state and therefore considered in terms of thermal resistances, the response in the ground is usually transient (Loveridge and Powrie, 2013). Heat transfer in soil involves several mechanisms as conduction, convection, radiation, vaporisation and condensation processes, ion exchange and freezing-thawing processes (Brandl 2006). However, the main heat transfer mechanisms in unfrozen soil are first conduction, followed by the convection.

The total heat transfer q_{tot} may defined according to Rees et al. (2000) through Equation 2-11:

Equation 2-11: $q_{tot} = q_{cond} + q_{1,conv} + q_{v,conv} + q_{lat}$

Where q_{cond} represents heat transfer by heat conduction, $q_{1,conv}$ is the heat transfer by liquid convection,$q_{v,conv}$ refers to heat transfer by vapour convection and q_{lat} is the latent heat transfer.

The heat conduction can be expressed according to Fourier's law reported in Equation 2-12:

Equation 2-12: $q_{cond} = \frac{Q}{At} = \frac{\dot{Q}}{A} = -\lambda \frac{\partial T}{\partial n}$

Where λ is the soil thermal conductivity and $\frac{\partial T}{\partial n}$ is the temperature gradient in the actual flow direction n defined as:

Equation 2-13: $\frac{\partial T}{\partial n} = \frac{\partial T}{\partial x} e_x + \frac{\partial T}{\partial y} e_y + \frac{\partial T}{\partial z} e_z = gradT$

where: e_x, e_y and e_z are the unit vectors.

If the grains and pores sizes are negligible in relation to the considered soil volume, the complex heat transfer process may be reduced to only conduction, which dominates in the case of thermo-active foundations (Brandl, 2006). Equation 2-12 can be written in rectangular coordinates as:

Equation 2-14: $\dot{q} = -\lambda \left(\frac{\partial T}{\partial x} e_x + \frac{\partial T}{\partial y} e_y + \frac{\partial T}{\partial z} e_z \right) = -\lambda gradT$

A temperature change is caused by an alteration of heat flux density within this period, leading to a change of internal energy that is expressed in Equation 2-15:

Equation 2-15$-\rho c \frac{\partial T}{\partial t} = \frac{\partial \dot{q}}{\partial x} + \frac{\partial \dot{q}}{\partial y} + \frac{\partial \dot{q}}{\partial z}$

Differentiating Equation 2-12 with respect to spatial coordinates and combining with Equation 2-15 and considering internal heat generation $\dot{Q}_i$ in the considered soil volume, the basic conduction equation becomes:

Equation 2-16: $\frac{\partial T}{\partial t} = \frac{\lambda}{\rho c} \left(\frac{\partial^2 T}{\partial x^2} + \frac{\partial^2 T}{\partial y^2} + \frac{\partial^2 T}{\partial z^2} \right) + \frac{\dot{Q}_i}{\rho c} = \frac{\lambda}{\rho c} div(grad\ T) + \frac{\dot{Q}_i}{\rho c}$

Where: $\frac{\lambda}{\rho c} = a$ is the thermal diffusivity, (m^2/s); λ is the soil thermal conductivity (W/ m °C); ρ is the density of the solid medium (kg/m^3) and c is the specific heat capacity (J/kg K).

The ground heat transfer mathematical description requires initial condition about the temperature distribution at time zero and boundary conditions (e.g., Dirichlet's boundary condition, Neumann's boundary condition and Cauchy's boundary condition). Surface temperature Ts depending only on time t or being constant are examples of Dirichlet's conditions. Assuming that the heat flux density q at the surface depends on time or is constant are generally named Neumann's boundaries condition. Assuming that at the surface liquid or gaseous surrounding soil surface exchange heat corresponds to the so-called Cauchy's boundaries conditions. Solutions for Equation 2-16 are possible only in some cases and adopting simplifying hypotheses.

The temperature change in the ground determined by applied thermal load could be described through *G-function*. Analytical solutions of the G-functions for EPs are derived with different methods and models as Infinite Line Source Method (ILS), Finite Line Source Model (FLS), Hollow Cylindrical Source Model (HCS) or Solid Cylindrical Source Model and Superposition Borehole Model (SBM). All the approaches assume a constant surface temperature as a boundary condition. ILS does not represent the limited length and the large diameter of EPs (at least compared to the very slender boreholes) and provide accurate results in short time periods. This method assumes an infinitely long and thin heat source embedded in a homogeneous medium. The FLS model represents the heat exchanger as a finite line. The HCS model is quite complicated compared to the ILS and FLS models and is recommended in cases where the pipe diameter is rather large, and the time of the transient analysis is rather short. In this model the EP is represented with a hollow cylinder with a diameter equals to that of the heat exchanger. Pile material is not modelled therefore the temperature profile inside the pile (cylinder) cannot be estimated but the effect of the diameter and the end effects are taken into account. The Solid Cylindrical Source Model assumes that the cylinder is no longer a cavity but is filled with a medium identical to that out of the cylinder so that the whole infinite domain is composed of a homogeneous medium (Man et al., 2010). The SBM model uses numerical solutions based on a finite heat source with superposition for multiple boreholes. This approach is widely used and well validated for borehole Design (Loveridge et al., 2020). Different improvements of the previously described analytical models are provided in literature. For example, the ILS model could be coupled with groundwater flow producing the moving line source model. It should be noted that generally such approaches are conservative in terms of energy assessment determining a design on the safe side. The fact that all these approaches assume a constant surface temperature as a boundary condition has two drawbacks. First, it is neglected the fluctuations throughout the year of the near surface temperature that may be significant in case of EPs. Second, most GEPs would be better represented considering heat flux from the building. However, uncertainty over the most appropriate boundary conditions also remains a barrier to further development of these simplified models (Loveridge et al., 2020).

2.1.3 Thermal properties of the soil

For the design of GS important quantities are the initial soil temperature which is generally the undisturbed ground temperature, the thermal conductivity and the heat capacity.

In most regions of Europe, the seasonal ground temperature remains relatively constant below a depth of 10-15 m. At depths of about 50 m temperature values between 10 °C and 15 °C predominate (Brandl, 2006). According to Popiel et al. (2001) the ground temperature distribution is affected by structure and physical properties of the ground, ground surface cover, e.g., bare ground (surface clear of vegetation) or lawn ground (with short grass cover), climate interaction determined by air temperature, wind, solar radiation, air humidity and rainfall. From the point of view of temperature distribution with depth, three ground zones could be defined:

- *Surface zone* reaching a depth of about 1-2 m, in which the ground temperature is very sensitive to short time changes of weather conditions. In this zone thermal diffusivity and permeability and surface condition, wind velocity and interaction with structures play a significant rule.
- *Shallow zone* extending from the depth of about 1-2 m to 8 m (for dry soil) or even 20 m (for soils below groundwater table) where the ground temperature is almost constant and close to average annual air temperature, in this zone the ground temperature distributions depend mainly on the seasonal cycle weather conditions. In this zone the influence of phreatic aquifer conditions and

ground water flow, underground thermal diffusivity and permeability has a prominent role. The effects of air temperature become almost negligible.

- *Deep zone* (below about 8-20 m), where the ground temperature is near to the constant average values. Increasing the depth, the interaction with structures and buildings becomes negligible.

A basis for the prediction of soil's thermal regime was proposed by Lettau (1962). Temperature at any depth z from ground surface and at any time t could be expressed according to the Equation 2-17:

Equation 2-17: $T(z,t) = \bar{T} + A_z \sin[wt + \varphi(z)]$

where $\bar{T}$is the average temperature of the surface for the period under consideration, $A_z$is the amplitude at z depth of the surface temperature fluctuation i.e., the range from maximum (or minimum) to average temperature, w is the radial frequency and φ is the phase angle.

Based on the solution for a transient heat conduction in a semi-infinite solid, temperature distribution provided by Baggs's (1983) is reported in Equation 2-18. Baggs (1983) introduced the vegetation coefficient k_v that depends on the proportion of vegetation shade cover. For a bare ground in full sun condition k_v is equal to unity.

Equation 2-18: $T(x,t) = (T_m \pm \Delta T_m) - 1.07 k_v A_s \, exp(-0.00031552 x a^{-0.5}) \, cos[\frac{2\pi}{365}(t - t_0 + 0.018333552 x a^{-0.5})]$

where: : $T(x,t)$ is the ground temperature (°C) at a given depth (x) below ground surface on a calendar day (t), x is is the depth below the ground surface (cm), t is the time of the year from day 1 that is (1st January), $Tm$is the average annual air temperature (°C), ΔT_m is the local site variable for ground temperature (°C), A_s is the amplitude of annual air temperature wave from mean average yearly maximum and minimum monthly basis (°C), a is the average thermal diffusivity for homogeneous undisturbed ground (10^{-2} cm $^{-2}$ sec^{-1}), $t0$ is the phase of air temperature wave (day).

Equation 2-18 was validated for the Australian continent, but the author provided suggestions for the application of the expression in different places.

Popiel et al. (2001) measured temperature distribution in the ground since summer of 1999 to spring of 2001 in Poznan in Poland and compared the experimental data with Bagg's temperature distribution finding a good agreement. Tinti et al. (2014) carried out site investigations in the geographic context of Italy with a special focus on Emilia Romagna Region providing ground temperature variations data with reference to daily and seasonal scale.

The data collected by the in-situ monitoring were compared with Baggs's equation and it is modified for European continent according to Equation 2-19 (Tinti et al., 2014).

*Equation 2-19*$T_g(d,t) = (T_m) - A_{o,s} \, exp\left(-d\sqrt{\frac{\pi}{365\,a}}\right) cos[\frac{2\pi}{365}\left(t - t_0 - \frac{d}{2}\sqrt{\frac{365}{\pi\,a}}\right)]$

where $T_g(\mathrm{d},t)$ is the daily average value of underground temperature (°C), $\mathrm{T_m}$ is the average external temperature measured value (°C) throughout the year, $\mathrm{A_{o,s}}$temperature wave amplitude (°C), d is the depth (m), t is the time on annual scale, $\mathrm{t_0}$ is the time of minimum external temperature throughout the year (number of day that corresponds to the minimum temperature), a is the equivalent underground thermal diffusivity (m^2/day).

Measuring the profile of the underground temperatures at different depths and times, the day of minimum temperature and the average temperature throughout the year, it is possible to estimate the average value of the underground thermal diffusivity. For instance, the values of thermal diffusivity for dry clay should be included between 0,023 m^2/day and 0,054 m^2/day (Tinti et al., 2014).

In most practical cases a single value of average ground temperature is used as design parameter (undisturbed ground temperature). It is determined in situ by methods like downhole temperature logging, the fluid circulation method (Spitler and Gehelin, 2015) or the Thermal Response Test (TRT).

Thermal conductivity in general is simply the proportionality factor between the rate at which heat is transferred and temperature gradient in a material (SI units W/m °C) (Rees et al., 2000). For soils, thermal conductivity typically varies between 0.2 and 3 W/ (m °C) and can rarely achieve values of 3.5 W/ (m^2 °C), while for rocks values greater than 5 W/ (m °C) are possible too. Typical values of thermal conductivity of different soil kinds are reported in Table 2-1.

Table 2-1: Thermal Conductivity of soils from Rotta Loria and Laloui (2019) and Phaud (2002).

Material	**Thermal Conductivity λ $[Wm\,°C]$**	
	Dry	*Saturated*
Clay	0.4-1	0.9-2.3
Silt	0.4-1	0.9-2.3
Sand	0.3-0.8	1.7-5
Gravel	0.4-0.5	1.8

This thermal property is mostly influenced by soil's dry density and water content (Coté and Konrad, 2005).

Thermal conductivity of dry soil is at list five time lower than that of saturated soils (Suryatriyastuti, 2013) because it increases with increasing water content. Dry soil makes deeper piles and larger area of the heat exchanger necessary. Depending on the soil properties the installation depth of the absorbers, 1 kW heating needs roughly between 20 m^2 (saturated soil) and 50 m^2 (dry sand) of the surface of concrete structures in contact with soil or groundwater (Brandl,2006). The mineral content, size and arrangement of particles, pore space distribution have a strong influence on the thermal conductivity too.

A prediction model of three phases medium thermal conductivity could be provided considering it as a function of conductivities and volume ratios of its constituents (Equation 2-20).

Equation 2-20: $\lambda = (1-n)\lambda_s + nS_r\lambda_w + n(1-S_r)\lambda_v$

Where: n is the soil's porosity (volume of voids/total volume), S_r is soil's degree of saturation (volume of water/ total volume), λ_s is the thermal conductivity of grains that generally varies from 1 to 5 $\frac{W}{m°C}$ (Coté and Konrad, 2005), $\lambda_w = 0.6\frac{W}{m\,°C}$ is thermal conductivity of water and $\lambda_v = 0.024\frac{W}{m\,°C}$ is thermal conductivity of vapour.

According to Equation 2-20 thermal conductivity of the porous medium (λ) depend on the heat conductivity in soil particles (λ_s) and the heat conductivities in the pore fluid i.e., water thermal conductivity (λ_w) and vapour thermal conductivity(λ_v). For dry soil or saturated soil Equation 2-20 becomes Equation 2-21 and Equation 2-22, respectively.

Equation 2-21 $\lambda = \lambda_{dry} = (1-n)\lambda_s$

Equation 2-22: $\lambda = \lambda_{sat} = (1-n)\lambda_s + nS_r\lambda_w$

Several models of different complexity have been provided in literature to predict the effective thermal conductivity of soil. De Vries (1952) expressed the thermal conductivity of a granular material as a function of the thermal conductivities and volume fractions of its constituents by making use of the analogy between the heat conductivity, electric conductivity, dielectric constant, magnetic permeability and diffusion coefficient. Johansen (1975) introduced the normalized thermal conductivity concept where the soil effective thermal conductivity can be evaluated from saturated (λ_{sat}) and dry (λ_{dry}) thermal conductivities and soil degree of saturation and quartz content. The upper bound for soil thermal conductivity corresponds to λ_{sat} while the lower bound corresponds to λ_{dry}.

According to Coté and Konrad (2005) Johansen's model (1975) gave the best overall prediction results for sands and fine-grained soils. They modified Johannsen's model to delete the logarithmic reliance on the saturation degree that provided not accurate predictions at low saturation degrees and introduced coefficients that account for particle shape and soil texture (Rotta Loria and Laloui, 2019).

For the preliminary design of complex EGs, or for the detailed design of standard geothermal systems, soil thermal conductivity could be estimated through diagrams considering water content, saturation density (ρ_d) and texture of the soil (coarse-grained soil and fine-grained soil, Figure 2-2 (a) and Figure 2-2 (b), respectively) (Brandl, 2006).

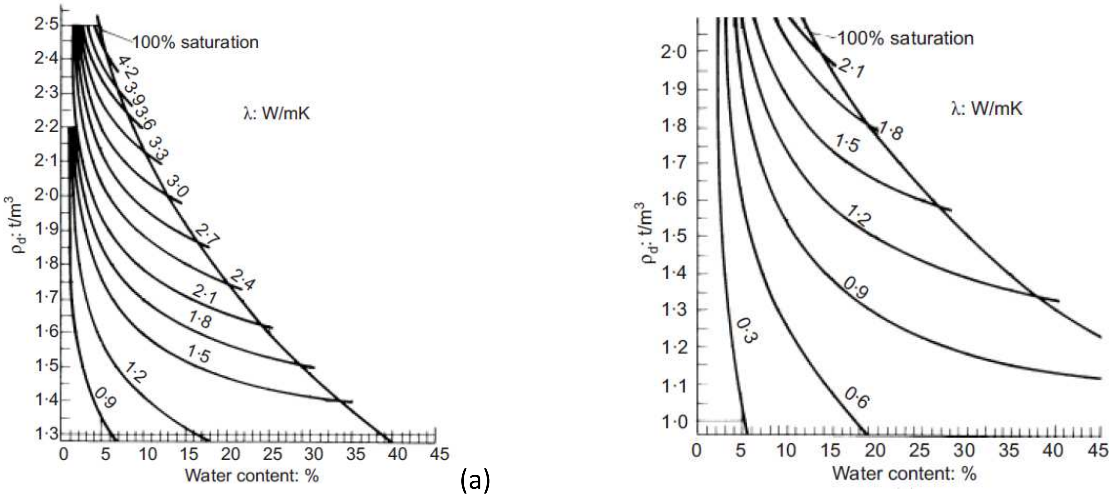

(a) (b)

Figure 2-2: Thermal conductivity against dry density and water content from Brandl (2006); (a) coarse-grained soil (b) fine-grained soil.

By using theoretical models or diagrams that consider water content, saturation density and texture of the soil, thermal conductivity can be usually determined to an acceptable level of accuracy. However, for larger scale projects, parameter values are best determined through laboratory and/or field testing (De Moel et al., 2010).

Laboratory measurement techniques can be classified into two main categories: steady state methods and transient state methods. Thermal conductivity, specific heat capacity and thermal diffusivity of all types of soils and rock can be determined using both methods.

Steady state techniques perform measurement when the temperature of the material measured does not change with time allowing the directly application of Fourier's law. The disadvantages of these techniques are that they need long time for single data points, and they need also a well-engineered setup. The principle used in all the steady state tests is to establish steady state one dimensional heat flow through a sample.

One of the steady state techniques is the Absolute technique that consists of circulating a steady state heat flow at one surface of a sample. To the opposite side of the sample a heat sink is placed, ideally no heat losses should occur ensuring a 1D heat flow. The temperature of the heat source (T1) and of the heat sink (T2) are constant, after an initial stage, and continuously monitored (Vieira et al., 2017). The sample of soil used during the tests needs to be circular or rectangular standard shape and enough large in cm scale. The guarded hot plate apparatus is a typical kind of apparatus for this kind of test. There are several apparatus variants on the absolute method.

Transient methods do not need to reach steady state and the measurements are usually performed during heating process. A large number of devices are available, the most commonly used are needle probe method or hot wire method and the transient plane source (TPS) (Vieira et al., 2017).

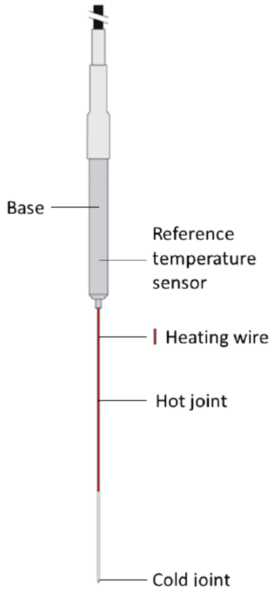

Figure 2-3:Needle Probe method.

The principle of the needle method is that a probe with constant dimensions and thermal properties contain a source of heat, and a thermometer is immersed in the medium whose constants are unknown. During the application of heat to the specimen temperature changes over time are monitored. The transient data are used to determine the heat conductivity by application of analytical solutions or heat diffusion equation (Low et al., 2014). The calculation of thermal conductivity is based on theory of an infinitely long, infinitely thin line source. If a constant power is applied to the heat source, the temperature increasing ΔT at time t after the start of heating, at a radial distance r from the heat source is provided by Equation 2-23:

Equation 2-23: $\Delta T = -\frac{q}{4\pi\lambda} E_i\left(\frac{-r^2}{4at}\right)$

Where: q is the power per unit length of heater, λ is the thermal conductivity of soil, a is the thermal diffusivity and E_i is the exponential integral.

After the power has been switched off (i.e., the start of the recovery phase), the temperature difference is given by:

Equation 2-24: $\Delta T = -\frac{q}{4\pi\lambda}[E_i\left(\frac{-r^2}{4at}\right) + E_i\left(\frac{-r^2}{4a(t-t_{heat})}\right)]$

Where: t_{heat} is the time at which the power is turned off. Equation 2-23 and Equation 2-24 cannot be solved explicitly for λ and a. Representing the exponential integral as a series expansion ΔT for $t > t_{heat}$ could be expressed as:

Equation 2-25: $\Delta T = -\frac{q}{4\pi\lambda} ln\left(\frac{t}{t-t_{heat}}\right)$

Thermal conductivity of soil is computed from graphs of the change in temperature versus $ln\left(\frac{t}{t-t_{heat}}\right)$.

Different size and kind of probes can be utilised. Standard needles are constructed with a minimum diameter of 2 mm and can vary to diameter about 6 mm and length of 45 mm or longer (Vieira et al., 2017). For soft soils, probes could be inserted directly into the material while for dense samples predrilling may be required. The minimum diameter of the sample is 40 mm and its minimum length is greater than 20% of probe length.

The time of the measurements depends on the expected thermal conductivity, varying from a few minutes to about 20 min for high magnitudes. The accuracy of the measurement is about 2-3%.

Following principles similar to those of the needle probes multi needle probes allow the measurement of soil properties within the same soil volume.

Heat capacity of soil (SI units J/kg K) can be evaluated by adding the heat capacities of the different constituents according to their volume fraction (Rees et al., 2000).

Equation 2-26 $c = (1-n)c_s + nS_r c_w + n(1-S_r)c_v$

Where: c is the effective specific heat capacity of the porous media, c_s is the specific heat capacity of grains, n is soil's porosity, S_r is soil's degree of saturation, $c_w = 4186 \frac{kJ}{kg} °C$ is water's specific heat capacity, $c_v = 1.256 \frac{kJ}{kg} °C$ is air's specific heat capacity.

The overall thermal capacity increases with the water content and decreases in the case of freezing (Brandl,2006). The volumetric capacity C_v is derived from the specific heat capacity and the bulk density of the soil and it increases with the water content as shown in Figure 2-4 (Brandl et al. 2006).

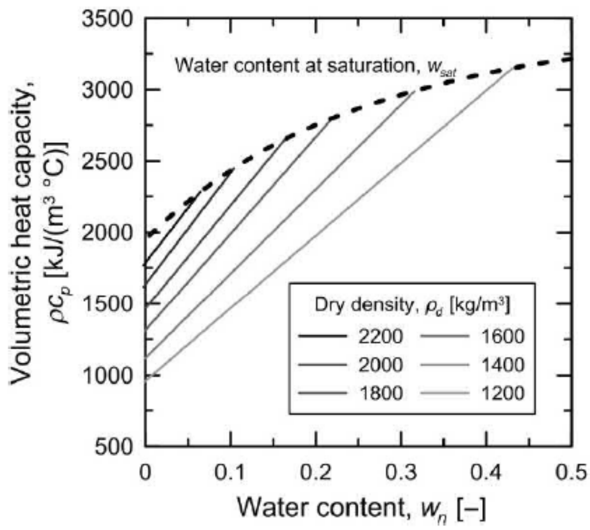

Figure 2-4: Volumetric heat capacity evolution with water content (reported as wn) from Rotta Loria and Laloui (2019).

Typical values of volumetric heat capacity of different soil kinds are reported in Table 2-2.

Table 2-2: Volumetric Heat Capacity of soils from Rotta Loria and Laloui (2019).

Material	**Volumetric heat capacity** cv $[MJm3\ °C]$	
	Dry	*Saturated*
Clay	1.5-1.6	1.6-3.4
Silt	1.5-1.6	1.6-3.4
Sand	1.3-1.6	2.2-2.9
Gravel	1.4-1.6	2.4

Thermal performance tests (TPT) are simple tests performed to obtain the energy capacity of a system. These tests may be subdivided into short term tests, where the duration of the experiment is no longer than three months, and longer-term observations, typically conducted during the full life of a heat exchanger system (Loveridge et al. 2020). The performance of the pile heat exchanger is tested by circulating fluid, usually entering the pile at constant temperature, through the heat transfer pipes and recording the resulting outlet temperature. From the outlet temperature and the knowledge of the flow rate and thermal properties of the fluid it is possible to calculate the heat transferred to the heat exchanger and the ground. The heat extraction or injection rate per pile meter i.e., the specific heat extraction or injection rate, is expressed in W/m. It depends on a wide range of factors including as the number and arrangements of pipes, the flow rate, the ground conditions, the temperature difference between the fluid and the ground and the test duration.

2.1.4 Piles thermal properties

The most common material used in GEP construction is reinforced concrete (Sani et al., 2019) where heat transfer occurs mainly by conduction. The thermal properties of concrete are of interest for a variety of reasons not all connected to the performance of energy geo-structures. Thermal conductivity and diffusivity are relevant to the development of temperature gradient, wrapping, thermal strains and cracking in the very early life of concrete. To determine the concrete thermal resistance a number of methods have been described in the technical literature (Loveridge and Powrie, 2014). Shonder and Back (1999) modelled the heat transfer problem considering that the temperature of the fluid in the pipe does not change with time and even without taking care of the actual positioning of the pipe. The geometrical problem is schematized considering the equivalent diameter approximation where all the exchanger pipes are modelled through a single pipe co-axial with the pile. In this hypothesis thermal resistance could be evaluated according to the Equation 2-27.

Equation 2-27: $$R_c = \frac{ln\left(\frac{r_p}{r_{eff}}\right)}{2\Pi\lambda_c}$$

where r_p is pile's radius, $r_{eff} = r_0\sqrt{N}$ is the effective radius, r_0 is the pipe outer radius N is the number of pipes and λ_c is the thermal conductivity of concrete.

The heat capacity of concrete is little affected by the mineralogic character of the aggregate, but it is considerably increased by an increase in the moisture content of the concrete. Specific heat increases with an increase in temperature and with a decrease in the density of concrete. The common range of values for ordinary concrete is between 840 and 1170 j/kg K (Neville, 1994).

The coefficient of thermal expansion of concrete depends both on the composition of the mix and on its hygral state at the time of temperature change. The coefficient of concrete is a resultant of the coefficients of the two main constituents (cement paste and aggregate). The thermal expansion coefficient of hydrated cement paste varies between $11x10^{-6}$ and $20x10^{-6}$ °C^{-1} and it is higher than the coefficient of the aggregate. The coefficient of concrete of the aggregate content in the mix is reported by Neville (1994) in Table 2-3.

Table 2-3: Influence of aggregate content on the coefficient of Thermal Expansion (Neville, 1994).

Cement sand Ratio	**Linear coefficient of Thermal Expansion at the age of 2 years [°C x 10^{-6}]**
Net cement	18,5
1 : 1	13,5
1 : 3	11,2
1 : 6	10,1

The coefficient decreases with the age due to the amount of crystalline material in the hardened paste. The effect of temperature on the coefficient of thermal expansion are observed above temperature of 150 °C with the coefficient that becomes negative for temperatures in the range of 200 to 500 °C. These phenomena can be neglected for energy geo-structures where maximum temperatures are certainly lower than this range. In terms of thermal stresses and strains it could be assumed that considering larger expansion coefficient is an assumption on the safe side. However, adequate design of energy piles requires to properly define the coefficient of thermal expansion of concrete. Free-expansion or contraction tests could be performed on the foundations by circulating heated or cooled water while thermal strains and temperature variation are monitored to determine the linear coefficient of thermal expansion of concrete. Goode and McCartney (2015) performed free expansion tests on model pile when the foundation was standing vertically on a rigid base, founding a coefficient of thermal expansion that ranges between $15x10^{-6}$ and $16x10^{-6}$ $°C^{-1}$.

Usually, the analysis of the variables that influence thermal conductivity are oriented to reduce thermal conductivity increasing the insulation of concrete to the aim of improving the thermal performance of the upper structure reducing the heat losses. In case of Energy geo-structures to improve the performance of the system thermal conductivity of concrete should be increased without modifying Pile mechanical performance (Di Girolamo et al., 2021).

Thermal properties of the concrete are influenced by the spatial spreading and by the volume ratio of its elements, such as aggregate, water cement and voids ratio. The value of thermal conductivity increases about 6% with each 1% increment in the moisture of concrete (Asadi et al.,2018). Mix design of the concrete could be modified mainly though the design of the aggregate because of its well-known higher thermal conductivity than other constituents of the concrete (e.g., cement). The nature of the aggregate appears to have a strong influence on thermal conductivity. The siliceous aggregate, compared to the carbonate one, having a more regular molecular structure (crystallinity), has greater thermal conductivity. Basalts and trachyte have a low conductivity, dolomite and limestone are in the middle (Neville, 1994). Even with an increase in the fine aggregate, an increase in thermal conductivity is obtained. Typical values of conductivity are listed in Table 2-4.

The degree of saturation of concrete, like for the soil aggregates, has a strong influence on the thermal conductivity because the conductivity of air is lower than that of water. Thermal conductivity increases when concrete voids are filled with water. Pile foundations made by concrete directly cast in place in soils below the groundwater table can boast greater performance as geothermal heat exchanger. It is possible to identify some precautions that mix design should have to optimize both the structural and the energy performance. The compactness to be maximized is certainly an advisable solution, which can be obtained following different procedures. High strength and significant compactness also make the cement matrix physically impenetrable to the aggressions of the environment, the microporosity being reduced too. Both are a guarantee of durability, a fundamental aspect of the performance for any concrete structural object and this is especially true for a foundation pile and even more in case of EPs. Lie and Kodur (1996) reported an interesting relationship between thermal conductivity and temperature in concrete in which the effects of steel fibers and the nature of the aggregate are added. The addition of steel fibers within the mix design of concrete improves both mechanical and thermal properties of concrete, with negligible influence on thermal capacity at low temperatures.

Table 2-4: Typical values of thermal conductivity of concrete (Neville,1994).

Type of aggregate	**Wet density of concrete**	**Conductivity**
	[kN/m³]	[W/m °C]
Quarzite	23,93	3,46
Dolomite	24,52	3,287
Limestone	24,03	3,114

Sandstone	23,54	2,941
Granite	23,73	2,595
Basalt	24,71	2,076
Barytes	29,81	2,076
Expanded shale	15,59	0,865

The geometrical size of the pile i.e., length and cross-section are designed on the basis of the design mechanical loads. More efficient thermal performances are generally achieved if the pile length extend beyond heterothermal zone (Sani et al., 2019). Pile's diameter influences the heat transfer and the storage capabilities due to the greater contact area with the ground and the possibility of increasing the number of energy loops to be incorporated within the foundation.

2.1.5 Thermal performance of GEP system and impact of the main design factors

The design of any GEP system needs to take into consideration both the geotechnical and thermal interactions of the system at the early design stages. Firstly, the impact of some vital factors should be carefully investigated (Dincer,2000). These factors include the definition of building hourly heating and cooling load, building usage, type of occupancy, possibility of heating losses that may occur in the system (usually factored into thermal loads), sustainability of components and sub-components in the system. If monodirectional (i.e., only heating or only cooling) mode is performed, high permeability ground and groundwater with a high hydraulic gradient are of advantage (Brandl,2006). The most economical and environmentally friendly is a seasonal operation (i.e., bidirectional mode) with an energy balance throughout the year, with heat extraction during winter and heat recharging into the ground during summer. In this case low-permeability ground and groundwater with only low hydraulic gradients maybe favourable. In addition to the above factors, an extensive geotechnical investigation of the construction site should be conducted to determine the subsoil condition and define the geotechnical model. As part of the design process, an evaluation of the system should be carried out to confirm the amount of heating and cooling the GEPs can supply. It is common practice to allow for some margin of error, between the energy demand and the predicted system capacity. A recommended practice is to allow for 10% margin between the required amount and the predicted output capacity of the system (Sani et al.,2019). The thermal performance of a GEP system can be assessed by relating the amount of useful energy obtained to the input power used in running the system, measured through field testing as thermal response test (TRT) or thermal performance test (TPT), analytical or numerical methods for a simulation of the system, and COP of the system.

Maximising the system performance can be achieved through optimisation of the individual components and the subcomponents of the system. Improving and modifying the heat transfer rate of the pile-concrete, heat carrier fluid, the number of installed pipes, flow velocity, pipe configurations, heat pump speed etc. could lead to higher performance. Similarly, utilising nanofluids as heat carrier fluids circulating in the pipes, and highly thermally conductive fillers in pipe manufacturing and concrete mix, were shown to significantly improve the convective and conductive heat transfer process of the liquid, the energy loops and the concrete pile. The thermal performance of a GEP was found to be influenced by factors including geometry, dimension, thermal and hydrological soil properties (Brandl, 2006). The geometrical sizes of piles (length and diameter) are governed by the mechanical loadings of the superstructure rather than the building demand.

The configuration and number of installed loops and fluid velocity are very important in defining the heat transfer efficiency of the GEP system (Gao et al., 2008).

Suryatriyastuti (2013) studied the influence of the absorber pipe on the heat diffusion considering three types of absorber pipes two U-shaped absorber pipes, four U-shaped absorber pipes and two W-shaped absorber pipes. It was found that the model with two W-shaped absorber pipes produces the highest average pile temperature.

Hamada et al. (2006) carried out field tests considering three types of heat exchangers U-shape d, double U-shaped and indirect double pipe types. It was found the U-shaped configuration was the best solution.

Gao et al. (2008) investigated on pile thermal performance provided by different heat exchanger configurations. Five years simulations of the ground temperatures for pile group were performed and the W-shaped type of heat exchanger with moderate medium flow rate appeared to be most efficient solution.

Cecinato and Loveridge (2015) used the software Abaqus to investigate the key factors that contribute significantly to heat transfer in GEPs. It was found that maximising the total pipe surface area available for heat transfer was the most important factor for increased energy efficiency

Zarella et al. (2013) investigated on the thermal behaviors of two types of energy pile equipped with helical configuration and triple U-tube coupled in parallel by means of the numerical CaRM model developed by the authors. The helical-pipe energy pile provided better thermal performance than the triple U-tube configuration.

Batini et al. (2015) performed series of numerical simulations to investigate the effects of different design solutions as different pipe configurations, aspect ratios of the foundation, fluid flow rates circulating in the pipes, and fluid mixture compositions both from thermal and geotechnical point of view. It was observed that the W-shaped pipe configuration resulted in an increase of up to 54% in the heat transfer rate compared with the single U-shaped configuration at the same flow rate. An increase of up to 11% in the heat transfer rate was obtained by increasing the fluid flow rate from 0.2 to 1 m/s with only slight differences in the results for the different pipe configurations. Nanoscale particles can be introduced in the primary circuit fluid to enhance thermal properties of the fluid. Nano particles in fluids (termed as nanofluids) has been extensively studied and has proven to lead to substantial improvement of the thermal properties of fluids with very low concentrations of particles.

2.1.6 Temperature related changes in soil mechanical behavior

The issue of mechanical effects due to thermal variations on EGs is relevant to EPs and all the kinds of EGs where thermal loads are added to the structural design loads. Because of soil multiphase constitution a complex Thermo-Hydro-Mechanical (THM) behavior arises and depends on several parameters as particle size, mineralogy, stress history, and so on.

A first approximation for evaluating thermo-mechanical soil response can be obtained by means of analytical solutions adopting the thermo-elasticity theory. Linear thermal strain is given by Equation 2-28 where α is the linear expansion coefficient in $°C^{-1}$ and ΔT is the temperature variation in °C.

Equation 2-28: $\varepsilon = \alpha \Delta T$

The coefficient of linear thermal expansion is therefore required to determine thermal strains (Agar,1984). For isotropic media the volumetric coefficient of thermal expansion (α_V) is given by Equation 2-29.

Equation 2-29: $\alpha_V = 3\alpha$

The volumetric thermal strain (ε_V) due to an applied thermal variation ΔT is given by Equation 2-30.

Equation 2-30: $\varepsilon_V = \alpha_V \Delta T$

The magnitude of thermal expansion in porous materials depends on the degree of mobility of the pore fluids. According to Agar (1986) thermal expansion coefficient upper and lower bounds can be determined conducting undrained and drained heating experiments, respectively. The author carried out drained heating experiments in high temperature consolidometer for temperatures ranging between 20 °C and 300 °C. During undrained heating tests pore fluid drainage from the samples was not permitted, therefore the sample mass remained constant although the volume increased. Two types of experiments were carried out undrained heating at a constant total stress and undrained heating at constant effective stresses. Confining stress were held constant by heating very slowly and allowing continuous vertical expansion of the sample. Both Campanella and Mitchell (1968) and Agar (1986) define pore pressure parameter expressed in terms of stress and temperature dependent volume changes of the component of soil.

Typical soil mechanics laboratory tests are properly adapted to temperature-controlled conditions providing a deeper insight of temperature effects on soil mechanical behavior. Soil testing devices for non-isothermal conditions are mainly direct or simple shear, triaxial device and oedometer. In terms of heating systems three main methods of applying thermal loadings are identified by Laloui et al. (2014) heating by circulating fluid, heating with internal heaters and heating with external heaters.

Most of the experimental evidence dealing with THM soil behavior involve wider temperature range with 100 °C as upper bound. During the operation of EGs, soil temperature varies typically in the range of 2°C and 45 °C (RottaLoria, 2019) therefore results referring to temperature variations higher than 45°C are not significant for such applications.

When fully saturated soil are investigated, drained conditions are generally adopted because thermal loadings are applied to such structures with sufficiently slow rate ensuring drainage of the water embedded in the soil pores and negligible pore water pressure build-ups (Rotta Loria and Laloui, 2017).These conditions are the result of testing procedures that do not cause excess pore water pressures upon thermal loading, despite the water present in the pores of soil matrices having a thermal expansion coefficient that is approximately 10 times greater than that of the solid particles and involving interactions with the solid phase. The mechanical behavior of soils under non isothermal conditions is described below dealing with the volumetric strains, shear strength and compressibility parameters for fine grained soils first and further for coarse-grained soils.

2.1.6.1 Effects of temperature variations on mechanical behavior of fine-grained soils

Burghignoli et al. (2000) summarized in their work the results of an extensive laboratory tests investigation of remoulded and natural clays (Todi clay, Fiumicino clay and Bologna clay) under non isothermal conditions with temperature ranging between 20 °C and 60 °C. Different overconsolidation ratios and recent stress histories produce significantly different behaviors. During heating void-ratio variations occurred is evidence of the rearrangement of particles that is responsible of the volume deformation. The void ratio changes produced by heating are not reversed during cooling phase, and hence they represent irreversible part of volume deformation induced by thermal cycle. The void ratio changes both in value and sign depends on the mechanical stress experienced by the soil prior to thermal cycle and in particular on the recent stress history (over consolidation ratio). Although the grains are expanding, the volumetric strains of soil can be expansion or contraction. Normally consolidated and lightly overconsolidated clays show generally contracting behavior upon heating while overconsolidated samples dilate.

Abuel Naga et al. (2007) investigated on the thermally induced volumetric strain of soft Bangkok clay specimens of different stress histories (OCR = 1, 2, 4, 8) prior to the application of a drained incremental heating–cooling cycle of 22 °C to 90 °C and back to 22 °C. The normally consolidated clays contracted irreversibly and nonlinearly upon heating, whereas the highly overconsolidated clays exhibited reversible expansion. Between these two cases there is the intermediate case of slightly OC soils that show an initial expansion and subsequent contraction when heated. Slightly OC soils behavior shows a transition between soils under NC and OC conditions. Cekerevac and Laloui (2004) performed laboratory tests at high temperature (90° C) and ambient temperature (22 °C) comparing the results to evaluate temperature effects on Kaolin (CM clay). The studies carried out show that fine-grained soils response to thermal loading is not unique but among other factors depends strongly on the overall and recent stress history experienced (Burghignoli et al., 2000). To describe the volumetric behavior of fine-grained soils under temperature variations thermal volumetric strains can be related to the OCR (stress history) as reported in Figure 2-5 (Rotta Loria and Laloui, 2019).

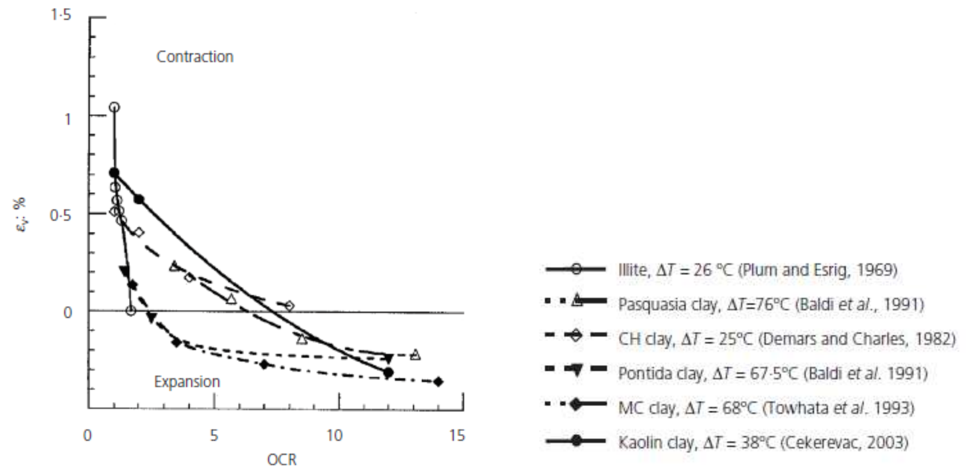

Figure 2-5:Influence of over consolidation ratio (OCR) on the thermal volumetric strain of clays from Cekerevac and Laloui (2004) and Abuel Naga et al. (2007)

Thermally induced volumetric strains of at least 6 % characterise NC clays for temperature variations of up to 80 °C. Thermal contraction of soil matrix occurred (Thermal Collapse). Thermally induced volumetric strains of up 0.5% characterise OC soils for temperature variations of up to 80 °C.

Extensive experimental evidence demonstrated that the apparent preconsolidation stress decreases at constant void ratio with increasing temperature (RottaLoria and Laloui, 2019). “Apparent preconsolidation stress” denotes that the applied mechanical load does not change, therefore the maximum mechanical stress occurred is always the same. From this perspective, Burghignoli et al. (2000) define as normally heated (NH) samples that have never been exposed to temperatures higher than the current temperature, and over-heated (OH) for samples that have experienced temperatures higher than the current temperature.

The effects of temperature on the apparent preconsolidation stress for a set of experimental investigation carried out on remoulded Kaolin, Swedish clays and natural Canadian showed a linear relationship between normalised preconsolidation stress ($\sigma'_C(T)/\sigma'_C(T_0)$) and the logarithm of normalised temperature (T/T_0) is essentially linear (Laloui and Cekerevac, 2003).

NC soils are characterised by a stress temperature state that lies on the yield surface (the applied mechanical load coincides with σ'_C). Drained heating under a constant mean effective stress induces thermoplastic strains. For thermal unloading under constant mean effective stress, the material becomes OC and strains are only partly recovered (Thermally overconsolidation). Heating of NC produced strain hardening because it causes plasticity and induces an increase of the elastic domain (Rotta Loria and Laloui,2019). Therefore, the volumetric behavior of NC is partly thermoelastic and partly thermoplastic. In case of highly OC soils a thermoelastic behavior is observed. OC soils are characterised by stress-temperature state that lies within the yield surface. Drained heating at a constant mean effective stress induces thermal strains but stress-temperature strains still remain within the yield surface. In case of energy geo-structures because the soil volumetric behavior is responsible for the eventual additional displacements of the over-structure, is of primary importance to evaluate the behavior under cyclic thermal loadings. Di Donna and Laloui (2015) investigated the response of natural clayey soils under thermal cyclic loading and proposed an extension of the constitutive model ACMEG-T to reproduce plastic accommodation under thermal loadings. For NC clayey soils it was shown that the material undergoes most of the thermal plastic deformation during the first heating-cooling cycle, followed by an accommodative behavior during the subsequent ones. Increments of irreversible strain are observed in the thermal cycles successive to the first one, which become smaller and smaller cycle after cycle until stabilisation. In the end, the material's stress point tends to remain inside the elastic domain showing a thermo-elastic expansion and contraction during heating and cooling.

The assessment of the shear strength of fine-grained soils under thermal cycles depends on the initial and current temperature level and general loading conditions. The initial OCR has a strong effect on the shear strength of the material after the application of one or more thermal cycles (Di donna and Laloui, 2013). If the material is initially under OC conditions the response is not affected because no permanent changes are induced in the void ratio. If the material is initially under slightly OC or NC conditions thermally induced overconsolidation occurs and therefore it is characterised by an increase in shear strength. Di donna and Laloui (2015) reported the evolution of the oedometric modulus during tests 20 °C, 40 °C and 60 °C not observing a defined effect of temperature on it. The compressibility parameters C_c (compression index), C_r (recompression index) and C_s (swelling index) appear to be insensitive to temperature variations (Di Donna and Laloui, 2013). The slope of the Critical State Line (CSL) may exhibit a slight dependence on temperature, but it could be considered negligible due to the significance involved (Rotta Loria and Laloui, 2019).

2.1.6.2 Effects of temperature variations on mechanical behavior of coarse-grained soils

The volumetric behavior of coarse-grained soils subjected to one or multiple thermal cycles were investigated by Agar et al. (1986), Ng et al. (2016), Liu et al. (2016) and Sittidumrong et al. (2019). About behavior of sand under drained cyclic thermal load, there are few studies (Marone et al., 2019) with respect to the investigations performed on clayey soils. Drained heating in coarse- grained soils produces expansive volume variations while cooling produces contractive volume variations. Liu et al. (2016) performed temperature-controlled hollow triaxial tests on dense saturated sand with temperatures ranging from 25 °C to 55 °C (Figure 2-6).

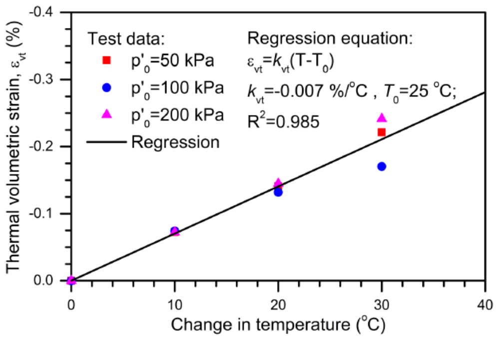

Figure 2-6: Thermal volumetric strain versus change in temperature from Liu et al. (2016).

Ng et al. (2016) investigated through temperature controlled triaxial tests the thermally induced volume changes of Toyoura sand carrying out tests at the same level of mean effective stress but at different initial density (21 %, 70% and 90%). The volumetric behavior observed by Ng et al. (2016) for different relatively sand densities are reported in Figure 2-7.

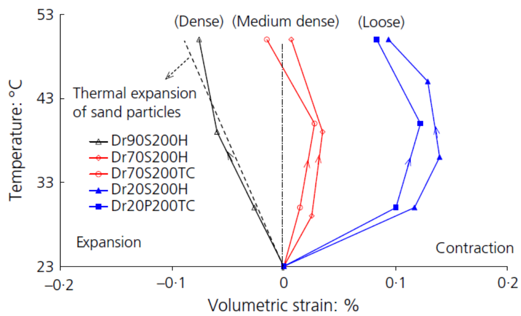

Figure 2-7: Heating induced volume changes of Toyoura sand with different densities at constant mean effective stress from Ng et al. (2016).

As the temperature rose from 23 to 35°C during the heating, loose and medium dense specimens showed contractive volumetric strains of about 0.15% and 0.05%, respectively. As the temperature increased further from 35 °C to 50 °C both specimens exhibited an expansive volumetric strain of about 0.05 %. Loose and medium dense sand sands started to expand after a certain temperature is reached (Ng et al., 2016). This phenomenon was explained by the authors considering that loose and medium dense sands are in some transitional state between expansion and contraction, similar to slightly over consolidated clay that contracts under heating after a certain temperature. For the dense sand only, expansion was observed as the temperature increase from 23 °C to 50 °C and the amount of thermal expansion is almost the same as that individual soil particles.

According to Liu et al. (2016), a linear increase of the volumetric thermal expansion coefficient of coarse-grained soils may be considered with the relatively density. According to the investigations carried out by Ng et al. (2016) thermal collapse of coarse-grained soils appears to depend on the mean effective stress (p'). Ng et al. (2016) reported the results of thermal controlled tests carried out on samples at the same relatively density (20 %) but different stresses (p'=50 kPa and 200 kPa). Heating induced larger strains at higher stress, with 0.15 % and 0.07% volumetric contraction at an effective stress of 200 kPa and 50 kPa, respectively. The stress effects were explained considering the state dependency of soil behavior. At a given relative density, a sand specimen at a higher stress behaves like looser sand, which has larger contractive volumetric strain under heating, therefore larger thermal volumetric contraction is observed when sand is under higher stress (Ng et al., 2016).

Experimental results about coarse-grained soils under cyclic thermal loads are presented by Ng et al. (2016) and Sittidumrong et al. (2019). The observed cyclic effects are due to the irreversible contraction induced by the first cycle of heating and cooling, during subsequent cycles the response of the soil becomes stiffer (Rotta Loria and Laloui, 2019). Sittidumrong et al. (2019) investigated on the influence of numerous thermal cycles (28-50-28 ◦C) on the volumetric behavior of Bangkok sand using temperature-controlled double oedometer tests. The authors found out that the first thermal cycle induced the largest strain increase while subsequent cycles gave rise to a progressively lower strain increase. Non isothermal tests were carried out both on undisturbed and reconstituted Bangkok sand samples at different relatively densities. The vertical strain induced by the first thermal cycle ranged between 0.12 % and 0.3 %. The samples with lower density exhibited larger thermally induced strains. The behavior observed during thermal tests carried out on the reconstituted sample at 50 % of relatively density is reported as example in Figure 2-8. The total strains observed in the thermal cycle tests are shown as dashed lines, while the time dependent strain at constant temperature is plotted as solid lines (Figure 2-8).

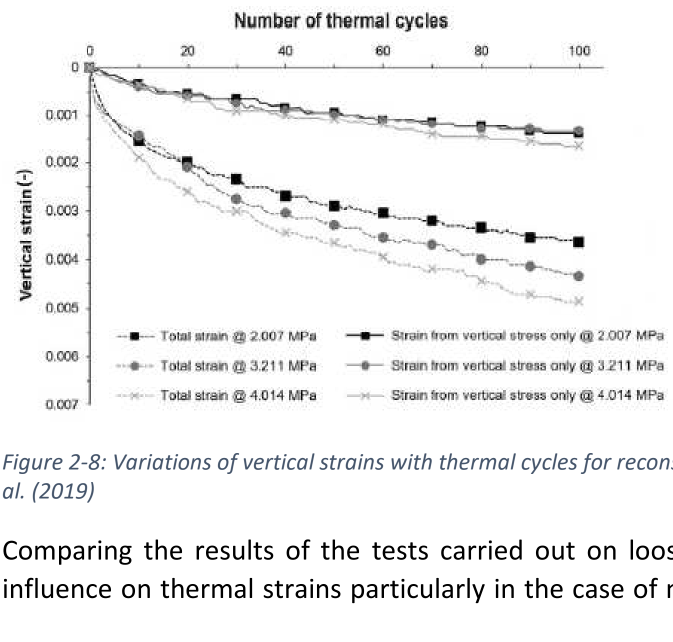

Figure 2-8: Variations of vertical strains with thermal cycles for reconstituted sand at relatively density of 50 % from Sittidumrong et al. (2019)

Comparing the results of the tests carried out on loose to dense sand the stress level appears to have influence on thermal strains particularly in the case of medium to dense samples. For loose samples, both reconstituted and undisturbed, thermal strains observed are larger and the effect of the stress level on strain was less clear. In this case the thermal cycle effects on strain were more prominent than the stress level's effect as the stress state would already be near the yield surface and thermal collapse would be more readily induced.

The stiffening effects are significant only within a limited range of stress and deformation increment, beyond which the behavior of the soil skeleton is no longer influenced by temperature history (Sittidumrong et al., 2019). Interestingly, the shake-down mechanism observed in this study is similar to those observed during repeated cyclic loading of sand under drained conditions in both laboratory triaxial compression, and pile load tests in the centrifuge and in-situ.

The temperature had no major impact on secant modulus for dense sand. The critical state line in the p'-q plane was not dependent on temperature, and the critical state friction angle was unaffected by temperature (Liu et al., 2016). These findings were consistent with previous studies on clay soils.

2.1.7 Temperature effects on concrete behavior

In practice concrete is mixed at a wide range of temperatures and remains in service at different temperatures while laboratory testing of concrete is usually performed at a controlled temperature (18°C to 21 °C). The effect of temperature on concrete could be considered both on fresh and hardened material. During the initial period of setting and hardening the influence of temperature (is to accelerate the development of strength. Several methods of applying heat to concrete for the purpose of accelerating the gain of strength exists (e.g., hot-mix method and methods of electrical curing). The knowledge of the strength of concrete may be required for different practical conditions of thermal exposure. Cylindric specimens heated at the rate of up to 20°C per hour show a steady loss of resistance with the temperature increase dependent on the water/cement ratio too. Smaller loss in compressive strength is observed for higher water/cement ratio (e.g., 0.6 compared to 0.45). The influence of water/cement ratio on the loss of strength is not noticeable in the splitting tensile test. An increase in the length of exposure to a temperature of 150 °C or higher increases determine the loss of compressive strength. A major part of the strength loss occurred within the 2 hours of the rise in temperature. Significative decrease of concrete strength is observed for temperature higher than 120 °C. However, one of the main changes occurs when the temperature rises to about 400 °C (decomposition of calcium hydroxide). For concrete in the range of 21 to 96 °C there is no difference in modulus of elasticity. It reduces at temperatures larger than 120 °C. At temperatures ranging from the freezing point of water down to about –200 °C, the strength of concrete is markedly higher than at room temperature. The compressive strength may be as high as two to three times the strength at room temperature when the concrete is moist while being chilled, but the increase of compressive strength of air-dry concrete is much less. According to ACI 306R-88 when concrete has reached a compressive strength of about 3.5 MPa is capable of withstanding one cycle of freezing and thawing. Considering that for GSHP systems the upper bound temperature is typically 30 °C –40°C and the lower bound temperature is generally taken as 0 °C to 2 °C (Loveridge et al.,2020) the effects of temperature on concrete mechanical properties could be neglected. During service EGs are subjected to thermal variations that can result in cracking of reinforced concrete when external restraint of thermal movement occurs. According to FitzGibbon (1975) concrete cracking may occur when the temperature difference exceeds 20 °C. Therefore, EP could be interested by such cracking phenomenon. Garbellini and Laloui (2020) illustrate that reinforced concrete post-cracking behavior can significantly impact the response of energy piles. The influence of such factor could be comparable to the influence of the soil–pile interface behavior. Therefore, reinforced concrete non-linearity should be considered for a correct assessment of the structural performance of the piles.

2.2 *Full scale pile tests on single EP*

Full-scale tests are the powerful tool to investigate the thermomechanical interaction between single pile or piles group and soil. In situ testing allows accounting for the real stress-strain state and the temperature conditions of the soil and applying different levels of mechanical loads. Few experimental studies refer to data collected from monitoring real energy piles installed as buildings' or structures' foundations. Most of the investigations concerns the installation of test EPs designed for research purposes. In several cases the pile response has been investigated before or during the construction of the building (Bourne Webb et al., 2009; Laloui et al., 2006; Wang et al., 2014; Faizal et al., 2016).

A wide range of instrumentation has been used during the experimental in situ tests including thermistors and fiberoptic sensors for temperature changes, vibrating wire strain gauges and fiberoptic sensors for axial and radial strain changes, and load cells for axial stress changes (Loveridge et al. 2020). Only one study used embedded Osterberg cells to evaluate the effect of thermal variations on pile shaft capacity (Wang et al. 2014). All the thermo-mechanical tests on energy piles reported in the literature are load (compression) tests; only Akrouch et al. (2014) performed pull-out tests which of course do not involve pile tip resistance.

Different aspects of the thermo-mechanical interaction have been analysed during in situ tests: general overview of pile response (Laloui et al.(2006); Bourne Webb et al (2009)), the effect of thermal loading on pile's shaft resistance (Wang et al. (2014), Akrouch et al. (2014)) , the restraint action at the piles ends on thermal observed strains (Sutman et al. 2019), the influence of different operation modes on piles thermal axial and radial stress and strains (Faizal et al., 2016-2018-2019), the installation technique (Jiang et al., 2021), the cyclic behavior (Faizal et al., 2019), and so on.

The simplest form of thermal action that can be considered is monotonic heating or cooling, as in Santiago et al. 2016. On the other hand, Faizal et al. (2016), for example, investigated about the impact of continuous versus intermittent cooling.

Recent review papers reported quantitative observations (Bourne-Webb et al. (2019), Bourne-Webb and Bodas Freitas (2020)) or focused on the range of conditions of in situ studies (Loveridge et al. (2020)).

In the following paragraphs different investigations about energy piles installed in situ are described and analysed.

2.2.1 Case studies

Two main site investigations of EPs have leaded the investigation in the field: The EPFL setup in Losanne (Laloui et al. (2003); Laloui et al. (2006)), and the Lambeth College setup in London (Bourne-Webb et al.,2009). Both studies have been used to characterise the main aspects of pile subjected to thermal loadings (Amatya et al., (2012)).

The test experiment built on the EPFL was on a bored pile located below the edge of a four-storey building, with a diameter of 0.88 m and a length of 25.8 m embedded in layered soil. The pile was a semi-floating pile equipped with four U-loops. Seven tests were carried out, T1 to T7.

The first test was different from the other tests because the head of the pile was completely free to move, and no mechanical loads were applied. In fact, the Figure 2-9 shows that displacements of the head of the pile in the first test are at least three time larger than those measured during the other tests. The maximum pile heave for a thermal increment of 21 °C was about 3.5 mm.

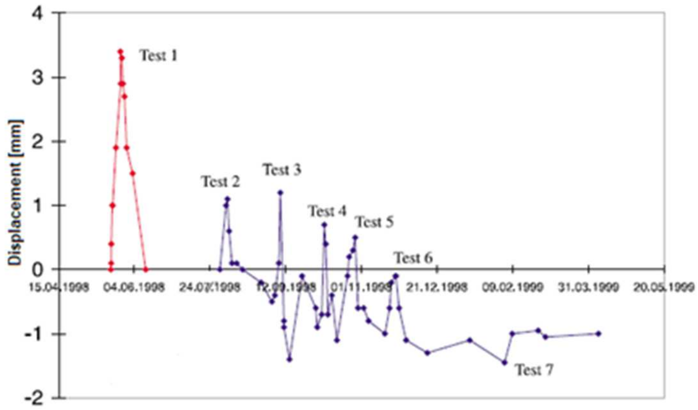

Figure 2-9: Pile Head displacements during test1, test 2, test 3, test 4, test 5, test 6 and test 7 (Laloui et al., 2003).

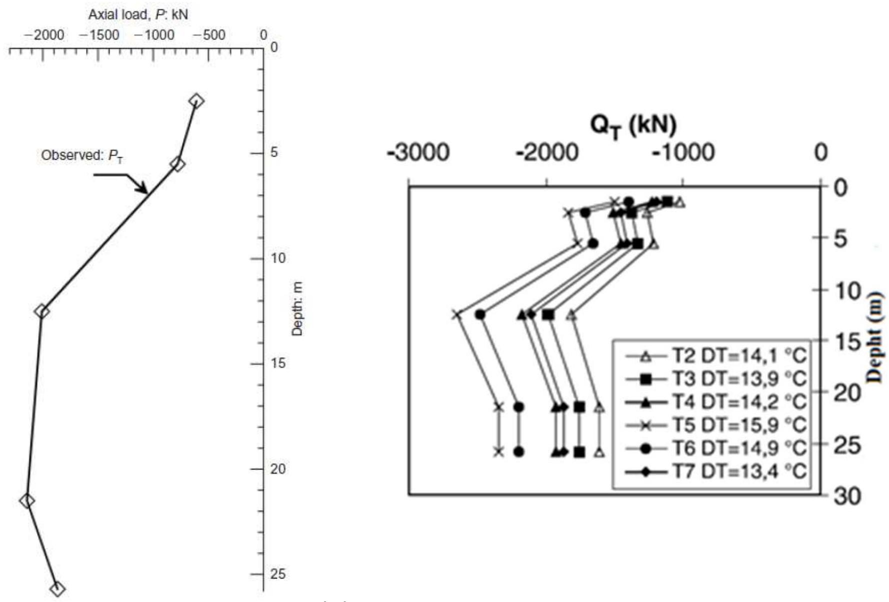

(b)

(a)

Figure 2-10: Thermal load during Test 1 (a) (Amatya et al., 2012) and Test 2, Test 3, Test 4, Test 5, Test 6 and Test 7(b) (Laloui et al., 2003).

The partially suppressed pile head movement leaded to an increase of the axial stress as the pile head constraint increased (Bourne-Webb et al. ,2019). The axial load profile during the construction phases is reported in Figure 2-10 (a and b). For Test T7, for example, the axial stress at the head of the pile is doubled compared to the case in which only mechanical load is applied. The axial load induced by thermal load of course can be quite large and in general cannot be neglected. The impact of the structure on the pile had a strong constraint action observed along almost the entire pile (Figure 2-10 b).

Observing the axial load at the head of pile during the tests, the restraint of the slab constructed at the step of test 1 had a smaller constraint action compared to those of the overall building. From the data of tests 5 and 6, 1 °C of temperature increase determines 100 kN of additional compressive stress (Laloui et al., 2006).

Bourne-Web et al. (2009) reported the experimental results of a test carried out at the Lambeth College in London within the framework of the construction of a five-storey building. The elements involved in the test are the test pile, a heat sink pile and four anchor piles. The main test pile and the heat sink pile were instrumented with a mix of either, conventional embedded vibrating wire gauges (VSWG) and thermistors, and/or optical fibre sensing cable (OFS) (Bourne-webb 2020). The soil layering was typical of London: a shallow, 4 m thick, sandy layer overlying a deep (down to 30 m) London clay layer. The test pile, 0.6 m diameter and 22 m length, was subjected to an initial load of 800 kN and then unloaded. Then a load of 1200 kN was applied and thermal loads were added to the mechanical one. The test was carried out combining to the mechanical load a first cooling cycle of 1 day and then one heating cycle of 1 day. Then a cooling cycle of 35 days and a heating cycle of 12 days were applied. The maximum and minimum temperatures were 40 °C and -6 °C, respectively. The evolution of pile head displacement with temperature variations imposed by the geothermal loops is reported in Figure 2-11 (Bourne-Webb et al., 2009). The pile had only the restraint of the surrounding soil while the pile's head was free to move, even if under a constant load of 1200 kN. A decrease in temperature of about 20°C determined a settlement of about 4 mm that is very close to the free shortening of the concrete pile. The thermo-mechanical axial loadings measured by the authors are reported in Figure 212. The residual strain profile was used as new baseline to examine the changes induced by the load and temperature variations. Cooling led to tensile forces being developed in the lower part of the pile shaft, with a maximum thermal load of 500 kN. During heating additional compression axial forces occurred. Consideration of the test data from the Lambeth College test pile leads to the conclusion that the pile is effectively floating in the ground, with little constraint on its movement at either end (Bourne-webb et al., 2009).

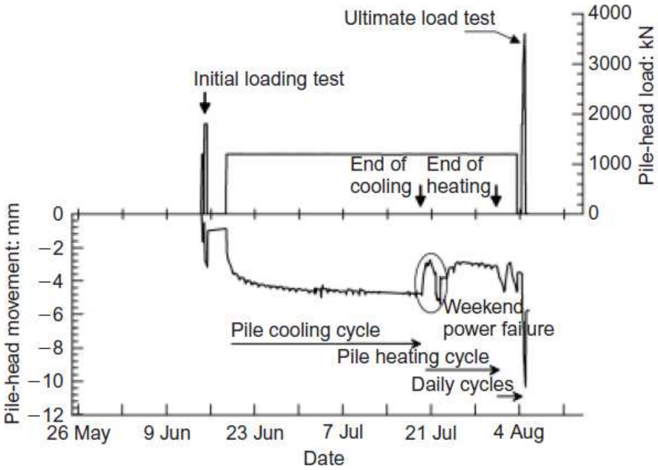

Figure 2-11: Load control and pile head displacement through test period (Bourne-Webb et al., (2009).

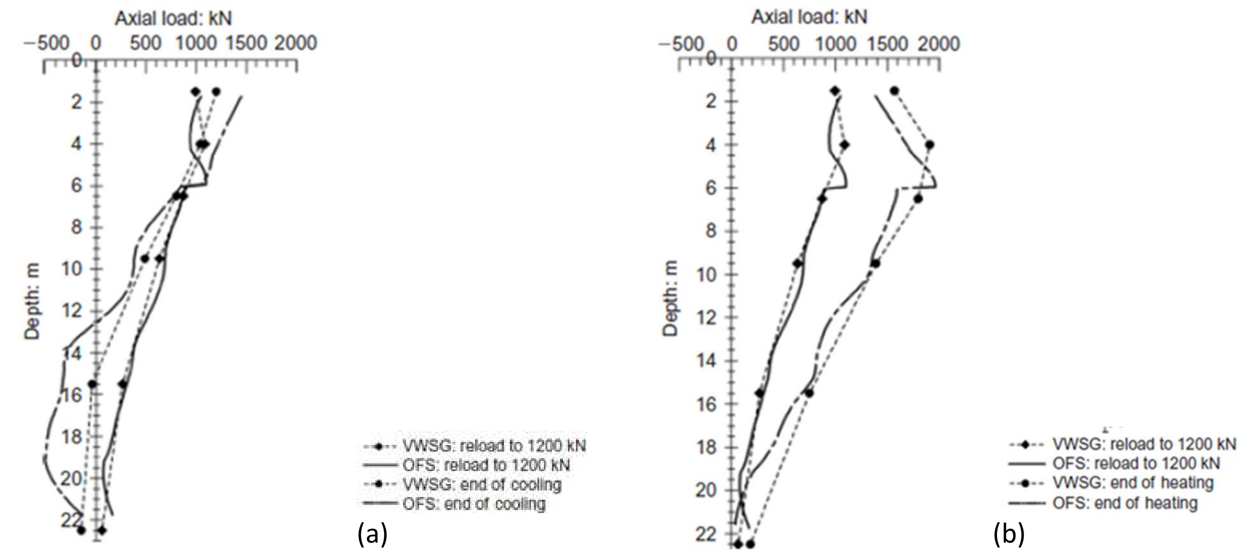

Figure 2-12: Axial load along the pile shaft measured by Optical Fiber Sensing cable (OFS) and Vibrating Wire Strain Gauge (VWSG); (a) Mechanical load and thermo-mechanical mechanical axial load at the end of cooling; (b) Mechanical load and thermo-mechanical mechanical axial load at the end of heating (Bourne-Webb et al., 2009).

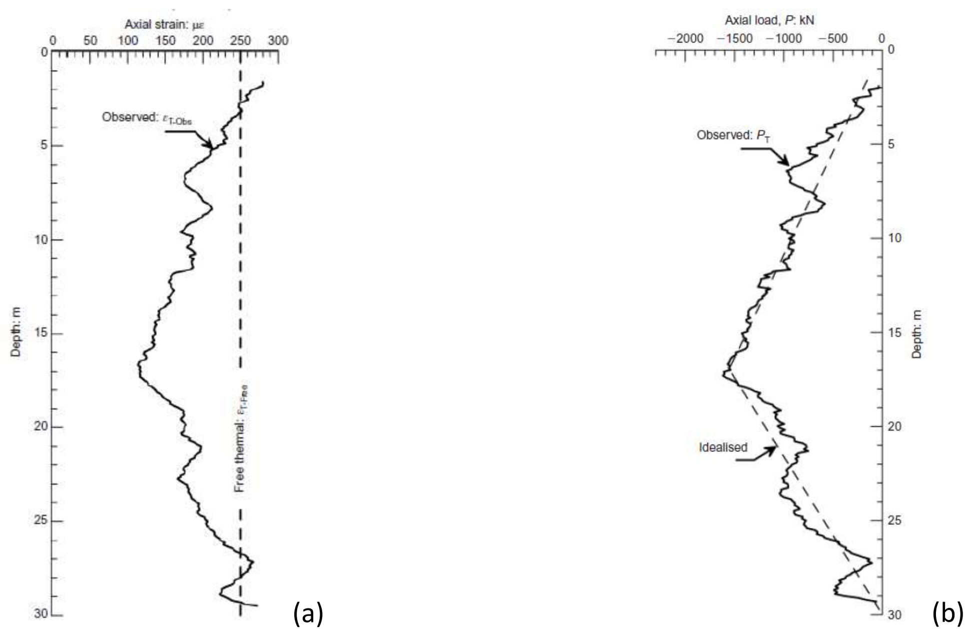

Figure 2-13: (a) Observed and free thermal strain profile and (b) thermal load and idealised thermal load profile for the heat sink pile at Lambeth college from Amatya et al. (2012).

The behavior of the heat sink pile, 0.6 m in diameter and 30 m deep, is reported by Amatya et al. (2012). The behavior during the first heating cycle for an imposed temperature change △T of +29.4 °C, was reported in terms of axial strains and load in Figure 2-13 (a) and Figure 2-13 (b), respectively. A triangular load profile with near-zero thermal load at both pile's ends was observed with 1550 kN of maximum thermal load below the mid depth.

Wang et al**.** (2015) investigated the impact of thermo-mechanical load on pile's shaft capacity through in situ testing. Test pile equipped with two level Osterberg cells, three U shaped loops and strain gauges was installed at Monash University, Melbourne. The pipes were installed 50 mm from the edge of the pile and down to the top of the lower Osterberg cell to a depth of 14.2 m. The ground conditions are a shallow sandy clay layer overlying dense sand. Groundwater was not encountered. The test pile is a bored pile with length of 16,1 m and 0.6 m diameter. The test program did not involve the extraction of heat from the ground, cooling cycles refer to pile temperatures dropping down to the initial ground temperature. Pile load tests were carried out by applying load and unload cycles before and after applying the thermal loads to assess the effects of thermal loading on the ultimate shaft resistance. After the purely mechanical test, the pile was heated continuously for nine days using a constant energy input, then five load and unload cycles were carried out. After one heating period of 9 days, the pile shaft gained a shaft resistance of at least 14 %. After heating, the pile was cooled naturally for 47 days. Three load and unload cycles were carried out finding that the pile shaft capacity is very close to that before heating. 52 days of heating and recovery were performed. The ultimate shaft resistance at the end of heating was higher than that computed in the previous test. Then pile was left to cool naturally for 78 days. Three load and unload cycles were carried out to assess the post-long-term recovery phase. The shaft resistance obtained returned closely to the initial value indicating a thermo elastic behavior. During these tests radial and axial thermal strains were measured. Thermal strains during 9 and 47days heating and recovery phases are reported in Figure 2-14 (a) and Figure 2-14 (b), respectively. During the long-term heating and recovery, the pile was heated continuously for of 52 days, with final fluid of about 46°C and then was cooled down naturally for 78 days. During this period, the circumferential and vertical thermal strains are plotted in Figure 2-14 (a). At the end of the long-term heating period, elongations were recorded, and the maximum vertical and horizontal strain increased by approximately 250 and 275 micro-strains.

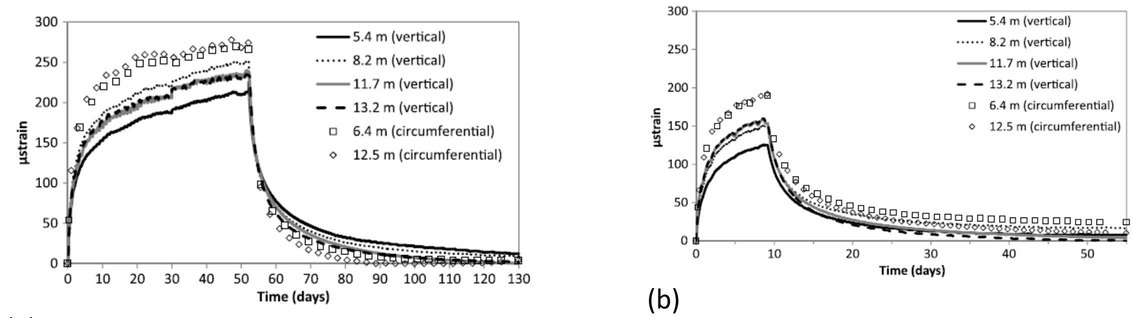

(a) (b)

Figure 2-14: Pile's vertical and circumferential (radial) thermal strains versus time, during (a) long-term heating and recovery and (b) short-term cooling and recovery.

At the end of the 9-days heating period, the maximum vertical and horizontal strain increased by approximately 150 and 192 micro-strains, for a final heating fluid temperature of approximately 38°C (Figure 2-14 b). The measures at the end of the recovery phases showed thermo elastic behavior.

Faizal et al. (2016) described the tests carried out on the same instrumented EP of Wang et al. (2015) to the aim of investigating the effects of intermittent and continuous operating modes on the thermal and mechanical behavior of EPs.

Two different kinds of operating modes: 24 h daily continuous operating mode (24 h mode) and intermittent modes (16 h mode and 8 h mode) were considered. Intermittent modes considered natural ground recovery and consisted of two different cases: 8 hours rest and 16 hours of operating (16 h mode) and 16 hours rest and 8 hours operating (8 h mode). For all operating modes, water was circulated at approximately 5 °C. Slightly variations temperature with depth were measured, with 1.5 °C of variation between different depths (5.4 m,8.2 m, 11.6 m and 13.3 m). For a given operating mode, there are differences in thermal strains and rates of decay between different depths (Figure 2-15).

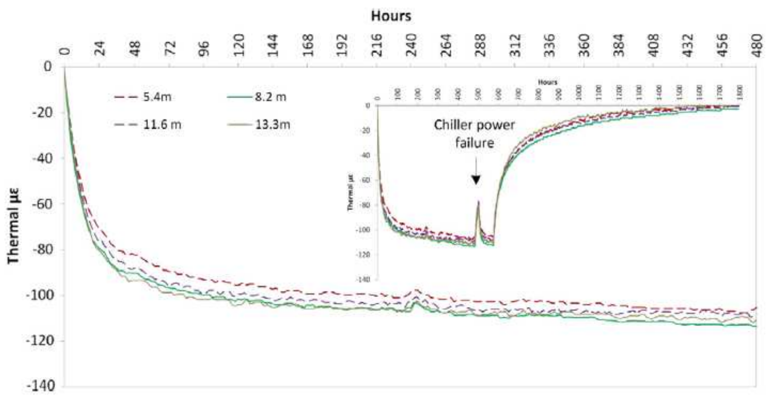

(a)

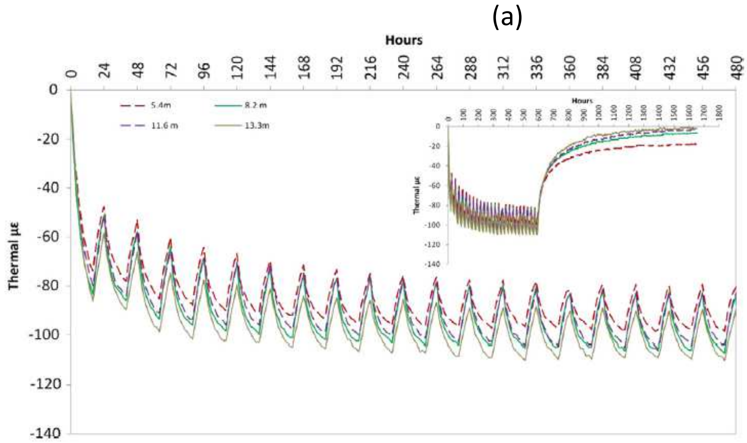

(b)

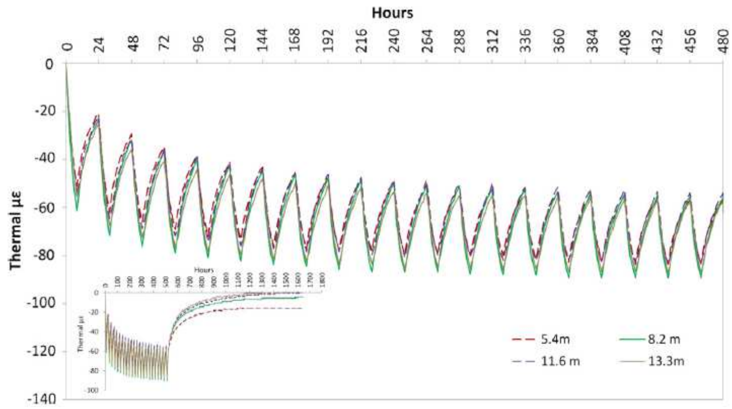

(c)

Figure 2-15: Transient axial thermal stresses at different depth for 24 h (a), 8 h (b) and 16 h (c) modes (Faizal et al. 2016).

The head of the pile was not loaded and was exposed to the atmosphere. Thermal strains recovered to near initial conditions at end of the tests (Figure 2-15).

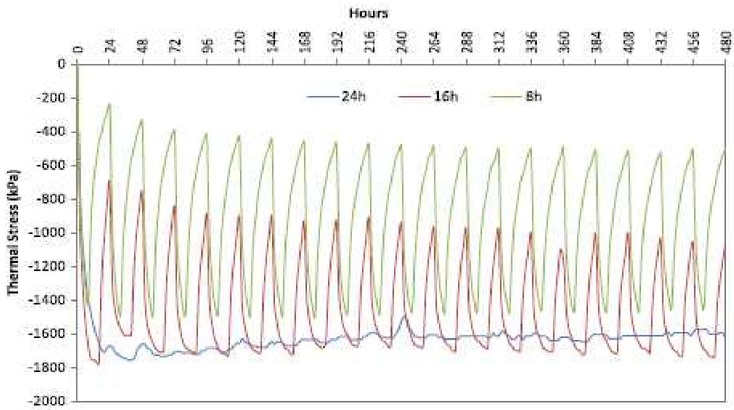

Figure 2-16: Thermal stresses for all modes for depth of 5.4 m (Faizal et al., 2016).

The change in thermal strains at the beginning of experiments is higher and gradually stabilises with minimal changes between consecutive days. The maximum axial stresses were observed where the largest constraint to axial strain is exerted (5.4 m depth) for all the operation modes. The cyclic changes in temperatures and thermal strains determined a cyclic behavior from end of cooling to end of recovery compared to continuous thermal stresses in the 24 h modes, for daily thermal cycles. At the depth of maximum thermal stress, the results of the three operating modes were compared in Figure 2-16. 24 h and 16 h operating modes determine similar maximum thermal stresses while 8 h operating mode always determines lower thermal stresses compared to the other operating modes. With increasing number of thermal cycles accumulation of thermal stress is observed. Comparing the experimental results, 8 h mode had the lowest thermal impact on the ground and the pile.

Studies conducted on GEPs have shown that the heat transfer is higher in intermittent operation compared to continuous operation due to ground temperature recoveries (Faizal et al.,2016). The energy extracted from the ground was 40.9% and 14.8% higher in the 8 h and 16 h modes, respectively, compared to the 24 h mode. From a thermo-mechanical point of view, it could be hypothesised that the intermittent operating modes will induce lower thermal loads on GEP due to frequent recovery (Faizal et al. 2016). The average thermal stresses induced in the pile shown was 12.2% lower in the 16 h mode and 42.3% lower in the 8 h mode compared to the 24 h mode, respectively. Lower temperatures are induced in the pile in the 8 h mode compared to 16 and 24 h modes as reported by the authors of the test.

Faizal et al. (2018) based on the site investigation of Faizal et al. (2016) focused on a comparison of the magnitudes of axial and radial thermal strains and stresses. It was concluded that the magnitudes of the radial thermal stresses developed in the pile are much lower than the axial thermal stresses and may be neglected.

Faizal et al. (2019) carried out full scale tests at Monash University, same site of Wang et al. (2011), Faizal et al. (2016) and Faizal et al. (2018) to investigate the effects of daily cyclic temperature changes on the axial and radial thermal responses of an energy pile installed under a six-story building. The EP was 0.6 m diameter and 10 m in length, equipped with four U loop pipes and instrumented with radial and axial vibrating wire gauges and thermocouples. Cyclic heating and cooling were conducted for 17 days and the pile was subjected daily to intermittent operation. The authors reported the profiles of temperatures, temperature variations, and axial and radial strains plotted against depth. In this study only axial strain and temperature variations profile are reported in Figure 2-17.

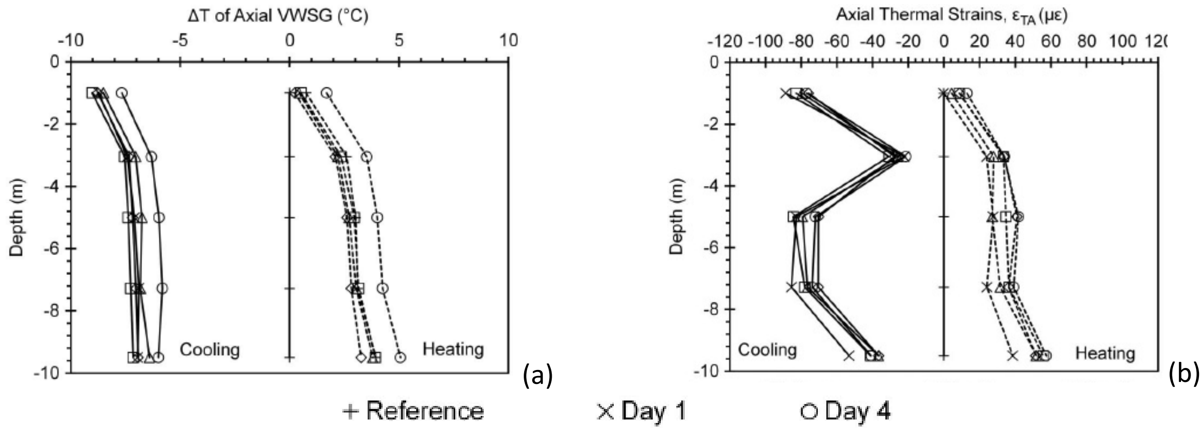

Figure 2-17:Change in pile temperatures △Ts from axial Vibrating Wire Gauges (a) and Axial thermal strains profile at four days intervals from Faizal et al. (2019).

Pile's temperature variations profiles showed in Figure 2-17 (a) indicate that the 16-h cooling cycle determined larger pile's ΔT up to −9°C than the 8-h heating cycle ΔT up to 5°C. The axial thermal strains at the end of cooling in Figure 2-17 (b) showed higher variations with depth compared with the end of heating, in fact larger ΔTs occurred during cooling cycles. At 3.05 m depth the most significant restriction to axial thermal strains was observed. A complex axial thermal strains profile is observed. Locations of high restrictions in axial thermal strains were not evident with depth at the end of heating.

The thermal stresses developed in the pile are shown in Figure 2-18 along with the purely mechanical stress profile imposed by the load of the building. Tensile stresses developed during cooling and compressive stresses developed during heating. The sign convention in this study is that compressive stresses are considered negative. The magnitudes for tensile axial thermal stresses at the end of cooling were greater than those for the compressive axial thermal stresses at the end of heating because of the differences in ΔT magnitudes.

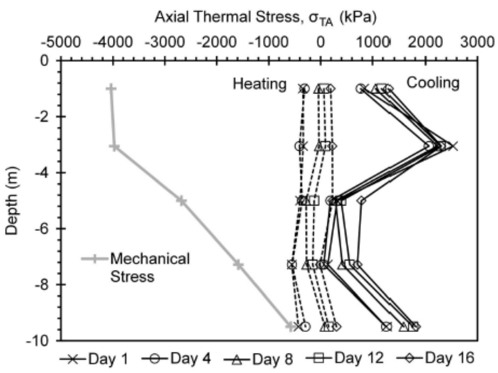

Figure 2-18: Axial thermal stress profile with depth at Day1, Day 4, Day 8, Day 12 and Day 16 during intermittent operation of cooling and heating, from Faizal et al. (2019).

The impact of daily cyclic temperature variations, ranging between – 8 °C (during cooling) and +5 °C (during heating), combined to a mechanical load corresponding to 52% the ultimate capacity does not induce significant plastic deformations. The magnitudes of radial thermal stresses were found to be insignificant in comparison with the magnitudes for axial thermal stresses developed in the pile at all depths. This finding indicates that radial thermal expansion and /or contraction of the pile did not have impact on pile's skin friction. Temperature distribution over the cross section of the pile showed a low range of variation that it could result in nonuniformly distributed axial stress across the cross section of the pile. For this study, the magnitudes of axial thermal stresses were within the ultimate capacities of the pile.

Sutman et al. (2019) reported the results of in situ testing on three EPs to the aim of further investigating the ends restraint effect on piles behavior, providing comparative results. The tests were performed in Houston, Texas. Two of the three test piles were constructed entirely in a stiff to a very stiff clay. One of the piles was bearing on a very dense sandy layer. All the three test piles were 0.457 m in diameter. Test Pile 1 and Test Pile 3 were 15.24 m in length while Test Pile 2 was 19,4 m in length extending in stiff to very stiff clay. In addition to three piles, eight reaction piles were installed for the conventional pile load test. Mechanical tests, thermal tests and thermomechanical tests were reported. To investigate the response of EP to multiple thermal cycles, Test Pile 1 was loaded to find its ultimate capacity (2558 kN), then the mechanical load was removed and 5 thermal cycles between 43 °C and 6 °C were applied during period over 6 weeks. After the thermal cycles were completed, the test pile was re-loaded to 2558 kN. Thermo mechanical tests were performed on test piles 2 and 3. During these tests, piles were loaded up to a live load corresponding to SF=2. Then single heating and cooling cycles were separately applied to the piles. During thermal test on Test Pile 1 (TP-1), thermally induced axial stress along the pile depth reported by the authors is plotted in Figure 2-19 (a) and Figure 2-19 (b) . Positive sign represents tensile axial stresses. The absence of mechanical load determines null observed thermal stress at the level of pile head where the observed strains are equal to the free thermal expansion of pile. Maximum thermally induced axial stress during heating and cooling episodes are -1600 kPa (during heating) and 1040 kPa (during cooling) at 8.7 m dept.

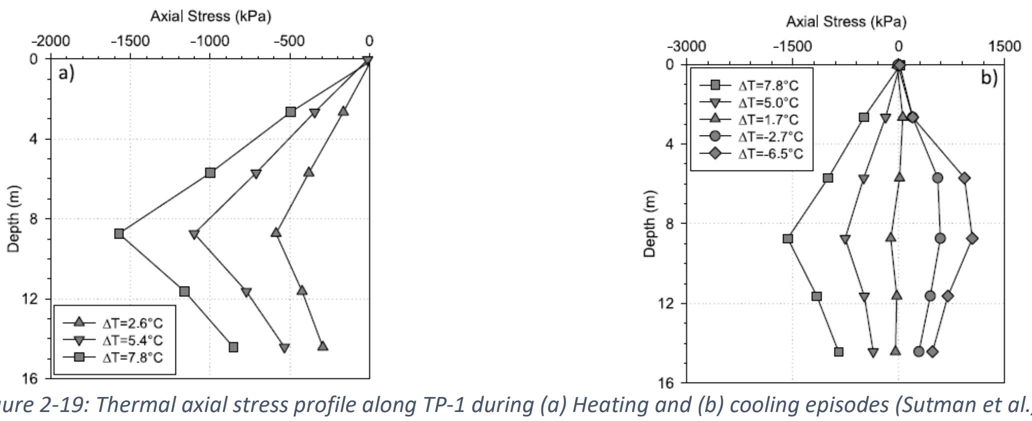

Figure 2-19: Thermal axial stress profile along TP-1 during (a) Heating and (b) cooling episodes (Sutman et al., 2019).

Thermo mechanical tests carried out on Test Pile 2 and Test Pile 3, (TP-1 and TP-2), allow the investigations of the mechanical load effect on the restraint conditions at piles head and toe. Comparing the obsrved response of TP-3 and TP-1 the effect of the head restraining conditions (mechanical load and null load at pile's head) can be investigated. The effects of the base restraining conditions on two piles subjected to similar thermal variaitons (TP-2 and TP-3) can be investigated comparing the behavior of TP-2 and TP-3.It is not entirely possible because the two piles have diverse degrees of freedom at the head, TP-2 and TP-3 did not have the same ultimate load capacity that is used to determine the design load applied. The effects of temperature changes, increasing during heating and decreasing during cooling, are deduced, by the authors, as the difference between the thermo-mechanical and the mechanical stresses.

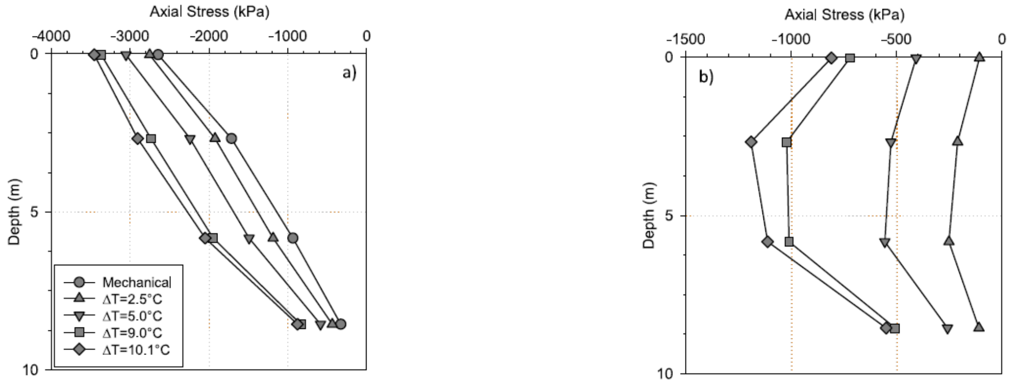

Figure 2-20: Axial stress profile along TP-2 during heating episode: (a) combined effects of mechanical and thermal loadings; (b) Thermal loading excluding the effects of mechanical loadings (Sutman et al., 2019).

Compressive axial stress with a magnitude of 2645 kPa is observed at TP-2 through the application of the mechanical load. The restraining effect of the maintined mechanical load on the thermal expansion of TP-2 results in 27 % increase in the axial compressive stresses (720 kPa), compared to the one induced by mechanical load (Figure 2-20 (a)). The maximum induced thermal stress due to heating is observed at level between 2.7 m and 5.8 m and it is in the order of 1200 kPa (Figure 2-20 (b)).

The thermomechanical and thermal axial stresses at the peaks of cooling episode are shown in Figure 2-21 (a) and (b) for TP-2. The most pronounced effect of cooling is observed at 5.8 m depth where the compressive axial stress is reduced by almost 190 kPa compared to the mechanical loading case.

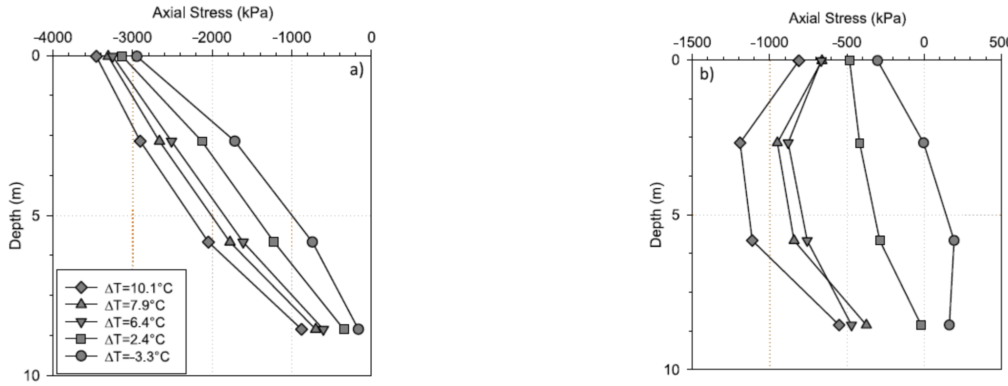

Figure 2-21: Axial stress profile along TP-2 during cooling episode: (a) combined effects of mechanical and thermal loadings; (b) Thermal loading excluding the effects of mechanical loadings (Sutman et al. 2019).

Axial stress profile for TP-3 is reported in Figure 2-22 considering both the thermo-mechanical effects (a) and purely thermal effects (b). Axial stress at pile head caused by mechanical loading, 6900 kPa, is increased by 1200 kPa, 17 %, at the peak heating episode.

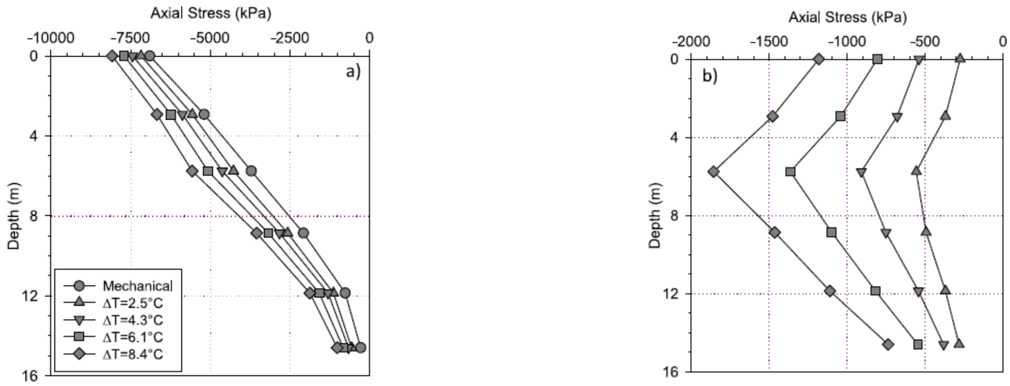

Figure 2-22: Axial stress profile along TP-3 during heating episode: (a) combined effects of mechanical and thermal loadings; (b) Thermal loading excluding the effects of mechanical loadings (Sutman et al. 2019).

The thermo mechanical and thermal stress during peak cooling are reported in Figure 2-23 (a) and (b), respectively. As occurred for TP-2, the compressive axial load at TP-3 head is slightly higher (100 kPa) than one induced by the mechanical loading. The decrease in compressive stress it is observed below the head of the pile. Maximum decrease in the compressive axial stresses of 490 kPa is observed at 8.9 m depth, compared to the mechanical loading case. A decrease in the compressive stresses caused by prior mechanical loading and heating is observed along piles length both for TP-2 and TP-3 during cooling. Heating episodes result in an increase in the compressive axial stresses at pile's head both in case of TP-2 and TP-3. At the peak cooling episode, the axial stress at the head of TP- 2 and TP-3 is observed both for TP-2 and TP-3.

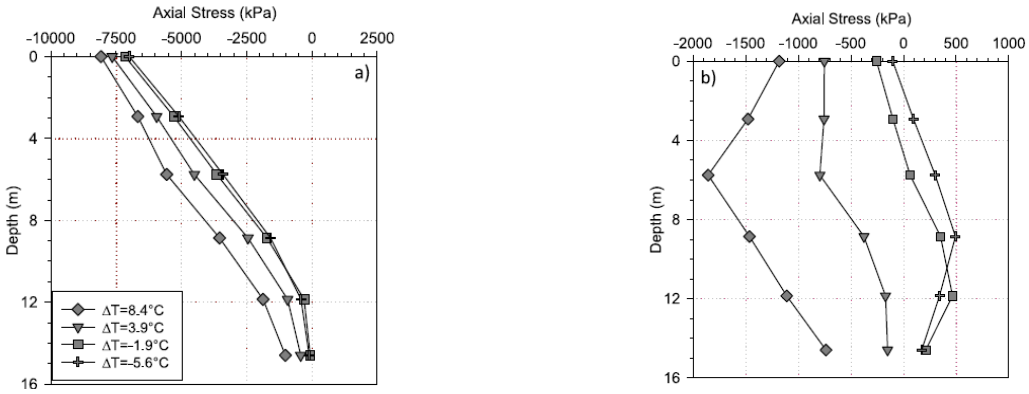

Figure 2-23: Axial stress profile along TP-3 during cooling episode: (a) combined effects of mechanical and thermal loadings; (b) thermal loading excluding the effects of mechanical loadings (Sutman et al., 2019).

The thermal compressive stress developed at pile's head is 200 kPa higher for TP-2 compared to TP-3 during peak cooling episode. According to the authors it is caused by the early termination of the cooling episode due the failure in closed loop system. For TP-2, the maximum thermal stresses are observed between 2.7 m and 5.8 m from pile's head. The stiff clay layer at the base of TP-2 results in an increase in compressive stresses compared to the mobilized base resistance due to only mechanical loading. For TP-3 the maximum thermal stresses are observed at 5.8 m depth which points out the depth of the highest imposed restriction on the expansion of TP-3 (NP position). During heating maximum decrease in the compressive axial stresses of 490 kPa is observed at 8.9 m therefore a variation of NP position during the transition from the heating to cooling episode is noted.

de Santiago et al. (2016) present the results of site investigations on a full-scale precast concrete energy pile of 0.35 m diameter and 17.4 m total length carried out in Valencia. The aim of the experiment was to improve the understanding of the effects of cooling and heating on precast piles subjected to mechanical loads. This test pile was made by reinforced concrete equipped with double U tubes, strain gauges and thermistors. Subsoil profile consisted of an alternance of sand, clay and gravel. The pile was subjected first to two static load tests (tests A and B), and then to thermo-mechanical tests (Test C) by maintaining the mechanical service load of 1000 kN. Strains, displacements, and temperatures are reported during strategic moments of the test named as: C_0, C_a, C_b, C_c, C_d and C_e. In terms of temperature changes, comparing the soil initial temperatures at different depths at time instant C_0, the first meters of pile show ΔT=17 °C, while ΔT=12 °C is registered in the lower part of the pile. These measures demonstrated that during the heating of the foundation, pile's temperature is strongly influenced by atmospheric temperature. Maximum temperature is 35-36°C in the upper meters and 30-31°C in the lower zone. Pile's head displacement time history induced by thermal variations is reported in Figure 2-24. The maximum displacement was 1.4 mm in Cb, after this moment all the measurements sensors showed a decreasing trend as the pile thermally recovered. Thermal daily variations of air temperature influenced the displacement trend during the recovery phase in fact cyclic oscillation were observed. At the end of monitoring the pile's head displacement did not return to its original elevation upon cooling maintaining about 0.4 mm of upward displacement.

Thermal strains measured at different depths are reported in Figure 2-25. The convention adopted by the authors is negative sign for shortenings or compression stresses. All strain profiles show elongations, with the exception of the Ce profile, corresponding to the recovery phase. The maximum elongation is measured in Cb, when the heat injection and temperature measured in the pile are maximum. Larger thermal strains are measured in the upper part of the pile, at all the heat injection curves, while the deeper part of the pile tends to show lower strain values.

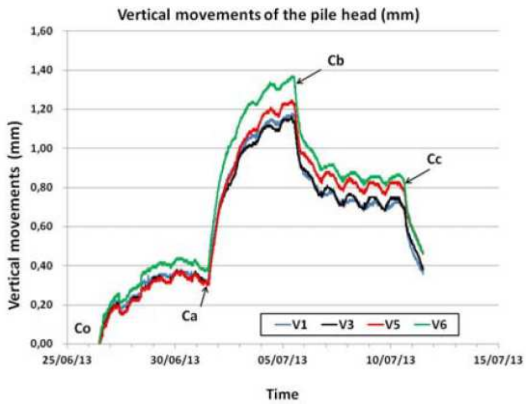

Figure 2-24:Vertical Displacements of pile's head due to thermal changes during test C (de Santiago et al., (2016)).

The average thermal axial stresses induced in the foundation by the temperature changes have been calculated from the measured strains at the location of each gauge (Figure 2-26).

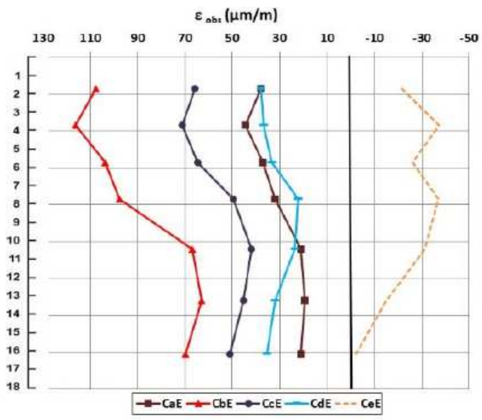

Figure 2-25: Observed thermal strains measured by the extensometer, during different moments (C_a, C_b, C_c, C_d and C_e) of the thermo-mechanical test reported by de Santiago et al. (2016).

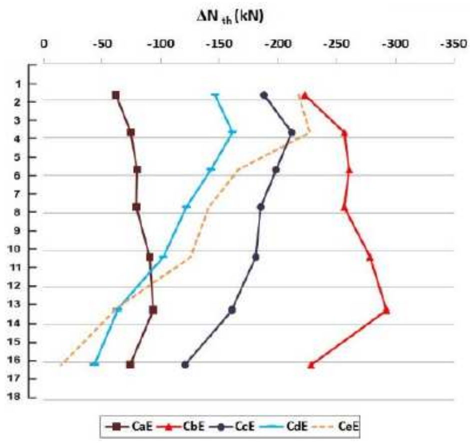

Figure 2-26: thermal axial load profile during different moments (C_a, C_b, C_c, C_d and C_e) of the thermo-mechanical test reported by de Santiago et al. (2016).

Murphy et al. (2015) reported the results of the in-situ testing performed in the framework of one-story building construction at the Field Engineering and Readiness Laboratory (FERL) of the US Air Force Academy (USAFA). The building could have been constructed with a shallow foundation, so the main purpose of incorporating drilled EPs as foundation system was to evaluate the thermo-mechanical response of EPs. Eight drilled shafts, each 15.2 m deep and 0.61 m in diameter, provide the foundation support for the structure. Site conditions are characterised by three prominent strata. The top layer is approximately 1 m thick and consists of sandy fill, the second layer is a very dense 1-m-thick sandy gravelly layer, and the deeper layer is sandstone. The profiles of measured thermal strains and axial load for the three equipped foundations are reported in Figure 2-27. Pile Foundation 3 was located at the corner of the building and had the lowest end restraint at the top compared with Pile Foundations 1 and 4 which are located in the central area. Larger thermal axial strain at the toe of foundation 1 and foundation 4 was observed. According to the authors this could be due to issues with thermistors measurements or could reflect the possibility that the toe of the foundations may be relatively soft. The thermal axial strains were used to calculate the thermal axial stresses induced in each foundation during heating considering Young's modulus of 30 GPa. The thermal axial stresses observed in these three foundations are below 33 % threshold of the compressive strength of reinforced concrete (21 MPa). The thermal axial stresses in Foundation 3 were observed to be lower than in the other two foundations (1 and 4). This could be attributed to the lower amount of restraint provided by the corner of the building compared with the centre of the grade beam, further, Foundations 5 and 8 were not heated, so they may provide greater constraint to Foundations 1 and 4 than to Foundation 3. The end restraint boundary conditions were found to play an important role in pile's thermo-mechanical response: foundation 3 has the lower head stiffness, and it was found to lead to a lower thermal axial stress along with a slightly greater displacement.

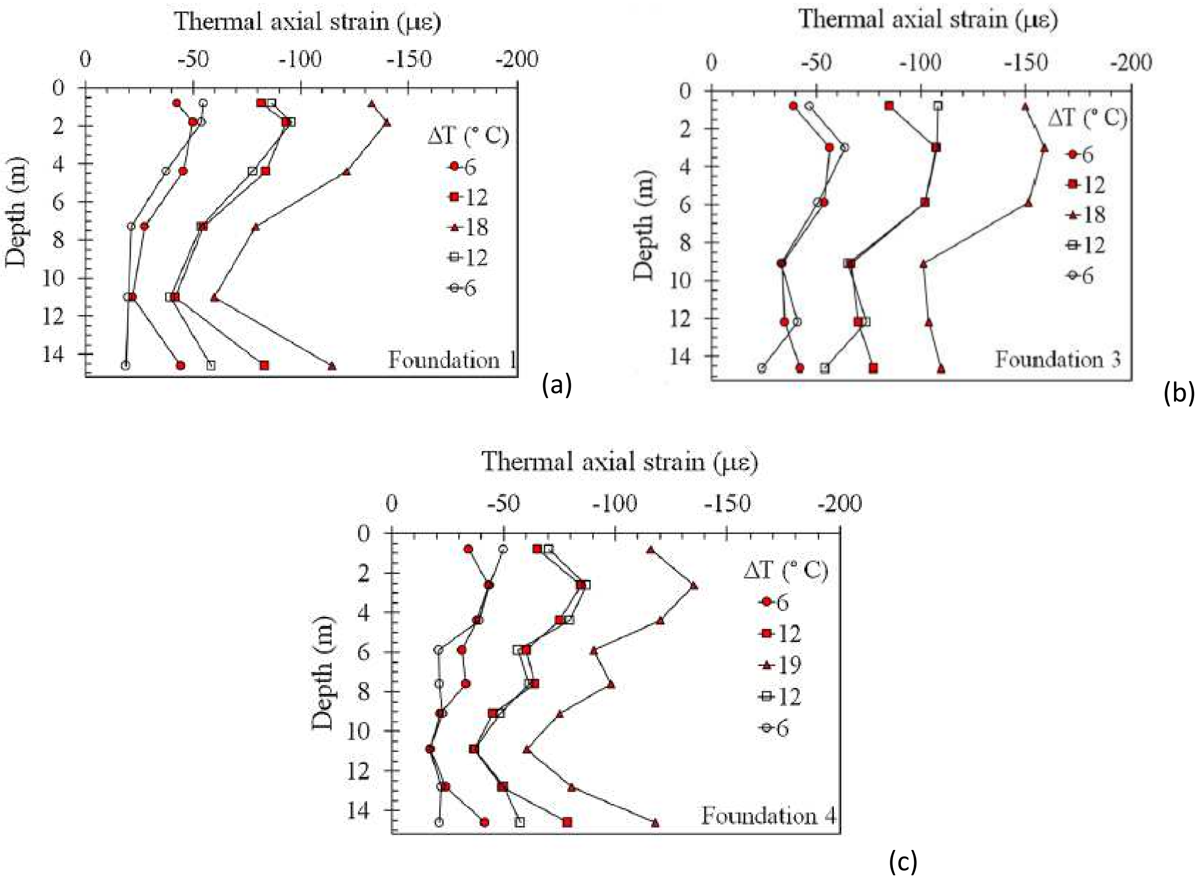

Figure 2-27: Profiles of thermal axial strain for different average changes in foundation temperature during heating (red) and cooling (open): (a) Foundation 1; (b) Foundation 3; (c) Foundation 4.

Jiang et al. (2021) carried full-scale tests on jacked Prestressed High Strength Concrete (PHC) EP to investigate on the behavior of driven energy piles under cyclic temperature changes and multiple mechanical loads. Within depth of 25 m, the subsurface soil was comprised of fill, silty clay, silt with sand, silty sand, and silt. The groundwater was located at 1 m an of depth from ground surface. The pile tip-bearing layer was silty sand. Two jacked driven piles were considered in this study, a reference pile tested using mechanical load and one EP subjected to heating-recovery cycles and cooling-recovery cycles at different mechanical loads. The test piles have 0.4 m and 0.21 m of outside diameter and inside diameter and with a length of 15 m. The EP was equipped with a single U-shape heat exchanger tube. During the heating-recovery tests the outflow temperature increased from 18.2 °C to 64.5 °C and then returned to 19.6 °C after the recovery phase.

Five mechanical loading levels were considered, 0%, 50%,150 % and 200% of the working load. For each level of mechanical load one cycle of heating-recovery was applied and when the head settlement reached stable stage during the recovery phase the next increment of mechanical load was applied. The results of the heating-recovery tests reported by the authors are showed in Figure 2-28. Positive pile's head displacement corresponds to settlement. According to the authors the change in pile settlement lagged slightly behind the change in temperature because the soil-pile system required a certain time to react to the quick thermal loading. Maximum heave of pile's head of 0.8 mm was recorded for null mechanical loading applied to the head of the pile. The results of the cooling-recovery tests reported by the authors are showed in Figure 2-29.

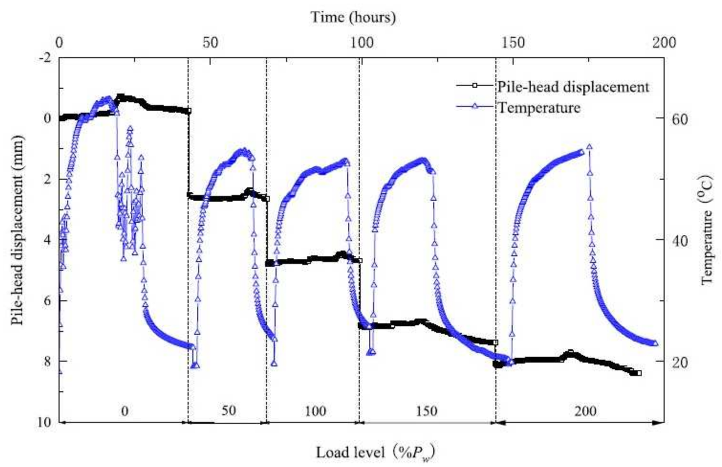

Figure 2-28:Variations of pile's head displacement and temperature during heating-recovery cycles at different levels of mechanical loadings from Jiang et al. (2021).

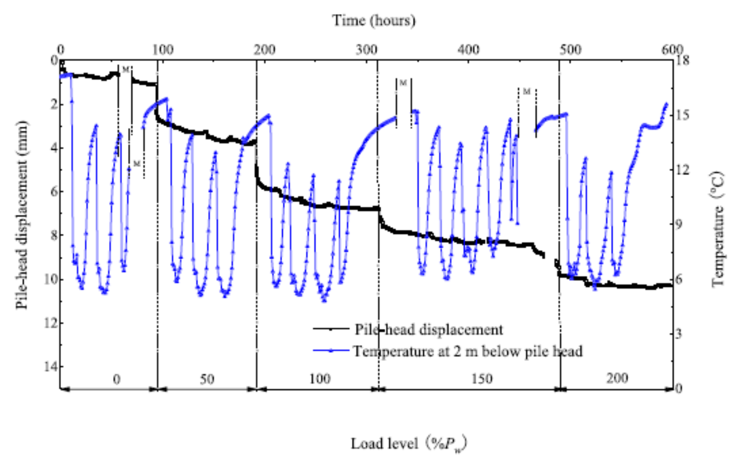

Figure 2-29: Variations of pile's head displacement and temperature during cooling-recovery cycles at different levels of mechanical loadings from Jiang et al. (2021).

For cooling-recovery tests additional 3-5 cycles were carried out under the same mechanical load level. During cooling the water temperature was decreased from 15.5 °C to 2-4 °C in the outflow temperature.

During the recovery phase the temperature was recovered to the initial temperature. The heating-recovery cycles resulted in elastic pile responses at mechanical loads smaller than working load. At the end of the recovery phases induced settlement was less than 5% of mechanical load induced settlement. For the cooling-recovery cycles apparent elastic–plastic pile responses were observed at a specific mechanical loading level, with the cooling-induced settlement being several times greater than the mechanical settlement.

In Table 2-5 all the tests described are listed. Pile characteristics are considered both in term of mechanical behavior (floating, end bearing or semi floating piles) and technology (drilled or driven piles).

Table 2-5: Field tests carried out in different conditions.

Authors	***Place***	***Kind of test***	***Site stratigraphy***	***Pile***
Laloui et al. (2003-2006)	Europe	During building construction	Alluvial soil, sandy gravelly moraine, molasse, groundwater table near surface	Drilled,semi-floating
Bourne-webb et al. (2009) **Amatya et al. (2012)**	Europe	Site investigation	Granular fill and sand, founded in stiff fissured silty clay, Groundwater table at a depth of 3 m	Drilled,semi-floating
Sutman et al. 2019	USA	Site investigation	Stiff sandy/silty clay, very dense sand, stiff to a very stiff clay, Groundwater table at depth of 3.7 m	Drilled, floating and end-bearing
Santiago et al. (2016)	Europe	Site investigation	Sandy gravel, stiff clay, soft and black organic clays, sandy gravels with some stiff clays' levels. Ground water table at a depth of 2.0 m.	Driven, semi-floating
Wang et al. (2015) **Faizal et al. (2016)** **Faizal et al. (2018)** **Faizal et al. (2019)**	Australia	Site investigation	Silty clay, sandy clay, dense sand and very dense sand. Groundwater not encountered	Drilled, floating
Akrouch et al. (2014)	USA	Site investigation	High plasticity clayey soils Groundwater not encountered	Drilled, semi-floating
Murphy et al. (2015)	USA	Buildings' foundations	Sandy soils and sandstone Groundwater not encountered	Drilled, semi-floating
Jiong et al. (2021)	China	Site investigation	Medium dense silt Groundwater table at depth of 1 m	Driven Floating

2.2.2 Pile-soil thermo-mechanical interaction

The experimental data of in situ testing could be analysed making some simple assumptions about the pile-soil thermo-mechanical interactions. It is possible to describe the likely thermo-mechanical response of isolated EPs through three dimensionless parameters reported in Equation 2-31 and Equation 2-32.

Equation 2-31: $DOF = \frac{\varepsilon_{th,0}}{\varepsilon_{th,free}}$; $DDR = \frac{y_{th,0}}{y_{th,free}}$

where DOF is the pile's *D*egree *O*f *F*reedom computed for a specific section along pile's length. To estimate DOF, thermal strain and temperature variation ΔT should be available in the considered section. $\varepsilon_{th,0}$ is the measured thermal strain, $\varepsilon_{th,free}$ is the maximum elongation or shortening strain computed assuming that the pile is a free column (free to expand or contract without any restraint provided by the surrounding soil).

DDR is the *D*imensionless *D*isplacement *R*atio at pile's head that depends on the entire pile shortening or elongation. $y_{th,0}$ is the thermal displacement measured at pile's head that depends on the thermo-mechanical interaction between pile and soil, $y_{th,free}$ is the maximum displacement of pile's head computed neglecting the interaction with surrounding soil and taking into account for the NP position (L_{np}).

Equation 2-32: $DSR = \frac{\sigma_{th,max}}{\sigma_{th,fixed}}$

where DSR is the Dimensionless Stress Ratio computed for a specific section where the measure of thermal stress and temperature variations are available. $\sigma_{th,max}$ is the maximum measured thermal stress in a specific section of the pile, $\sigma_{th,fixed}$ is the maximum stress change computed in the hypothesis that the pile body is perfectly constrained both respect to the thermal elongations or the thermal shortenings. It is computed as the product of $\varepsilon_{th,free}$ and pile's Young modulus.

The DOF is a parameter that represents the thermo-mechanical behavior of single EP from the deformation point of view. If thermal strains measurements are available along pile's depth, DOF provides a measure of the constraint action of the surrounding soil on pile with depth. If measurements of strains are not available along pile's depth DDR provides summarised and dimensionless information about the constraint action of the soil on pile thermal movements. It must be highlighted that this parameter is also directly dependent on the constraint action at pile's head due to the foundation system if the pile under observation is inserted into a foundation group for example.

The DSR is a parameter that represents the thermo-mechanical behavior of a single EP from the induced thermal stress point of view. DSR accounts for the maximum normal stress induced by thermal loads and it is obviously related again to the constraint action of the surrounding soil.

Plie's free thermal strain $\varepsilon_{th,free}$ is computed according to Equation 2-33.

Equation 2-33: $\varepsilon_{th,free} = \alpha_p \cdot \Delta T$

Where α_p (°C^{-1}) is expansion thermal coefficient of the pile in and ΔT (°C) is the temperature variation measured in a specific section.

The maximum displacement of pile's head $y_{th,free}$ neglecting pile-soil interaction is computed according to Equation 2-34.

Equation 2-34: $y_{th,free} = \alpha_p \cdot \Delta T \cdot L_{np}$

Where ΔT is the temperature difference evaluated as an average of the temperature differences along pile's depth in °C and L_{np} is the depth of the NP with respect to pile's head in the same units of the displacement.

ΔTs considered are the maximum thermal variations, applied to the pile, occurring during a thermal cycle. In case of the in situ test they are computed as the difference between the initial undisturbed soil temperature and, the maximum temperature (in case of heating) or minimum temperature (in case of cooling) applied to the pile during the thermal cycles.

Comparing *DSR* and *DOFs* a complementarity of thermal deformation restraint and mobilised stress change is expected. In other words, larger pile head movements are associated with lower internal stress change.

2.2.3 Experimental observations about in situ thermo-mechanical response of isolated piles

Site investigation studies provide several experimental data that are used to investigate about the thermo-mechanical response of single energy pile. Dimensionless ratios DOF, DDR and DSR have been computed as key parameters for assessing structural impacts (DSR), potential impacts on the overlying structure (DDR and DOF) (Bourne Webb and Bodas Freitas, 2020) and constraint action of soil on pile free expansion or contraction (DOF).

The tests carried out in Losanne and reported by Laloui et al. (2003,2006) and Amatya et al. (2012), described in the previous paragraph, provide several experimental data obtained from in situ measurements. DDRs are computed considering the maximum thermal variations that occur during each thermal test (test 1, test 2, tests 3, tests 4, test 5, test 6 and test 7) for the heating mode. DOFs are computed for five different depths. DDR Computed by Bourne Webb and Bodas Freitas (2020) agree with DDRs computed considering the pile's head displacements and the maximum thermal variations.

DSRs increase during the construction steps. During heating, the increasing of mechanical loading determines a reduction of head displacement (DSR) and thermal strains and increase of thermal axial stress observed as DSRs increase. During the construction Step a decrease of the DOFs is observed at all depths along pile length. At pile toe the variation the DOF is almost negligible demonstrating that the different restraint provided by the foundation system during the construction steps lightly influence the allowed thermal strain at toe.

Lambeth college experimental test reported by Bourne-webb et al. (2009) are used to evaluate DDRs for cooling and heating phase. To evaluate DDR, NP positions were obtained from the profile of the axial load reported by the authors assuming NP position corresponding to the depth at which the maximum thermal load occurred. DDR in case of heating is two times those reported in the review of Bourne-Webb (2019) and it is connected to the hypothesis about NP position. From the restrained thermal strains reported by the authors, the observed thermal strains of pile are computed assuming constant $\triangle$Ts along pile's depth thus allowing DOFs estimation too. Along pile's mid depth (z/L=0.5) DOFs computed during heating are smaller than DOFs computed during cooling. DSR were computed considering the maximum stresses developed along pile's shaft at the end of cooling and heating. It is highlighted that during cooling, tensile stresses are observed with maximum value at pile's toe (about 300 kN).

Thermal tests performed by Wang et al. (2015) allow computing DOFs and DSR during the peak of long-term and short-term heating for four different depths. For the computation of the dimensionless ratios a constant $\triangle$T was assumed along pile depth both for long-term (52 days) and short-term heating (9 days). DSRs are computed considering the minimum thermal strains and free thermal elongation of the pile. Minimum thermal strain is observed at a depth of 5.4 m from pile's head. Even if Pile's Young modulus was not reported in this study, in the subsequent research carried out on the same model pile (Faizal et al. 2016), the authors stated that 30 Gpa Young's Modulus can be assumed for the concrete. From the Computation of the DOFs it is observed that the greater DOFs occurred at all depths for the long-term heating with respect to the short term.

Faizal et al. (2016) analysed the thermo-mechanical and energetic aspect of three different kinds of operation mode: 24 h, 16 h and 8 h. DOFs are computed for three different depths that corresponded to the position of thermal strains and temperature measurements. DOFs increase with the number of thermal cycles while DSRs decrease with increasing thermal cycles. This trend was observed for each operating mode.

Faizal et al. (2019) presented the results of full-scale test carried out at Monash University the same site of previous studies (Faizal et al., (2016) and Wang et al., (2014)). The authors focused on different aspects of the thermo-mechanical interaction as the cyclic behavior, the effect of radial expansion or contraction of the pile on the skin friction of the pile and the temperature distribution in the cross sectional of the pile and its effect on thermal stresses distribution. The data provided by this study allow computing DOFs and DSR both for heating and cooling modes. These two dimensionless parameters are reported for the first thermal cycle both for heating and cooling mode.

Sutman et al. (2019) investigated the effects of restrictions of pile head and toe through site tests. The authors provided degree of freedom (DOF) computed for each VWG level. According to the authors of the test the test the restriction action at the head and throughout the pile is connected to the application of the mechanical loading. The effect of the mechanical loading can determine a different mobilization of the shaft friction along pile's length, but it does not provide any cinematic restrain to the expansion or contraction of the pile at its head. If the Pile is heated and mechanical loading are applied at the head the mobilization of the shaft friction can be evaluated separating the effect of the mechanical load and thermal load. In the part above the NP position thermal heating load determines downward shaft friction while mechanical loading determines upward shaft friction. Therefore, the global mobilised shaft friction in the upper part of the pile will be different in the case of thermomechanical and purely thermal heating loads leading to a global different constraint action and observed displacement. In the upper part of TP-1 (at the first 8.9 m) DOFs are always larger than those computed for TP-3. Proceeding further down, the two piles have almost the same DOFs since the effect of the mechanical load is less pronounced. For TP-2, DOF near to pile head is larger for cooling episode (0.90) than for heating episode (0.79). Along TP-2's depth DOFs decrease and subsequently increase next to pile's toe about 0.85 both for heating and cooling. This trend was observed also for TP-1 and TP-3 therefore it could be connected to the pile's execution technique of each test piles and not only to the stiffness properties of the different soil layers (very dense sand in the case of TP-1 and TP-3 and very stiff clay in the case of TP-2). It should be outlined that even if the trend of the DOFs profiles is similar for each test pile the effect of the different stiffness of soil layer at pile's tip is noticed comparing the magnitude of the DOFs for the three cases. in the case of TP-2 DOF at pile's tip is about 116% of TP-1 and TP-2 DOF. DSRS are computed considering the maximum thermal stress along TP-1, TP-2 and TP-3. For TP-1 the maximum DSR is observed at 7.80 m and both for cooling and heating episodes is about 0.4. For TP-2, DSR is about 0.3 during heating and 0.26 during cooling at depth ranging between 2.70 m and 5.80 m. During heating of TP-3 the maximum DSR is observed close to pile's head (0.8). During cooling of TP-3 DSR at pile's head is about 0.20 and it is maximum at 8.9 m depth (0.38). DOFs and DSRs have exact opposite behavior.

In the case by de Santiago et al. (2016) the moment indicated as Cb, where the maximum thermal variation occurs, is considered to evaluate DDR, DSR and DOF. The strains measured along pile shaft allow evaluating the total pile's elongation that is 1.6 mm. The maximum thermal stress, obtained in the Clays and Gravels layer, is observed at depth of about 13 m. DDR is obtained considering the NP position and an average ΔT along pile length. DOFs are computed along pile's depth as ratio between the observed thermal strains to free thermal elongation reported by the authors. DOFs decrease along pile's depth as soil constraint action on pile's elongation increase with depth.

Akrouch et al. (2014) performed tension load tests on pile, at different mechanical and heating loadings. Strains and temperature distribution during the tests were monitored at different positions but data were reported by the authors only at 1.4 m and 2.4 m depth from pile head and only for tests 4 and 5. Increasing DOF is observed with increasing tension load. DSRs are computed, for each of the five thermo-mechanical tests, considering the pile's head displacements reported by the authors.

Murphy et al. (2015) investigated the thermo-mechanical behavior of three EPs during building operations. For this study DSR, DOFs, DSRs are computed for foundation 1, foundation 3 and foundation 4 for the maximum thermal variation during heating (18-19 °C). During the cooling of the pile, because of the preceding heating phase all the piles are characterised by shortening strains that decrease with increase of cooling. The profiles of foundation temperature reported by the authors show that the temperature is relatively constant along depth, in except for the base of the foundations, and slight variations in the top of the foundation due to surface temperature effects (Murphy et al., 2015). Therefore, a constant ΔT was assumed along pile's depth for each foundation. Displacement of the head of the pile was calculated by integrating the thermal axial strain profiles (Murphy et al., 2015). Maximum displacements and strains are observed for foundation 3. For foundation 4 and foundation 1 smaller displacements are observed demonstrating the influence of the head restraint provided by adjacent piles. DSR for each foundation during the peak heating were computed assuming the NP position between 11 m and 13 m from piles' head. DOFs are computed for each foundation and maximum values correspond to those calculated for foundation 3.

In the case by Jiang et al. (2021) it was possible to compute DSR for each level of mechanical loads and both during cooling and heating modes. During heating the increase of the mechanical loads determine a decrease of DSR while during cooling modes the increase of the mechanical load level determines larger DSR.

DDRs are computed as described above and reported in Figure 2-30 versus the computed thermal variation ΔT in °C.

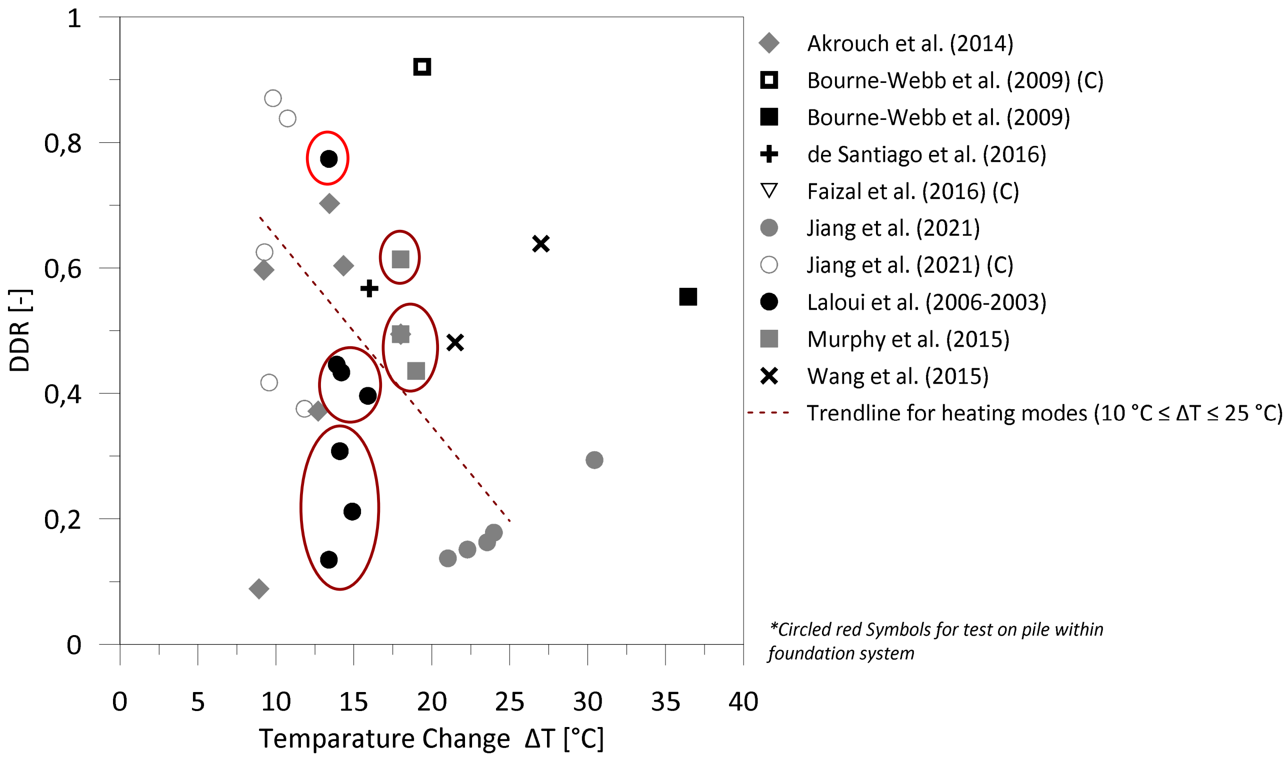

Figure 2-30: DDRs versus temperature computed for site investigations.

The temperature difference plotted in Figure 2-30 is considered in absolute value i.e., positive thermal variations are reported both for heating and cooling modes. As could be observed by the data reported in Figure 2-30, the larger DDR are observed in the case of cooling. Even if a potential influence of subsoil nature and test condition and last but not least pile's technology could be likely hypothesized the available data do not allow a clear summary. This finding was also highlighted by Bourne-webb et al. (2019) in their review study. On the average the DDR for cooling cases was about 65 %. In case of heating the DDR is more scattered and cover the range between 10% and 80% with and average weighted value slightly less than 40%. The maximum DDR in case of heating is observed in the case of Laloui et al. (2006) for the test 1 where null mechanical load is applied. The progressive construction of the overlying building between each thermal heating test (test 1 to test 7) suppressed the observed pile head movement as could be observed comparing DDR without load (circled light red symbol) to DDRs computed when mechanical loads are applied (circled dark red symbol). Of course, as it could be expected, the movement limit defined by the pile head being perfectly unrestrained appears a reasonable upper limit for both heating and cooling (Bourne-webb et al., 2019).In the case of heating mode, between 10 °C and 25 °C where more date are available, DDR decreases with increasing ΔT as plotted in Figure 2-30 by the dotted red line.

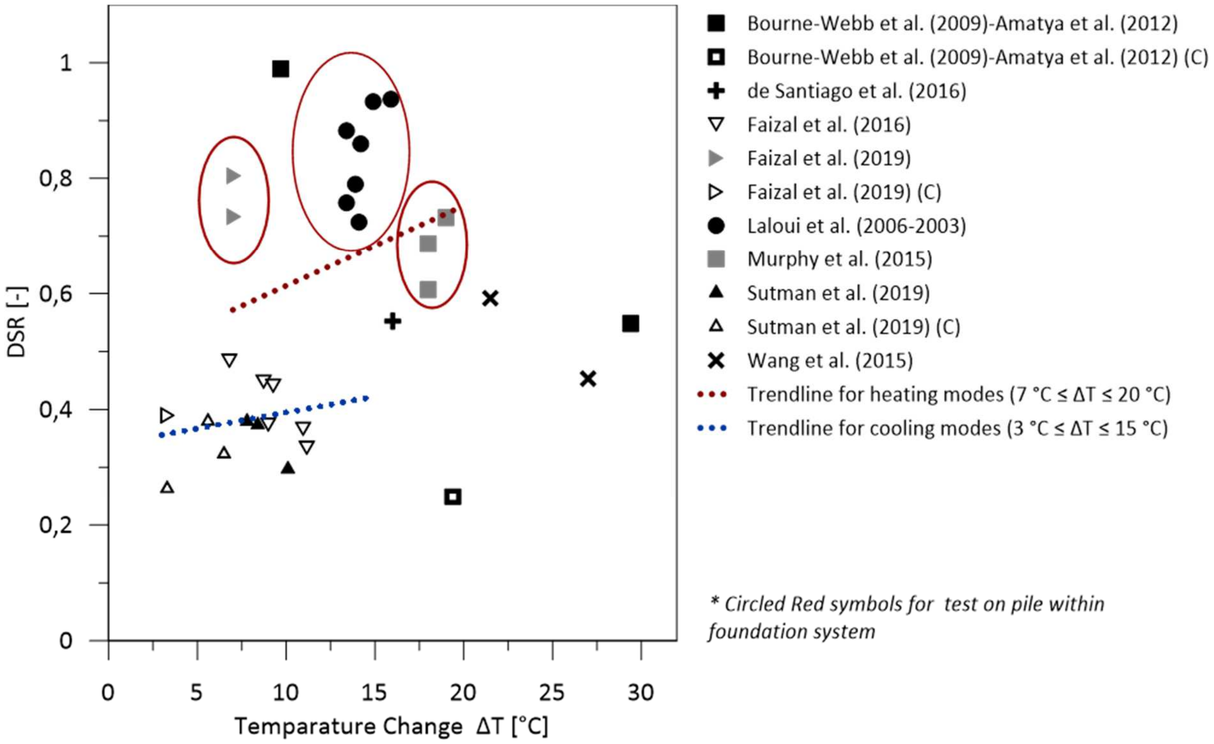

Figure 2-31: DSRs computed from data of site investigations test for both heating and cooling (C) modes.

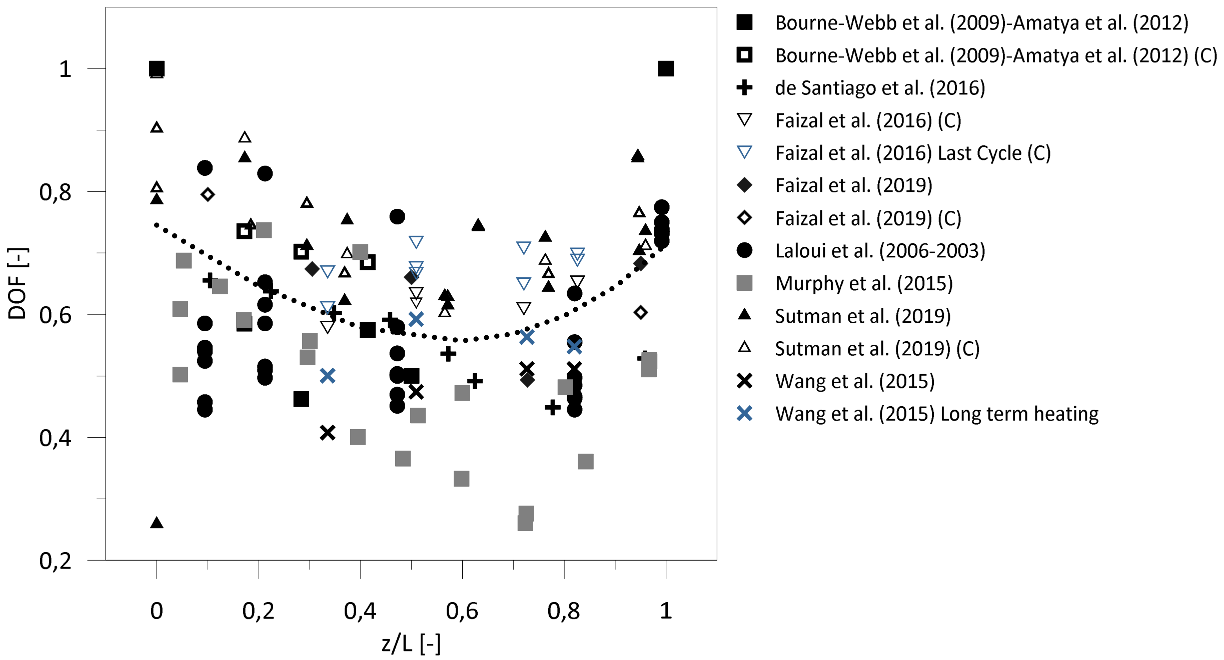

Figure 2-32:DOFs data versus z/L dimensionless depth.

The DSRs are summarized in Figure 2-31, for the case of cooling smaller and less scattered DSRs are calculated by the experimental data. In Figure 2-31 linear regression is plotted for the cooling data between 3 °C and 15 °C where more data are available. With increasing temperature changes, in absolute value, DSR slightly increases. For cooling episodes the DSR ranges between 20% and 50% with a weighted average slightly less than 40%. In the case of heating the maximum thermal induced stress ranges between 40%-100% of the ideal thermal stress induced in a perfectly constrained condition ($\sigma_{th,fixed}$). With increasing △Ts, as in the case of cooling, an increase of DSR is observed (Dotted red line in Figure 2-31).

Finally, DOFs are reported as function of the dimensionless depth z/L defined as the ratio between the depth of measure with respect to the total pile length (Figure 2-32). z/L=0 corresponds to the head of the pile while z/L=1 corresponds to pile's toe. The experimental studies of Faizal et al. (2016) and Wang (2015) provide thermal strains along pile depth for subsequent thermal cycles and for short term and long-term heating, respectively. DOFs computed for subsequent thermal cycles are reported with coloured blue symbols while the black ones correspond to the first cycle. Maximum DOFs among the collected cases are found for the sink pile installed at Lambeth college (Amatya et al. (2012)). From the experimental data reported the maximum local thermal strain are observed both at pile's head and toe. The fact that the pile's head is free to deform matches with the fact that at pile's head no external constraint are present. At pile toe the DOFs range in the same field found for the pile head, i.e., 45%-100%. At the pile's toe may be less expected than in some cases the DOF is close to one certifying that the soil does not exert any constraint to the free expansion of the pile. The less constraint at pile's toe could be caused to issues during the excavation and concreting in the case of displacement piles. Smaller DOFs are expected in the case of driven pile or for pile with socket depth in hard soils or soft rocks. The latter case is not among the experimental studies investigated while driven EP were employed by de Santiago et al. (2016) and Jiang et al. (2021). Experimental data to compute the DOF at pile's tip of driven pile was provided only by Santiago e al. (2016) close to pile's tip a reduction of the DOF occurred with respect to shallower depth demonstrating the influence of pile's technology. For all the experimental investigations close head DOFs range between 45% and 100% leaving apart a few points. The smaller DOF occurred in the experimental test where the pile belongs to a foundation system e.g., Laloui et al. (2006) and Murphy et al. (2015).

The data of computed DOFs reported in Figure 2-32, however, can be summarized considering that, apart from some outliers the general distribution with depth is described by a concave shape which gets the lower values in the middle of the pile (about 0.60) and moves from 0.75 and 0.70 at the pile head and toe, respectively.

2.3 *Small scale Physical modelling for EPs*

The thermo-mechanical behavior of pile foundation has been largely studied also by small-scale tests. They are valuable tools, especially for research purposes, to study soil-pile interaction in a controlled environment and thus limiting the unknown variables. Advanced physical models may be used to establish predictions of soil-structure interaction, environmental geotechnical response and for problems that can benefit from a multi-scaled, multi-modelling method approach (Mayne *et al.*, 2009)

Early physical modelling focused on small scale model tests to investigate processes, explore physical response to loading and to develop fundamental in soil mechanics, i.e., for example lateral earth pressure (Terzaghi, 1934) or bearing capacity of shallow foundation (Vesic, 1963).

Several Physical models at laboratory scale are possible: 1g small scale models, calibration chamber models and 1 g shaking table or centrifuge models. Each of these models is characterised by advantages and disadvantages. Among these approaches this study is focused on physical modelling at small scale under 1g mainly because most of the available studies are made on such models. In all the experimental studies the model piles and the soil are placed in a container box and the soil surface is free of stress. The geometry of the model implies that the stress state in the soil is significantly lower than that in the field, this affects the soil pile interaction since the mechanical behavior of the interface is influenced by the stress range (Laloui and Di Donna, 2013). Such models are suitable for making predictions in which in situ stress is not greatly significant (Mayne et al. 2009). The lack of scale factors for generalising the results obtained via a little model to a prototype is another limiting factor for this kind of test. But on the other hand, they provide the possibility of doing tests under known stress strain histories and controlled boundary conditions differently from in situ testing. In several cases, soil is contained in a tank of rigid walls, and the deformation of tank's walls is considered negligible under mechanical loading of the pile.

The diameter of the pile and the soil's container should be chosen in a way that minimizes boundary effect and minimize the effect of rigid walls to minimize the size effect.

Physical modelling has been largely used to investigate the behavior of EPs from different perspectives as thermal exchange and energy performances and thermo-mechanical interaction between pile and soil. In both cases the boundary conditions connected to the heat transfer should be considered. A small boundary distance can certainly affect both thermal and mechanical performance of a model geothermal pile or at least, limit the thermal response study only to the short term behavior (Kramer and Basu, 2014). Common solutions that allow to neglect thermal boundary effects are using a soil container large enough to consider that the temperature at walls and bottom does not induce any thermal variation or using tank's walls and bottom thermally insulated.

In terms of thermal boundary effects, the heat transfer at the soil surface should be considered as a design parameter for the test. When the soil surface is on direct contact to the laboratory room environment the effects of room temperature should be considered in the evaluation of the heat exchange process. Wang, et al., (2011) show that a fluctuation of approximately 2°C to 3 °C of room temperature between 10 and 17 hours causes a change in soil temperature of about 0.5 °C- 1 °C.

2.3.1 Small scale test case studies: layout of the tests and experimental results

Different experimental studies on small scale energy piles are presented and summarized in this section. For each test the setup of the tests, the soil and pile properties, the thermal and mechanical loadings applied, and main experimental results are briefly described. All the tests considered in this study are listed in Table 2-6. The material, behavior (floating or end bearing) and the size of small-scale energy piles, the soil type and condition (dry, saturated or unsaturated) and the primary circuit material and configuration are reported (Table 2-6).

Table 2-6: Experimental research considered in this study

		Pile			***Soil***			***Primary Circuit***	
Authors	**Test**	*Material and behavior*	*d [mm]*	*L [mm]*	*type*	*condition*	*DR or Ip [-]*	*material*	*configuration*
Kalantidou et al. 2012	4	Aluminium (floating)	20	600	*sand*	*dry*	46%	Polyethilene	U
Yavari et al. 2014	2	Aluminium (floatig)	20	600	*sand*	*dry*	50%	aluminium	U
Yavari et al. 2016	5	Aluminium (floating)	20	600	*clay*	*saturated*	24%	aluminium	U

Nguyen et al. 2017	4	Aluminium (floating)	20	600	*sand*	*dry*	50%	aluminium	U
Liu et al. 2018	4	Concrete (floating)	104	1400	*sand*	*satured*	64%	Polyethilene and Polyethilene embedded in steel	U
Fei and Dai 2018	1	Cement Mortar (floating)	100	900	*sand*	*dry*	30%	Polyethilene	U
Bao et al. 2020	1	Precast Concrete (floating)	200	1300	*sand*	*satured*	62%	Polyethilene	Double U
Huang et al. 2018	4	Aluminium (Floating)	50	1000	*sand*	*saturated*	80%	Copper	U
Wu et al. 2018	6	Aluminium (floating and end bearing)	23	450	*lower layer sand and upper layer clay*	*saturated*	69% and 26,9	Copper	U
Wang et al. 2016	2	Concrete (floating)	104	1400	*Najing Sand*	*dry*	63%	Polyethilene	U
Wang et al. 2017	3	Aluminium (floating)	104	1400	*Najing Sand*	*dry*	61%	Polyethilene	U, spiral and W

Thermo-mechanical behavior of energy piles through physical modelling was firstly investigated by Kalantidou et al. (2012). Four small scale tests were performed on aluminium pile in dry sand subjected to thermal and mechanical loadings. During the four tests: Test 1, Test 2, Test 3 and Test 4, mechanical loadings of 0 N, 200 N, 400 N and 500 N were applied, respectively. The pile's head displacement measured during the four tests are reported in Figure 2-33. The small pile is an aluminium closed end pile equipped with a metallic "U" tube. The ultimate load of the pile is assumed to be 525 N that corresponds to a head settlement of 10% D. The experimental box was filled with dry Fointainblue sand deposed at 46% relative density. The sand initial temperature was fixed to 25 °C. The temperature variations applied to the pile are in the range of 25 ° C to 53 °C. Two thermal cycles of heating and cooling were applied to the pile through circulating water within the PC. The experimental responses showed that when the mechanical load is less than 40% of the ultimate resistance the behavior of the pile is thermo-elastic, while, when the mechanical loads exceed 40% of the ultimate resistance the observed response is thermo-plastic because the temperature induced strains are partially non reversible. According to the authors the effect of many cycles of loading needs to be investigated to confirm their finding and further work is needed to decouple temperature effects and creep. An analysis on the time dependent behavior of the pile in Tests 1 and 2 showed a slight difference between the first and the second thermal cycle of each test.

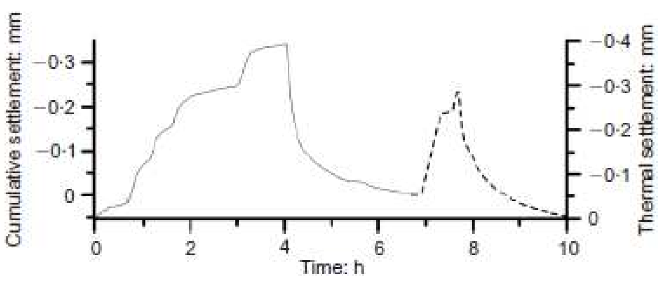

(a)

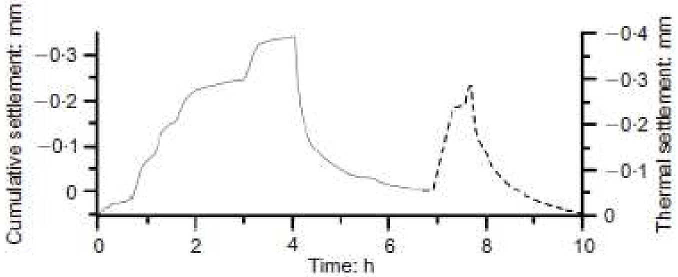

(b)

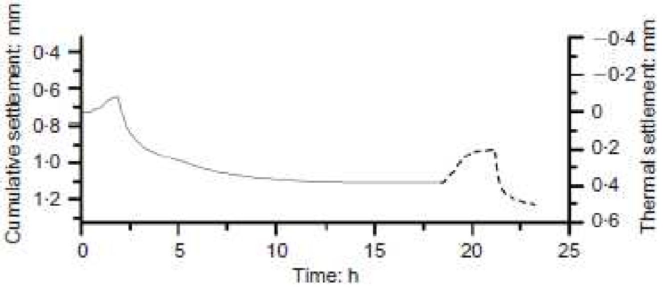

(c)

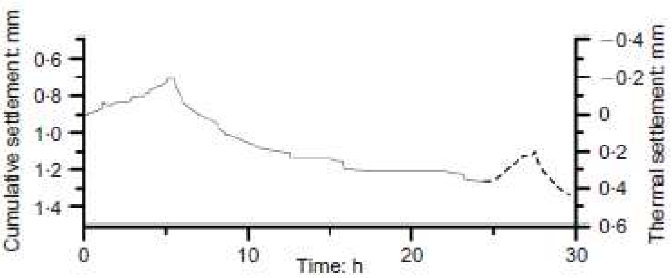

(d)

Figure 2-33: Pile's head thermal and cumulative displacements from Kalantidou et al. (2012) measured during tests: (a) Test 1, (b) Test 2, (c) Test 3 and (d) Test 4.

Yavari et al. (2014) reported a study on a model pile similar to that presented by Kalantidou et al. (2012). Three set of experiments are reported: purely mechanical test where the pile is loaded axially until failure (E1), pure thermal test (E2) where only thermal loadings are applied to the pile and thermo-mechanical tests (E3, E4, E5, E6 and E7) where constant vertical load are combined to thermal loadings. From E2 to E7 the axial head load ranges between 0 to 70% of the pile estimated bearing capacity.

The model pile was a closed-end aluminium tube of 800 mm length with outer and inner diameters of 20 mm and 18 mm, respectively. The pile was embedded only for 600 mm in the soil, a "U" shaped thin aluminium tube containing water was installed inside it. The pile-soil bearing capacity, (450 N), was conventionally taken as the load that corresponds to a vertical displacement equal to 10% of the pile diameter (2 mm), under the ambient temperature (Yavari et al., 2014). The soil filling the cylindrical experimental container is dry Fontainebleau sand compacted at 50 % of relatively density.

Yavari et al. (2014) reported the time histories of the thermal variations only for the test E2 (at zero head load) and test E6 (at 250 N). For this reason, only data from these two tests were analysed in this study. Pile's head displacements measured during the thermal test (E2) and thermo-mechanical test (E6) are reported in Figure 2-34.

During test E2 two thermal cycles were applied to the pile as follows: a cooling phase down to 6 °C, a heating phase up to 31°C, a cooling phase down to 13 °C, a heating phase up to 31°C and a cooling phase down to 13

°C. During test E6 two thermal cycles were applied to the pile, during each cycle a cooling phase down to 14 °C and a heating phase up to 30°C were performed.

In the case of test E2, heaves and settlements observed during the first and second cycle are of the same amount, showing a reversible thermo-mechanical response. In the case of test E6 irreversible settlement occurs already in the first thermal cycle and increases further in the second thermal cycle, there is a clear coupling between mechanical and thermal loading.

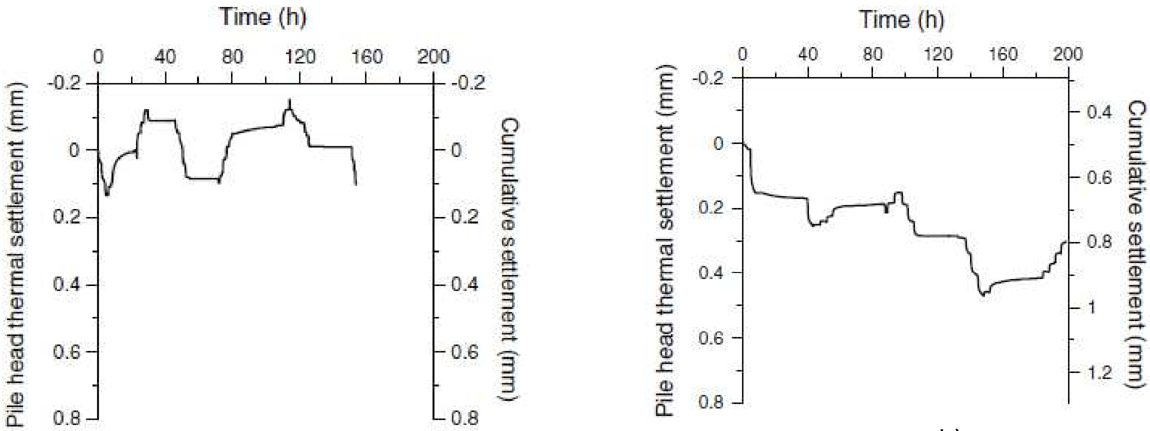

a) b)

Figure 2-34: Pile's head thermal and cumulative displacements from Yavari et al. (2014) measured during tests E2 a) and E6 b).

Yavari et al. (2016**)** reported the results of seven experimental tests performed using a layout similar to those used by Yavari et al. (2014). The geometry of the model pile and primary circuit are the same of that used by Yavari et al. (2014) but saturated Kaolin clay with a liquid limit and plastic limit of 57% and 33%, respectively, was used. Different kinds of test were carried out: two mechanical tests (tests F1 and F2) and five thermo-mechanical tests with a constant mechanical load of 100 N (test F3), 150 N (test F4), 200 N (test F5), 250 N (test F6) and 300 N (test F7), respectively. From the results of test F1 and F2, considering 2 mm as the pile settlement at failure, the pile's resistance can be estimated as 500-550 N. Each thermomechanical test included the following steps: increase of the axial load to a given value, which was maintained constant during the subsequent thermal cycle, heating the pile from 22 °C to about 27 °C, cooling the pile to about 17 °C and then heating the pile to its initial temperature (22 °C). Pile's head displacements measured during all the tests are reported in Figure 2-35 (Yavari *et al.*, 2016). From the experimental results presented by the authors seems that the pile immediately reacts to the temperature change and heaves with the first heating. When the pile is cooled it settles and under low mechanical loading, 100 N, the slope of the cooling brunch is close to that of the heating. This slope becomes higher at higher pile's head loadings.

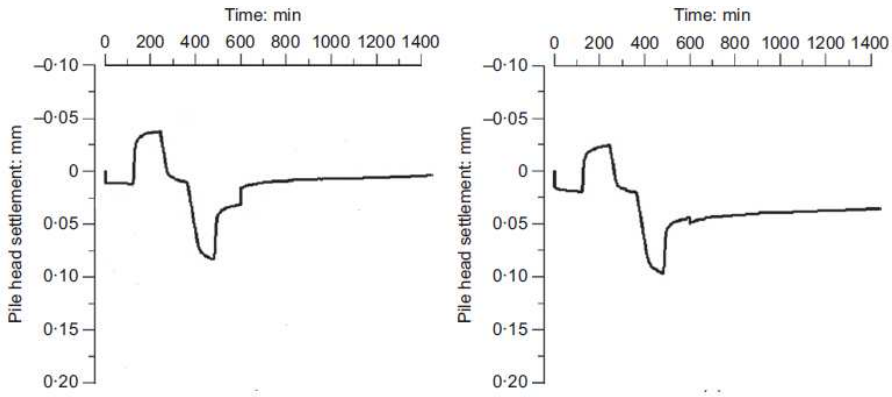

a) b)

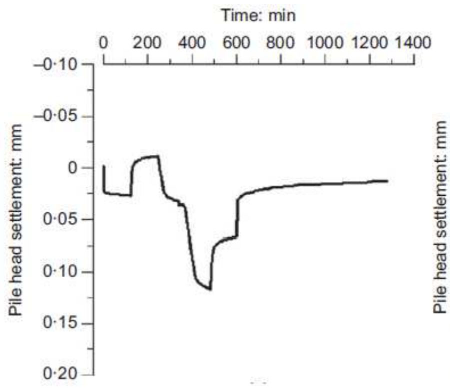

c)

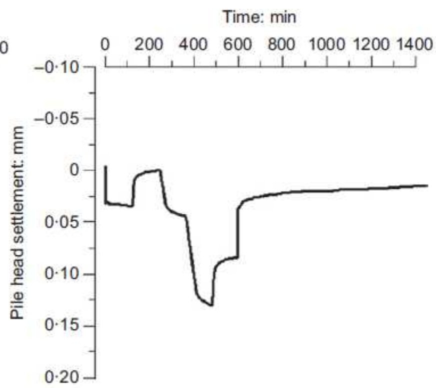

d)

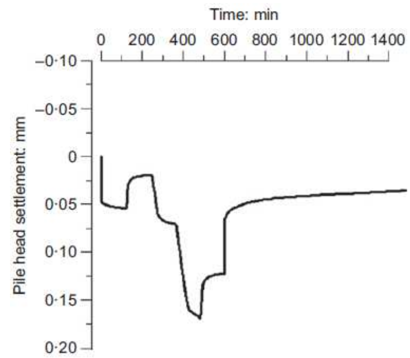

e)

Figure 2-35: Pile's head cumulative displacements from Yavari et al. (2016) measured during tests F3 a), F4 b), F5 c), F6 d) and F7 e).

Nguyen et al. (2017) investigated the behavior of a small-scale EP installed in dry sand and subjected to 30 thermal cycles applied while the pile's head load was maintained at 0, 20, 40 and 60% of the pile ultimate bearing capacity, respectively. The pile ultimate bearing capacity estimated through mechanical load test is assumed 500 N corresponding to a pile's head settlement of 2 mm. The pile is an aluminium tube sealed at the bottom of 600 mm length, with internal and external of 18 mm and 20 mm, respectively. A metallic U tube is used as heat exchanger and the entire pile was filled with water. The soil sample was Fointainbleau sand at relatively density of 46%. Before starting thermal tests, pile's temperature was fixed at 20°C for two days to ensure the homogeneity of temperature distribution inside the experimental box. After this phase, the pile was first heated from 20°C to 21 °C (for 4 hours) and then cooled to 19°C (for 4 hours), finally the initial temperature was imposed to for at least 16 hours. Thirty thermal cycles were applied to the pile. Thermo-mechanical tests were performed in successive stage. First 100 N axial head load was applied to the pile and kept constant then the same thirty thermal cycles were applied. The same procedure was repeated at pile head loads of 200 N and 300 N. This is considered as one thermo-mechanical test named by the authors as T3. The results of the pile head settlement during the first thermal cycle for the different level of stress reported by the authors are shown in Figure 2-36.

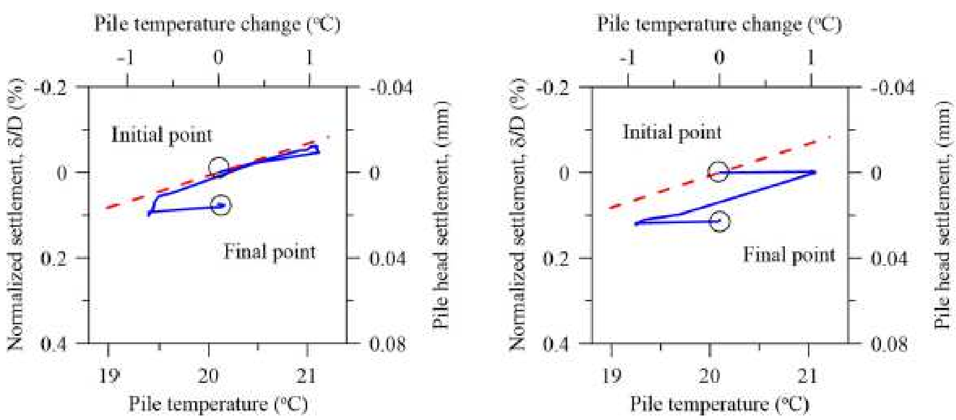

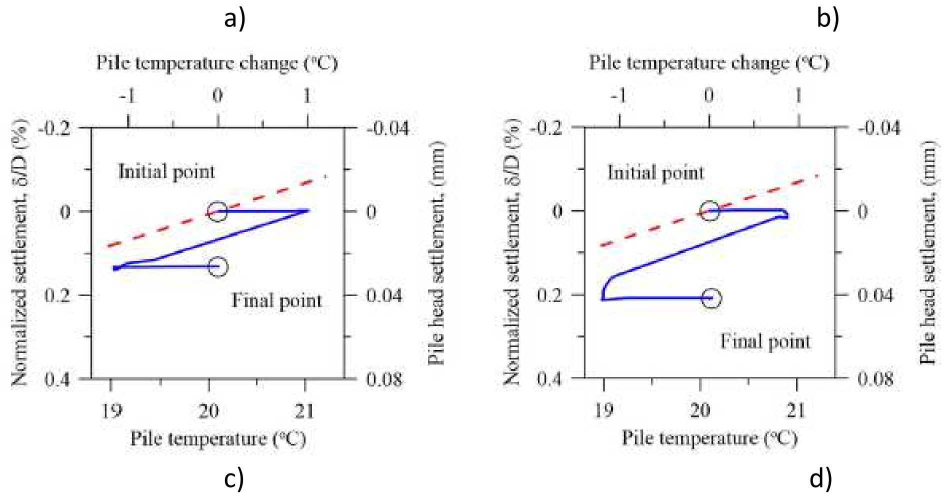

Figure 2-36: Pile's head thermal displacements (blu line) and pile thermal expansion curve (red dotted line) during the first thermal cycle from Nguyen et al. (2017):Thermal test without mechanical load applied at pile's head a) ; thermo-mechanical test with a mechanical load applied to the pile's head of 100 N; b); thermo-mechanical test with a mechanical load applied to the pile's head of 200 N c); thermo-mechanical test with a mechanical load applied to the pile's head of 200 N d) .

Figure 2-36 shows that the pile head heaves only when the mechanical loading applied is zero, while cooling induces a settlement that follows the pile's temperature variation. For all the level of stress it could be observed that the first heating/cooling cycle induces irreversible displacements. The residual displacements are negligible only in the case of zero mechanical loading.

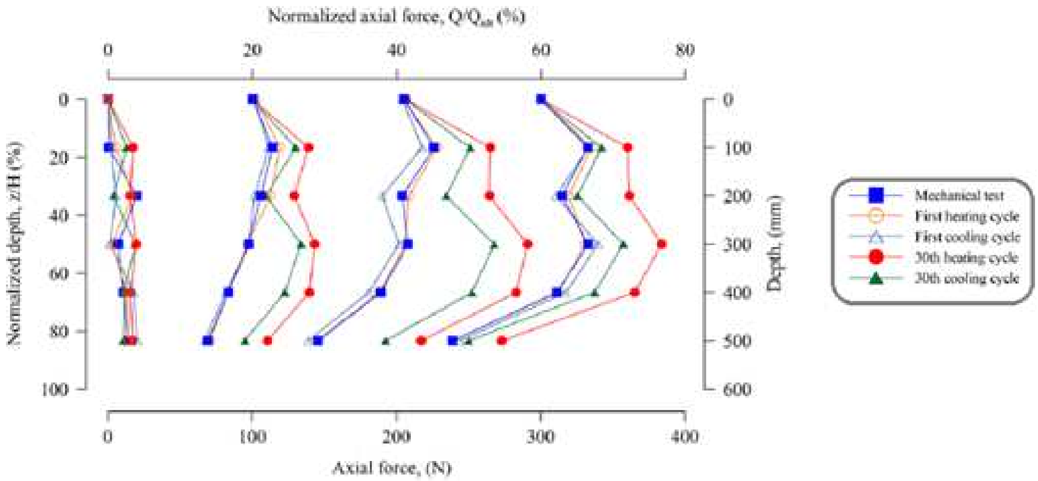

Figure 2-37:Axial force profile during thermal cycle from Nguyen et al. (2017).

The axial load along the pile shaft reported by the authors, at the end of first cooling and heating cycle and at the end of the 30th heating and cooling cycle for different level of mechanical loading (0 % Q_{ult} ,20% Q_{ult} ,40 %$Q_{ult,}$ and 60 % Q_{ult}) are shown in Figure 2-37. Both cooling and heating induce very small compressive stresses (Nguyen et al., 2017). In the cases of SF=5, SF=2.5 and SF=1.7 a slight increase of the axial force is observed at the end of the first heating comparing the thermo-mechanical axial loading to the mechanical axial loading. At the end of cooling an opposite trend is observed (a slight decrease). In all the thermomechanical cases at the end of the 30th cycle the axial loading increases both in case of cooling and heating.

Liu et al. (2018) studied the thermo-mechanical behavior of two model EPs in saturated sand characterised by the same geometry but different configuration of the PC. The response of a small EP equipped with the heat exchangers attached to reinforcing cages (conventional energy pile) was compared to an EP equipped with exchanger pipes embedded in steel tubes (improved energy pile). According to the authors the improved EP can protect the pipes from being damaged during the construction process and the steel tubes are also helpful to reduce concrete corrosion. The model piles were concrete piles with an embedded length of 1400 mm and 104 mm diameter. In the model test medium dense Najing sand was used. The two piles were tested with and without mechanical loading applied to the pile head. The mechanical load of 10 kN was applied to each pile in increment of 1kN.The thermal loading was applied circulating water at temperature between 55 °C and 4 °C. Heaves and settlements were measured during heating and cooling, respectively (Figure 2-38). According to the authors, comparing the thermal tests with the thermo mechanical tests it is shown that the mechanical loads influence the magnitude of pile's head displacement. Without vertical loading the pile's heaves were greater than the displacements that occur with a mechanical load. The opposite trend it is observed during cooling: the settlements were lower in the case of null mechanical loadings.

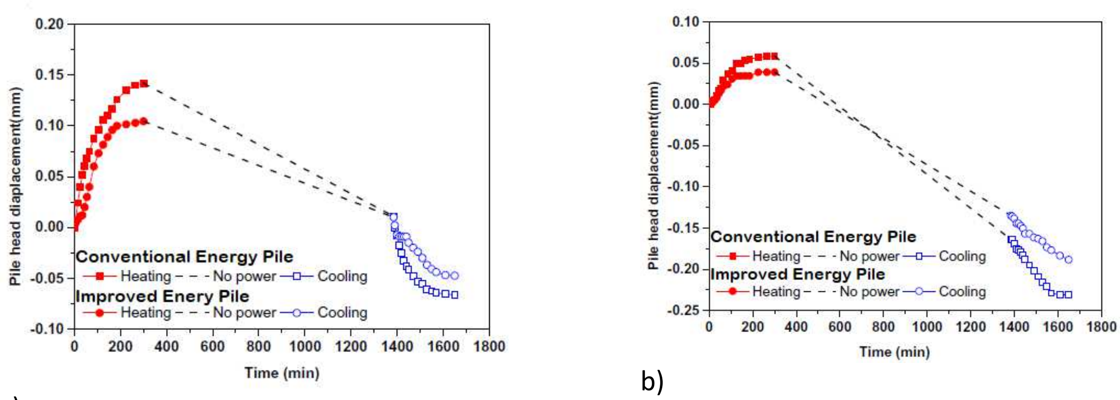

b)

a)

Figure 2-38:thermal displacements of pile's head from Liu et al. (2018): a) thermal displacements measured during thermal test for conventional and improved energy pile; b) thermal displacements measured during thermo-mechanical tests for conventional and improved energy pile.

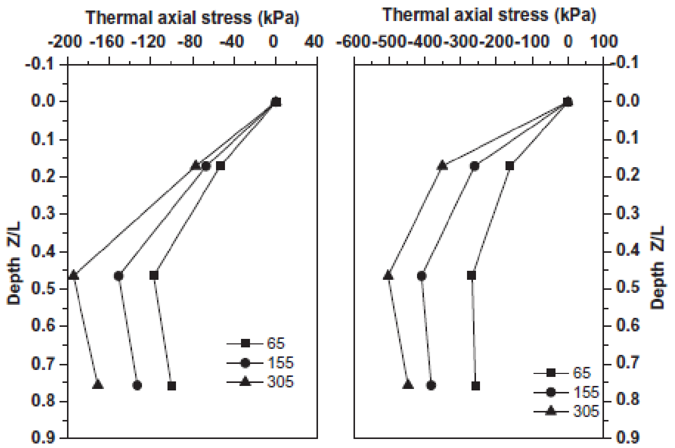

a) b)

Figure 2-39: thermal axial stress along the improved energy piles for heating mode: a) Without mechanical load b) with mechanical load from Liu et al. (2019).

During heating and cooling, the two piles showed similar thermal responses, but the conventional energy pile generally changed a little more severely than the improved one (Liu *et al.*, 2018). The thermal stress distribution reported by the authors is shown in Figure 2-39 for different instants of time of the heating mode during thermal cycle for the improved energy pile.

The compressive stress produced during heating was negative while the tension stress produced during cooling was positive. Under null mechanical load the thermal stress at depth z/L=0 was defined as 0 kPa because free expansion at pile head was assumed. With mechanical load, the same assumption was adopted because of the slight stiffness constraint at pile head. The thermal stress during heating is compressive and increases with time whether a mechanical load is applied or not. The constrain effect of the soil is more significant in the lower half of the pile than the upper part in fact larger thermal stresses are observed in the lower half.

The thermal stress distribution for the improved energy pile is shown in Figure 2-40 considering different instants of time of the cooling mode during thermal cycle.

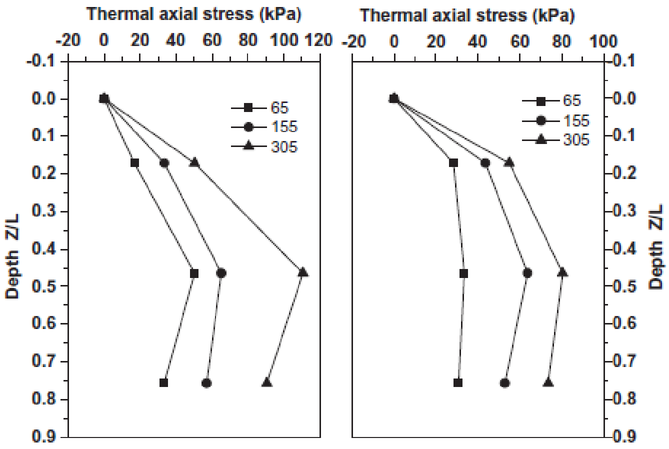

Figure 2-40: Thermal axial stress along the improved energy piles for cooling mode: a) Without mechanical load b) with mechanical load from Liu et al. (2019)

Fei and Dai (2018) performed small scale tests to obtain insights into the effects of thermal cycles on the settlement and the capacity of EPs. Two kinds of test were performed: vertical load tests (mechanical test) and then thermo mechanical tests at a working load of 0.8 kN. The thermo mechanical tests were carried out applying to the pile three thermal cycles lasting 24 hours each. The model pile was 1000 mm long, with an embedded length of 900 mm, and 100 mm in diameter and was made of cement mortar. From the mechanical test the pile ultimate resistance was found to be 1.70 kN. The soil used in the experimental tests was Yangzhou dry sand rained to achieve a relative density of 30%. U- tube polyethylene pipes embedded in the pile were used as PC and the temperature of the pile was increased of about 15 °C by cycling hot water through these pipes. The heating mode was followed by a recovery phase where the initial temperature was decreased naturally to the indoor temperature. The pile's head displacements during the three thermal cycles reported are shown in Figure 2-41. First heating caused 0.06 mm of pile's head displacement smaller than the displacement computed considering that the pile is free to expand (Fei and Dai, 2018).

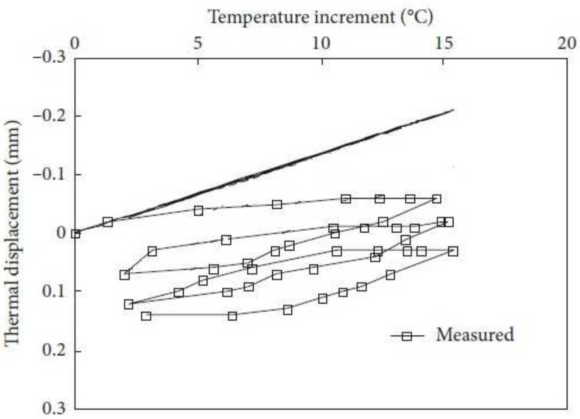

Figure 2-41: Pile's head thermal displacement during thermal cycles from Fei and Dai (2018).

During the cooling process the pile contracted, and the head of the pile settled. Figure 2-41 suggests that the cyclic temperature variation induces irreversible pile settlements. The measured displacements are compared to the pile's free thermal expansion (black straight line). At the end of the test the cumulative settlement was 0.14 mm which is approximately 44% of the settlement under mechanical loading (0.32 mm).

Bao et al. (2020) conducted model tests to evaluate the thermo-mechanical behavior of EPs. Mechanical and thermomechanical tests were carried out. In this study a large section concrete pile with a diameter of 200 mm and length of 1500 mm was pre-cast. The embedded depth of the pile was 1300 mm, and the top of the pile was 200 mm higher than soil surface. The thermal load is applied circulating fluid in a double-U-shaped polyethylene tube. The experiment involved the simulation of the summer cooling case for a structure from which thermal energy was drawn and injected into the soil through the pile. The soil is saturated silica sand poured into the model box at a relatively density of 62%. Prior to heating a dead load of 6 kN was applied to the pile determining 0.863 mm of head settlement. Heating tests were carried out with a constant inlet temperature of 55 °C. The initial room temperature of the soil was 31 °C. After heating for 48 hours, the temperature circulation control machine was turned off, and the pile naturally cooled down. Then three thermal cycles were carried out lasting 216 hours. The pile head displacements during the thermal cycles are reported in Figure 2-42. It could be noticed that the overall displacement was mainly upward with a value of approximately 0.02 mm at the end of the first cycle (Bao et al., 2020).

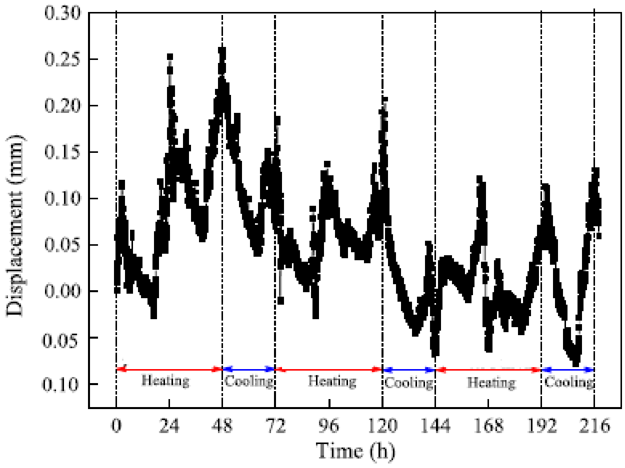

Figure 2-42: pile head thermal displacements during thermal cycles from Bao et al. (2020).

Strains of the pile were monitored at different locations in the cross section at depth of 433 mm and 866 mm below the soil surface. The relative temperature difference at the cross section of the pile was approximately 2 °C. Non-uniform distribution of the strain in the cross section indicated a large stress difference within the pile body, which may have an influence on the work function of energy pile when subjected to large loads.

Wu et al. (2019) investigated the thermo-mechanical behavior of EP under three kinds of climatic conditions through physical modelling.). Small-scale floating energy pile and small-scale end bearing energy pile embedded in normally consolidated clay were subjected to cyclic heating/cooling, heating/recovery and cooling/recovery to simulate the energy pile work in the regions of warm/cold balanced climate, warm-dominated climate and cold-dominated climate, respectively. The thermal response and the mechanical response of EP under different climatic conditions, as well as the different response between the floating energy pile and the end-bearing energy pile, were analysed (Wu *et al.*, 2019).

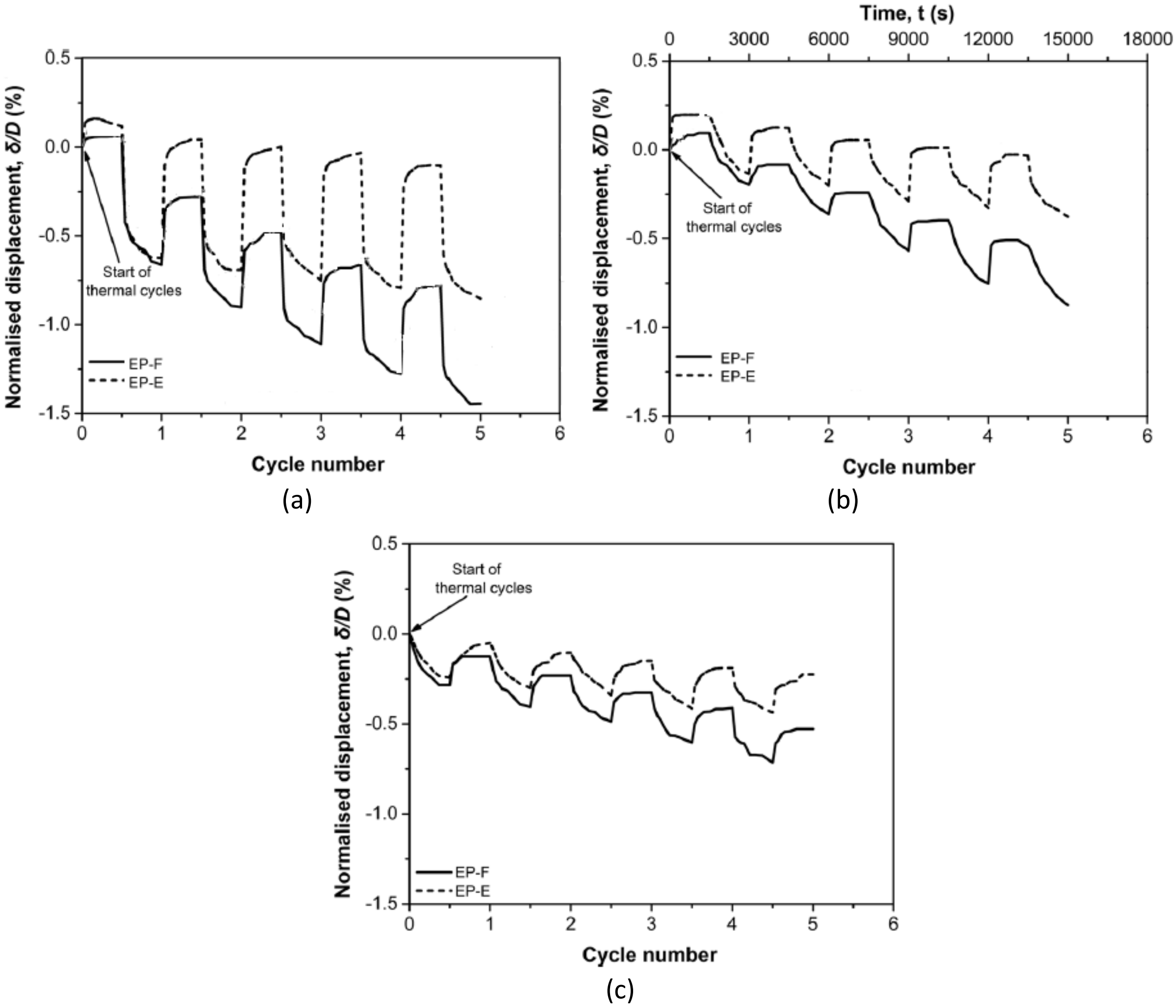

Figure 2-43: Normalised pile head displacement during heating-cooling cycle (a), heating cycle (b) and cooling cycle (c) for Floating Energy Pile (EP-F) and End bearing Energy Pile (E-EP) from Wu et al. (2019).

The small-scale instrumented energy pile was prefabricated from a steel tube with outer and inner diameters of 23 mm and 21 mm, respectively. The pile length was 550 mm, but only 450 mm was embedded in the soil. The heat exchanger was a U-shaped copper tube. Free expansion heating tests were performed to measure the free expansion of the pile (1.51×10^{5} °C^{-1}). 450 mm thickness of remolded clay was deposited on a layer of dense sand of 50 mm. The sand was pluviated and then saturated achieving a relatively density of 69%. Six thermo-mechanical tests (Test 1 – Test 6) and two reference tests (Test 7 and Test 8) were performed in this study. The reference tests are purely mechanical tests where piles were subjected to mechanical loadings at room temperature of 25 °C. During the thermo-mechanical tests, the pile was subjected to 147 N of working load and then to five thermal cycles of cyclic heating/cooling or heating/recovery or cooling/recovery. During these tests, temperature variations ranged between -20 °C and + 20 °C and the pile head moved correspondingly (Figure 2-43).

Huang et al. (2018) performed mechanical, thermo-mechanical and thermal tests on pipe EPs in saturated sandy soils at 80% of relative density. The model energy piles were prefabricated from aluminium alloy tubes with inner diameter of 40 mm and outer diameter of 50 mm. The length of the model energy pile was 1000 mm, and only 900 mm were embedded in the sand. A copper pipe was put into the pile as heat exchangers. One load test was carried out under the ambient temperature of 15 °C (mechanical test) and three thermo mechanical tests were carried out on EPs indicated as PEP1, PEP2 and PEP3 that were heated up or cooled down to temperatures of 35 °C ,50 °C and 5 C°, respectively and then the piles are loaded to failure. The observed responses were compared to the purely mechanical load test where the pile was loaded to failure at a temperature of 15°C. The failure conditions were assumed as the load that corresponded to head pile displacement of 50 mm (pile diameter). When the pile settlement is less than 5 mm (10% diameter) all the model piles behaved linearly, the difference of the pile settlements being not significant among the thermomechanical cases. When the pile cooled down the radius expansion would leave place to radius contraction and a dropping down of the shaft resistance was expected. The results reported by the authors shows that for tests carried out at 50 °C evident changes in the bearing capacity occurred. According to the authors this phenomenon may be caused also by the preparation of the sandy soil that had a higher relative density than the other tests. The increasing of the pile bearing capacity does not depend only on the heating applied to the pile (Huang *et al.*, 2018). Two additional thermal tests were carried out applying a heating load to the pile to evaluate the thermal response of the pile. A thermo-mechanical test was performed applying heating phase at 35°C, recovery phase and cooling at 5 C° and finally a thermal recovery to the ambient temperature. During this test, a working load of 1200 N was applied to the pile head. The pile's head displacement measured during the heating/cooling cycle is reported in Figure 2-44.

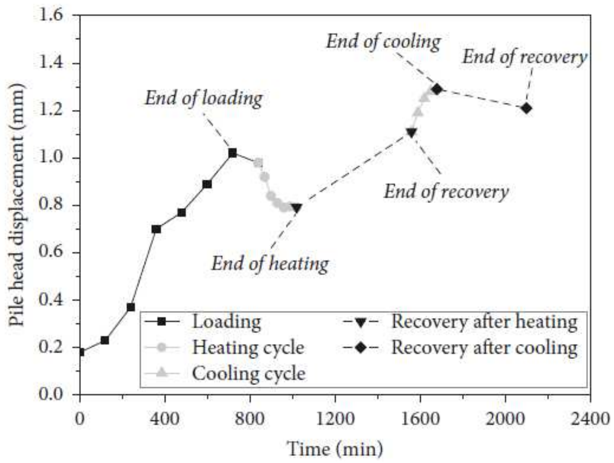

Figure 2-44: Pile's head displacement during the heating cooling cycle from Huang et al. (2018).

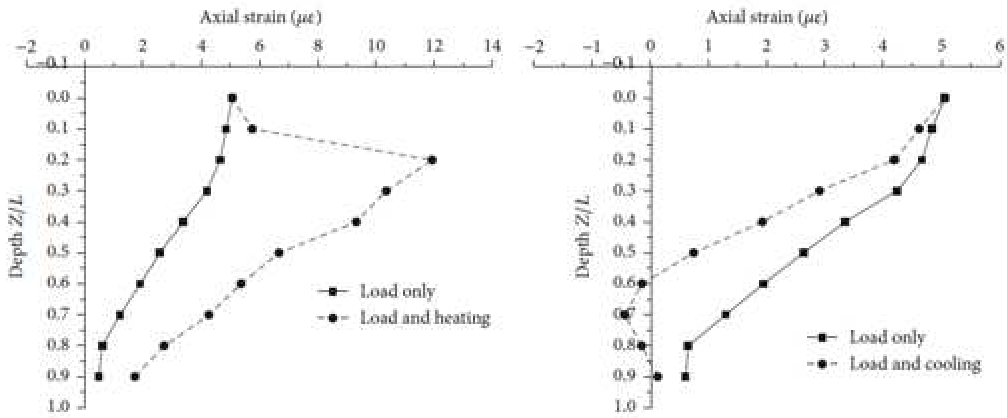

a) b)

Figure 2-45: Axial strain distributions during heating (a) and cooling (b) from Huang et al. (2018).

The pile head heaves during heating and settles during recoveries and cooling. At the end of the process the settlement of pile was more than the upward displacement, which means that uncovered plastic displacements were induced (Huang *et al.*, 2018).

The axial strains along the pile under purely mechanical and thermo-mechanical loadings are reported in Figure 2-45. The axial strains distribution shows that when the mechanical load was applied to the pile, the axial strains decreased with dept. After heating, the axial strains increased along the pile depth, while after cooling, the axial strain decreased along depth and the direction of axial strain even changed at the toe part of the pile. Plastic deformations also occurred along the pile and according to the authors they are likely caused by the contraction of soil during the thermal cycles which need to be studied further in the future.

Wang et al. (2016) investigated the behavior of concrete piles in dry sand during a heating and cooling cycle. Different kinds of small-scale test were performed: mechanical test, purely thermal test and thermo mechanical test. One Mechanical test was carried out to evaluate the ultimate resistance of pile-soil (20 kN). A vertical load of 10 kN was derived as the 50% of the ultimate resistance (SF=2) and was applied to the head of the pile during the thermo-mechanical test. The Thermal test was carried out applying thermal variations to the pile without axial loading. The Tests were performed on concrete model piles of 1600 mm length, with embedded length of 1400 mm and a diameter of 104 mm. U- shaped loops were fitted as heat exchangers. The temperature of the water travelling through the piles during heating and cooling was 55 °C and 5 °C, respectively. Dry Nanjing sand was used in the model tests that were prepared using the pluvial deposition method reaching 63% of relative density. Temperature variations along pile depth less than 1 °C were measured by the authors. The upper part of the pile was under the influence of the air temperature. Different temperatures were also recorded if the vertical load is applied or not to the pile head. In Figure 2-46 the variations of pile-head displacement against time with and without vertical loads are reported (Wang *et al.*, 2016). The heave amplitude under no load was 0.199 mm (143% of the thermomechanical displacement during heating). After natural recovery phase the final settlement under no load was 0.006 indicating that under no load the deformations were nearly completely reversed. Under a vertical load the final settlement was -0.117 mm indicating that the plastic deformations occurred During cooling, the settlement under no load was 0.065 mm which was only 64% of that under vertical load.

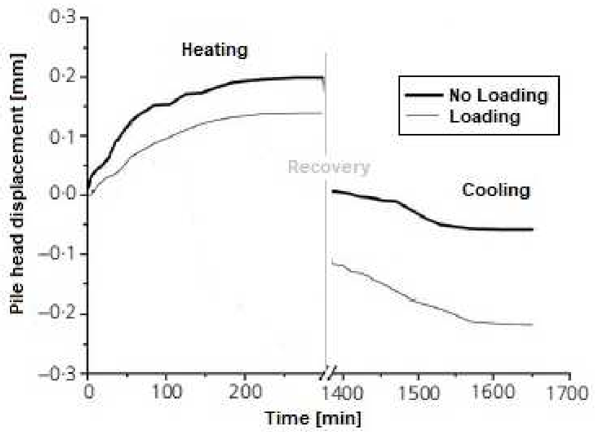

Figure 2-46: Pile head displacement measured during purely thermal test (No Loading) and thermo-mechanical test (Loading) from Wang et al. (2016).

From the thermal strains along pile depth, the authors computed the restrained axial strains as difference between theorical free expansions or contractions and observed (measured) strains. The axial thermal stress is derived from the restrained thermal strains. During heating compressive stress was produced and assumed as negative. Under null vertical load, during heating, thermal stress increased along pile shaft to a maximum of −544 kPa, and the NP moved downward. During cooling, the maximum stress of 242 kPa appeared at 650 mm from the soil surface which was away from the pile tip. Under vertical load, during heating and cooling, the maximum stresses were, respectively, −450 kPa and 360 kPa, near the halfway point of the pile. After heating, thermal stress in the upper half of the pile was larger under a vertical load than under no load (Figure 2-47).

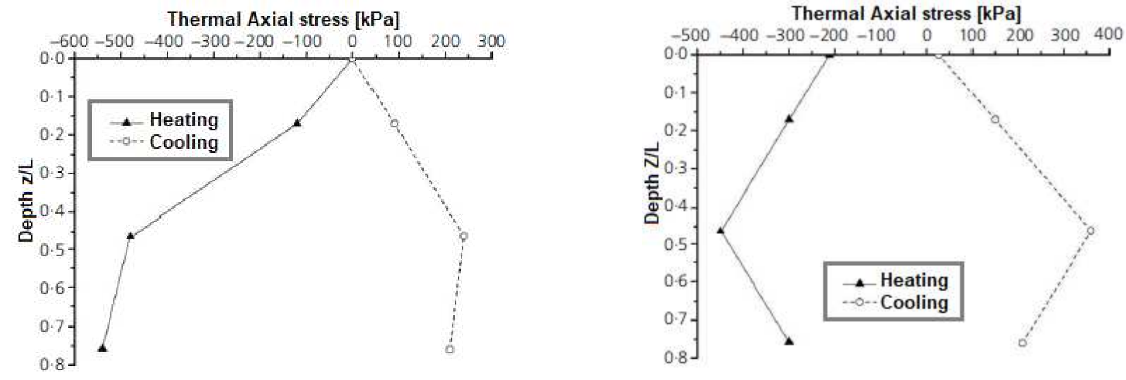

(a) (b)

Figure 2-47: Profiles of thermal axial stress under (a) no load and (b) vertical load from Wang et al. (2016)

Wang et al. (2017) carried out experimental tests on small-scale EPs equipped with heat exchangers in U-shaped, spiral and W-shaped configurations subjected to three heating and cooling cycles at a constant working load. The piles had embedded length of 1400 mm and a diameter of 104 mm. The inlet water temperature in the pipes was kept constant during heating and cooling at 55 °C and 4 °C, respectively. The model test was prepared using pluvial deposition method to cast in place Najing sand at a constant relatively density of 61 %. One mechanical test, at constant room temperature, was carried out to evaluate the pile-soil ultimate bearing capacity. The failure criterion of 10 % D was used to assess the capacity from the load-settlement curve (19 kN). Thus, for the thermo-mechanical tests the working load was set to be 9.5 kN. Each of the three thermomechanical tests consists of a loading phase followed by heating for 5 hours, natural recovery for 8 hours, cooling for 4,5 hours and then natural recovery for 6.5 hours. Then the second and third cycles started for a total time of 72 hours. Piles head displacements measured during the tests is reported in Figure 2-48.

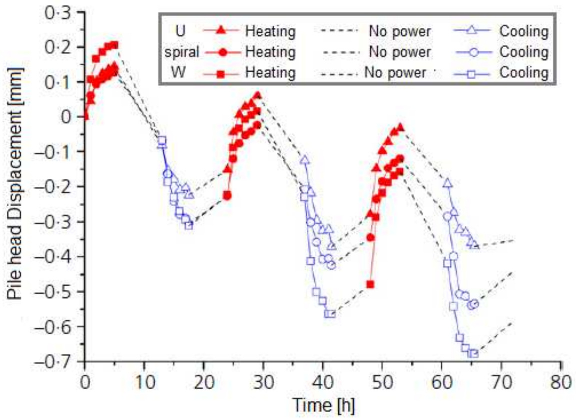

Figure 2-48: Displacement at pile head with heating-cooling cycles for energy piles with different primary circuit configurations shaped, Spiral and W shaped (Wang et al., 2017).

The EP equipped with spiral primary circuit showed greater displacements than the other two piles (equipped with W-shaped and U-shaped heat exchanger). It could be noticed that the heave during heating and settlement during cooling in the subsequent cycle were larger than those measured during the previous cycle. According to the authors this could be due to the plastic contraction of the soil.

2.3.2 Pile-soil thermo-mechanical interaction: Interpretation of the experimental results

The experimental results of the described small-scale tests are analysed in terms of soil-pile thermo-mechanical interaction characterized by a balancing between movement and the alteration of the internal stresses within the pile (Bourne-Webb et al., 2019). As suggested by Bourne-Webb et al., (2019) the expression of this interaction could be examined in terms of the pile head movement and changes in internal stress due to thermal loadings. To this aim reference is made to the two dimensionless parameters DDR and

DSR introduced in 2.2.3. These ratios are computed and reported for all the experimental studies where the available data allow the calculation. In some cases, because of the lack of data or the uncomplete understanding of the experimental measures only *DDRs* and/or *DSRs* have been reported. DSRs and DDRs versus temperature variations in °C are reported in Figure 2-49 and Figure 2-50, respectively.

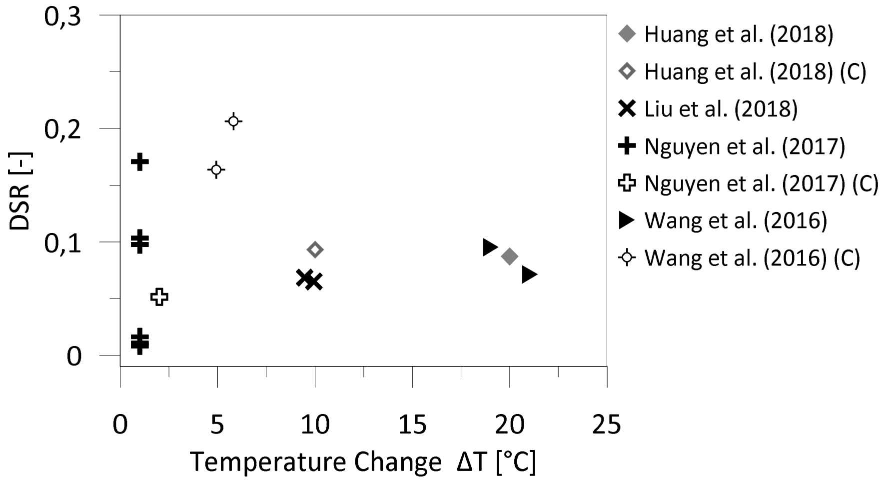

Figure 2-49:DSR versus temperature changes for the experimental small-scale tests.

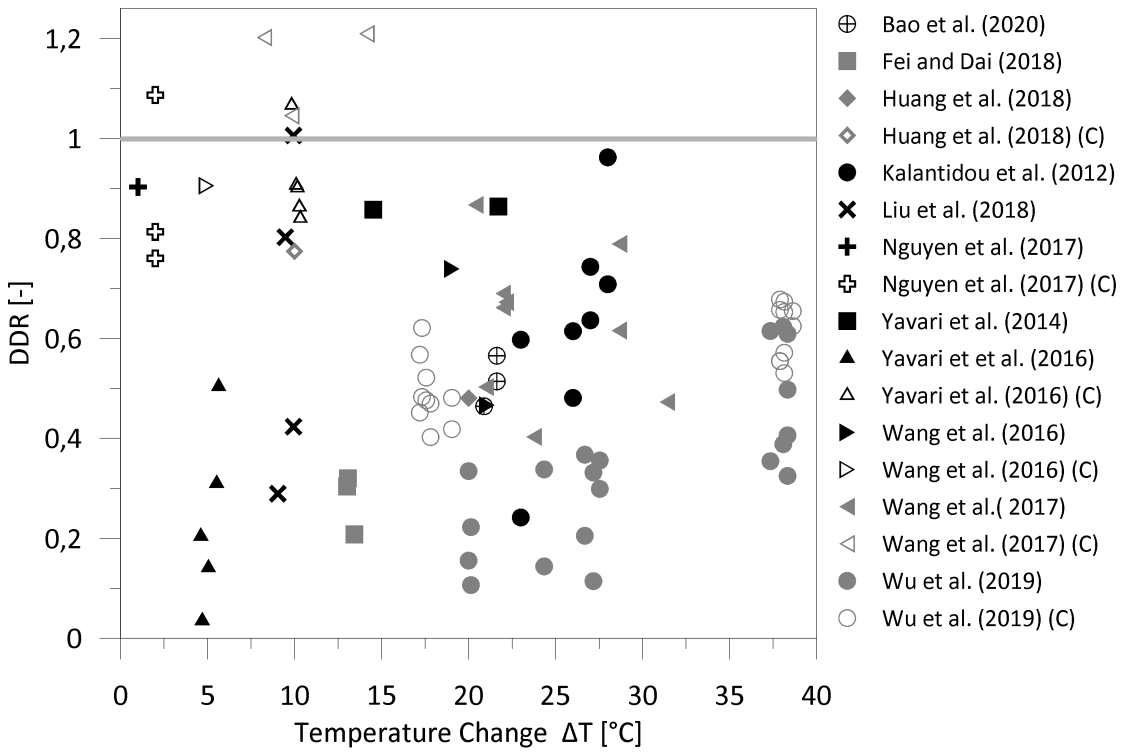

Figure 2-50:DDR versus temperature changes for the experimental small-scale tests.

DDRs are computed considering that the NP position corresponds to the depth of maximum stress. If strains and stress measurement along pile depth does not allow or are not provided to estimate the NP, the total pile length is considered for the estimation of the free head displacement. ΔT is the maximum thermal variation, applied to the pile, that occurs during a thermal cycle. It is the difference between the maximum temperature (in case of heating) or minimum temperature (in case of cooling) and the initial undisturbed soil temperature. Temperature difference in this section is considered in absolute value i.e., ΔT during cooling episodes are not considered as negative. The thermal displacement measured at pile head is assumed zeroing all the alterations that could occur during the experimental tests. In the case of thermomechanical loading, when the thermal displacement of the pile is not reported, the pile thermal displacement is computed applying the superimposition effect principle. The total displacement is considered as the summation of the thermal displacement induced by the thermal variations and mechanical displacement induced by the vertical axial loading. The thermal displacement is computed as the difference from the total observed displacement and the mechanical displacement. DDRs ratios when more than one thermal cycle is applied to the pile are computed during the first and the subsequent cycles.

From Kalantidou et al. (2012) only the DDR ratios are computed because the vertical pile's head displacements are the only displayed measures. DDRs are computed during the first and the second thermal cycles only for the heating mode. Considering the second thermal cycle, it is possible to identify a trend passing from first to second thermal cycle. With the increasing number of thermal cycles, the DDRs decrease. For the test 1, where no external mechanical load is present, DDR obtained from the first cycle is greater than the DDR obtained during the second thermal cycle (from 0.74 to 0.64). Thermal variations applied to the pile determine a response that is not purely reversible and elastic. The thermal displacement of pile head decreases with ascending number of cycles. The decreasing of the DDR could be also attributed to the fact that the pile temperature could not come back to the initial temperature at the end of the first thermal cycle determining slightly different thermal variation.

From Yavari et al. (2014) only the results of the thermal test E2 and the thermo-mechanical test E6 are considered to compute the DDRs. DDRs are computed for both tests, (E2 and E6), considering the maximum thermal variations occurred referring both to cooling and heating modes. In case of heating the DDRs computed are lower than the unity. During cooling, for both the tests considered, DDRs are larger than the unity. According to Bourne-Webb et al. (2019) some of the data appears to suggest that the pile could expand or contract more the free expansion or contraction value and this may be due to additional thermal effects in the surrounding soil mass. The fact that the soil expand/contracts leading to a greater pile movement can be postulated considering that if the shaft resistance on pile is fully mobilized by external loading, than it is possible that when cooled, the measured thermal settlement of the pile head could exceed the free thermal movement, because the pile will settle downwards as the pile toe tries to contract upwards (Bourne Webb et al. 2019) .According to Bourne Webb et al. (2019) it appears during cooling in the case of Yavari et al.(2014) where the reported settlement is greater than the free thermal contraction. For the cooling episode of the test E6 DDR is 1.4. The residual displacement observed during the first unloading phase showed that the behavior of the pile, also under purely mechanical loads, for the level of mechanical stress applied, is not elastic. In this study DDR greater than 1.2 are not reported in Figure 2-50.

Data provided by Yavari et al. (2016) allows to compute the DDRs for similar thermal variations and different stress level (SF). Pile's head displacements measured during each test (F4, F5, F6 and F7), are obtained zeroing the initial mechanical displacement induced by the application of the mechanical loading. The DDRs are computed both for heating and cooling considering the displacements corresponding to the maximum thermal variations. The variation of DDR between heating and cooling clearly shows the different response of the pile when cooled or heated and the effect of the mechanical stress level. During cooling an increase of DDR with decreasing FS is observed, while, during heating, a decrease of DDR with increasing mechanical loadings is observed. This remark concerns a range of thermal variations of about 5 °C. In the case of heating DDRs are less than or at least equal to 0.5 and decrease with the increasing of mechanical stress level.

From Nguyen et al. (2017) the results of thermo-mechanical tests carried out for different mechanical loadings i.e., SF, are considered to compute DDRs and DSRs. In terms of DDR the displacements of the head of the pile, for both cooling and heating, are reported only for the first thermal cycle. The trend of displacement of the head of the pile for different level of mechanical loadings, shows again the relationship of the observed behavior from the level of mechanical stress. The displacements of the head of the pile induced by thermal variations are characterised by thermal movements only in the case of cooling when the pile temperature decreases of 2 °C. When the pile is heated to the starting temperature (after cooling) or heated up of 1 °C no movements of the pile's head occur (cases of SF=5, SF=2.5 and SF=1.7). Nguyen et al. (2017) explained this effect considering that the thermal upward movement of the pile may be balanced by the vertical load applied to pile head. For the purely thermal test, DDRs of 0.76 and 0.90 are computed during heating and cooling, respectively. For the other cases, during cooling DDRs increase with the increasing of mechanical loading (decreasing of SF).

Liu et al. (2018) reported the results of the experimental tests in terms of displacements and axial strains and stresses in the case of purely thermal and thermomechanical loadings for both the two model energy piles described in the previous paragraph. Without mechanical loading, DDR and DSR are computed both for heating and cooling. Between heating and cooling a recovery phase is interposed, and the pile come back to its initial temperature. This allows a separate evaluation of the cooling and heating thermal effects. At the end of the first recovery phase the residual thermal displacement of the head of the pile is 0.01 mm. The behavior could be considered reversible. The authors provided data only on the room temperature that ranges from 8.7 °C to 13.2 °C. Therefore, to compute the DDRs the thermal variations assumed are those reported by the authors. DDRs are lower than one and are greater in the case of improved pile with respect to the conventional pile. The DSRs are consistent with DDRs, because to greater observed displacements correspond lower observed stresses.

The experimental results reported by Bao et al. (2020) are used to compute DDRs during the heating mode for each of the three thermal cycles. Strains of the pile were monitored at different locations in the cross section at two different depths (433 mm and 866 mm) (Bao *et al.*, 2020). The DDRs are computed considering the displacement of the head of the pile reported by the authors where there is not a matching between the thermal variations applied and the thermal displacement measurements (Figure 2-42). DDRs for each thermal cycle are evaluated considering the thermal variation reported by the authors and the thermal displacement measured at the beginning of the heating phase.

Wu et al. (2019) reported the thermal displacement of pile's head considering end bearing and floating piles. Experimental tests on small scale pile fixed at toe have been reported for the first time in this study. The result of thermo-mechanical heating-cooling, heating- recovery and cooling-recovery tests have been used to compare DDRs ratio evaluated for a fixed SF=2.5 with the increasing of thermal cycle. The observed behavior with the increasing thermal cycles depends on thermal loading applied (magnitude of thermal variations) and end restraint condition (end bearing or floating). Both in the case of end bearing and floating pile when the thermal variations applied on the pile are around 40 °C and with the increasing number of thermal cycles, DDRs increase both in case of heating and cooling. For SF=2.5 and thermal variations around 40 °C the behavior of the pile is governed by thermal loading. Thermal displacements of the pile head do not stabilise at the end of the fifth cycle and continue to increase with the number of thermal cycle (Figure 2-43).

Huang et al. (2018) reported the cumulative displacements of the pile subjected to constant heating or cooling with increasing mechanical loading. For this kind of test the thermal displacements of the pile could be evaluated as the difference between the cumulative displacement and the mechanical displacement corresponding to the displacement observed under isothermal conditons. DDRs for these tests are computed applying the superimposition effects principle. The values of the computed DDRs demonstrate that for high level of the mechanical stress it is not possible to compute the thermal displacements as the difference between the cumulative movements and the mechanical settlements. DDRs considered in this study, refer only to the test where cooling, heating and recovery phases are combined to a constant mechanical loading. The DDR computed in the case of heating and cooling are 0.48 and 0.77, respectively. The axial strains induced by the thermo-mechanical load are considered to compute the thermal stress induced in the pile in order to evaluate DSRs during heating and cooling. In order to compute the maximum DSR along the pile shaft, the minimum observed thermo-mechanical strain has been considered. The observed minimum thermal deformation has been subtracted from the free contraction(cooling) or expansion(heating) to estimate the restrained thermal strain that is used to compute the axial thermal stress. DDRs computed are lower than 1% of the theorical maximum stress both in the case of heating and cooling.

Wang et al. (2016) reported the behavior of small scale EP with(SF= 2) and without (SF=) mechanical loading. Increasing the SF DDRs decrease during heating mode. During cooling, an opposite trend it is observed the DDRS increase with the deacreasing of SF. The value of the thermal stresses reported by the authors are used to evaluate DSRs. The values of DSR computed from the experimental data reported by the authors are not in agreement with DDRs, for this reason they are considered in this study (Wang et al., 2016).

The experimental results reported by Wang et al. (2017) are used to evaluate DDRs of small scale piles equipped with different kinds of heat exchanger pipe (U-shaped, Spiral and W-shaped). DDRs are evaluated for a constant SF=2 and during the three thermal cycles. DDRs computed both in case of heating and cooling increase with the number of thermal cycles regardless of primary circuit configuration. DDR's trend demonstrates that a cumulative settlement occurs at the end of each cycle. DDRs during cooling mode are greater than unity. This could be also explained accounting for the coupling between mechanical and thermal loading. Different kinds of small-scale test performed on EPs have been considered in this section. Most of the tests have been performed on floating piles, except for Wu et al. (2018) that carried out their experimental study on both floating and end bearing model-piles.

Kalantidou et al. (2012), Yavari et al. (2014), Yavari et al. (2016), Fei and Dai (2018), Huang et al. (2018), Wu et al. (2019) Wang et al. (2016), Wang et al. (2017) and Nguyen et al. (2017) carried out load test on the model piles determining the pile-soil bearing capacity. For these studies, for each thermo-mechanical test reported it is possible to compute the SF. In Figure 2-51 and Figure 2-52 DDRs are plotted as function of the SF during the first cycle of heating or cooling episodes, respectively. In the case of cooling a general trend could be identified: DDRs increase with descending values of SF. The increasing of the DDRS with the level of mechanical loading is observed for most of the tests. This phenomenon is a clear effect of the thermo-mechanical coupling. Mechanical loading determines an increase of the downward displacements of the pile head when combined to thermal loads of cooling. DDRs larger than unity could be observed with decreasing SF and only for cooling. In the case of heating, is not completely possible to identify a trend of DDR with increasing SF.

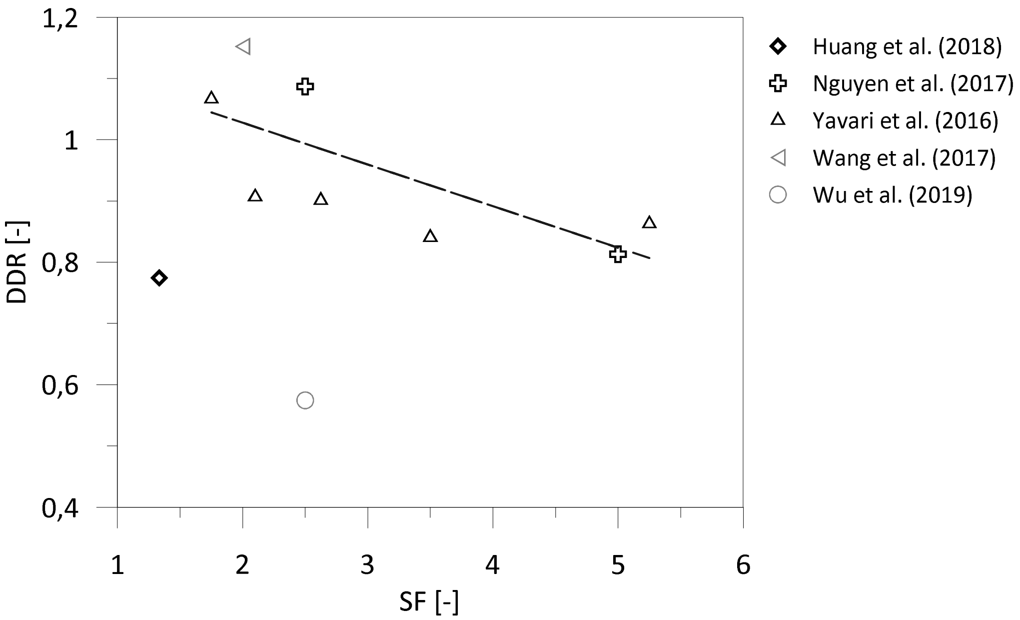

Figure 2-51: DDRs computed during the first cooling phases and related to the SF.

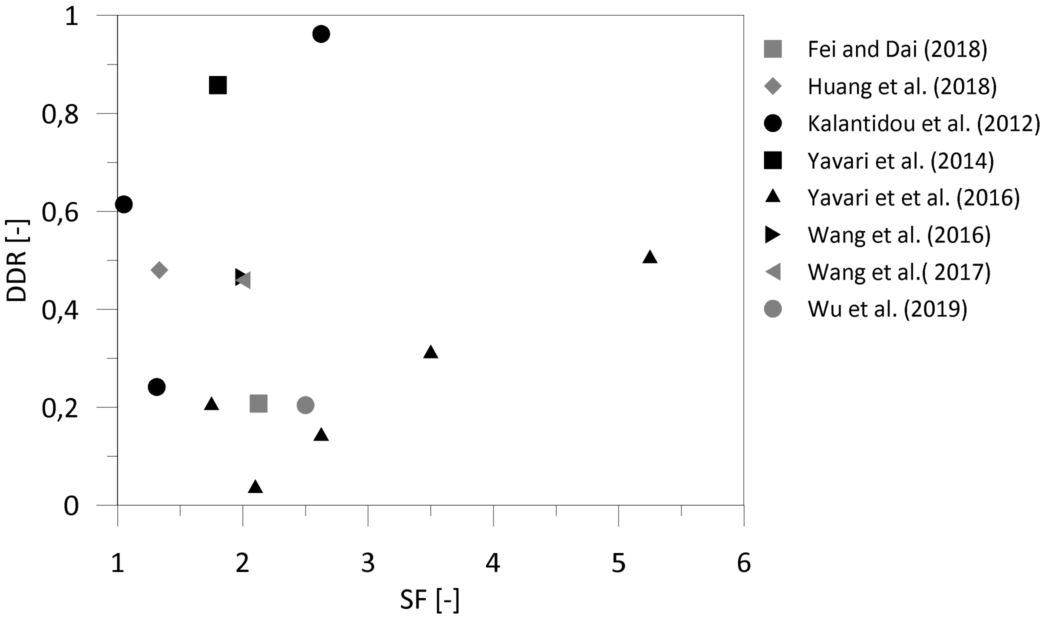

Figure 2-52: DDRs computed during the first heating modes and related to the SF.

In the case of Wang et al. (2017), the DDR considered is an average of those computed for different pile's PC configuration (U-shaped, W shaped and spiral). In the case of Wu et al. (2019), different DDR values correspond to different kinds of toe constraint (floating pile and end bearing pile) an average value was considered in order to focus only to the relationship between DDR and SF.

With increasing number of thermal cycles, the evolution of the pile mechanical behavior could be represented by DDRs. With increasing number of thermal cycles different mechanisms at the pile–soil interface could be induced as, for example, the degradation of the pile–soil interface resistance with irreversible displacements. Nguyen et al. (2017) applied to the pile thirty heating/cooling cycles under various constant pile head loads varying from 0 to 60% of pile resistance. They observed that thermal cycles, under constant head load, induce irreversible settlement of the pile head that head is higher at higher pile head load. Nguyen et al. (2017) also noticed that the first thermal cycle induces the highest irreversible pile head settlement. The incremental irreversible settlement, accumulating after each thermal cycle, decreases when the number of cycles increases and becomes negligible at high number of thermal cycles and/or low pile head load. The experimental results of Nguyen et al. (2017) are confirmed by the experimental results of Kalantidou et al. (2012). DDRs during heating computed for the experimental tests of Kalantidou et al. (2012) do not follow a precise trend with increasing thermal cycles, therefore are not considered in this study. DDRs computed referring to the experimental study of Bao et al. (2020) show a decreasing passing from the first to the second thermal and very small increasing passing from the second to the third thermal cycle. In the case of Wang et al. (2017) the evolution of pile settlement could be related to the magnitude of thermal variations and to the toe restraint condition (floating pile and end bearing pile). In the case of thermal variations around 40 °C DDRs increase with increasing number of thermal cycles both for end bearing and floating pile. When thermal variations of 20 °C are applied to the floating model pile, DDRs decrease with the number of cycles for the first three cycles. When thermal variations of 20 °C are applied to the end- bearing model pile, DDRs increase with the number of cycles. Fei and Dai (2019) and Wang et al. (2017) tests show that DDRs increase with the number of thermal cycles. DDRs versus increasing number of thermal cycles are plotted for heating and cooling modes in Figure 2-53 (a) and Figure 2-53 (b), respectively.

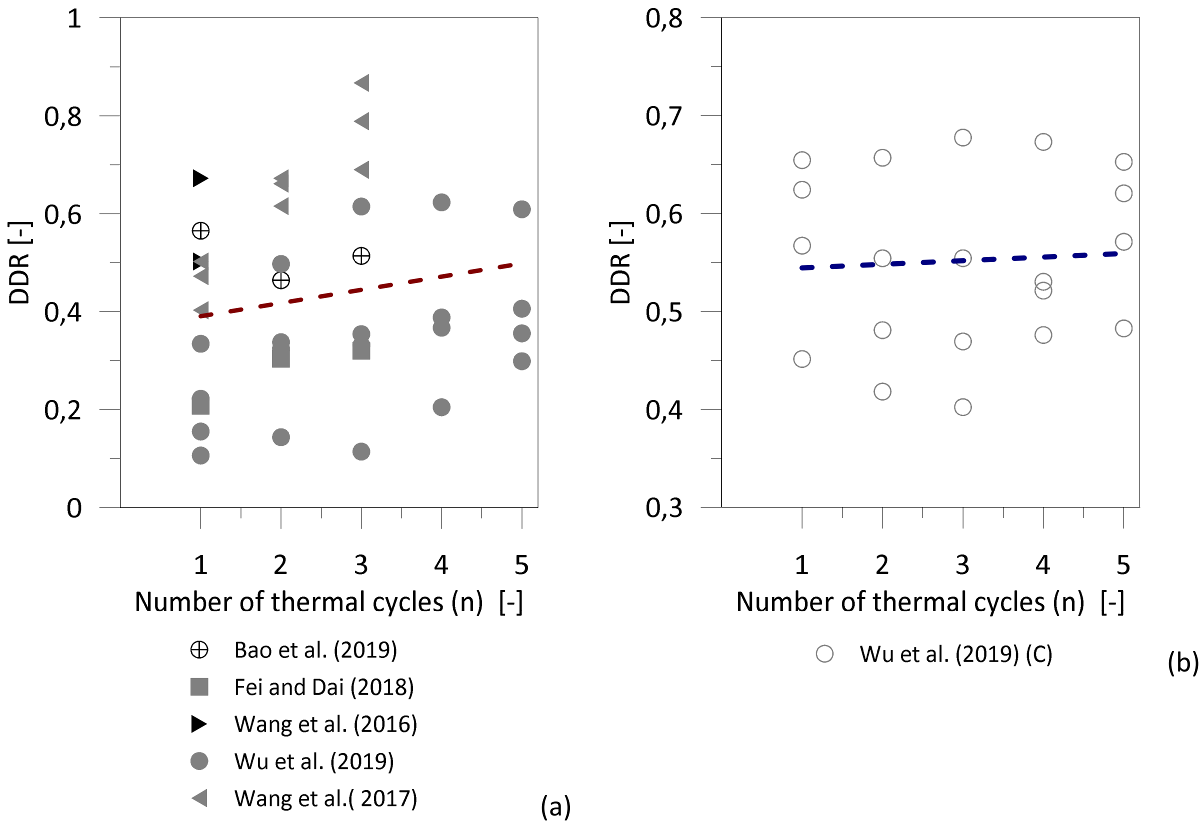

Figure 2-53: DDRs with increasing number of thermal cycles for (a) heating and (b) cooling modes.

From the data collected in this study it could be concluded that the evolution of thermal displacements with the number of thermal cycles is also connected to the pile's end restraint conditions and to the magnitude of thermal variations. A general trend of DDRs with increasing number of thermal cycles can be identified as plotted in Figure 2-53 (a) and Figure 2-53 (b). DSR increases with increasing number of thermal cycles. It means that the mobilised thermal expansion coefficient of the pile increases with the evolution of thermal cycle and therefore the constraint action provided by the soil decreased. It should be highlighted that this behavior is observed from few cases therefore further investigations are needed. Additional physical testing should be addressed to investigate the effects of realistic thermal cycles on pile's displacement evolution to provide a general trend with increasing number of thermal cycles. The effect of the SF particularly in the case of heating needs further investigations too.

2.4 *Numerical analyses on EPs*

The main full scale field experiments (2.2) along with small experimental set-ups (2.3) have provided an invaluable insight into the behavior of EPs. Through the preceding description of existing studies, it was demonstrated that both thermal-induced displacements and stresses must be taken into account in the geotechnical design of EPs. The variations in the bearing characteristics of EPs, additional displacements, axial force and pile shaft friction mobilisation along depth, are complex, being closely related to the site's engineering geological conditions (Wang et al.,2019). Aspects of the interaction between the pile and the surrounding soil require further investigation, especially in terms of the long-term performance under operational conditions (Gawecka et al., 2017). In order to improve the understanding of thermo-active piles mechanical and thermal behavior, numerous numerical studies have been performed.

A simplified geotechnical analysis method for heat exchanger piles based on the load transfer method was introduced by Knellwolf et al. (2011). For EPs Knellwolf et al. (2011) modified the original load-transfer method by *Coyle and Reese (1966)* to allow the calculation of heat exchanger pile displacements and mobilized efforts. The method is based on different assumptions: radial displacements and pile's weight are neglected, and the mechanical properties of the pile do not vary with temperature. Plaseid (2012) developed a load transfer analysis which provides an improvement over the tau-z curves proposed by Knellwolf et al. (2011). Nonlinear springs are adopted, side shear and toe resistance were represented by hyperbolic curves and the radial expansion of the pile elements are considered. According to Suryatriyastuti (2013) in the present time there exist only two tau-z functions able to model cyclic loading and unloading path (Randolph and Wroth (1978) and the Frank and Zhao (1982)). Tau-z curves under two-way cyclic loading should satisfy a series of conditions connected to the main aspect observed for a cyclic behavior as the reduction of the shaft friction with increasing number of cycles, the degradation of pile-soil resistance and soil modulus with increasing cycles, the accumulation of permanent displacements and the loading rate effect. To this aim Suryatriyastuti (2013) proposed a new formulation of tau-z function in which the available resistance can be specified to deteriorate. In this instance, the model again yields accumulating increments of settlement with cycles of thermal loading. As the pile ratchets downwards and shaft restraint is lost, there is an accumulation of load reaction at the base of the pile. Chen et al. (2016) updated the load transfer analysis described by to better identify NP location. The model was calibrated to evaluate the expected soil-structure interaction response of four case studies: one field test and three centrifuge studies. Chen et al. (2016) performed a parametric study on the influence of the soil shear strength parameters, toe stiffness, head stiffness, radial expansion and other issues as the magnitude of temperature change. It was observed that the thermo-mechanical axial stresses increase with an increasing friction angle or the undrained shear strength. The effect of stiffness on maximum values of axial stresses is an increase. The effect of toe stiffness on maximum value of axial stresses is that if the stiffness increases the axial stress increases. The effect of radial expansion on maximum values of axial stresses and total axial strains indicates that the radial expansion has a negligible influence on axial stresses and total axial strains. The analysed methods provide a simplified approach to evaluate the complex problem of pile-soil interaction under thermo-mechanical loadings. As an example, it is not possible to take into account the heat transfer phenomenon. Oliaei et al. (2018) proposed a method in which heat transfer analysis was accompanied by a thermomechanical analysis of the pile behavior. Sutman et al. (2018) proposed an experimental approach based on load transfer curves for the analysis of cyclic behavior of EPs. The comparison of the results of experimental and numerical analysis shows that the load transfer method is suitable to analyse the cyclic thermal behavior of energy piles.

The finite element method (FEM) has been largely employed both to reproduce or back-analyse full- or small-scale tests, or to explore other conditions and parameters to investigate on of various aspects of the soil–structure interaction. These numerical analyses vary in complexity in terms of both the finite-element formulation and the modelling approach.

FEM was firstly employed and validated by Laloui et al. (2006) who compared the numerical results with the observed behavior of Losanne in situ test (2.2). They employed a fully coupled thermo-hydro-mechanical formulation, and the experimental results were globally well reproduced. Gawecka et al. (2017) performed coupled thermo-hydro-mechanical analyses to back analyse the Lambeth College test described by Bourne-Webb et al. (2009). They demonstrated that the use of the Mohr-Coulomb failure criterion is acceptable to predict the ground movements. Adinolfi et al. (2018) validated FE tool able to numerically investigate the thermo-hydro-mechanical behavior of a single EP comparing the numerical results to the data available from field tests. Gunawan and Gouw (2019) used three different constitutive models and the FEM software to back-analyse a centrifuge experimental test. Comparing the measured results to the back-analysis the HS with small strain model better reproduce the thermal observed settlement. Bodas Freitas et al. (2013) used a simple elastic model to investigate on the effects of the thermal boundary condition considering either zero heat flow (perfect insulation) or constant temperature (no change relative to starting temperature) on the ground surface and the relative thermal expansion between the soil and the pile. The results of this study showed that the temperature field in the vicinity of the pile was crucial in determining the response of the pile. While heating a pile in a soil with higher coefficient of thermal expansion than the pile itself compressive stress were predicted only when a constant boundary condition was applied at ground surface. The results presented highlighted also that there is a complex interaction between the foundation and soil and the degree of fixity against thermal expansion that can be mobilised depends on the pile's shaft requiring deeper investigations (Bodas Freitas et al., 2013).

Di donna and Laloui (2014) performed FE analyses to investigate on the effects of the thermo-mechanical behavior of soils and pile–soil interface on the geotechnical performance of EPs. Normally-consolidated Clayey soil was modelled by the Advanced Constitutive Model for Environmental Geomechanics, with temperature effects included (ACMEG-T model). This model was also adopted for the thin layer of elements that simulate the pile-soil interface. The thermal load is applied in terms of injected and extracted thermal power, while applied mechanical load is 750 kN. The same cyclic thermal loading is repeated for 10 years with the purpose to study the long-term response. The maximum and minimum temperatures reached inside the pile are 25 and -2 °C, respectively. The pile has reversible upwards (heating) and downwards (cooling) displacements of during thermal cycles of about 4mm. The effect of the subsequent thermal cycles on the thermoplastic response of the soil (accommodation) is subtle. The majority of the effect is seen in the first heating cycle, as the subsequent annual heating cycles reach approximately the same temperature and thus, do not provoke significant additional thermal consolidation. The pore water pressure is unaffected by temperature, the horizontal effective stress varies cyclically because of the interaction with the pile i.e., the radial thermal expansion of the pile, in accordance with the constant normal stiffness (Di donna and Laloui, 2014). Cooling determines tensile stress in the lower part of the pile; but the authors highlighted that it depends on the entity of the mechanical load and on the boundary conditions. The thermal-induced total stresses inside the pile remain constant cycle after cycle. Olgun et al. (2015) performed energy demand analyses coupled with finite element analyses to investigate the long-term performance of heat exchanger piles. The results showed that the heat exchange operations can lose efficiency over time unless preventive measures are taken as recharging approach to balancing the ground temperature. Thermo-mechanical analyses suggest that the pile shows pure elastic elongation over the operation period and the considered long-term energy operations do not have much influence on the geotechnical performance of the heat exchanger piles. Wang et al. (2019) from laboratory measurements showed that the concrete-soil interface resistance was not influenced by temperature variation and that the temperature at the interface increase with time tends to be constant after heating for a certain time. Based on these results, A FE model developed to simulate the behavior of an §EP equipped with spiral heat exchanger. The effect of the liquid flow on the temperature distribution in the heated pipe was neglected as often occurred in FE analyses focused on the geotechnical performances. The pile and uniform layer of dry sandy soil were modelled by linear elastic model and Mohr-Coulomb elastoplastic model, respectively. The application of the thermal loadings consists of twelve hours of heating followed by twelve hours of natural cooling; repeated for thirty days. Different levels of mechanical loadings were combined to the thermal loadings and it was concluded that cyclic heating and cooling would lead to additional displacements when heavy loads are applied at the energy pile top, at which non-linear settlements began to occur (Wang et al., 2019). Additional simulations were performed heating the pile for ten days and naturally cooling for thirty days. At the end of the long thermal recovery all the thermal displacements observed during hating were almost recovered demonstrating that the displacement caused by heating could be eliminated with the process of naturally cooling at lower load level.

Saggu and Chakraborty (2015) carried out a parametric study on the effects of different end conditions of the pile, relative densities of the soil, coefficients of lateral earth pressure of the ground, lengths and diameters of the pile, thermal loads, coefficients of friction at the pile-soil interface, critical-state friction angles of soil, thermal conductivity of soil, specific heat of soil and thermal conductivity of the pile on the stress response of soil, deformation of the pile and soil, and strains in the pile through axisymmetric model. The concrete energy pile was modelled as linearly elastic while the soil is uniform layer of Ottawa sand through the CASM model based on the critical-state soil mechanics. The study assumed that the pile-soil system behaves thermo-elastically which is a valid assumption for sand (Saggu and Chakraborty, 2015). Pile length and relative density of soil play key role in deciding the behavior of the piles under thermal loading. Thermal loads on pile and soil friction angle influenced strongly the pile soil interaction. The coefficient of earth lateral pressure increased under increasing thermal loadings. For friction angles that increased from 30° to 35° the coefficient of lateral earth pressure increases for piles with both ends fixed. The change in soil thermal conductivity and pile's heat specific heat and thermal conductivity has a negligible effect on the coefficient of lateral earth pressure.

Batini et al. (2015) performed numerical sensitivity analyses to investigate the thermo-mechanical response of a full-scale EP for different pipe configurations, foundation aspect ratios, mass flow rates of the fluid circulating in the pipes and fluid mixture compositions. The dimensions of the EP and the subsoil condition considered in this study corresponded to the experimental site of EPFL located in Losanne (2.2). Both the pile and soil are assumed to behave as thermo elastic materials. It was assumed to be representative of the analysed problem in view of the experimental evidence that was obtained through in-situ tests performed at the site (Batini et al., 2015). 3-D Transient FE simulations was performed over 15 days in winter, this period has been proven to be sufficient to reach steady-state within the EP domain. The thermo-mechanical behavior of a single energy pile equipped with a single U, a double U and W-shaped pipes was investigated. The configuration of the pipes was the most important factor influencing the thermo-mechanical behavior of the EPs. The increase of the foundation aspect ratio resulted in an approximately linear increase of the exchanged. However, a lengthening or shortening of the energy pile resulted in markedly different responses of the foundation to the thermomechanical loads. higher and less homogeneous evolutions of stresses and displacements were observed for the higher aspect ratios. No remarkable variations of the vertical stress and strain distributions in the foundation were observed with the variation in the fluid flow rates and heat carrier fluid compositions.

Bourne-Webb et al. (2016) explored further the temperature field around the pile along with the effect of the soil thermal expansion coefficient to provide a baseline set of predictions that examine the impact of a limited set of thermal and thermomechanical parameters on the thermomechanical behavior of EPs. Fe simulations are performed assuming that the soil is purely cohesive and thermally elastic, and the pile is located centrally under a building of larger dimensions and a constant surface temperature can be assumed. The results of this study showed that the difference between the initial ground temperature field and the thermal conditions imposed by any overlying building determine thermal effect within the foundation element which affects the subsequent response when the pile is heated and cooled. The volume response of the soil i.e., the coefficient of linear expansion should be appropriate because it could lead to incorrect prediction of pile-soil interaction under thermal loadings. According to the authors the results presented are illustrative and further investigations are needed taking into account transient heating and cooling and soil temperature conditions (Bourne-webb et al., 2016). Gawecka et al. (2017) investigated the behavior of a single thermo-active pile placing particular emphasis on reproducing ground conditions typical of the London basin. The modelling approach, in terms of both the analysis type (i.e., coupled as opposed to uncoupled) and the method of thermal load application, can have a large influence on the computed results, and therefore potentially also on the design of such piles. For example, in the case where the transient phenomena in the soil were not considered the changes in stresses caused by temperature were significantly higher than those predicted by a fully coupled THM analysis. For the ground conditions typical of the London basin, varying thermal conductivity and permeability does not affect the behavior of the pile as significantly as changing the modelling approach.

Rammal et al. (2017) investigated about the influence of thermal solicitations on the design of EPs. To this aim an isolated EP installed in saturated sandy soil was modelled via the finite difference code FLAC. The constitutive law used to model the ground behavior included an isotropic elastic part, the conventional Mohr Coulomb failure criterion and a non-associated flow rule. The pile was modelled as linear elastic. The mechanical properties are assigned at measured at site investigations on CFA pile in sand. The difference between the numerical results and experimental data is not negligible but according to the authors of the test it can be assumed to be sufficiently for their study where the mechanical load is 33 % of the ultimate bearing capacity. Three types of thermal solicitations are compared: constant pile temperature with rest phase (krenel solicitations), constant pile temperatures without rest between heating and cooling phase, continuous sinusoidal temperature variation taking into account various scale: year, day and hours. Considering ten years of operations and yearly time scaling the pile's head displacements slowly increased during ten consecutive thermal cycles. no cyclic constitutive law is used, the pile head displacement is not stabilised after 10 cycles while the rate and the amplitude of displacement tend to decrease indicating similar effects to those of ratcheting. In terms of energy pile design, these results are quite interesting and significant since they show that cyclic effects can be observed even if the constitutive law considered to simulate the ground behavior does not deal with these aspects and were almost stabilised at the end of the period. This trend was observed with any kind of solicitations. From the results of this study, it was worth noting that after each rest phase the displacement is not totally recovered since the temperature of the pile is not recovered too. The absolute values of axial forces increase between the first and the tenth cycle, with higher magnitude in the case of heating in agreement with the observed experimental results. According to the authors, further studies should be carried to analyse the influence of the thermal solicitation type on the behavior of single pile with other boundary conditions at the head.

Several numerical studies investigating different aspect of thermo-mechanical behavior of EPs are reported in literature. The soil behavior under thermal variations is mainly modelled as thermo elastic because the range of temperature considered do not significantly modify the mechanical properties of soil with respect to isothermal conditions. Most of the studies consider simplified subsoil conditions modelling a single soil layer and thermal loadings. This choice is particularly common dealing with parametric analyses. In these kinds of studies, the soil and pile behavior are modelled as linear elastic. Several aspects about the thermo mechanical interaction should be investigated as the thermal interaction with the overlying structure or the long behavior under cyclic thermal variations. What is emerged is that thermal loading combined to mechanical loading is mainly a serviceability connected problem that should be deeply investigated taking into account the long-term behavior.

References

Abuel-Naga, H., Raouf, M.I.N., Raouf, A.M.I., Nasser, A.G., 2015. Energy piles: Current state of knowledge and design challenges. Environ. Geotech. 2, 195–210. https://doi.org/10.1680/envgeo.13.00019

Abuel-Naga, H.M., Bergado, D.T., Bouazza, A., Ramana, G. V., 2007. Volume change behavior of saturated clays under drained heating conditions: Experimental results and constitutive modeling. Can. Geotech. J. 44, 942–956. https://doi.org/10.1139/T07-031

Adinolfi, M., Maiorano, R.M.S., Mauro, A., Massarotti, N., Aversa, S., 2018. On the influence of thermal cycles on the yearly performance of an energy pile. Geomech. Energy Environ. 16, 32–44. https://doi.org/10.1016/j.gete.2018.03.004

Akrouch, G.A., Sánchez, M., Briaud, J.L., 2014. Thermo-mechanical behavior of energy piles in high plasticity clays. Acta Geotech. 9, 399–412. https://doi.org/10.1007/s11440-014-0312-5

Amatya, B.L., Soga, K., Bourne-Webb, P.J., Amis, T., Laloui, L., 2012. Thermo-mechanical behavior of energy piles. Geotechnique 62, 503–519. https://doi.org/10.1680/geot.10.P.116

Asadi, I., Shafigh, P., Hassan, Z. F. B. A., Mahyuddin, N. B. 2018. Thermal conductivity of concrete – a review Journal of Building Engineering, 20**,** 81–93.

Baggs, S.A., 1983. Remote prediction of ground temperature in Australian soils and mapping its distribution. Sol. Energy 30, 351–366. https://doi.org/10.1016/0038-092X(83)90189-5

Bao, X., Li, Y., Feng, T., Cui, H., Chen, X., 2020. Investigation on thermo-mechanical behavior of reinforced concrete energy pile with large cross-section in saturated sandy soil by model experiments. Undergr. Sp. 5, 229–241. https://doi.org/10.1016/j.undsp.2019.03.009

Batini, N., Rotta Loria, A.F., Conti, P., Testi, D., Grassi, W., Laloui, L., 2015. Energy and geotechnical behavior of energy piles for different design solutions. Appl. Therm. Eng. 86, 199–213. https://doi.org/10.1016/j.applthermaleng.2015.04.050

Bouazza, A., Singh, R.M., Wang, B., Barry-Macaulay, D., Haberfield, C., Chapman, G., Baycan, S., Carden, Y., 2011. Harnessing on site renewable energy through pile foundations. Aust. Geomech. J. 46, 79–89.

Bourne-Webb, P.J., Bodas Freitas, T.M., 2020. Thermally-activated piles and pile groups under monotonic and cyclic thermal loading–A review. Renew. Energy 147, 2572–2581. https://doi.org/10.1016/j.renene.2018.11.025

Bourne-Webb, P. J., Bodas Freitas, T.M., Assunção, R.M.F., 2016. Soil-pile thermal interactions in energy foundations. Geotechnique 66, 167–171. https://doi.org/10.1680/jgeot.15.T.017

Bourne-Webb, P.J., Bodas Freitas, T.M., Freitas Assunção, R.M., 2019. A review of pile-soil interactions in isolated, thermally-activated piles. Comput. Geotech. 108, 61–74. https://doi.org/10.1016/j.compgeo.2018.12.008

Burghignoli, A., Desideri, A., Miliziano, S., 2000. A laboratory study on the thermomechanical behavior of clayey soils. Can. Geotech. J. 37, 764–780. https://doi.org/10.1139/t00-010

Brandl, H., 2006. Energy foundations and other thermo-active ground structures. Geotechnique 56, 81–122. https://doi.org/10.1680/geot.2006.56.2.81

Cecinato, F., Loveridge, F.A., 2015. Influences on the thermal efficiency of energy piles. Energy 82, 1021–1033. https://doi.org/10.1016/j.energy.2015.02.001

Cekerevac, C., Laloui, L., 2004. Experimental study of thermal effects on the mechanical behavior of a clay. Int. J. Numer. Anal. Methods Geomech. 28, 209–228. https://doi.org/10.1002/nag.332

Cervera, C.P., Sinnathamby, G., Gustavsson, H., Korkiala-Tanttu, L., 2014. Ground thermal modelling and analysis of energy pile foundations. Numer. Methods Geotech. Eng. - Proc. 8th Eur. Conf. Numer. Methods Geotech. Eng. NUMGE 2014 2, 965–970. https://doi.org/10.1201/b17017-172

Chen, D., McCartney, J.S., 2017. Parameters for Load Transfer Analysis of Energy Piles in Uniform Nonplastic Soils. Int. J. Geomech. 17, 04016159. https://doi.org/10.1061/(asce)gm.1943-5622.0000873

Coyle, H. M., Reese. L. C. 1966. Load transfer for axially loaded piles in clay. J. Soil Mech. and Found. Div., 92(2), 1–26.

Côté, J., Konrad, J.M., 2005. A generalized thermal conductivity model for soils and construction materials. Can. Geotech. J. 42, 443–458. https://doi.org/10.1139/t04-106

Coulibaly, J.B., Shah, M., Rotta Loria, A.F., 2020. Thermal cycling effects on the structure and physical properties of granular materials. Granul. Matter 22. https://doi.org/10.1007/s10035-020-01054-6

De Santiago, C., De Santayana, F.P., Groot, M. , Urchueguía, J., Badenes, B., Magraner, T., Arcos, J.L., Martín, F., 2016. Thermo-mechanical behavior of a thermo-active precast pile. Eur. Geotherm. Congr. 2016 48, 41–54.

Di Girolamo L., Ausiello G., Russo G., Marone G. 2021. High Thermal Conductivity Concrete for Energy Piles. fib International Conference on Concrete Sustainability Prague, Czech Republic, 8-10 September 2021 (Accepted).

De Moel, M., Bach, P.M., Bouazza, A., Singh, R.M., Sun, J.O., 2010. Technological advances and applications of geothermal energy pile foundations and their feasibility in Australia. Renew. Sustain. Energy Rev. 14, 2683–2696. https://doi.org/10.1016/j.rser.2010.07.027

Di Donna, A., Laloui, L., 2015. Response of soil subjected to thermal cyclic loading: Experimental and constitutive study. Eng. Geol. 190, 65–76. https://doi.org/10.1016/j.enggeo.2015.03.003

Dincer, I., 2000. Renewable energy and sustainable development: A crucial review. Renew. Sustain. energy Rev. 4, 157–175. https://doi.org/10.1016/S1364-0321(99)00011-8

Faizal, M., Bouazza, A., Haberfield, C., McCartney, J.S., 2018. Axial and Radial Thermal Responses of a Field-Scale Energy Pile under Monotonic and Cyclic Temperature Changes. J. Geotech. Geoenvironmental Eng. 144, 04018072. https://doi.org/10.1061/(asce)gt.1943-5606.0001952

Faizal, M., Bouazza, A., McCartney, J.S., Haberfield, C., 2019. Effects of Cyclic Temperature Variations on Thermal Response of an Energy Pile under a Residential Building. J. Geotech. Geoenvironmental Eng. 145, 04019066. https://doi.org/10.1061/(asce)gt.1943-5606.0002147

Faizal, M., Bouazza, A., Singh, R.M., 2016a. An experimental investigation of the influence of intermittent and continuous operating modes on the thermal behavior of a full scale geothermal energy pile. Geomech.

Energy Environ. 8, 8–29. https://doi.org/10.1016/j.gete.2016.08.001

Faizal, M., Bouazza, A., Singh, R.M., 2016b. Heat transfer enhancement of geothermal energy piles. Renew. Sustain. Energy Rev. 57, 16–33. https://doi.org/10.1016/j.rser.2015.12.065

Fei, K., Dai, D., 2018. Experimental and Numerical Study on the Behavior of Energy Piles Subjected to Thermal Cycles. Adv. Civ. Eng. 2018. https://doi.org/10.1155/2018/3424528

Fitzgibbon, M.E., 1975. Thermal Curing of Massive Structural Concrete. Batim Int/Build Res Pr. 3, 344. https://doi.org/10.1080/09613217508550426

Frank R., and Zhao S. R. 1982. Estimation par les paramètres pressiométriques de l'enfoncement sous charge axiale de pieux forés dans des sols fins. Bull. Liaison Lab. Ponts Chaussees, 119, 17–24.

Freitas, B.T.M., Silva, C.F., Bourne-Webb, P.J., 2013. The response of energy foundations under thermo-mechanical loading. 18th Int. Conf. Soil Mech. Geotech. Eng. Challenges Innov. Geotech. ICSMGE 2013 4, 3347–3350.

Gao, J., Zhang, X., Liu, J., Li, K., Yang, J., 2008a. Numerical and experimental assessment of thermal performance of vertical energy piles: An application. Appl. Energy 85, 901–910. https://doi.org/10.1016/j.apenergy.2008.02.010

Gao, J., Zhang, X., Liu, J., Li, K.S., Yang, J., 2008b. Thermal performance and ground temperature of vertical pile-foundation heat exchangers: A case study. Appl. Therm. Eng. 28, 2295–2304. https://doi.org/10.1016/j.applthermaleng.2008.01.013

Garbellini, C., Laloui, L., 2021. Thermal stress analysis of energy piles. Géotechnique 1–12. https://doi.org/10.1680/jgeot.19.p.208

Gawecka, K.A., Taborda, D.M.G., Potts, D.M., Cui, W., Zdravković, L., Haji Kasri, M.S., 2017. Numerical modelling of thermo-active piles in London clay. Proc. Inst. Civ. Eng. Geotech. Eng. 170, 201–219. https://doi.org/10.1680/jgeen.16.00096

GSHP Association, 2012. Thermal pile design, installation and materials standards. Gr. Source Heat Pump Assoc. Milt. Keynes 82.

GSHP Association, 2011. Closed-loop vertical borehole design, installation & materials standards 1–45.

Gunawan, A., Gouw, T.L., 2020. Numerical modelling of energy pile by different constitutive models. 16th Asian Reg. Conf. Soil Mech. Geotech. Eng. ARC 2019 2016–2019.

Hamada, Y., Saitoh, H., Nakamura, M., Kubota, H., Ochifuji, K., 2007. Field performance of an energy pile system for space heating. Energy Build. 39, 517–524. https://doi.org/10.1016/j.enbuild.2006.09.006

Huang, X., Wu, Y., Peng, H., Hao, Y., Lu, C., 2018. Thermomechanical Behavior of Energy Pile Embedded in Sandy Soil. Math. Probl. Eng. 2018. https://doi.org/10.1155/2018/5341642

Kramer,C., Basu, P., 2014.Experimental Characterization of Energy Output from a Model Geothermal Pile.Geo Congress 2014,GSP ASCE 2014 ://doi.org/10.1061/9780784413272.359

J.E., L., Loveridge, F.A., Powrie, W., 2015. Title: Thermal conductivity of soils by the needle probe method, for energy foundation applications for inclusion in the 32, in: 32nd International Thermal Conductivity Conference and the 20th International Thermal Expansion Symposium Authors: https://doi.org/10.5703/1288284315539

Jiang, G., Lin, C., Shao, D., Huang, M., Lu, H., Chen, G., Zong, C., 2021. Thermo-mechanical behavior of driven energy piles from full-scale load tests. Energy Build. 233, 110668. https://doi.org/10.1016/j.enbuild.2020.110668

Kalantidou, A., Tang, A.M., Pereira, J.M., Hassen, G., 2012. Preliminary study on the mechanical behavior of heat exchanger pile in physical model. Geotechnique 62, 1047–1051. https://doi.org/10.1680/geot.11.T.013

Knellwolf, C., Peron, H., Laloui, L., 2011. Geotechnical Analysis of Heat Exchanger Piles. J. Geotech. Geoenvironmental Eng. 137, 890–902. https://doi.org/10.1061/(asce)gt.1943-5606.0000513

Laloui, L., Cekerevac, C., 2003. Thermo-plasticity of clays: An isotropic yield mechanism. Comput. Geotech. 30, 649–660. https://doi.org/10.1016/j.compgeo.2003.09.001

Laloui, L., Di Donna, A., 2013. Energy Geostructures: Innovation in Underground Engineering, Wiley. John Wiley & Sons, Inc. https://doi.org/10.1002/9781118761809

Laloui, L., Moreni, M., Vulliet, L., 2003. Behavior of a bi-functional pile, foundation and heat exchanger. Can. Geotech. J. 40, 388–402. https://doi.org/10.1139/t02-117

Laloui, L., Nuth, M., Vulliet, L., 2006. Experimental and numerical investigations of the behavior of a heat exchanger pile. Int. J. Numer. Anal. Methods Geomech. 30, 763–781. https://doi.org/10.1002/nag.499

Laloui, L., Olgun, C.G., Sutman, M., McCartney, J.S., Coccia, C.J., Abuel-Naga, H.M., Bowers, G.A., 2014. Issues involved with thermoactive geotechnical systems: characterization of thermomechanical soil behavior and soil-structure interface behavior. DFI J. - J. Deep Found. Inst. 8, 108–120. https://doi.org/10.1179/1937525514y.0000000010

Laloui, L., Rotta Loria, A.F., 2020. Thermohydromechanical behavior of soils and soil–structure interfaces, Analysis and Design of Energy Geostructures. https://doi.org/10.1016/b978-0-12-816223-1.00005-9

Laloui, L., Rotta Loria, A.F., 2019. Analysis and Design of energy Geostructures, Accademic. ed.

Lettau H., 1954. Improved models of Thermal Diffusion in the soil. Trans. Am. Geophys. Union 35, 121–132.

Lie, T.T., Kodur, V.K.R., 1996. Thermal and mechanical properties of lightweight foamed concrete at elevated temperatures. Can. J. Civ. Eng. 23, 511–517. https://doi.org/10.1139/l96-055

Liu, H. long, Wang, C. long, Kong, G. qiang, Ng, C.W.W., Che, P., 2018. Model tests on thermo-mechanical behavior of an improved energy pile. Eur. J. Environ. Civ. Eng. 22, 1257–1272. https://doi.org/10.1080/19648189.2016.1248792

Liu, H., Liu, Hanlong, Xiao, Y., McCartney, J.S., 2018. Effects of temperature on the shear strength of saturated sand. Soils Found. 58, 1326–1338. https://doi.org/10.1016/j.sandf.2018.07.010

Loveridge, F., 2012. The Thermal Performance of Foundation Piles used as Heat Exchangers in Ground Energy Systems. Univ. Southhampt. 206.

Loveridge, F., McCartney, J.S., Narsilio, G.A., Sanchez, M., 2020. Energy geostructures: A review of analysis approaches, in situ testing and model scale experiments. Geomech. Energy Environ. 22, 100173. https://doi.org/10.1016/j.gete.2019.100173

Loveridge, F., Powrie, W., 2013. Pile heat exchangers: Thermal behavior and interactions. Proc. Inst. Civ. Eng. Geotech. Eng. 166, 178–196. https://doi.org/10.1680/geng.11.00042

Loveridge, F., Powrie, W., Nicholson, D., 2014. Comparison of two different models for pile thermal response test interpretation. Acta Geotech. 9, 367–384. https://doi.org/10.1007/s11440-014-0306-3

Man, Y., Yang, H., Diao, N., Liu, J., Fang, Z., 2010. A new model and analytical solutions for borehole and pile ground heat exchangers. Int. J. Heat Mass Transf. 53, 2593–2601. https://doi.org/10.1016/j.ijheatmasstransfer.2010.03.001

Mayne, P.W., Coop, M.R., Springman, S., Huang, A.-B., Zornberg, J., 2009. State-of-the-Art Paper (SOA-1): GeoMaterial Behavior and Testing. Proc. 17th Intl. Conf. Soil Mech. Geotech. Eng. 4, 2777–2872.

Murphy, K.D., McCartney, J.S., Henry, K.S., 2015. Evaluation of thermo-mechanical and thermal behavior of full-scale energy foundations. Acta Geotech. 10, 179–195. https://doi.org/10.1007/s11440-013-0298-4

Neville, A.M.1994. Properties of Concrete. 3rd ed. Harlow, UK: Longman Scientific & Technical.

Ng, C.W.W., Wang, S.H., Zhou, C., 2016. Volume change behavior of saturated sand under thermal cycles. Geotech. Lett. 6, 124–131. https://doi.org/10.1680/jgele.15.00148

Nguyen, V.T., Tang, A.M., Pereira, J.M., 2017. Long-term thermo-mechanical behavior of energy pile in dry sand. Acta Geotech. 12, 729–737. https://doi.org/10.1007/s11440-017-0539-z

Olgun, C.G., Ozudogru, T.Y., Abdelaziz, S.L., Senol, A., 2015. Long-term performance of heat exchanger piles. Acta Geotech. 10, 553–569. https://doi.org/10.1007/s11440-014-0334-z

Oliaei, M., Kiani, M.A., Torkaman, M., 2019. Advanced finite difference method for study energy piles behavior in temperature dependent soils. Springer Ser. Geomech. Geoengin. 0, 105–112. https://doi.org/10.1007/978-3-319-99670-7_14

Park, H., Lee, S.R., Yoon, S., Choi, J.C., 2013. Evaluation of thermal response and performance of PHC energy pile: Field experiments and numerical simulation. Appl. Energy 103, 12–24. https://doi.org/10.1016/j.apenergy.2012.10.012

Pasten, C., Santamarina, J.C., 2014. Thermally Induced Long-Term Displacement of Thermoactive Piles. J. Geotech. Geoenvironmental Eng. 140, 06014003. https://doi.org/10.1061/(asce)gt.1943-5606.0001092

Plaseied, N., 2012. Load-Transfer Analysis of Energy Foundations.Thesis.University of Colorado Boulder.

Rammal, D., Mroueh, H., Burlon, S., 2018. Impact of thermal solicitations on the design of energy piles. Renew. Sustain. Energy Rev. https://doi.org/10.1016/j.rser.2018.04.049

Randolph, M. F., Wroth, C. P. 1978. Analysis of deformation of vertically loaded piles. J. Geotech. Eng., 104(GT12), 1465–1488.

Rees, S.W., Adjali, M.H., Zhou, Z., Davies, M., Thomas, H.R., 2000. Ground heat transfer effects on the thermal performance of earth-contact structures. Renew. Sustain. energy Rev. 4, 213–265. https://doi.org/10.1016/S1364-0321(99)00018-0

Rotta Loria, A.F., Laloui, L., 2017. Thermally induced group effects among energy piles. Geotechnique 67, 374–393. https://doi.org/10.1680/jgeot.16.P.039

Saggu, R., Chakraborty, T., 2015. Thermal analysis of energy piles in sand. Geomech. Geoengin. 10, 10–29. https://doi.org/10.1080/17486025.2014.923586

Sani, A.K., Singh, R.M., Amis, T., Cavarretta, I., 2019. A review on the performance of geothermal energy pile foundation, its design process and applications. Renew. Sustain. Energy Rev. 106, 54–78. https://doi.org/10.1016/j.rser.2019.02.008

Shonder, J. A., Beck, J. V. 1999. Determining effective soil formation properties from field data using a parameter estimations technique. ASHRAE Transactions, 105, 1, 458–466.

Sittidumrong, J., Jotisankasa, A., Chantawarangul, K., 2019. Effect of thermal cycles on volumetric behavior of Bangkok sand. Geomech. Energy Environ. 20, 100127. https://doi.org/10.1016/j.gete.2019.100127

Spitler, J.D., Gehlin, S.E.A., 2015. Thermal response testing for ground source heat pump systems - An historical review. Renew. Sustain. Energy Rev. 50, 1125–1137. https://doi.org/10.1016/j.rser.2015.05.061

Stearns, C.R., 1969. Application of Lettau's Theoretical Model of thermal diffusion to soil profiles of temperature and heat flux. J. Geophys. Res. 74, 532–541. https://doi.org/10.1029/jb074i002p00532

Suryatriyastuti, M.E., 2013. NUMERICAL STUDY OF THE THERMO-ACTIVE PILES BEHAVIOR IN COHESIONLESS SOILS. Université Lillel Sciances and Technologies.

Suryatriyastuti, M.E., Mroueh, H., Burlon, S., 2014. A load transfer approach for studying the cyclic behavior of thermo-active piles. Comput. Geotech. 55, 378–391. https://doi.org/10.1016/j.compgeo.2013.09.021

Sutman, M., Brettmann, T., Olgun, C.G., 2019a. Full-scale in-situ tests on energy piles: Head and base-restraining effects on the structural behavior of three energy piles. Geomech. Energy Environ. 18, 56–68. https://doi.org/10.1016/j.gete.2018.08.002

Sutman, M., Olgun, C.G., Laloui, L., 2019b. Cyclic Load–Transfer Approach for the Analysis of Energy Piles. J. Geotech. Geoenvironmental Eng. 145, 04018101. https://doi.org/10.1061/(asce)gt.1943-5606.0001992

Terzaghi, K. 1943. Theoretical Soil Mechanics, John Wiley and Sons, New York.

Tinti, F., Barbaresi, A., Benni, S., Torreggiani, D., Bruno, R., Tassinari, P., 2014. Experimental analysis of shallow underground temperature for the assessment of energy efficiency potential of underground wine cellars. Energy Build. 80, 451–460. https://doi.org/10.1016/j.enbuild.2014.06.002

Vasilescu, A.R., 2019. Design and execution of energy piles: Validation by in-situ and laboratory experiments.PhD Thesis. Ecole centrale de Nantes.

Vesic, A.B. 1963. Bearing Capacity of Deep Foundations in Sand.Highway Research Record, Washington, DC.

Vieira, A., Alberdi-Pagola, M., Christodoulides, P., Javed, S., Loveridge, F., Nguyen, F., Cecinato, F., Maranha, J., Florides, G., Prodan, I., Van Lysebetten, G., Ramalho, E., Salciarini, D., Georgiev, A., Rosin-Paumier, S., Popov, R., Lenart, S., Poulsen, S.E., Radioti, G., 2017. Characterisation of ground thermal and thermo-mechanical behavior for shallow geothermal energy applications. Energies 10. https://doi.org/10.3390/en10122044

Wang, B., Bouazza, A., Singh, R.M., Haberfield, C., Barry-Macaulay, D., Baycan, S., 2015. Posttemperature Effects on Shaft Capacity of a Full-Scale Geothermal Energy Pile. J. Geotech. Geoenvironmental Eng. 141, 1–12. https://doi.org/10.1061/(ASCE)GT.1943-5606.0001266

Wang, C. long, Ng, C.W.W., Liu, H. long, Wu, D., Kong, G. qiang, 2016. Model tests of energy piles with and without a vertical load. Environ. Geotech. 3, 203–213. https://doi.org/10.1680/jenge.15.00020

Wang, C.L., Liu, H.L., Kong, G.Q., Ng, C.W.W., 2017. Different types of energy piles with heating-cooling cycles. Proc. Inst. Civ. Eng. Geotech. Eng. 170, 220–231. https://doi.org/10.1680/jgeen.16.00061

Wang, Z.J., Zhang, R.H., Fang, P.F., Wang, W.J., Wang, H.Y., 2019. Analysis of an energy pile enduring cyclic temperature loads. Geotech. Res. 6, 227–233. https://doi.org/10.1680/jgere.18.00043

Wu, D., Liu, H., Kong, G., Li, C., 2019. Thermo-mechanical behavior of energy pile under different climatic conditions. Acta Geotech. 14, 1495–1508. https://doi.org/10.1007/s11440-018-0731-9

Yavari, Neda, Tang, A.M., Pereira, J.M., Hassen, G., 2016. Effect of temperature on the shear strength of soils and the soil–structure interface. Can. Geotech. J. 53, 1186–1194. https://doi.org/10.1139/cgj-2015-0355

Yavari, N., Tang, A.M., Pereira, J.M., Hassen, G., 2016. Mechanical behavior of a small-scale energy pile in saturated clay. Geotechnique 66, 878–887. https://doi.org/10.1680/jgeot.15.T.026

Yavari, N., Tang, A.M., Pereira, J.M., Hassen, G., 2014. Experimental study on the mechanical behavior of a heat exchanger pile using physical modelling. Acta Geotech. 9, 385–398. https://doi.org/10.1007/s11440-014-0310-7

Zarrella, A., De Carli, M., Galgaro, A., 2013. Thermal performance of two types of energy foundation pile: Helical pipe and triple U-tube. Appl. Therm. Eng. 61, 301–310. https://doi.org/10.1016/j.applthermaleng.2013.08.011

3 Thermo-hydro-mechanical FE analyses

3.1 *Introduction*

Numerical analyses are a powerful tool to investigate several aspects of thermo-mechanical interaction between EPs and soil allowing long term prediction and parametric study in a time effective manner. During operational conditions distinct features of the thermo-mechanical behavior should be analysed to predict thermal, structural, and geotechnical performance of such foundations. The thermal module introduced in 2015 in the commercially available FEM package PLAXIS 2D/axi-symmetrical allows simulating thermo-mechanical interaction under transient conditions. The thermal module implements several features as thermo-hydro-mechanical coupling for both saturated and unsaturated soil and fully coupled formulation and implementation. The effects of temperature on the retention curve and on mechanical properties are not taken into account by the software but generally it could be assumed as a reasonable simplification for the range of temperature variations of geothermal piles. The results of transient thermo-hydro-mechanical FE analyses carried out by PLAXIS 2D are presented in this section. Simulations carried out with different thermo-elastic constitutive soil models confirm the possibility of reproducing the experimental response observed during experimental studies. The laboratory case reported by Yavari et al. (2014), in situ monitoring by Murphy and McCartney (2015) and Lambeth college test of Bourne-Webb et al., (2009) are back-analysed in this section. A simple procedure to calibrate the model's parameter is also proposed and validated. The results of a parametric study, focusing on the impact of different parameters on pile-soil thermo-mechanical interaction, are also presented.

3.2 *Thermo-mechanical simulations with PLAXIS 2D thermal*

3.2.1 FE Analyses with PLAXIS 2D

The Plaxis 2D program uses automatic generation of FE meshes based on a robust triangulation. The mesh generator requires a global meshing parameter, I_e, which is calculated from the outer geometry dimensions and the Relative element size factor according to Equation 3-1.

Equation 3-1: $I_e = r_e \cdot 0.06 \cdot \sqrt{(x_{max} - x_{min})^2 + (y_{max} - y_{min})^2}$

The basic elements to model soil layers and other volume clusters are either 15-Node or 6-Node triangular elements. Each node has a number of degrees of freedom that correspond to discrete values of the unknowns in the boundary value problem to be solved (in 2D FE model only two translational degrees of freedom per node). The 15-node triangle, default element, provides a fourth order interpolation for displacements and the numerical integration involves twelve Gauss points. A mesh composed of 15-node elements gives a finer distribution of nodes and therefore more accurate results than a similar mesh composed by an equal number of 6-node elements. In areas where large strain or stresses could be expected to occur a finer element mesh is required. The definition of a local Coarseness factor allows to locally refine the mesh. By default, this factor is set to unity because the relative element size corresponds to the target element size, decreasing this factor the element size is reduced respect to the target element size. A Value of 0.5 corresponds to element size that are half of the target element size. For a proper modelling of soil-structure interaction interfaces joint elements could be added to the model.

The interface elements are numerically integrated using 6-point Gauss integration. The distance between the two nodes of a node pair is zero. Each node has three translational degrees of freedom (ux, uy, uz). As a result, interface elements allow for differential displacements between the node pairs (slipping and gapping).

The material properties of the interface can be assigned according two options available in the software: *From adjacent soil* where the roughness of the interaction is modelled by choosing a suitable value for the strength reduction factor or Custom where a material dataset can be assigned directly. The interface could be "*rigid*" if the strength of the interface is not reduced respect that of the surrounding soil according to the software manual. It could be "*not rigid*", through a strength reduction factor has to be fixed small than unity, to simulate that the interface is weaker than the surrounding soil.

The analyses can be based on several types of calculations: initial phase, plastic equilibrium phase, safety and transient fully coupled phase (described in the following chapter).

The initial phase corresponds to the initial stress state generation (*K_0 procedure*, *Gravity loading* and *Field stress*). *K_0 procedure* is adopted in the simulations performed in this chapter *and it is based on the* definition of vertical stresses that are in equilibrium with the self-weight of soil and horizontal stresses by the k_0 values specified in the tab sheet of the material. This procedure is particularly suitable in cases with horizontal surface and groundwater level parallel to surface when dealing with non-horizontal surfaces and weight stratifications the procedure is not recommended. The stress field equilibrium is not checked at the end of the phase leading in some cases, as K_0 values greater than unity, to out of balance forces and plastic points. A plastic nil-phase, where no additional load is applied, is advisable, after this phase, to perform equilibrium corrections.

Plastic calculation is used to carry out elastic-plastic analysis in which is not necessary considering change of pore pressure with time when external loading is applied. The load can be defined in the sense of changing the load combination, stress state, weight, strength or stiffness of elements. The total load level is reached at the end of the calculation phase and is defined by a new load configuration.

Thermo Hydraulic coupling may be used to analyse the effects of temperature change on stress, deformation and groundwater flow simultaneously through a fully coupled analysis type.

3.2.2 Transient thermo-hydro-mechanical analyses

The thermal module extension allows implementation of flow-deformation analyses that take into account non-isothermal unsaturated ground water flow, heat transport, thermal deformations and effects of temperature on stress and deformation. The computation of heat exchanging problems is based on the principle of local thermodynamic equilibrium where each phase, solid, gas (constant pressure) and liquid, has the same temperature. The variables of the problem are temperature, displacement and pore water pressure. PLAXIS 2D allows for fully coupled transient *Thermo-Hydro-*M*echanical* (THM) calculations of problems in which the time-dependent effect of changes of temperature on stress, deformation and groundwater flow are to be taken into account simultaneously. The constitutive relation in terms of effective stress is function of the thermal strains defined through the drained thermal linear expansion coefficient of soil skeleton in x, y and z directions. The governing equation for the deformation model is obtained as difference of the total strain of the soil skeleton and the thermal strain caused by temperature increase.

The heat transport balance equation accounts for the conductive heat flow, the advective internal flux in the water and a heat source term. In case of unsaturated porous media, the total heat flux is the sum of diffusive heat flux and advective flux.

Transient thermal calculations are based on thermal flow boundary conditions assigned in the model. Different kinds of conditions can be assigned: constant temperature or thermal functions, closed boundary (perfectly insulated), convective boundary, thermosyphons that become closed boundary when the air temperature is higher than a fixed limit value, Inflow when a prescribed heat flux adds energy to the model, Outflow when a prescribed heat flux absorbs energy from the model.

The climate option can be used to specify a general convective condition simulating the exposition to the outdoor weather condition; typically, this option is used for the boundaries that represent the ground surface.

3.2.3 Modelling of soil mechanical behavior

The mechanical behavior of the soil may be modelled through fourteen available constitutive models or additional user defined model. In this study Mohr-Coulomb (MC) and Hardening soil model (HS) have been adopted. The linear elastic perfectly - plastic Mohr-Coulomb model could be considered as a first order of approximation of soil behavior. The linear elastic part of MC model is based on Hooke's law of isotropic elasticity. The perfectly plastic part is based on the Mohr-Coulomb failure criterion, formulated in a non-associated plasticity theory. The yield condition consists of six yield functions formulated in terms of principal stresses and two plastic parameters, friction angle and cohesion. In principal stress space the yield surface is a fixed hexagonal cone. In addition to the yield function six plastic potential functions depend on principal stress state and dilatancy angle. The standard Mohr-Coulomb criterion allows for tension in case of cohesive soils. This behavior cold be included in PLAXIS specifying a tension cut-off introducing three additional yield functions. This model requires the definition of five parameters: Young's modulus (E), Poisson's ratio (ν), Cohesion (c), Shear strength angle (φ) , Dilatancy angle (ψ), and Tensile strength (σ_T).

The value of the Young's modulus adopted in the calculation requires particular attention because in this model is possible only to account for the increasing of stiffness with depth while soil nonlinearity requires the definition of an equivalent average modulus. A suggested value for the Young's modulus, adopted in many simulations of live conditions is the secant stiffness at 50% of strength. In the MC model is not possible to simulate the end of dilatancy when the critical state is reached, and the soil continues to dilate as long as shear deformation occurs.

The Hardening Soil model is an advanced model suitable to simulate the behavior of different type of soil (Shanz ,1998). The background is the hyperbolic relationship between vertical strain and deviatoric stress in primary triaxial loading. In contrast to an elastic perfectly plastic model through shear and compression hardening, HS model has yield surface not fixed in the principal stress space because it could expand due to plastic straining. Shear hardening is connected to the irreversible strains due to primary deviatoric loading, while compression hardening is connected to plastic strains due to isotropic or eodometric loadings. The model allows to account for: stress dependent stiffness according to an input parameter (m) that defines the shape of the yield loci, plastic straining due to primary deviatoric loading via the modulus E_{50}^{ref}, Plastic straining due to primary compression via the modulus E_{oed}^{ref}, Elastic unloading/reloading input parameters via the modulus E_{ur}^{ref}, Failure according to Mohr-Coulomb criterion via the usual parameters c, φ and ψ.

The plastic straining due to primary deviatoric loading is simulated through the confining stress dependent stiffness modulus for primary loading which is function of the reference stiffness modulus E_{50}^{ref} corresponding to the reference confining pressure p_{ref}. The amount of stress dependency is connected to the power m which could be considered in a range of 0.5-1. The ultimate deviatoric stress is derived from the Mohr-Coulomb failure Criterion involving the shear strength angle and cohesion. For Unloading-reloading stress path the stress dependent stiffness modulus is used E_{ur}^{ref}. The material model manual of the software suggests that this modulus should be at least three times E_{50}^{ref}. In the HS model an associated flow rule is defined as linear relation between rates of plastic shear strain γ^P and plastic volumetric strain ε_v^P(

Equation 3-2).

Equation 3-2 : $\varepsilon_v^P = \gamma^P \sin\psi_m$

Where ψ_m is the mobilized dilatancy angle which depends on the critical state shear strength angle and the mobilized shear strength angle. The parameters of the model are listed in Table 3-1.

Table 3-1: Basic parameters of the HS model

E_{50}^{ref}	Secant Stiffness reference module	[kN/m²]
E_{oed}^{ref}	Tangent Stiffness for primary oedometer loading	[kN/m²]
E_{ur}^{ref}	Unloading reloading reference stiffness	[kN/m²]
ν_{ur}	Poisson's ratio for unloading reloading	[-]
c	Cohesion	[kN/m²]
φ	Shear Strength Angle	[°]
ψ	Dilatancy angle	[°]
σ_T	Tensile strength	[kN/m²]
m	Power for stress level dependency of stiffness	[-]
p_{ref}	Reference stress (default=100 kPa)	[kN/m²]

The oedometer stiffness is related to the compaction hardening part. On the other hand, Secant Stiffness and Unloading-reloading stiffness are related to the frictional hardening part. To explain the plastic volumetric strain in isotropic compression, a second type of yield surface must be introduced to close the elastic region (compaction hardening). The yield surface is mainly controlled by the Secant Stiffness modulus, the eodometer modulus controls the cap yield surface.

3.2.4 Modelling of thermo-mechanical problems for single EP

In this chapter numerical simulations of the single pile behavior are performed using axial-symmetric models. The step calculation sequence adopted in the analysed cases is always the same with some minor differences connected to the time duration of the imposed thermal variations and the presence of mechanical loadings. In any case the initial stress state of the soil is modelled through the k_0 procedure. When full scale cases are simulated, k_0, for different soil layers, is assigned manually with values judged adequate according to the change of the in-situ stress conditions induced by the installation of pile. When external mechanical loadings are applied to the pile head, a plastic step is performed. During the plastic phase at the pile-soil contact interfaces are activated to model the intense shear zone. In such a case interfaces are modelled through M-C constitutive model and assuming zero dilatancy. To model the application of thermal variations on the pile and the effects of the geothermal system operation on soil temperature fully coupled phases are calculated. The temperature distribution is calculated by means of transient thermal flow FE calculation based on the input thermal flow boundary conditions and assigning appropriate thermal model parameters to pile and soil (e.g.,3.5.1). The thermal calculation starts from an initial temperature defined in previous phases that is assumed to be constant or variable with depth through the definition of earth gradient per meter of soil depth. The input thermal conditions are applied inside the pile to model the presence of the heat exchanging circuit. The difference between the inlet and outlet temperature of the heat career fluid is neglected as the thermal resistance of the plastic pipe in which the fluid is circulating. Thermal conditions are applied to all the boundary of the model and its sizes are assumed sufficiently large to neglect the effect of the thermal boundary conditions on the pile-soil thermal and mechanical interaction. Thermal variations on the shallow part of the model are considered through the climate option that allow the interaction with the external environment (building or outdoor air) through the definition of the heat transfer coefficient.

3.3 *Numerical modelling of small-scale EP in dry sand (Test of Yavari et al., 2014)*

The small-scale laboratory experiments published by Yavari et al. (2014) and described in 2.3.1 were chosen for back-analyses purposes both because of the thermo-mechanical coupling and because the dry sandy soil used in the chamber is widely known and investigated (Fointaiblue sand). Yavari et al. (2014) reported the detailed time histories of the thermal cycles only for the test E2 (at zero head load) and test E6 (at 250 N). For this reason, in the following sections numerical back-analyses are carried out with reference only to these two tests. The main soil physical and mechanical parameters for the sand as reported by De Gennaro et al. (2008) are listed in Table 3-2.

In the case of the model tests by De Gennaro et al. (2008) however the sand was indeed subjected in a sort of calibration chamber to a confining isotropic state of stress p'=100 kPa.

Table 3-2: Soil parameters for Fointanbleu sand at DR=50% (De Gennaro et al. 2008)

	γ [kN/m^3]	c [kPa]	φ [°]	ψ [°]	E [MPa]	K_0 [-]	p' [kPa]
Fointanbleu dry sand	15	-	36.5	6	34	0.5	100

On the other hand, in the case of Yavari et al. (2014) the stress level in the box of the model was significantly lower. For this reason, soil stiffness was fixed on the basis of the mechanical load tests results and used in the back-analysis of the thermomechanical tests. The analyses were carried out adopting two different constitutive models for the sandy soil: the elastic-perfectly plastic Mohr-Coulomb (M-C) model and the Isotropic Hardening (H-S) model. A fine mesh of 3574 triangular (15-noded) elements was used to discretize the axial symmetric model. The size of the FEM model was assumed equal to the size of the experimental container. Interface elements were adopted to allow slip at the pile-soil contact and to simulate the thin zone of intensely sheared material at the contact between the pile and the surrounding soil.

The pure mechanical axial load test E1 was used to calibrate strength and stiffness parameters of the elastic-plastic M-C and H-S soil models. A classical best fit procedure based on the trial-and-error method was adopted to simulate the test E1, which can be considered as an *I*deal *L*oad *T*est, *ILT*, according to the definition by Russo (2013). After several attempts the set of parameters listed in table 5.2 was obtained. The aluminium pipe was assumed linear elastic and an equivalent Young's modulus was assigned for the pile modelled as a solid cylinder.

Table 3-3: Soil parameters for Fointanbleu dry sand obtained from the calibration procedure and pile properties used in the FEM model

	γ [kN/m^3]	c [kPa]	φ [°]	ψ [°]	E (M-C) [MPa]	E_{50}=E_{oed} (H-S) [MPa]	E_{ur} (H-S) [MPa]
Fointanbleu dry sand	15	0,1	37	7	4	4	12
Aluminium pile	20	-	-		23000	-	-

For each soil models the interface was activated allowing relative vertical displacements between the pile and the surrounding soil but keeping the same shear strength and stiffness parameters of the Mohr-Coulomb model adopted for the Fointanbleu sand. As an example of the sensitivity study conducted at this stage, just three different predictions obtained via the simple M-C model are compared.

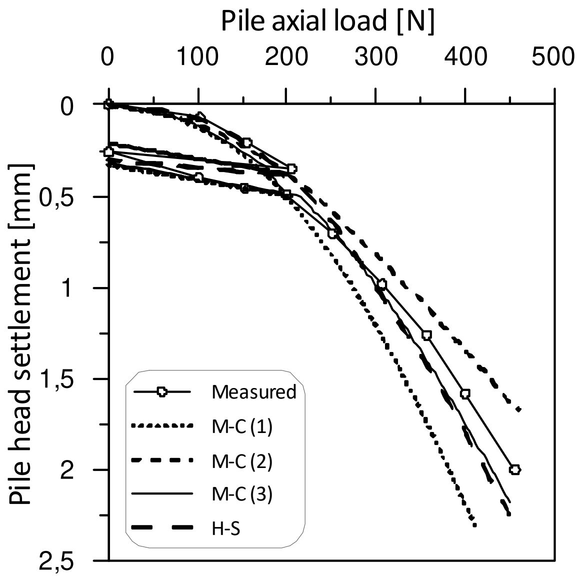

Figure 3-1: Comparison between measured and calculated load settlement relationship for test E1.

The differences among the predictions derive from the adoption of three values of shear strenght angle φ and of dilatancy angle ψ. M-C (3) is the final prediction which is also the one showing the best agreement with the experimental curve and is obtained by assuming the values reported in Table 3-2(i.e., φ =37° and ψ =7°). M-C (1) and M-C (2) are the predictions obtained by assuming φ =36° and ψ =6° and φ =38° and ψ =8°, respectively. The two soil models M-C and H-S were then used for back-analysing the thermal experiments E2 and E6. The Thermal properties reported by Yavari et al. (2014) are assigned to the dry sandy soil and aluminium pile. Thermal simulations are carried out defining thermal boundary conditions. More precisely in the FEM model (Figure 3-3) a time dependent thermal boundary condition along the axis of symmetry of the pile was applied.

Below the pile tip, the axis of symmetry was defined as a closed flow boundary while the bottom and right boundaries of the model were set as constant temperature boundaries, the constant selected value corresponding to the environment temperature of the experimental setup. The thermal histories applied to the model pile in tests E2 and E6 correspond to the temperature functions reported by Yavari et al. (2014) (Figure 3-2 (a) and Figure 3-2 (b)). The numerical analyses were carried out using the transient flow option being the applied thermal history characterized by rather quick changes of the imposed temperature.

The FEM results are documented in terms of the head settlement time history (Figure 3-4 a and Figure 3-4 c) and head settlement versus temperature (Figure 3-4 b and Figure 3-4 d). The computed results are also compared with the available experimental measurements obtained considering the two soil constitutive models.

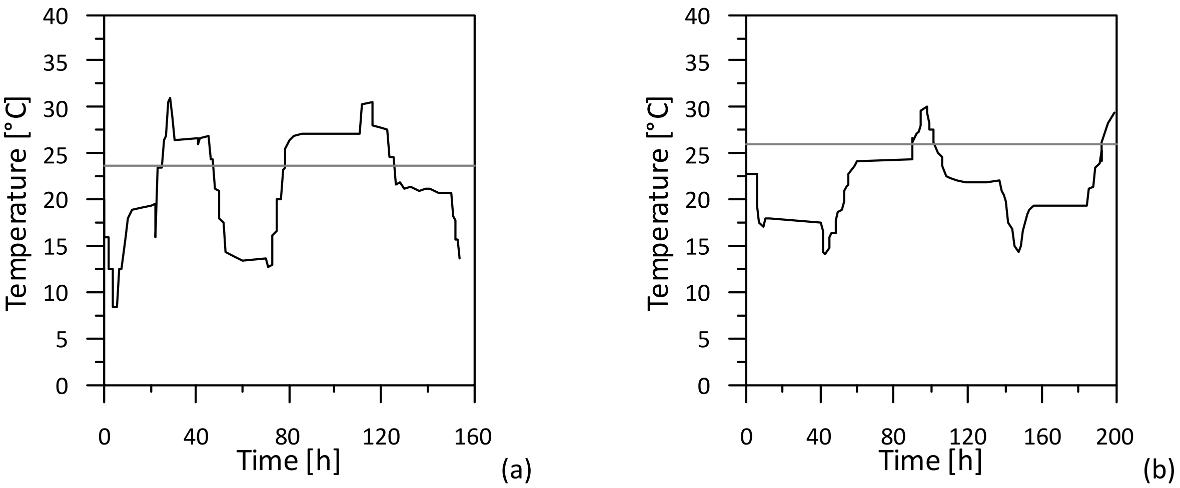

Figure 3-2: Temperature history applied to the pile during (a) Test E2 (b) and Test E6.

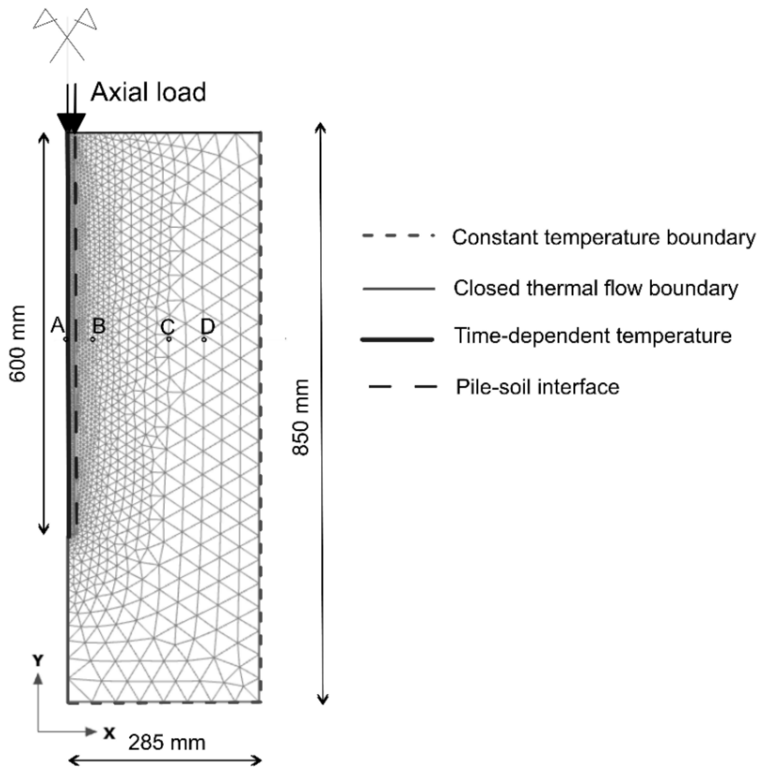

Figure 3-3: Finite element mesh and thermal boundary conditions used to simulate the model-scale problem

As shown by Figure 3-4 (b) the observed pile head movements with the temperature change were essentially reversible for test E2. The full excursion range being just a bit smaller than the theoretical free thermal expansion curve obtained by imposing thermal change to an ideally free aluminium pile. This is an expected result considering that surrounding soil i.e., soil-pile interaction acts as partial constraint to the free expansion of pile. The calculated pile head settlement, for both soil models, are very similar. Not largely different are observed by an engineering point of view. The largest difference between computed and measured head settlement, however, occur at the end of the first cooling step and correspond to around 30% of the measured value (Russo et al., 2019).

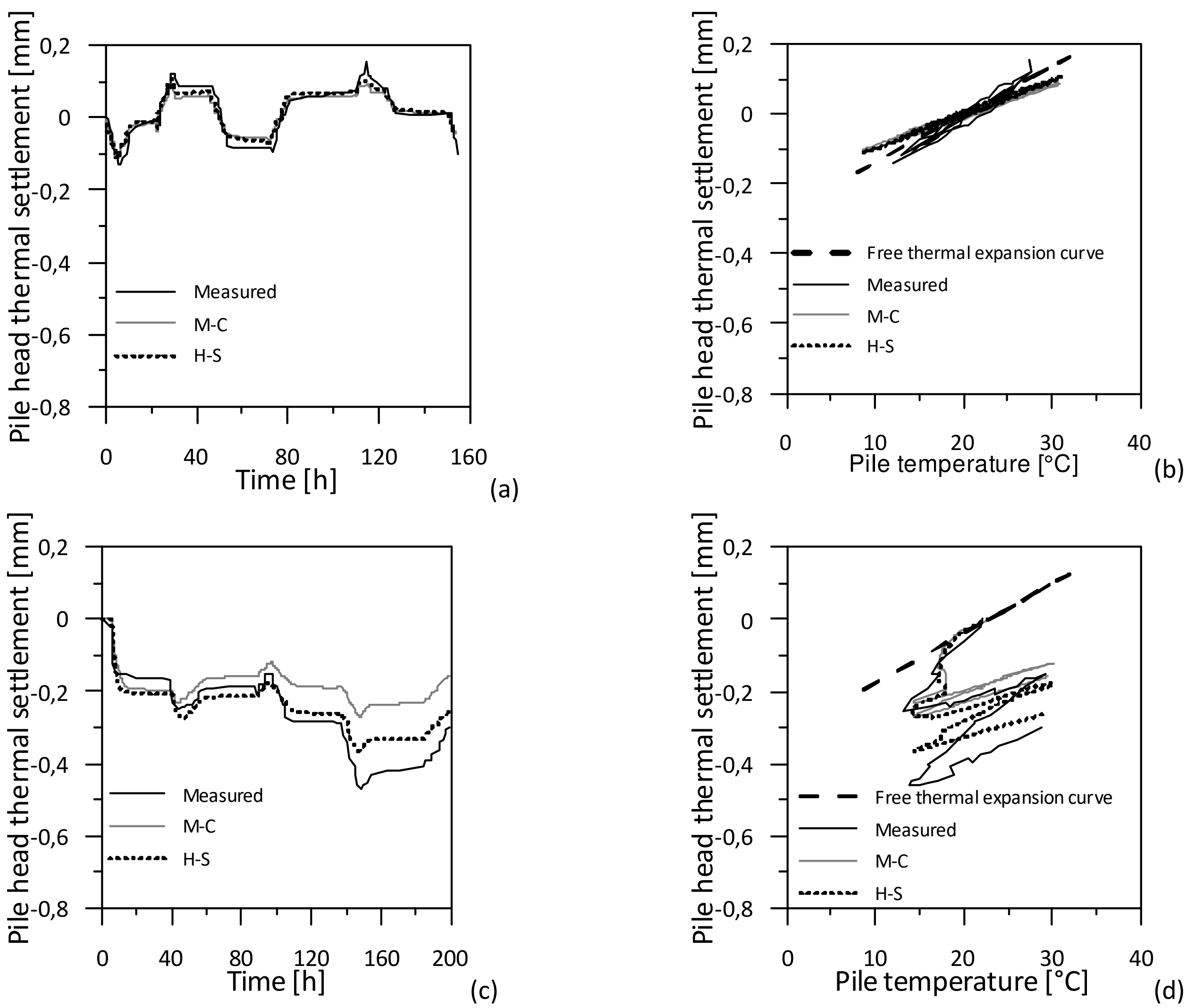

Figure 3-4: Comparisons between measured and calculated pile head thermal settlement for tests E2 (a and b) and E6 (c and d).

In the case of test E6 the thermal calculations followed the application of 250 N axial load corresponding to one half of the pile measured axial bearing capacity. As shown by Figure 3-4 (c), irreversible settlements have already occurred in the first thermal cycle and increases further in the second thermal cycle. Being the thermal cycles very similar to the ones adopted in the test E2, there is a clear coupling between mechanical and thermal loading even for this single free head pile test. In the case of test E6 however the comparison between the two models shows that the H-S model is better than the M-C model in predicting the amount of irreversible strains. At the end of the thermal history the H-S computed final settlement is only 20% smaller than the observed value while for the M-C model the difference increases to more than 40%.

3.4 *Numerical modelling of full-scale tests on EP*

With the aim to establish procedures to analyse the thermo-mechanical problems by numerical methods and to fix criteria for the calibration of the parameters to be introduced in the model further to validate the fully coupled thermo-hydro-mechanical module of FEM package PLAXIS 2D, the experimental data of Lambeth College test in London (Bourne-Webb et al., 2009) and McCartney and Murphy (2014) in Denver are back analysed in the following sections.

3.4.1 Simulations of energy foundations during building operations housing authority case in Colorado

The case study of Murphy and McCartney (2014) and McCartney and Murphy (2012) represents one of the few well detailed thermo-mechanical monitoring reported in literature on existing EGs. Two piles as a part of the foundation of the eight-story Housing Authority in Denver were coupled into a conventional GSHP system. Foundation A is under the centre of the building while Foundation B is located under an exterior wall of the building slab. Foundation B was considered in this study, it was 13.4 m long and had a diameter equal to 0.91 m. The pile includes four loops of polyethylene tubing installed within the reinforcing cage. Six concrete embedment vibrating wire strain gages (VWGs) and thermistors were incorporated into the foundation to monitor the axial strain profile under mechanical and thermo-mechanical loadings. A datalogger was used to record data hourly from December 29, 2011 to October 19, 2013, even though there was an interruption of data recording right after April 27, 2012. The soil stratigraphy at the site consists of an upper layer 3 m thick of urban fill, intermediate layer 4.6 m thick of medium dense sand and gravel and a final layer of Denver claystone. Groundwater table was encountered at 7.6 m below the ground surface. The thicknesses of the soil layers along with the measurements from field tests are reported by Murphy and McCartney (2014). Seasonal changes in the temperature profiles within the foundations before operation of the heat pump started were reported by McCartney and Murphy (2012). They observed that the depth of shallow zone was located at 5 m -6 m and characterized by 15 °C of temperature. An insulating effect of the building slab was observed in the near-surface foundation temperatures. For Foundation A compared to Foundation B temperature is more sensitive to outdoor air variations. Air temperature data reported by the authors were assigned as surface thermal boundary condition.

Figure 3-5 shows the geometry, FE mesh and the thermal boundary conditions adopted for the analyses.

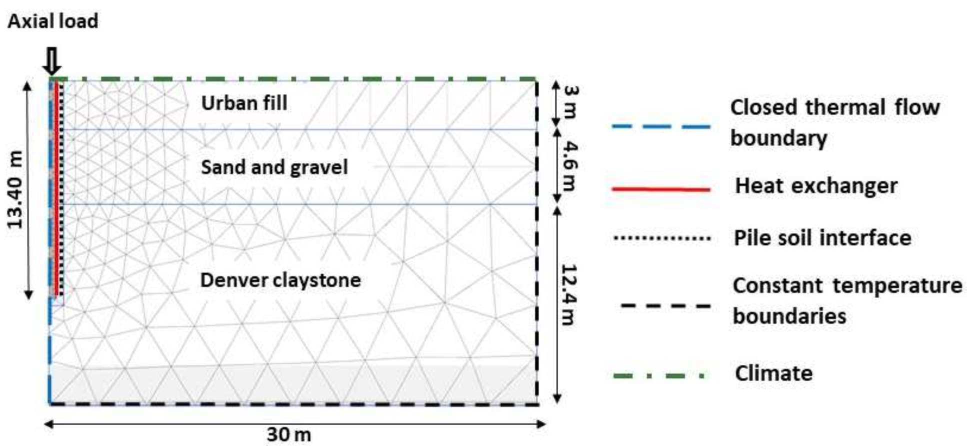

Figure 3-5: Finite element mesh used for the Denver Housing Authority test.

The calculations were carried out in four phases: Initial phase (K_0 procedure), plastic phase (nil step), plastic step and fully coupled flow-deformation step. During the second plastic step a mechanical load corresponding to the presence of the building (7.2 MPa) was applied and kept constant during the following fully coupled step. During the coupled thermo-mechanical phase temperature function was applied to the pile and the air ambient temperature was assigned at soil surface as reported in Figure 3-6. The thermal loading considered was the temperature recorded by the thermistors inside the test pile. M-C model was used for the soil layers while the pile was modelled as linear elastic (LE). The materials' properties (Table 3-4) were defined on the basis of the data available from Murphy and McCartney (2014). For the Denver Claystone Abu-Hejleh and Attwooll (2005) report was used to calibrate stiffness and resistance parameters.

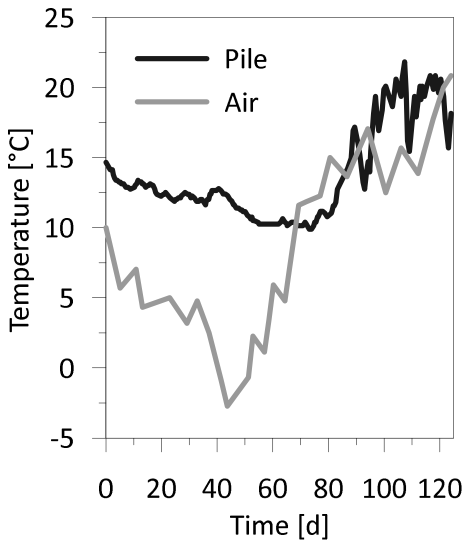

Figure 3-6: Temperature function applied during the fully coupled calculation phase, temperatures applied to the pile (Pile) and to the ground surface (Air).

Table 3-4: Material parameters used for the back-analysis of the Denver Housing Authority.

	Unit weight (γ) [kN/m³]	Shear Strength angle (φ) [°]	Cohesion (c') [°]	Young modulus (E) [Mpa]	Thermal conductivity (λ) [W/m°C]	Specific heat capacity (c_s) [J kg^{-1} °C^{-1}]	Thermal expansion coefficient ($_s$) [°C^{-1}]
Urban Fill	16	35	-	7.2	0.2	4.44	1.17E-05
Sand and gravel	18	42	-	66	0.3	6.39	5.25E-04
Denver Claystone	21	38	200	190	0.25	6.07	1.13E-04
Concrete	25	-	-	30000	1.8	800	1.00E-05

The analysis has been focused on the 124 days of the heat pump operation, starting from December 29, 2011 until a programming issue with the datalogger stopped the data-recording for about three months.

Foundation B observed behavior in terms of mechanical stress and strains is compared to the results of numerical analysis in Figure 3-7. The measured values reasonably match with the computed values. The measurement at 3 m depth was different to those obtained from numerical results. Experimental strains measured during the elapsed are compared to the numerical results in Figure 3-7 a, Figure 3-7 b, Figure 3-7 c, Figure 3-7 d, Figure 3-7 e and Figure 3-7 f. All the depth of measures were compared. A reasonable agreement between the experimental and numerical results is observed.

Overall, results in terms of contraction during cooling of the pile seem to be well simulated. During the heating of the pile FE analysis gives a slightly underestimation of induced thermally axial strains in the upper third of the EP.

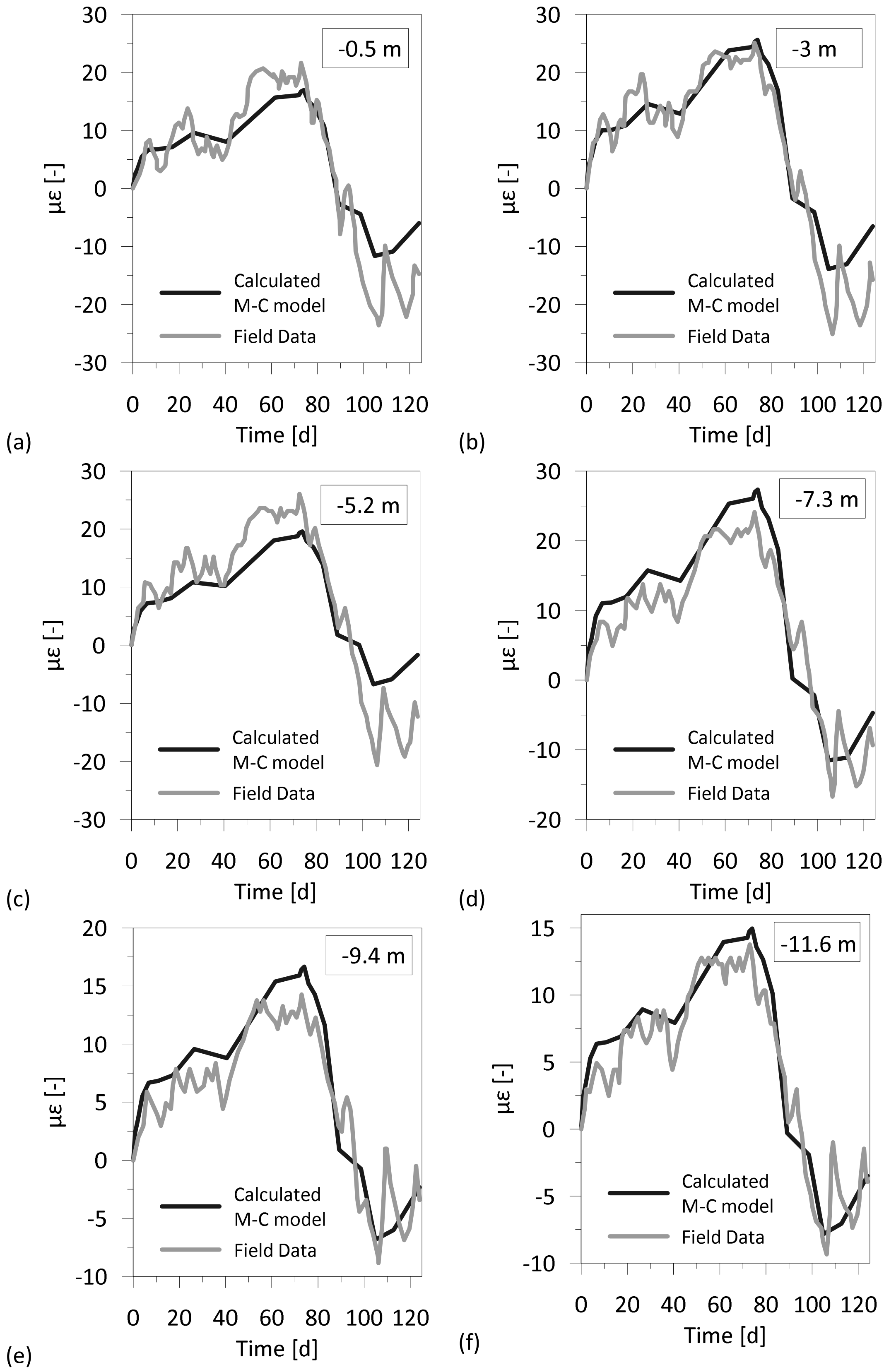

-0.5 m
-3 m
-5.2 m
-7.3 m
-9.4 m
-11.6 m
Calculated
M-C model
Field Data
με [-]
Time [d]
(a)
(b)
(c)
(d)
(e)
(f)

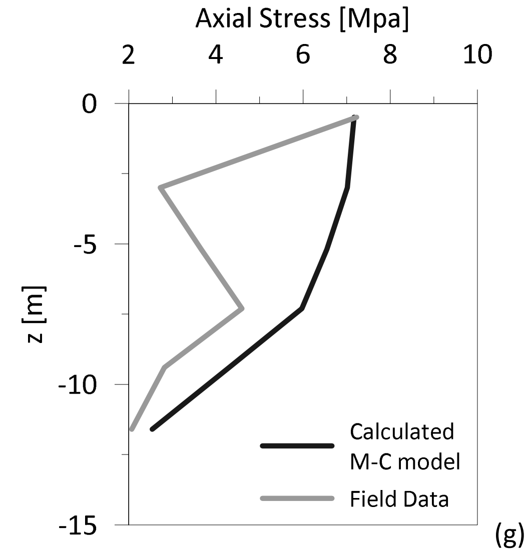

Figure 3-7: Comparison between the experimental and simulated results; Thermal strains at 0.5 m (a), 3 m (b), 5.2 m (c),7.3 m (d), 9.4 m (e) and 11. 6 m (f) and (g) Mechanical stress profile induced by the weight of the building.

3.4.2 Simulations of Lambeth college Case (Bourne-Webb et al. 2009)

The Lambeth College test was described in more details in 2.2.1 was back analysed in this section. Thermal and mechanical load time history are reported in Figure 3-8 (Maiorano et al., 2019).

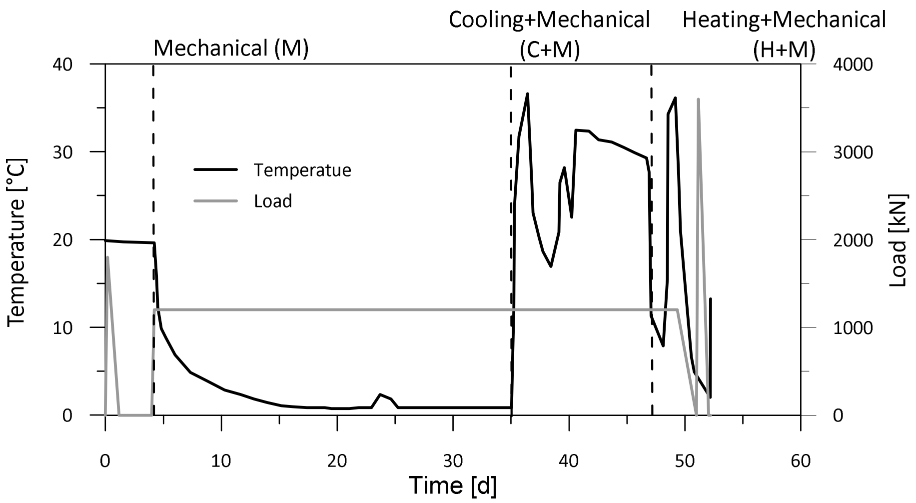

Figure 3-8: Pile load and temperature recorded in the Lambeth College test pile vs. time.

The thermal loading considered was the temperature recorded by the thermistors inside the test pile. The initial ground temperature assigned to the whole model was 20 °C as reported by the authors of the test. Figure 3-9 shows the finite element mesh and the thermal boundary conditions adopted for the analyses. M-C model was adopted for the soil layers while the pile was modelled as LE. The material properties (Table 3-5) corresponded to those adopted by Gawecka et al., (2017) and Adinolfi et al. (2018). The pile stiffness EA is calculated on the basis of the back-calculated value of the Young's modulus E, equal to 40 GPa (Bourne-Webb et al., 2009), and, obviously of the transverse area A of the pile section.

Table 3-5: Material parameters used for the back-analysis of the Lambeth College Test.

	Pile	River deposits	London clay	units
Unit weight (γ)	20	19	19	[kN/m^3]
Young modulus (E)	40000	13	70	[MPa]

Thermal expansion coefficient (α)	8.5 x 10^{-6}	1.7 x 10^{-5}	1.7 x 10^{-5}	[$°C^{-1}$]
Thermal conductivity (λ)	2.33	1.40	1.79	[W $m^{-1}°C^{-1}$]
Specific heat capacity (c_s)	960	950	910	[J kg^{-1} $°C^{-1}$]
Permeability (k)	-	1 x 10^{-5}	1 x 10^{-9}	[m/s]
Cohesion (c')	-	1	5	[kPa]

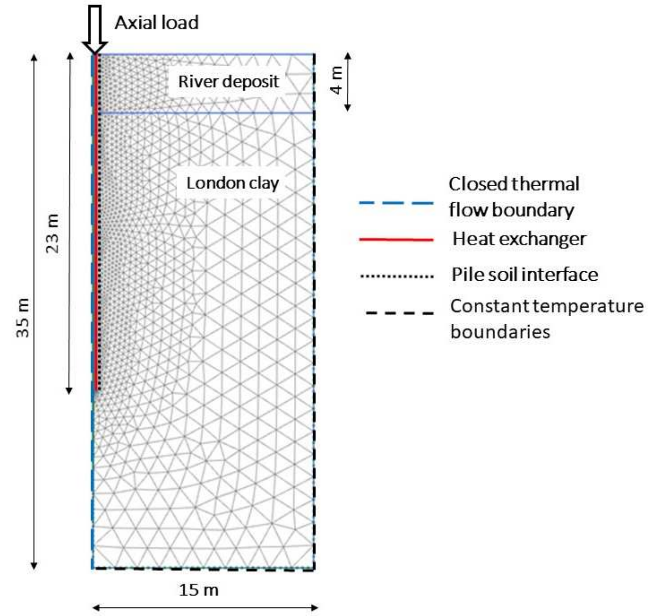

Figure 3-9: Finite element mesh used for the Lambeth College test.

The initial temperature of 20 °C is assumed to be constant over the whole FE mesh. Numerical analysis reproduces the same conditions occurred during the experiment. All the thermomechanical stages were performed using a fully coupled-thermo-hydro-mechanical analysis. The mechanical loading, unloading and reloading steps were modelled as plastic phases under isothermal conditions. Thermal loadings were applied to the pile as temperature time function at the location of the PC. Numerical results are compared to measurements on site in terms pile's head displacement and axial load, in Figure 3-9 and Figure 3-10, respectively. The displacement of the pile head during the initial loading is over predicted by the FE analyses while during the subsequent unloading phase a good agreement is observed. During the cooling phase FE analysis overestimated pile's head settlement while the subsequent heating phase is better reproduced.

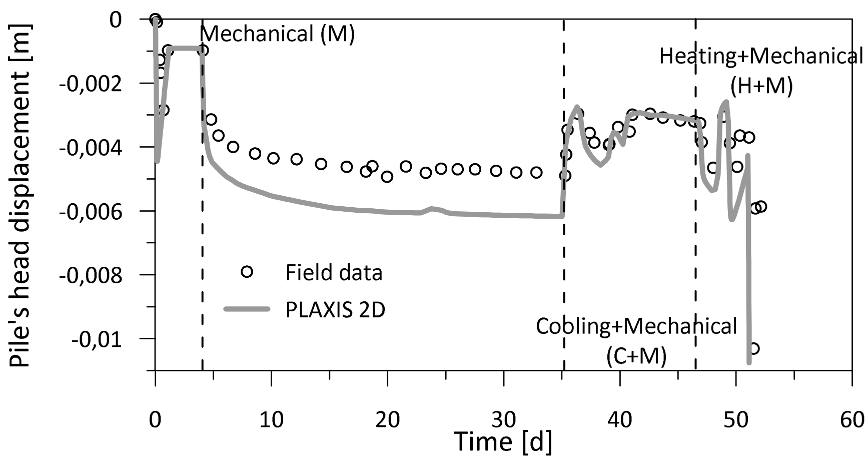

Figure 3-10: Pile head vertical displacements comparison between Field data and calculated by FEM (PLAXIS 2D) results during the end of reloading stage (M), the end of cooling (C+M) and heating (H+M) phases.

The fact that pile's head displacements are over predicted in the heating phase can be attributed to the assumed constant stiffness that does not depend on the strain level (Maiorano et al., 2019).

In Figure 3-11 (a) mechanical axial load profiles obtained from the FEM simulation compared to the experimental data. The numerical data are in good agreement with measurements. In Figure 3-11 (b) and Figure 3- 11 (c) experimental thermomechanical load profiles are compared to the numerical results during cooling and heating episodes, respectively.

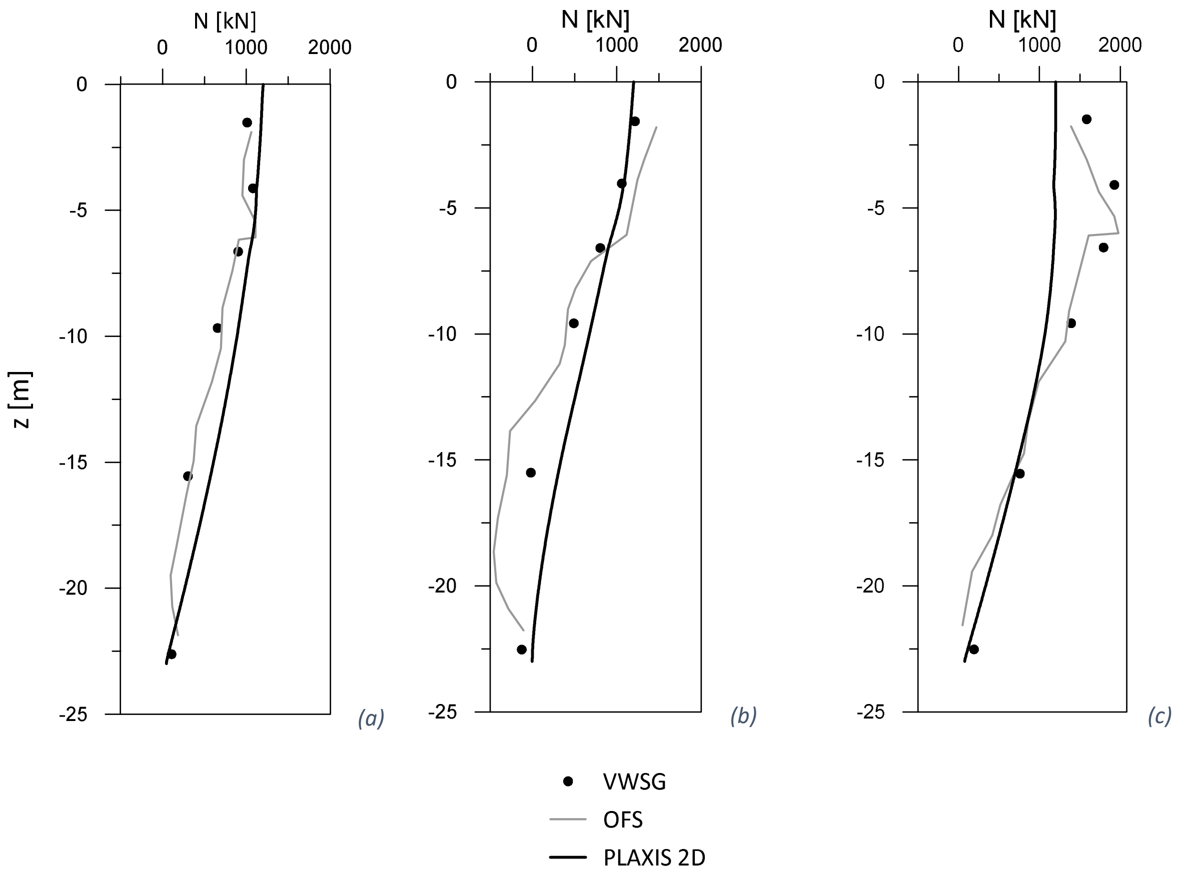

Figure 3-11: Comparisons between experimental (OFS and VWG) and calculated by FEM (PLAXIS 2D) result, during the end of reloading stage (a), at the end of the cooling phase (b) and heating (c) phases.

The major differences between computed and observed results are observed for the axial load profiles during heating phase, while under purely mechanical loadings and cooling mode the agreement is rather satisfactory (Maiorano et al., 2019).

3.5 *Thermo-mechanical analyses of a real CFA pile in pyroclastic sand*

In sections 3.3 and 3.4, results of the laboratory small scale test of Yavari et al. (2014) and field test performed in London, UK and Denver USA are used to validate thermo-hydro-mechanical analysis with PLAXIS 2D. Of course, the term "validate" is not referred to the calculation algorithm but is mainly oriented towards the overall process of back-analysis which include the choice of constitutive soil model, the criteria for selecting the parameters, the boundary conditions and so on.

In order to investigate the response of a potential EP installed in the area of Napoli, numerical simulations have been done considering typical subsoil condition and widely used pile type. To this aim the results of site investigations and failure load test performed on Continuous Flight Auger (CFA) pile in Napoli, IT reported by

Russo (2013) are considered for the simulations. The numerical model parameters were defined on the basis of the experimental results through a trials and errors procedure, and then the effects of daily thermo-mechanical coupling are shown in terms of axial load profiles and pile's head displacements.

3.5.1 Axisymmetric FE model and calibration of soil parameters

To investigate on the thermo-mechanical interaction of a potential energy piles installed in the subsoil conditions typical of the urban area of Napoli the site investigations and load to failure test performed in the framework of the design of the foundations of a new trade centre were considered. Herein the main results of one load test to failure and site investigation are described. Russo (2013) reported the results of three COnventional top-down static Load Tests (COLTs) and two Osterberg's cell Load Tests (OLTs) on the same pile type (CFA piles) in the same subsoil conditions.

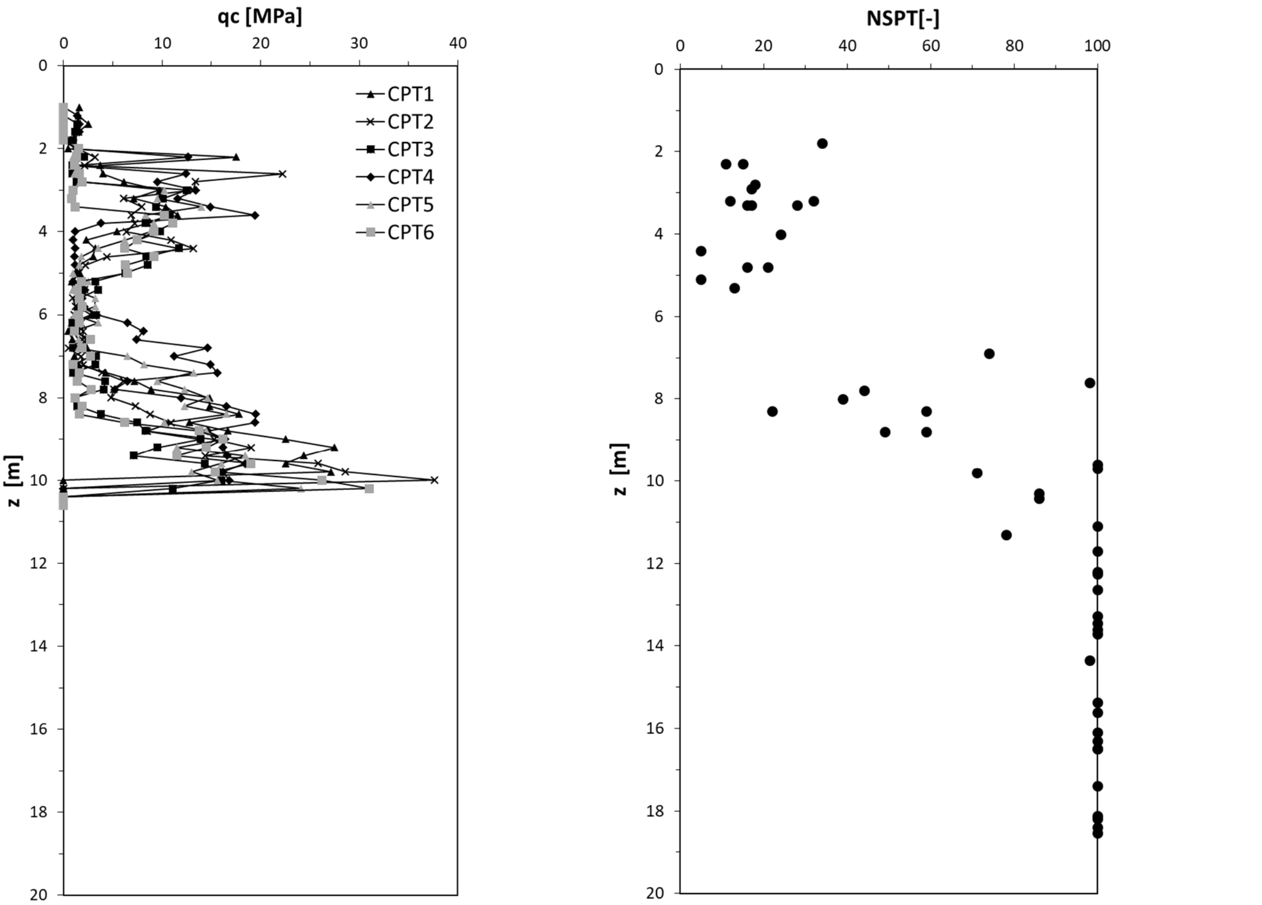

(a) (b)

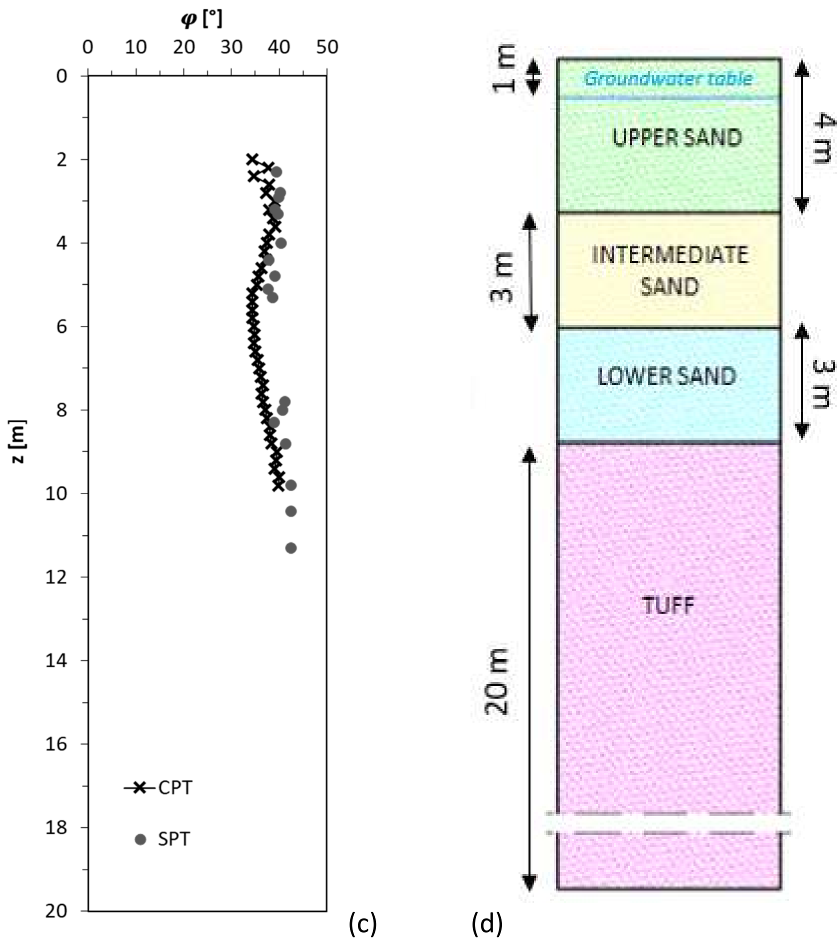

Figure 3-12:Results of site investigations from Russo (2013); (a) CPTs, (b) SPTs, (c) shear strength angle deduced by penetration tests and schematic soil profile (d).

The test site is located in the plain east of Napoli where the subsoil is composed by products of the Vesuvius and Phlegrean volcanoes. The groundwater table is located close to the ground surface. Eleven boreholes allow to describe the soil profile on the whole area. Made ground is first found in all the boreholes with thickness ranging between 1 m and 3 m. A second layer with a total thickness ranging between 8 and 11 m consists of pyroclastic sandy soil. Finally, at a depth ranging between 10 and 12 m below the ground surface, the bedrock is encountered. It is a volcanic grey tuff characterized by a rather variable degree of cementation in the upper few meters. A few deep boreholes show that the thickness of the tuff layer is rather uniform on the whole area and on the average equal to at least 20 m. The results of CPTs and SPTs against the depth, reported by Russo (2013), are plotted in Figure 3 12 (a) and Figure 3 12 (b). In Figure 3 12 (c), the values of the shear strength angles plotted versus the depth are shown. The values were deduced by Kulhawy and Mayne (1990) correlation with the soil densities derived by the average end resistance measured during CPTs and by the NSPT measured during the SPTs.

The values derived by the correlations based on SPTs are slightly larger than those derived by the correlations based on CPTs, even if the trend with the depth is rather similar, this result is quite common in pyroclastic soils (Russo, 2013). On the basis of CPTs, it can be summarised that the shear strength angle ranges between 31° and 37° for all the soil layers above the tuff. In the upper layer and in the lower part of the pyroclastic sand, the shear strength angle approaches the upper bound of the range while in the middle of pyroclastic sand layer the shear strength angle approaches the lower bound (Russo and Marone, 2018). The underlying layer of volcanic tuff was not directly investigated, but it represents a very common and well-known formation in the urban area of Napoli. The strength of such a material is typically characterised by a Mohr-Coulomb envelope with an effective cohesion c'=400-800 kPa and a shear strength angle φ=27-28° (Russo,2013). The subsoil schematic model, deduced by the investigations, is plotted in Figure 3-12(e).

From the results of the load tests, showed by Russo (2013), only for one load test the shaft friction has been fully mobilised. This test is Conventional load test performed with the CFA pile of 13 m of length and 0.6 m of diameter; therefore, this test pile was taken as reference for the calibration of the numerical model. The pile, as well as the other test piles, was instrumented with vibrating wire gauges (VWGs) to measure the load transfer along the piles length and embedded in tuff layer with 3 m of socket depth. The load transfer curves derived by the load test for each of the three main soil layers are plotted in Figure 3-13.

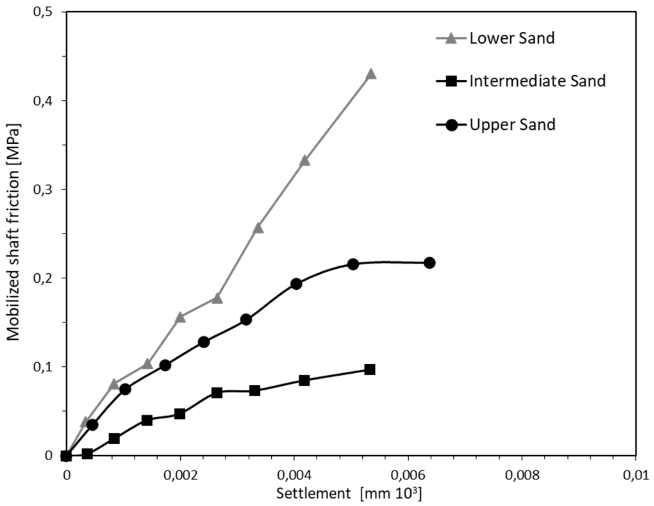

Figure 3-13:Mobilized shaft friction for each of the main soil layers: Lower Sand, Intermediate Sand and Upper Sand.

The mobilized friction observed from the load transfer curve is higher than the local ultimate value obtained using the static formulas or the simple β Method. This latter approach, that is worldwide diffused, consists of multiplying β= 0.3 to the effective vertical stress. Being $\beta = k \cdot \mu$, instead of separately evaluating K and μ,in routine design practice it is often suggested to refer to a lumped parameter β. This method does not work properly for such piles in pyroclastic sandy soil (Russo, 2013). As a matter of fact, in the upper sand and in the intermediate sand layer, the ultimate values of shaft friction, computed according to this method, are 16 kPa and 25 kPa, respectively, while the experimental values are about 0.2 MPa and 0.09 MPa, respectively. Rollins et al. (2005) suggested different depth depending β curves from the results of more than one hundred load tests on bored piles in sands and gravels. Experimental evidence obtained from load tests on drilled piles shows that β values could be very high for depths ranging between 8 m and 10 m (Russo and Callisto, 2016). Chen and Kulhawy (1994) showed that β values could range between 5 and 7, from the results of about ninety load tests on drilled piles in sands and gravels. Caputo et al. (1993) on the basis of fourteen load tests on bored piles in pyroclastic soils found out β values near the ground surface higher ten times than those suggested by the traditional method.

The results of the conventional load test are showed in Figure 3-14. The load settlement curve shows that the shaft friction is fully mobilised, with a sudden increase of the settlement at a maximum load of about 6000 kN. Although conventionally small, the settlement can be considered representative of the mobilization of both lateral and tip resistance of the pile.

An axi-symmetrical model characterised by fine triangular mesh of 15-noded elements was used to discretize the soil and the pile. The subsoil was modelled as a four layers system with ground water table set at 1 m depth from ground surface (Figure 3-12 (e)). Two different constitutive models were used, for the three layers of pyroclastic sands the H-S model was adopted, while, for the tuff layer M-C constitutive model was used. Through defining the coarseness factor, the mesh around the pile was refined. The calibration of the soil stiffness and resistance parameters was carried out on the basis of the experimental results i.e., site investigations and load-settlement and mobilised friction settlement relationships.

In order to achieve a satisfactory agreement with the experimental results the stiffness and resistance parameters of the soil were changed until the PLAXIS load- settlement curve shows an adequate matching with the Experimental curve (Figure 3-14). After several attempts the trials and error procedure allowed the determination of the set of parameters listed in Table 3-6.

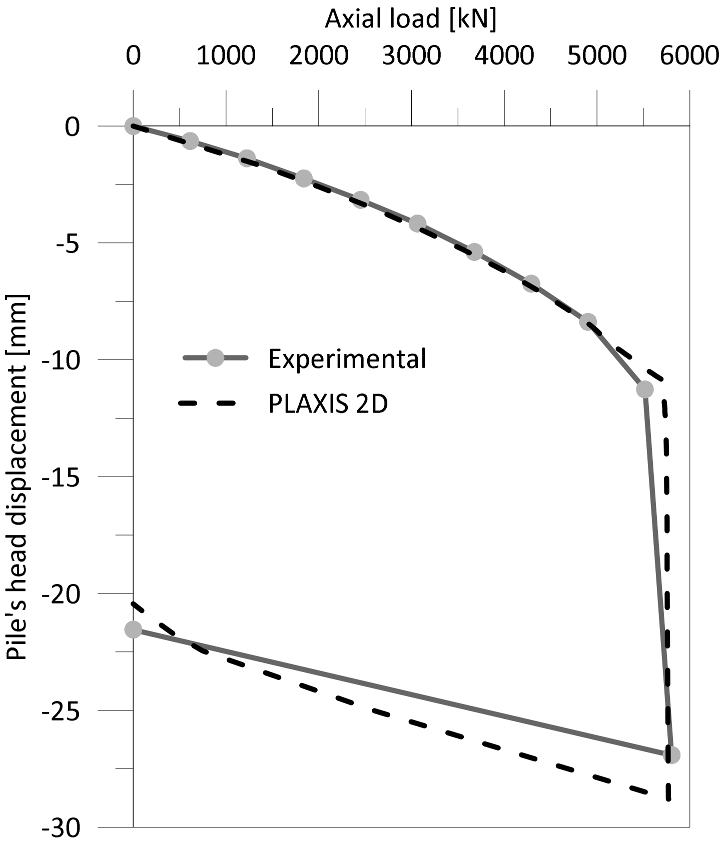

Figure 3-14: Load-settlement relationship obtained from the load test (Experimental) and numerical analyses (PLAXIS 2D).

Table 3-6:Material parameters obtained from the site investigations and calibration procedure.

	Pile	Upper sand	Intermediate sand	Lower sand	Tuff
Unit weight (γ) [kN/m^3]	24	19	18	19	17
Young modulus (E_{50}) [MPa]	30000	31.85	9.10	53.30	5000
Young modulus (Eur) [MPa]	-	95.55	27.30	159.90	-
Cohesion (c') [kPa]	-	10	-	-	100
Shear Strength angle (φ')[°]	-	37	32	37	28
Dilatancy angle (ψ)[°]	-	7	2	7	-

In the H-S model the possibility to account for the stress level influence on the moduli E_{50}=E_{oed}=E_{ur}/3 was also used, while the ratio among the values of the three moduli were kept equal to the suggested value (Brinkgreve et al., 2018). Bolton expression (1984) have been assumed to evaluate dilatancy angle of sands. The unloading path is satisfactory simulated assuming that the unloading reloading stiffness E_{ur} is three times the Secant stiffness E_{50}. For a proper modelling of soil-pile interaction at the contact between pile and surrounding soil an interface is added. M-C constitutive model was used for the interface considering a roughness equal to the shear strenght angle of the adjacent soil. The comparison between “Experimental” and “PLAXIS 2D” curves, Figure 3-14 , shows that the agreement with the experimental behavior is rather satisfactory both in the loading and unloading path. The adopted stiffness reported in Table 3-6, and particularly the ratios between the Young moduli and the average qc values reported in Figure 3-12 (a) could seem high (Marone and Russo, 2018). These values are in agreement with the values adopted to estimate low strain Young’s moduli of the pyroclastic sandy soils (Russo, 2013). Mancuso et al. (1999) showed that the initial stiffness derived by load-settlement relationships measured during conventional load tests is predicted in a BEM linear analysis adopting low strain Young's moduli (Russo, 2013).

The very high ultimate shaft friction measured during the tests was substantially matched adopting fitted β values. According to Russo (2013) β or k values should be appropriate for displacement piles to get a better agreement with the measured values. Pile installation and loading are processes that cause complex stress changes in the soil around the pile from in situ condition to failure (Mascarucci et al., 2014). The shaft resistance could be expressed considering different contributions that depend on the pile installation process and loading (Equation 3-3).

Equation 3-3: $q_s = \sigma'_{hf} \cdot tan\delta = (\sigma'_{h0} + \Delta\sigma'_{hc} + \Delta\sigma'_{hl}) \cdot tan\delta$

Where $\Delta\sigma'_{hc}$ is the stress change depending on the drilling operation as well as on the concrete casing and properties (e.g., water cement/ratio), $\Delta\sigma'_{hl}$ is the stress change attributed to Poisson's effect connected to the Poisson's ratio strains in the pile and to dilation of the soil close to the pile where strains localize (Mascarucci et al., 2014). Several attempts to quantify the increase of horizontal stress responsible of higher shaft resistance are proposed in literature. Herein this aspect is not deeply investigated but the FE analyses are addressed to simply model the horizontal stress increase achieving a good agreement with the experimental results. Therefore, during the numerical simulation, higher horizontal stresses were modelled adopting the k_0 procedure and defining K_0 values fitted on the experimental load transfer curves. The total load (Q), total side resistance (S) and total tip load (P) calculated by PLAXIS are plotted in Figure 3-15 (a).

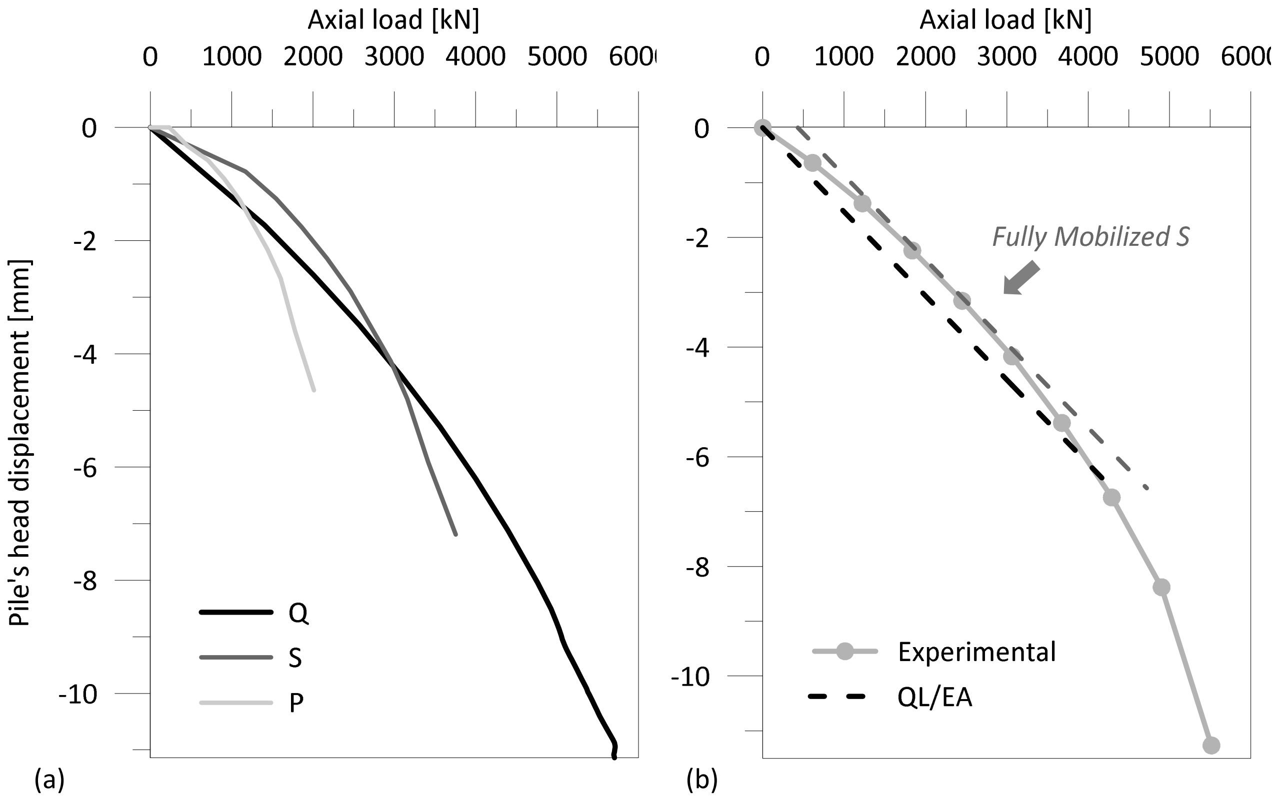

Figure 3-15: (a) Total load (Q), total side resistance (S) and Total Point Resistance (P) obtained from the PLAXIS; (b) Mobilization of total side resistance evaluated from the experimental results.

From the load settlement curve, it is possible to evaluate when the total side resistance is fully mobilized (Viggiani, 2013). When the load settlement curve is parallel to the elastic shortening of the pile (it can be assumed that the side resistance is fully mobilised (Figure 3-15 b). The total side resistance reported in Figure 3-15 (a) is in agreement with the range of fully mobilization obtained from the experimental results Figure 3-15 (b).

3.5.2 Numerical prediction of the short-term thermo-mechanical behavior

The pile-soil system load tested and described in the previous section is used here in for the analysis of time dependent effects of changes of temperature on stresses and deformations.The short-term thermo-mechanical behavior was investigated coupling the service load to heating or cooling loads. The magnitude of the service gravity load to be applied is defined as a fraction of the ultimate bearing capacity (about 6000 kN). Assuming an overall SF=2.5 the live load is 2400 kN. The modelling was carried out performing an initial phase (k_0 procedure), a subsequent nil step to guarantee the equilibrium and then applying the mechanical load during a plastic calculation phase carried out in isothermal conditions. This load was kept constant and combined to heating or cooling loadings in fully a coupled phase. To model the thermo-mechanical interaction and particularly transient heat transfer phenomena occurring between pile and soil or vice versa thermal properties as well as thermal boundary conditions are assigned, (3.2.4). Thermal properties of soils were not measured in situ and therefore thermal conductivity and heat capacity as well as the linear thermal expansion coefficient for each layer of soil were assigned based on values provided in literature. McCombie et al. (2016) investigated the thermo-physical characteristics of Pyroclastic soils, the effective thermal conductivity of Pozzolana's minerals was assessed to be about 2.14 W/m °C. The transient thermal probe method was applied to measure the thermal conductivity over a full range of degree of saturation and porosities of 0.44 and 0.50. For saturated samples and porosity of 50% the average conductivity of soil was about 1.15 W/m °C. For the yellow tuff Colombo (2010) reported 1.47-1.5 W/m °C of heat conductivity measured on saturated tuff. For the tuff layer a thermal conductivity of 1.5 W/m °C was assumed. Aversa and Evangelista (1993) evaluated the thermal expansion coefficient of Neapolitan yellow tuff through drained expansion tests using a particular apparatus called "expansion cell" and oedometer and undrained thermal expansion test in triaxial cell. The thermal expansion coefficient of saturated tuff samples ranges between 310^{-4} and 10^{-3} °C^{-1} at 20 °C and 200°C, respectively (Aversa and Evangelista,1993). Agar (1986) reported thermal expansion coefficient of sand ranging between 2.4 10^{-5} °C^{-1} and 2.4 10^{-4}°C^{-1}. Bournewebb et al. (2019) reported the coefficient of thermal expansion of soils adopted for energy piles-soil interaction studies defining a wide range of magnitudes, between 10^{-3}°C^{-1} and 5 10^{-7}°C^{-1}. In this study the coefficient of thermal expansion for the three layers of sands was assumed 4 10^{-5}°C^{-1}. According to the data provided by Colombo (2010) a volumetric heat capacity of 2000 and 2600 kJ/m^3 °C was assigned to the three layers of Pozzolana and tuff, respectively.

For the concrete pile the specific heat capacity, thermal conductivity and linear expansion coefficient assigned are 800 kJ/m^3 °C ,2.4 W/m °c and 1.2 10^{-5}°C^{-1}, respectively.

The set of thermal boundary conditions assigned are plotted in Figure 3-16. The surface boundary was considered as exposed to the outdoor air temperature. Two different outdoor sinusoidal temperature functions were imposed at ground surface. For the cooling mode of the superstructure, that corresponds to heating of the pile, at the soil-surface a daily temperature variation, representative of typical summer day, was assigned. For the heating mode of the superstructure, that corresponds to cooling of the pile, at the soil surface a daily temperature variation, representative of a typical winter day, was assigned. The heating and cooling thermal loadings are imposed as a temperature -time variable functions on a straight line inside the pile body roughly corresponding to the operational location of the primary circuit inside the energy pile (Marone et al., 2019). The heat exchanger reproduces a coil-type primary circuit. The helix circuit has been shown to represent the configuration with a higher specific heat/extraction rejection rate (Fadejev et al., 2017) compared to single U shape pipes. This more efficient configuration, when the pitch of the coil is very small can be simulated via a cylindric constant temperature surface (in the axisymmetric model a simple straight line) (Marone et al. 2019).

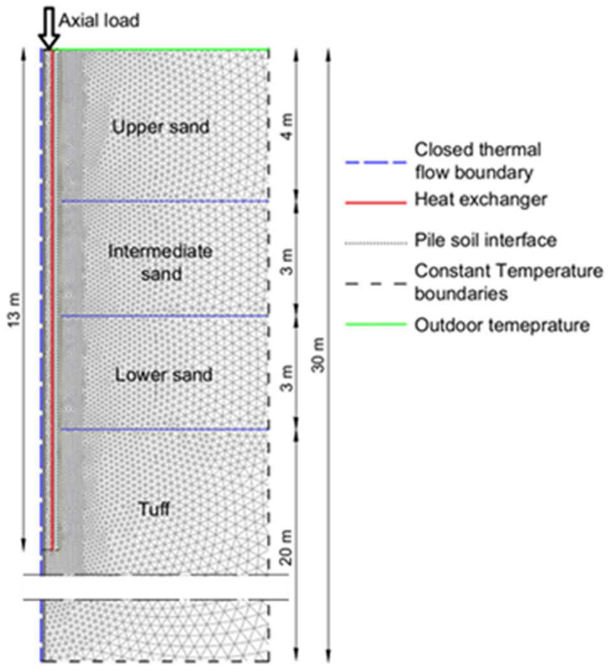

Figure 3-16: Thermal Boundary conditions assigned during the Thermo-Hydro-Mechanical (THM) simulations of short-term analyses.

Dirichlet boundary conditions are applied to the vertical right side and the bottom boundary assigning a constant temperature of 17°C. The size of the soil domain is defined to be large enough at distance (forty-three times the pile diameter from the pile-soil interface) where the heat exchange options have no effects such as to avoid any boundary effects. Axial symmetry is used in all the models.

The temperature is applied uniformly along the pile shaft since the real presence and configuration of the heat exchangers tubes is neglected, which is a common assumption for the design and remains acceptable because the difference between the inlet and the outlet temperature is usually less than 4°C (Rammal et al. 2018). The thermal loads were defined considering daily operations and both cooling and heating mode. Crenel temperature variations were considered, according to the numerical study carried out by Rammal et al. (2018). Temperature functions assigned at ground surface (Outdoor temperature) and to the pile during heating and cooling modes are reported in Figure 3-17 (a) and Figure 3-17 (b), respectively.

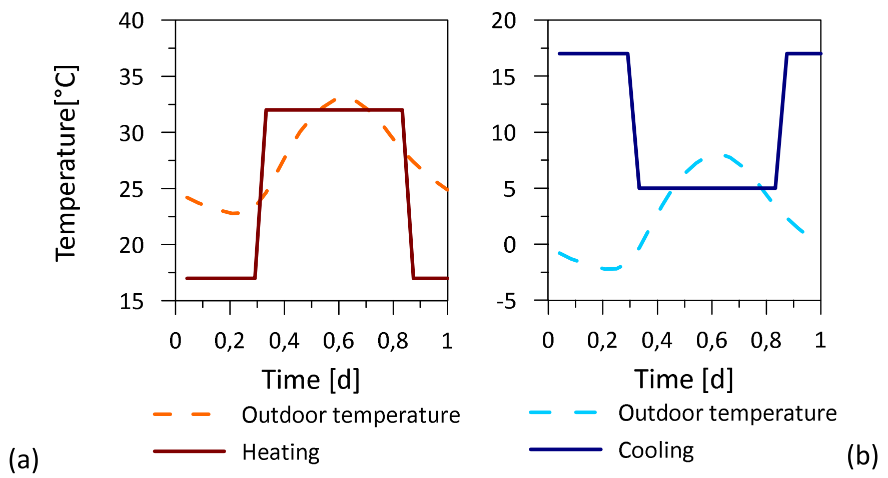

Figure 3-17:Temperature functions assigned at ground surface (Outdoor temperature) and to the pile (Heating and Cooling) during (a) heating and (b) cooling modes.

In case of heating the temperature function assigned to the pile ranges between 17 °C and 32 °C while during cooling between 17°C and 5 °C. It was considered that the geothermal system works twelve hours per day both during heating and cooling mode. The initial and final temperature of 17 °C assigned as temperature function correspond to the undisturbed soil temperature of the deep zone measured in the urban area of Napoli that is included in the range of 17-18 °C (Colombo, 2010).

During the heating mode of the pile the air ambient temperature assigned as thermal boundary condition at soil surface ranges between a minimum temperature of 22.8 °C and a maximum temperature of 33.1 °C. During the cooling, the air ambient temperature assigned at soil surface ranges between a minimum temperature of -2 °C and a maximum temperature of 8.1 °C. During the heating mode the maximum thermal variation with respect to the initial soil temperature is about 15 °C. During cooling the minimum thermal variation with respect to the initial soil temperature is about 12 °C. The temperature variation applied to the pile are included in the range of typical temperature changing occurring during the operational condition of GSHP. The results of the thermo-mechanical tests are reported in terms of displacements at the head and toe of the pile (Figure 3-18 (a) and Figure 3-18 (b)) and axial loading profiles (Figure 3-19 (a)Figure 3-18 and Figure 3-19 (b)).

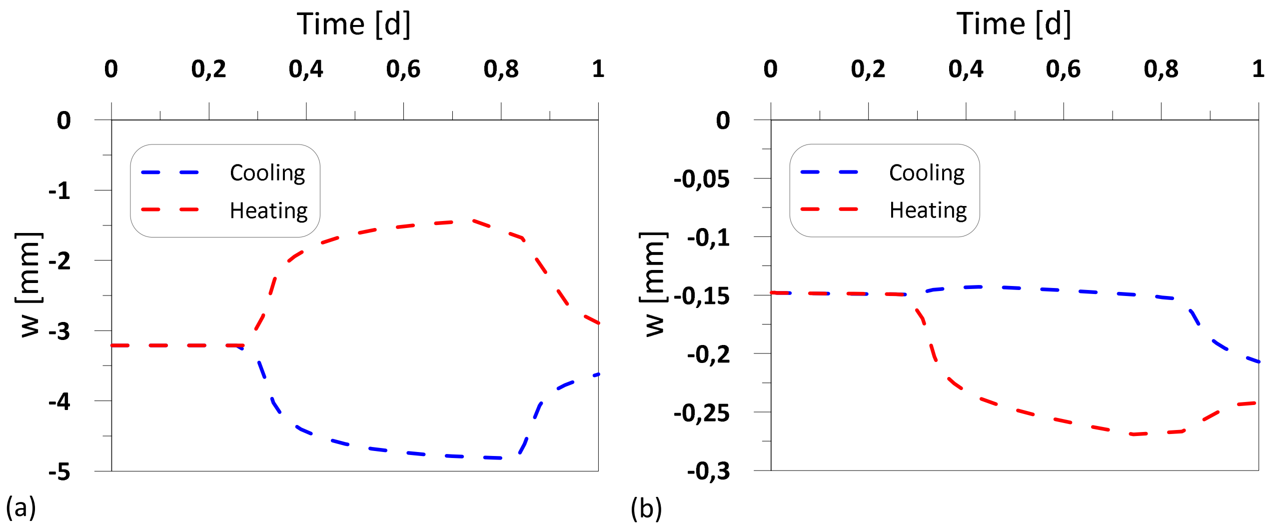

Figure 3-18:Pile's thermo-mechanical displacement (w) versus time for the heating mode (Heating) and cooling mode (Cooling) at the head (a) and toe (b).

Both during heating and cooling cycles the displacement history of pile's head starts from the initial mechanical settlement of -3.21 mm determined by the application of the service load. The pile head moves upward when heated and settles during cooling. During the heating, the thermal heave of pile's head is about 1.7 mm, while during cooling the additional thermal settlement is about -1.6 mm. The maximum and minimum thermo-mechanical displacements are -1.5 mm and -4.90 mm during heating and cooling, respectively. The maximum upward thermal displacement is about 53% of mechanical displacement while the minimum downward thermal displacement is about 49% of the mechanical displacement, during heating and cooling respectively. In Figure 3-18 b the displacements of pile's toe are plotted both for heating and cooling mode. The initial settlement of -0.15 mm is determined by the initial mechanical load. During heating the toe settles while during cooling heaves demonstrating that the pile is expanding during heating and contracting during cooling, as expected. The thermo mechanical maximum and minimum displacements are -0.15 mm and -0.27 mm during cooling and heating, respectively. The minimum thermal settlement during heating is -0.12 mm while the maximum thermal heave during cooling is about 0.06 mm. The thermal displacement observed at pile's toe is lower of about one order of magnitude than those observed at pile's head. Particularly in the case of cooling the upward thermal displacement is very low. The pile toe as described in the previous section has a socket depth of about 3 m, and the thermal displacement are strongly restrained by the tuff.

The axial load profile is plotted in the case of purely mechanical load in isothermal condition as black straight line ("M"). The thermo mechanical load profile at the end and at mid time of the heating is named as EH and

H, respectively (Figure 3-19 a). The thermo mechanical load profile at the end and at mid time of the cooling is named as EC and C, respectively (Figure 3-19 b). The mechanical axial load profile is maximum at pile's head and decrease with depth, at the toe 27% of the load is transmitted.

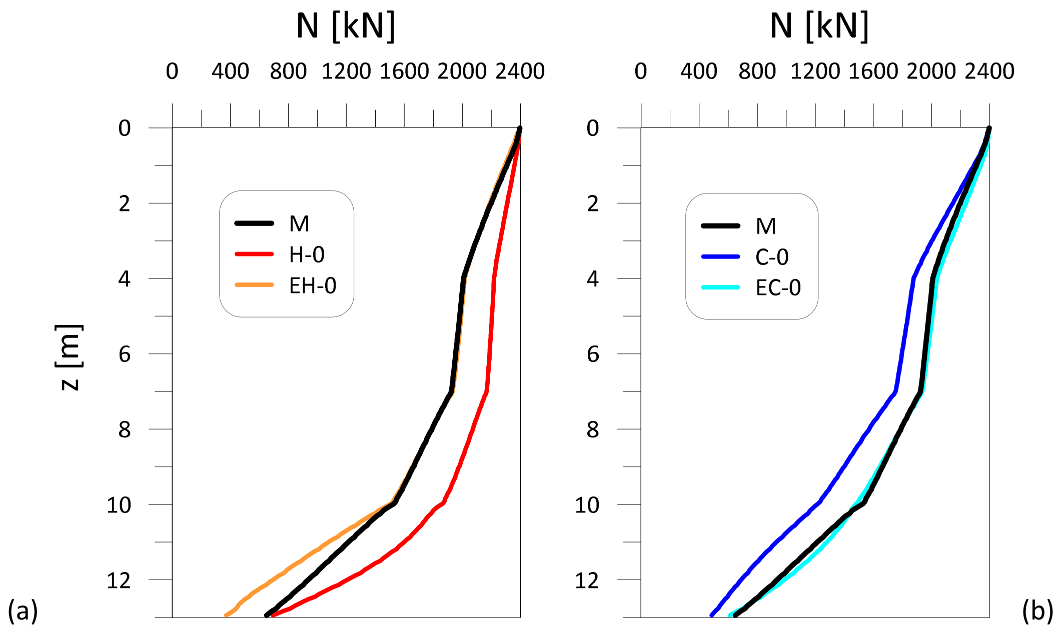

Figure 3-19:Axial Load Profile during (a) Heating and (b) Cooling at different time instant (mid time "H" and "C" and at the end "EH" and "EC") for Case 0 along with the mechanical load profile (M) for isothermal conditions.

As expected during the peak of heating additional compressive load are observed while at the peak of cooling episode the compressive axial load decreases. At the peak of the heating the maximum additional compressive load is about 385 kN. At the peak of the cooling episode, the largest decrease of the compressive axial load is about 311 kN at depth of about 10 m. The largest variations of the axial load are observed in the tuff layer, as expected from the history of thermo-mechanical displacements at pile's toe. The soil surrounding the pile restrained the free contraction and expansion of the pile and the maximum action of restraint occurred in the stiffer layer (tuff). Comparing the observed pile's head displacement to the free elongation or contraction, obtained neglecting the interaction with the surrounding soil, it is observed that the thermal displacement is about 72 % and 78% of the free elongation and contraction during heating and cooling, respectively. The magnitude of the residual thermal displacements at the end of heating and cooling are very small compared to the settlement induced by the mechanical loadings and could be considered as negligible. At the end of the heating, some residual thermal stresses are observed close to the pile toe (see Figure 3-19 a).

3.5.2.1 Parametric study for short-term conditions

The heating and cooling Thermo-mechanical analyses presented in the previous paragraph (3.5.2) are herein defined as CASE 0. Starting from this initial case, a parametric study has been carried out investigating several aspects involved in the design of EPs. The numerical simulations carried out are based on the hypotheses of free head pile with no cinematic restraint to pile's head movements, spiral primary circuit, single heating or cooling cycles and a specific thermal conductivity of the concrete of the pile (CASE 0). The FE models of the parametric analysis is basically the same presented in section 3.5.2. The parameters that have been varied concern the configuration of the primary circuit, the constraint action provided by the foundation system (slab and piles), the sequence of thermal loadings, the effect of the rest phase between heating and cooling modes or vice versa, the thermal boundary condition at ground surface and the thermal conductivity of the pile.

The configuration of the pipes embedded within energy piles is a very important aspect of the design (Batini et al., 2015). Herein two types of primary circuits have been considered single coaxial or U-shaped pipe placed at pile's middle section and spiral configuration attached to the reinforcing cage (CASE 0).

The constraint action at pile's head is among the most important factors that influence the pile-soil interaction. The end restraint conditions also govern the significance of the stress, strain and displacement variations (Rotta Loria et al.,2019). The case of free head pile presented in the previous section is rather unreal because the pile is at least partially constrained by the foundation system. The effect of the constraint action provided by the structure and foundation system was well documented by Laloui et al. (2006) through monitoring the behavior of an energy pile during the construction steps of the upper structure. Herein two different degrees of constraint are considered, 50% and 100%. Both cases are simply modelled assigning a prescribed displacement during the fully coupled phase. The 50% and 0% of the free head thermal displacements are allowed to model 50 % and 100% degree of constraint, respectively. The free thermal displacement is provided by the simulations of CASE 0.

The loading magnitude and sequence critically characterise THM behavior of EPs because the loading sequence can also involve different responses of energy piles (Rotta Loria and Laloui, 2019). The effect of the sequence of thermal loads is investigated comparing the heating mode of the CASE 0 to different sequences made by combination of heating, cooling and recovery phases. On this aspect interesting is the experimental investigations by Faizal et al. (2016). The energy extracted from continuous operations is lower compared to the intermittent operations while the average thermal stresses in the pile for the intermittent modes are lower compared to the continues mode.

Rammal et al. (2017) performed three-dimensional FE analyses of energy piles considering that the surface boundary is exposed to external air temperature. CASE 0 was also modelled assuming that at ground surface the temperature corresponds to the outdoor air temperature during summer and winter for the geographical area assumed as a reference location (i.e., Napoli area). Several further cases were analysed highlighting the differences on mechanical performance.

Finally, the thermal conductivity of reinforced concrete is increased of 20%, 50% and 100% with respect to the CASE 0. On the same topic Abdelaziz et al. (2011) performed three-dimensional FE analyses on piles with different materials.

3.5.2.2 Effect of the configuration of exchanger pipes

The thermo mechanical behavior of the single energy CFA pile equipped with two different configurations of pipes, U (or coaxial) and spiral, was investigated both in heating and cooling mode (Figure 3-20).

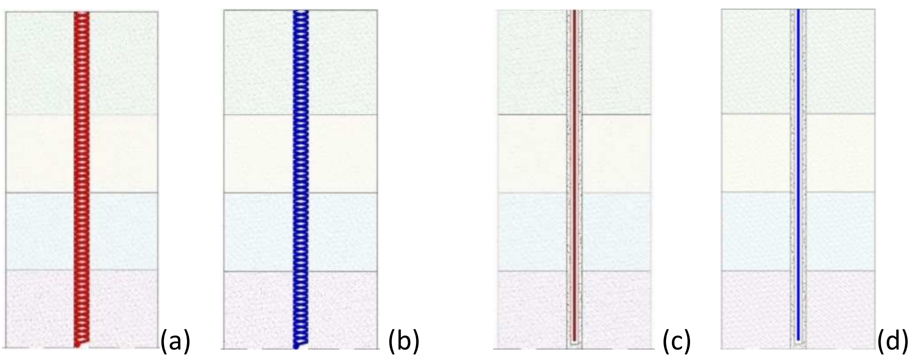

Figure 3-20: (a and b) Spiral and (b and c) coaxial/U pipe configurations.

The *U* or coaxial configuration can be modelled considering that the temperature functions (Figure 3-17) i.e., the transient thermal boundary condition is applied along a straight line in the middle of the pile. The spiral configuration is modelled as described in 3.5.2.

The temperature evolution along pile cross section at location of pile's head is plotted in Figure 3-21. The temperature variations along the cross section of half pile (axisymmetric model) are considered at mid time of both heating and cooling modes for the two positions and configurations of the PC.

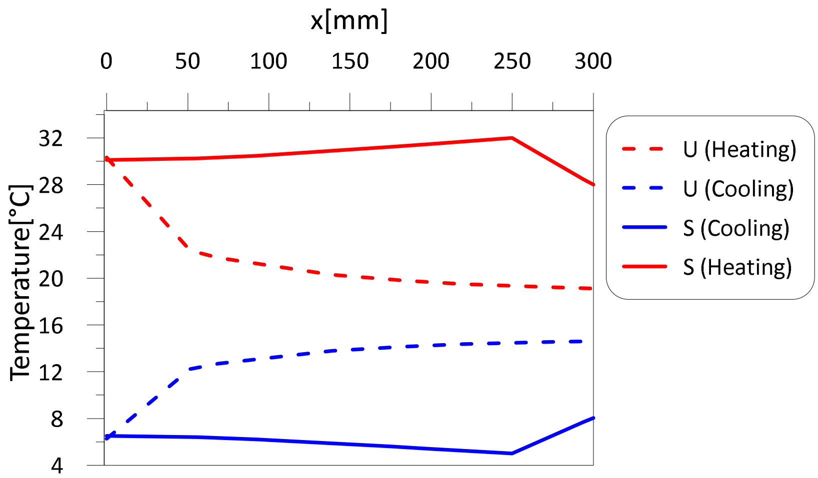

Figure 3-21:Temperature evolution along half pile cross section for the U-shaped configuration (U) and the spiral configuration (S) for both heating and cooling mode at mid-time of each episode.

As could be easily expected the two kinds of PC provide different temperature distributions along the cross section. From Figure 3-21 for daily operation the heat exchange from pile and surrounding soil is characterised by a very low amount in the case of central U pipe. The temperature of the concrete pile at contact with soil (300 mm) does not change (initial temperature is 17°C) and therefore, the exchange mechanism is very limited. Pile's head displacement in the central area of the pile and 50 mm from the pile edge, with reference to the pile head are plotted in Figure 3-22 (a) and Figure 3-22 (b), for U and Spiral configurations respectively.

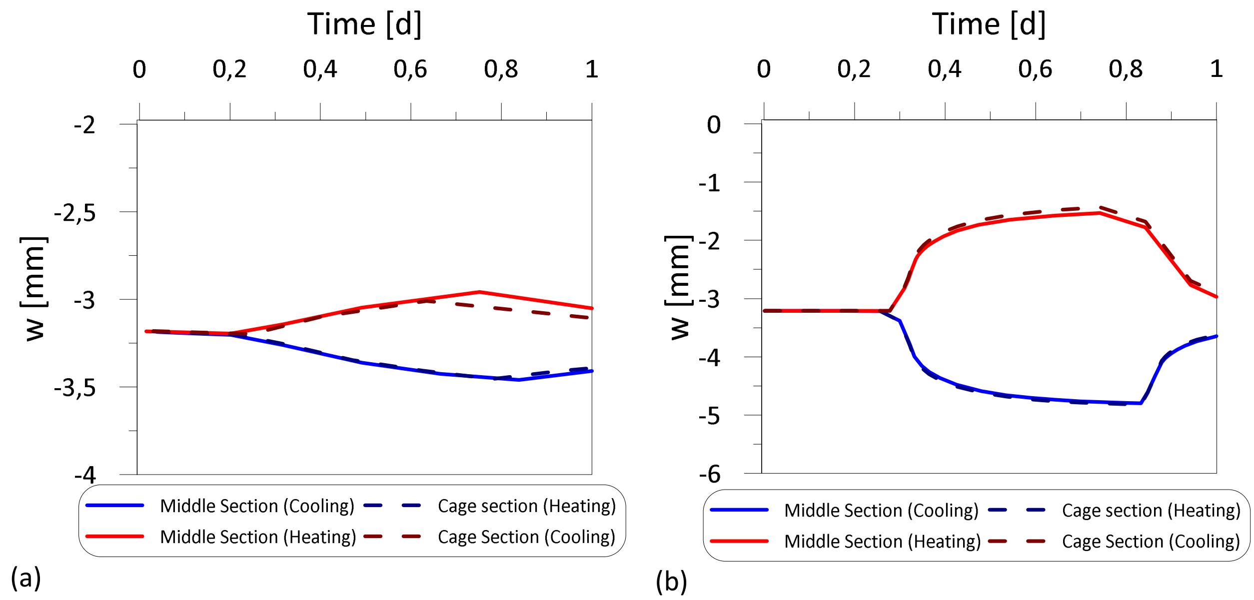

Figure 3-22:Pile's head displacement at different location along the cross section: middle and 50 mm from pile edge (reinforcing cage location) for the U-shaped configuration (a) and spiral shaped configuration (b).

There is a clear influence of the different layout on the displacement profile at the pile (Figure 3-22 (a) and Figure 3-22 (b)). For both pipes configurations greater displacements are observed at the location of the heat exchanging pipes even if the differences are in both cases rather small. The axial load profiles for both the U-shaped (U) and Spiral configurations (S) are plotted in Figure 3-23 (a) and Figure 3-23 (b) for heating and cooling modes, respectively. As described in 3.5.2 the axial load thermo-mechanical profiles are compared to the purely mechanical load in isothermal condition plotted as black straight line and named "M" (Figure 3-23 (a) and Figure 3-23 (b)). The thermo mechanical load profiles for both the configurations of pipes are considered at the end and at mid time of the heating EH and H, respectively (Figure 3-23 (a)) and at the end and at mid time of the cooling EC and C, respectively (Figure 3-23 (b)). For the case U, both during cooling and heating the thermomechanical loads along piles depth are almost matching the mechanical profile. The thermo-mechanical load slightly increases and decreases with respect to the mechanical load during heating and cooling, respectively. During heating episode, the maximum thermal stress at the mid time and end is 43 kN and 63 kN, respectively. During colling episode, the minimum thermal stress at the mid time and end is 38 kN and 43 kN, respectively.

For daily operation the U-shaped configuration induces negligible effects in terms both of stresses and displacements. Smaller energy performance, connected to the position of the pipes inside the pile, are connected to smaller thermo-mechanical interaction.

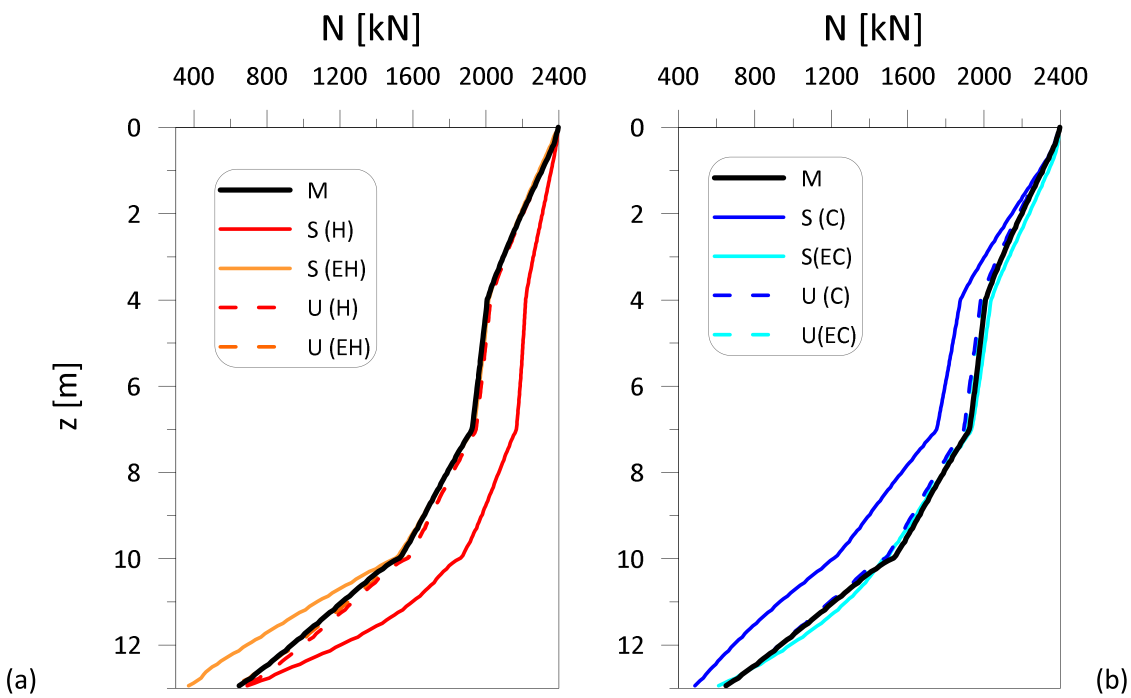

Figure 3-23 :Thermo-mechanical load profiles during (a) heating and (b) cooling episodes for the U-shaped configuration of pipe and CASE 0 at different time instants (mid time and end) of the thermal episodes.

The results of the thermo-mechanical simulations agree both with the results of the small-scale laboratory tests of Wang et al. (2017) and the numerical simulations carried out by Batini et al. (2015). Lower amounts of energy were removed from the ground through the single U-shaped pipe configuration with respect to double U shaped and W shaped pipes (Batini et al., 2015).

3.5.2.3 Effect of the constraint action at pile's head

Three different cases of head constraint are compared. The CASE 0 presented in 3.5.2 corresponds to the free head pile and therefore to 0% of degree of constraint. This case will be named as 0%. This condition is obviously not representative of the operating conditions of an energy pile as part of a foundation system. Depending on many factors such as the rigidity of the slab and the presence and distance of other piles equipped with heat exchangers, a certain constraining action may be exerted at the head of the pile with respect to the displacements induced by the temperature. The fully constrained head pile is the case of 100 % of constraint where no thermal displacements are allowed at the head of the pile and it will be named as 100%. This condition represents another extreme situation where for example the interaction with adjacent piles, that are not thermally loaded, provide a strong constraint action avoiding additional thermal displacements. These two cases represent extreme situations where the pile is completely free or perfectly constrained with respect to head thermal movements (both upward and downward). The bounds defined by fully unrestrained and perfectly restrained pile thermal deformation are likely to be a good support for a safe, though possibly somewhat conservative, design (Bourne-Webb and Bodas Freitas, 2020). The Partial constraint of the thermal displacement at pile's head is included between the two bounds of 0% and 100% and it is named as 50%. When the pile's head is not completely free to expand or contract (100 % and 50 % degree of constraints), thermal loads determine additional stresses at pile's head. In Figure 3-21 the temperatures evolution along the pile's cross section at the peak of the heating and of the cooling step at pile's head is plotted. As could be observed from Figure 3-21, considering the blue and red straight lines, the temperature distribution along pile's cross section is not homogeneous. From the displacements reported in 3.5.2.2 it was concluded that negligible variations at the head displacement occur at two different points of the cross section (Figure 3-22 (b)). When the stress distribution is considered, the temperature differences between different points along the pile's cross section provides different thermal stress. Therefore, a constant distribution of thermo-mechanical axial stress cannot be assumed and thermal axial load for the 100% and 50 % cases at the head of pile is computed according to Equation 3-4. Maximum and minimum magnitudes of stress are observed at the location of the maximum and minimum temperature i.e., location of the primary circuit. Thermal axial load for the 100% and 50 % cases at the head of pile is computed according to Equation 3-4.

Equation 3-4: N= $\int_A \sigma_z dA$

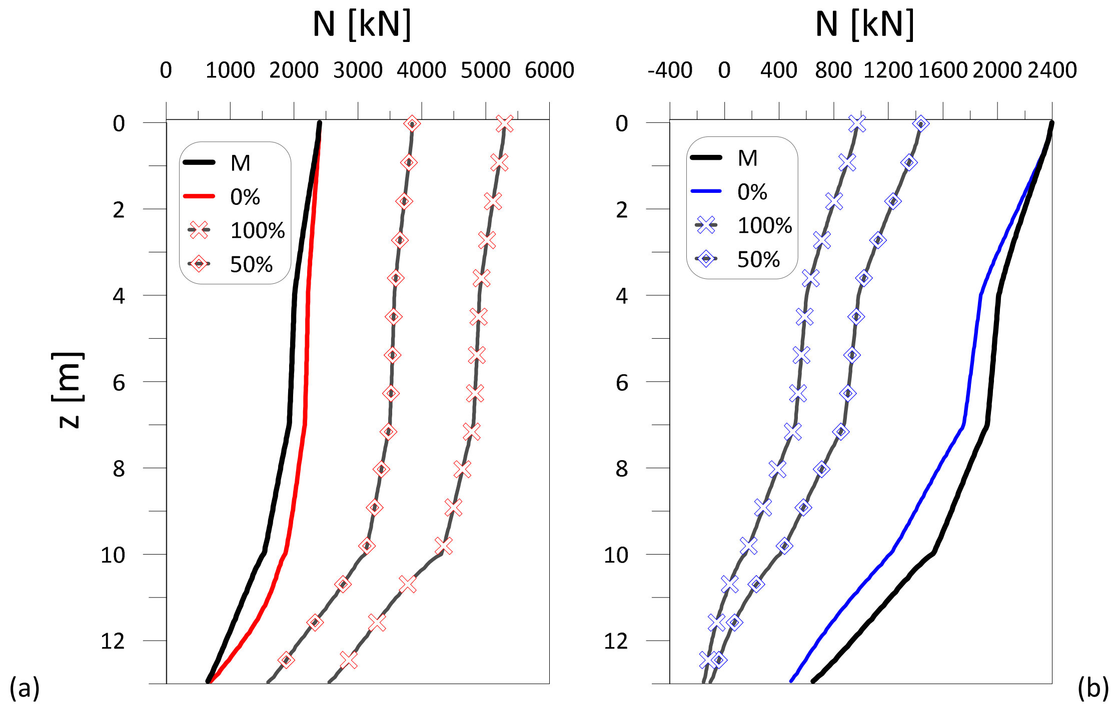

Figure 3-24:Thermo-mechanical load profiles at the peak of heating (a) and Cooling (b) for different degree of constraint modelled at pile's heat (0% (free head), 100 % (fully constrained head) and 50 % (partially constrained)).

The thermomechanical axial profiles are reported in Figure 3-24 (a) and Figure 3-24 (b) considering the three cases, 0%, 50% and 100%, and the peak of heating and cooling episodes, respectively. All the cases are compared to the purely mechanical case M. 100% case is characterised by the maximum variations of the head axial load. For the peak of heating the additional thermal load is about 2899 kN while for the peak of cooling a decrease of 1425 kN is obtained. The total thermomechanical load during the peak of heating is 5299 kN while during cooling is 974 kN. As observed during the monitoring performed by Laloui et al. (2006) the maximum degree of constraint determines a total axial load that is twice the mechanical load during heating. The thermal loads of cooling determine a decrease of the compressive axial load at the head and throughout pile's length determining tensile loadings at toe. 50 % constraint is characterised by a thermomechanical axial at the head of 3849 kN and 1444 kN during the peak of heating and cooling, respectively. The increase of axial loading is observed along the entire pile's length during heating while during cooling a decrease it is observed. For the 50% also tensile load is observed close to the pile's toe. Form experimental study in situ, are not available data about the cooling effects on pile's foundations. Murphy and McCartney (2014) monitored the heating and cooling cycles of two piles foundation during building operation as described in 3.4.1. According to the authors it was not possible to accurately evaluate the tensile thermal axial stresses during cooling, but they are not relevant for the structural performance of these foundations. From the results of thermo-mechanical simulations, the minimum tensile stresses occur for the 100% case and it is about -0.6 Mpa. This magnitude of stress does not exceed the tensile design resistance of concrete, as Murphy and McCartney (2014). As well as the maximum compressive stress (about 19 Mpa) does not exceed the compressive design resistance of concrete.

Therefore, for daily operations, the degree of constraint determines a significant changing of thermo-mechanical loading along the entire pile length but does not compromise the structural integrity of the foundation.

3.5.2.4 Effect of the sequence of thermal loadings

Considering that the GSHP system works both in heating and cooling mode, the effects of the sequence of heating and cooling modes and vice versa and the presence of a recovery phase between two modes are herein modelled considering daily operation. Four additional cases are defined and compared with the heating and cooling of CASE 0. One cooling and heating cycle corresponding to temperature functions of Figure 3-17 (b) and Figure 3-17 (a) are performed in CASE CH**.** One cooling followed by a recovery phase and heating are modelled in CASE CRH**.** The temperature functions applied to the pile and at ground surface are plotted in Figure 3-25 (a) and Figure 3-25 (b) for the cases CH and CRH, respectively.

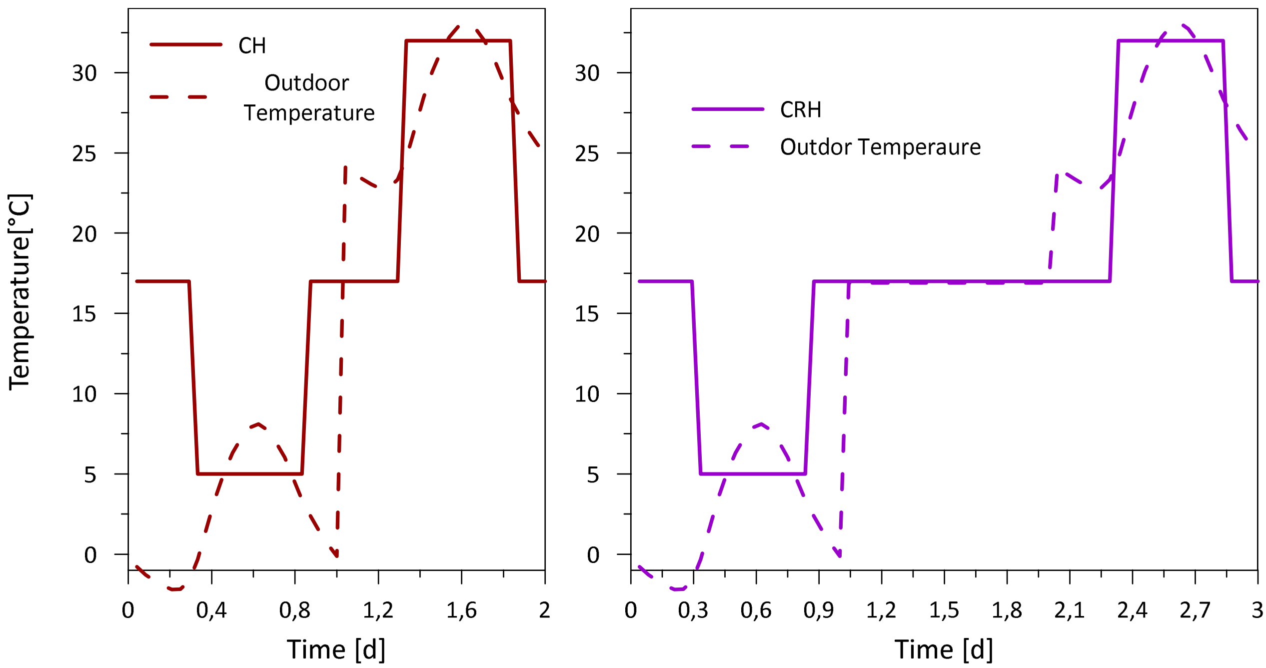

(a) (b)

Figure 3-25:Temperature functions applied to the pile (Heating) and Ground Surface (Outdoor Temperature) for the case CH (a) and CRH (b).

One heating and cooling cycle corresponding to temperature functions of Figure 3-17 (b) and Figure 3-17 (a) are performed in CASE HC**.** One heating followed by a recovery phase and cooling are modelled in CASE HRC**.** The temperature functions applied to the pile and at ground surface are plotted in Figure 3-26 (a) and Figure 3-26 (b) for the cases HC and HRC, respectively. For each of the four additional cases, CH, CRH, HC and HRC, the thermal boundary conditions correspond to those applied in the CASE 0 (Figure 3-16). For CH and HC the transient analyses are carried out for a total time duration of two days and the upper boundary conditions applied at ground surface correspond to those applied in the CASE 0 for cooling and heating or vice versa. For CRH and HRC the transient analyses are carried out for a total time duration of three days and the upper boundary conditions applied at ground surface correspond to those applied in the CASE 0 during cooling and heating episodes or vice versa, while for the recovery phase a constant temperature of 17 °C was assumed. The results of CH and CRH are compared to the results of the heating of CASE 0 in terms of pile's head displacements and thermo-mechanical axial load profile considering at the end of each case. The results of HC and HRC are compared to the results of the cooling of CASE 0 in terms of pile's head displacements and thermo-mechanical axial load profile considering at the end of each case.

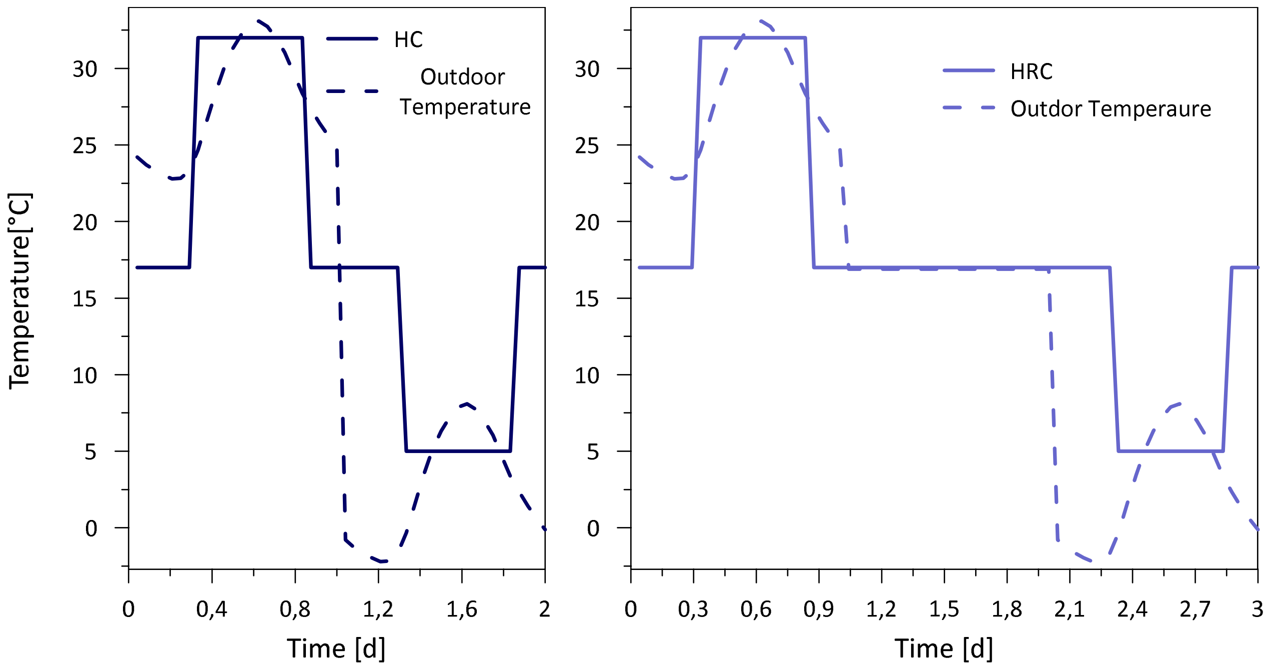

(a) (b)

Figure 3-26: Temperature functions applied to the pile (Cooling) and Ground Surface (Outdoor Temperature) for the case HC (a) and HRC (b).

Pile's head displacements are compared during the last heating cycle for cases CH and CHR (Figure 3-27 (a)), while for cases HC and HRC the last cooling cycle is considered (Figure 3-27 (b)).

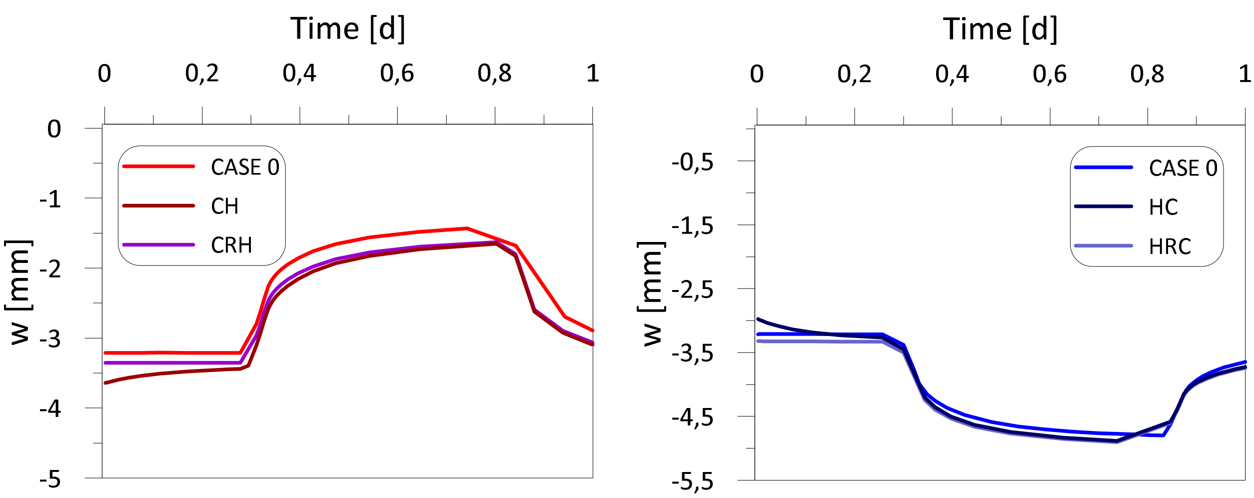

(a) (b)

Figure 3-27:Pile's head displacement during the heating cycle for cases CH, CHR and heating of CASE 0 (a) and cooling cycle for cases HC, HRC and cooling of CASE 0.

Both for heating and cooling mode the difference between the cases of Figure 3-27 (a) and Figure 3-27 (b) are practically negligible. Comparing the final settlement of cases CH and CRH the difference is about 0.03 mm. The final settlements of cases HC and HRC differ of 0.01 mm. The recovery has no effect on the settlement of the pile. While the cooling before heating determines slightly greater pile's heaves of about 0.10 mm. The heating phase before cooling determines slightly greater settlement of about 0.11 mm.

The axial load profiles at the end of heating are plotted in Figure 3-28 (a) for cases CH, CRH and CASE 0. The axial load profiles at the end of cooling phase are plotted in Figure 3-28 (b) for cases HC, HRC and CASE 0.

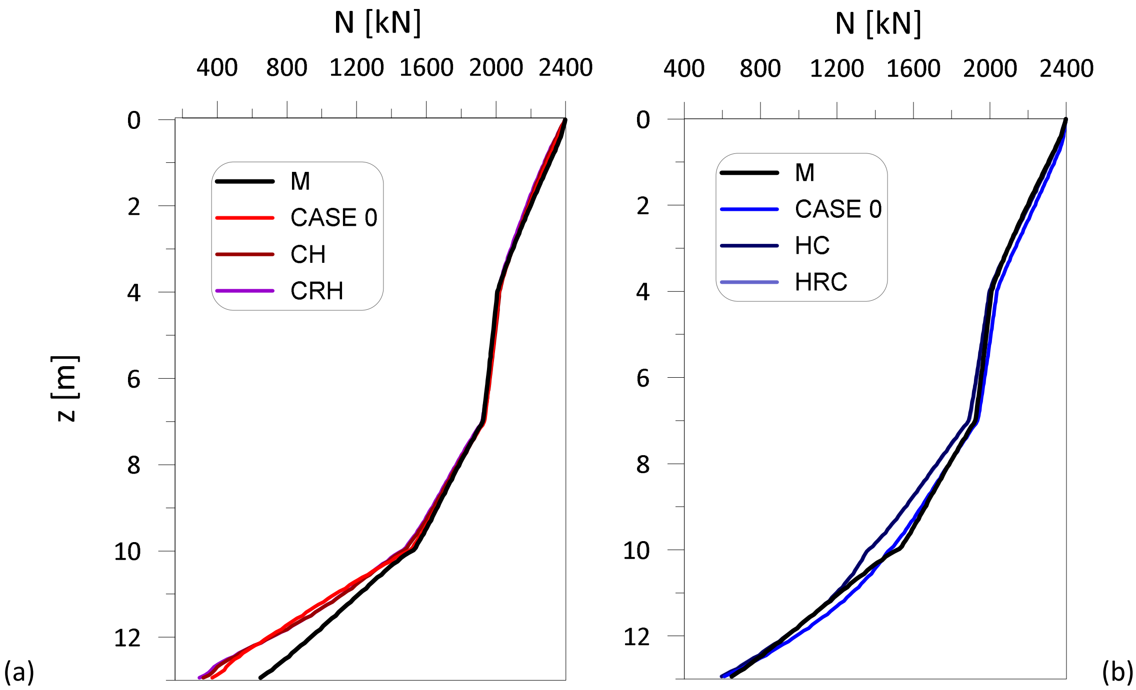

Figure 3-28:Thermo-mechanical axial load profiles at the end of heating for cases CH, CRH and CASE 0(a) and at the end of cooling for cases HC, HRC and CASE 0 along with the purely mechanical profile (M).

The comparison of the results shows that the succession of the phases determines a slight variation with respect to the cases of cooling or heating only, while the heat recovery phase between two cycles is practically irrelevant from the geotechnical point of view (Marone at al.,2019).

3.5.2.5 Effect of the thermal boundary condition at ground surface

The effects of thermal boundary condition on the pile's soil interaction are herein evaluated simply comparing the heating and cooling of CASE 0 to two additional cases BH and BC. The convective boundary condition assigned at soil surface corresponds to a constant temperature of 26 °C and 20 °C for the cases BH and BC, respectively. The pile's head displacement during heating and cooling of CASE 0 are compared to the displacements of BH and BC in Figure 3-29 (a). Axial load profiles at peak of heating and cooling for CASE 0 are compared to the axial load of cases BH and BC in Figure 3-29 (b). All the thermo-mechanical stresses are compared to the purely mechanical stress (M) (Figure 3-29 (b)).

From Figure 3-29 (a) it could be observed that the displacements of the three cases, CASE 0, BH and BC are very similar. The thermal boundary conditions applied in cases BH and BC determine slightly lower pile's heave and greater pile's settlement. The maximum and minimum thermo-mechanical displacement is -1.53 mm and -4.79 mm for BH and BC, respectively.

As shown by Figure 3-29 (b) the axial load profiles of the CASE 0 are practically equal to the profiles of the new cases.

For daily thermal operation and with reference to single isolated pile the boundary thermal conditions do not significantly affect the results of the pile-soil thermo-mechanical interaction.

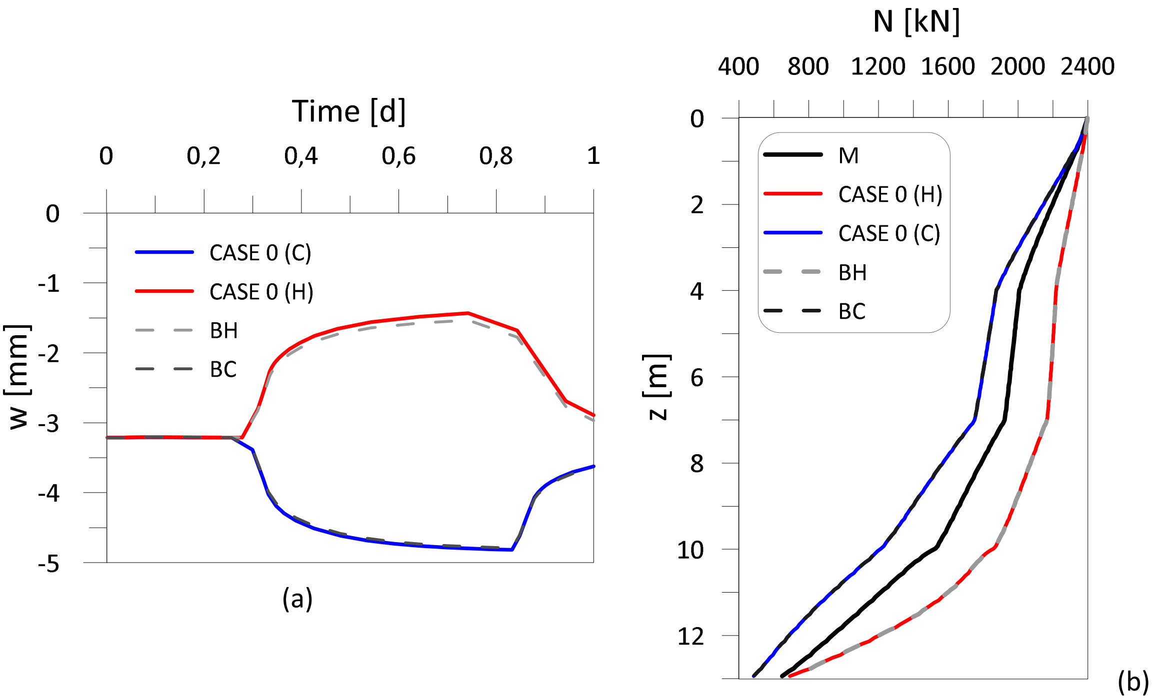

Figure 3-29:Effects of ground surface thermal condition on pile-soil interaction; (a) pile's head displacement during heating and cooling for cases BH and BC and CASE 0, (b) thermo-mechanical load profiles at peak of heating for cases BH and CASE 0 and at peak of cooling episode for cases BC and CASE 0 along with the purely mechanical load profile (M).

3.5.2.6 *Effect of the pile's thermal conductivity*

The impact of concrete thermal conductivity on pile-soil mechanical interaction is herein investigated.

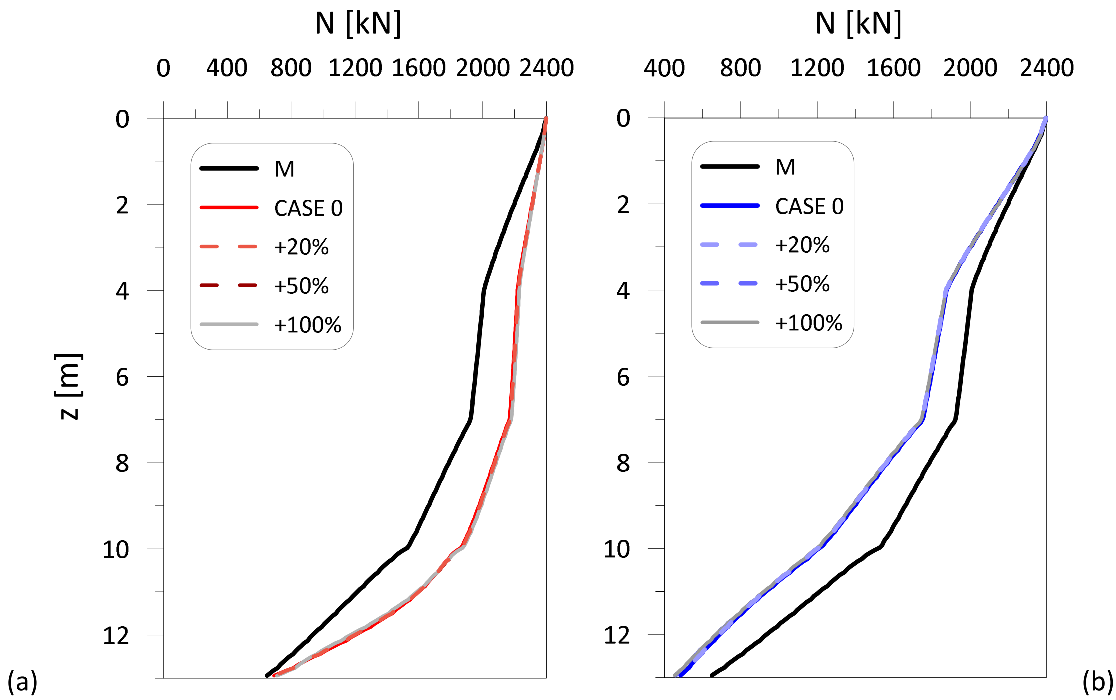

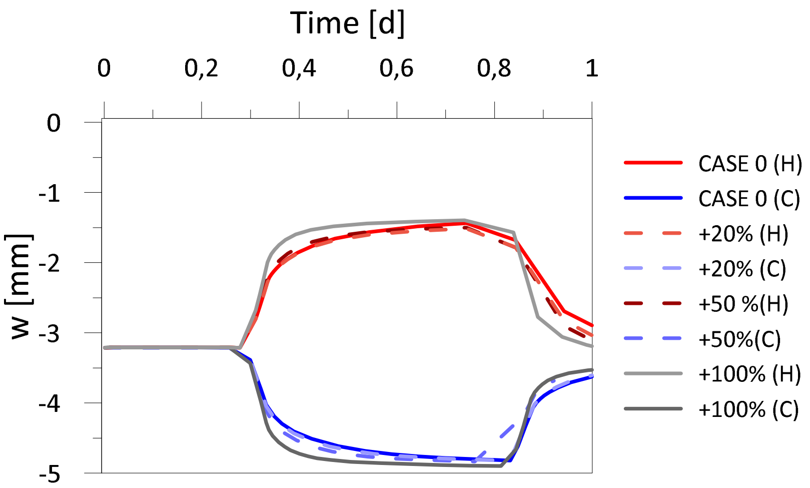

Figure 3-30: Effects of improved concrete thermal conductivity on pile-soil interaction; (a) thermo-mechanical load profiles at peak of heating for cases +20%, +50%, +100% and CASE 0 and (b) thermo-mechanical load profiles at peak of cooling episode for cases +20%, +50%, +100% and CASE 0 along with the purely mechanical load profile (M); (c) pile's head displacement for cases +20%, +50%, +100% and CASE 0 during heating (H) and cooling (C) episodes.

Three cases of increased thermal conductivity are considered: 20%, 50% and 100% of increment of the thermal conductivity with respect to the magnitude assumed for CASE 0. These cases are compared to the CASE 0 both in terms of displacements (Figure 3-30 (c)) and axial loadings along the depth (Figure 3-30 (a) and Figure 3-30 (b)). From Figure 3-30 (a) and Figure 3-30 (b) it could be observed that the increased thermal conductivity has negligible effects in terms of mechanical response in comparison to CASE 0. Both the maximum thermal stress and the displacement computed for the CASE 0 are confirmed for the other cases.

3.5.2.7 Concluding remarks about short term THM analyses

Daily operational conditions have been modelled to simulate the behavior of a typical EP installed in the urban area of Napoli. The service mechanical load is coupled to thermal loadings both in the case of heating and of cooling. Crenel solicitations considering twelve hours of working per day have been applied. The main effects on thermo-mechanical interactions have been investigated through the displacements of pile's head and toe and the load transfer along pile's depth. Heating and cooling determine additional displacements and axial loadings. Within the limits of the simulated behavior the relevance of several factors on the pile mechanical performance has been assessed. Among the factors considered the head constraint and the configuration of the PC influenced strongly the thermo-mechanical interaction while the boundary conditions at the ground surface and the thermal conductivity showed only minimal effects (in a single day simulation). With the single U-shaped or coaxial pipe configuration placed in the middle of the pile the smallest effect was observed as confirmed also by Batini et al. (2015). The spiral shaped pipe configuration generally appears superior from the perspective of the energy harvesting (Rotta Loria and Laloui, 2019) compared to U or W pipe configurations. Wang et al. (2017) investigated the thermo-mechanical behavior of U, W and spiral types of heat exchangers configurations. The strain of the W-shaped and spiral heat exchanger pile showed the largest thermal strains under the same heat input along the depth. The degree of the head constraint may have a relevant role and at the same time apart from upper and lower bound the exact condition is not easily defined. Scarce data are available about the long-term monitoring and particularly about the effects of cooling loadings in term of thermo-mechanical interaction. The FE THM simulations performed do not provide tensile stresses in the case of free head pile. When a constraint is modelled at pile's head tensile axial loadings are observed even if the compressive mechanical loading is applied. However, the tensile loadings observed i.e., the tensile stresses are smaller than the medium tensile strength of concrete. Additional monitoring will permit the evaluation of whether cyclic heating and cooling will lead to a greater increase in thermomechanical stresses over time (Murphy and McCartney, 2014). Even if from the daily thermo-mechanical analyses, the thermal boundary condition at soil surface does not provide relevant effects in terms of thermo-mechanical investigations, further investigations about this topic are needed considering long term analyses. The boundary conditions at ground surface could determine additional loadings whose effects on thermo-mechanical interaction should be further investigated.

3.6 *FE long term analyses*

3.6.1 Introduction

Understanding the impact of cycles of heating and cooling on the behavior of EPs is a necessary line of inquiry, because during the operational conditions the piles will be subjected to seasonal cycles of heating and cooling, and therefore the impact of these cycles on the foundation performance must be understood (Bournewebb and Bodas Freitas, 2020). The cyclic thermal response of single piles has been examined using numerical analysis (Saggu and Chakraborty (2015), Di Donna and Laloui (2014), Olgun et al. (2015), Rammal et al. (2017)). As a widespread habit it should be remarked that the temperature changes adopted in numerical modelling of EPs have been only rarely justified based on realistic heating and cooling demands of live buildings (Marone et al.,2020). Among the rare case Olgun et al. (2015) estimated thermal loadings on the basis of energy demand calculations. To address the investigation on thermo-mechanical response FE analyses are carried out considering thermal loadings defined on the heating and cooling demands of a building located in Napoli. The axisymmetric model presented in 3.53.5 was adopted for the simulations. Thermal loads have been determined by means of Design Builder software. The intermittent operation of the heat pump over different time scaling, hourly or daily, is modelled and compared in terms of thermo-mechanical interaction. A sensitivity analysis has been carried out to investigate the effects of the surface thermal boundary conditions on pile-soil interaction. The two bounds condition of free head pile and completely blocked at head pile were investigated for yearly operations. Then the results of FE analyses carried out on different piles type, end bearing and floating, subjected to the same level of mechanical and thermal loadings are compared. The results of long-term numerical simulations are also presented in order to provide previsions of such systems installed in the considered geographic area and subsoil conditions.

3.6.2 Yearly thermo-mechanical simulation of single energy pile under operational condition

The same axisymmetric model presented in 3.5 was used for performing yearly thermo-mechanical analyses. The mechanical service load was combined to the thermal loadings defined on the energetic demand of an office building for the geographical area of Napoli. The calculation of the energetic demand along with the main results of numerical simulations in terms of pile-soil interaction are firstly presented. Then different time scaling of thermal variations, thermal upper boundary conditions and head's restraint are compared.

3.6.3 Thermal loading definition

The nature of the thermal loads applied to a GSHP system has a large impact on its performance (Loveridge et al., 2020). From the thermal performance point of view, a system dominated by one way heat transfer will show decreasing performance over time while a system that is balanced between heat injection and heat extraction will always operate at greater efficiency. Energy geo-structures and GSHP design is therefore dependent on the thermal load requirements. Reliable prediction of the heating and cooling demands is extremely difficult, current approaches often lead to an underestimation. Therefore, designers often assess the risk of underestimation including a SF to be applied to the thermal loads. GSHP for the base thermal load and an auxiliary system for the balance could be used to cover peaky thermal loads. The phenomena caused by thermal loads involve effects that are coupled with those of mechanical loads and that can be comparable to the effects of mechanical loads (Rotta Loria et al.,2019). Thus, the importance of the definition of amplitude, numbers, and duration of thermal cycles.

The software used to perform the energetic simulation is Design Builder 9 that includes energy-plus tool able to model building cooling, heating, lighting, ventilation and other energy flow. The software was firstly used to calculate heating and cooling equipment sizes and then detailed simulation of the HVAC (Heating Ventilation Air Conditioning) was performed. Prior to determine the sizes of the equipment several input parameters have been assigned to the model. A four-storey building with a rectangular shape in plan of 9.00

m x 16.25 m is modelled. The transmittance of walls, slabs, windows was assigned according to the minimum required from the Italian Laws and guidelines (D.M. 26/06/2015) on building energy performance. One year of operation of the HVAC system was assumed. The GSHP was set in daily "on/off" mode from 8:00 a.m. to 18:00 p.m., from Monday to Friday defining the occupancy schedule of the building. Furthermore, the system was assumed to not work in April, May and October. For the Upper-structure five operational modes were considered: first heating cycle of ninety days, first recovery phase of sixty-one days, cooling cycle of one hundred twenty-two days, second recovery cycle of thirty-one days and second heating cycle of sixty-one days. The activities in the building have been set to "Generic Office Area" with an occupant density of 0,111 person/m^2. Target temperatures have been assigned to the internal air of the building according to the provisions of UNI / TS 113000 and they are 20 °C and 26 °C for heating in the wintertime and cooling in the summertime, respectively.

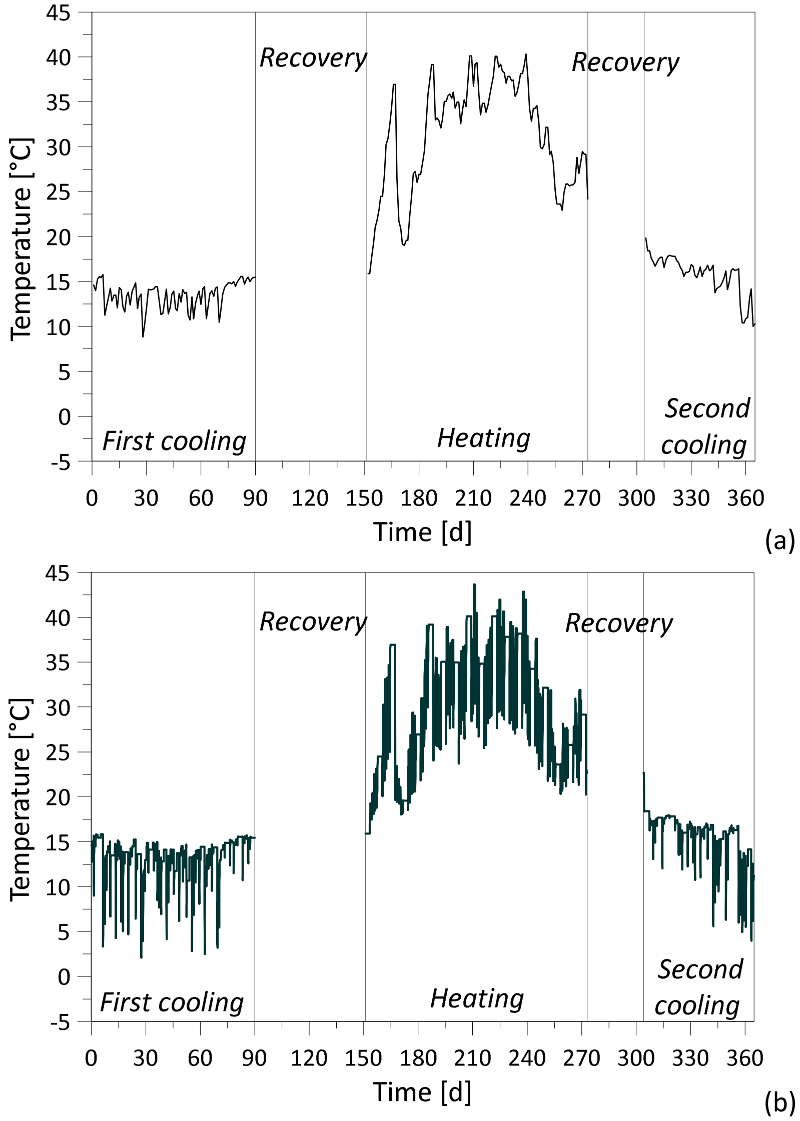

Figure 3-31:Inlet temperature used as temperature function applied to the pile (Thermal loading) at daily (a) and (b) hourly time scaling.

Heating calculations are carried out using a simple convective heating system to achieve the temperature set point. Cooling design calculations are carried out to determine the capacity of cooling equipment to meet the hottest summer design weather conditions at the site location. Designed the HVAC system as well as the geothermal heat exchangers, Dynamic simulations have been performed and the hourly and daily inlet temperatures of the fluid entering the underground collector (heat exchanger system) and indoor mean air temperature have been obtained. The inlet temperature at daily (DTV) and hourly (HTV) time scaling is plotted in Figure 3-31(a) and Figure 3-31 (b), respectively.

The inlet fluid temperature was assumed as the temperature function to assign to the pile in order to define thermal loadings. The small difference occurring between the inlet and outlet temperatures of the fluid was neglected. This is of course a minor approximation considering its mechanical implications. The temperature history is divided into three functions: First cooling (from January to March), heating (from July to September) and second cooling (November and December). The heating of the pile corresponds to the cooling of the upper structure and vice versa. Peaks thermal loadings obtained from the simulation are greater for the case of cooling of the upper-structure and smaller for heating, as could be expected for the considered climatic area. Therefore, greater thermal variations are observed in the case of heating of the pile and smaller in the case of cooling of the pile. During the heating of the pile temperature ranges between 14°C and 43 °C while during cooling between 2°C and 17 °C and. Three recovery phases are defined for the months of April, May and October. During these periods, the GS is not working.

The Indoor and Outdoor air temperatures at different times scaling are plotted in Figure 3-32 (a) and Figure 3-32 (b), respectively.

The Outdoor temperatures have been obtained from data base of air temperature measurements for the Urban area of Napoli while the indoor temperature derived from the energetic simulations considering the operational of the HVAC system. The Indoor temperature ranges between 13.7 °C and 24.5 °C for the first cooling of pile between January and March. During the months from July to September ranges between 32 °C and 22.3 °C. During the second cooling of the pile indoor temperature maximum and minimum values are 15.3 °C and 26 °C, respectively. During the operational of the GSHP outdoor air temperature is greater than the indoor air temperature for the heating of the upper structure. During the heating of the pile internal air temperatures are lower than the outdoor temperatures.

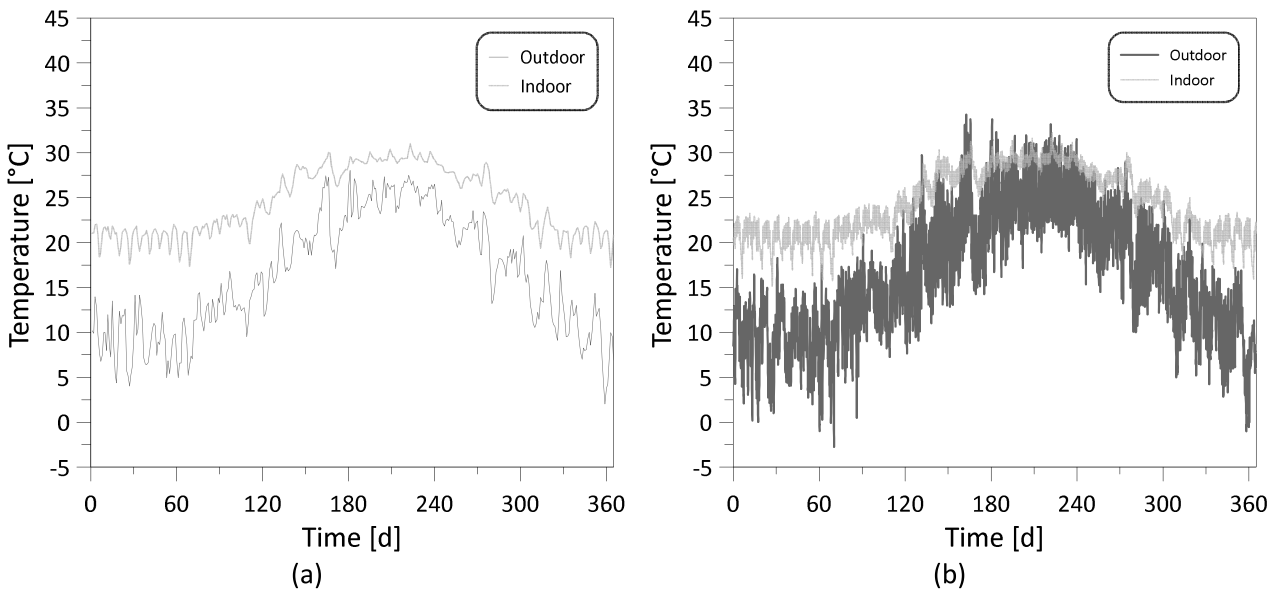

Figure 3-32:Indoor and Outdoor air temperature at daily (a) and hourly (b) time scaling.

3.6.4 Analysis of pile-soil interaction under different thermal variations

Long-term predictions of energy piles' performance imply cyclic thermal loadings and consequently pile-soil interaction under cyclic quasi-static conditions. For instance, the thermally induced cyclic movements may cause cumulative degradation of the side friction leading to the alteration of shaft resistance. The thermal response of soil, subjected to numerous thermal cycles could contribute to further pile plastic displacements accumulation in long term condition and to changes in the mobilized frictional resistance. Experimental studies on sand under drained cyclic thermal load described in 2.1.6.2 showed cyclic accumulation of strains. Therefore, given the relatively small but realistic temperature range, and the magnitude of strains accumulation in sand, relatively simple and thermo-elastic constitutive models are adopted for soils layers (H-S). The axisymmetric model adopted for daily simulations (3.5) was developed to perform longer analyses. Two Cases, corresponding to different time scaling of thermal loadings, are reported: cycles with Hourly Thermal Variations (HTV, Figure 3-31 (b)) and cycles with Daily Thermal Variations (DTV, Figure 3-31so (a)). For both cases, the same live mechanical load (2400 kN) applied during the daily analyses was applied to the head of the pile and kept constant during the yearly thermal cycle. The transient thermo-mechanical analyses have been carried out assigning the same thermal boundary described in section 3.5 except for temperature functions applied to the pile and at soil surface. At soil surface the outdoor main temperature of air in Napoli was assigned (Figure 3-32 (a) and (Figure 3-32 (b)). Thermal loadings imposed as temperature-time variable functions correspond to the inlet fluid temperatures (HTV or DTV Figure 3-31 (b) and Figure 3-31 (a)). During one year of the operation, two recovery phases of 61 and 31 days are considered and simulated not applying any thermal conditions to the pile. During these phases all the others thermal boundary conditions are applied to the model to simulate the effective thermal recovery of the system. The effects of the two different types of thermal load variations, DTV and HTV, are compared in terms of pile head displacements and axial load profiles in Figure 3-33 and Figure 3-34, respectively. From Figure 3-33 it is possible to notice that the trend of the pile head displacement follows the pile expansion and contraction induced by the thermal variations. The maximum incremental displacement observed for DTV is 4.40 mm and 4.86 mm for HTV. Comparing the displacement induced by the thermo-mechanical coupling to the displacement induced by mechanical loading (3.21 mm), DTV and HTV determine an additional displacement equal to 37 % and 51% of the mechanical displacement, respectively (Marone et al., 2020).However, the absolute value of the difference between the maximum thermo-mechanical displacement induced by HTV and DTV is generally less than 0.3 mm and therefore it could be considered almost negligible for engineering applications. Different time instants of the yearly thermal cycles, both in case of HTV or DTV, are chosen to illustrate the distribution of the axial load within the pile during heating, cooling and recovery phases (Figure 3-34). The axial load along the pile induced by DTV and HTV combined to mechanical loading are compared with the case where only the live load is applied to the head of the pile (Mechanical case). For both kinds of thermal variations, DTV and HTV, heating the pile increases the axial loading along the shaft, and this effect is only slightly higher under hourly variations (Figure 3-34). In the case of cooling the axial load for both DTV and HTV decreases with respect to the mechanical case (Figure 3-34).

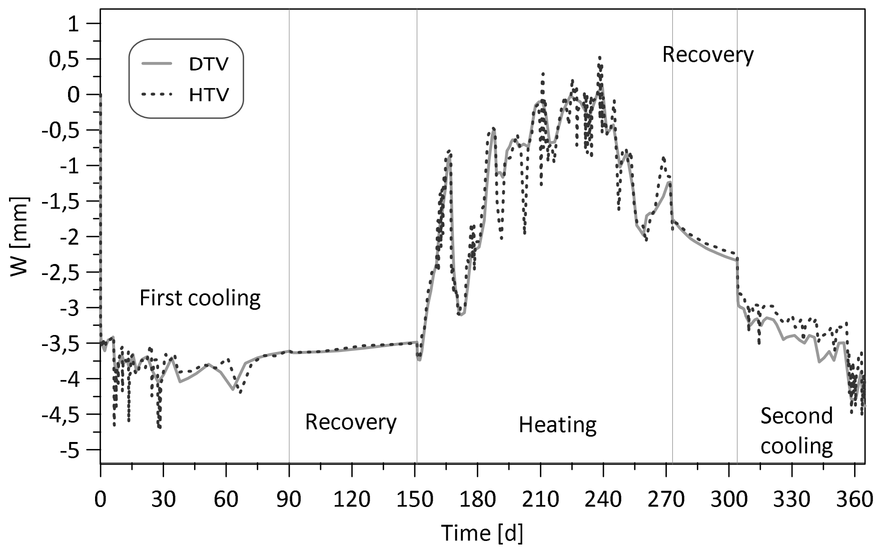

Figure 3-33: Pile's head thermo-mechanical displacement for DTV and HTV during one year of operational.

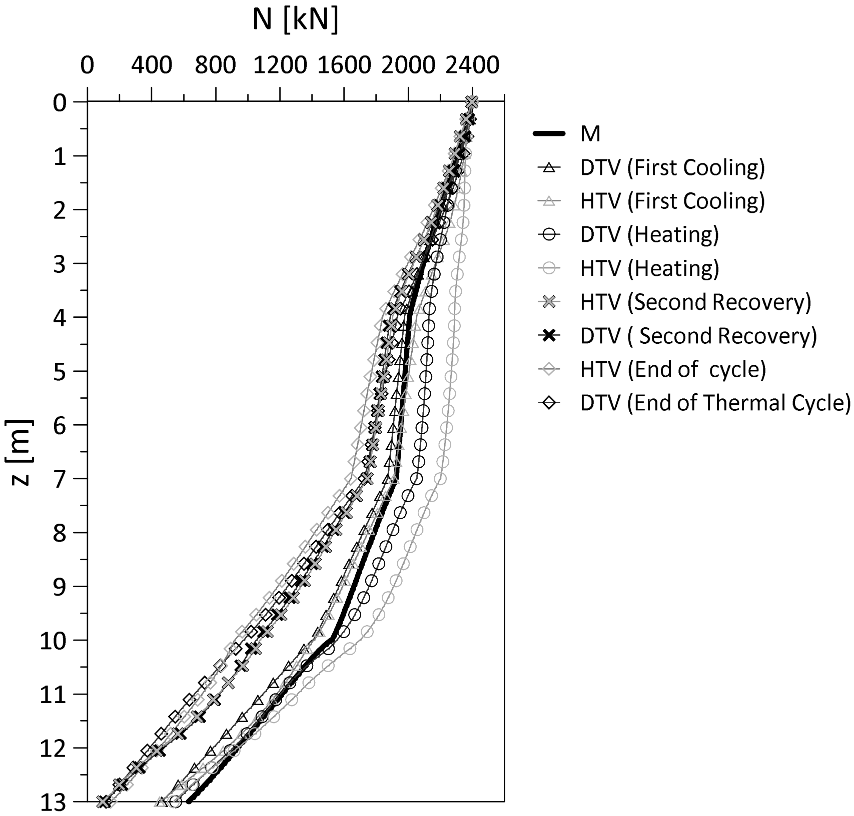

Figure 3-34:Thermomechanical axial load at different time of the yearly operation (First Cooling, Heating, Second Recovery and at the end) for the DTV and HTV.

The axial load is reported also at the end of the second recovery phase (Figure 3-34) where no thermal loadings are directly applied to the pile. During this phase, the axial load is not overlapped to the mechanical case, within the pile there is still a thermal variation induced by the previous loading. At the end of the yearly operational condition, for both DTV and HTV the axial loading is smaller than the mechanical case (Marone et al., 2020). This effect could be attributed to the cooling at the end of thermal cycle i.e., the temperature of the pile is not back to the initial value. As a matter of fact, also in terms of axial loading, DTV and HTV determine different axial load variations, but their amount could be assumed negligible. From the observed response, applying DTV or HTV does not determine substantial difference in terms of additional displacements and axial load variations along the pile shaft. Carrying out FE analyses with hourly thermal variations significantly increases the calculation efforts and the time needed and does not lead to a noticeable difference when compared to the simpler case of daily temperature variations. Zanchini and Iazzari (2013) demonstrated that varying the amplitude over short periods (month, days or hours) in numerical models increases the computational time with no effect on the predicted overall long- term performance. The results of the investigations about the thermo-mechanical interaction provide the same findings from the geotechnical performance point of view, therefore DTV could be considered to provide previsions about soil-pile thermo-mechanical interaction.

3.6.5 Analysis of pile-soil interaction for different ground surface thermal conditions

Another aspect that needs to be further investigated is the possible coupling of the effects of the imposed surface boundary condition and the pile thermal loadings on pile-soil thermo-mechanical interaction. According to Bourne-Webb et al. (2019) thermo-mechanical response observed in the pile could be affected by the superposition of the heat flow from the structure and the thermal loading within the pile (Bourne-Webb et al., 2019). Therefore, additional numerical investigations are carried out considering the superposition of effects of thermal interaction between heated or cooled energy pile and the upper structure for longer operational (one year instead of one day). In this study, for the surface boundary conditions two extreme cases were defined: (i) the surface temperature corresponds to the outdoor temperature (the results discussed in 3.6.4), (ii) the surface temperature corresponds to the building indoor temperature. The former case could be considered representative of a pile foundation located under an exterior wall of the building that is more sensitive to variations in ambient air temperature. Murphy and McCartney (2014) observed that greater changes in temperature occur for EPs under an exterior wall of the building compared to piles that are under the central area of the building slab. Therefore, the latter boundary condition could be representative of a pile that under the middle of the slab. The interaction with the upper structure is modelled in a simple way considering that the temperature of the air inside the building (Figure 3-32) is applied at ground surface. The indoor temperature function is applied as convective boundary considering a surface heat transfer of 2 W/m^2 °C. For these thermal surface boundary conditions, the results of DTV analyses are firstly reported.

In Figure 3-35, the thermal surface effects are compared in terms of pile head displacements.

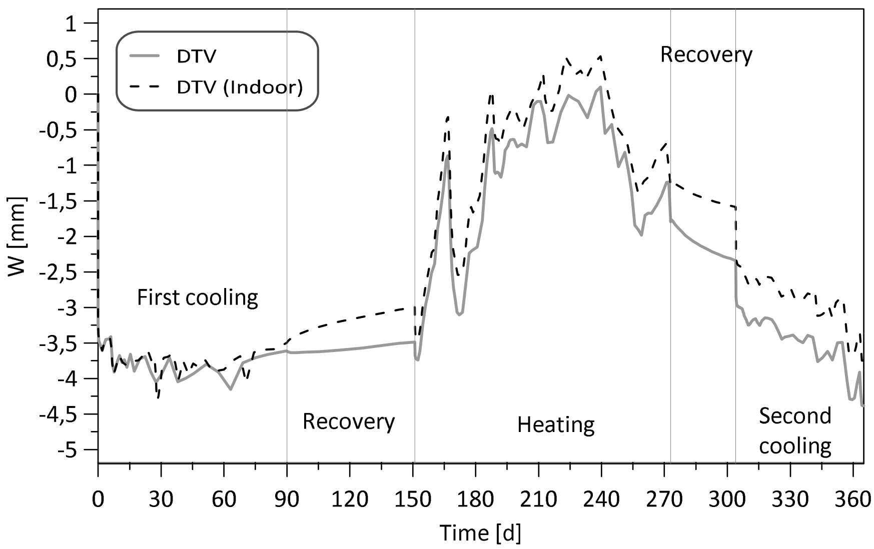

Figure 3-35:Pile's head thermomechanical displacements for DTV and different upper thermal boundary conditions outdoor air temperature (DTV) and Indoor temperature (DTV (Indoor)).

The displacement history shows that when the indoor condition is applied at soil surface higher heaves occur during the heating phase. During the cooling phases the settlements observed applying the outdoor temperature at soil surface are smaller. The greater difference of the two thermal boundary conditions is observed during the recovery phases, in terms of head displacements of the pile head. The maximum pile head settlement considering Indoor temperature variations at soil surface is however -4.31 mm. The largest difference between the two different boundary conditions is slightly less than 1 mm which is about 23% of the maximum displacement recorded during the overall time history.

The influence of the different boundary conditions is explored in terms of axial load along the pile shaft in Figure 3-36. The axial load thermomechanical profile is reported for different phases of the thermal cycle (first cooling, heating and recovery phases). The two thermal boundary conditions are compared in terms of axial loading profile considering the same instant of time for each mode considered.

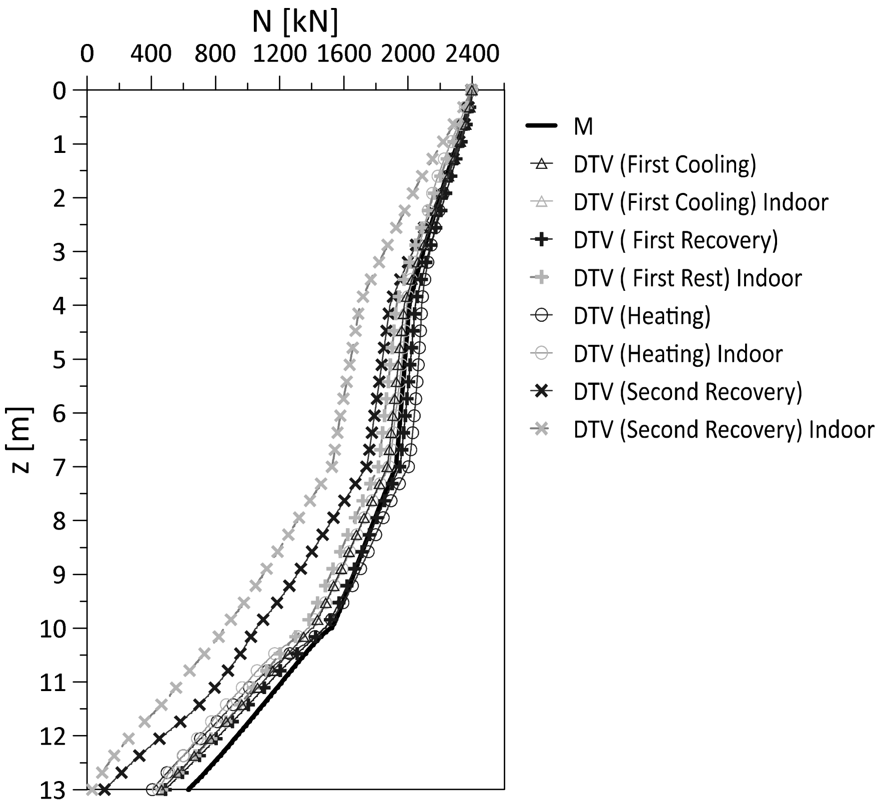

Figure 3-36:Thermomechanical axial loads for different thermal boundary conditions at ground surface and time instant of the yearly operational (First Cooling, First Rest, Heating and Second Recovery).

During the two recovery phases the assigned surface boundary condition has a more pronounced effect on the axial loading distribution. This finding is in agreement with the displacement histories. Comparing the axial load along the shaft, during the different phases, it could be noticed that the difference between the two simulated surface conditions is in the range of 10% to 15 %. In the case of heating, applying the indoor thermal variations to the top of the domain determines a lower axial load compared to the outdoor thermal case. During cooling modes, the difference between the two cases is smaller, the indoor temperature assumption determines a smaller axial load compared to the outdoor temperature assumption. During both first cooling and heating cycles, as shown by the results plotted in Figure 3-36, the effect of the surface boundary condition is mitigated. The largest difference between the two thermal conditions at soil surface occurs during the two recovery phases. In fact, when the system does not work the surface boundary is the only thermal loading applied to the system. This is evident in Figure 3-37 (b) and Figure 3-37 (d) where the field temperature during the second recovery phase is plotted in a vertical section passing through the pile axis. When indoor temperature is considered at the boundary the temperature values computed down in the subsoil are higher than the corresponding values under outdoor conditions. On the other hand, Figure 3-37 (a) and Figure 3-37 (c) clearly show the smaller influence of the thermal boundary conditions during the heating phase which is presumably governed by the heating load applied within the pile. As concluding remark, from the results both in terms of axial loading and pile head displacement, the outdoor temperature variation assumed as surface boundary condition seems to be the most conservative design assumption.

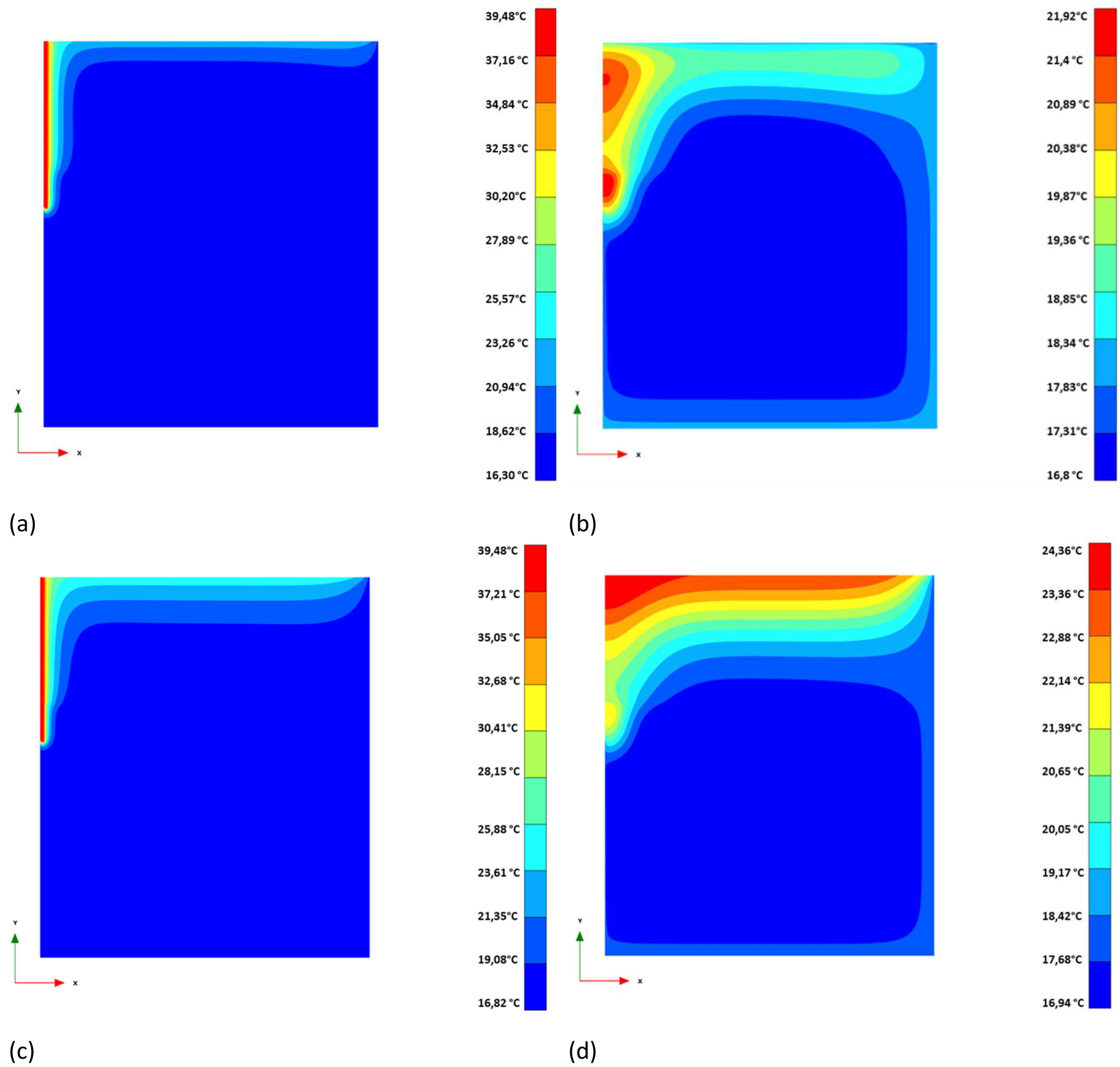

Figure 3-37: Temperature fields: Peak of the heating phase and end of second recovery phase for the outdoor boundary condition (a and b) and indoor boundary condition (c and d).

3.6.6 Analysis of pile-soil interaction for different head constraint

The pile-soil interaction under two extreme conditions, free head pile and fully constrained pile head, is herein investigated considering one operational year. The free head pile model corresponds to those described in 3.6.5. DTV are considered on the basis of the previous results because assigning HTV increase only the calculation efforts without significant effects on the thermomechanical interaction. The thermal boundary conditions applied correspond to those described in 3.6.5. The model of fully constrained pile differs to the free head pile only for the degree of freedom modelled at its head. Thermal displacements are completely blocked at pile's head. The comparison of pile response for fully constrained case (FC) and free head case (FH) is provided in terms of thermo-mechanical axil profiles and pile's displacement. During the yearly operation, the end of the first cooling cycle, the peak of heating and the end of the second cooling cycle (end of the thermal history) are considered to evaluate the axial loading along the depth (Figure 3-38).

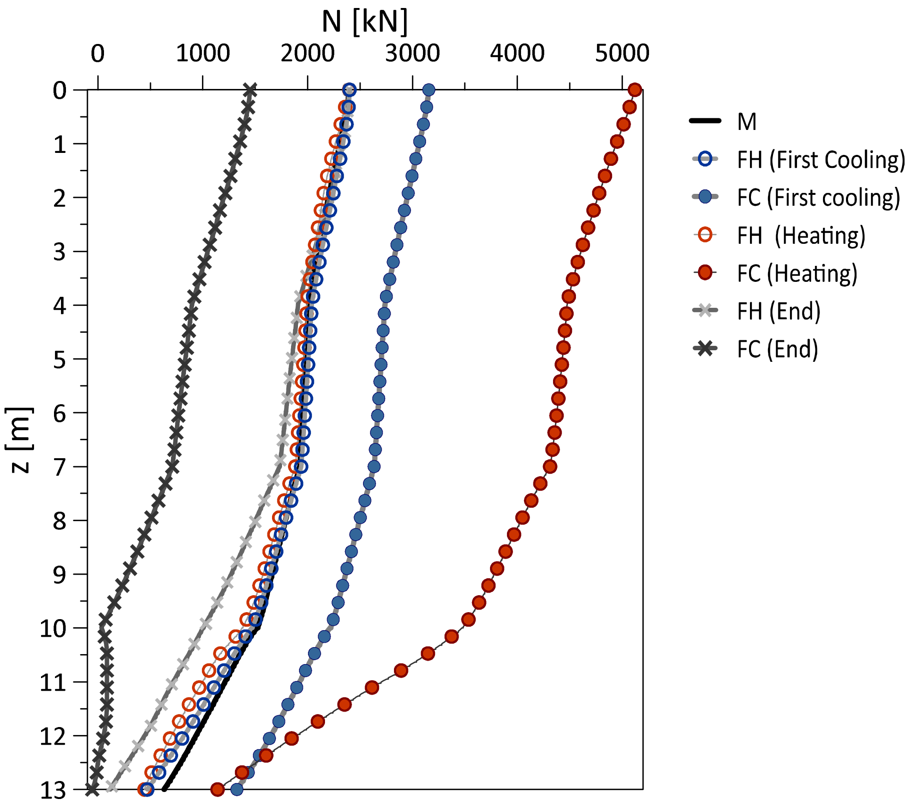

Figure 3-38: Thermomechanical axial load profile for the FH (Free Head) and FC (Fully Constrained head) cases at the same time instants of the yearly operational : at the end of the first cooling phase (first cooling), at the peak of the heating phase 8Heating) and at the of the thermal history (End).

The pile's head blocked thermal movement determines additional compressive axial load during heating while a complete recover is observed at the end of the thermal history. The end of the thermal history corresponds to the end of the second cooling phase and in this case the temperature is lower than the initial one and therefore a reduction of the compressive axial load is expected and observed. Comparing the thermomechanical stress to the purely mechanical stress observed for the FH case, it could be observed that the greater change occurs during heating. At the peak of heating the axial loading at pile head is 5126 kN. At the end of cooling the thermomechanical load at the head is about 1454 kN while at the end of the first cooling it is about 3158 kN. At the peak of heating the load computed in the constrained case doubles the purely mechanical loading. At the end of the thermal cycle the thermomechanical loading at the head is about 60 % of the purely mechanical load, while at the end of the first cooling is about 30% of increment with respect to the purely mechanical load.

In Figure 3-39 the thermomechanical displacement of pile's toe versus the elapsed time is plotted for the FC and FH cases. The constraint at pile's head determined higher displacement at pile's toe. The thermomechanical minimum settlement in the case of FH pile is about -0.81 mm while in the case of FC pile is -1.31 mm. The initial small mechanical settlement (-0.49 mm) is almost tripled in the case of FC while in the case of the FH is almost doubled. The higher displacements at pile's toe are expected in the case of the FC pile because of the constraint modelled at pile's head. In both cases the values of the displacements of the single analysed pile are very small at the pile's toe and it should be kept in mind that it is a pile with the pile's tip in the yellow tuff. The difference in magnitude of the FH and FC toe's displacement change during the simulated year. It is smaller at the operational beginning and increase with the elapsed time.

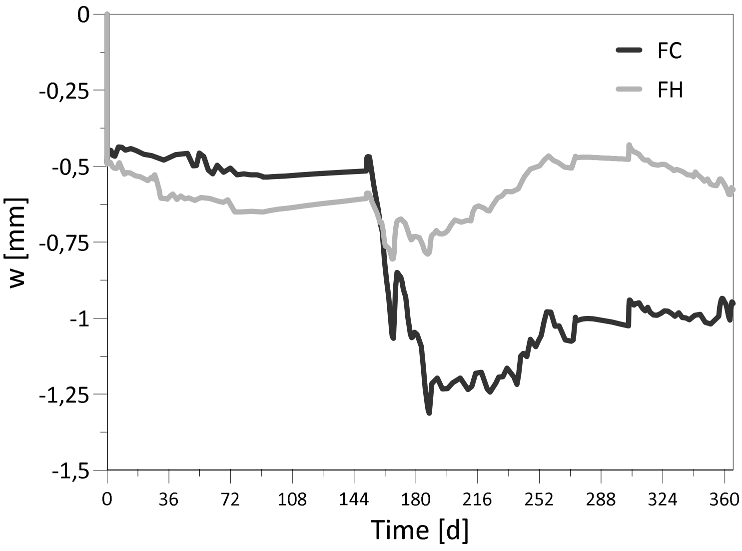

Figure 3-39:Thermomechanical toe's displacement for the FH (Free Head) and FC (Fully Constrained head) cases.

During the heating phase higher displacements occurs at pile's toe in the FC pile demonstrating the different mobilization of the shaft friction. The mobilised shaft friction and the dimensionless mobilised shaft friction are plotted versus pile's depth for the FC and FH cases in Figure 3-40 (a) Figure 3-40 (b).

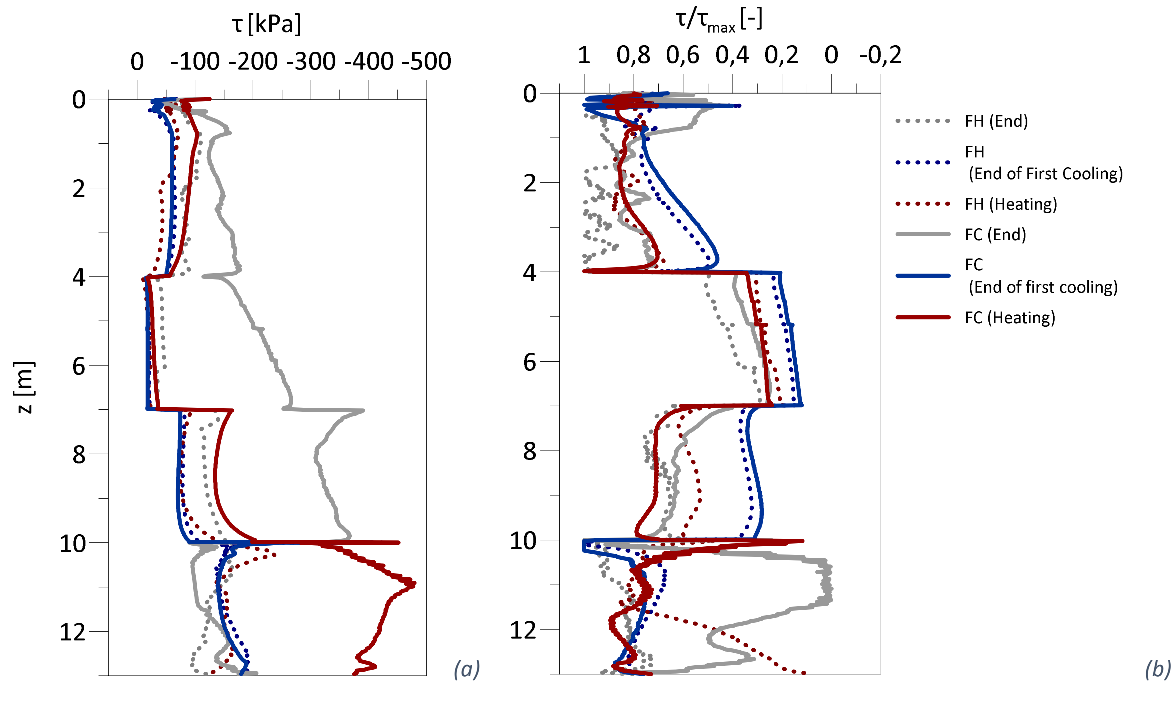

Figure 3-40: (a) Mobilized shaft friction and (b) dimensionless mobilized shaft friction versus pile's depth for the FH and FC cases at the end of the first cooling phase (End of first cooling), at the peak of the heating phase (Heating) and at the of the thermal history (End).

The same time instants of Figure 3-38 are taken into account. The dimensionless mobilised shaft friction (τ/τ_{MAX}) on the abscissa axis is the ratio between the mobilised friction and the maximum shaft friction at each depth. During the first cooling of the pile the mobilised shaft friction of the FC and FH piles are very close. This could be explained considering that during the first cooling the amount of the thermal loading is reduced and therefore the magnitude of constrained thermal strains is small. With the increasing in temperature changing during the yearly operation the different head constraint conditions determine different degree of mobilization of the shaft friction (Figure 3-40 (b)). At the peak of heating episode and at the end of the operational, the larger difference between FH and FC is observed close to the pile's toe.

The effect of the constrained head determines higher displacements at pile's toe along with higher variations of thermal loading at this location with respect to the FH case. During the peak of heating and the end of the thermal cycle higher mobilization in lower part of the pile along with higher toe displacements occurred demonstrating the predominant effect of the degree of constraint at pile's head.

3.6.6.1 FE analyses on a typical floating pile

The thermo-mechanical interaction under different degree of constraint at pile's toe is investigated considering two typical situations: pile with socket depth in tuff and pile without socket depth in tuff layer These two conditions will be named as end bearing and floating pile. To an end bearing pile are dedicated all the previous sections: i.e., a pile with 3 m of socket depth in the tuff layer. The term "end bearing" is only used to emphasize that the pile has socket depth in the tuff layer. The behavior of the pile is of semi-floating pile type. That is a typical layout for piles in the urban area of Napoli. A new axisymmetric model representing the condition of a floating pile is considered in the following. Floating pile is used to emphasize that in this case the pile has not socket depth in tuff. The real behavior of this pile too is semi-floating pile. Thermo mechanical transient analyses are carried out considering the same level of mechanical loadings and thermal loads. Temperature functions to be applied to the pile are defined following the procedure described in 3.6.3.

3.6.6.1.1 Floating pile modelling and calibration of the subsoil parameters

In the frame of the design stage of the pile foundations of a new mall and a touristic facility at Torre Annunziata south of Napoli, close to Pompeii archaeological park, geotechnical investigations and pile tests to failure on floating piles were performed. In this area the shallow soil layer is very soft while subsoil below 6-8 m is rather stiff and partially cemented due to the volcanic origins and the high temperature at the time of areal deposition. For this reason, at the design stage a hybrid pile technology was purposely conceived. The upper part of the pile is a typical large stem pipe pile with the pipe simply pushed in the ground without soil removal while the lower part is a classical CFA pile with a significant volume of soil removed in the step when the installation tool is retrieved upwards. The hybrid technique adopted allowed a better mechanical performance in the upper soft layers due to the displacement type of pile which induce soil densification.

The mechanical performance of the foundation pile was experimentally evaluated performing three design tests. All the tests were carried out by means of a hydraulic jack where the reaction to the compressive load on pile is obtained via a thick spreading beam anchored to a couple of tension piles. Among the performed load tests, for the calibration of the FE model the longest tested pile (16 m length and 0.6 m diameter) was selected as reference. The geotechnical subsoil model parameters were also defined on the basis of the results of site investigations. Eight continuous coring boreholes and down-hole geophysical tests, standard penetration tests, Cone Penetration Tests (CPTU) on twelve verticals and two Casagrande type piezometers for the groundwater table investigation were carried out at the site. The results of CPTs and SPTs are plotted in Figure 3-41 (a) and Figure 3-41 (b), respectively.

SPTs were stopped at 50 blows as shown in Figure 3-41 (b). From Figure 3-41 (a) it is possible to notice that CPTs were stopped between 7 m and 10-11 m because coarse material (i.e., sandy soil with pumices) was encountered. The results from CPTs and SPTs allowed the determination of soil stiffness and strength parameters. Relative density for each soil layer was computed through Gibbs and Holtz (1957) and Kulhawy and Mayne (1990) expressions considering the mean blow count and cone tip resistance Q_c, respectively, for each soil layer. Friction angle for each soil layer was computed as mean value between those obtained from API (1987) and Schmertmann (1979) relationships considering the average relative density.

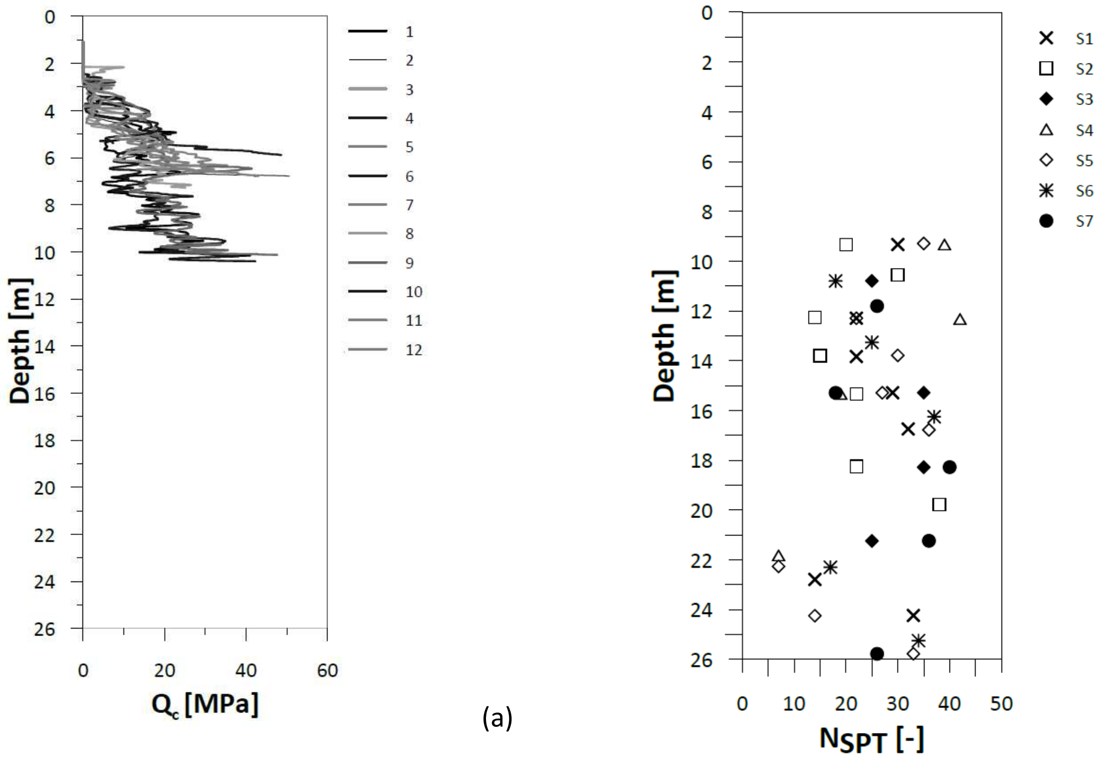

(a)

(b)

Figure 3-41: Site investigations results; (a) CPTs and (b)SPTs.

For each soil layer secant Young modulus Es was obtained from De Beer (1965). Five main soil layers are identified. For each soil layer, soil physical and mechanical properties are summarised in Table 3-7.

Table 3-7: Soil layering and mechanical properties

Layer	Soil Type	Depth		ɣ	φ	C'	E_s	E^*_0
[-]	[-]	Top [m]	Bottom [m]	[kN/m³]	[°]	[kPa]	[MPa]	[MPa]
1	*Upper soil*	0	1	18	30	-	10	-
2	*Pumice 1*	1	3	16	32	-	20	180
3	*Sand and Gravel*	3	10	17,5	35	-	45	460
4	*Pumice 2*	10	12	16	32	-	35	-
5	*Fine Sand*	12	22	17	35	-	50	850

*Initial Stiffness obtained by Down-hole geophysical tests.

The load-settlement relationship curve obtained from the load test on the hybrid test pile is plotted in Figure 3-42(a).

Even if the maximum test load was not sufficient to activate all the components of the pile resistance, a conventional pile bearing capacity of 6189 kN corresponding to -30.62 mm of head's settlement is assumed. The axial load along the pile shaft at the service and at the ultimate load is plotted in Figure 3-42(b).

The mechanical behavior observed during the load test and the site investigations were used for calibrating the strength and the stiffness parameters of the FE model developed. The aim of this investigation is to provide as realistic as possible FE model to study thermo-mechanical interaction of floating energy pile installed in the urban area of Napoli. A fine triangular mesh of 15-noded elements was used to discretize the axisymmetric model. Around the pile an additional mesh refinement was assigned to provide more accurate results. For the five layers of pyroclastic soil H-S constitutive model was adopted, while, for the pile the simple linear elastic model was used. The Young's modulus of the concrete pile was fixed at 30.000 MPa.

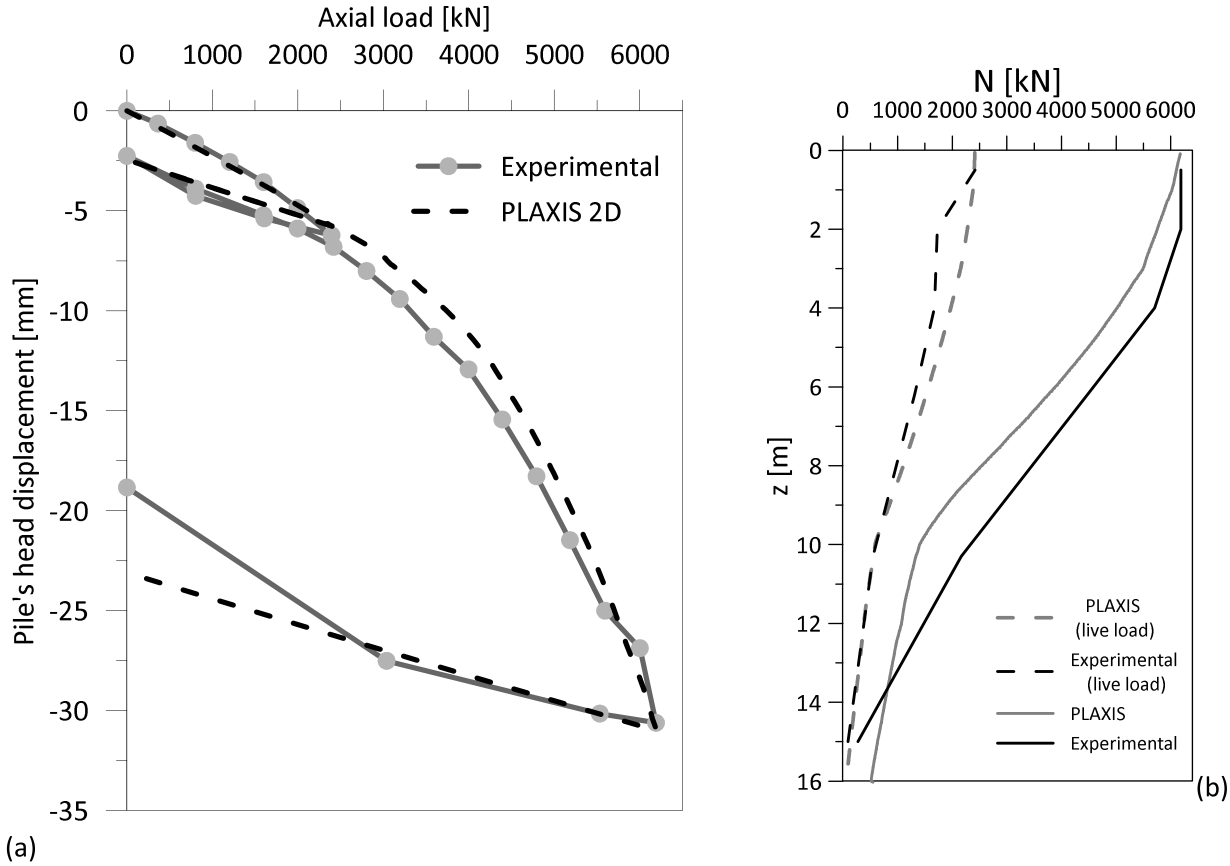

Figure 3-42: Experimental and numerical (PLAXIS 2D) results. (a) Load-settlement relationship and (b) axial load along pile shaft during live load and ultimate condition.

Best fit procedure based on the trial-and-error method was adopted to obtain the set of stiffness parameters listed in Table 3-8. Interface elements have been adopted to allow vertical relative displacements between the pile and the surrounding soil. For these elements, the same strength parameters of the surrounding soil were kept for all the soil layers.

Table 3-8:Subsoil geotechnical model, stiffness and resistance parameters of the H-S model.

Soil Type	Depth		ɣ	φ	ψ	E_{50}	E_{ur}
[-]	Top [m]	Bottom [m]	[kN/m³]	[°]	[°]	[MPa]	[MPa]
Upper soil	0	1	18	30	-	10	30
Pumice 1	1	3	16	32	2	20	60
Sand and Gravel	3	10	17,5	35	4	70	210
Pumice 2	10	12	16	32	2	80	240
Fine Sand	12	22	17	35	4	100	300

The hybrid pile execution was simulated by high levels of the horizontal stress fixed through the earth pressure coefficient at rest used in the K_0-procedure. The dilatancy angles, ψ, are estimated from the peak shear strength angles reported in Table 3-7 using Bolton (1986) expression. The parameter m of the H-S model for soft soil is assumed considering for the stress dependency a linear relationship, i.e., m=1 (Brinkgreve et al., (2010). The ratio among the values of the E_{50} and Eur moduli were kept E_{50} =E_{ur}/3 (Brinkgreve et al., 2010). The secant stiffness values (E_{50}) obtained from the calibration procedure are slightly larger than those reported in Table 3-7.

In Figure 3-42 (a) and Figure 3-42 (b) the load-settlement curve and the axial load profiles obtained by PLAXIS at the end of the calibration procedure are compared with the experimental curves. The test pile was equipped with vibrating strain gauges that allow estimating the load transfer mechanism along the pile. The axial load profile obtained from the measurements of the gauges is plotted in Figure 3-42 (b). The comparison shows that the agreement with the experiment is rather satisfactory both in term of load-settlement and load transfer. The general trend of both the primary loading and unloading-reloading branches is satisfactory reproduced by the H-S model that allows a good fitting particularly in the first loading – unloading branch (Figure 3-42 (a)). The axial load profiles along the pile shaft, calculated by the FE simulation (PLAXIS) and measured during the experimental test (Experimental), are reported for two different loading steps, i.e., 40 % of the ultimate test load, assumed as live load for the pile, and ultimate load. The comparison is rather satisfactory particularly at live load.

3.6.6.1.2 Thermo-mechanical analyses

The described calibration procedure allows developing the model used for the thermo-mechanical analyses on the floating energy pile (FEP). The operational conditions of FEP were modelled following the same procedure described for the end bearing pile (EBEP). A plastic phase was used to model the application of the live loading (2417 kN) to the head of the pile. Before this calculation phase the stress state of the soil induced by the installation of the pile was modelled through a K_0 procedure. A nil plastic step was also modelled to ensure the equilibrium. The plastic step was followed by fully coupled phase where the mechanical load was combined to thermal loadings.

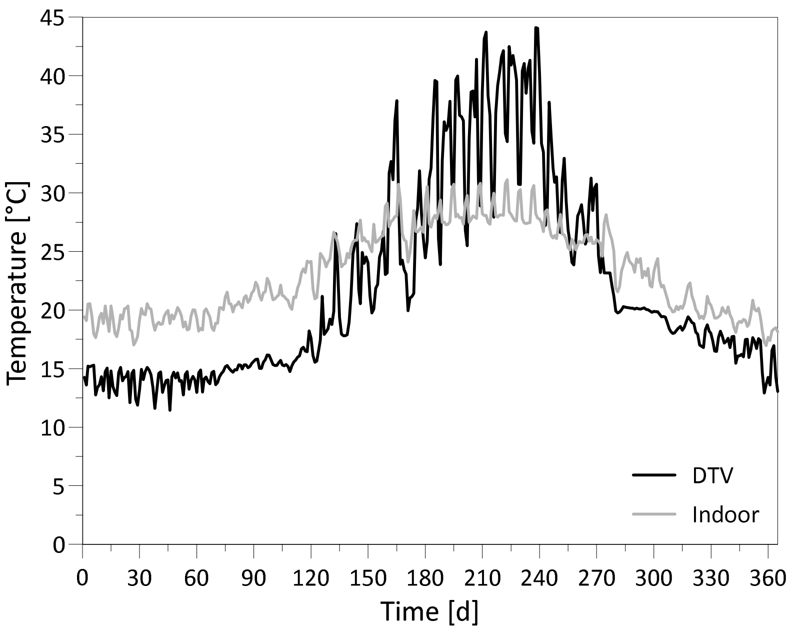

Figure 3-43: Inlet pile temperature variations (DTV) and Indoor temperatures during one year of operation.

The application of thermal loadings consists of applying temperature function along a straight line corresponding to the primary circuit. Temperature function corresponds to inlet temperature of fluid in the primary circuit. The definition of thermal loadings is based on the same procedure described in section 3.6.3 and dynamic energy simulations are carried out by means of Design Builder software. One year of operation for the city of Napoli was considered. Therefore, the same geographic area was considered but different upper structure, schedule and activities are modelled. The GSHP was assumed to work in intermittent mode “on/off” from 8:00 a.m. to 22:00 p.m. for all days of the week. Thermal recovery phases are not modelled during the year of operational. To simulate the activities carried out and the occupancy density the “Retail-Mall common area” was chosen. The inlet fluid temperature i.e., thermal loadings and the indoor temperature of the mall are plotted in Figure 3-43. The inlet temperature ranges between 11 °C and 44 °C while the indoor temperature between 31 °C and 17 °C. In Figure 3-44 a cross section of the FEM model with the thermal boundary conditions is sketched. At the ground surface a convection boundary condition with an appropriate heat transfer coefficient was assigned assuming as temperature variable function the indoor temperature (Figure 3-44). Closed flow boundary thermal conditions are assigned at the sides of the model, while at the bottom a constant temperature condition was set (17 °C). The thermal properties of the soil are those typical of saturated pyroclastic sandy soils (Colombo, 2010; McCombie et al., 2016). i.e., and correspond to the thermal properties assigned for the sands layer surrounding the EBEP. For the concrete pile the same thermal properties of EBEP are assigned.

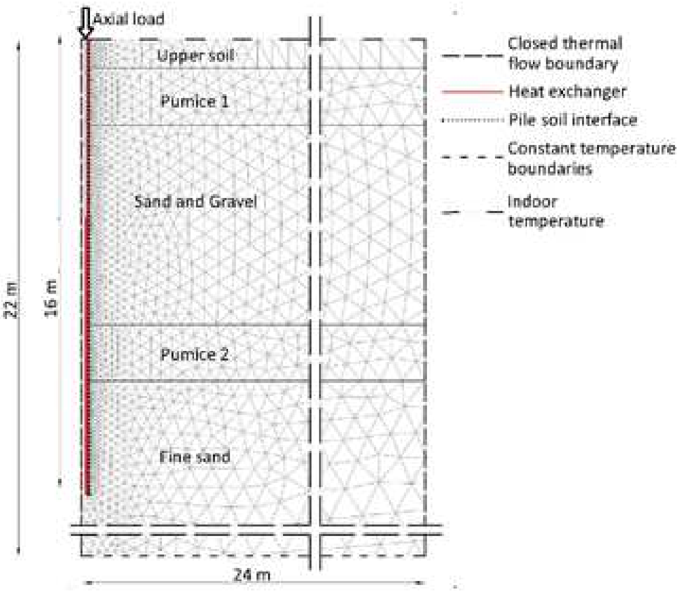

Figure 3-44: FE model and thermal boundary conditions for the FEP.

Pile head and toe displacements during one year of operation are plotted in Figure 3-45. The initial settlement of the pile, induced by the service load (mechanical), is about -4.78 mm. Therefore, being the plastic phase that simulate the application of the mechanical load not time dependent, the initial settlement at the instant zero corresponds to the purely mechanical one. The application of the mechanical loading determines a settlement at toe of the pile that is -2.58 mm. Therefore, the total pile's elastic shortening induced by the mechanical service load is about 2.5 mm.

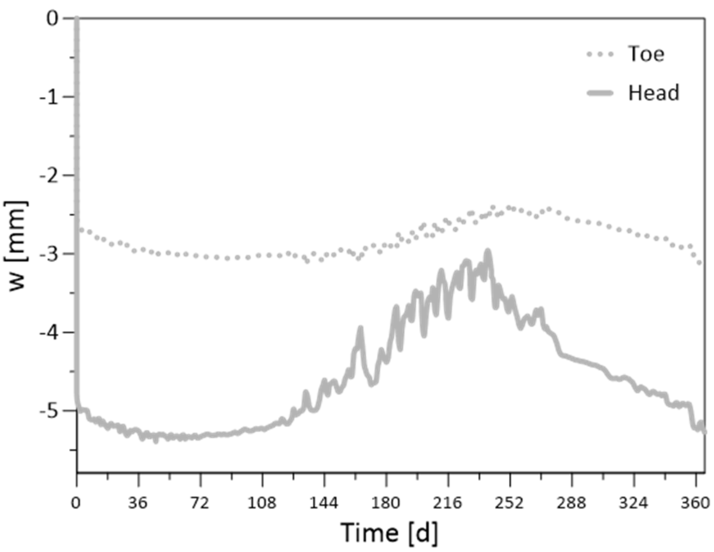

Figure 3-45:Pile's head and toe thermo-mechanical displacement during the operational of the FEP.

When the mechanical load is coupled to the thermal loads pile's displacement at toe and head follows the trend of temperature function (Figure 3-43). When the pile is heated the head of the pile heaves while during cooling settles. The maximum changing in displacements are observed during the peak of heating episodes.

The maximum thermomechanical displacement is about -0.55 mm that correspond to a thermal displacement upward of 4.23 mm. The minimum thermomechanical displacement observed during cooling is about -5.40 mm that corresponds to downward displacement of -0.61 mm. At the end of year of operational the settlement pile's head settlement is -5.28 mm, determining 10% increment of the mechanical settlement. After one year of operation the thermomechanical settlement observed is about 0.5 mm different from the initial mechanical settlement, i.e., negligible from a practical point of view.

Pile's head displacement of the EBEP subjected to the same thermal loads and level of mechanical load is plotted in Figure 3-46.

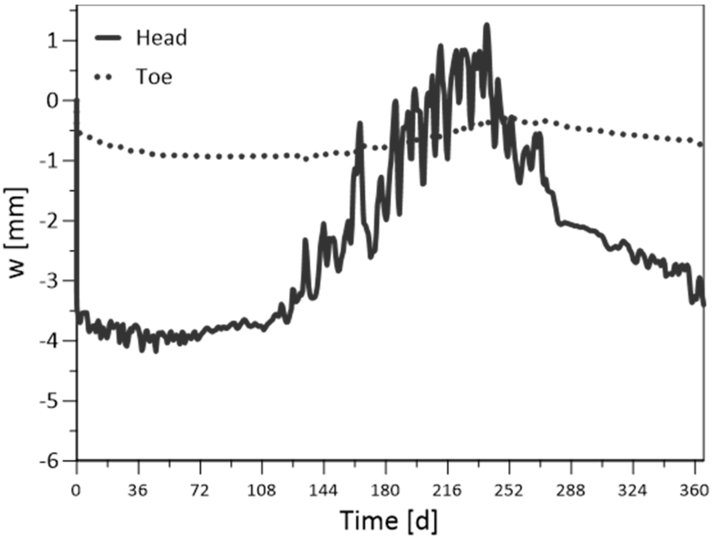

Figure 3-46: Pile's head and toe thermo-mechanical displacement during the operational of the EBEP.

In the case of the EBEP, as observed from the results of the previous numerical analyses (3.5.2), the magnitude of the displacement at pile's toe is very small. The pile's head settlement follows the trend of temperature function with upward displacement during the heating of the pile and downward displacement during cooling. The thermo-mechanical settlement observed at the end of yearly operation is -3.40 mm and corresponds to 0.06% of variation with respect to the mechanical initial settlement. The maximum thermomechanical displacement observed during heating is 1.26 mm and corresponds to 4.47 mm of upward thermal displacement. During cooling the minimum thermomechanical displacement observed is -4.18 mm that corresponds to downward thermal displacement of about – 1mm.

Comparing the magnitude of displacements occurring for the EBEP and FEP, the same thermal variation and level of mechanical stress determine higher thermal displacements in absolute value at pile head when the degree of constraint is higher at pile's toe i.e., EBEP. To provide a better comparison between thermal displacements occurring in the two cases the dimensionless displacements of EBEP and FEP are plotted together in Figure 3-47.The dimensionless displacement is defined as the ratio of the thermomechanical displacement to the mechanical settlement induced by the service load.

In terms of induced stress, the thermomechanical axial load at different time instant is plotted along with the purely mechanical load profile (M) in Figure 3-48 (a). The time instants considered are: 46 days, 165 days, 284 days and the end of the thermal history, i.e., 365 days. As can be observed from Figure 3-48 (a) thermal loadings combined to service load determine changings in the axial load profile. The thermomechanical axial load at different time instants during the operation is smaller than the mechanical load profile. At the end of the yearly operation 226 kN is the maximum variation in absolute value with respect to the mechanical axial load (less than 10% of the maximum mechanical axial load). At 46 days the minimum variation with respect to the mechanical axial profile i.e., the minimum thermal axial load along pile depth is about -60 kN.

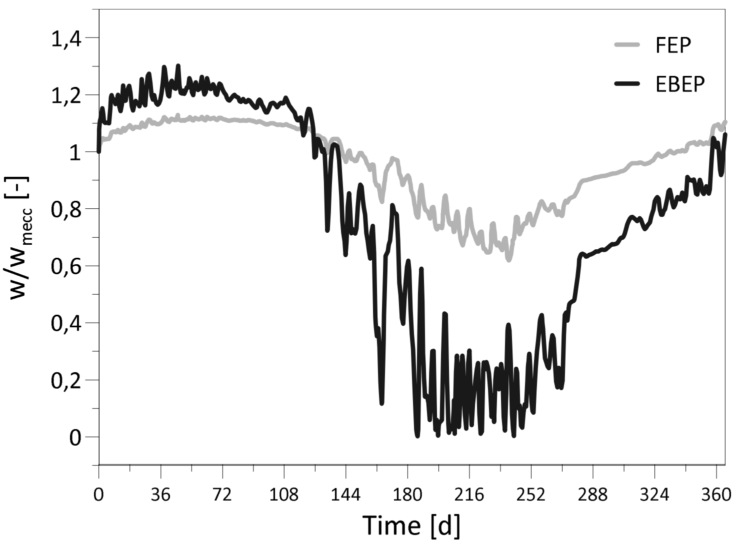

Figure 3-47: Dimensionless thermo-mechanical displacement of EBEP and FEP versus elapsed time.

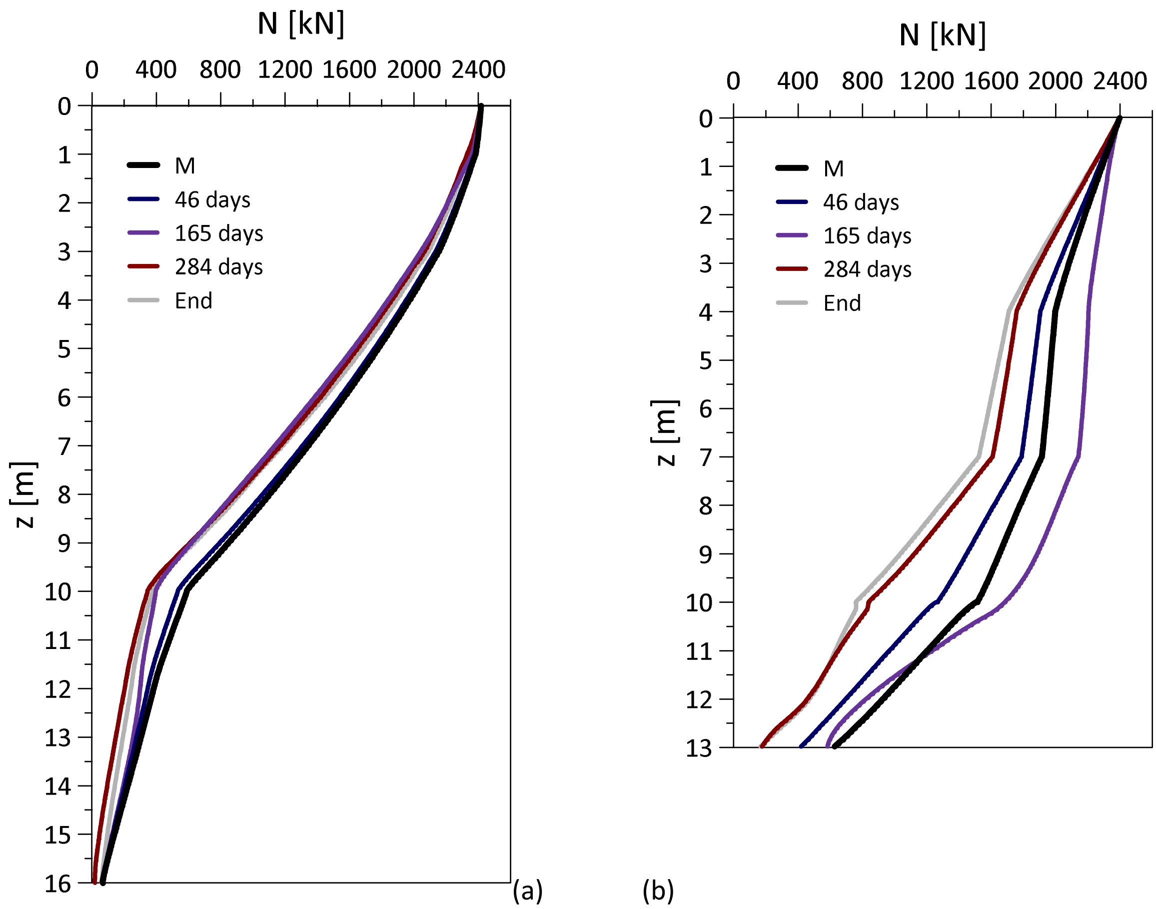

Figure 3-48: Thermomechanical axial load profile at 46 days,165 days,284 days and the end of the yearly operation along with the purely mechanical load profile (M) for the case (a) FEP and (b) EBEP.

At 165 days the minimum axial thermal load induced is -230 kN while the maximum is about 5 kN. At 284 days the minimum axial thermal load along pile length is 254 kN. The maximum changing in absolute value with respect to the maximum mechanical loading (2417 kN) is about 10 %.

The thermomechanical axial loading profiles are plotted in Figure 3-48 (b) for the EBEP at the same time instants of Figure 3-48 (a) along with the purely mechanical load profile (M).

The first observation is that the magnitude of changings in the axial load profile is larger for the case of the EBEP when mechanical and thermal loadings are combined. At 165 days, for example the maximum and minimum thermal load is about 240 kN and -800 kN, respectively (10 % and 30% of the maximum mechanical loading). In the case of EBEP, the greater constraint effect induced by the tuff layer, induced additional loading in the lower part of the pile. In the case of the FEP the maximum changing of the axial load, i.e., greater induced thermal loadings are observed in the upper part of the pile. At pile's toe the thermomechanical axial load corresponds to the mechanical load.

The effects of thermomechanical interaction in terms of mobilized shaft friction and axial loading are compared for the two cases with normalized curves in the Figure 3-49 (a) and Figure 3-49(b).

In Figure 3-49 (a) the normalized or dimensionless axial load is defined as as the ratio of the thermomechanical load to the head mechanical load. In Figure 3-49 (a) the dimensionless depth (z/z_{max}) is introduced to compare the axial load profiles of the EBEP and FEP of different lengths. The dimensionless depth is defined as the ratio of the depth to pile length. The loading transfer mechanism under purely mechanical load is also plotted in Figure 3-49 (a) both for the EBEP and FEP (M (EBEP) and M (FEP), respectively). The dimensionless profiles of EBEP and FEP are compared at mid time and the end of the yearly operation. At mid time of the cycle the EBEP is characterized by increasing load in the upper part and decreasing at the toe with respect to mechanical case. For the FEP, as discussed before, smaller changing of axial load occurs with respect to the mechanical case. At mid time of the operation a slightly increasing is observed close to the pile's toe while at the head decreasing occurred. Therefore, an opposite trend it is observed for the EBEP and FEP along piles' length. This could be also expected observing the displacements of pile's toe occurring in the two cases. To provide a wider comparison the dimensionless shaft friction profiles at the same time instants are plotted in Figure 3-49(b) and Figure 3-49(c) for the FEP and EBEP, respectively. The dimensionless mobilized shaft friction on the y axis was defined in 3.6.6. As the constraint action at the head the degree of constraint depending on the surrounding soil at pile's toe determines clear effects on the interaction.

Both for the FEP at the end and mid time of thermal cycle the mobilized shaft friction increased with respect to the mechanical case in the upper part of the pile. At the location of the NP a trend reversal is observed in the lower part of the pile, i.e., lower mobilized shaft friction with respect to the purely mechanical case (Figure 3-49 (b)). The greatest variation of mobilized shaft friction it is observed at mid time of the operational that corresponds to higher thermal variations with respect to the end of the year. For the EBEP at mid time of thermal cycle a lower mobilization of the shaft friction it is observed in the upper part and lower part of the pile with a significant decrease close to the pile's toe (Figure 3-49 (c)). At the end of the yearly operation the mobilized shaft friction is greater than those mobilized in the purely mechanical case throughout the entire pile's length except the pile's toe. At pile's toe a decrease of the mobilized shaft friction it is observed both at the end and mid time. This trend it is observed both for the EBEP and FEP but the largest changings in magnitude are observed in the case of the EBEP (Figure 3-49 (b) and Figure 3-49 (c)).

For each case, the different soil layering is evident from the shaft friction profile as well as the different pile behavior (EBEP and FEP). Larger changing in the mobilized friction and thermomechanical axial loadings are observed for the EBEP. Another observation is about the different location of the NP for the two cases. From Figure 3-49(a) and Figure 3-49(b) is possible to define the NP position of each pile type. For the EBEP the NP is located at about 60% of pile length and remains at this depth during the operational. While for the EBEP the NP position along pile's can be assumed at about 80% of pile's length where mobilized friction is reversed.

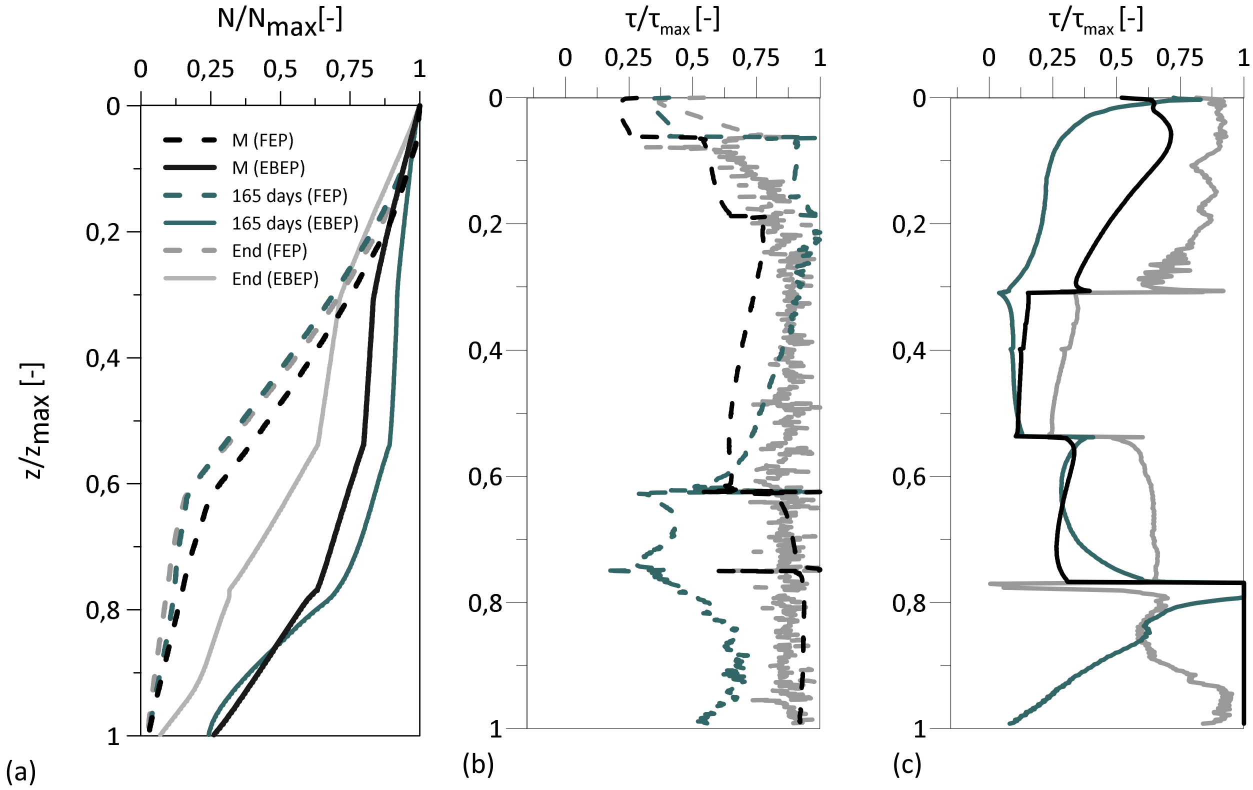

Figure 3-49:Comparisons between the load transfer mechanism in EBEP and FEP; (a) dimensionless axial load profiles and (b) and (c) dimensionless mobilized friction profile at the end and mid time (165 days) of the operational along with purely mechanical case (M).

3.6.6.2 Long term behavior

Taking into account that the ordinary life of a mal is generally in the range between 30 to 50 years the likely displacement accumulated in the case of EBEP is very significant and can be a problem for the pile as a foundation system of the above superstructure. The coupled thermal and mechanical loadings effects on the pile soil interaction are evaluated for the case of the EBEP model where higher induced displacements at pile head and higher induced stress are expected in comparison to the FEP case. Therefore, assuming constant building energy demand over the entire operational period, the yearly thermal loadings are repeated 50 times as well as the indoor temperature at soil surface. This is a common assumption, e.g., Lazzari et al. (2010) and Zanchini et al. (2012) have adopted the same hypothesis in their models to evaluate the long-term thermal performance of boreholes. The EBEP model was developed in order to perform long term simulations. The applied thermal load and surface boundary condition over fifty years are plotted in Figure 3-50 (a) and Figure 3-50 (b), respectively.

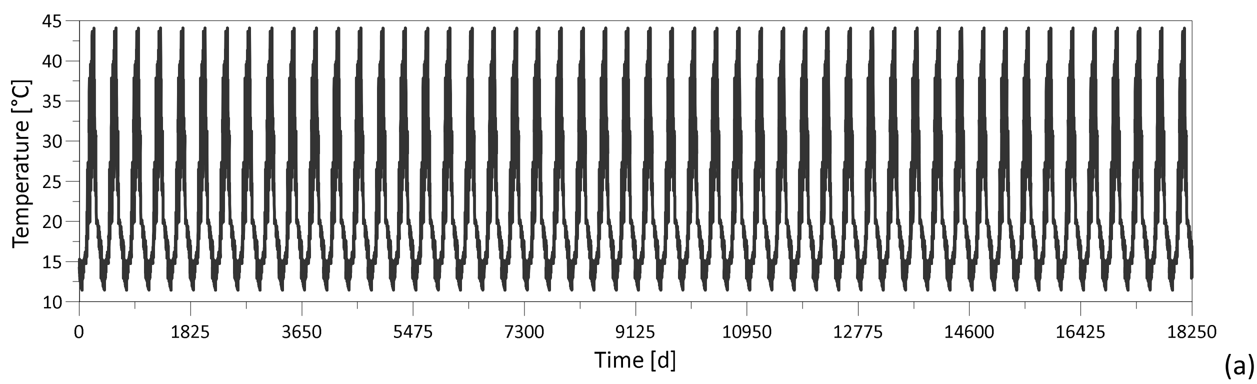

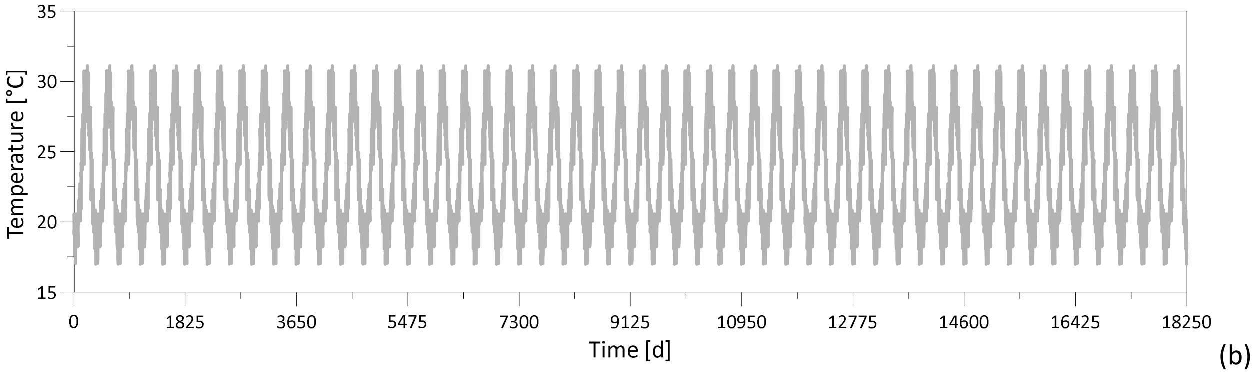

Figure 3-50: Thermal loadings (A) and indoor temperature(b) functions for 50 years of operational.

The thermal boundary conditions applied to the axisymmetric model along with the service mechanical load correspond to those described in 3.6.6.1.2. The thermomechanical interaction over the entire operational period is investigated and the main effects in terms of pile's head and toe displacements, axial load profile and mobilized shaft friction are reported.

The thermomechanical pile's head and toe displacement is plotted in Figure 3-51. The initial settlement of the pile head is -3.21 mm which is obtained under the service load. Pile's elongation is observed over fifty years of operation. The elongation of the pile shaft is clearly represented by the difference in the displacement of the pile toe and of the pile head. This sort of ratcheting is induced by the cyclic thermal strain in the pile caused by the temperature condition applied. The maximum rate of increase of pile's heave occurred during the first twenty years of operational. Then heaves of pile's head continue to rise but at lower rate. An accumulation of displacements due to the thermomechanical effects is observed throughout the fifty years of operation. During the first year the final displacement of pile's head is about -3.4 mm. At the end of the second year the final settlement of pile's head is about -2.8 mm, while at the end of the third year is about -2.3 mm. At the end of fifth year the pile's settlement increased, the final settlement is about -1.3 mm. At the end of the tenth and twentieth years the final displacement is -0.4 mm and 2.24 mm. When the operation of fifty years ends the final pile's head thermomechanical displacement is on the average about 5 mm. From these results different observations can be made. Firstly, the coupling effects determine a changing in pile's head displacement that is upwards. The accumulation is likely produced by the hardening part of the model adopted for the sandy material. The cyclic shearing produces enlargement of the yield envelope which in turn produces a stiffer response for the soil involved. As a matter this interpretation is confirmed by the axial force along the shaft and the shear stress distribution in Figure 3-52. However, even if the accumulation of plastic displacement occurred, it should be highlighted that the maximum pile's head displacement during the operational is about 9 mm i.e., less than 1 cm that could be considered as a warning threshold. With the increasing number of thermal cycles, the accumulation of plastic displacement between subsequent cycle decreases, this trend is also confirmed by experimental study as Nguyen et al. (2017). The numerical algorithm for cyclic thermal displacement developed by Pasten and Santamarina (2014) showed that most of the thermally induced plastic displacements take place in the first few cycles, typically less than 10–20 cycles for standard applications.

Olgun at al. (2015) performed FE analyses taking into account also heating load and the displacement trend observed agrees with the results reported in Figure 3-51. The accumulation of thermally induced plastic displacements affects the long-term thermo active pile performance. Cumulative plastic displacements seem to be next to approach shakedown conditions with asymptotic displacements. According to Pasten and Santamarina (2014) in cases prone to shakedown, the evolution of the pile head displacement follows an exponential function in terms of the number of thermal cycles.

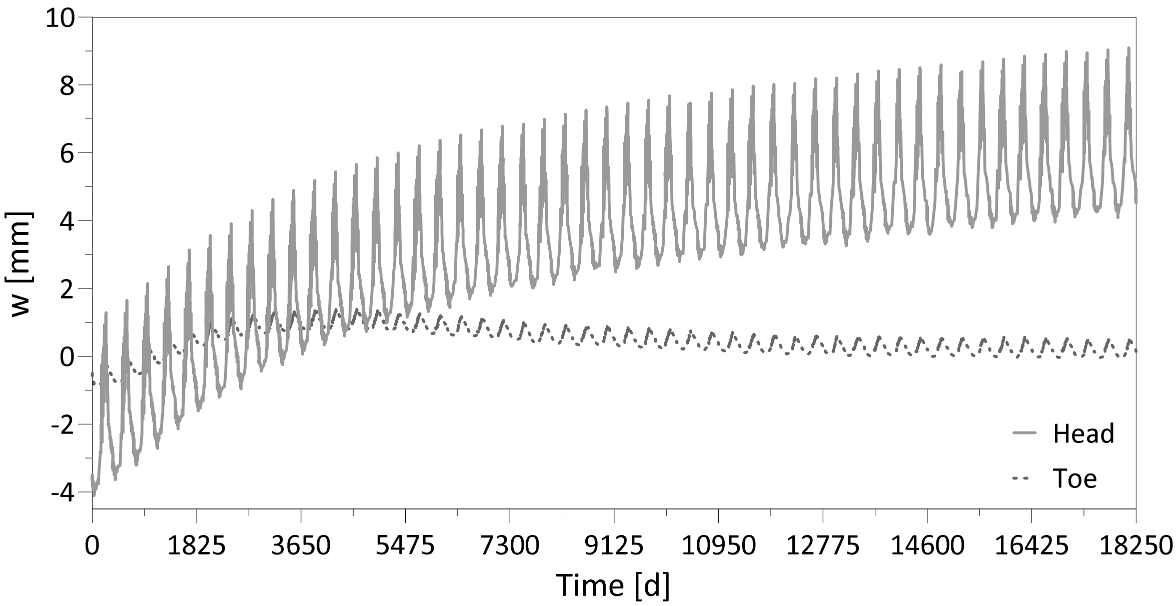

Figure 3-51:Thermomechanical pile's head and toe displacement over fifty years of operational.

The thermomechanical axial load at different time instants of the operational along with the purely mechanical profile are plotted in Figure 3-52 (a). The thermomechanical axial load along depth is plotted at: 365 days, 3650 days, 7300 days and 18250 days. With respect to the purely mechanical case (M) the thermal loadings combined to the service load determine a decrease of the axial load at the end of the first (365 days), tenth (3650 days), twentieth (7300 days), and fiftieth (18250 days) thermal cycle.

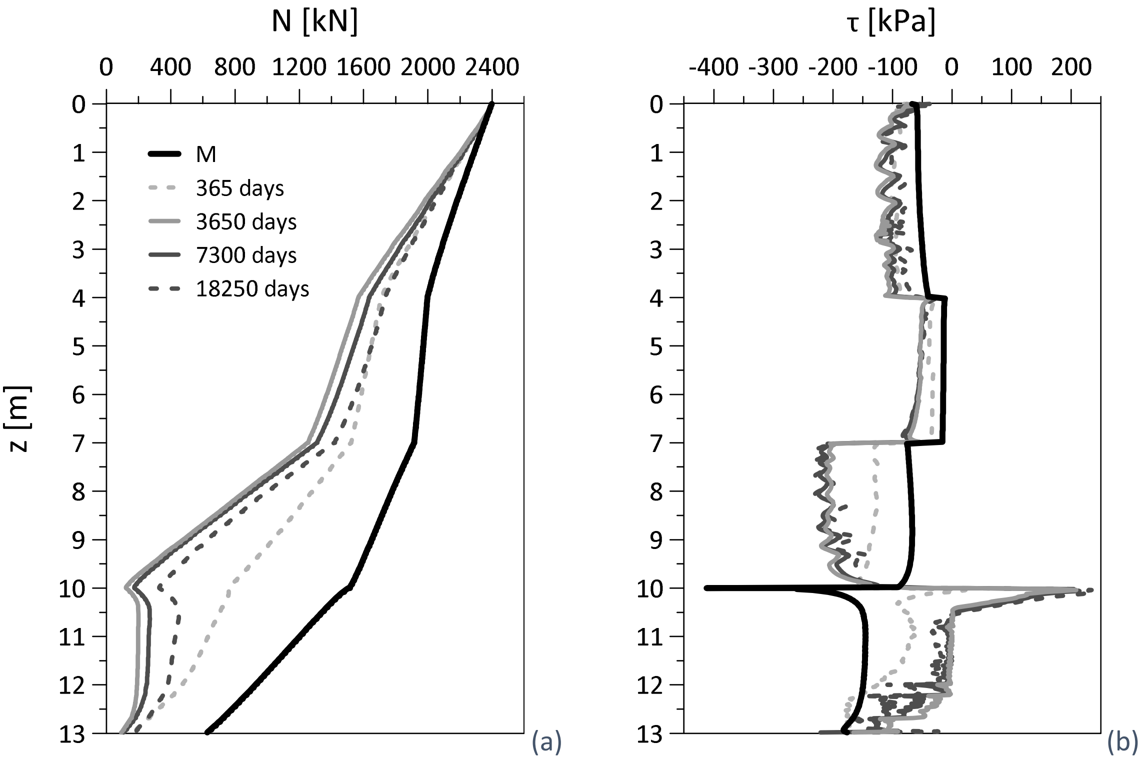

Figure 3-52: Thermo mechanical and mechanical axial load profile (a) and mobilised shaft friction (b) at different time instant at different time instants (365 days,3650 days,7300 days and 18250 days).

The maximum variation in axial load with respect to the mechanical case it is observed at the end of the first year of operational, i.e., first annual thermal cycle. Between the first and the tenth thermal cycle an additional decrease in axial loading is observed (Figure 3-52 (a)). The trends here are similar to the already discusses displacement trends and can be partially explained by the hardening part of the model used for the sandy layers. The stiffer response of the soil under cyclic shear, due to the deviatoric hardening part of the model, produces increase of the shear stress along the pile shaft (see Figure 3-52b). This increase is of course the responsible of the decrease of the axial stress along the pile (see Figure 3-52 a) which is clearly related to the already discussed pile elongation. At the end of the simulation a decrease of axial load along pile's depth it is observed with about 0% load transmitted at pile's toe. Similarly, decrease in axial stresses is observed by Olgun et al. (2015) where the thermal loads are heating dominated. This phenomenon already discussed above can be partially explained also by the difference in the thermal expansion coefficients of the pile and the soil (Olgun et al.,2015).

The mobilised shaft friction at different time instants of the operational along with the purely mechanical friction are plotted in Figure 3-52 (b). The mobilized shaft friction at the end of the first year of operational is greater, in absolute value, than the shaft friction mobilised by the purely mechanical load.

Temperature profile at different distance away from the pile are reported in Figure 3-53. At 50 mm from the pile the influence of thermal loading is very strong, and the combination of thermal load of the pile and upper structure thermal interaction determine an increase of soil temperature. The larger increase is observed between the first and the tenth year, later the temperature seems to be close to the steady state. At 600 mm away from the pile, i.e., 1 D, the influence of the thermal activation of the pile is lighter. At increasing distance from the pile's edge, the thermal profile is becoming less and less influenced by the thermal activation of the pile. However, it should be highlighted that during the operational changings in temperature profile are observed at each distance from the pile.

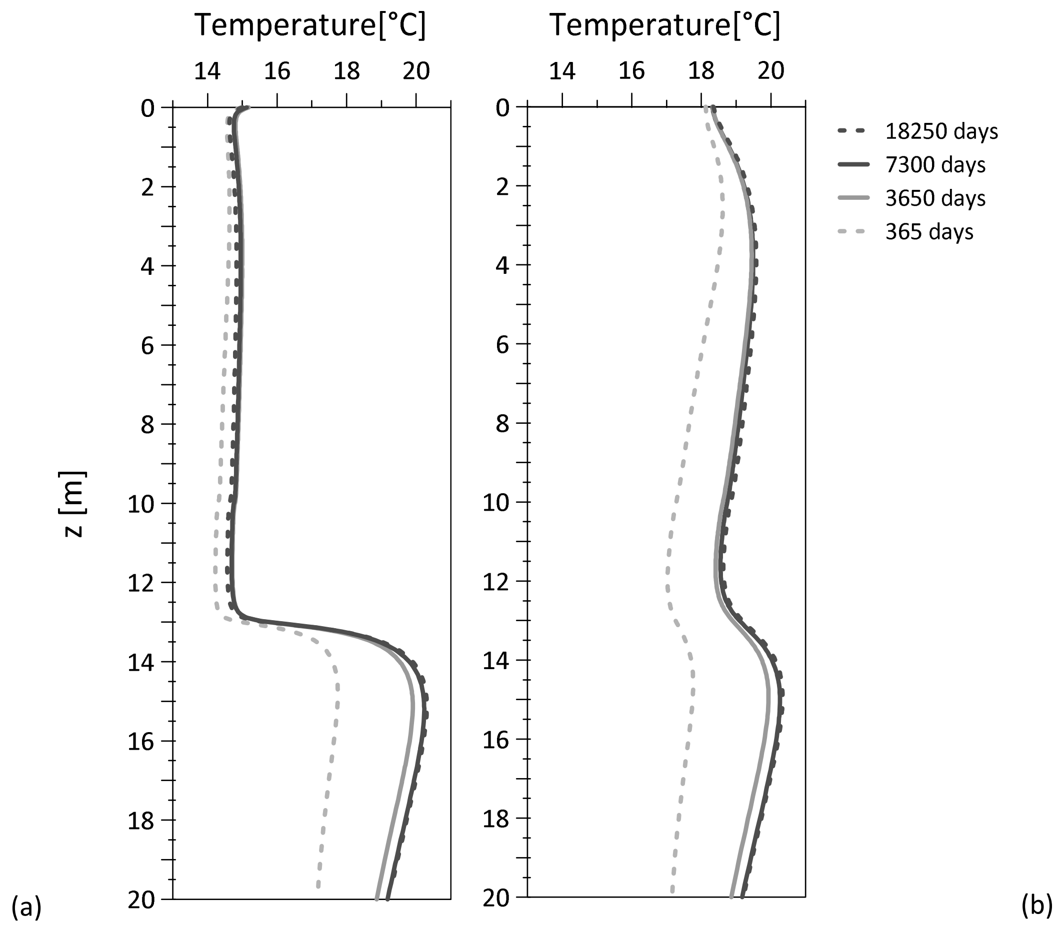

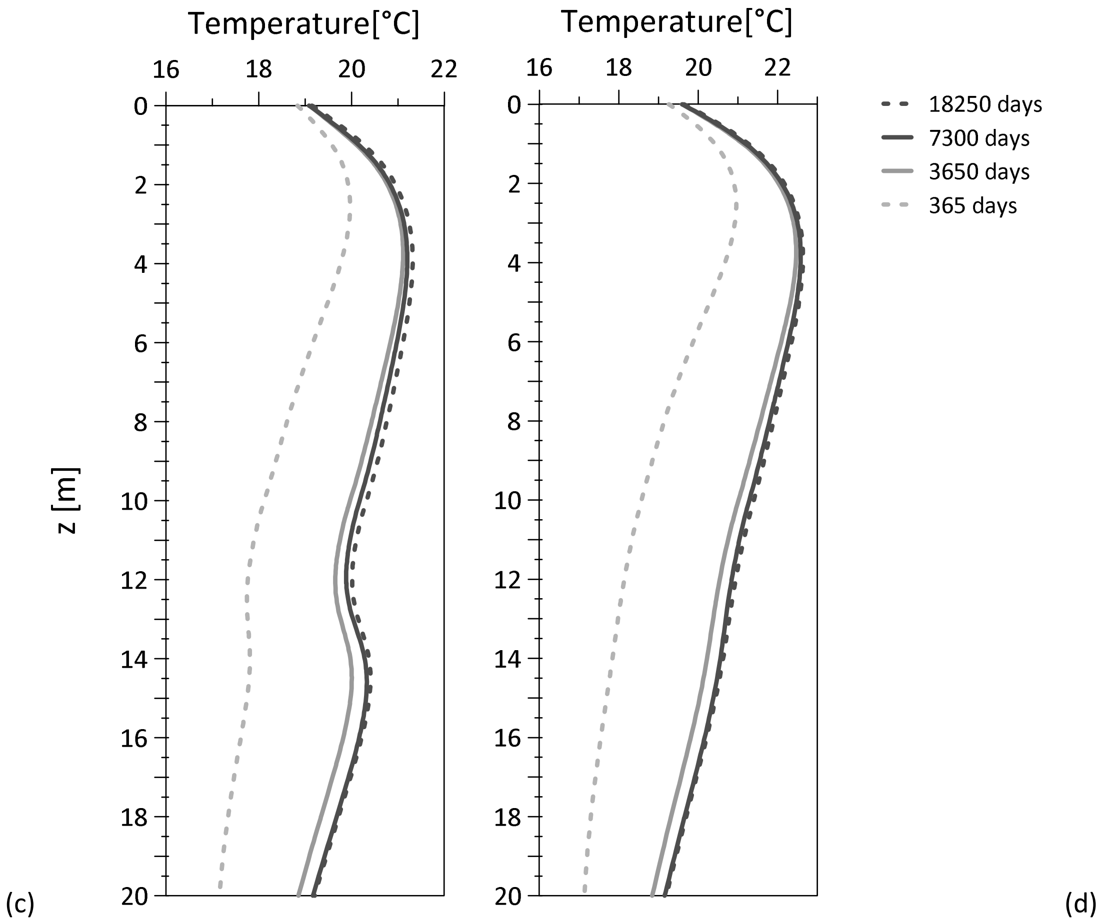

Figure 3-53: Soil temperature profiles at different time instant during the fifty years of operational, 365 days, 3650 days, 7300 days and 18250 day at (a) 0.05 m, (b)0.6 m, (c)1.20 m and (d)2.40 m from pile's edge.

This effect is connected to the activation of the thermal pile over the operational period of fifty years without modelling recovery thermal phases. The thermal loadings are defined here with the aim of improving the understanding of the structural and the geotechnical performances.

It is worthy underlining that the thermal interaction with the upper structure, founded on piles, may determines important changes in soil temperature profiles. This aspect which is often neglected in literature may be considered as important as the thermal activation of the energy pile. Therefore, in long term condition the variation of soil temperature should be evaluated taking into proper account the thermal interaction with the building along with the activation of several energy piles together. Of course, also the single pile displacement should be considered only as an element for the definition of the overall performance of a pile group where many piles are usually activated as heat exchangers.

References

Abu-hejleh, N., Attwooll, W.J., 2005. Colorado's Axial Load Tests on Drilled Shafts Socketed in Weak Rocks: Synthesis and Future Needs. Color. Dep. Transp.

Adinolfi, M., Maiorano, R.M.S., Mauro, A., Massarotti, N., Aversa, S., 2018. On the influence of thermal cycles on the yearly performance of an energy pile. Geomech. Energy Environ. 16, 32–44. https://doi.org/10.1016/j.gete.2018.03.004

Agar, J.G., Morgenstern, N.R., Scott, J.D., 1986. Thermal expansion and pore pressure generation in oil sands. Can. Geotech. J. 23, 327–333. https://doi.org/10.1139/t86-046

API, 1987. Recommended practice for planning, designing, and constructing fixed offshore platforms. API RP2A, 17th edn. American Petroleum Institute, Washington, DC

Aversa, S., Evangelista, A., 1993. Thermal expansion of Neapolitan Yellow Tuff. Rock Mech. Rock Eng. 26, 281–306. https://doi.org/10.1007/BF01027114

Batini, N., Rotta Loria, A.F., Conti, P., Testi, D., Grassi, W., Laloui, L., 2015. Energy and geotechnical behavior of energy piles for different design solutions. Appl. Therm. Eng. 86, 199–213. https://doi.org/10.1016/j.applthermaleng.2015.04.050

Bolton, M.D., 1986. The strength and dilatancy of sands, Geotechnique, 36, 1, 65-78

Bourne-Webb, P.J., Amatya, B., Soga, K., Amis, T., Davidson, C., Payne, P., 2009. Energy pile test at lambeth college, London: Geotechnical and thermodynamic aspects of pile response to heat cycles. Geotechnique 59, 237–248. https://doi.org/10.1680/geot.2009.59.3.237

Bourne-Webb, P.J., Bodas Freitas, T.M., 2020. Thermally-activated piles and pile groups under monotonic and cyclic thermal loading–A review. Renew. Energy 147, 2572–2581. https://doi.org/10.1016/j.renene.2018.11.025

Bourne-Webb, P.J., Bodas Freitas, T.M., Freitas Assunção, R.M., 2019. A review of pile-soil interactions in isolated, thermally-activated piles. Comput. Geotech. 108, 61–74. https://doi.org/10.1016/j.compgeo.2018.12.008

Brinkgreve, R.B.J., Engin, E., Engin, H.K. 2010. Validation of empirical formulas to derive model parameters for sands. Numer. Methods Geotech. Eng. - Proc. 7th Eur. Conf. Numer. Methods Geotech. Eng. 137–142. https://doi.org/10.1201/b10551-25

Brinkgreve, R. B. J., Kumarswamy, S., Swolfs, W. M. and Foria, F. (2018). PLAXIS 2D 2018 User Manual.

Caputo V., Mandolini A., Viggiani C. (1993). Large diameters bored piles in pyroclastic soils. Deep Foundations on Bored and Auger Piles, Van Impe ed., Milpress, Rotterdam, pp. 227-232.

Chen, Y.J., Kulhawy, F.H. (1994). Case history evaluation of the behavior of drilled shafts under axial and lateral loading. Final report, Project 1493-04, EPRI TR-104601, Geotechnical Group, Cornell University, Ithaca

Colombo, G., 2010. Il congelamento artificiale del terreno negli scavi della metropolitana di Napoli : valutazioni teoriche e risultati sperimentali. Riv. Ital. di Geotec. 4, 42–62.

DeBeer, E.E., 1965. Bearing Capacity and Settlement of Shallow Foundations on Sand. Proceedings of the Symposium on Bearing Capacity and Settlement of Foundations, Duke University, 15-33

DesignBuilder Help - Intro https://designbuilder.co.uk/helpv6.0 (accessed 7.17.20).

De Gennaro, V., Frank, R., 2005. Finite element modelling of the soil-pile interaction. Bull. Des Lab. Des Ponts Chaussées 107–133.

Edition, C., 2020. CONNECT Edition V20.02 1–23.

Fadejev, J., Simson, R., Kurnitski, J., Haghighat, F., 2017. A review on energy piles design, sizing and modelling. Energy 122, 390–407. https://doi.org/10.1016/j.energy.2017.01.097

Faizal, M., Bouazza, A., Singh, R.M., 2016. An experimental investigation of the influence of intermittent and continuous operating modes on the thermal behavior of a full scale geothermal energy pile. Geomech. Energy Environ. 8, 8–29. https://doi.org/10.1016/j.gete.2016.08.001

Gawecka, K.A., Taborda, D.M.G., Potts, D.M., Cui, W., Zdravković, L., Haji Kasri, M.S., 2017. Numerical modelling of thermo-active piles in London clay. Proc. Inst. Civ. Eng. Geotech. Eng. 170, 201–219. https://doi.org/10.1680/jgeen.16.00096

Gibbs, KJ., and Holtz, WG., 1957. Research on determining the density of sands by spoon penetration testing. Proceedings of the 4th International Conference on Soil Mechanics and Foundation Engineering, London, 35–39

Kulhawy, F.H., Mayne, P.W., 1990. Manual on Estimating Soil Properties for Foundation Design. Ostigov. https://doi.org/EPRI-EL-6800

Laloui, L., Nuth, M., Vulliet, L., 2006. Experimental and numerical investigations of the behavior of a heat exchanger pile. Int. J. Numer. Anal. Methods Geomech. 30, 763–781. https://doi.org/10.1002/nag.499

Laloui, l., Rotta Loria, A. F., 2019. Analysis and Design of Energy Geostructures, Theoretical Essentials and Practical Application. Ed. Elsevier Academic Press.

Lazzari, S., Priarone, A., Zanchini, E., 2010. Long-term performance of BHE (borehole heat exchanger) fields with negligible groundwater movement. J. Energy 35 (12),4966–4974.

Loveridge, F., McCartney, J.S., Narsilio, G.A., Sanchez, M., 2020. Energy geostructures: A review of analysis approaches, in situ testing and model scale experiments. Geomech. Energy Environ. 22, 100173. https://doi.org/10.1016/j.gete.2019.100173

Maiorano, R.M.S., Marone, G., Russo, G., Di Girolamo, L., 2019. Experimental behavior and numerical analysis of energy piles, in: Proceedings of the XVII ECSMGE-2019. pp. 1–8. https://doi.org/10.32075/17ECSMGE-2019-0819

Mancuso, C., Mandolini, A., Silvestri, F., Viggiani, C. 1999. Prediction and performance of axially loaded piles under working loads. In: Lo Presti D (ed) Proceedings of II international symposium on prefailure deformation of geomaterials, Torino, vol 1. Balkema, Rotterdam.

Marone, G., Russo, G. Di Girolamo, L. 2018. Carichi termici e carichi meccanici per un palo CFA attestato a tufo.in IARG 2018, Genova.

Marone, G., Di Girolamo L., Russo G., 2019. Studio parametrico del comportamento di un palo singolo sottoposto a carichi termo-meccanici, in:IX IAGIG. Napoli, 81-84.

Marone, G., Di Girolamo, L., Pirone, M., Russo, G., 2020. Numerical modelling of heat exchanger pile in pyroclastic soil. E3S Web Conf. 205, 1–7. https://doi.org/10.1051/e3sconf/202020505014

Mascarucci, Y., Miliziano, S., Mandolini, A., 2014. A numerical approach to estimate shaft friction of bored piles in sands. Acta Geotech. 9, 547–560. https://doi.org/10.1007/s11440-014-0305-4

McCartney, J.S., Murphy, K.D., 2012. Strain Distributions in Full-Scale Energy Foundations (DFI Young Professor Paper Competition 2012). DFI J. - J. Deep Found. Inst. 6, 26–38. https://doi.org/10.1179/dfi.2012.008

McCombie, M.L., Tarnawski, V.R., Bovesecchi, G., Coppa, P., Leong, W.H., 2017. Thermal Conductivity of Pyroclastic Soil (Pozzolana) from the Environs of Rome. Int. J. Thermophys. 38. https://doi.org/10.1007/s10765-016-2161-y

Murphy, K.D., McCartney, J.S., 2015. Seasonal Response of Energy Foundations During Building Operation. Geotech. Geol. Eng. 33, 343–356. https://doi.org/10.1007/s10706-014-9802-3

Murphy, K.D., McCartney, J.S., Henry, K.S., 2014. Thermo-Mechanical Characterization of a Full-Scale Energy Foundation 617–628. https://doi.org/10.1061/9780784413265.050

Nguyen, V.T., Tang, A.M., Pereira, J.M., 2017. Long-term thermo-mechanical behavior of energy pile in dry sand. Acta Geotech. 12, 729–737. https://doi.org/10.1007/s11440-017-0539-z

Olgun, C.G., Ozudogru, T.Y., Abdelaziz, S.L., Senol, A., 2015. Long-term performance of heat exchanger piles. Acta Geotech. 10, 553–569. https://doi.org/10.1007/s11440-014-0334-z

Pasten, C., Santamarina, C.J. 2014. Thermally induced long term displacement of thermoactive piles. J. Geotech. Geoenviron. Eng. 2014.140-5. https://doi.org/10.1061/(ASCE)GT.1943-5606.0001092

Rammal, D., Mroueh, H., Burlon, S., 2018. Impact of thermal solicitations on the design of energy piles. Renew. Sustain. Energy Rev. 92, 111–120. https://doi.org/10.1016/j.rser.2018.04.049

Rollins, K.M., Clayton, R.J., Mikesell, R.C., Blaise, B.C., 2005. Drilled Shaft Side Friction in Gravelly Soils. J. Geotech. Geoenvironmental Eng. 131, 987–1003. https://doi.org/10.1061/(asce)1090-0241(2005)131:8(987)

Rotta Loria, A.F., Bocco, M., Garbellini, C., Muttoni, A., Laloui, L., 2020. The role of thermal loads in the performance-based design of energy piles. Geomech. Energy Environ. 21. https://doi.org/10.1016/j.gete.2019.100153

Russo G., Callisto, L. 2006. Relazione Generale al Convegno Nazionale dei Ricercatori di Ingegneria Geotecnica: Fondazioni su pali: osservazioni sperimentali. pp.231- 349 CNRIG - BARI, SETTEMBRE 2006

Russo, G., 2013. Experimental investigations and analysis on different pile load testing procedures. Acta Geotech. 8, 17–31. https://doi.org/10.1007/s11440-012-0177-4

Russo, G., Maiorano, R., Marone, G., 2019. Analysis of thermo-mechanical behavior of energy piles. Geotech. Eng. J. SEAGS AGSSEA 50, 110–117.

Russo, G., Marone, G., 2018. Experimental comparison on different pile load testing methods, in: Proceedings of DFI-EFFC Int. Conf. on Deep Found. and Ground Improvement: Urbanization and Infrastructure Development-Future -Challanges. Rome, pp. 159–169.

Saggu, R., Chakraborty, T., 2015. Cyclic Thermo-Mechanical Analysis of Energy Piles in Sand. Geotech. Geol. Eng. 33, 321–342. https://doi.org/10.1007/s10706-014-9798-8

Schmertmann, J.H., 1979. Statics of SPT. J. Geotech. Eng. Div. ASCE., 105,5, 655-670

Sittidumrong, J., Jotisankasa, A., Chantawarangul, K., 2019. Effect of thermal cycles on volumetric behavior of Bangkok sand. Geomech. Energy Environ. 20. https://doi.org/10.1016/j.gete.2019.100127

Viggiani, C., Mandolini, A., Russo, G. (2012). Piles and pile foundations. Ed. Spon Press, Taylor & Francis, London.

Wang, C.L., Liu, H.L., Kong, G.Q., Ng, C.W.W., 2017. Different types of energy piles with heating-cooling cycles. Proc. Inst. Civ. Eng. Geotech. Eng. 170, 220–231. https://doi.org/10.1680/jgeen.16.00061

Yang, W., Zhang, L., Zhang, H., Wang, F., Li, X., 2020. Numerical investigations of the effects of different factors on the displacement of energy pile under the thermo-mechanical loads. Case Stud. Therm. Eng. 21, 1–14. https://doi.org/10.1016/j.csite.2020.100711

Yavari, N., Tang, A.M., Pereira, J.M., Hassen, G., 2014. Experimental study on the mechanical behavior of a heat exchanger pile using physical modelling. Acta Geotech. 9, 385–398. https://doi.org/10.1007/s11440-014-0310-7

Zanchini, E., Lazzari, S., 2013. Temperature distribution in a field of long borehole heat exchangers (BHEs) subjected to a monthly averaged heat flux. J. Energy 59,570–580.

4 Small scale tests

4.1 *Introduction*

In this chapter a small-scale physical model designed to perform laboratory tests on model EP is described. The experimental setup was designed and realized to the aim of exploring the thermo-mechanical response of an isolated EP in pyroclastic soil in controlled boundary conditions. The small-scale model is composed by an aluminum tube pile, closed at the end by a conic tip, embedded in natural dry pyroclastic sand placed by air pluviation inside a transparent parallelepiped pvc box. During the test piles' head displacements, strains and temperatures were measured. Soils' temperatures at different depths and distances from the pile were also measured along with the volumetric water content.

The experimental layout has developed based on previous similar experimental investigations as Kalantidou et al., (2012) and Yavari et al., (2014). Advancements have been made for instance the application of thermal variations are estimated taking into account the potential operational conditions of a simulated GSHP system in a specific geographic area. The testing program aimed at the evaluation of the cyclic effect of heating or cooling, the estimation of the mean effective soil stress along with the effect of the mechanical stress level coupled with thermal loadings on pile behavior. All the tests were performed in the geotechnical laboratory of University of Napoli Federico II.

4.2 *Experimental Test set up*

4.2.1 Description of the physical model

The physical model consists of a small aluminum pipe installed in a container filled by pyroclastic sandy soil. The soil physical, mechanical and thermal characterization are reported in 4.3.

After several trials, the sand was rained through air pluviation technique at a constant height of fall to reach a dry density of 9.3 kN/m^3. Before the installation, the natural soil was prepared for the raining procedure through drying in the oven and sieving the fraction greater than 5 mm. This was done taking into account the diameter of the model aluminum pile to be installed (i.e., 30 mm) The deposition technique was carried out in seven steps, during each step one soil layer of 100 mm height was rained. The layers of soil were materialized using seven strips of adhesive tape stuck on the four PMMA walls of the container as shown in figure Figure 4-1(a). This procedure was carried out to ensure an acceptable uniformity of soil density throughout the tank. Before and after each step the weight of the soil to be pluviated was checked, hence under the container box was placed a platform weight scale (Figure 4-1 (a)). When the *Pozzolana* reached a total eight of 300 mm, i.e. ended up the first three steps of pluviation, the pile was placed in the middle of the tank and fixed at the desired depth ,300 mm from the bottom of the container, supported by a steel frame (Figure 4-1 (b)). The installation of the pile was followed by the pluviation of four additional soil layers reaching the target height of 700 mm (Figure 4-1 (c)). At last, the pile was fully surrounded by soil. The method of installation is typically used in small scale tests as representative of non-displacement piles, as a matter of fact installed without horizontal stress relief (Fioravante, 2002).

The test container has length, width, and height respectively of 1000 mm x 1000 mm x 700 mm. The experimental box was designed to minimize thermal and mechanical boundary effects caused by walls and bottom following suggestions provided in literature. According to Parkin and Lunne (1982) to enable the soil in the container to get the same deformation of the unbounded soil the ratio between the diameter of the container and the diameter of the pile must be at least 20 for loose sands. Le Kouby et al. (2004) suggested a distance between the pile toe and base of the container 10 times the pile diameter. The dimension of the box is 1000 mm so that the ratio between the diameter of the test pile and the length of the container is greater than 33. The height of the box was 700 mm so that the distance between the pile toe and the box toe is at list 10 times the diameter. The container is made by PMMA walls of 20 mm thickness to avoid lateral displacements of soil.


(a)


(b)


(c)

Figure 4-1:Experimental layout: (a) Box, scale platform and steel frame before installation of pile and soil (b) PMMA box, scale platform, steel frame equipped pile after the installation of pile and soil and before the installation of the last four soil layers (c) PMMA box, scale platform, steel frame equipped pile after the installation of pile and soil

During thermal and mechanical tests, only pile vertical displacements were allowed thanks to two flanged axial ball bearings bolded on steel plates welded to the beams of the frame. The steel frame (S235) made by two UPN 65 beams and two UPN 65 columns was placed as shown in Figure 4-1 and Figure 4-2. The beams of the frame were used as support for the displacements' devices and flanged ball bearings. The experimental set up is reported in Figure 4-2.

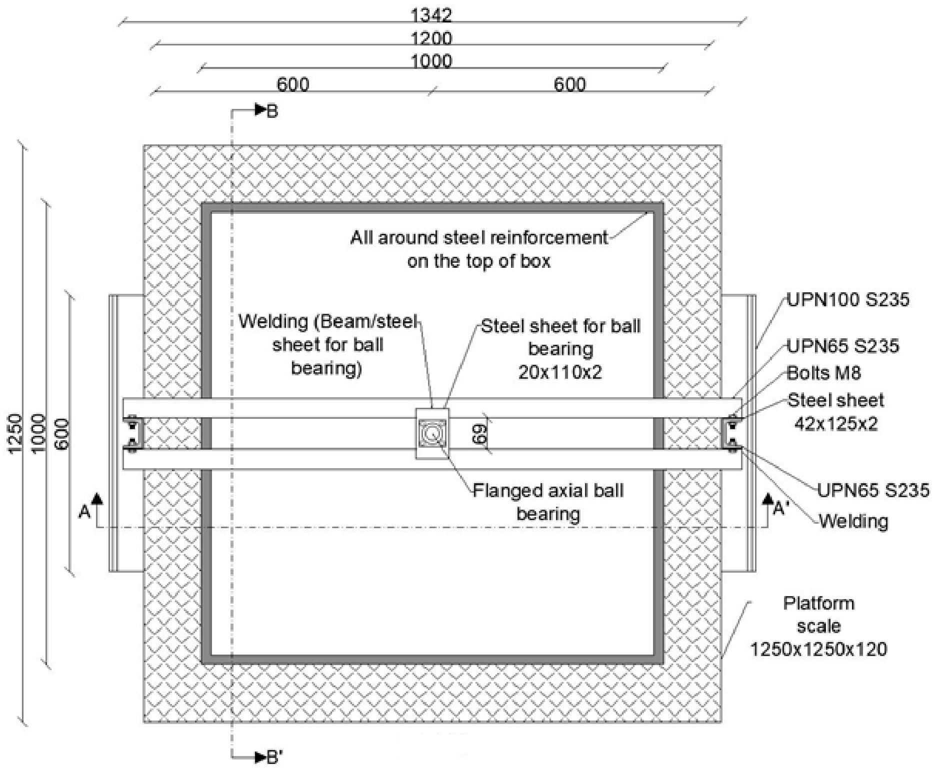

(a)

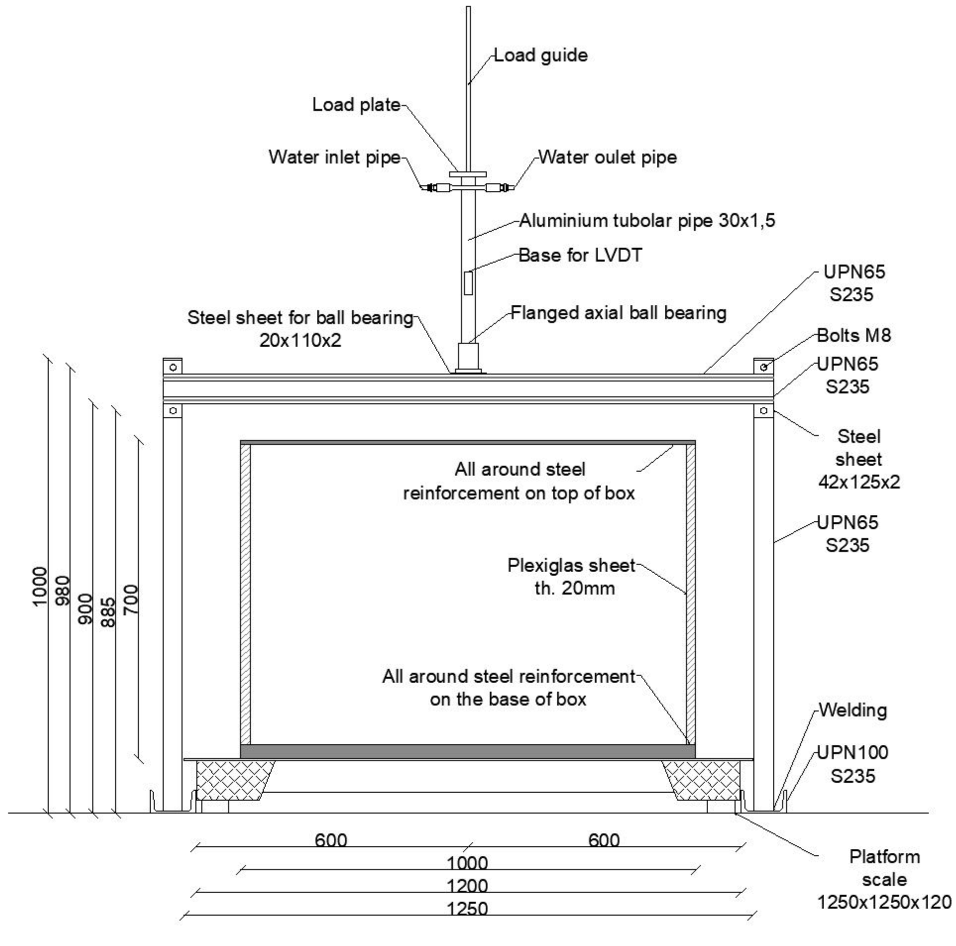

(b)

Figure 4-2:Experimental set-up, (a) Plan and (b) Section A-A' (measurements in mm).

During the tests, strains at different depths along the pile shaft, pile and soil temperature and pile head displacements were measured and recorded. Vertical and radial strains along pile shaft were measured by electrical strain gauges (Figure 4-3 (a)). Seven quarter-bridge strain gauges, SG1, SG2, SG3, SG4, SG5, SG5 bis and SG5 tris, were attached to the outer surface of the pile in vertical direction at 10 mm, 105 mm, 200 mm, 295 mm and 390 mm from the pile toe, respectively (Figure 4-4 (b)). Vertical gauges were installed at an interval of 95 mm circa. Two additional strain gauges, SG1o and SG3o, were attached in horizontal direction at 10 mm and 200 mm from pile toe (Figure 4-4 (b)). Seven thermocouples (Tc1, Tc2, Tc3, Tc4, Tc5, Tc6 and Tc7) were arranged at different horizontal distances from the pile and depth from soil surface as shown in Figure 4-4 (a) and (b). The thermocouples are k type, Nickel Chromium conductors, with mineral (MgO) insulated junction to prevent earth loops and suit applications without impairing performance. The probe is stainless steel AIS316 with diameter of 3 mm and length of 100 mm (Figure 4-3 (b)). Thermocouples TC2 and TC3, as shown in Figure 4-4, are placed at pile soil interface to monitor soil temperature changings adjacent to the pile.

Displacements at the head of the pile were measured using two Linear Variable Displacement Transducer (LDVT), calibrated using a micrometric screw before the installation. LVDTs were located as shown in Figure 4-2 (c), to measure the vertical displacement of two metal flaps which were tightly fixed at the pile body. The fixed support basis of each displacements' sensors was placed on the two UPN beams of the steel frame (Figure 4-3 (c)).

The arrangement of all measurements sensors is sketched in Figure 4-4.

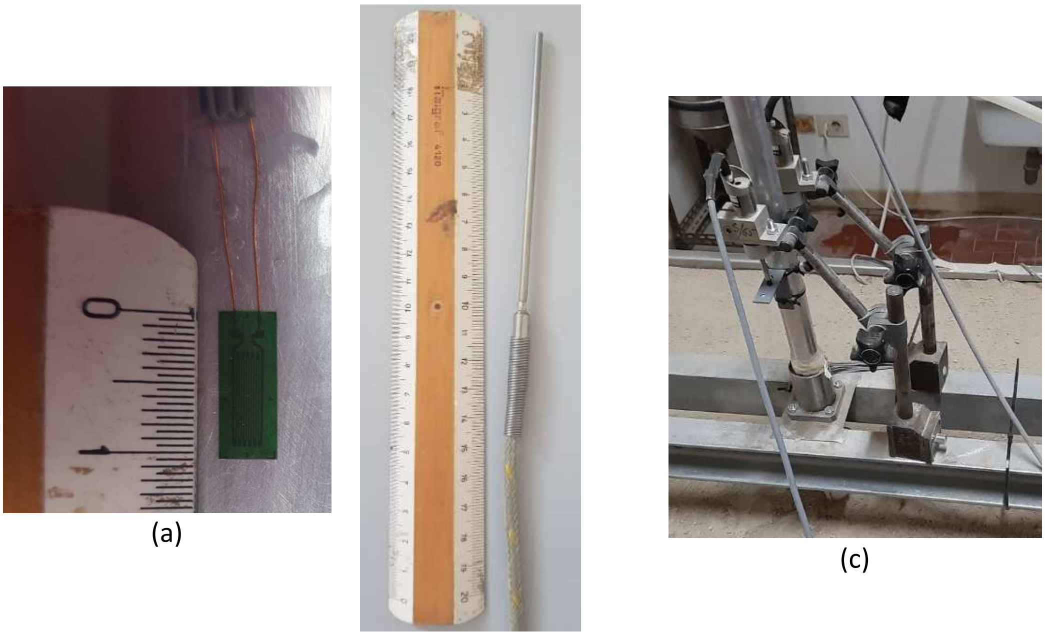

(a) (b) (c)

Figure 4-3 : (a) Quarter Bridge Strain Gauge (SG), (b) Thermocouple K and (c) LVDTs used during the tests.

Heating and cooling modes during thermal and thermo-mechanical tests were performed through refrigerated and heating bath circulator of Lab Companion. This device allows to control and maintain liquid heating or cooling inside its bath though temperature sensor and regulator. The water circulation is allowed by inlet and outlet connection to plastic pipe that were adequately thermally insulated and connected to the pile. The circulating pump can supply a pressure up to 100 kPa and a flow rate from 0 l/min to 28 l/min by setting the pump circulating level from 0 to 5 level.

The tests were planned into dry sand but in order to check the variation in time of the volumetric water content of the soil surrounding the energy pile three time-domain reflectometer (TDR1, TDR2 and TDR3) that were installed in different position inside the experimental box (Figure 4-4).

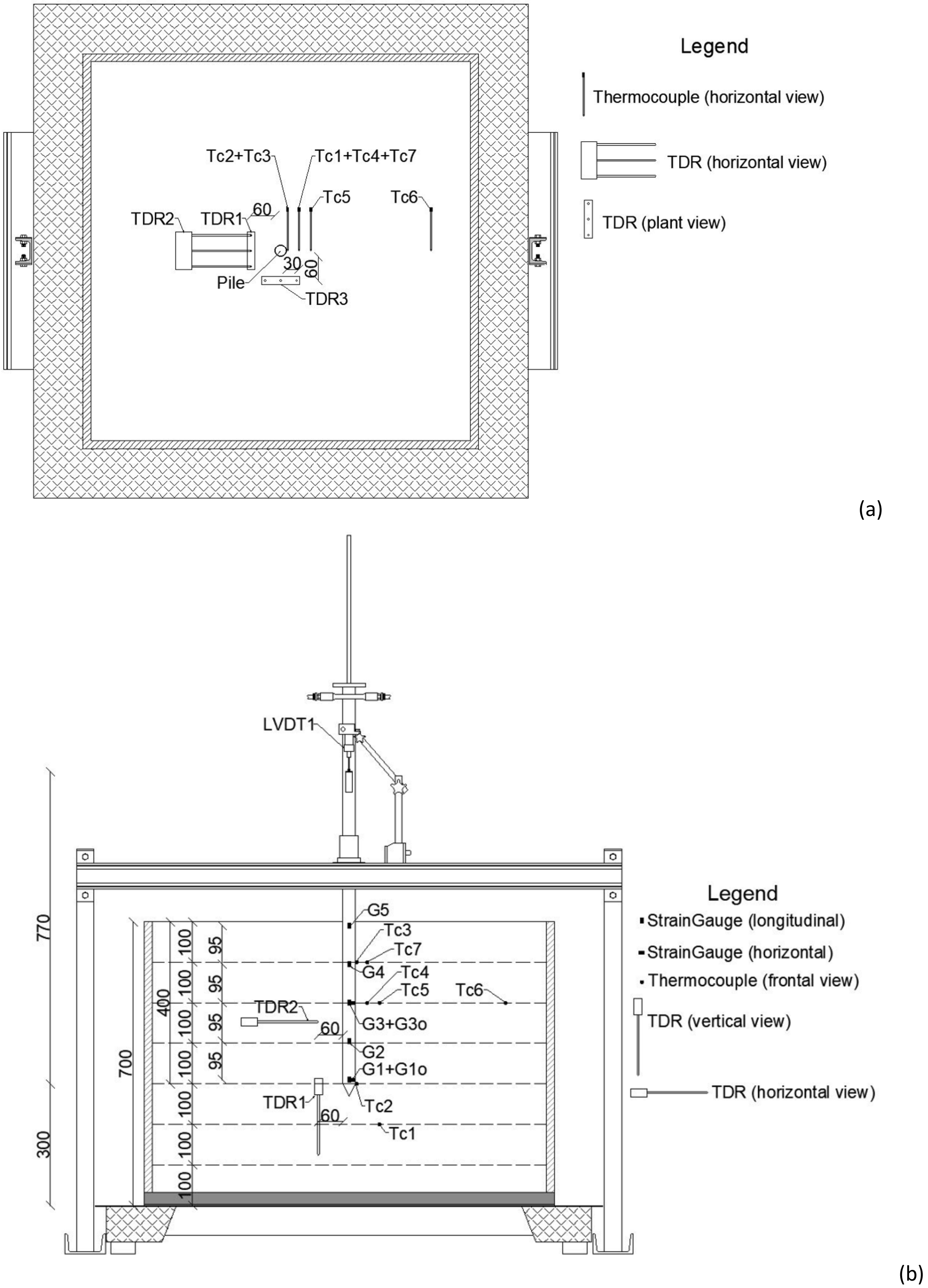

Figure 4-4: Experimental Layout; (a) Plan View with sensors arrangement (b) Section with layout of thermocouples (TC), LVDT, Strain Gauges (SGs) and TDR.

4.2.2 Model Pile

The pile is a closed-ended aluminum tube with inner diameter of 27 mm, outer diameter of 30 mm, total length of 950 mm and embedded depth of 400 mm.

(b)

(a)

Figure 4-5 (a) Model pile (b) Metal tip inserted at pile toe.

An end cone was fitted to the pile's toe ensuring also water tightness being the aluminum pipe pile filled with water during the thermal tests (Figure 4-5 b).

The test pile was a bar of extruded aluminum alloy EN AW-6060 characterized by Young's modulus (E) of 69000 MPa, a medium tensile strength (Rm) of 120 MPa, a linear expansion coefficient ($\boldsymbol{\alpha}$) of $23 \cdot 10^{-6}$ °C^{-1} and thermal conductivity ($\boldsymbol{\lambda}$) of 200 W/m °C (Table 4-1).

Table 4-1 :Mechanical properties of the aluminum pile.

R_m	E	α	γ	C_v	λ
[Mpa]	[Mpa]	[°C^{-1}]	[kN/m^3]	[J/kg K]	[W/ cm °C]
120	69000	23x10^{-06}	27	890	2

To avoid the grain size scale effects Fioravante (2002) suggested that the ratio between the pile diameter and the median diameter of sand particles D_{50} should be greater than 50. The median diameter of pozzolana soil is 0.3 mm and the pile diameter is 30 mm. Thus, the ratio between pile's diameter and soil's D_{50} is two times greater (100) than the Fioravante's suggested value.

To increase the roughness of the aluminum pile, a coat of plaster mixed with Pozzolana was coated on its outside surface (Figure 4-2). The coat covers all the gauges and the wires. The mobilization of the shaft friction is controlled by a thin area of soil adjacent to the pile surface that is subjected to large plastic strains and whose thickness depends on the pile surface roughness (grater thickness for rough piles). The ultimate shear stress mobilized in a soil structure interface depends on the Normalized Roughness, Rn, that is the ratio between the maximum surface roughness (measured as the height between two sequent peaks over a skin length from 0.8 mm to 2.5 mm) and the mean particle size of the sand D_{50}. According to Fioravante (2002) the interface is totally rough if $R_n > 0.1$. The final layout of the model pile covered by the plaster satisfied the requisite and could be considered as perfectly rough. In this situation the shear strength angle of the pile-soil interface can be assumed as equal to the friction angle of the soil. Only the embedded part of the alloy tube was coated while the upper portion of the tube was indeed covered by grease to minimize the friction between the pipe and the flanged bearings (Figure 4-6).

Figure 4-6: Model pile covered with mix of plaster and sand.

At the head of the pile a steel plate connected to a load guide was constructed to apply weights to perform mechanical and thermo-mechanical tests (Figure 4-7).

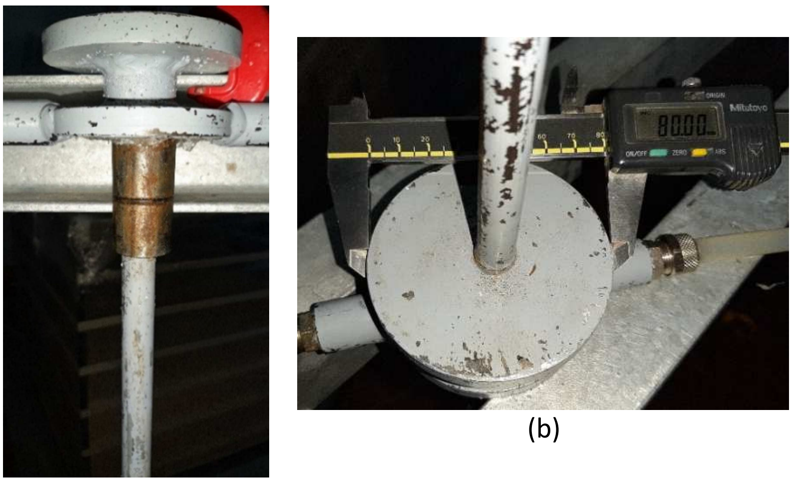

(b)

(a)

Figure 4-7 : (a)Steel plate for the application of weights at the head of the pile, (b) steel plate and load guide.

In such a way the load was applied by using controlled steel weights and there was no need to measure.

The heating and/or cooling modes were performed circulating water inside the pile through a refrigerated and heating bath circulator. Water circulation occurred through two circuits. One circuit is placed outside the pile (Outer Circuit) while the other one is placed inside the aluminum tube (Inner Circuit). The Outer Circuit is composed by two plastic tubes both connected to the circulating bath and to the Inner Circuit. One pipe allows the water to enter inside the inner circuit (water inlet pipe) while the other allows the water to exit from the pile (water outlet pipe). The Inner Circuit is composed by a nozzle that allows the water to enter in the pile and an inner tube placed in the inner part that reached the pile's toe and allows the exit of water from the pile (Figure 4-6 (a), (b), (c)).

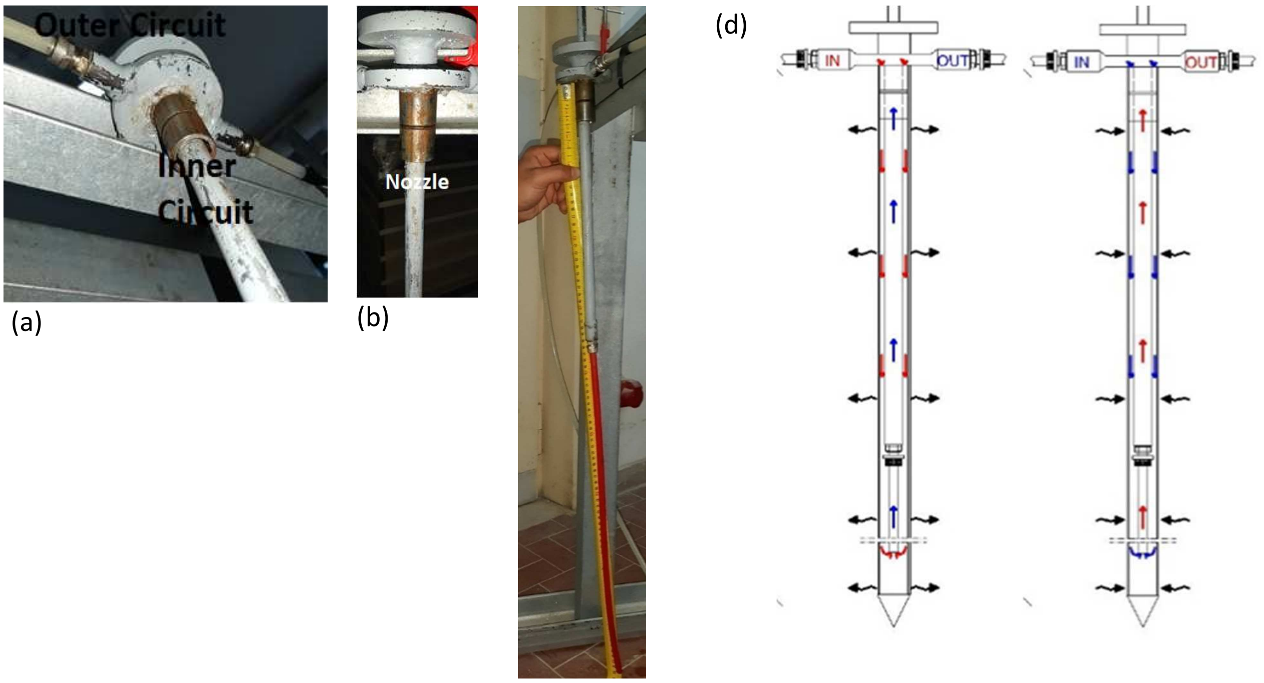

(c)

Figure 4-8: (a) Inner and Outer Circuits that allow the circulation of water, (b) Nozzle that allows the water to enter inside the pile, (c) Inner tube that allows the water exit from the pile and (d) Water circulation mechanism .

4.2.3 Electrical Strain Gauges (SG) installation and calibration

The electrical strain gauges (SG) are single *FLAB-6-23-3LJCT-F* of 6 mm length, 4.6 mm width, backing length of 12.5 mm, backing width of 4.3 mm and resistance of 120 Ω.

The gages' full potential for accurate strain measurement can be realized only if they are properly installed. The installation procedure follows different steps. The preparation of the surface for strain gage bonding consists of cleaning the gauging area though degreaser, abrading the surface through abrasive paper, marking trough a pencil the point that will correspond to the barycenter of the gage and cleaning again though different cleaning agents. Cleanliness is essential throughout the installation. When the surface is prepared the bonding process started, then a coating it is applied to protect the gage in the laboratory environment and to ensure the durability of the devices.

These gauges employ Cu-Ni alloy foil for the grid and special plastics for the backing and were integrated with lead-wires. A wide range of operating temperature from -196 to +150°C is possible. This alloy minimizes the thermal output over a wide temperature range when bonded to test materials with thermal expansion coefficients for which they are intended (in this case aluminum). Strain gauges employing these specially processed alloys are referred to as self-temperature-compensated. Since the advent of the self-compensated strain gauge, the requirement for matching unrestrained dummy gage in the adjacent arm of the Wheatstone bridge has been relaxed considerably. Now it is normal practice when making strain measurements at or near room temperature to use a single self-temperature compensated gage in quarter bridge arrangement completing the circuit with a stable fixed resistor in the adjacent arm.

When the self- temperature-compensated strain gage is bonded to material having the thermal expansion coefficient for which the gage is intended, and when operated within the temperature range of effective compensation, strain measurements can often be made without the necessity of correcting for thermal output. There are basically two methods of calibration available direct and indirect. With direct calibration, a precisely known mechanical input is applied to the sensing elements of the measurement system, and the instrument output is compared to this for verification or adjustment purposes. Indirect calibration is carried out by applying a simulated strain gage output to the input terminals of the instrument. This method, known as shunt calibration, is very versatile in application and generally simple to implement.

Figure 4-9 illustrates a representative situation in which an active gauge, in a three-wire circuit, is remote from the instrument and connected to it by lead wires of resistance R_L.

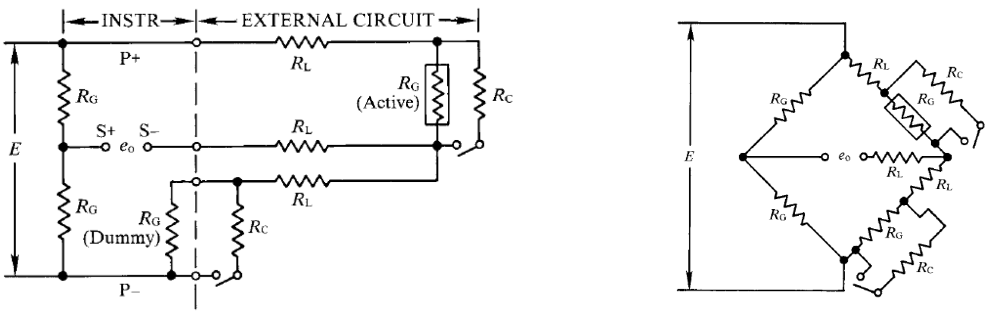

Figure 4-9: Quarter bridge circuit with active gage remote from instrument

If all leadwire resistances are nominally equal i.e., the same amount of leadwire resistance is in series with both the active gauge and the dummy (Equation 4-1).

Equation 4-1: $R_1 = R_L + R_G$ and $R_2 = R_L + R_G$

There is also leadwire resistance in the bridge output connection to the S– instrument terminal.

The latter resistance has no effect, however, since the input impedance of the instrument applied across the output terminals of the bridge circuit is taken to be infinite. Thus, no current flows through the instrument leads. The active gauge is shunted by a calibration resistor of 11880 Ω or selected for the strain magnitude of 5000 με. After adjusting the sensitivity of the instrument to register the calibration strain, the effect of the lead-wire resistance is eliminated from all subsequent strain measurements.

Prior to installing the model pile inside the model box, all the gauges were calibrated by subjecting the pile to compressive loadings at a constant ambient temperature. Calibration is used to adjust the sensitivity of the instrument so that it properly registers the strain signal produced by the gage.

The output of each gauge was also monitored under thermal variations close to that applied during thermal and thermo-mechanical tests.

Thermal output is caused by two algebraically additive effects that are expressed in Equation 4-2. The first depends on the electrical resistivity of the grid conductor that is temperature dependent (first term of Equation 4-2). The second contribution is due to thermal expansion between the grid conductor and the test material to which gauge is bonded (second term of Equation 4-2).

Equation 4-2: $\frac{\Delta R}{R_0} = \beta_G \Delta T + \left[K_G \left(\frac{1+K_t}{1-\upsilon_0 K_t}\right) (\alpha_M - \alpha_G)\right] \Delta T$

Where:

- $\beta_G \, \Delta T$: gage resistance with temperature

- $\left[K_G\left(\frac{1+K_t}{1-\upsilon_0 K_t}\right)(\alpha_M-\alpha_G)\right]\Delta T$: Resistance change proportional to the differential expansion
- $\frac{\Delta R}{R_0}$ Unit change in resistance from the initial reference resistance, R0, caused by change in temperature resulting in thermal output.
- β_GTemperature coefficient of resistance of the grid conductor
- K_G Gage factor of the strain gauge
- K_t transverse sensitivity of the strain gauge for its gage factor
- υ_0 Poisson's Ratio of the standard test material used in calibrating the gauge
- α_M Thermal expansion coefficient of the test material
- α_G Thermal expansion coefficient of the grid
- ΔT Temperature change from an arbitrary initial reference temperature
- $\left(\frac{1+K_t}{1-\upsilon_0 K_t}\right)$ is the correction factor for transverse sensitivity to account that the strain in the gage grid due to differential thermal expansion is biaxial.
- Thermal output is usually expressed in strain units ($\mu\varepsilon$) as the ratio of Equation 4-1 and the gauge factor setting of the instrument (K):

Equation 4-3: $$\varepsilon_T=\frac{\frac{\Delta R}{R_0}}{K}=\frac{\left[\beta_G+K_G\left(\frac{1+K_t}{1-\upsilon_0 K_t}\right)(\alpha_M-\alpha_G)\right]\Delta T}{K}$$

Equation 4-3 provides thermal output in strains units when the gauge is subjected to a temperature change ΔT under conditions of free thermal expansion or contraction for the substrate.

The equation demonstrates that the thermal output should not be linear with temperature change, because the coefficients are themselves function of temperature. The thermal output clearly depends not only on the nature of the gauge but also on the material to which the gauge is bonded. In the case of self-temperature-compensated gauges, thermal output is only function of gage resistance variation with temperature. The thermal expansion coefficient of the tests material is equal to the thermal expansion coefficient of the grid therefore, the second term of Equation 4-2 is null and thermal output just depends on the nature of the gauge. Heating and cooling thermal tests in "nearly" free expansion and contraction conditions were performed on the foundations by circulating cooled or heated when the foundation was standing vertically on a rigid base and thermal outputs were recorded. To account for this behavior thermal corrections were applied so that the measurements from the gauges would yield strains that are consistent.

4.2.4 Time-Domain Reflectometry (TDR)

The time domain reflectometry was used to determine the dielectric constant (relative permittivity) that is related to the volumetric water content of soil (θ). A pulse is sent through a coaxial cable connected to the TDR probe (Dias et al., 2018). The signal is then reflected and detected by an oscilloscope. The signal round-time is the travel time of an electromagnetic pulse along a metallic waveguide expressed by Equation 4-4.

Equation 4-4: $$\Delta t=2L\frac{\sqrt{K_a}}{c}$$

Where L is the probe length, K_a is the apparent dielectric constant and $\mathrm{c}=3\cdot10^8 m/s$ is the velocity of electromagnetic signal in free space.

Comparing the dielectric constant of water to those of minerals it is very hight, therefore, changes in volumetric water content can be directly related to the change in dielectric constant of soil. Different relationship between the volumetric water content and dielectric constant have been proposed in literature e.g., Ledieu et al. (1986) but studies as Papa and Nicotera (2012) have shown that those relations are unsatisfactory when applied to some types of soils as volcanic soils, Dias et al. (2018) have demonstrated that the volumetric water content was underestimated.

The software PCTDR 3.0 by Campbell Scientific Inc. suggested procedure was used to calibrate the probe constants because the probes used were not standard. The TDR probes used in the experiments are characterised by three rods of 150 mm length, 5 mm diameter and spaced by 32 mm. The calibrated *probe length* in m and the calibrated *probe offset* are required by the software for the interpretation of the recorded signal. The former constant is the rods length while the latter is used to correct the effect of the probe head on the measurements. Once the TDRs were calibrated the relative permittivity was measured. The calibration polynomial function proposed by Dias et al. (2018) for pyroclastic soil with grain size distribution close to those of soil in the experimental box (Equation 4-5) was used to estimate θ.

Equation 4-5: $\theta = a\, k_a^3 + b\, K_a^2 + c\, K_a + d$

Where: $a = 4.132 \cdot 10^{-6}$, $b = -5.748 \cdot 10^{-4}$, $c = 2.986\ \cdot 10^{-2}$, and $d = 1.500\ \cdot 10^{-2}$.

4.3 *Soil Physical, mechanical and thermal characterization*

Physical modelling, usually, is carried out on sands and clays that are traditional “laboratory” soils mainly provided by industrial suppliers to a given specification (Mayne et al., 2009). Typically, these soils are characterised by a relatively uniform grain size distribution. In this study a well graded grain-size distribution characterised the soil sample.

Small scale tests were carried out on soil of pyroclastic origin and typical of Campania region named as *Pozzolana* which is generally a sandy silt or more often a silty sand or sand and silt. Soil samples were collected from a site located at north of Napoli (Pascarola, Caivano) in the *ASI* industrial area (Figure 4-10). In the same site about two cubic meters of remoulded soil was taken from the shallow layers and carried into geotechnical lab to be used for the model preparation. research study (Raucci, 2017). Two boreholes, S1 and S2, and four CPTs along with laboratory investigations were performed. Drained triaxial consolidated tests (CID) and 1D compression tests on undisturbed samples were carried out in the geotechnical laboratory of University of Napoli Federico II. Borings and CPTs showed that the subsoil profile consisted of alternance of pyroclastic silty sands and volcanic ashes layers occupying a thickness of about 5.50 m. Below this layer, from 5.5 to 9 m, grey tuff was detected overlying a sandy layer placed at 9 m up to 12 m. Below 12 m the grey tuff was again found. Using the results of the four CPTs, Durgunoglu and Mitchell (1975) and Robertson and Campanella (1983) methods provide an average peak shear strength angle φ=35° for the shallow sandy layers (i.e., until 2.6 m depth). The in situ Relative density DR has been estimated as equal to 4%, using data from the penetration tests, (Lancellotta (1983); Baldi et al. (1986)). Young’s and oedometric modulus, E=3.1 MPa and Eed=3.7 Mpa respectively, have been computed by means of standard De Beer (1965) suggestion. From the undisturbed samples collected at two different depths above the groundwater table, three specimens were used to perform drained triaxial consolidated tests (CID). Three CID tests have been carried out by applying different cell pressures (i.e., 50 kPa, 100 kPa and 200 kPa). The value of the critical state and of the peak friction angles determined are 29.4° and 33.3°respectively.

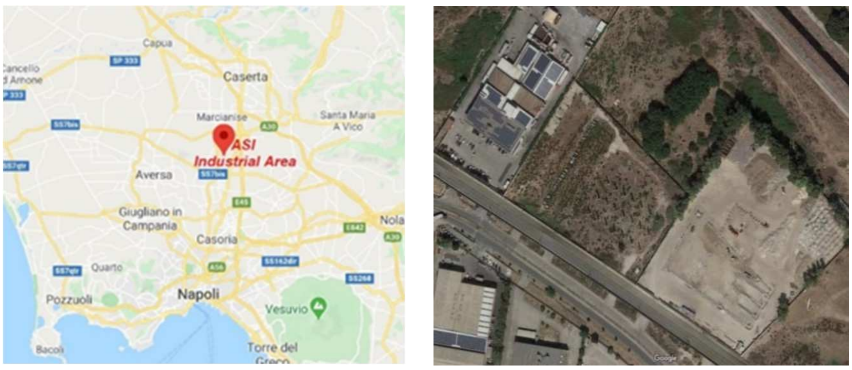

Figure 4-10: Geographical framework of ASI industrial area in Caivano (Napoli).

Investigations were carried out in the frame of this thesis and the soil profile was basically confirmed with boreholes down to 10-12 m. Soils samples were taken by using an Osterberg piston sampler as usual in *Pozzolana* above the groundwater table. Particle size analyses were performed on various soil samples taken at different depths (1.50-2 m, 2-2.50 m and 5-5.60 m). Mainly on the basis of the grain size distribution it was decided to collect the soil for the model test in the lab in the range between 2 and 2.5 m depth from the ground surface (Figure 4-11).

Figure 4-11: Excavation process and extraction of the soil.

The grain size distribution of soil collected in situ at depth ranging between 2-2.50 m and used for the small-scale model is reported in Figure 4-12.

In the lab the soil density was measured as$G_s = 2.54 \frac{gr}{cm^3}$. Maximum void ratio ($e_{max} = 1.70$) and minimum void ratio ($e_{min} = 1.08$) were obtained according to the standard test methods provided by the ASTM 4253-00 and 4254-00. The maximum index density or unit weight, according to ASTM 4253-00 standards, could be determined through four alternative methods. Among these the method based on the oven dried soil with aa vibrating table is used. This method is applicable to soils that may contain up to 15%, on dry mass, of soil passing at 75 μm sieve. The minimum index dry density /unit weight, according to ASTM 4254-00 procedures, could be determined through three methods. Among these methods the one based on the use of a funnel pouring device to place the material in the mold was used. This method is the preferred procedure for determining minimum index density and it is applicable to soils in which 100%of soil particles pass a 75 mm sieve and which may contain up to 30%, on dry mass, of soil particles retained on a 37.5 mm sieve (ASTM D4254-00).

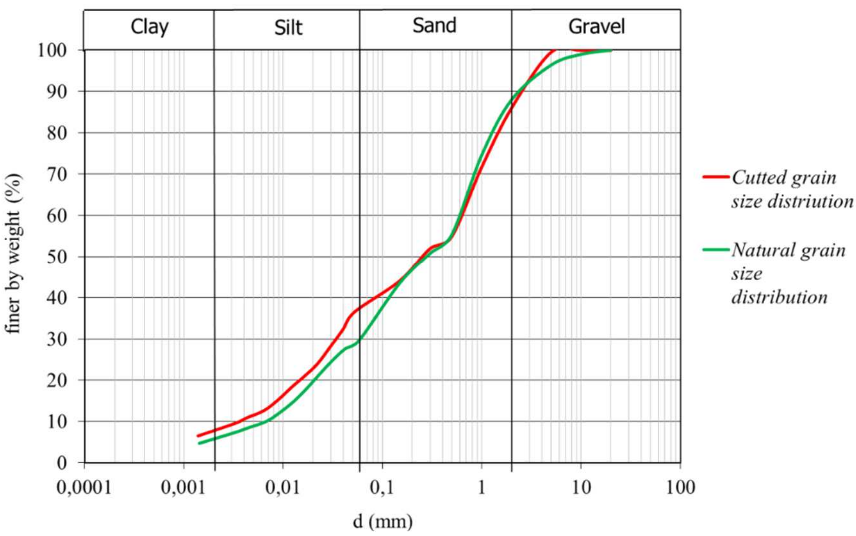

Figure 4-12: Grain size distribution of the Natural soil and the sieved soil used for the experimental tests.

The values of these state parameters are compared to the values reported in literature for *Pozzolana* collected by Nicotera (2002). Data collected from more than 44 sites located in the geographical area of Napoli have been divided in three classes: CLASS A data obtained from samples collected from depth less than 15 m, CLASS B data obtained from samples collected from depth between 15 m and 25 m AND CLASS C data obtained from samples collected from depth greater than 25 m (Nicotera, 2002). The collected data in terms of some of the Pozzolana state parameters are reported in the Table 4-2.

Table 4-2: Maximum and minimum particle density (Gs), initial void index (e_0), dry weight (γ_d), total weight for unit of volume (γ), water content (w_0) for CLASS A, CLASS B and CLASS C samples from Nicotera (2002).

		G_s [gr/cm3]		e_0 [-]		γ_d[kN/m^3]		γ [kN/m^3]		w_0 [-]		S_{r0} [-]	
		min	*max*	*min*	*max*	*min*	*max*	*min*	*max*	*min*	*max*	*min*	*max*
A	*Natural water content*	2.25	2.66	0.573	2.344	7.59	15.64	9.24	18.44	0.101	0.618	0.21	0.888
B	*Natural water content*	2.23	2.6	0.739	2.412	7.44	14.26	9.02	17.27	0.051	0.515	0.15	0.878
C	*Natural water content*	2.23	2.54	0.653	2.251	7.81	15.36	10.38	18.41	0.131	0.615	0.33	0.9
A	*Saturated in lab*	2.45	2.52	0.998	1.603	9.27	12.22	12.15	17.19	0.183	0.301	0.33	1
B	*Saturated in lab*	2.43	2.5	1.095	1.765	8.79	11.71	10.61	14.29	0.191	0.478	0.29	0.766

The values of the particle density G_s and packing limits e_{max} and e_{min}obtained in this study are comparable to the value reported in Table 4-2 for CLASS A samples saturated in laboratory.

In the preparation of the model for several reasons also depending on the diameter of the tested pile it was decided to use only a fraction of the collected soil mass. The fraction used correspond to the cutted grain size distribution passing at the 5 mm sieve, (Cutted grain size distribution, Figure 4-12). On this fraction the lab analyses were repeated and soil density maximal void ratio and minimal void ratio of 2.525 gr/cm^3, 0.9 and 1.7 were respectively found. The values of the packing limits are still comparable with the data reported by Nicotera (2002). It should be noted however that natural soils may well get to maximum void ratios that in the laboratory are not easy to obtain in remoulded samples.

The maximum and minimum void ratios are used only as reference quantities target to reproduce “loose” and “dense” state for the sand.

In this work the decision to concentrate the experimental efforts first on loose state was taken. After several trials a reference void index of 1.63 was assumed as a target quantity for the so called “loose” state. The loose state was chosen as first choice also because it is known that in such a condition of relatively low stiffness the thermo-mechanical strains are enhanced. The mechanical properties of loose *Pozzolana,* used for the experimental tests, were evaluated through direct shear tests on dry reconstituted samples.

Direct shear tests were performed with direct shear testing machine AUTOSHEAR 27-WF2160 on dry loose reconstituted samples in the geotechnical laboratory of the University of Napoli Federico II. The samples were prepared using air pluviation as placement technique. The sand was directly poured into the square shear box, 60 mm x 60 mm. All the Samples were prepared at dry density of 9.3 kN/m^3.

All the tests were carried out at a constant rate of shearing deformation of 0.133 mm /min. According to ASTM D3080/D3080M the rate of shearing must be slow enough to ensure drained conditions so that insignificant excess pore pressure exists at failure. In this case the tests are performed on dry specimens where pore pressure dissipation does not occur, therefore all the tests are designed to reach the maximum shear displacement in one hour. Shear tests were performed on reconstituted, to the same void index, specimens applying different normal stress levels.

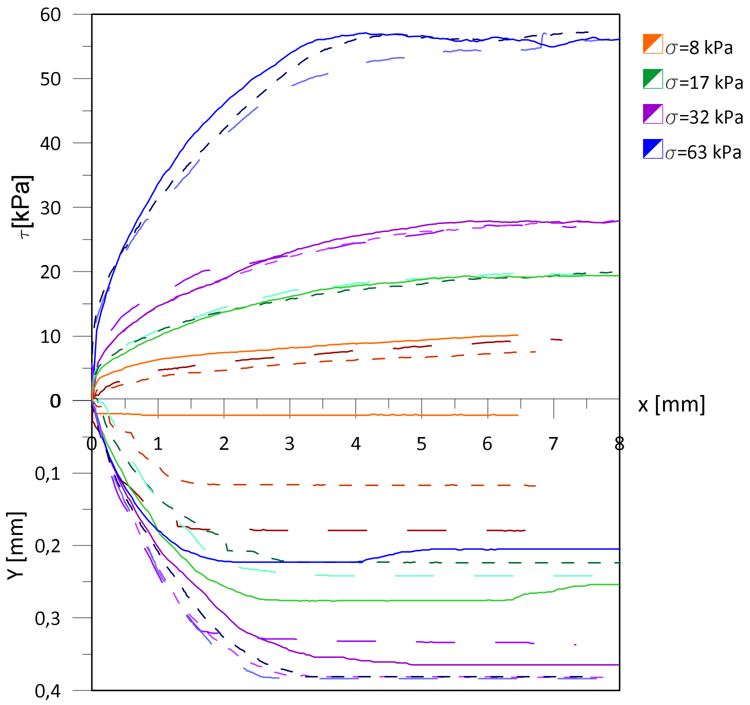

Figure 4-13: Results of direct shear tests: shear stress and vertical displacement plotted against the shear displacement at different level of nominal normal stresses.

Three tests are performed for each normal stress level on the reconstituted specimens described above. The vertical loads applied are: 8.17 kPa, 17.03 kPa, 32.02 kPa and 63.34 kPa. The three tests were carried to verify the accuracy and the repeatability of the procedure adopted to reconstitute the sample at a given density.

Figure 4-13 shows the typical set of results of direct shear tests. As it is widely appreciated from Figure 4-13 it could be observed that increasing the applied normal force increases the initial stiffness and the maximum shear stress. At all stress level it could be noticed that the shear stress increases with shear displacement to a maximum value and then remains constant (there is no peak). Consistently the volume of the specimen gradually decreases to a certain value and remains approximately constant thereafter.

From the shear tests results the shear strength of the loose pozzolana was evaluated. Within a dry approach, i.e., null water pressure assumed, the shear strength angle φ= 41 °C is obtained from the Mohr-Coulomb criterion considering no cohesion. Shear strength angle values reported by Nicotera (2002) for saturated and unsaturated *pozzolana* samples varies between 32°-40°. The rather large friction angle obtained from the shear tests on “nearly” dry samples is slightly greater and it could be related to the matrix suction that occurs in residual conditions. Unsaturated soils shear strength is influenced by their suction and degree of saturation. Even if the mechanical tests are not performed monitoring matrix suction and degree of saturation, the effects of these parameters maybe present in the determined high value of the shear strength angle obtained with a linear regression on the shear tests couples τ,σ without accounting for an intercept.

The thermal properties of dry Pozzolana soil are determined in terms of thermal conductivity (and thermal resistivity) Thermal conductivity of dry soil depends also on the void ratio because the amount of void filled by air between the soil particles obviously influences the total thermal properties of soil. The thermal conductivity (or thermal resistivity) of reconstituted dry soil specimens is determined by the thermal needle probe procedure. Tests were performed on dry reconstituted samples to 1.6 and 1.05 void index. These tests allow determining thermal conductivity by a variation of the line source method using a needle probe having a large length to diameter ratio to simulate conditions for an infinitely long heat source (as described in chapter 2). The probe consists of a heating element and a temperature measuring element. A known current and voltage are applied to the probe and the temperature rise with time is recorded over all the time intervals while the probe is inside the soil sample. Thermal conductivity is obtained from an analysis of the temperature time series data during the heating cycle. Considering that the change in temperature after the constant amount of heat had been applied to the mass of the specimen over a period of time and approximating the exponential integral by the most of significant term of its series expansion is possible to compute the thermal conductivity λ by the Equation 4-6:

Equation 4-6: $\lambda = \frac{q(lnt_2 - lnt_1)}{4\pi(T_2 - T_1)}$

Where: q is heat input per unit length of heater (W/m), t_1 and $t_2$are subsequent Instants of time recorded during the tests (s), T_1 and T_2 in K are subsequent temperatures recorded during the test. The heat input per unit length during the tests was 4,49 W/m.

The specimens' preparation is carried out according to ASTM D53334-14 that suggests compacting the specimen to the desired dry density (and gravimetric water content) in a thin-walled metal or plastic tube using an appropriate compaction technique. The tube shall have a minimum diameter of 50 mm and a length of 20030 mm. Plastic tube of 200 mm diameter and 700 mm length are used. Loose samples are prepared by air pluviation and gentle tamping (Figure 4-14 b). Dense samples are prepared through air pluviation maintaining free fall of the soil of 700 mm and energetic tamping (Figure 4-14 a). All the samples are prepared in seven layers in order to achieve a constant relatively density (void index) for the whole sample height.

According to ASTM D53334-14 the total heating time should be appropriated to the thermal needle probe size. For a diameter greater than 2.54 mm the heating duration should be longer than 60 seconds. However, this method is only valid if the thermal pulse does not encounter the boundaries of the specimen, so care must be taken not to choose too long a heating duration. To these aims a tests duration of 300 seconds was assumed with 248 temperatures measurements. The thermal conductivity obtained for the loose samples is 0.222 W/m °C while for the dense samples is 0.226 W/m °C. The soil thermal resistivity computed for the loose and dense samples is 4.505 m °C / W and 4.425 m °C/ W.

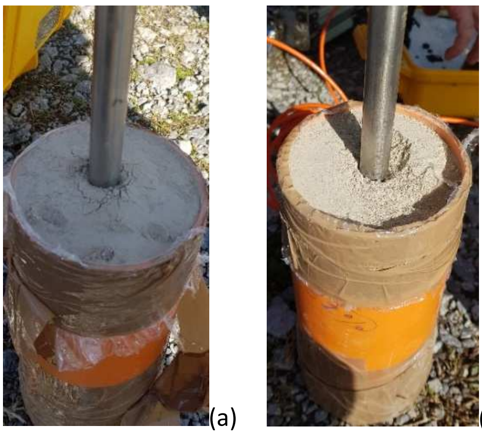
(a) (b)

Figure 4-14: (a) Dense and (b) loose samples used for the thermal needle tests.

As could be expected the thermal conductivity is a decreasing function of the porosity. The larger the porosity the lower the conductivity (i.e., the larger the resistivity). The valued obtained from the experimental tests are in agreement with the typical data obtained for a dry sand taking in account the high porosity of the loose sample.

4.4 *Testing program*

The experimental tests carried out on the small-scale pile are divided into two categories: tests carried out without loadings at ground surface (Model A) and tests carried out with dead loads applied at the ground surface (Model B). The thermal and thermo-mechanical pile-soil interaction was evaluated considering different level of soil mean effective stress. In the Model A, the stress state is very low with mean vertical effective stress at pile's mid depth less than 2 kPa. As known the small-scale tests carried out at 1 g because of the geometry of the model implies that the stress state in the soil is significantly lower than that in the field. Even if the level of stress of the field are not reached a slightly increase of the stress state was performed applying at the soil surface iron cast circular weights arranged symmetrically with respect to the pile (Figure 4-15).

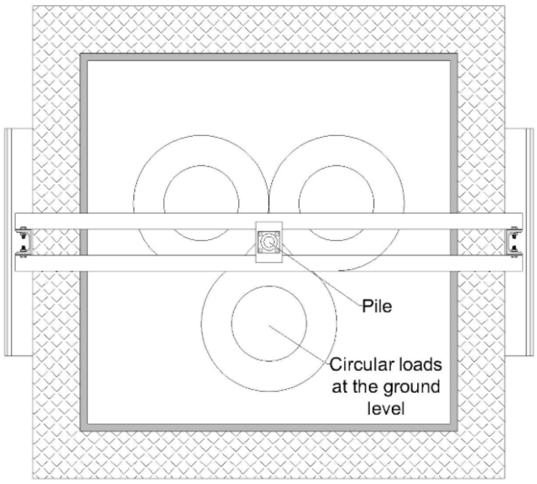

Figure 4-15:Arrangment of iron-cast weight with respect to the model pile (Model B).

Three circular weights of 637.39 N are arranged as shown in Figure 4-15.The vertical stress increase ($\Delta\sigma_z'$) induced by the dead loads along a vertical of soil placed at contact with pile (soil-pile interface) is plotted in Figure 4-17. $\Delta\sigma_z'$ is obtained by means of DEFRET included in FONDAZIONI of CFSYSTEM that is the application to solve elastic stress increments induced by rectangular or circular loads.

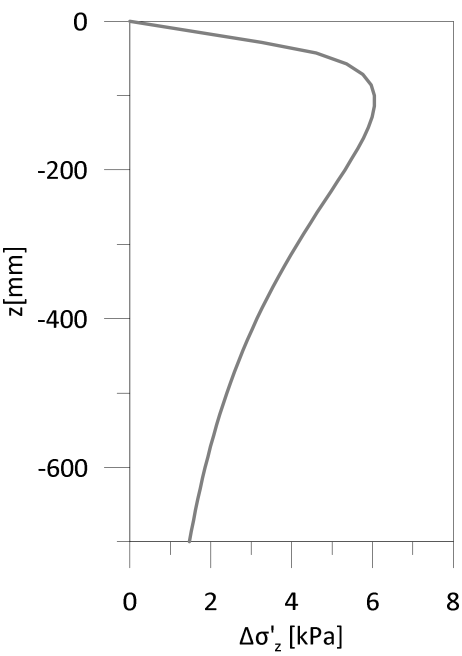

Figure 4-16: Vertical stress induced by the application of the weights at soil surface in Model B.

The application of the loads at ground surface determines an increment of vertical stress. The combination of the lithostatic stress and the induced increment produce a vertical stress σ_z' = 7.2 kPa and σ_z' =6.9 kPa at mid depth and toe of the pile, respectively. The laboratory tests were firstly performed on Model A. Before performing tests on Model B, the pile was extracted, the soil container was emptied, and all the transducers were removed. The soil was pluviated again following the same procedure described in 4.2.1 but applying the weights at soil surface. An additional thermocouple was installed to monitor the outlet water temperature to estimate the thermal performance of the small pile. All the thermal and thermo-mechanical tests were carried out at constant flowrate of 5.6 l/min (9.33 10^{-5} m^3/s). The heat flow, Q in W is estimated according to Equation 4-7:

Equation 4-7: $Q = \rho c_w \Delta T\ v$

Where: ρ is the density of water (ρ=997 kg/m^3,) c_w is the specific heat capacity of water (c_w=4185 j/kg °C), ΔT is the difference between the inlet and outlet water temperature expressed in °C and v is the water flow rate (v= 9.33 10^{-5} m^3/s).

During the tests, the average volumetric water content (θ) was estimated by means of TDR (4.2.4) installed in different positions inside the experimental box as showed in Figure 4-4 . The matric suction was also monitored by means of miniature tensiometer.

Both in case of Model A and Model B, purely mechanical test is carried out to evaluate the bearing capacity of the small pile and investigate about the soil-pile interaction under conventional loadings. Different kinds of tests were performed, mechanical tests (characterized by purely mechanical loadings), thermal tests (characterized by purely thermal loadings), and thermo-mechanical tests (characterized by coupled thermal and mechanical loadings). On Model A two kinds of thermal tests and one thermomechanical test were performed. One Model B, two kinds of cyclic thermo-mechanical tests were performed. The tests performed on Model A and Model B are reported in Table 4-3.

During each test carried out under non isothermal conditions the temperature of the soil was continuously monitored by means of thermocouples placed in the soil as shown in Figure 4 4. The thermocouples acquisition system allowed recording only four channels. For both Model a and Model B temperature in each thermocouple was recorded when the circulating bath was turned off. The environmental air temperature was recorded too. Because of the number of channels of the acquisition system only the thermocouples that are closer to the pile were continuously recorded. Prior circulating the cooled or heated water inside the pile, soil temperature was recorded in each thermocouple to measure the average undisturbed temperature of the soil. During the tests on Model A malfunctioning of some sensors as Tc3 and SG1 were detected. Therefore, these measures were not reported.

During each test reported in Table 4-3 pile's head displacements were monitored by means of the two LVDTs placed at pile's head as showed in Figure 4-4. The measured thermal displacement is assumed as the average of the displacement measured by LVDT 1 and LVDT 2. Axial loadings were obtained by means of the SGs that were continuously recorded by means of Micro-Measurements P3-D4 acquisition system by Luchsinger.

Table 4-3: Testing program.

Test type	***Model A***	***Model B***
Load test to failure	Mechanical test in isothermal condition	Mechanical test in isothermal condition
	Heating	

Thermal test at constant temperature	Cooling	
Thermal test at variable temperature	Heating	
	Cooling	
Thermo-mechanical test at variable temperature	Heating SF=3	
Cyclic Thermo-mechanical test		Heating SF=3 (CTM-H)
		Cooling SF= 3 (CTM-C)
Simplified Cyclic Thermal and Thermo-mechanical test		Heating (S1)
		Heating at SF=6 (S2)
		Heating at SF=3 (S3)
		Heating at SF=2 (S4)

4.4.1 Load Test to failure

Load tests to failure are purely mechanical tests performed under isothermal conditions both on Model A and Model B. The tests were carried out applying at pile's head dead load made by iron-cast weight while pile's head displacements and mechanical strains were recorded. The bearing capacity of pile-soil system and the load transfer mechanism are evaluated.

4.4.2 Thermal tests at constant temperature

Thermal tests at constant temperature are performed applying purely thermal loadings during the tests of heating and cooling. Temperatures reported in Figure 4-18 are set at circulating bath that allowed to heat or cool the water to the desired temperature value. The Heating Thermal test at constant temperature is carried out circulating heated water ranging between 38.8 °C and 40.6 °C (Figure 4-17 (red line). The Cooling Thermal test at constant temperature was characterised by small temperature changes because of a programming issue with the circulating bath. The inlet water temperature ranged between 3.9 °C and 6.7 °C as showed in Figure 4-17 (blue line).

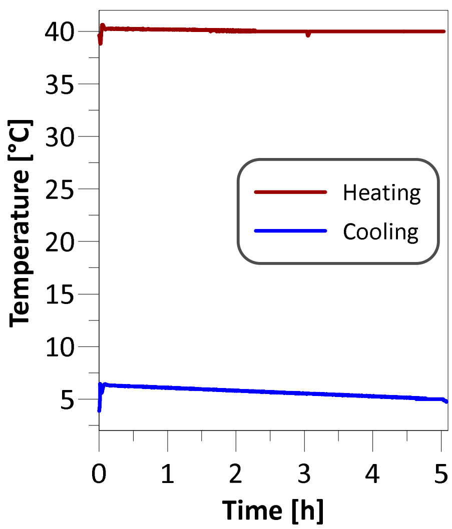

Figure 4-17:Inlet water temperature during heating (dark red line) and cooling (blue line) tests at constant temperature.

These tests are not representative of the real operation condition, the aim of these tests was to evaluate the thermal interaction under the simplest thermal loading condition.

4.4.3 Thermal tests at variable temperature

Magnitude of temperatures, number and duration of thermal cycles influence the thermo-mechanical behavior of EPs. Thermal tests in this study, even if the level of stress is not representative of real in situ conditions, are performed applying temperature variations that could occur in a real GEP system in operational conditions for the climatic area of Napoli. Therefore, thermal loads have been determined by dynamic energy simulations of an office building in Napoli by means of Design Builder software as described in section 3.6.3. Two days of operation one during Winter and the other during Summer were considered to define the thermal loads to be applied. The inlet water temperature during heating and cooling is plotted in Figure 4-18 in red and blue line, respectively.

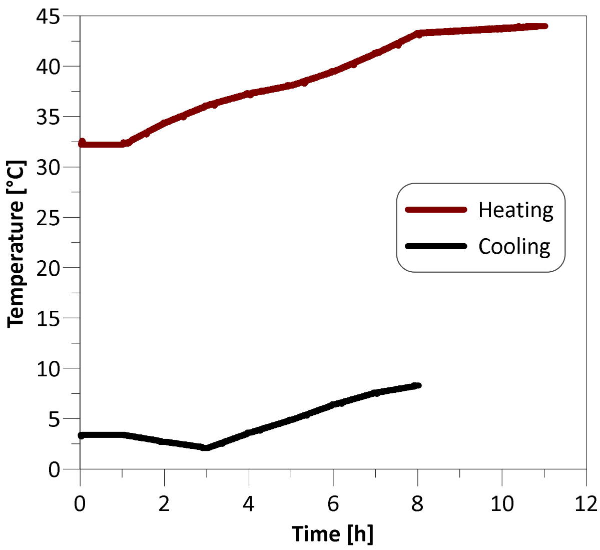

Figure 4-18: Inlet water temperature during the thermal tests at variable temperature (heating and cooling).

During heating temperatures range from 32 °C to 44°C. The temperature trend during the elapsed time is characterized by a temperature variation that is always increasing. This trend reflects what is the operation of a real heat pump in summer mode considering a daily operation starting from the early morning hours (8-9 am). The first hours are characterized by a lower temperature than the following hours which will be much warmer determining higher thermal loads. In the case of the cooling, winter operation is characterized by a thermal load trend that has a peak in the coldest hours and a gradual decrease of the load due to the increase in temperature during the day (with reference to the Mediterranean climate). During cooling, temperatures range from 2 °C to 8 °C. As could be noticed from Figure 4-18 heating loads are greater than cooling loads and it is obviously connected to the features of climatic area.

4.4.4 Thermo-mechanical tests

Thermo-mechanical tests are carried out in different steps. The first step is purely mechanical: iron cast weights are applied at pile's head. The load to be applied is defined as a percentage of the estimated pile's bearing capacity. The second step is thermo-mechanical: thermal loads are applied by circulating heated or cooled water inside the pile while the gravity load, applied during the previous phase, is kept constant. During the mechanical step pile's head mechanical displacements and strains were measured by means of the two LVDTs placed at pile's head. During the thermo-mechanical phase both SG and LVDTs were not zeroed. The purely thermal displacements and stresses were evaluated as differences between the results measures in the two steps and basically relying, as a first approximation, on the superposition principle effects.

4.4.4.1 Thermo-mechanical test at variable temperature

During the thermo-mechanical heating test at variable temperature the heating history reported Figure 4-18 is combined to a mechanical load of 48.17 N (i.e., an overall SF=3).

4.4.4.2 Cyclic Thermo-mechanical test

Two Cyclic thermomechanical tests of heating and cooling were performed on Model B. During the first step 96.67 N of head load was applied, corresponding to an overall SF=3. During the second step thermal cycles reported in Figure 4-19 were applied keeping constant the mechanical load. One thermal cycle corresponds to the daily thermal history of the thermal tests at variable temperature (Figure 4-18).

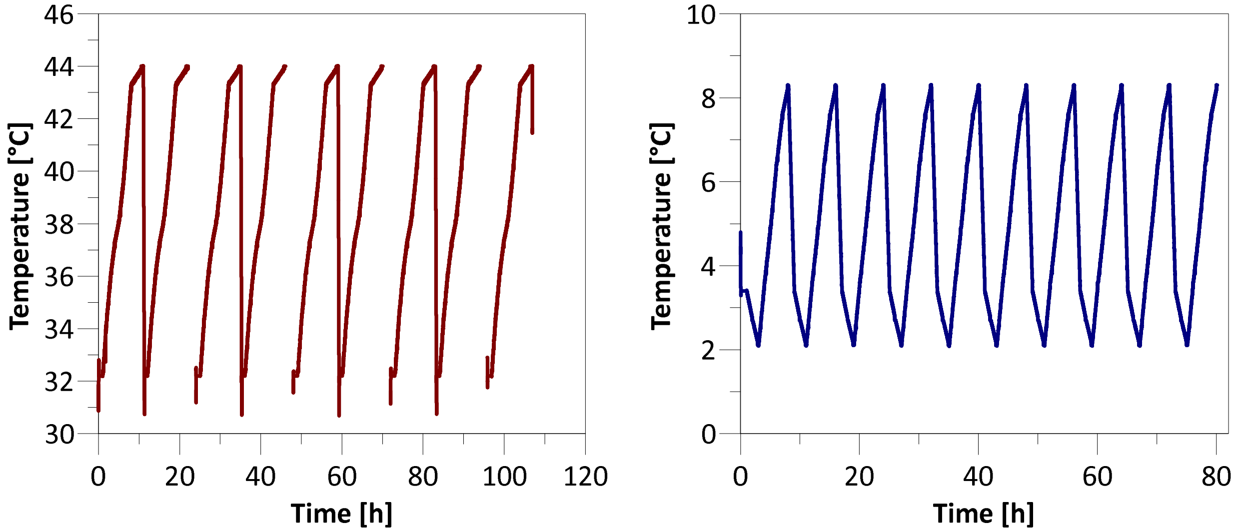

(a) (b)

Figure 4-19:Thermal cycles performed during the cyclic thermo mechanical tests; (a) heating and (b) cooling.

During the cyclic thermo mechanical tests of heating the temperature function repeated for nine times under the constant vertical load (Figure 4-19 (a)). During this test, a power lack occurred and the test was interrupted before the tenth cycle was performed. Between two subsequent cycles two hours of rest were performed. The test lasts about five days (Figure 4-19 (a)). During the cyclic thermo mechanical test of cooling the temperature function applied during the thermal test of cooling at variable temperature was repeated ten times as showed in Figure 4-19 (b). During this test, no rest phases were performed, and ten cycles of cooling (Figure 4-19 (b)) were repeated under a constant vertical load of 96.67 N (SF=3).

4.4.4.3 Simplified Cyclic Thermal and Thermo-mechanical test

The thermal loads evaluated through dynamic simulation as explained in 4.4.2 allow defining simplified solicitations showed in Figure 4-20. Additional thermo-mechanical and thermal cyclic tests were performed (simplified cyclic tests). Each heating cycle lasts six hours, during the first three hours the temperature ranges between 32 °C and 44 °C while in the last three hours between 44 °C and 32 °C. Eleven cycles were performed for a total time duration of about three days (Figure 4-20). Different level of mechanical stress was combined to the simplified cyclic solicitations as showed in Figure 4-22. One thermal Cyclic test and three thermo-mechanical cyclic tests were performed: S1, S2, S3 and S4 (Figure 4-22). During the test S1, null mechanical load was applied, only thermal solicitations were imposed to the pile (SF=∞). Test S2 was performed in two steps. During the first step a mechanical loading corresponding to SF=6 was applied. During the second step the mechanical load is kept constant and combined with cyclic thermal loads. Tests S3 and S4 were performed as described for test S2 but different level of mechanical loadings were applied, SF=3 and SF=2, respectively. During Test S3 the load level corresponds to SF=3 while during Test S4 a SF of two corresponds to the dead load.

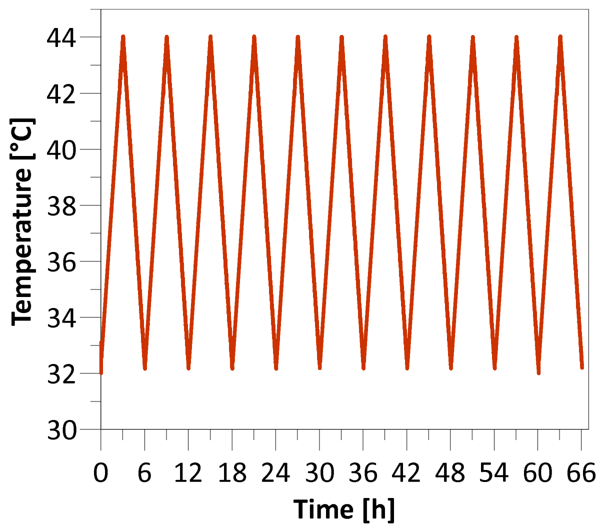

Figure 4-20:Simplified heating solicitations applied during the simplified cyclic thermal and thermo-mechanical tests.

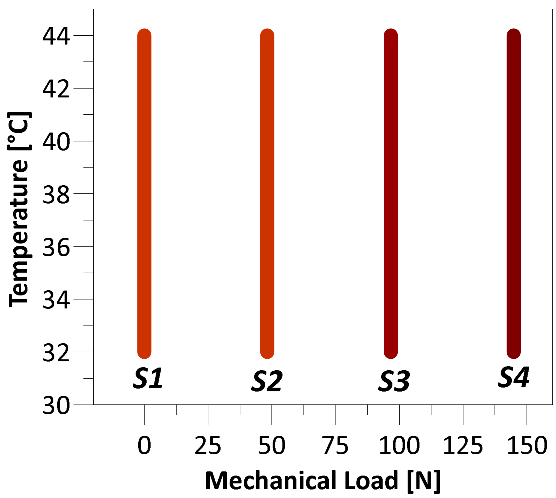

Figure 4-21:Cyclic thermal and thermo-mechanical tests carried out at different mechanical load level, Test S1 at SF=, Test S2 at SF=6, Test S3 at SF=3 and Test S4 at SF=2.

4.5 *Laboratory tests on Model A*

4.5.1 Load Test to failure

The aim of the test is to determine the bearing capacity of the pile and its load settlement relationship and the transfer curves of the side shear. The maintained load test is the most common procedure in which the load is applied in steps and each load step is kept constant for a certain time while settlement is measured (Viggiani et al., 2012). A fixed duration is adopted for each load step so that the duration is of the order of one hour. According to Viggiani et al. (2012) the practice of performing intermediate un-loading reloading cycles is of doubtful usefulness and it is suggested to adopt a load history consisting in a single loading cycle from zero to the maximum load test, followed by unloading to zero. This is the procedure adopted for the loading test. The loads are applied to the pile through iron-cast weights of about 10.79 N placed on the still plate at the head of pile and inserted in the load guide to keep nearly vertical the loading direction. This load test can be defined as an Ideal Load Test (ILT) where no reaction is provided to the applied top load (Russo, 2013). Load was applied in fifteen increments taking the load to 74.07 kPa, 158.49 kPa, 231.65 kPa, 315.78 kPa, 390.82 kPa, 475.02 kPa, 559.05 kPa, 643.44 kPa, 727.47 kPa, 800.48 kPa, 884.33 kPa, 968.83 kPa, 1052.94 kPa, 1136.79 kPa and 1209.86 kPa. Being the loading procedure based on dead weights the unloading is carried out following the same number of steps of the loading part. The loading procedure is sketched in Figure 4-22.

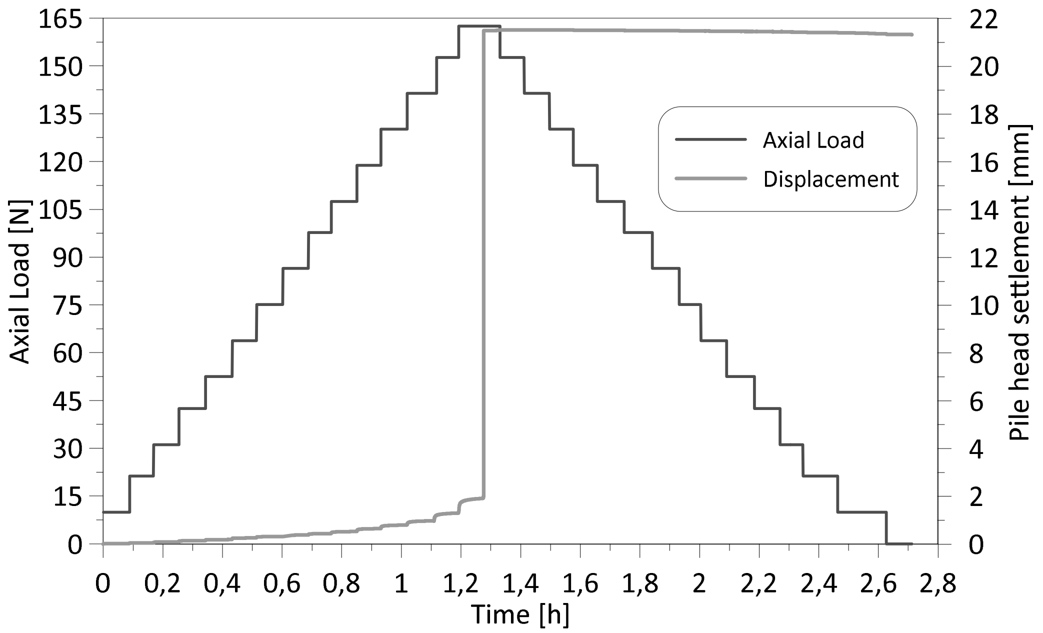

Figure 4-22:Loading procedure for the purely mechanical test. Load steps and measured displacement during the time duration of the test.

The pile bearing capacity is the summation of two components the shaft or skin load (Q_s) and the base or point load (Q_p). At the design stage (referred to the laboratory model) the skin load was estimated through the well-known β−method while the base load was evaluated through Berezantsev et al. 1961.

Equation 4-8: : $Q = Q_s + Q_p - \sum W = \left(s \ \cdot \pi d L_{pile}\right) + \left(p \cdot \ \pi d^2\right) - \sum W = \left(k\sigma'_v \mu \cdot \pi dL\right) + \left(N_q L_{pile} \gamma' \cdot \pi d^2\right) - \sum W$

where: s is the ultimate unit shaft resistance, p is the ultimate unit base resistance, W is the pile weight, d and L_{pile} are the pile diameter and embedded length, respectively, k=0.5 depends on the method of pile installation and soil properties, μ=0.87 depends on the interface properties and N_q is a function of the pile slenderness ratio and of the soil friction angle.

As described in the previous chapter the model pile was assumed as a displacement pile type and the interface friction angle may be assumed as corresponding to the shear strength angle of the surrounding soil. The measured load settlement relationship is plotted in Figure 4-23. For a load of 162,49 N a sudden increase in the measured settlement is observed therefore this load level is assumed as the ultimate bearing capacity. During the unloading to zero the residual pile head settlement almost corresponds to the total settlement measured at 162,49 N. Base load is completely mobilised and the soil below the pile tip is obviously compressed.

The axial load distribution along the model pile shaft at the end of each load step is shown in Figure 4-24.

The mobilized side friction is evaluated from the axial load dividing the pile in four zones. For the first 10 mm of the pile, over G5, the mobilisation of side friction is neglected, and the load applied to the head of the pile corresponds to the axial load measured by G5.

All the sensors remained operational during the test except G1 therefore the load transfer is reported only for the upper 300 mm of pile. During the last loading step 56 % of the load is transmitted at 300 mm depth from pile head (G2). Three zones are considered for the estimation of the side shear friction: zone 1 that ranges between G5 and G4, zone 2 that ranges between G4 and G3 and zone 2 that ranges between G3 and G2 (Figure 4-25).

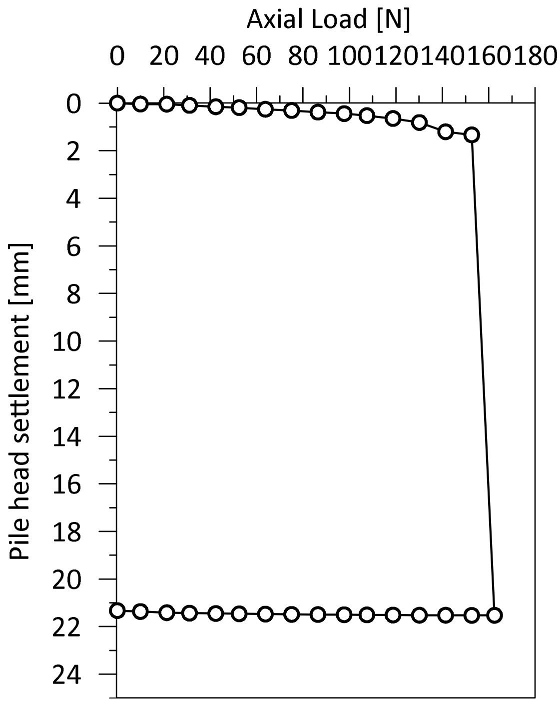

Figure 4-23:Results from the loading test, load-displacement curve.

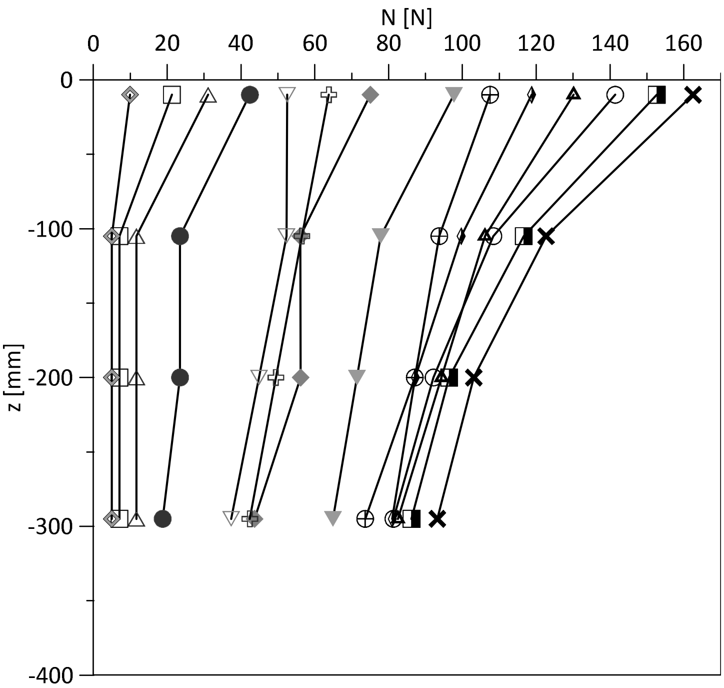

Figure 4-24:Axial force distribution along pile's depth.

The τ-w curves for zones 1, 2 and 3 are plotted in Figure 4-26 (a), Figure 4-26 (b) and Figure 4-26 (c), respectively. All the curves are plotted until a maximum displacement of 6 mm and are characterised by last part of the diagram that is black dotted lines to highlight that the displacement of pile's head continues to higher values (about 20 mm).

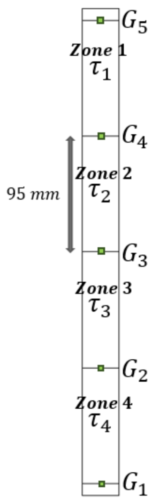

Figure 4-25: Zones of the pile defined to calculate the mobilised friction.

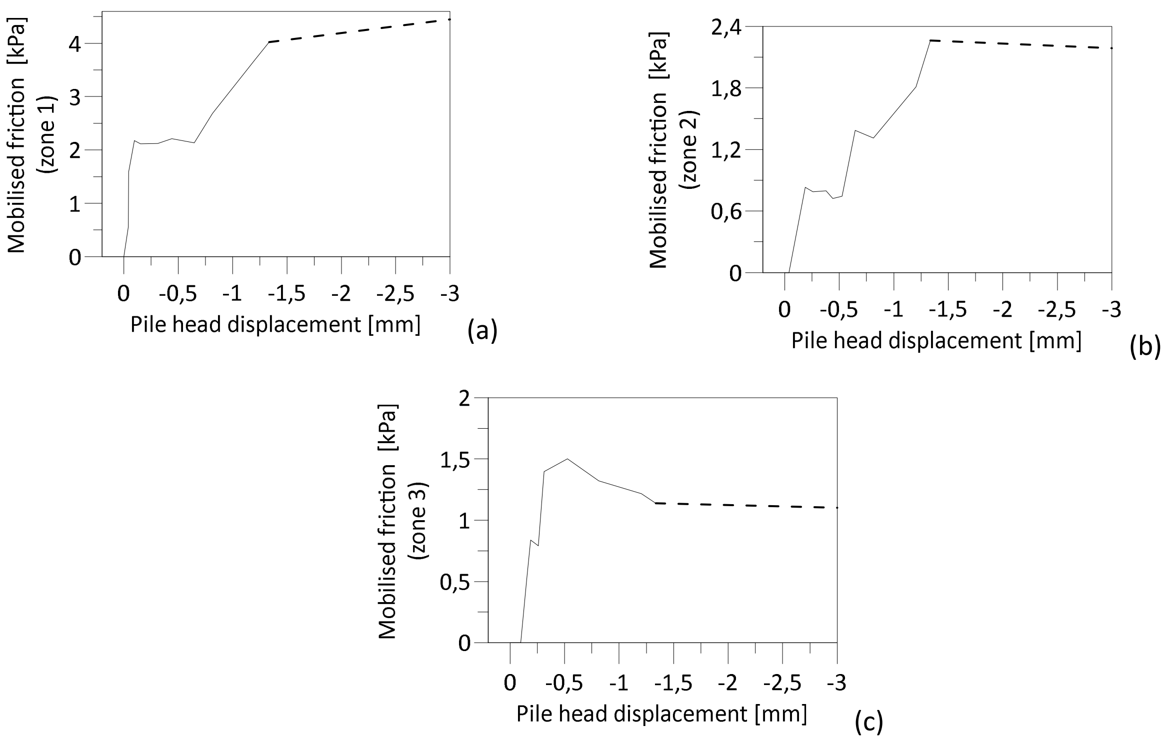

Figure 4-26: τ-w curves a at different depths: (a) zone 1, (b) zone 2 and (c) zone 3.

Mobilised friction is computed using vertical equilibrium between two subsequent gauges. The mobilised friction increased progressively with the increasing of pile head displacement which is used as a term of reference on the x axis for all the τ-w curves.

4.5.2 Purely thermal tests at constant temperature

In this section the results of the two thermal tests of heating and cooling at constant temperature are presented. During the tests pile's head displacements were monitored by the two LVDTs placed at pile's head, thermal along pile depth were measured by G5, G4, G3 and G2. Temperature of the soil were measured by thermocouples Tc1, Tc2, Tc3, Tc4, Tc5, Tc6 and Tc7 (Figure 4-4). Air ambient temperature were also measured during the tests. Inlet temperature applied during heating and cooling tests at constant temperature are plotted in Figure 4-17.

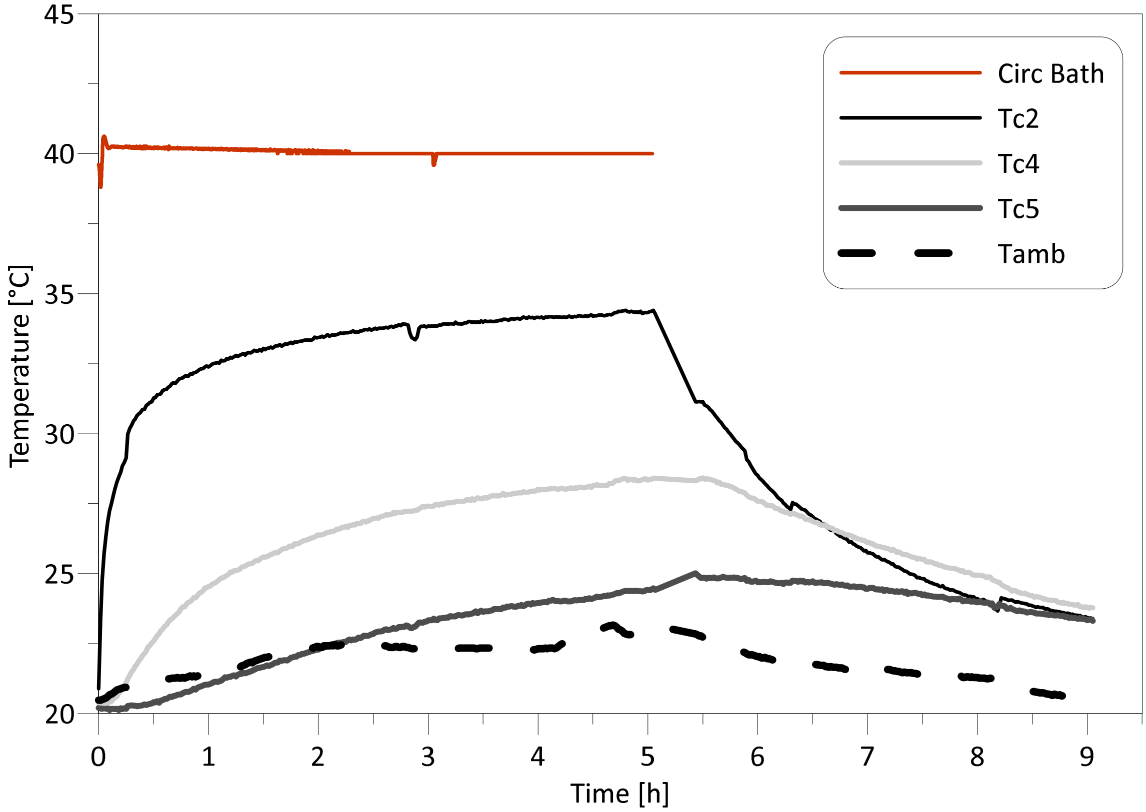

Figure 4-27: Soil temperature changes during heating test at toe of pile-soil interface (Tc2), at 1D and 2D from pile and 200 mm depth from ground surface (Tc4 and Tc5) along with ambient air temperature (Tamb) and Inlet water temperature (Circ Bath).

Before starting the heating test the average undisturbed soil temperature was 19.74 °C while prior to cooling test it was 20.62 °C. In both cases the time duration of the test was about 5 hours during which 4 thermocouples were continuously monitored and recorded. During the heating test Tc2, Tc3, Tc4 and Tc5 thermocouples were connected to the acquisition system and recorded for a total time duration of about nine hours (five hours of heating and four hours of thermal recovery). The temperatures recorded during the heating test are plotted in Figure 4-27. At the end of the heating test, soil temperatures were monitored to investigate about the heat transfer mechanism inside the experimental box. Temperature increase was measured by all the thermocouples, with larger temperature at pile soil interface and lower with increasing distance from the pile. Temperature variations occurred at 1D and 2D of distance from the pile.

Temperature measured by thermocouples Tc2, Tc4 and Tc5 during the cooling test are plotted in Figure 4-28. The monitoring of temperature after cooling of the pile was longer than those performed at the end of heating. The heat transfer evolution in the experimental box was monitored for seventeen hours from the end of cooling. Temperature's decrease was measured by all the thermocouples with larger temperature at pile soil interface and lower with increasing distance from the pile. Temperature variation occurred at 1D and 2D distance from the pile. At the end of monitoring both thermocouples Tc4 and Tc5 return almost to the initial temperature prior to cooling. Comparing the average soil temperature at the end of monitoring and prior to cooling 1 °C decrease occurred. From both tests, monitored temperatures are characterised by a sudden increase and decrease for heating and cooling, respectively. With Increasing distance from the pile, the magnitude of changing is smaller and slower, as expected.

Thermal pile's head displacement was monitored during the heating and cooling and the subsequent thermal recovery. Measured thermal displacement is related to free expansion of the pile considering two different locations of the NP: mid depth and pile's toe. The former displacement is named as displacement of floating pile ($y_{Floating}$) while the latter as end-bearing ($y_{End-bearing}$). The displacement of the Floating pile is computed according to Equation 4-9 while the displacement of the End Bearing pile according to Equation 4-10.

Equation 4-9: $y_{Floating} = \alpha_p \cdot \Delta T \cdot \frac{L_{pile}}{2}$

Equation 4-10: $y_{End-bearing} = \alpha_p \cdot \Delta T \cdot L_{pile}$

Where: α_p is the linear expansion coefficient of the pile in °C^{-1}, ΔT is the average temperature variation computed as the difference between the inlet water temperature and the initial soil temperature in °C and L_{pile} is the pile length in mm. Pile's length accounts for the length above and below the soil and the position of the LVDTs.

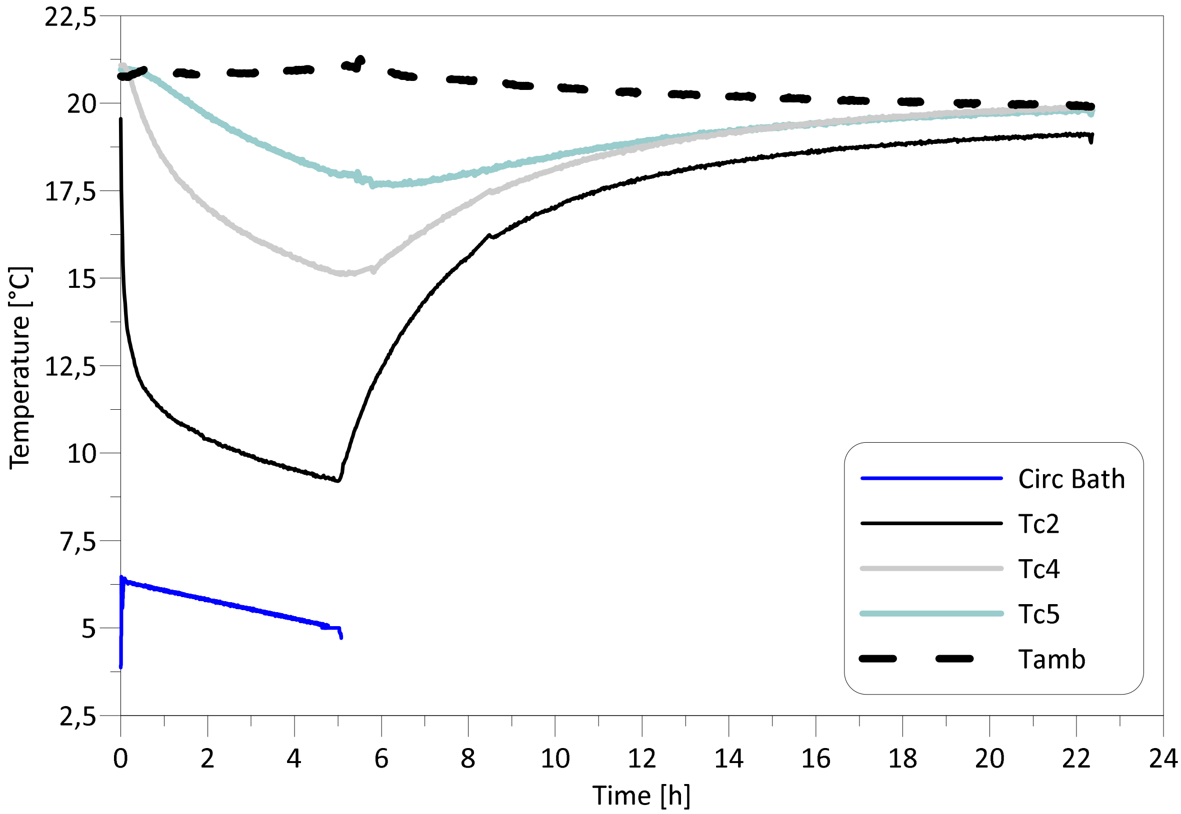

Figure 4-28: Soil temperature changes during cooling test at toe of pile-soil interface (Tc2), at 1D and 2D from pile and 200 mm depth from ground surface (Tc4 and Tc5) along with ambient air temperature (Tamb) and Inlet water temperature (Circ Bath).

$y_{Floating}$ and $y_{End-bearing}$ are considered as reference magnitudes of displacement. Pile's soil thermo-mechanical interaction defines both the NP position and the degree of mobilization of the free expansion coefficient of the material of the pile. Theoretically if the thermal loads are constant along pile's depth and soil mechanical properties do not vary with depth and tip resistance is null the NP position corresponds to mid length of the pile. Therefore, this condition, for thermally activated piles is commonly denoted as floating pile. If the maximum degree of constraint acts at pile's tip the NP position is at pile's toe (End bearing pile).

However, it is important to highlight that $y_{Floating}$ and $y_{End-bearing}$ quantities defined above, are theoretical quantities that corresponds to the maximum displacement that can occur depending on the NP location and do not account for the constraint action of the surrounding soil on the pile strains and displacements. The interaction with surrounding soil does not allow the free expansion or contraction of the pile. This can be expressed by the mobilised linear expansion coefficient of the pile that is smaller than the free linear expansion coefficient of the aluminium.

$y_{Floating}$ and $y_{End-bearing}$ are plotted along with the measured displacement and the water inlet temperature in Figure 4-29 and Figure 4-30 for heating and cooling tests at constant temperature, respectively.

The sign convention is that heating temperature variations are considered positive while temperature decrease during cooling are assumed negative. Upward displacements are considered positive while downward displacements are assumed negative.

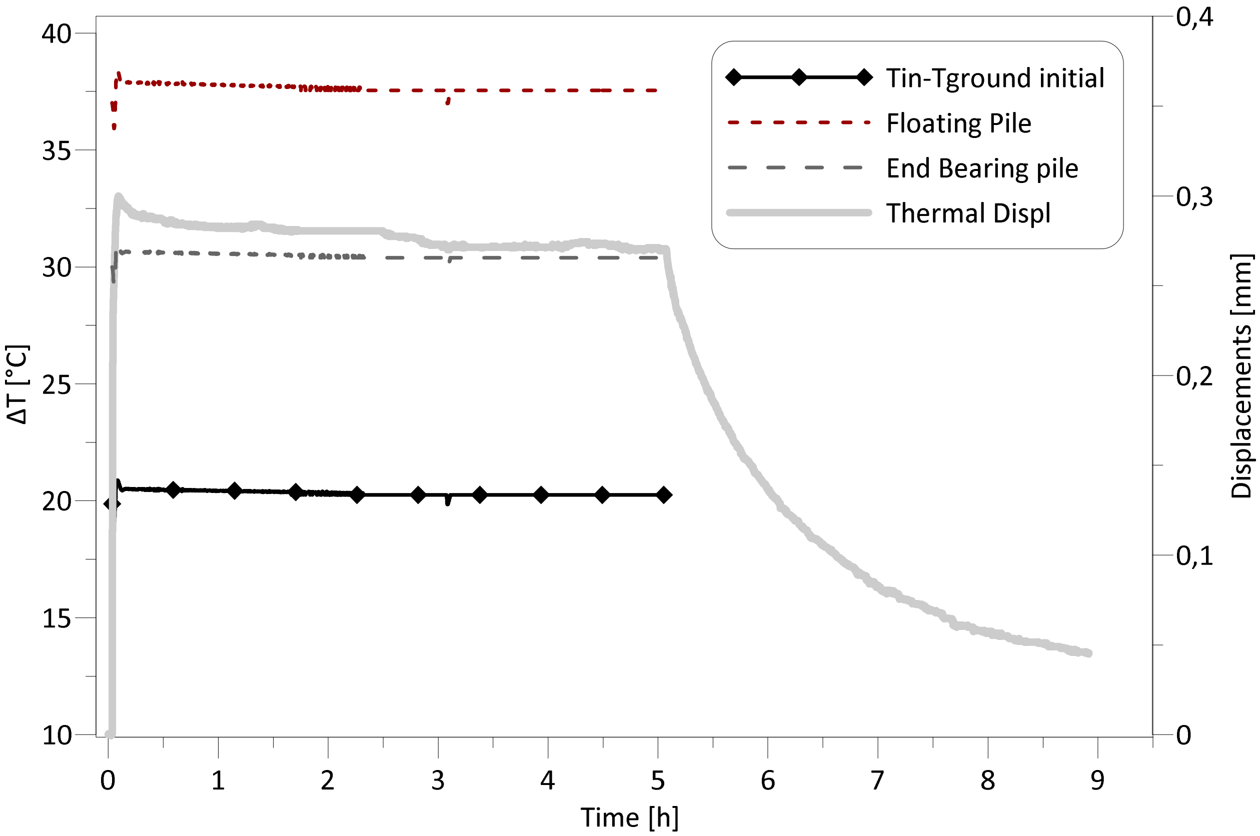

Figure 4-29: Pile's head thermal displacement (Thermal displ), Floating pile thermal displacement (Floating pile) and End-bearing pile thermal displacement (End Bearing pile) along with average temperature variation (Tin-Tground initial) during heating test at constant temperature.

Pile head displacement variations versus elapsed time follow the temperature variation trend for both heating and cooling tests at constant temperature. During heating pile head heaves while during cooling settles. The magnitude of the maximum and minimum thermal displacements during heating and cooling is 0.3 mm and -0.19 mm, respectively. The maximum temperature variation during heating is about 21 °C. The minimum temperature variation during cooling is -16.8 °C.

The thermal load profiles are plotted during heating and cooling episodes considering the maximum and minimum variations in Figure 4-31 (a) and Figure 4-31 (b), respectively.

The axial force during heating and cooling are obtained from the measurements of the SG applying the thermal correction as described in section 4.2.3. The sign convention is that compressive axial forces are positive.

As expected during heating compressive thermal loads are observed while during cooling tensile loadings occur. The maximum thermal load during heating is observed at 295 mm of depth (G2) and is 314 N. The minimum tensile load during cooling is -280 N at pile's mid depth (G3).

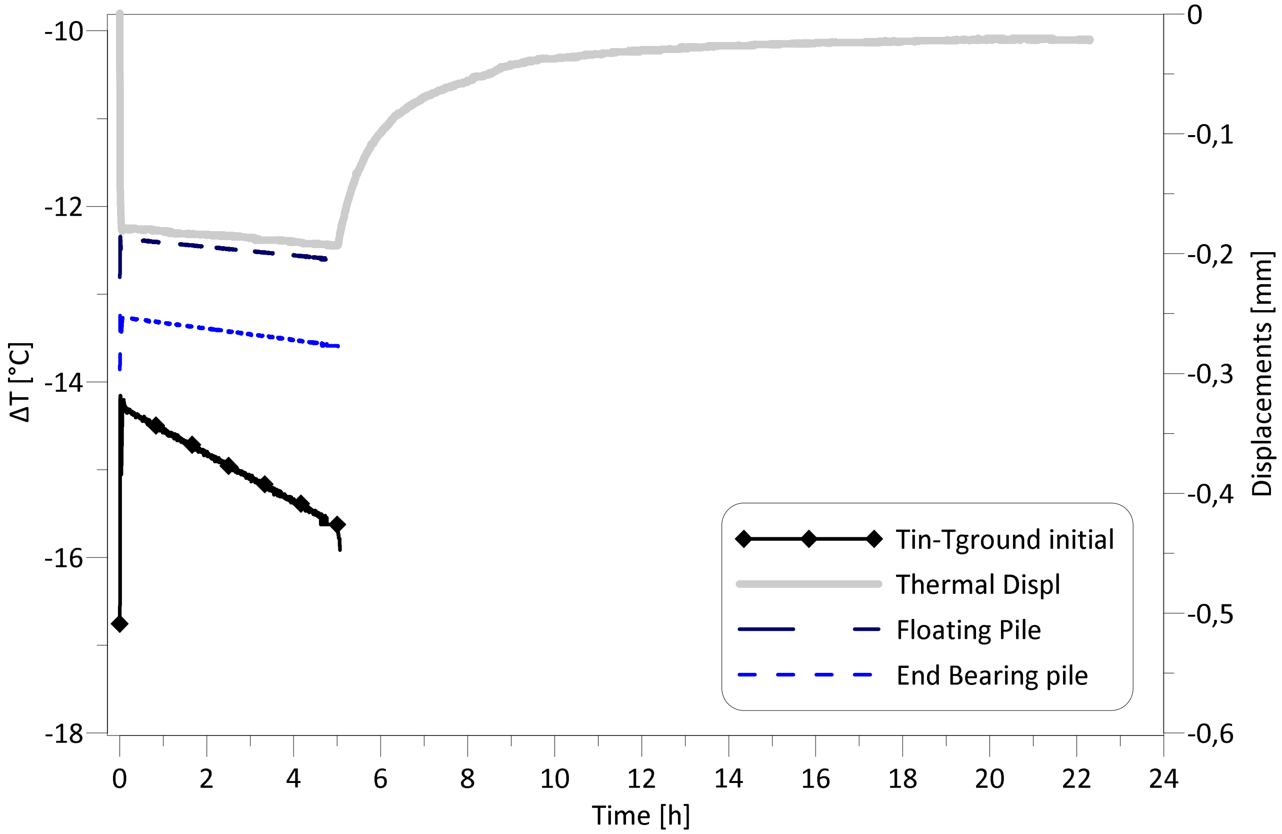

Figure 4-30: Pile's head thermal displacement (Thermal displ), Floating pile thermal displacement (Floating pile) and End-bearing pile thermal displacement (End Bearing pile) along with average temperature variation (Tin-Tground initial) during cooling test at constant temperature.

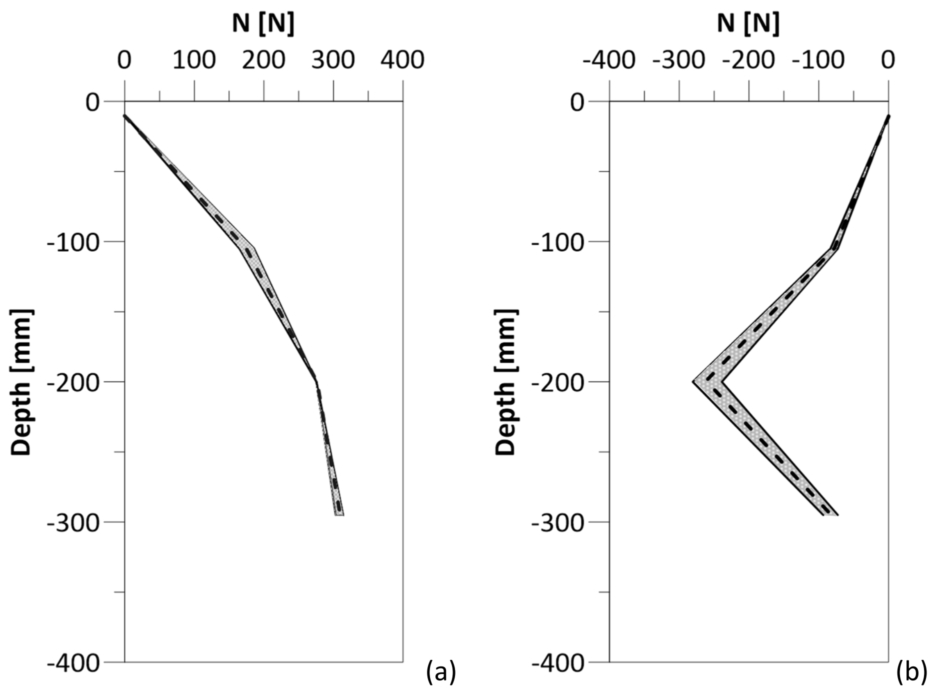

Figure 4-31: Thermal load profiles during (a) heating and (b) cooling thermal tests at constant temperature.

These magnitudes depend on the different level of thermal variations that are greater during the heating episode. During each thermal test, a slightly reduction of the axial load is observed. It could be observed that the SG measurements are in agreement with the measures of pile's head thermal displacements. During the heating test the measured displacement is very close to the end bearing displacement estimated assuming the NP at pile's toe. The maximum thermal load is observed at G2 depth which is the last gage working.

During the cooling test the evolution of measured displacement is closer to the floating pile displacement and the minimum thermal load is observed at pile's mid depth. These results are consistent and demonstrate the good quality of the measured performance considering a higher mobilization of pile's linear expansion coefficient.

4.5.3 Thermal tests at variable temperature

The results of the heating and cooling thermal tests at variable temperature are showed in this section. The assigned inlet water temperature during heating and cooling are plotted in Figure 4-18. Temperature of the soil were recorded by thermocouples Tc2, Tc7, Tc4 and Tc5. During the heating Tc3 acquisitions were replaced by Tc7. Air ambient temperature were also monitored during the tests. Soil temperature variations during the heating and cooling tests are plotted in Figure 4-32 and Figure 4-33, respectively along with ambient air temperature and inlet water temperature.

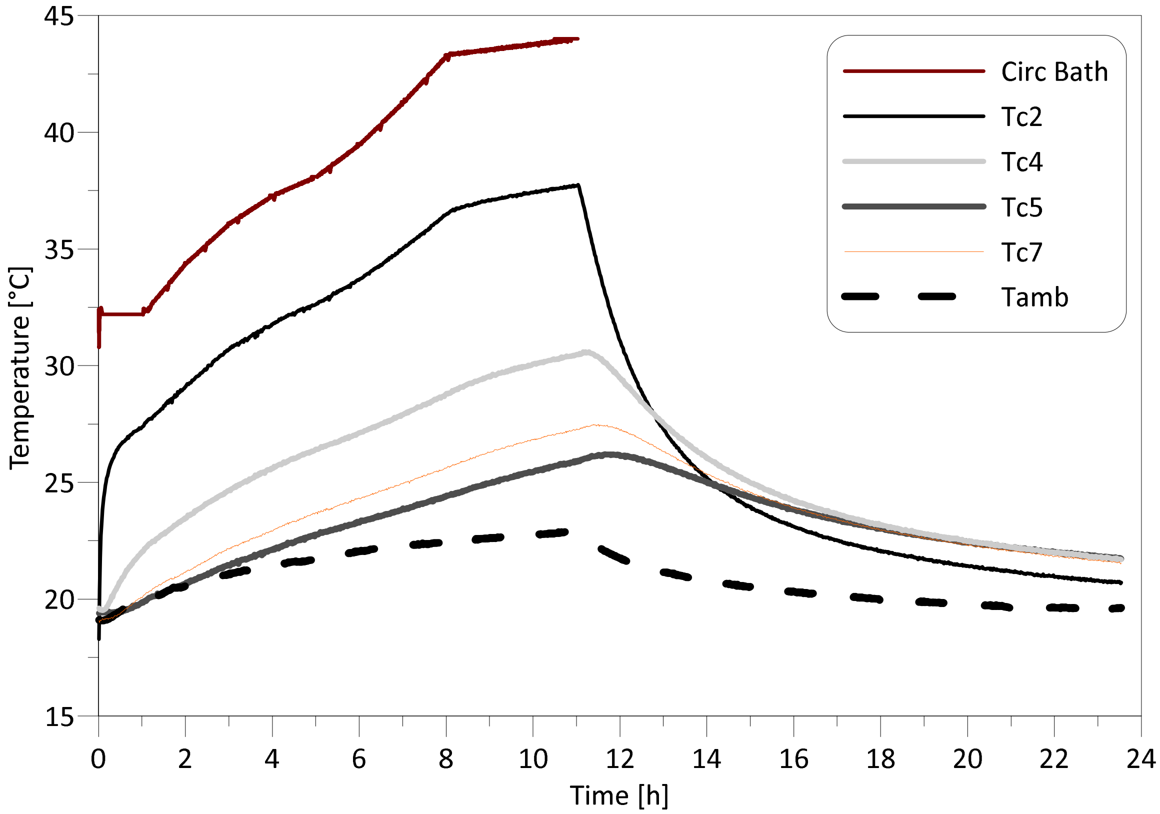

Figure 4-32: Soil temperature changes during heating thermal history at toe of pile-soil interface (Tc2), at 1D from pile and 200 mm depth from ground surface (Tc4), at 2D from pile and 200 mm and 100 mm depth from ground surface and (Tc5 and Tc7) along with ambient air temperature (Tamb) and Inlet water temperature (Circ Bath).

Before starting the heating test at variable temperature, the average soil temperature was 19.2 °C. For the heating thermal history, 1 day of monitoring during thermal rest was performed. At the end of the heating episode soil temperature measured by Tc2 was 37.7 °C. At 1D of distance from the pile the temperature measured by Tc4 was 30.5 °C. At 2D of distance from the pile the temperature measure by Tc5 and Tc7 was 25.9 °C and 25.3 °C. Twelve hours later soil temperature at Tc2, Tc4, Tc5 and Tc7 were 20.7 °C, 21.7°C, 21.7 °C and 21.5 °C, respectively. Temperature difference between Tc7 and Tc5, because the two thermocouples are placed at the same horizontal distance from the pile, can be caused both by the influence of the air ambient temperature that decreases with depth and by the heat transfer mechanism occurring in vertical direction along the heated pile. Prior to cool down the pile the average ground temperature was measured by means of all thermocouples except of Tc3. The initial soil temperature was 20.6 °C. After the end of the cooling history temperature of the soil and ambient air were monitored for twelve hours. At the end of the test Tc2 recorded 11.6 °C, at the end of the thermal recovery the temperature was 18.29 °C. Prior to cooling pile temperature measured by Tc2 was 18.9 °C. Considering that air ambient temperature before the test was 20.34 °C and after the recovery phase was 20.34 °C, it means that after 12 hours temperature of soil is still influenced by the cooling. Before starting the test and at the end of the recovery phase Tc1 measured 18.9 °C and 18.2°C therefore the heat transfer process is still occurring. The average temperature of soil at the end of the monitoring is 18.9 °C i.e., an average decrease of 0.7 °C was determined by eight hours of cooling.

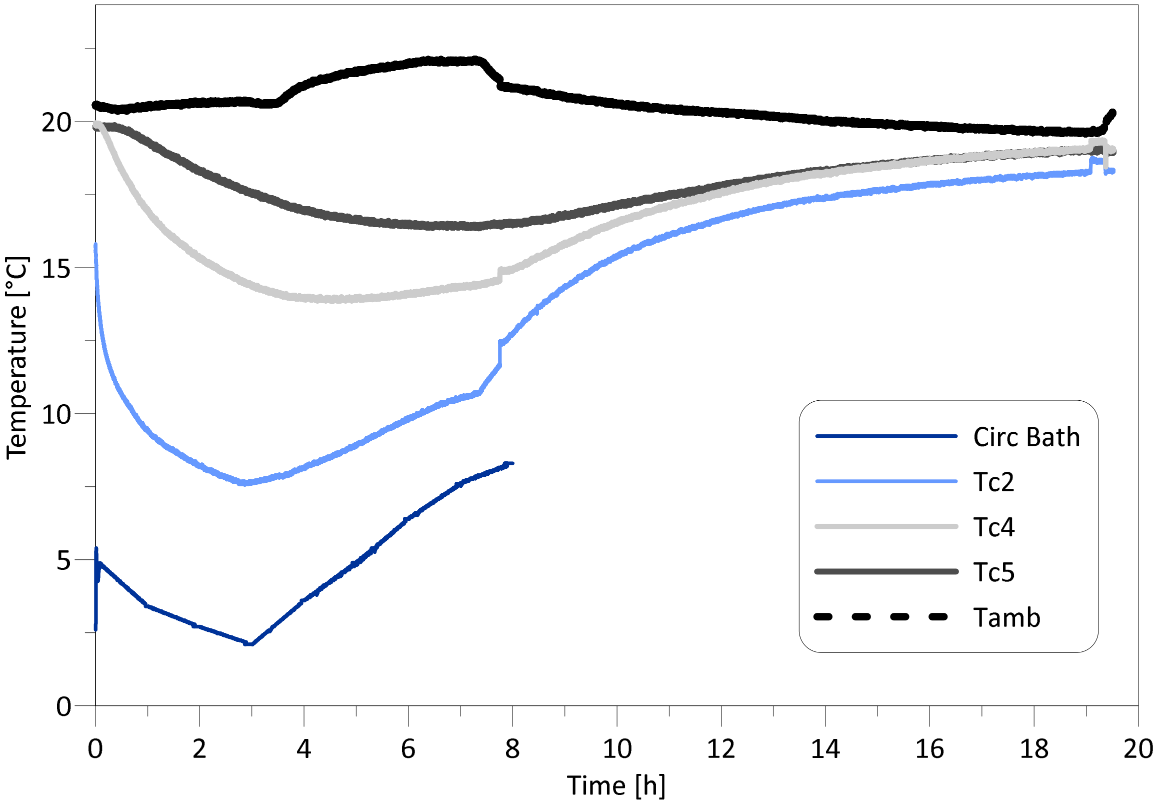

Figure 4-33: Soil temperature changes during cooling history test at toe of pile-soil interface (Tc2), at 1D and 2D from pile and 200 mm depth from ground surface (Tc4 and Tc5) along with ambient air temperature (Tamb) and Inlet water temperature (Circ Bath).

Thermal pile's head displacement was recorded during the heating and cooling thermal histories and the subsequent thermal recovery. Measured thermal displacement is related to $y_{Floating}$ and $y_{End-bearing}$ in Figure 4-34 and Figure 4-35 along with the thermal history of heating and cooling, respectively.The monitoring of pile's head displacement was performed for the same time duration of temperature's monitoring. The aim is to evaluate the displacement of the pile caused by temperature variations induced in the surrounding soil. The maximum and minimum temperature changing is 24 °C and - 17.8 C during heating and cooling test at variable temperature, respectively. The maximum pile's heave is 0.30 mm during heating. The minimum pile's settlement is -0.20 during the cooling test. For the heating episode at the end of the recovery phase a residual settlement of -0.01 mm is observed. In case of cooling at the end of monitoring the residual settlements is -0.0056 mm.

The axial force during heating and cooling are obtained from the measurements of the SGs and are plotted in Figure 4-36 (a) and Figure 4-36 (b), respectively. For each thermal history both the minimum and maximum values of the axial load along depth are plotted. During the cooling episode the thermal load profile is characterised by slightly variations that follow the evolution of thermal variations applied to the pile. As expected during heating compressive thermal loads are observed while during cooling tensile loadings occur.

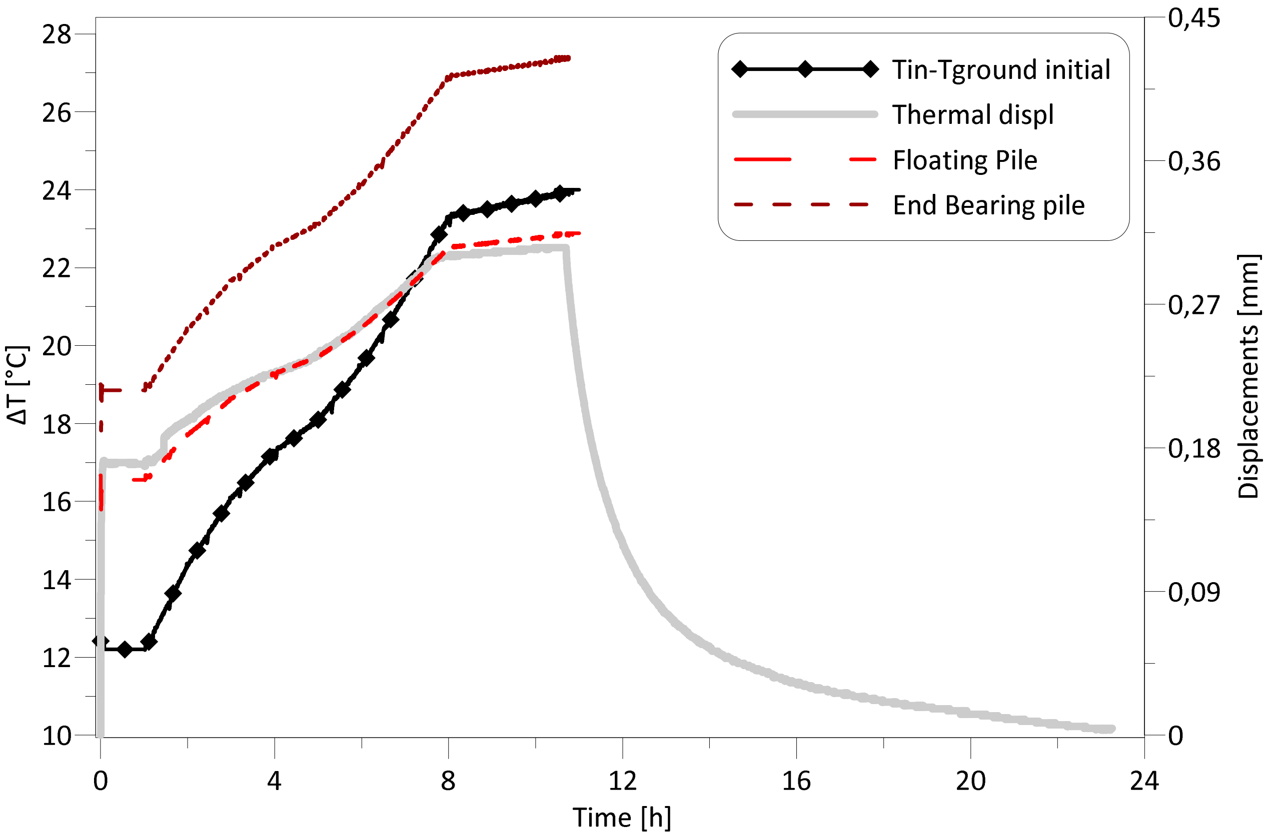

Figure 4-34: Pile's head thermal displacement (Thermal displ), Floating pile thermal displacement (Floating pile) and End-bearing pile thermal displacement (End Bearing pile) along with average temperature variation (Tin-Tground initial) during heating history.

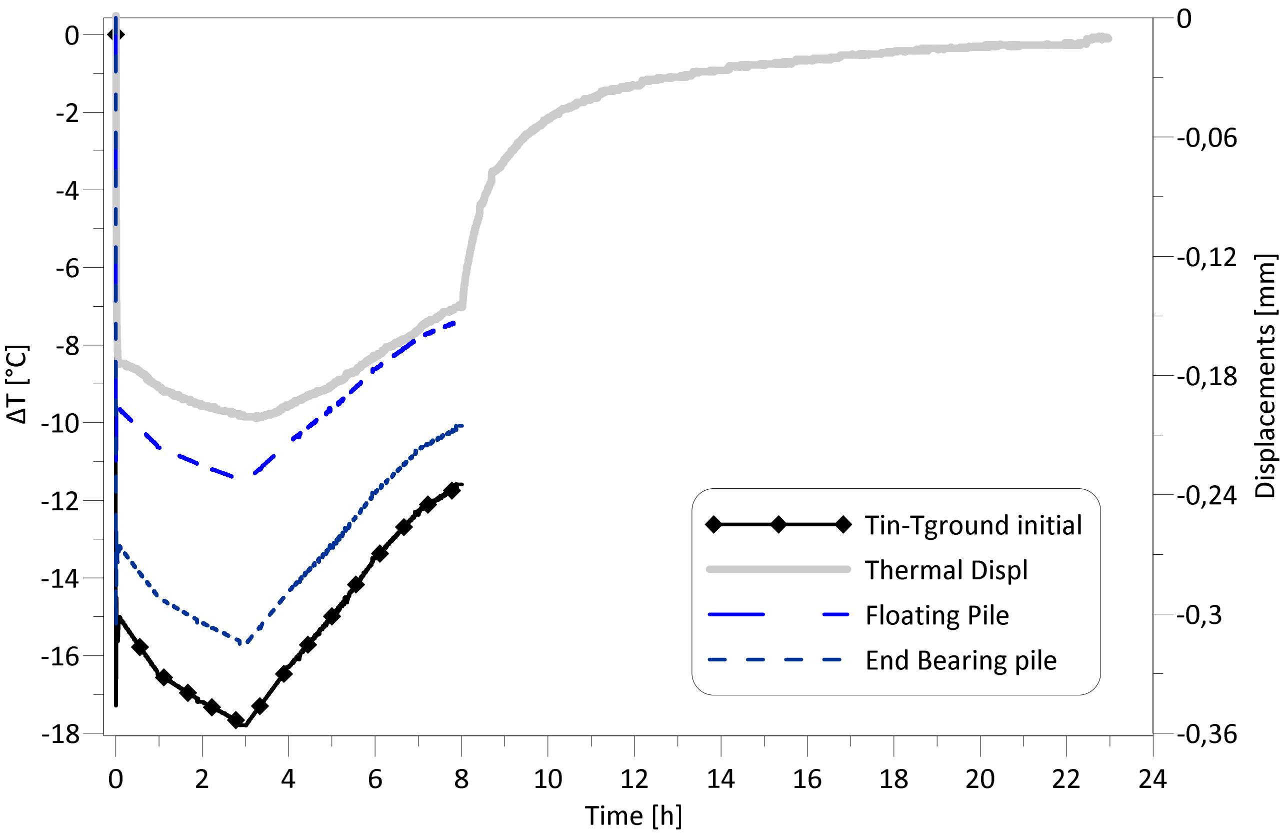

Figure 4-35: Pile's head thermal displacement (LVDT ave), Floating pile thermal displacement (Floating pile) and End-bearing pile thermal displacement (End Bearing pile) along with average temperature variation (Tin-Tground initial) during cooling history.

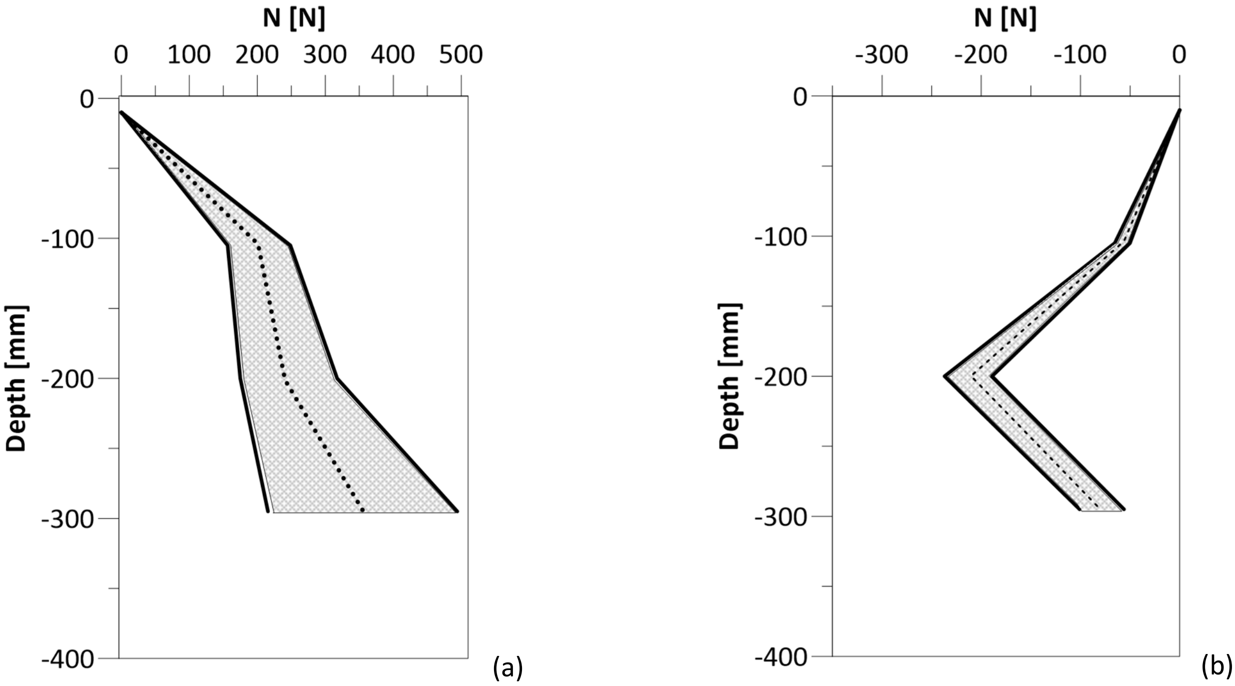

Figure 4-36: Thermal load profile during (a) heating and (b) cooling tests at variable temperature.

The maximum thermal load during heating is observed at 295 mm of depth (G2) and it is 494 N. The minimum tensile load during cooling is -238 N at pile's mid depth (G3). These magnitudes depend on the different level of thermal variations that are greater during the heating episode. Different thermal load transfer is observed during cooling and heating episode. During the heating test the measured displacement is closer to the floating displacement with respect to the end bearing pile, the maximum thermal load is observed at G2 depth i.e., high mobilization of the pile's linear expansion coefficient. During the cooling test the evolution of measured displacement is closer to the floating pile displacement and the minimum thermal load is observed at pile's mid depth i.e., high mobilization of the linear expansion coefficient of the pile.

4.5.4 Thermo-mechanical heating test at variable temperature

Thermo mechanical heating test was performed in three steps. During the first step the mechanical load is applied to the head while mechanical strains and displacements are monitored. During the second step the application of thermal variations is combined to the mechanical load. The third step corresponds to thermal recovery of about ten hours while the mechanical load is kept constant. During the first step, head load equal to 48.17 N is applied. This value corresponds to an allowable load using a SF=3. During the second step, while the mechanical load is kept constant, thermal loadings are imposed circulating heated water inside the pile. The applied thermal loading is reported in Figure 4-18 (red line). Prior to applying thermal variations, the mechanical load induced head settlement. The application of the mechanical load, step 1, is considered as the zero-time instant while thermal loadings have a time history.

During the test, the temperature of the pile and of the surrounding soil was continuously monitored by Tc1, Tc2, Tc4 and Tc5 (Figure 4-37). Prior to applying the thermal variations, the soil average temperature was about 18.85 °C. At Tc2 location a sudden increase of temperature is observed, reaching at the end of the eleven hours of heating 37.4 °C. Tc1, Tc4 and Tc5 maximum temperatures are 22.7 °C, 30 °C and 25.3 °C, respectively. After 10 hours from the end of heating the temperatures at Tc1, Tc2, Tc4 and Tc5 were 20° C, 20.2 °C, 21.1 °C and 21.1 °C, respectively.

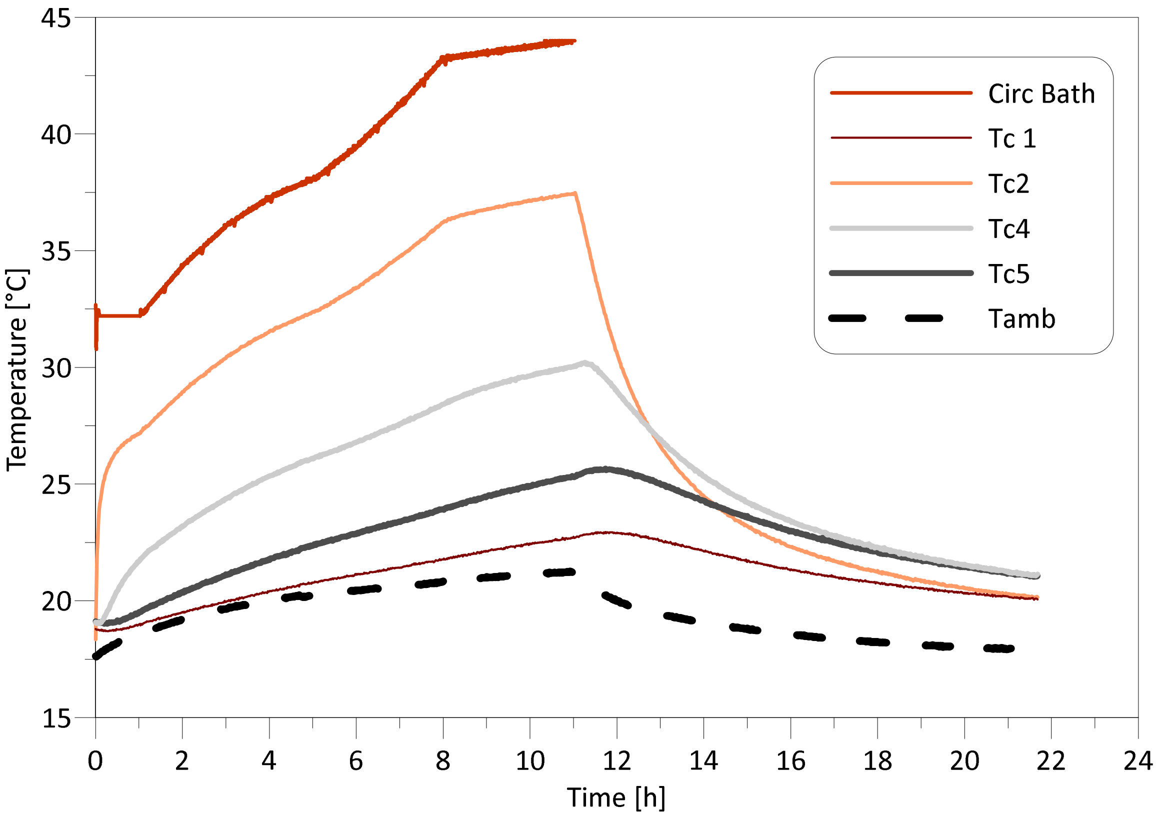

Figure 4-37: Soil temperature changes during thermo-mechanical heating at toe of pile-soil interface (Tc2), at 1D from pile and 200 mm depth from ground surface (Tc4), at 2D from pile and 200 mm depth from ground surface (Tc5), at 2D from the pile and 500 mm depth from ground surface (Tc1) along with ambient air temperature (Tamb) and Inlet water temperature (Circ Bath).

Pile thermal and thermomechanical displacements were monitored only during the first and second step of the test because of a power lack it was not possible to record LVDTs. Thermal and thermomechanical displacements are plotted in Figure 4-38. The full history of head displacement is represented by the light grey curve (*Total displ*). In fact, at time t=0 there is the downwards movement of the piled head caused by head mechanical load (about- 0,09 mm) while later the curve responds to the uplift caused by the heating. The black curve called *Thermal displ* is simply obtained by the difference between the measured total displacement and the settlement measured at the end of mechanical loading. The maximum thermal variation that occurred during test is 25.15 °C and the maximum thermo-mechanical displacement is 0.29 mm while the maximum thermal displacement is 0.38 mm.

Pile's head purely thermal displacement is plotted along with the displacement of the end bearing and floating pile and temperature changing in Figure 4-39. As the thermal load is applied the pile head heaves and a sudden upward pile's displacement is observed. Thermal displacement measured versus elapsed time lies between the displacement of the Floating and End Bearing. Therefore, if the mobilised thermal expansion coefficient of the pile is close to the free expansion coefficient of the aluminium the NP position is expected to be between pile's mid depth and toe. NP position is observed from the thermal load profile, i.e., the location of the maximum thermal axial load.

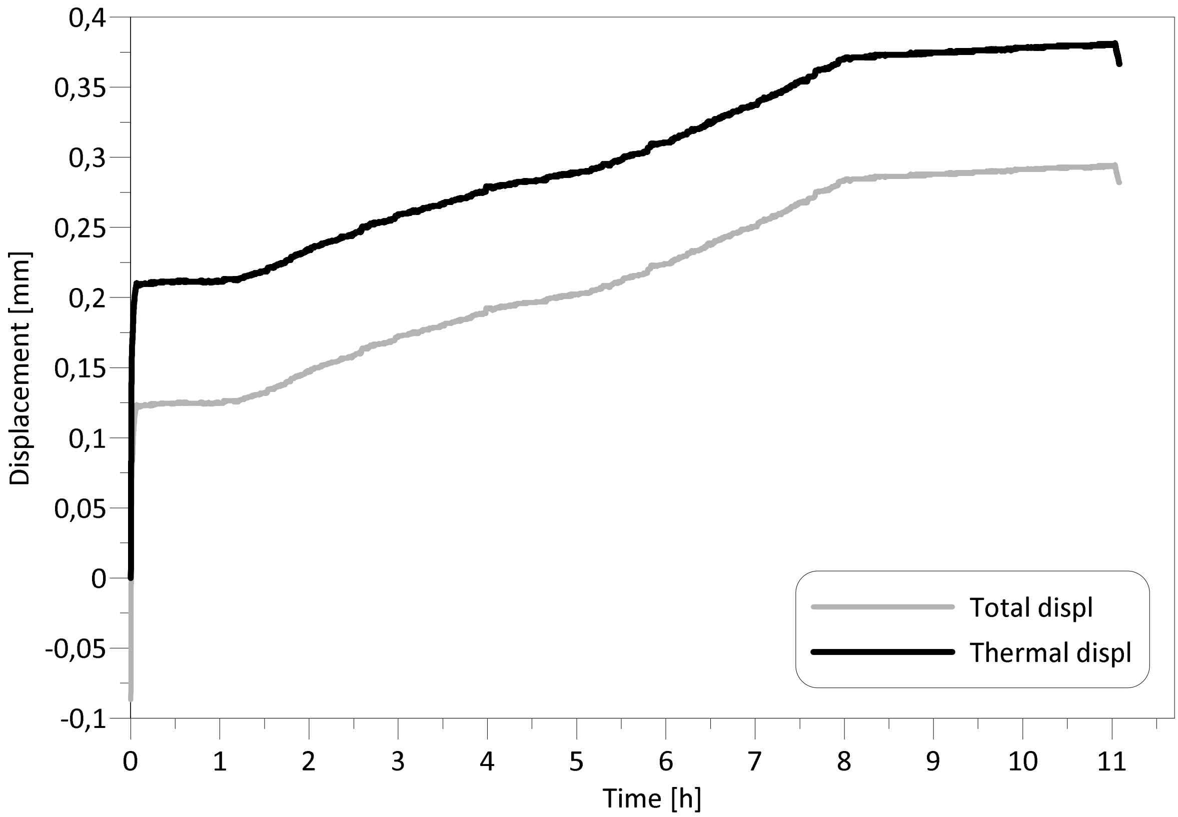

Figure 4-38: Thermal (Thermal displ) and thermo-mechanical (Total displ) pile's head displacements versus elapsed time.

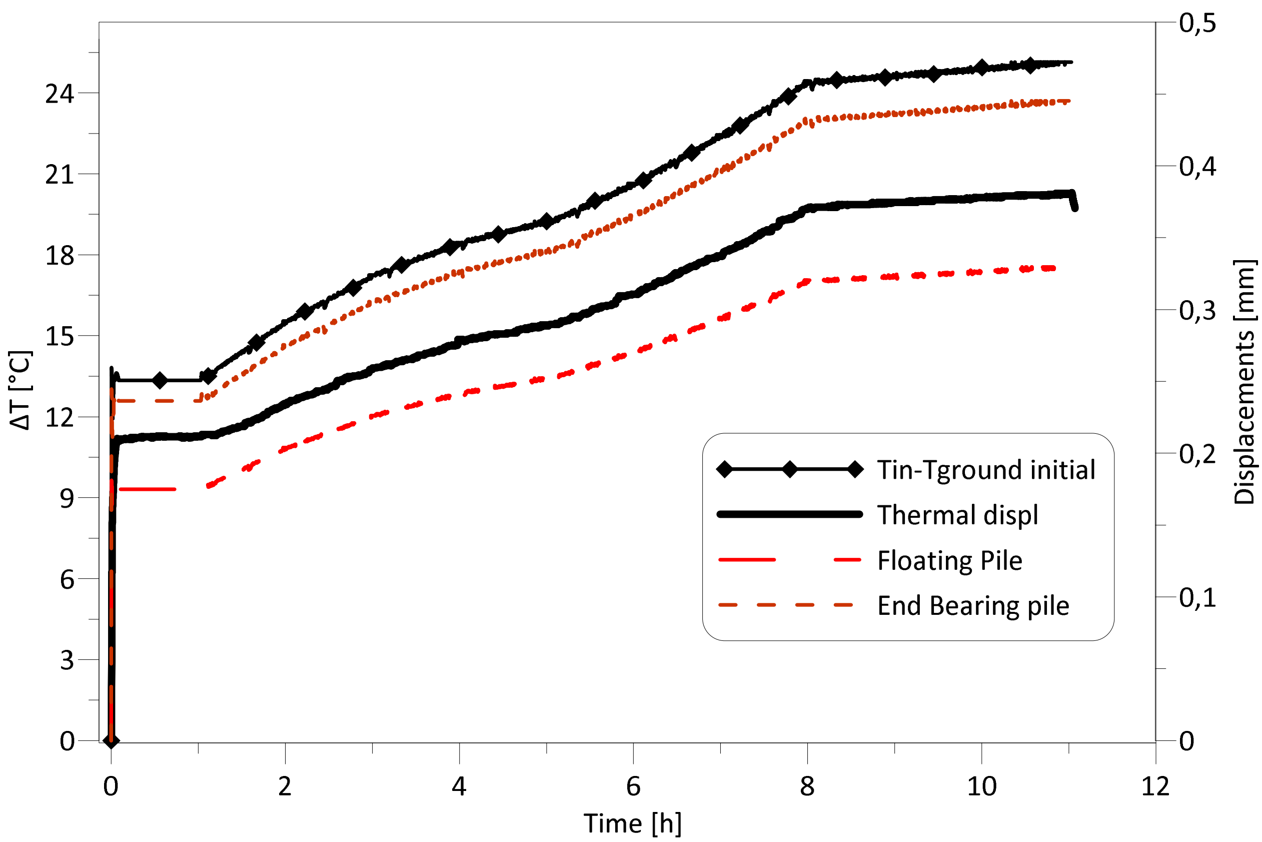

Figure 4-39: Pile's head thermal displacement (Thermal displ), Floating pile thermal displacement (Floating pile) and End-bearing pile thermal displacement (End Bearing pile) along with average temperature variation (Tin-Tground initial) during the thermo-mechanical test.

In Figure 4-40 (a) thermomechanical axial profiles corresponding to the minimum and maximum profiles occurring during the test are plotted as black straight lines. The purely thermal maximum and minimum load profiles are reported in Figure 4-40 (b).

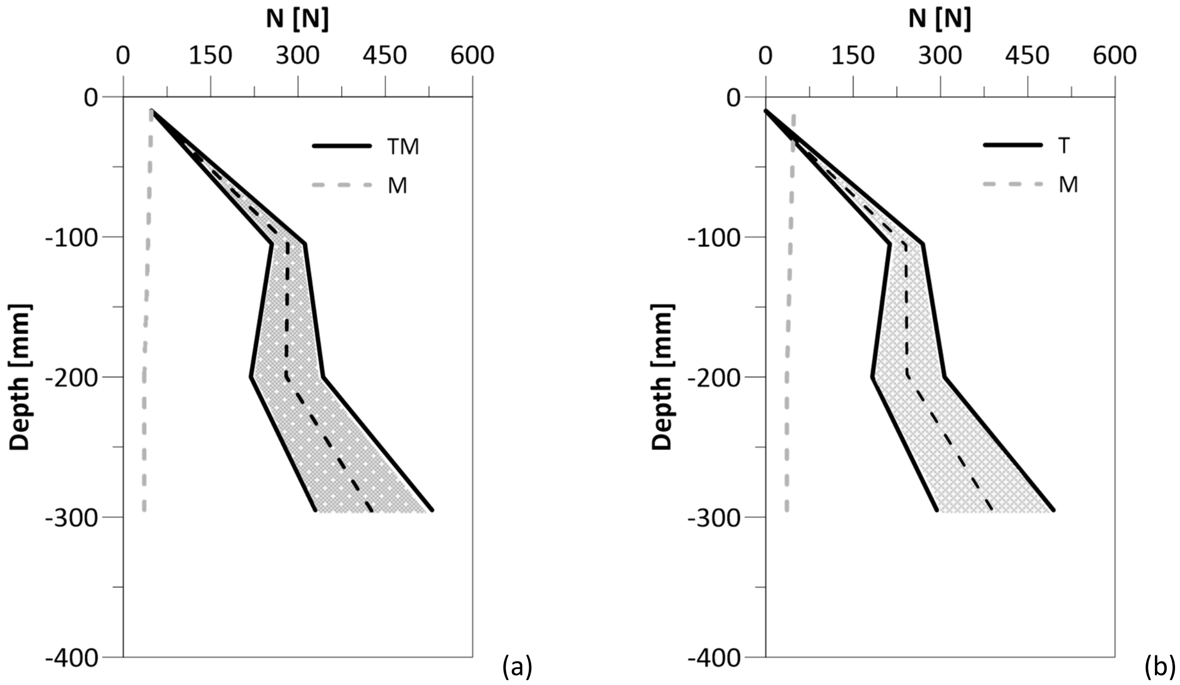

Figure 4-40: (a) Thermomechanical (TM) and (b) thermal (T) load profiles envelope during the thermomechanical heating history along with the purely mechanical (M) profile obtained in the first step of the test.

Both thermal and thermomechanical profiles are plotted along with the axial load profile (M) obtained during the first step and induced by purely mechanical load (Figure 4-40 a and Figure 4-40 b). The axial loadings induced by the thermal variations are larger of one order of magnitude with respect to the mechanical loadings. This is of course connected to the pile's dimensions and aluminium's linear expansion coefficient. About 530 N is the maximum thermomechanical load and it is observed at the end of the test. The maximum thermal load at the same instant and depth is 494 N. Both for thermal and thermomechanical cases, Figure 4-40 (a) and Figure 4-40 (b), it is observed that the maximum axial load occurred at 300 mm (G2) of depth from pile's head. Therefore, the NP is located a depth that ranges between pile's mid depth and pile's toe, demonstrating that the higher mobilization of the coefficient of thermal expansion.

4.5.5 Mobilised side friction and influence of matric suction

The mobilised side friction was estimated for the three elements (zones) reported in Figure 4-25 during each test. In Figure 4-41 (a) and Figure 4-41 (b) the envelope of the mobilized side friction during thermal tests at constant temperature (4.5.2) is plotted for the heating and cooling episode, respectively. The sign convection adopted is that downward shaft friction is assumed as negative. In Figure 4-41 (a) the maximum mobilization of shaft friction occurred in the first zone where the maximum friction is about 21 kPa. The mobilised friction decreases with depth, in the second and third zones 11.2 KPa and 7.8 kPa are the maximum frictions in absolute value. In the case of cooling test at constant temperature, the maximum mobilised thermal friction in absolute value occurred in the second third zones with the maximum friction reached in the deeper zone (about 21 KPa). At mid depth, mobilised friction is reversed, in the upper part of the pile, first and second zones, the mobilised friction is upward. In the lower part, third zone, mobilized friction is downward.

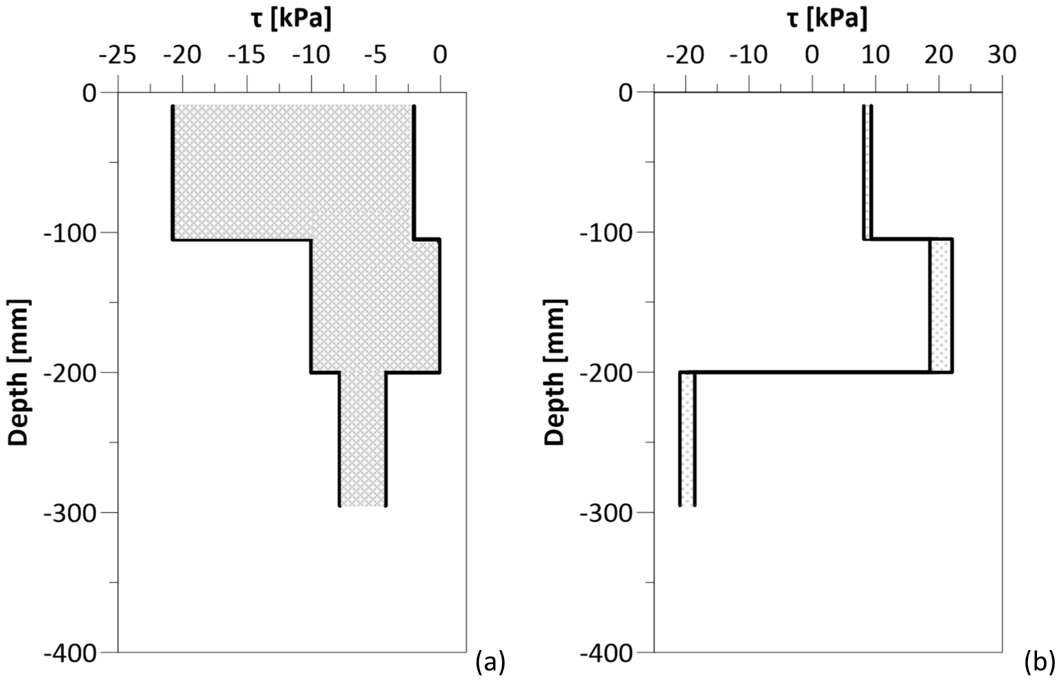

Figure 4-41: Thermal mobilized friction during (a) heating and (b) cooling thermal tests at constant temperature.

In Figure 4-42 (a) and Figure 4-42 (b) the envelope of the mobilized side friction during thermal tests at variable temperature (4.5.4) is plotted for the heating and cooling episode, respectively.

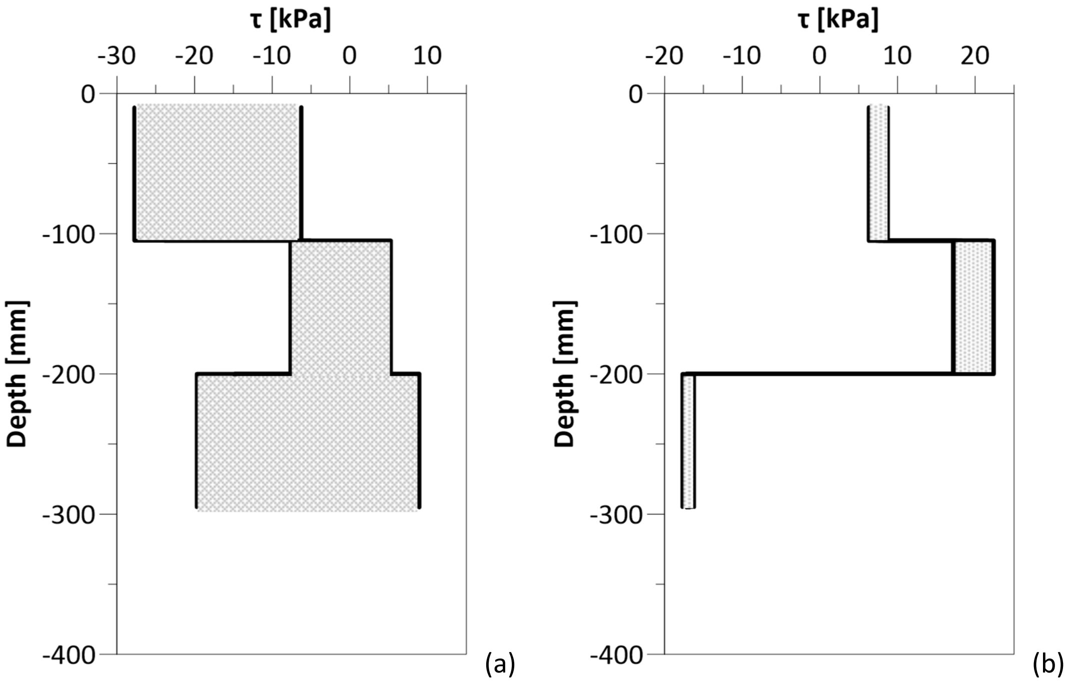

Figure 4-42: Thermal mobilized friction during (a) heating and (b) cooling thermal histories.

During the heating thermal test at variable temperature, the higher mobilization of shaft friction is observed in the first and second zone where the minimum thermal friction is about -28 kPa and -20 kPa, respectively. During the cooling thermal test at variable temperature, the mobilized friction along pile's shaft is very similar to those observed during the thermal test of cooling at constant temperature (Figure 4-41 (b)). At mid depth the mobilized side friction is reversed. From the envelope of side shear Figure 4-42 (b) the maximum and minimum thermal frictions are 18 kPa and -22 kPa, respectively.

The thermal (T) and purely mechanical (M) and thermomechanical mobilized side friction during the thermomechanical heating test at variable temperature (4.5.4) are plotted in Figure 4-43 (a) and Figure 4-43 (b), respectively.

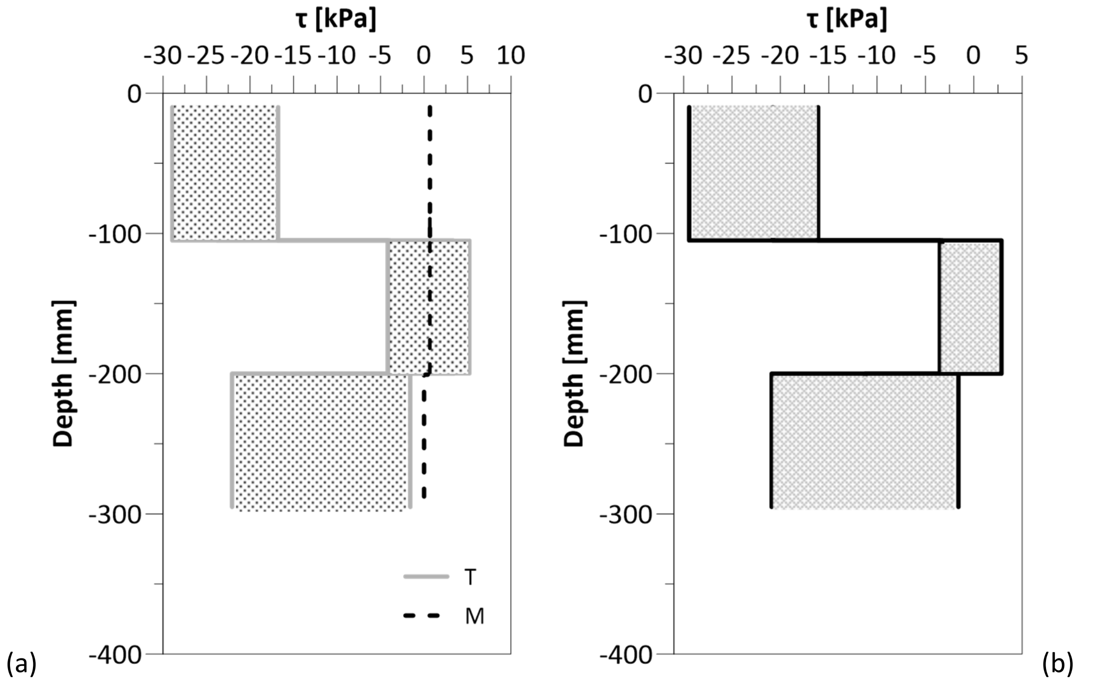

Figure 4-43:Mobilized side friction during the thermomechanical heating test (a) thermal (T) and purely mechanical (M) profiles and (b) thermomechanical profiles

The mechanical mobilised friction is lower than 1 kPa as could be observed from Figure 4-43 (a). The mobilization of side shear occurs only in the first and second zones, in the third zone, as observed during the loading test the side friction in not mobilised by the mechanical load applied at pile's head. Thermal side friction is computed from the thermal axial load. In the third zone the thermomechanical and thermal side friction match because side friction is not mobilised by the purely mechanical loading. The thermal loads mobilised higher side friction with respect to the mechanical load as could be observed by Figure 4-43 (a). The higher mobilization occurs in the first and third zones where the minimum side friction is about -22 kPa and -29 kPa, respectively.

The observed mobilised shaft frictions along pile's depth are larger of one order of magnitude with respect to those mobilised by the purely mechanical loading. According to Laloui and Sutman (2020) it should be acknowledged that lower end-restraint not only means higher axial displacements but also larger mobilization of shaft resistance due to the relative displacement of the pile with respect to the surrounding soil.

The magnitude of mobilised shaft friction along the pile-soil interface could seem not in agreement with the average shaft resistance of the model pile. If the ultimate shaft resistance is computed according to the well-known β Method, the average ultimate shaft resistance is about 1.4 kPa. Typically, pile foundations are designed assuming saturated or dry conditions. Vanapalli et al. (2011) proposed a simple technique to estimate the shaft resistance in unsaturated soil conditions using the SWCC (Soil-Water Characteristic Curve) i.e., the degree of saturation (S_r) and the matric suction ($u_a - u_w$). The total skin friction of piles in unsaturated sands (s_{ftot}) can be estimated as the summation of two contributes according to Equation 4-11.

Equation 4-11: $s_{ftot} = s_f + s_{(u_a - u_w)}$

Where: s_f is the skin friction computed according to the β Method and $s_{(u_a-u_w)}$ is the contribution of ultimate shaft resistance due to matric suction. $s_{(u_a-u_w)}$ can be estimated extending the approach proposed by Vanapalli et al. (1996) for predicting shear strength of unsaturated soils using the SWCC and the effective shear strength parameters as written in Equation 4-12.

Equation 4-12: $s_{(u_a-u_w)} = (u_a - u_w)(S_r)tan\phi$

Where: $u_a - u_w$ is the matric suction in kPa, $S_r$is the degree of saturation and ϕ is the angle of internal friction.

The degree of saturation of soil can be estimated from the volumetric water content (θ) and soil porosity (n) according Equation 4-13.

Equation 4-13: $S_r = \frac{\theta}{n}$

During the test 0.11 average volumetric water content was monitored by means of the TDRs installed in the soil. Knowing the initial porosity, n, at which the soil was pluviated in the experimental box it was possible to estimate $S_r = 18\ \%$ according to Equation 4-13. During the tests 206 kPa of matrix suction was also measured by means of a miniature tensiometer. Assuming the measured values for the matric suction and degree of saturation, the contribution to skin resistance due to matrix suction can be easily computed according to Equation 4-12. The additional skin resistance provided by the matrix suction is about 30 kPa.

Taking into account the experimental results of Vanapalli et al. (2011) and the measured suction and degree of saturation the thermal and thermomechanical mobilised shaft friction monitored during the experimental campaign never exceed the ultimate side capacity of the pile.

4.5.6 Concluding remarks and observations about tests on Model A

For all thermal and thermomechanical tests different behavior is observed under cooling and heating. Two reference schemes are considered for comparisons: floating pile - i.e., a pile where the NP is exactly in the middle with the upper half of the shaft moving upwards and the lower half moving downwards - and end bearing pile – i.e., a pile where NP is close to the pile tip. During heating pile's head moves upward, measured thermal displacement is closer to the displacement of the end bearing pile. During cooling pile's head moves downward and the measured thermal displacement is closer to the displacement of the floating pile.

Different thermal load transfer is of course observed with maximum stress location placed at different depths along pile's length. During cooling the NP is located almost at mid depth while during heating the NP position is closer to pile's toe as confirmed from the shaft friction diagrams. DDRs during cooling and heating are 0.88 and 0.78, respectively. This finding agrees on previous laboratory investigations as showed from the literature review of chapter 2. In most of the investigations carried out the mechanisms for pile response outlined predicts larger pile movements during cooling compared with heating (Bourne-Webb and Bodas Freitas, 2020) and smaller stresses along pile's depth. The NP different depth during cooling and heating could be attributed to the different contribution of the tip resistance during heating and cooling. The conical shape of pile's tip contributes to this phenomenon determining different behavior during the expansion and contraction of the pile.

During both thermal and thermo-mechanical tests at the location of pile's head (G5 location) the measurements provided by the sensor allow considering that the pile's head is free to expand or contract. No additional stresses are measured, demonstrating that the design of the system and the devices used allow to really minimize friction between the guide system and the pile. The thermo mechanical test carried out demonstrate the effects of the mechanical loading on the pile thermal behavior, compared to the those induced by thermal variations, are almost negligible both in terms of axial loadings and thermal displacements of the head. The maximum thermal load observed during purely thermal test of heating and thermo-mechanical heating is comparable, demonstrating that the thermal loads induce greater effects with respect to the mechanical loadings in the case of small-scale test. DSRs computed both during heating and cooling are smaller than 0.10 on average with slightly higher magnitudes in the case of heating. The mobilized shaft friction observed during the tests agrees on the skin friction computed taking into account the additional contribute due to matric suction. During the test in fact the monitoring of soil permittivity along with matric suction allows estimating the total shaft friction resistance (4.5.5).

Purely thermal and geotechnical aspects should be monitored at the end of the heating and cooling to evaluate the heat transfer process evolution and its effect on pile-soil interaction (reversible or irreversible effects). The longest recovery phases were monitored in case of purely thermal tests at variable temperature. In both cases a small and practically negligible residual settlement was observed. This value was slightly different in the heating test compared to the cooling one but in both cases of the order of a few percentage points with respect to the maximum value recorded under the maximum thermal load.

4.6 *Small scale tests on Model B*

4.6.1 Load Test to Failure

The aim of the test is to determine the pile bearing capacity, its load settlement relationship, and the transfer curves of the side shear on Model B. As described in section 4.4 the applied loads determine an increase of soil stress state, therefore higher pile capacity along with different load transfer mechanism with respect to Model A are expected. As on Model A, maintained load test is carried out and the load history consists in a single loading cycle from zero to the maximum load test, followed by unloading steps down to zero. The loads are applied to the pile in the same way, through iron-cast weights of about 23.53 N placed on the still plate at the head of pile and inserted in the load guide. Load was applied in eleven increments taking the load to 233.73 kPa, 467.30 kPa, 701.34 kPa, 881.58 kPa, 1061.18 kPa, 1240.79 kPa, 1419.96 kPa, 1600.10 kPa, 1780.12 kPa, 1960.33 kPa and 2107.61 kPa. Unloading is carried out following the same number of steps of loading. The loading procedure is plotted in Figure 4-44.

The load settlement relationship is plotted in Figure 4-45. The load of 282,91 N was assumed as the conventional ultimate bearing capacity that corresponds to a settlement of 10% D. During the unloading to zero the residual pile head settlement was very close to the total settlement measured at 282,91 N (2.8 mm). Because the soil is in a loose state punching failure is observed at pile's toe therefore the pile's head settlement is almost irreversible. Prior to starting the load test, the pile was loaded to 58.84 N and unloaded. Therefore, during the first three steps the loading-settlement relationship is a reloading path, characterised by greater stiffness.

The application of the weight at soil surface determines, as expected, an increase of the pile's bearing capacity. An estimate of the increase of pile's resistance depending on the increase of the stress level can be obtained by the Equation 4-14.

Equation 4-14: $$Q = Q_s + Q_p - \sum W = \left(s \cdot \pi d L_{pile}\right) + \left(p \cdot \pi d^2\right) - \sum W = \left[k\left(\frac{\gamma' L_{pile}}{2} + \Delta\boldsymbol{\sigma}'\boldsymbol{z}\right)\mu \cdot \pi d L\right] + \left[N_q\left(\gamma' L_{pile} + \Delta\boldsymbol{\sigma}'\boldsymbol{z}\right) \cdot \pi d^2\right] - \sum W$$

As described for Model A, the pile could be ideally divided into four zones comprised between two subsequent SGs. The vertical effective stress increase determined by the weights applied at soil surface along the soil vertical adjacent to soil pile-interface is reported in Table 4-4 for each zone of the pile.

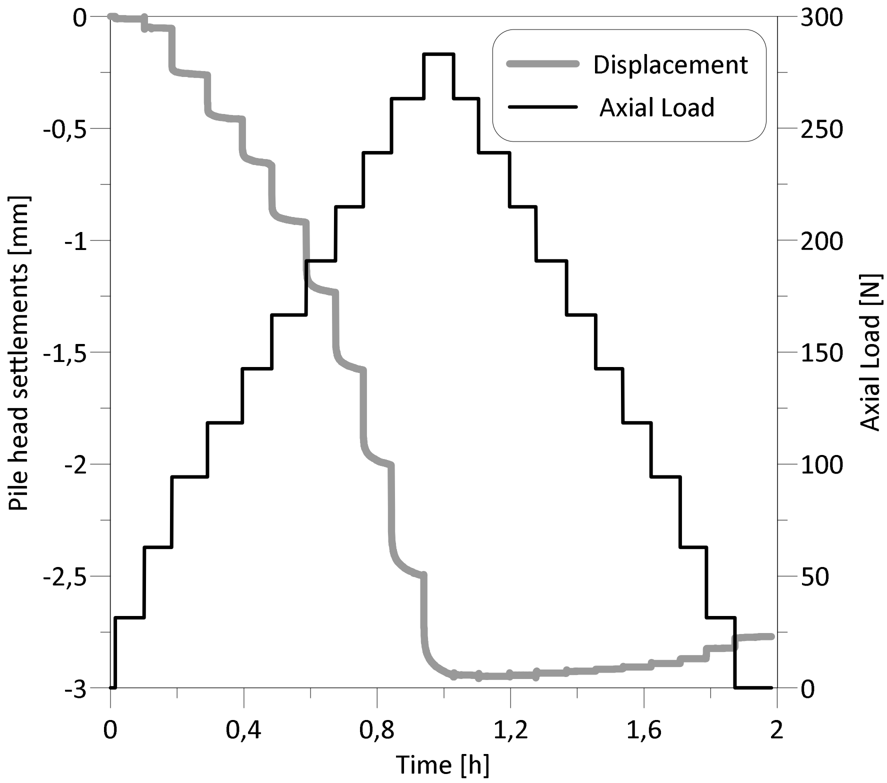

Figure 4-44: Loading procedure for the purely mechanical test. Load steps and measured displacement during the time duration of the test.

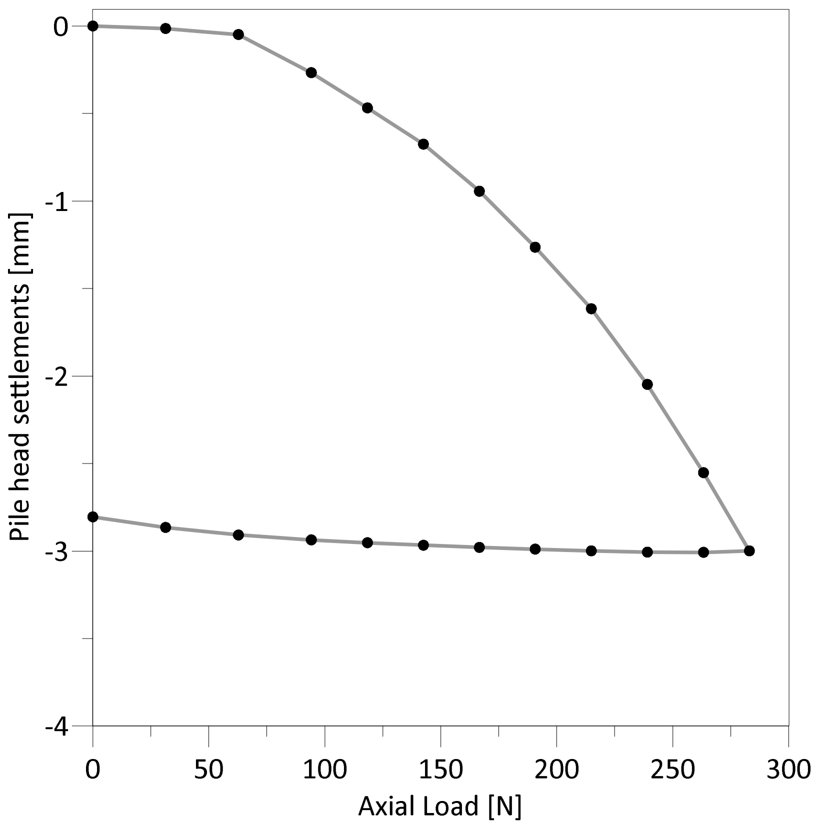

Figure 4-45: Load-Displacement Curve from load test to failure on Model B.

Table 4-4: Increase of vertical stress (Δσ'z) induced by the load applied at soil surface.

Zone	Δσ'z average [kPa]
1	3.59
2	5.93
3	5.73
4	4.64

The term $\Delta\boldsymbol{\sigma}'\mathbf{z}$ of Equation 4-14 corresponds to Δσ'z average at zone 2 (Table 4-4) in the case of shaft friction. For the toe resistance the term $\Delta\boldsymbol{\sigma}'\mathbf{z}$ of Equation 4-14 refers to the fourth pile zone of Table 4-4.

The increase of the confining stress induced by the loads applied at soil surface determines soil stiffness increase. The soil secant stiffness at 50% of the ultimate pile's bearing capacity is increased of about 40%-with respect to Model A.

The load distribution along the test pile length at the end of each load step is shown in Figure 4-46.As the load increases, shaft friction starts to be mobilised in the first zone between pile head (G5) and 105 mm depth (G4) and slightly in the second zone between 105 mm (G4) and 200 mm (G3). With increasing number of loading steps, the shaft friction mobilization along pile depth is observed. During the last loading step 75 % of the load is transmitted at 300 mm depth from pile head (G2).

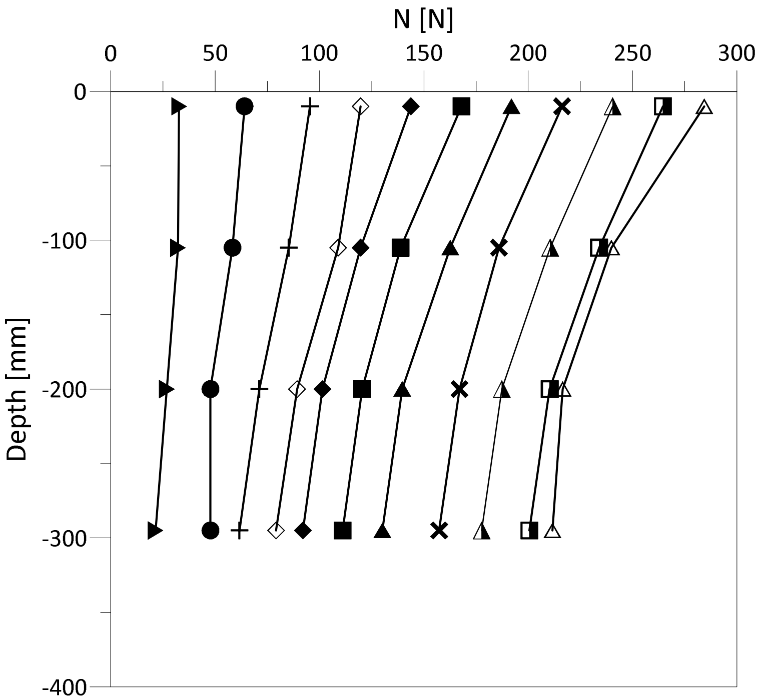

Figure 4-46: Axial force distribution along pile's depth

The mobilized side friction is evaluated at zones 1,2 and 3 and plotted in Figure 4-47 (a), Figure 4-47 (b) and Figure 4-47 (c), respectively. The effect of the weights at soil surface is greater on the second zone. The shaft friction mobilised in the second zone is higher with respect to the shaft friction mobilised in the other zones. In the second zone of the pile the greater increase of vertical stress, caused by the weights at soil surface, occurred with respect to the first zone and the third zone.

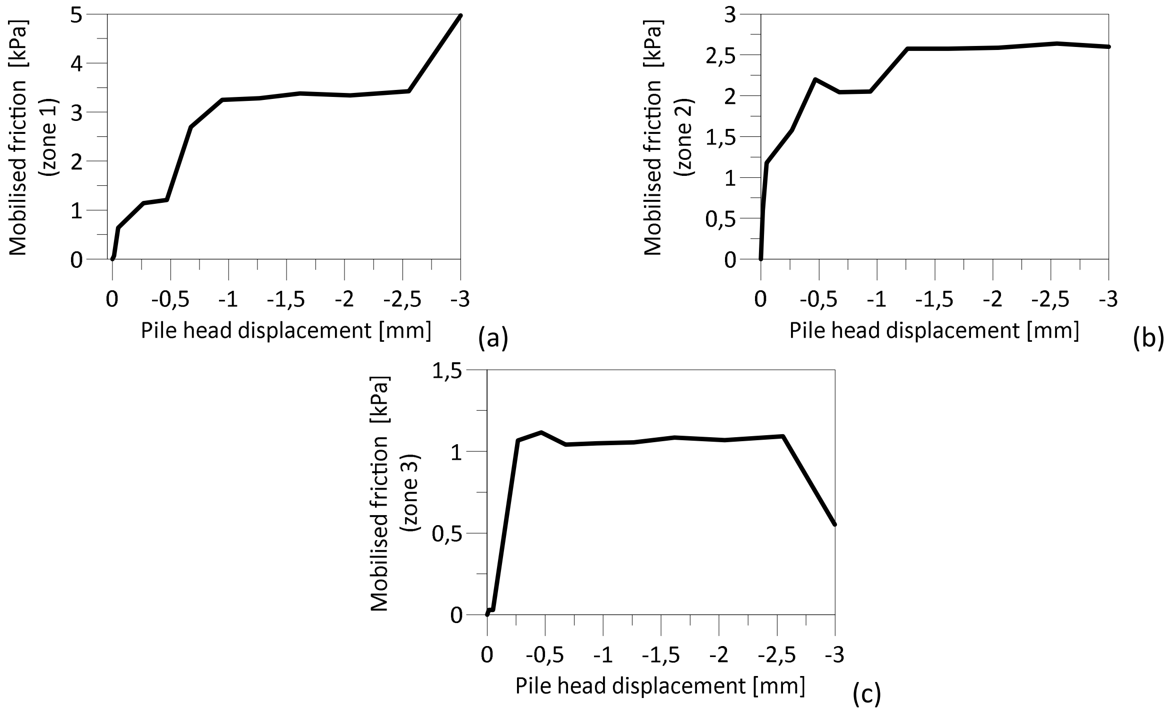

Figure 4-47:Mobilised friction along the pile: (a) at zone 1, (b) zone 2 and (c) zone 3.

The mobilised friction at different pile's zones is plotted considering both Models A and B in Figure 4-48.

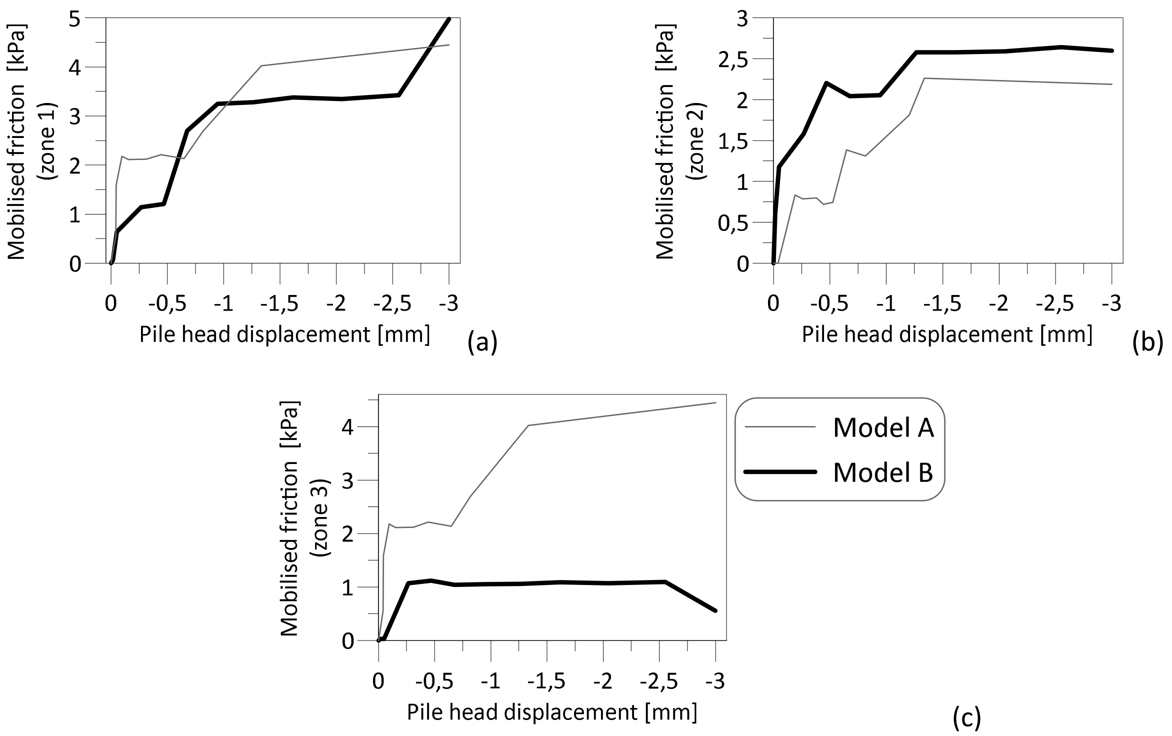

Figure 4-48:Comparison between Mobilised friction along the pile in Model A and Model B: at zone 1 (a), zone 2 (b) and zone 3 (c).

The main effect of surface loads is a greater mobilisation of the shaft friction in the second zone of the pile and a reduction in the third zone. The load transfer mechanism, as expected, is different between free field and loaded surface conditions. One of the main benefits of loaded surface, is reached in terms of soil stiffness, that being higher in this configuration, allows applying higher mechanical loads and increase the effects of the interaction between pile and soil.

The axial load at depth of SG1 i.e., close to pile's depth was not provided because the transducer was not replaced before starting the tests on Model B. To replace SG the coat of the pile must be removed and to avoid modifying the roughness of pile and to the aim of comparing the results provided by the two models the coat was not removed.

4.6.2 Cyclic Thermo-mechanical heating test

As described in 4.4.4, all the thermo-mechanical tests are carried out performing a first mechanical step. During this first step a dead load of 96.67 N, corresponding to 30% of the pile-soil system conventional resistance, is applied to the head of pile while pile's head settlement, mechanical strains and undisturbed soil temperature were monitored. Pile's head average mechanical settlement is about -0.07 mm while the initial average temperature of the soil is about 15.14 °C. The total time duration of the cyclic thermal part is about 106 hours during which the mechanical load applied in the previous phase is kept constant and combined to the cyclic thermal loading of Figure 4-19 (a). The last step of the test corresponds to a recovery phase where thermal loads are not applied to the pile, mechanical load is kept constant, and temperatures of soil and ambient air are monitored. During this phase it was not possible to monitor displacements and deformations of the pile but only air and ground temperatures.

During the test soil temperature at different locations were measured by Tc2, Tc3 and Tc4. The outlet temperature of water was also measured during the test and plotted in Figure 4-49 along with the air temperature, the inlet water temperature and soil temperatures.

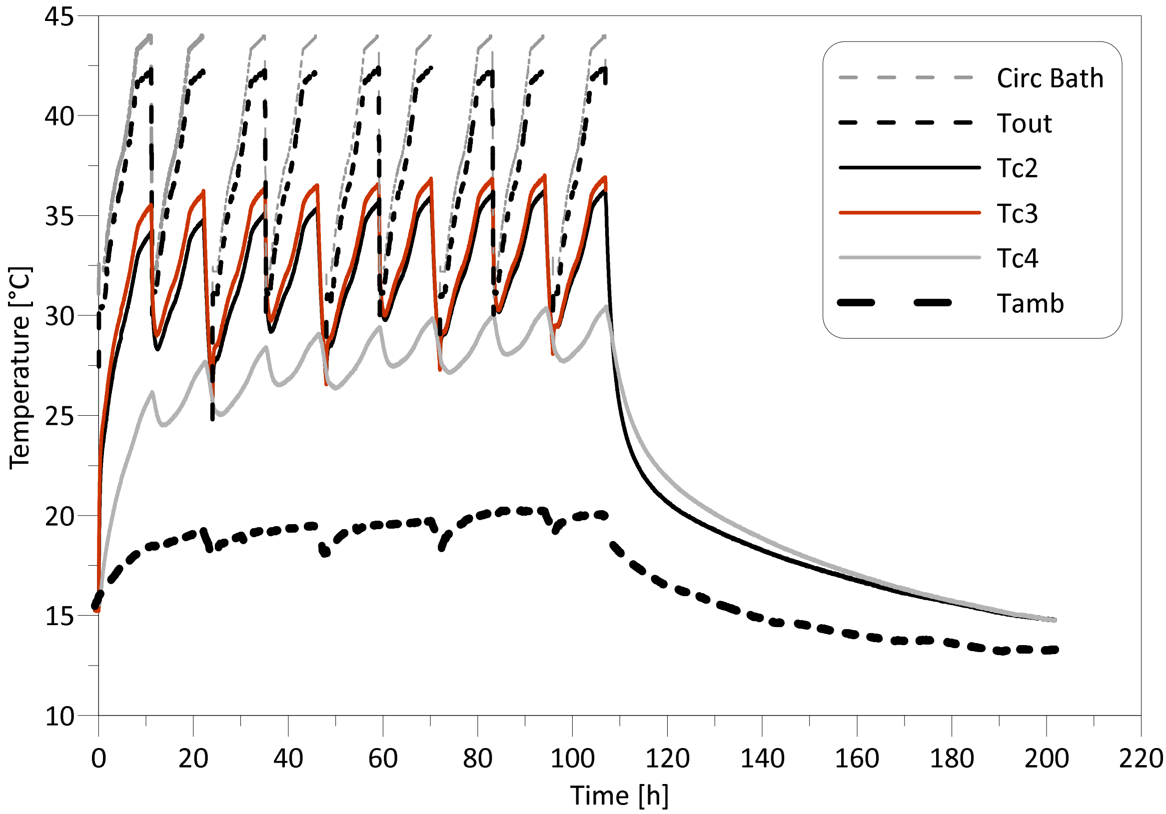

Figure 4-49: Temperature evolution during the cyclic thermo-mechanical heating test, temperature of soil at soil pile interface (Tc2 and Tc3) and at 1D away from the pile (Tc4), outlet water temperature (Tout), inlet water temperature (Circ Bath) and air temperature (T amb).

Soil temperatures measured at the end of each thermal cycle and at the end of the whole thermal history are summarized in Table 4-5.

Table 4-5: Temperature of soil at the end of each thermal cycle and during the rest phase

Time	Temperature Tc2	Temperature Tc3	Temperature Tc4
[h]	[°C]	[°C]	[°C]

11	34.16	35.53	25.99
22	34.75	36.06	27.5
35	35.07	36.3	28.36
46	35.35	36.5	28.97
59	35.61	36.52	29.34
70	35.91	36.74	29.7
83	36.09	36.8	29.95
94	36.19	36.9	30.24
106	36.03	36.69	30.13
130	19.27	-	20.09
150	17.42	-	17.83
180	15.64	-	15.73
200	14.8	-	14.85

From the temperature measured by Tc2 and Tc3 a difference of 1.37 °C is observed at the end of the first thermal cycle. This difference decreases with increasing thermal cycles. At the end of the last thermal cycle, it is about 0.66 °C. The difference observed between Tc2 and Tc3 depends both on thermal interaction with the ambient air and the heat exchange between pile and soil measured from inlet and outlet water temperatures. The difference between inlet and outlet water temperature decreases with the number of thermal cycles, showing a trend similar to that observed for Tc2 and Tc3 difference. At the end of the first heating cycle the difference between the inlet and outlet temperature of water is about 1.76 °C. At the end of the ninth thermal cycle, it slightly decreases to 1.52 °C. The temperature measured at 1D away from the pile (Tc4) is smaller of 8.8 °C than the average temperature measured at pile's soil interface. At the end of the last thermal cycle the difference between average temperature at pile-soil interface and the temperature of soil at 1D away from the pile decreases to 6.23 °C. At the end of the ninth thermal cycle soil temperature at 1D from the pile increases of 6 °C.

After one day from the end of the cyclic heating history soil temperature at 1D away from the pile is still increasing demonstrating that the transient heat transfer is still occurring in radial direction. After three days from the end of the last heating cycle soil temperature at 1D from the pile corresponds to the temperature measured by TC2 and Tc3. After four days from the end of the thermal cycle average soil temperature is about 14.8 °C i.e., it is lower than those measured at the beginning of the test.

During the test, the inlet and outlet temperatures measurements allow TPT. The difference (***ΔT***= T_{in}-T_{out}) is reported in Figure 4-50 and allows determining the heating power injected into the laboratory model according to Equation 4-7. At the start and end of each test, the difference between the inlet and the outlet pile temperature is higher due to the high initial inlet water temperature. The average heating power during the first two thermal cycles is about 589 W. During the Third and fourth thermal cycles the average heating power is about 564 W. A recovery thermal phase of about two hours was performed between any two cycles of heating. A slightly decrease of the average heating power injected into the soil sample occurred passing from the first two thermal cycles to the subsequent cycles. The higher decrease it is noticed between the first two cycles and the average heating power monitored during the third and fourth heating cycles. Several studies investigated about the heat exchanges rates of EPs during continuous and intermittent operations (e.g., Brandl, 2006; Faizal et al., 2016). Therefore, it is known that the heat exchange decreases with time until a steady state is reached, and intermittent operation allows improving the efficiency of the system. Faizal et al. (2016) compared the heat extracted for continuous and intermittent modes (with 16 hours and 8 hours of thermal recovery). The average energy extracted for 16 hours of recovery per day provided 30 % higher of additional energy extracted. Herein the time duration of the thermal recovery between two subsequent cycles was not enough to mitigate the decreasing of heat power with increasing cycles. Heat power measurements agree on thermal performance of small-scale energy piles measured in laboratory. Rate of heat exchange of 470 W/m was measured during the first five hours of heating thermal tests at constant temperature of 36 °C performed on concrete pile in saturated sand by (Elzeiny et. Al, 2020). Yang et al. (2016) investigating the thermal performance of spiral coil energy pile showed that for inlet temperatures of 37 °C, 32 °C and 27 °C the heat release rate is about 324 W, 272 W and 220 W, respectively.

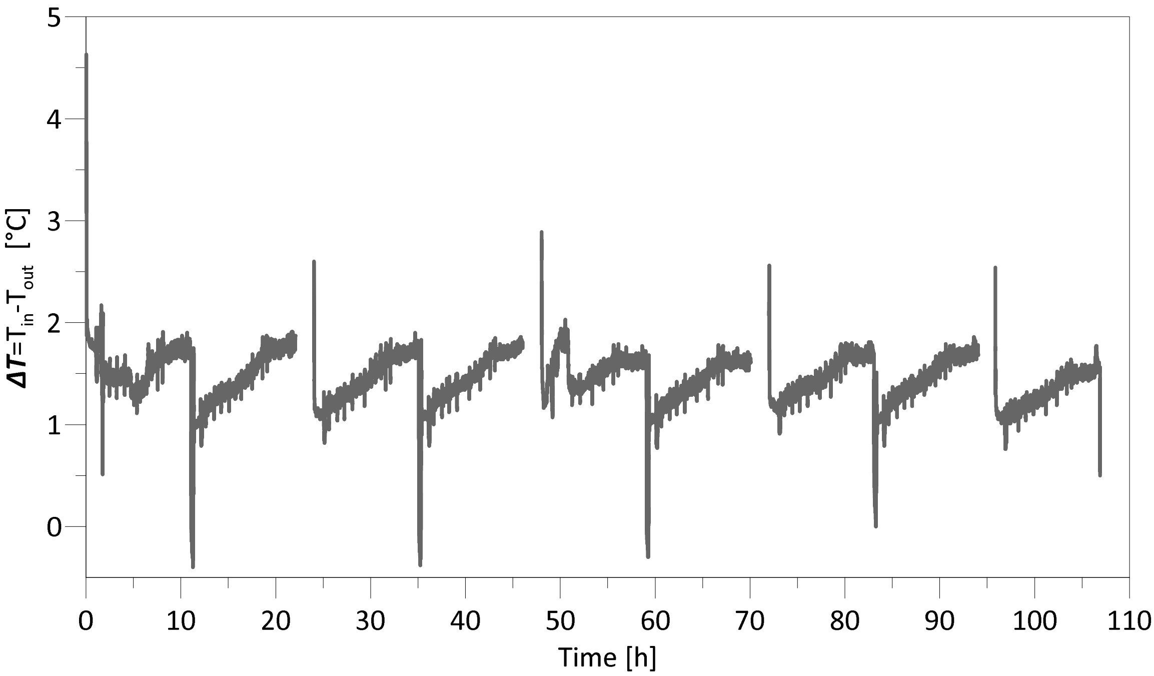

Figure 4-50: Thermal Performance of the test pile. Difference between inlet and outlet water temperature (Tin -Tout) versus elapsed time.

During the first step the mechanical load induced pile's head settlement that was not zeroed in the following thermo-mechanical step. Therefore, the Total displacement is the light grey curve in Figure 4-51. The thermal change is obtained by zeroing the movement after the mechanical part of the test (Figure 4-51). The maximum heave is 0.29 mm, and it is observed at the end of the first heating history. At the end of the test the thermal heave is 0.27 mm. With the increasing number of thermal cycles, the heaves of the pile decrease, at the end of the nineth thermal cycle the average Total displacement is about 0.18 mm. During the recovery phases the pile settles because of temperature decrease with respect to the previous stage. However, the settlement of the pile is very small (about -0.02 -0.01 mm). The measured settlement keeps higher than the settlement measured at the end of the mechanical step because the two hours of thermal recovery are not enough to allow the temperature of the pile to return to the initial temperature as showed in Figure 4-49. The average temperature measured by Tc2 and Tc3, placed at soil pile interface, is 26.3 °C, 26.8 °C, 27.5 °C,28.9 °C at the end of the first, second, third and fourth recovery phases, respectively.

Thermal displacement during the second step of the test is plotted along with the displacements of the end bearing and of the floating pile and the difference between inlet water temperature and the initial pile's temperature (Figure 4-52). Thermal displacement of the end bearing and floating pile are reported only during the heating of the pile where the thermal variations are computed as difference between the temperature of the heated water and pile's initial temperature. The thermal displacement of the pile is closer to the floating pile displacement (Figure 4-52).

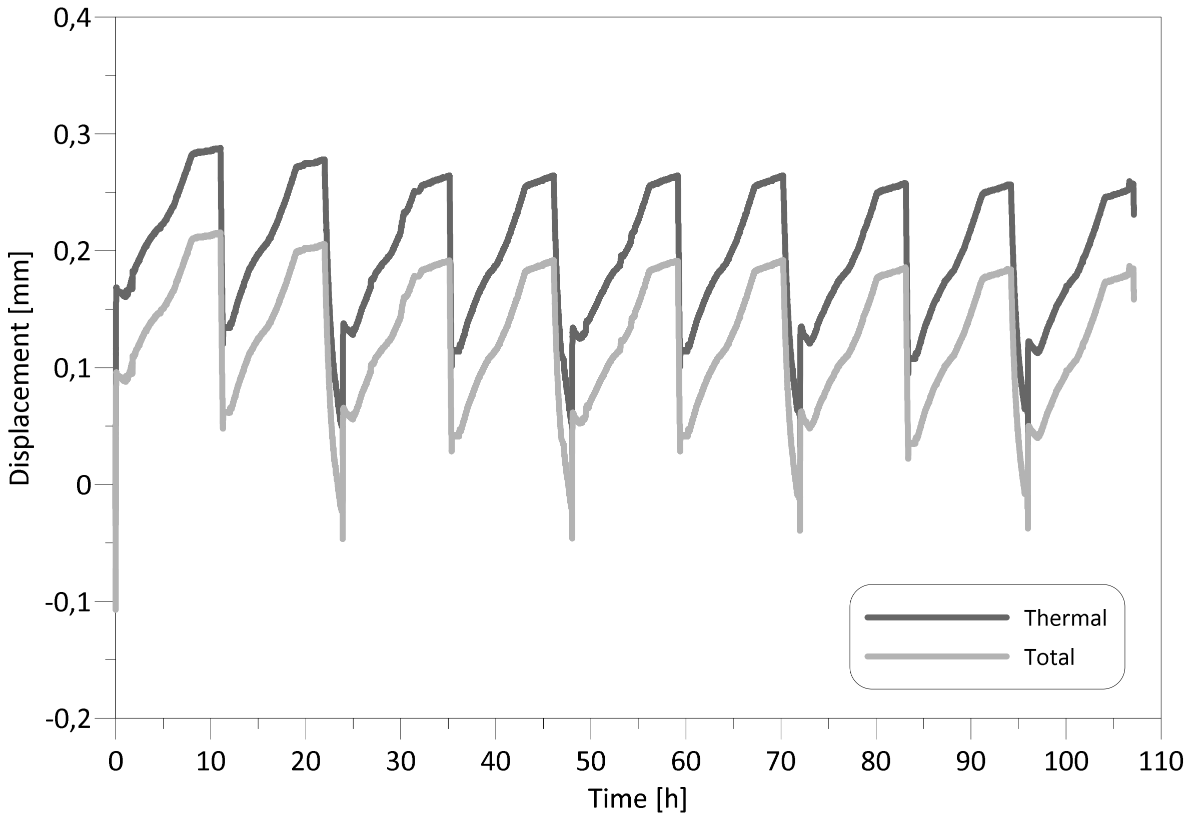

Figure 4-51:Pile's head thermal and thermo-mechanical (Total) displacements versus elapsed time during the cyclic thermo-mechanical heating history.

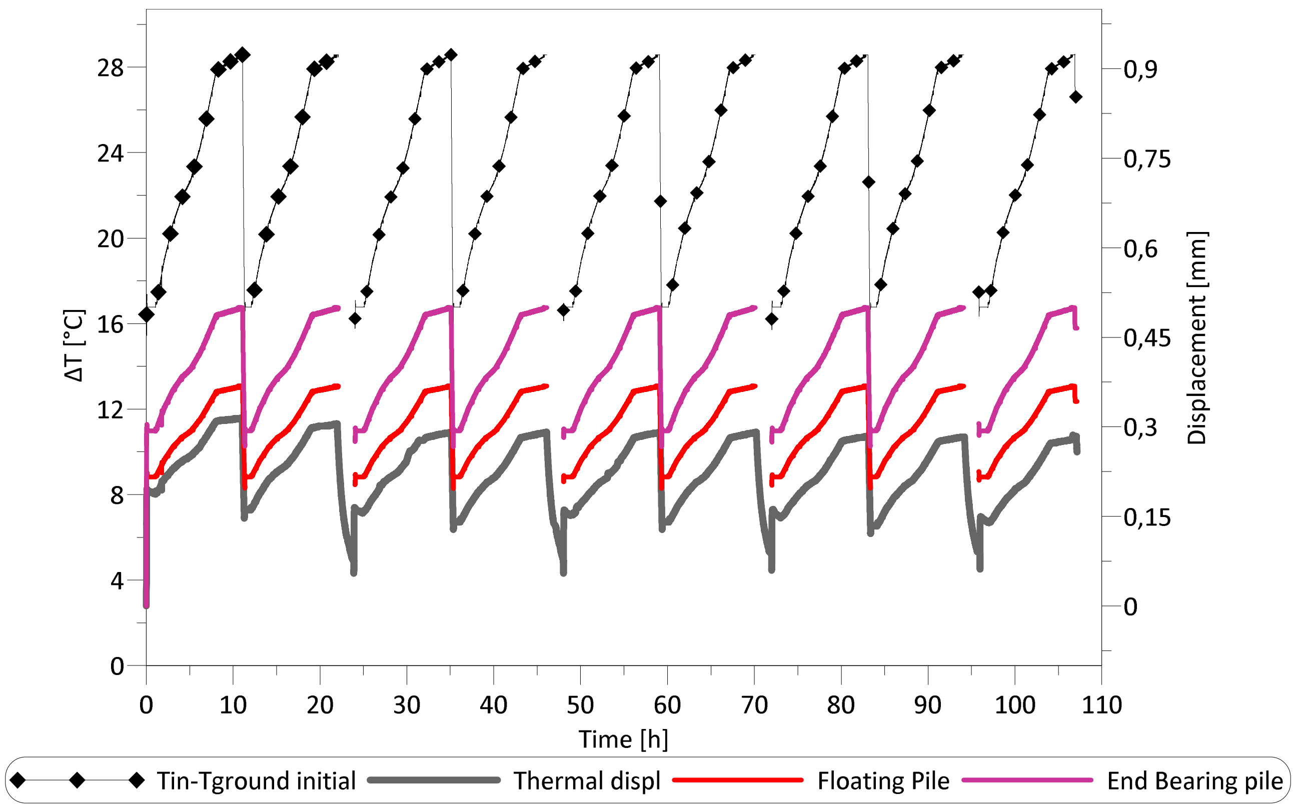

Figure 4-52:Pile's head thermal displacements (Thermal displ), Floating and End bearing Pile displacements (Floating Pile and End Bearing Pile) along with temperature variations.

Thermal and thermo-mechanical axial load profiles at the end of each thermal cycle are plotted in Figure 4-53 (a) Figure 4-53(b), respectively. The mobilised thermal and thermomechanical shaft friction along pile's depth is plotted in Figure 4-54 (a) and Figure 4-54 (b), respectively.

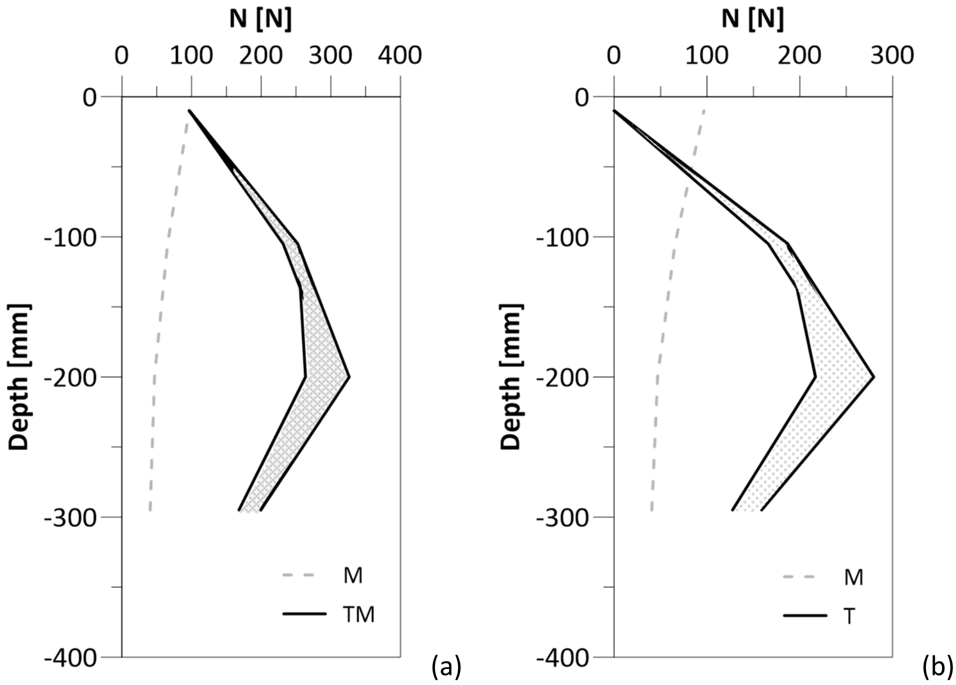

Figure 4-53:Thermal (b) and Thermo-mechanical (a) load profiles at the end of each thermal cycle.

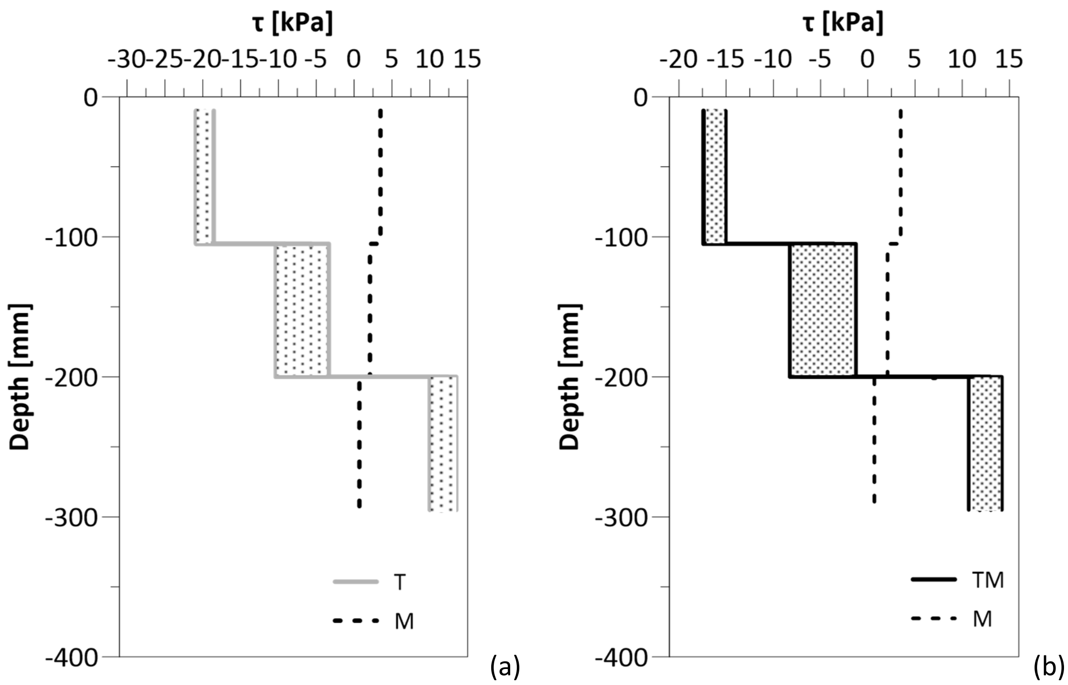

Figure 4-54:Envelope of mobilized side friction (a) thermal (T) and mechanical (M) shaft friction and (b) thermomechanical (TM) and mechanical(M) shaft friction.

The upper and lower bounds of the thermal and thermomechanical load profiles are shown as black straight lines that include all the axial loading measured at the peak of each thermal cycle. The maximum thermal load is observed at the depth of the G3, i.e., pile's mid depth. The maximum thermal and thermomechanical axial load at this depth is 326 N and 257 N respectively. Comparing the results of the test to the thermo-mechanical test at variable temperature on Model A, an upward shift of the NP occurred. The NP depth is at pile's mid length while in Model A it is about 300 mm depth from pile's head.

As for the axial load profile the maximum and minimum shaft friction at the peak of each thermal cycle is plotted in Figure 4-54. The higher mobilization of shaft friction is observed in the first zone of the pile with minimum values of about -21 kPa. At pile's mid depth, i.e., NP position, the shaft friction is reversed. In the second zone the minimum mobilised thermal and thermomechanical shaft friction is -10 kPa and – 8 KPa, respectively. In the third zone upward shaft friction is observed and the maximum thermal and thermomechanical stress is 13.50 kPa and 14.20 kPa.

4.6.3 Cyclic Thermo-mechanical cooling test

During the first mechanical step, 96.67 N, is applied to the head of pile while pile's head settlement, mechanical strains and undisturbed soil temperature were monitored. In the second part of the test mechanical load was combined to the thermal loadings for a total time interval of eighty hours. Temperatures assigned to the circulating bath i.e., inlet water temperatures are reported in Figure 4-19 (b)**Errore. L'origine riferimento non è stata trovata.**. Recovery phases are not modelled, and thermal cycles are continuously repeated. The average soil temperature before starting the cyclic thermo mechanical cooling test was 15.8 °C. At the end of the full thermomechanical stage (i.e., 80 hours), a third step dedicated to the thermal recovery was carried out for a total of sixty-three hours. During the recovery stage the evolution of the heat transfer process was evaluated through the monitoring of soil temperatures. Tc2, Tc3 and Tc4 were recorded during the test. Temperatures of the soil, ambient air, inlet and outlet water temperatures are plotted in Figure 4-55.

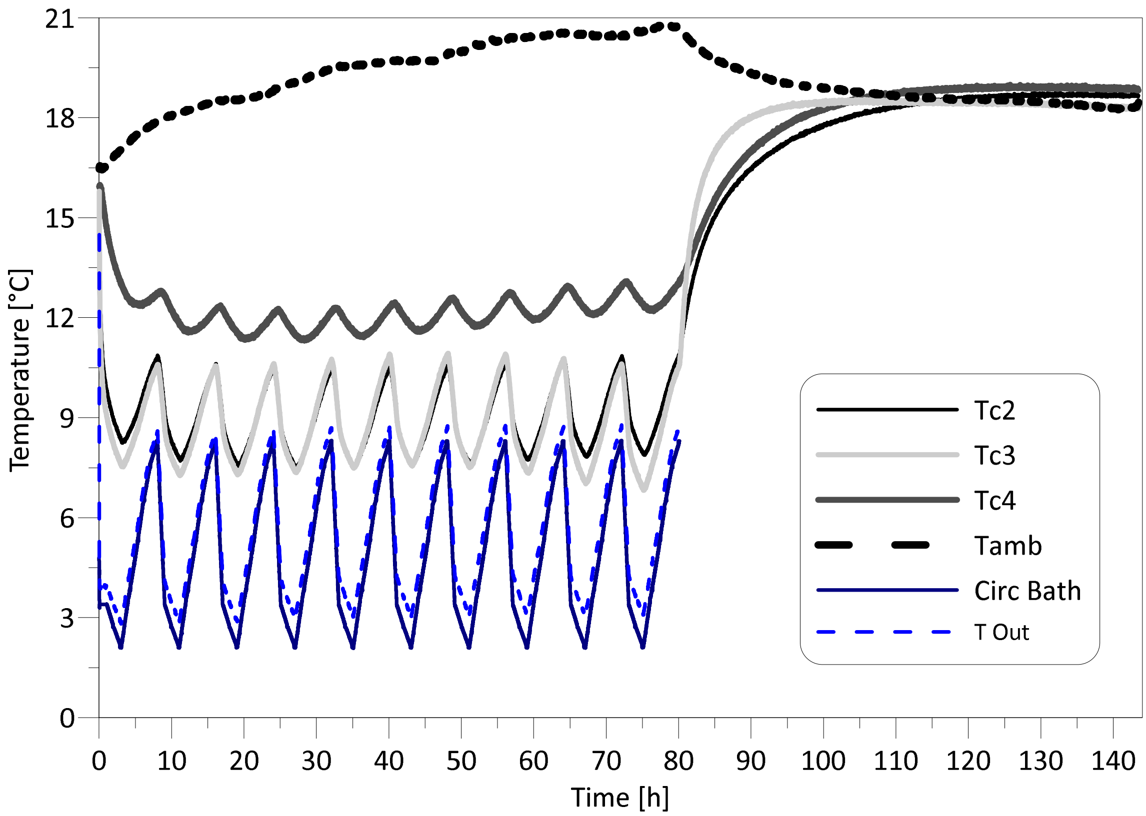

Figure 4-55: Temperature evolution during the cyclic thermo-mechanical cooling test, temperature of soil at soil pile interface (Tc2 and Tc3) and at 1D away from the pile (Tc4), outlet water temperature (Tout), inlet water temperature (Circ Bath) and air temperature (T amb).

Soil temperatures measured during each thermal cycle, at the end of the thermal history and during the first eight hours of the recovery step are reported in Table 4-6.

Table 4-6: Temperature of soil during the cyclic cooling thermal history.

Time	Temperature Tc2	Temperature Tc3	Temperature Tc4
[h]	[°C]	[°C]	[°C]
4	8.51	7.87	12.61
8	10.79	10.55	12.71
12	8.04	7.69	11.63
16	10.5	10.47	12.22
20	7.89	7.68	11.36
24	10.42	10.54	12.13
28	7.78	7.74	11.36
32	10.39	10.63	12.14
36	7.87	7.84	11.47
40	10.43	10.8	12.28
44	7.83	7.94	11.58
48	10.51	10.83	12.44
52	7.94	7.93	11.79
56	10.57	10.84	12.59
60	8.06	7.76	11.94
64	10.68	10.71	12.78
68	8.11	7.42	12.13
72	10.76	10.49	12.91
76	8.19	7.31	12.22
80	10.83	10.5	13.02
84	14.59	16.5	15.09
88	16	17.79	16.5

From Tc2 and Tc3 a difference of 0.64 °C is observed at the end of the first thermal cycle. This difference decreases with increasing thermal cycles, in fact, at the end of the last thermal cycle, it is about 0.33 °C. Temperature measured at 100 mm from pile's toe (Tc2) is always higher than those measured at 100 mm from pile's head (Tc3). Soil temperature at 1D away from the pile (Tc4) is about 3 °C higher than the average temperature measured at pile's soil interface after four hours from the beginning of the test. At the end of the last thermal cycle temperature measured by Tc4 is only 1.34°C higher than that measured at pile-soil interface. After 2.6 days from the end of the cyclic cooling history average soil temperature is about 18.4 °C which is very similar to the air temperature that is 18.55 °C. As from Figure 4-55 at the end of the rest phase the thermal equilibrium is fully obtained.

During the test the inlet water temperature is lower than the outlet water temperature because heat is transferred from the soil to the pile, therefore $\boldsymbol{\Delta T}= T_{in}-T_{out}$ is negative. The temperature difference, $\boldsymbol{\Delta T}= T_{in}-T_{out}$, is plotted in Figure 4-56. Minimum cooling power it is observed during the peak of cooling and at the beginning of the test at it is about -310 W. The average cooling power during the first thermal cycle is about -200 W. During the last cycle the average cooling power is about -280 W. The estimation of the cooling power corroborates that the system can be used for both heat rejection and extraction to and from the ground with higher performance in the former case. The temperature difference between inlet and outlet water increased with the number of thermal cycles. It was supposed that the heat exchange during each cycle was slightly smaller than the previous cycle. This phenomenon depends on the soil temperature decrease around the pile induced by cooling that increase the temperature gradient between the pile and the surrounding soil. The trend of temperature difference, $\boldsymbol{\Delta T}$= T_{in}-T_{out}, in Figure 4-56 could be explained taking into account the thermal interaction between the ambient air and the soil.

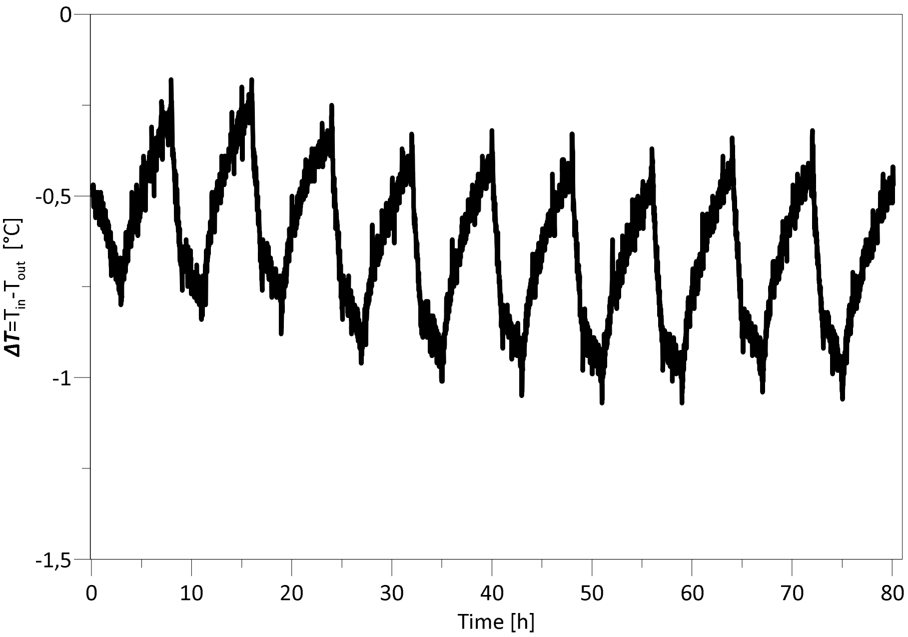

Figure 4-56: Thermal Performance of the test pile, Difference between inlet and outlet temperature (Tin -Tout) versus elapsed time.

Total and thermal displacement of pile's head are plotted in Figure 4-57.

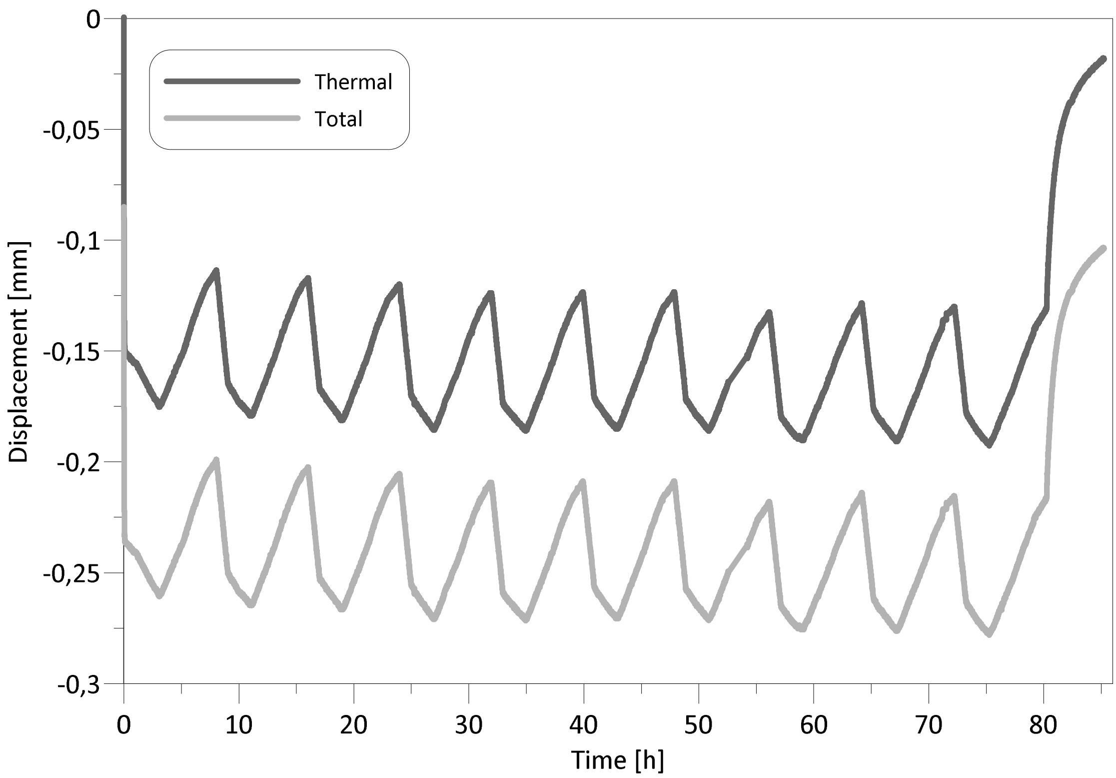

Figure 4-57: Pile's head thermal and thermo-mechanical (Total) displacements during the cyclic thermo-mechanical cooling history.

Thermo-mechanical displacement and thermal displacement in the middle and at the end of the first cooling cycle is -0.25 mm and -0.17 mm and -0.20 mm and - 0.11 mm, respectively. Thermo-mechanical displacement and thermal displacement in the middle and at the end of the tenth cooling cycle is -0.27 mm and -0.18 mm and -0.22 mm and - 0.14 mm, respectively.

With increasing number of thermal cycles, pile's head settlement increase. After ten cycles of cooling the thermal settlement of pile's head is increased of about 16%. Pile head displacement was also recorded during the early five hours of the recovery step. At the end of recovery (i.e., the temperature was nearly back to the initial value), the residual settlement is about -0.01 mm. The measured settlement under the mechanical load which was kept constant is about -0.10 mm nearly matching the mechanical settlement induced in the first part of the experiment.

Thermal displacement measured during the second stage of the thermo-mechanical test is plotted along with the displacement of the end bearing and floating pile and the difference between inlet and outlet water temperature in Figure 4-58.

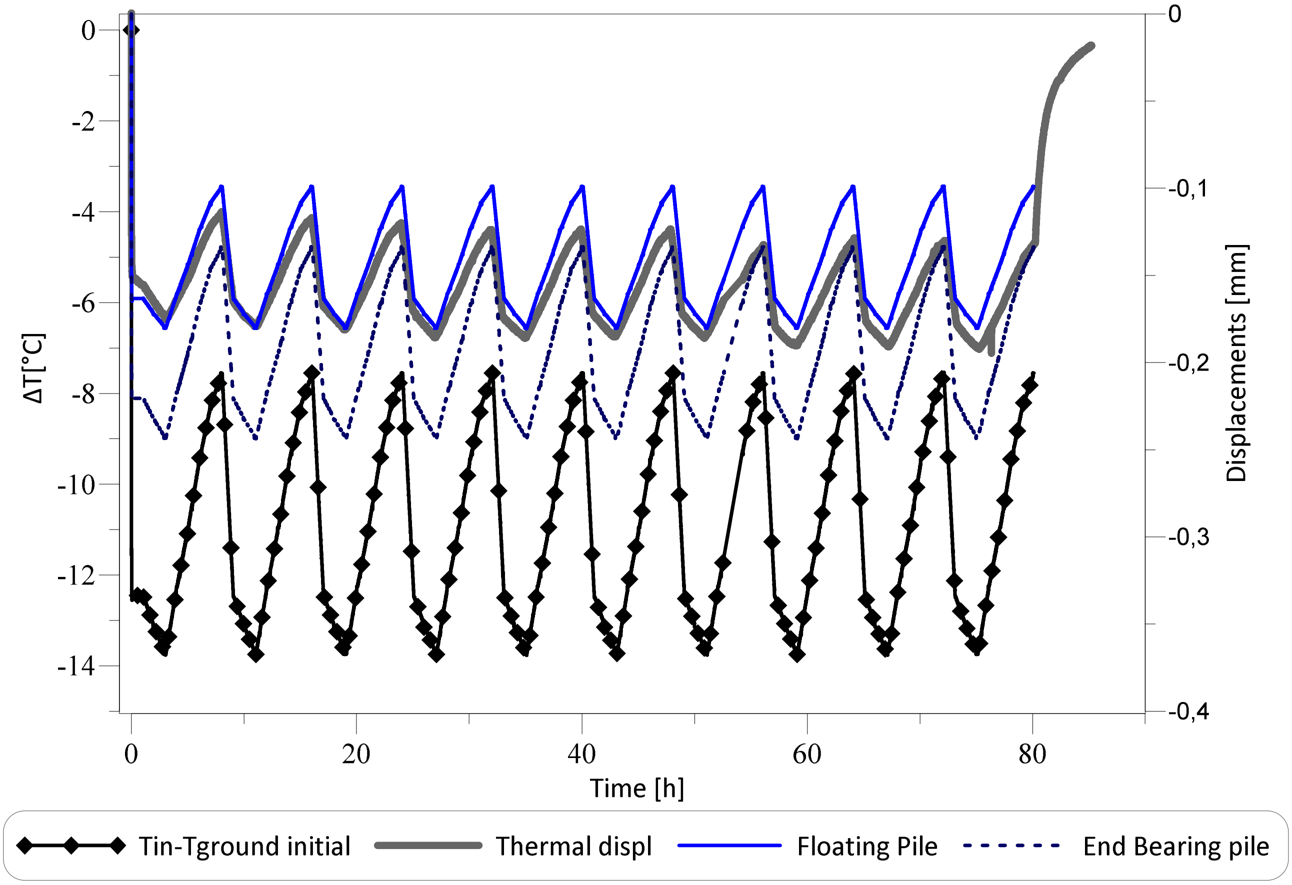

Figure 4-58: Pile's head thermal displacements (Thermal displ), Floating and End bearing Pile displacements (Floating Pile and End Bearing Pile) along with temperature variations (Tin-Tground initial).

Pile's head thermal displacement is close to the floating pile's displacement; therefore, the NP is expected in agreement with the mobilized thermal expansion coefficient close to the pile's mid depth.

Thermal and Thermomechanical load profile envelope is reported in Figure 4-59 (a) and Figure 4-59 (b).

During the first step, the pile is subjected to mechanical load that determines compressive axial loading (dotted black profile in Figure 4-59 (a) and Figure 4-59 (b)). During the thermomechanical step, the cooling applied to the pile determines decreasing of the compressive axial load and tensile load at pile's mid depth. The minimum tensile load i.e., the maximum tensile thermal stress in absolute value, it is observed at pile's mid depth. The minimum axial load occurring during the first thermal cycle is about -199 N. At the end of the tenth thermal cycle the tensile thermal load is about -167 N. The thermomechanical tensile axial load is about -131 N and -100 N during the first and tenth thermal cycle.

Therefore, during the cooling cyclic test, with increasing number of thermal cycles pile's head settlement increases and an increase of thermal tensile loadings is also observed (reduction of tensile loadings).

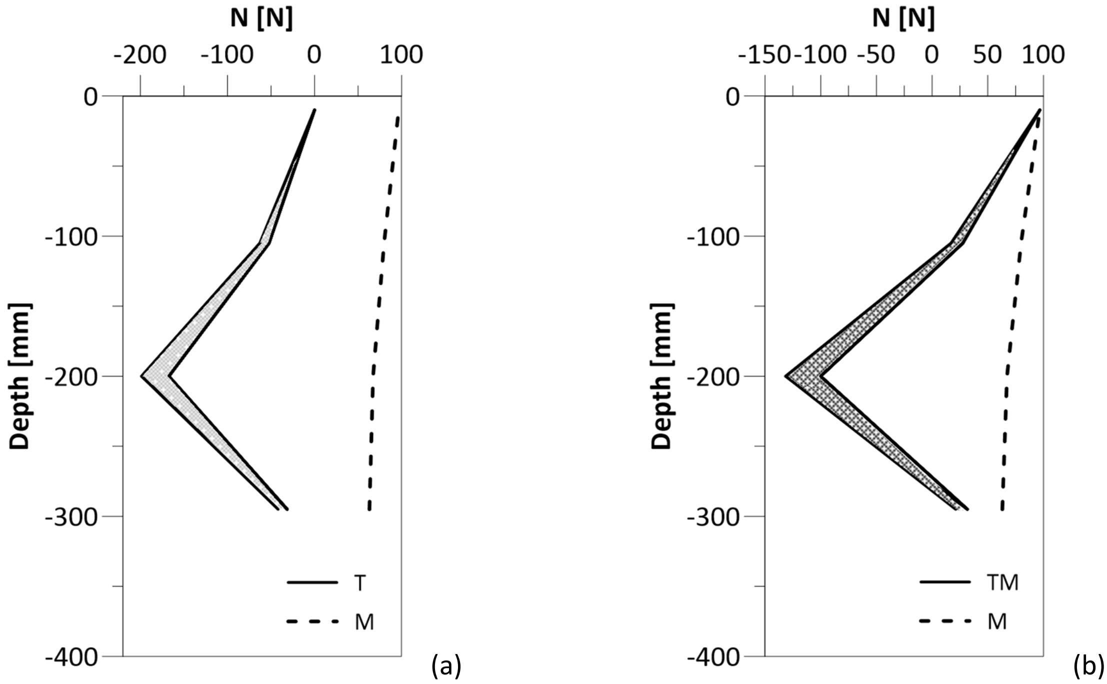

Figure 4-59:Axial load envelope; Thermal (b) and Thermo-mechanical (a) load profiles at the end of each thermal cycle.

The envelope of the thermal and thermomechanical mobilized friction is plotted in Figure 4-60 (a) and Figure 4-60 (b), respectively.

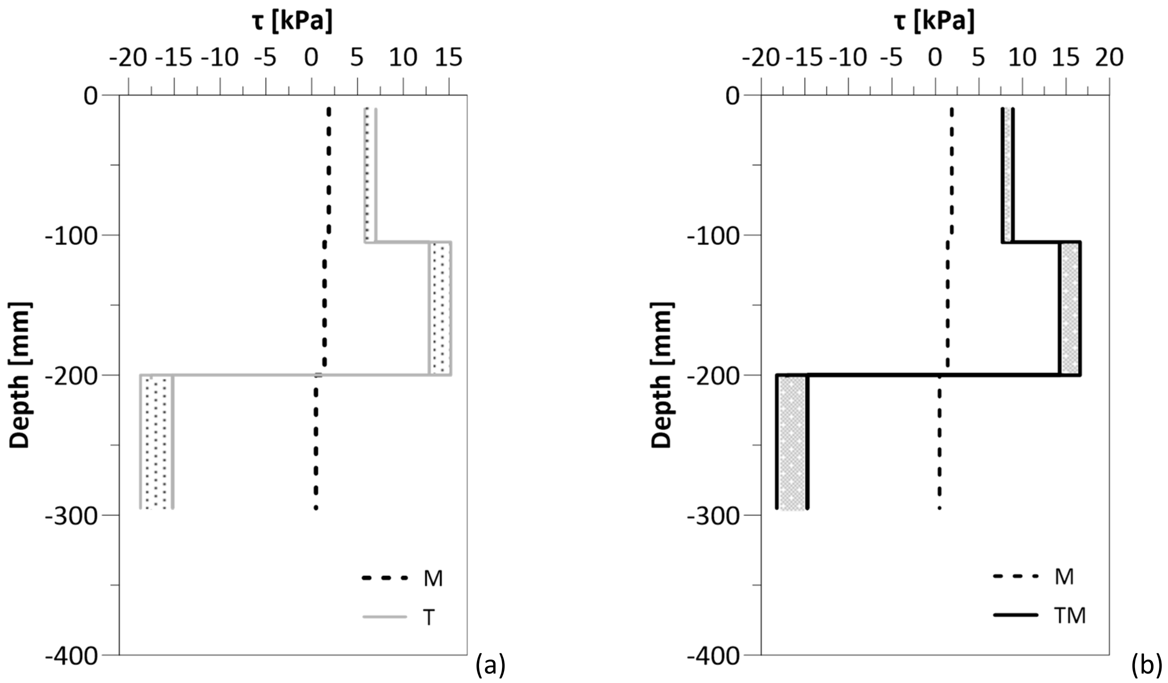

Figure 4-60: Mobilized skin friction envelope during the test;(a) Thermal (T) and Mechanical friction and (b) Thermomechanical (TM) and Mechanical (M).

The thermal mobilized friction is upward in the first and second pile’s zones while are downward in the third zone. Maximum thermal skin friction is about 7 kPa and 15 kPa in the first and second zones, respectively. The minimum thermal friction occurring in the third zone is about -18.7 kPa. The maximum thermomechanical mobilized friction is about 8.9 kPa and 16.6 kPa in the first and second zones, respectively. In the third zone the minimum thermomechanical friction is about -18.2 kPa.

4.6.4 Thermo-mechanical cyclic test

Cyclic thermo-mechanical tests are performed using the same thermal history while keeping different amount of applied mechanical head load (Figure 4-20). Each test consists of two or three stages as summarised in. Test S1 is performed in two stages, while S2, S3 and S4 consist of three stages. The last stage is always a stage dedicated to the thermal recovery and it lasted differently as reported in Table 4-7. During mechanical stage, i.e., first step in test S2, S3 and S4, mechanical load is applied. Each test is characterised by a different safety factor (SF) as reported in Table 4-7. During this stage, the initial undisturbed soil temperature was measured by means of all the thermocouples installed into the experimental box. During the mechanical stage pile's head settlement and strains along the pile shaft were also monitored and the step was considered as ended when all these measurements showed stationary values. Being the pile embedded in sand, as it could be expected, the stabilisation under mechanical head load occurred rather quickly. Therefore, it is assumed conventionally that the stage 1 under mechanical load is fully concluded at time t=0.

Table 4-7:Thermo-mechanical cyclic test stages.

Cyclic heating Test	**Stages**						
	Mechanical			*Thermal/Thermo-mechanical*		*Recovery*	
	SF	Load [N]	T av soil in [°C]	Time duration [h]	ΔT max [°C]	Time duration [h]	T av soil end [°C]
S1	-	-	17.79	66	26.29	59.9	18.48
S2	6	48.17	16.05	66	28	105	19.19
S3	3	96.68	14.7	66	29.4	39	17.6
S4	2	144.89	18.02	66	26.02	26	19.86

The thermal history applied after the mechanical head load is very similar in all the experiments (**Errore. L'origine riferimento non è stata trovata.**). Slightly different maximum temperature variations (ΔT_{max}) occurred for the 4 cyclic experiments. Temperature variations are the difference between the temperature of the inlet water, measured by the temperature sensor placed at the entrance of the outer circuit, and the average initial soil temperature. Thermal performance measured for each test was not reported in the following sections, 600 W is the average heat injection rate. The thermal interaction with ambient air influenced soil's temperature. Therefore, slightly different temperature variation occurred because air ambient temperatures varied. Herein the main results of tests S1, S2, S3 and S4 are reported.

4.6.4.1 Simplified Thermal Cyclic Test S1

S1 is a purely thermal test performed in two thermal stages. During the first stage cyclic thermal variations were applied while during the second stage thermal recovery was performed. During both stages pile's head settlement, strains and soil and air temperatures are monitored. Soil temperature were measured by means of Tc2, Tc3 and Tc4 during the first step. During the recovery step no water was circulated inside the pile, therefore the measure of the outlet water was replaced by the Tc5. Soil temperatures during S1 along with inlet and outlet water and air ambient temperatures are plotted in Figure 4-61.

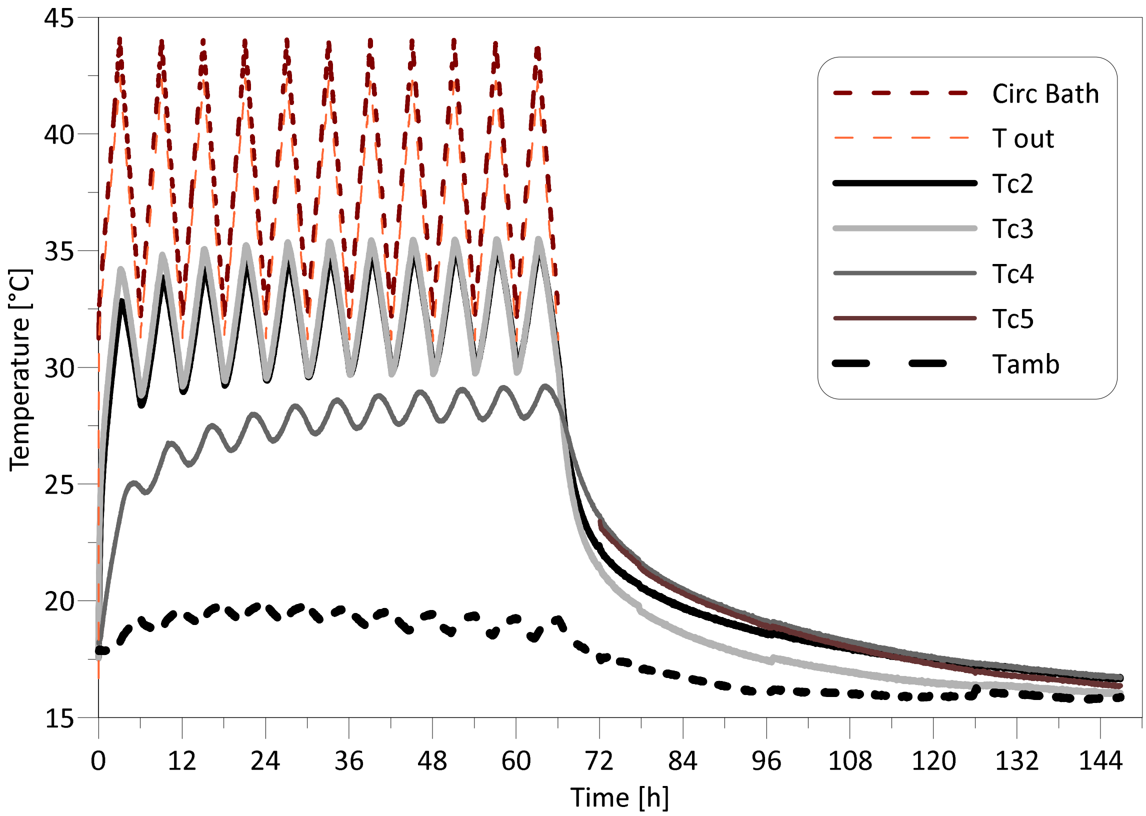

Figure 4-61: Temperature evolution during the cyclic thermal heating test S1. Temperature of soil at soil pile interface (Tc2 and Tc3) and at 1D away from the pile (Tc4), outlet water temperature (Tout) and inlet water temperature (Circ Bath) during the first step and air temperature (T amb); Temperature at 2D away from the pile (TC5) during the recovery step.

Soil temperatures measured by Tc2, Tc3 and Tc4 during the cyclic stage of the test are reported in Table 4-8.

Table 4-8: Temperature of soil during the first stage of test S1

Time	Temperature Tc2	Temperature Tc3	Temperature Tc4
[h]	[°C]	[°C]	[°C]
3.03	32.52	33.96	23.53
6.03	28.51	28.89	24.86
9.04	33.6	34.63	25.97
12.04	29.07	29.26	26.19
15.04	34	34.9	26.87
18.04	29.39	29.52	26.82
21.04	34.22	35.04	27.4
24.04	29.57	29.65	27.27
27.04	34.41	35.12	27.73
30.05	29.71	29.71	27.61
33.05	34.54	35.25	28.02
36.05	29.88	29.78	27.83
39.05	34.63	35.22	28.23
42.06	30.01	29.79	28.02
45.06	34.74	35.26	28.41
48.07	30.05	29.79	28.16

51.07	34.84	35.3	28.5
54.07	30.12	29.84	28.25
57.07	34.89	35.31	28.62
60.08	30.2	29.8	28.37
63.08	34.92	35.29	28.66
66.08	30.25	29.87	28.39

Temperature of soil measured by Tc2, Tc3, Tc4 and Tc5 during the recovery stage of the test are reported in Table 4-9.

Table 4-9: Temperature of soil and ambient air during the third second of test S1.

Time	Temperature Tc2	Temperature Tc3	Temperature Tc4	Temperature Tc5	Air Temperature
[h]	[°C]	[°C]	[°C]	[°C]	[°C]
75	21.22	20.36	22.45	22.24	17.415
80	20.27	19.17	21.13	20.98	16.987
85	19.62	18.5	20.31	20.19	16.654
90	19.1	17.94	19.76	19.54	16.368
95	18.65	17.54	19.22	19.01	16.129
100	18.46	17.38	18.81	18.65	16.106
105	18.13	17.12	18.46	18.19	16.082
110	17.84	16.85	18.12	17.86	16.01
115	17.59	16.63	17.81	17.6	15.891
120	17.38	16.53	17.57	17.28	15.891
125	17.22	16.38	17.35	17.03	15.891
130	17.15	16.4	17.22	16.82	16.034
135	17.01	16.28	17.03	16.71	15.915
140	16.85	16.14	16.92	16.54	15.819
145	16.71	16.04	16.74	16.4	15.843

As could be observed from the measures reported in Table 4-9 and Figure 4-61 thermal equilibrium between soil and the environment is not fully reached at the end of the recovery phase.

The thermal settlement during the first and the second stages is plotted in Figure 4-62. The maximum thermal settlement is 0.33 mm. The residual displacement measured at the end of the recovery step is 0.02 mm.

At increasing number of thermal cycles, a small increase of thermal heave is observed. At the peak of the first thermal cycle the head upward displacement was 0.31 mm while at the peak of the eleventh thermal cycle the displacement is 0.33 mm. Between the tenth and eleventh cycle no increase of the peak upward displacement was observed.

Thermal displacement during the second step of the test is plotted along with the displacement of the end bearing and floating pile and the difference between inlet and outlet water temperature in Figure 4-63.Pile's head thermal displacement measured during the test is closer to the displacement of the floating pile particularly at the peak of heating. The trend of increasing heaves of pile's head could be also observed comparing the measured displacement to floating pile displacement, at the end of the test the measured displacement increased and almost matched to the displacement of the floating pile.

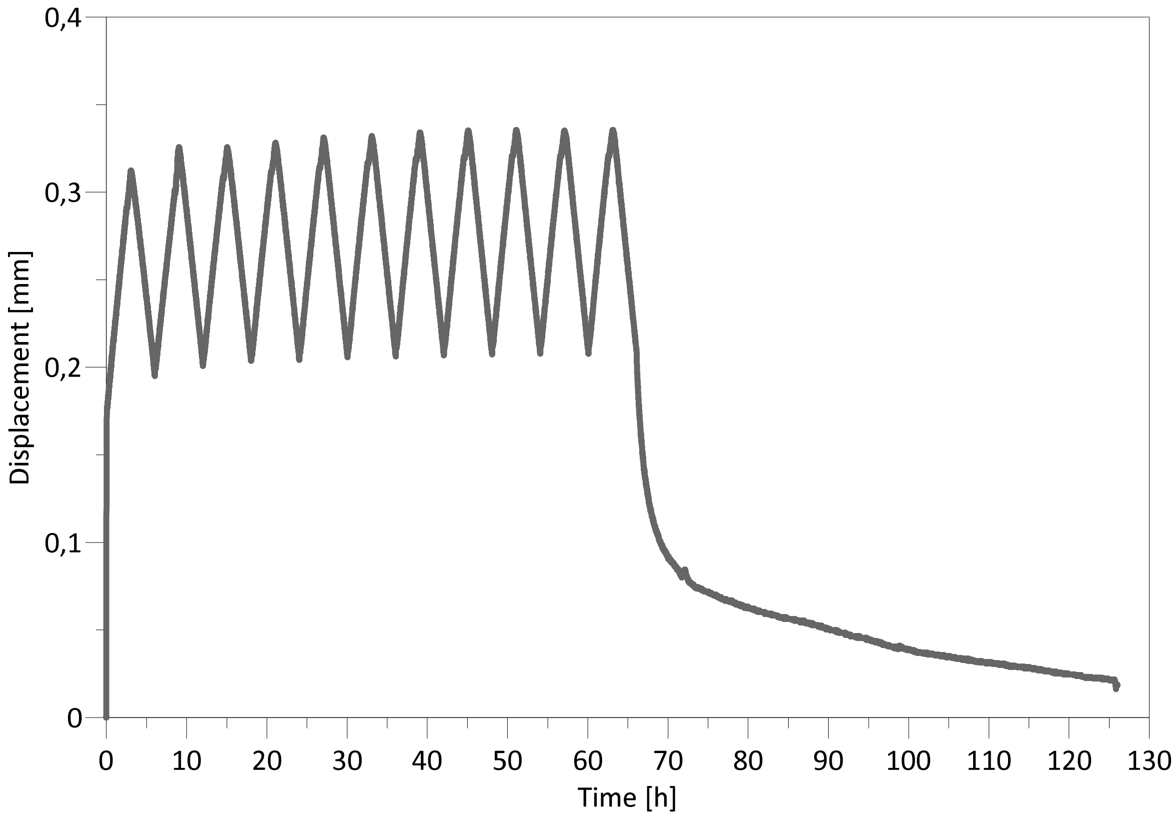

Figure 4-62:Pile's head thermal displacement measured during test S1 (thermal step and recovery step).

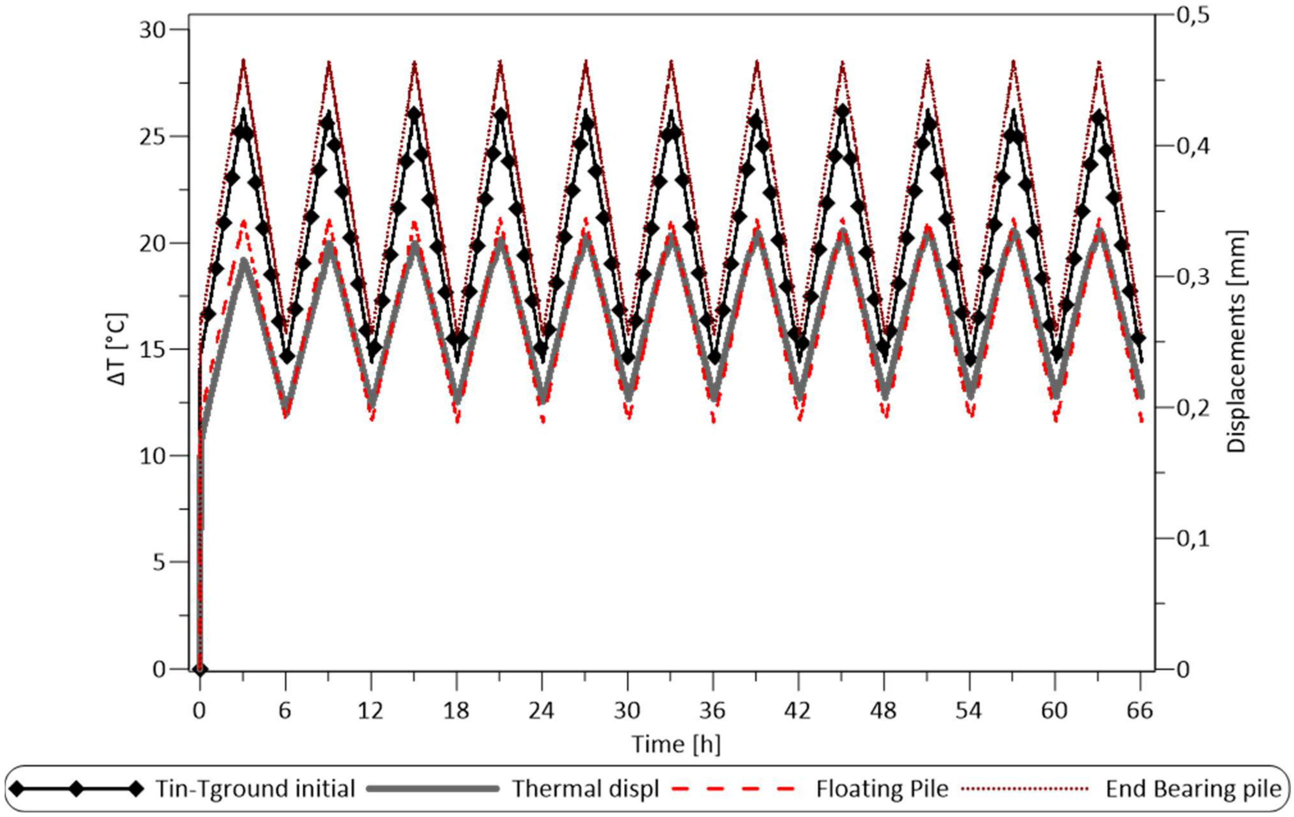

Figure 4-63: Pile's head thermal displacements (Thermal displ), Floating and End bearing Pile displacements (Floating Pile and End Bearing Pile) along with temperature variations (Tin-Tground initial) during test S1 (first step).

Thermal load profile envelope during the test is plotted Figure 4-64 (a). The mobilised thermal friction envelope estimated form the axial load is plotted in Figure 4-64 (b). At the mid-time of each thermal cycle

NP is located at 105 mm depth (Figure 4-64 (a)). At this depth thermal frictions are reversed, in the first zone skin friction is downward while in the second and third zones mobilised frictions are upward.

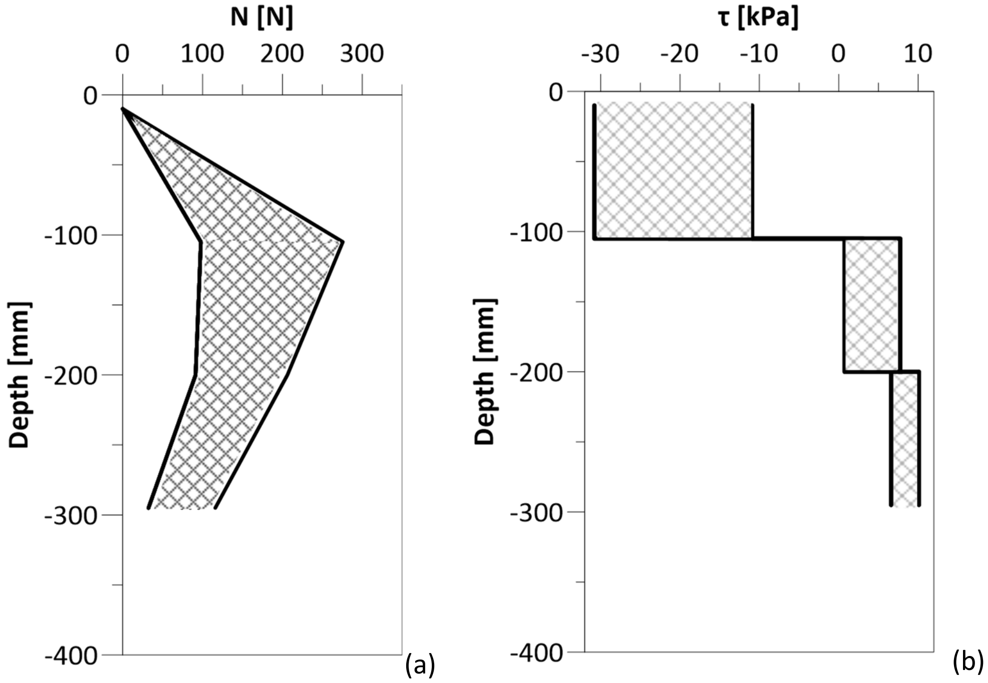

Figure 4-64:Thermal Loading profile envelope (a) and Mobilized friction profile envelope(b) during test S1.

The maximum axial load is about 276 N and occurred at the location of NP, the maximum mobilised thermal friction in absolute value occurred in the first zone and is about -31 kPa. With the increasing number of thermal cycle a reduction of thermal axial load and shaft friction occurred as reported by the lower bound of the envelopes in Figure 4-64 (a) and Figure 4-64 (b). At the peak of the last thermal cycle the thermal load at 105 mm depth is about 99 N. Thermal loads decreasing with increasing thermal cycles is observed along the entire depth of measure.

4.6.4.2 Simplified Thermo-mechanical Cyclic Test S2

The Cyclic thermo-mechanical test S2 is carried out in three steps. The first step is purely mechanical, the second step is thermo-mechanical, and the third step is the thermal recovery monitoring.

During the first step the axial load applied (48.17 N) corresponds to SF=6 and determines a mechanical settlement of -0.06 mm. During this step, the average soil temperature was 16.05 °C.

During the second step the variation of soil temperature along with air temperature and water inlet and outlet water temperatures were also measured. All the temperature measures during the test are plotted in Figure 4-65.

Soil temperature measured by thermocouples Tc2, Tc3 and Tc4, at mid-time and end of each thermal cycles is reported in Table 4-10.

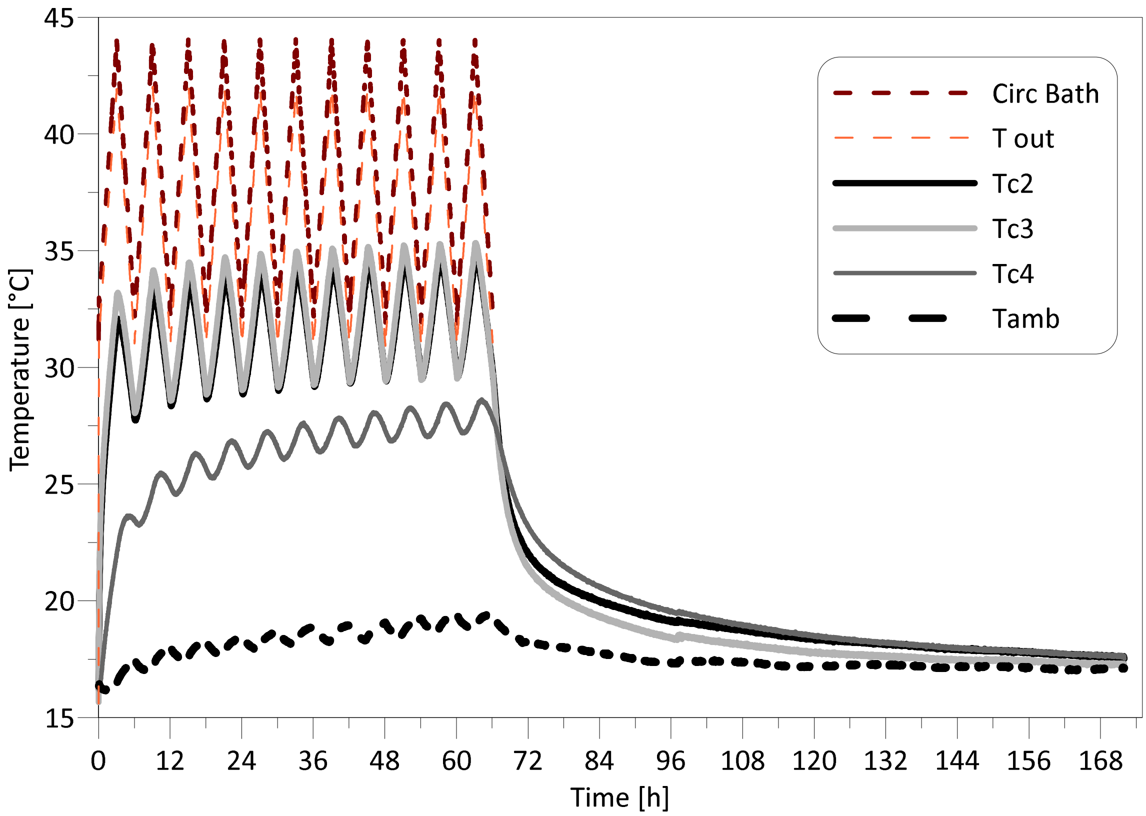

Figure 4-65: Temperature evolution during the cyclic thermo-mechanical heating test S2. Temperature of soil at soil pile interface (Tc2 and Tc3) and at 1D away from the pile (Tc4), outlet water temperature (Tout) and inlet water temperature (Circ Bath) during the first step and air temperature (T amb).

As observed in the previous thermal and thermo-mechanical test the temperature difference between Tc2 and Tc3 is maximum during the first thermal cycle, about 1.2 °C and decrease with the increasing number of cycles. At the heating peak of the eleventh thermal cycle the difference is about 0.7 °C.

Table 4-10: Temperature of soil during the second step of test S2

Time	Temperature Tc2	Temperature Tc3	Temperature Tc4
[h]	[°C]	[°C]	[°C]
3.03	31.78	32.93	21.97
6.03	27.88	28.12	23.44
9.04	32.98	34.01	24.7
12.04	28.45	28.63	24.89
15.04	33.43	34.35	25.65
18.04	28.8	28.93	25.64
21.04	33.65	34.52	26.25
24.04	29.02	29.13	26.14
27.04	33.78	34.67	26.68
30.05	29.14	29.22	26.5
33.05	33.91	34.72	26.99
36.05	29.38	29.37	26.81
39.05	34.05	34.87	27.21
42.06	29.49	29.46	27.09
45.06	34.21	34.91	27.49

48.07	29.59	29.51	27.29
51.07	34.35	35.03	27.69
54.07	29.72	29.6	27.49
57.07	34.45	35.06	27.86
60.08	29.77	29.6	27.64
63.08	34.5	35.15	28.03
66.08	29.88	29.68	27.79

Temperature of soil during the third step was measured also by thermocouples Tc5 placed 2D away from the pile. Temperatures of soil and ambient air are reported in Table 4-11. As could be observed by the magnitudes of soil and ambient air temperatures, reported in Figure 4-65 and Table 4-11 at ,the end of recovery phase, after about four days from the end of the heating, thermal equilibrium between soil and ambient air is almost reached.

Table 4-11: Temperature of soil and ambient air during the third step of test S2.

Time	Temperature Tc2	Temperature Tc3	Temperature Tc4	Temperature Tc5	Air Temperature
[h]	[°C]	[°C]	[°C]	[°C]	[°C]
75	21.22	20.58	22.16	21.65	18.105
80	20.42	19.78	21.16	20.72	17.915
85	19.91	19.27	20.47	20.11	17.724
90	19.48	18.79	19.97	19.64	17.486
95	19.16	18.49	19.61	19.24	17.32
100	19.06	18.43	19.37	18.99	17.391
105	18.83	18.22	19.07	18.76	17.368
110	18.66	18.05	18.87	18.48	17.296
115	18.49	17.89	18.68	18.29	17.201
120	18.33	17.81	18.51	18.09	17.177
125	18.29	17.68	18.32	17.93	17.225
130	18.17	17.66	18.27	17.84	17.272
135	18.09	17.56	18.19	17.69	17.249
140	18	17.51	18.08	17.57	17.13
145	17.93	17.47	17.96	17.53	17.153
150	17.9	17.44	17.87	17.47	17.201
155	17.8	17.42	17.85	17.35	17.153
160	17.71	17.34	17.76	17.31	17.082
165	17.64	17.29	17.68	17.23	17.034
170	17.6	17.26	17.64	17.16	17.106

Pile's head thermal and thermomechanical displacements are plotted in Figure 4-66.The maximum thermal and thermomechanical displacement measured during the test is 0.31 mm and 19 mm, respectively. The thermal displacement during the peak of each thermal cycle is almost constant with increasing of thermal cycles. At the end of the test thermal lightly decrease during the tenth and eleventh cycle (0.6 % of variation). Comparing the thermal displacement at the end of each thermal cycle a slightly decrease of about 2 % is observed between the first and the eleventh cycle.

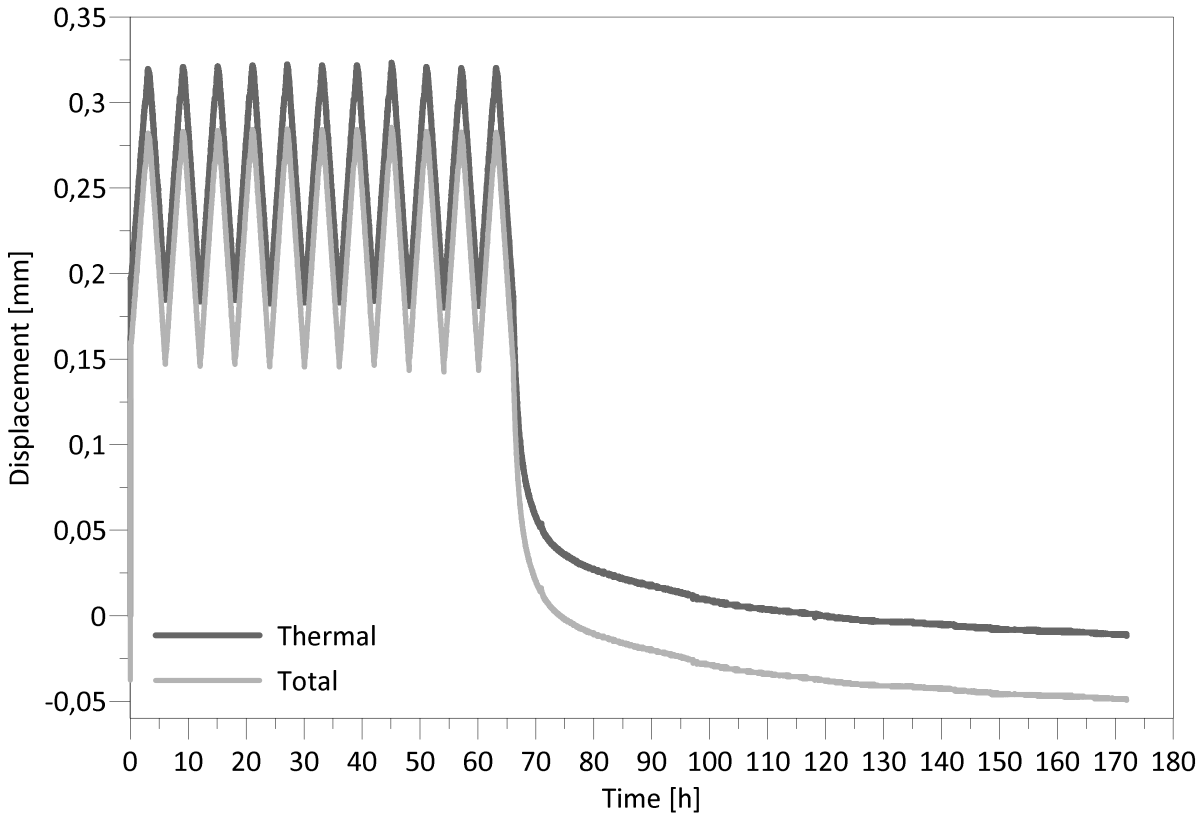

Figure 4-66:Pile's head thermal and Thermo-mechanical displacements measured during test S2.

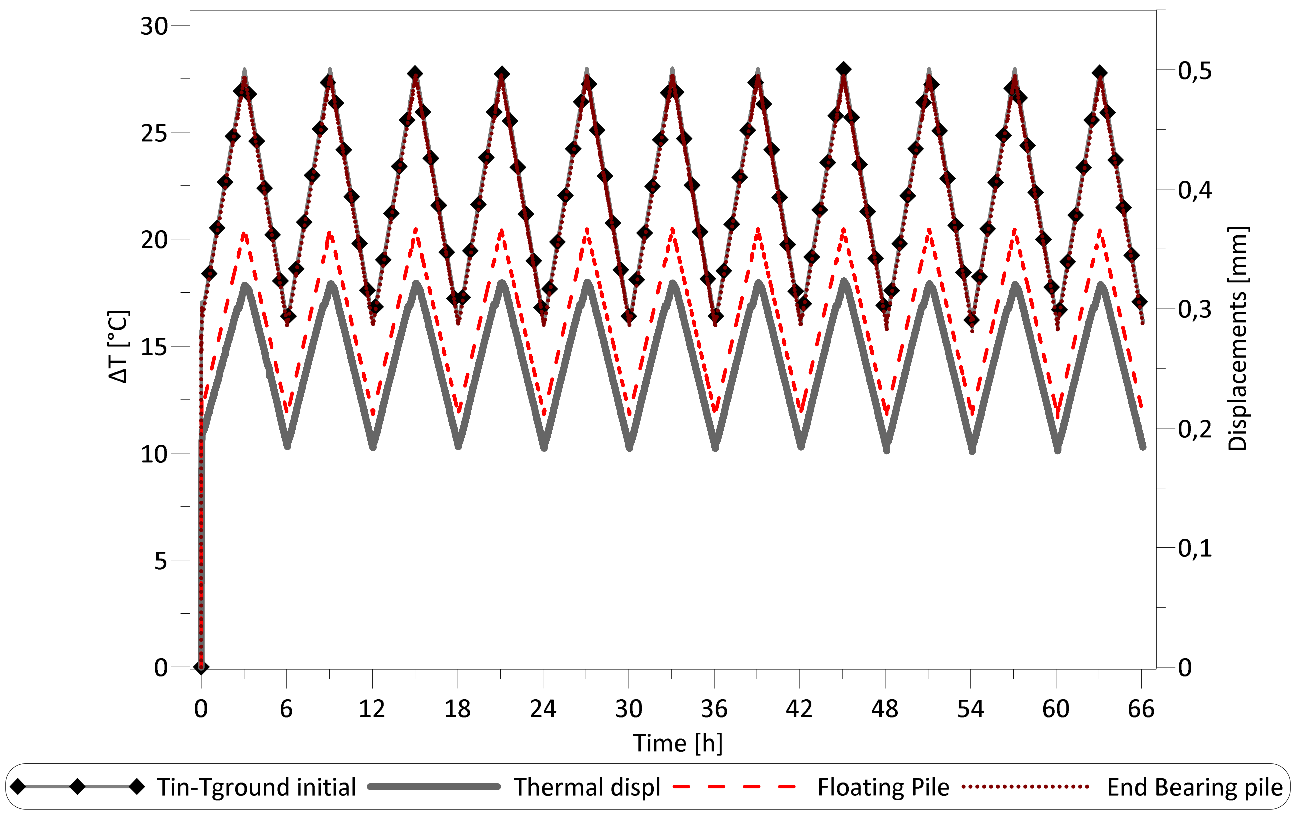

Figure 4-67: Pile's head thermal displacements (Thermal displ), Floating and End bearing Pile displacements (Floating Pile and End Bearing Pile) along with temperature variations (Tin-Tground initial) during the second step of test S2.

Thermal displacement and end bearing and floating pile's displacements along with thermal variations during the second step of the test are plotted in Figure 4-67. Thermal displacement is closer to the displacement of the floating pile. Therefore, in agreement with the mobilization of the thermal expansion coefficient the NP depth is attended at depth above pile's mid depth.

Thermal and thermomechanical loading profile envelope is plotted in Figure 4-68 (b) and Figure 4-68 (a), respectively.

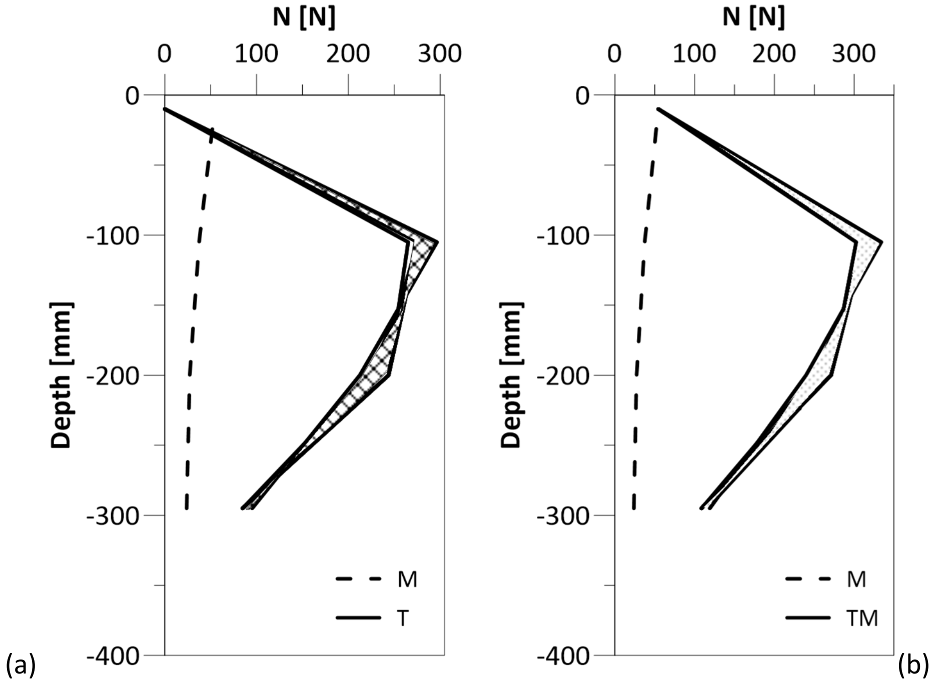

Figure 4-68:Axial Loading profile envelopes; (a) Thermal envelope(T) and purely mechanical profile (M) and (b) Thermomechanical envelope (TM) and purely mechanical profile (M).

The axial load during the first step of the test is plotted both in Figure 4-68 (a) and Figure 4-68 (b) in dotted black line and named as "M". The axial load envelope included the upper and lower bounds of the thermal and thermomechanical loading at the peak of each thermal cycle. The maximum thermal and thermomechanical axial load occurred at 105 mm depth from pile head i.e., NP position. The maximum thermomechanical load of 334 N at 105 mm depth occurred at the peak of the first heating episode. With increasing number of thermal cycles, the thermomechanical axial load at 105 mm of depth decreased to 304 N. At the location of G3 (200 mm of depth from pile's head) the thermomechanical axial load increased with the number of thermal cycles. At the peak of the first thermal cycle, it is 240 N while at the end of the last thermal cycle it is about 271 N. The maximum thermal load observed during the test is about 297 N at 105 mm of depth from pile's head.

The mobilised friction during the peak of each thermal cycle is plotted in Figure 4-69 (a) and Figure 4-69 (b) taking into account the upper and lower thermal and thermomechanical shaft friction, respectively.

The skin friction mobilised during the first step of the test i.e., the purely mechanical friction (M) is plotted both in Figure 4-69 (a) and Figure 4-69 (b) as black dotted line.

The maximum mobilization of shaft friction occurred at the first zone while in the second and third the mobilised skin friction is lower. At the NP position estimated from the axial load profile the skin friction is reversed. The maximum thermal thermomechanical friction in absolute value is about 33 kPa and 31 kPa. In the second and third zones, where the friction is upward, the thermomechanical stress is greater than the thermal stress. The thermomechanical friction is about 10 kPa and 18 kPa in the second and third pile's zones, respectively.

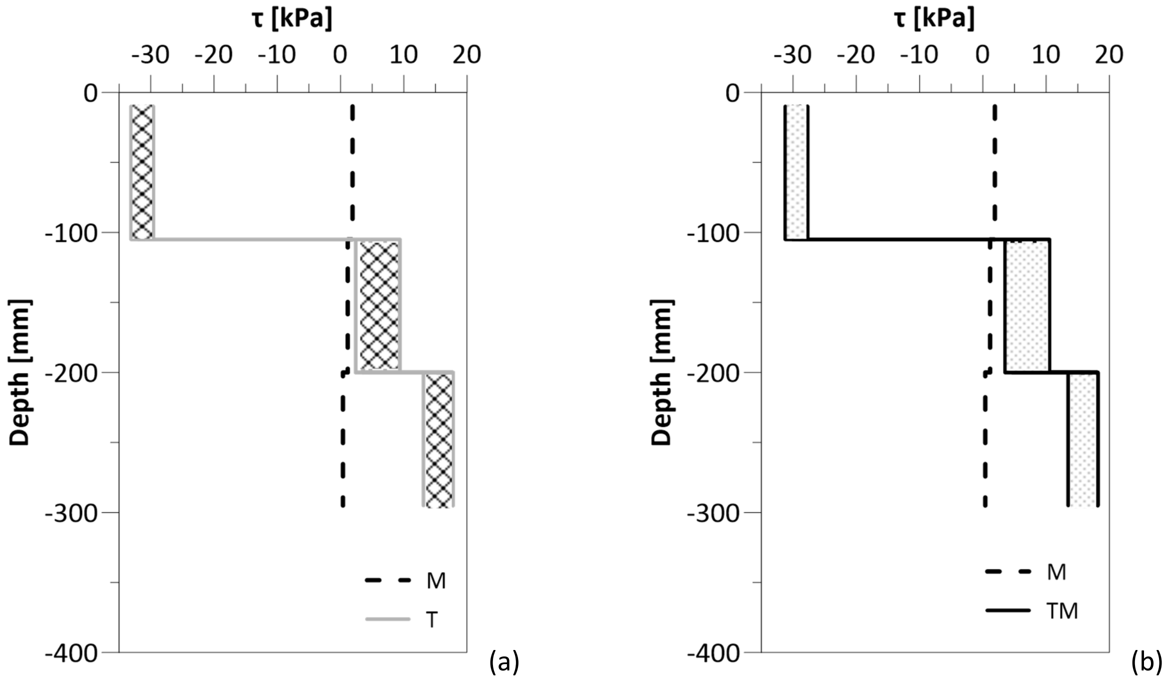

Figure 4-69:Envelope of mobilised shaft friction during the test S2; (a) thermal envelope (T) and purely mechanical profile (M) and (b) thermomechanical envelope (TM) and purely mechanical profile (M).

The shaft friction in the first zone decreased with the increasing number of thermal cycles, reaching -27.7 kPa at the peak of the last thermal cycle. In the second zone the mobilised friction follows the same trend of the first zone reaching 3.5 kPa at the peak of the last heating cycle. In the third zone the thermomechanical mobilised side friction increased with the increasing number of thermal cycle and at the peak of the last thermal cycle the mobilised friction is about 18 kPa.

4.6.4.3 Simplified Thermo-mechanical Cyclic test S3

During the first step of the test the mechanical settlement induced by 96.68 N was -0.08 mm. The average initial soil temperature was 14.7 °C. during the second and third step of the test the temperature of the soil was measured by Tc2, Tc3 and Tc4. The temperature of the soil along with inlet and outlet water temperature and ambient air temperature are plotted in Figure 4-70.

After one hour from the starting of the test the temperature at Tc2, Tc3 and Tc4 was 25.1 °c, 26.1 ° C and 16.8 °C. From the beginning of the test soil temperature at 1D away from the pile is increased of about 2 °C.

Temperature measured in Tc2 was always lower to those measured in Tc3. The difference between Tc3 and Tc2 temperature is maximum during the peak of the first thermal cycle (1.6 °C) and decrease with the increasing number of thermal cycles reaching 0.7 °C at the end of the eleventh thermal cycle. Temperature of soil during the second step of test are reported in Table 4-12.

Table 4-12: Temperature of soil during the second step of test S3.

Time	Temperature Tc2	Temperature Tc3	Temperature Tc4
[h]	[°C]	[°C]	[°C]
0.1	17.61	19.16	14.81
1	25.1	26.41	16.83
3	30.97	32.58	20.82
6	27.32	27.99	22.47
9	32.33	33.67	23.65
12	28.07	28.67	24.08

15	32.82	34.17	24.8
18	28.46	28.99	24.97
21	33.13	34.38	25.49
24	28.69	29.22	25.58
27	33.31	34.51	26.02
30	28.91	29.32	25.99
33	33.48	34.62	26.41
36	29.08	29.47	26.32
39	33.58	34.69	26.76
42	29.26	29.51	26.67
45	33.78	34.75	26.96
48	29.45	29.6	26.89
51	33.88	34.73	27.2
54	29.58	29.69	27.07
57	34.01	34.83	27.4
60	29.73	29.75	27.27
63	34.12	34.83	27.54
66	29.83	29.78	27.46

Temperature of soil and ambient air during the third step are reported in Table 4-13. At the end of the thermal recovery thermal equilibrium was not reached because both the temperature at different distances from the pile were different and the air ambient temperature was smaller.

Table 4-13: Temperature of soil and ambient air during the third step of test S3.

Time	**Temperature Tc2**	**Temperature Tc3**	**Temperature Tc4**	**Temperature Tc5**	**Air Temperature**
[h]	[°C]	[°C]	[°C]	[°C]	[°C]
66	29.83	29.78	27.46	-	18.557
71	21.83	21.26	23.06	-	17.368
76	20.31	19.84	21.26	20.91	17.439
81	19.51	19.03	20.21	19.94	16.868
86	19.01	18.43	19.57	19.28	16.654
91	18.57	18.01	19.08	18.82	16.463
96	18.27	17.55	18.61	18.23	16.511
101	18.11	17.39	18.32	17.93	16.654
104	18.03	17.34	18.17	17.79	16.677

Pile's head thermal and thermo-mechanical displacements are plotted in Figure 4-71. Thermal displacement, floating and end bearing pile's displacements are plotted in Figure 4-72 along with the thermal variations applied during the second step of test S3. The maximum thermal displacement is 0.34 and it is observed during the peak of the first thermal cycle. With the increasing number of thermal cycles, the thermal heave of pile's head decreases. At the peak of the eleventh thermal cycle the upward displacement of pile head is 0.31 mm. At the end of the recovery phase the residual displacement measured is about 0.05 mm. From Figure 4-72 it could be observed that the thermal pile's head displacement is closer to the displacement of the floating pile. Therefore, the NP position could be attended above pile's mid depth depending on the degree of mobilization of the coefficient of free thermal expansion of aluminium.

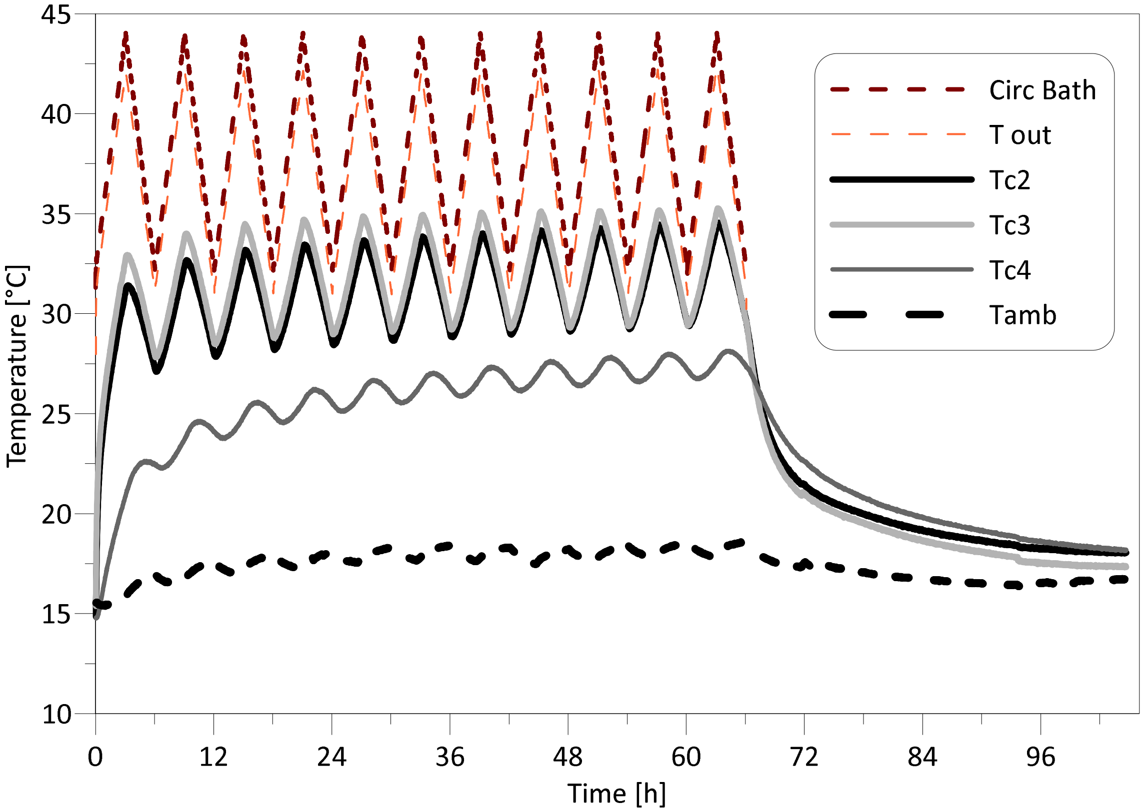

Figure 4-70: Temperature evolution during the cyclic thermo-mechanical heating test S3. Temperature of soil at soil pile interface (Tc2 and Tc3) and at 1D away from the pile (Tc4), outlet water temperature (Tout) and inlet water temperature (Circ Bath) during the first step and air temperature (T amb).

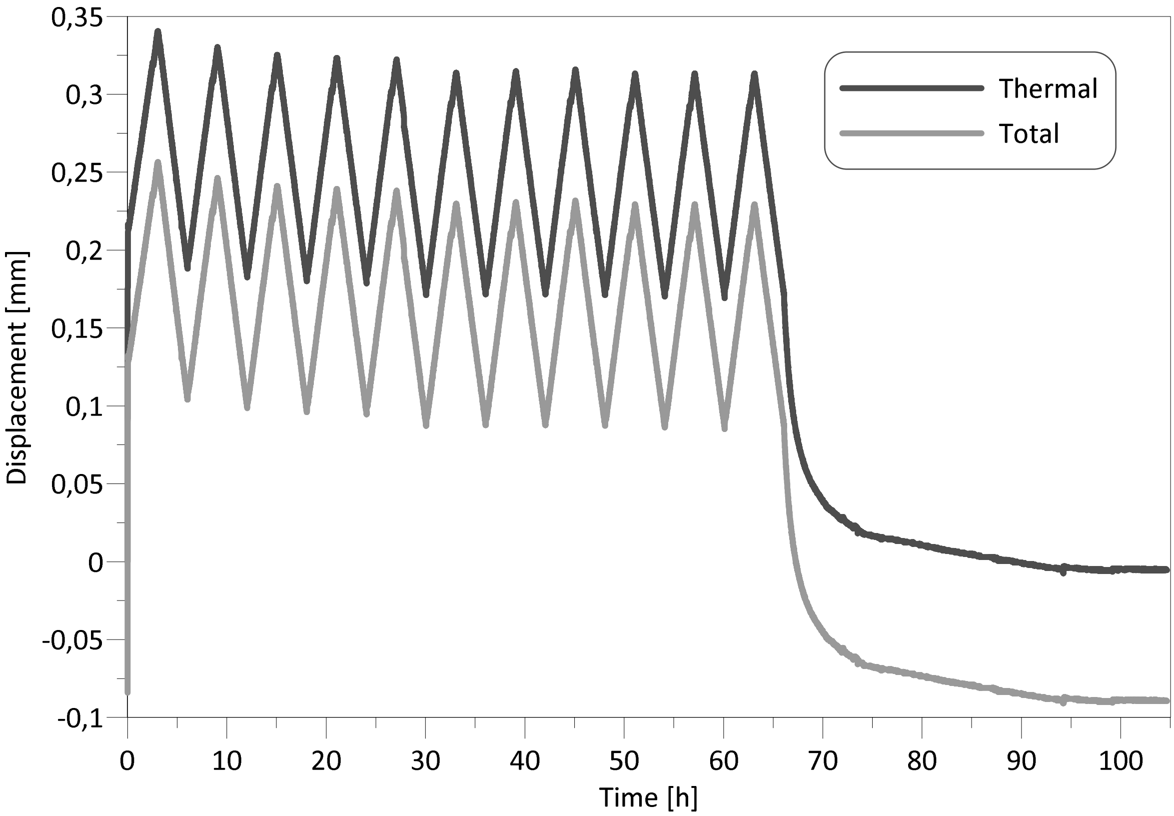

Figure 4-71:Pile's head thermal and Thermo-mechanical (Total) displacements measured during test S3.

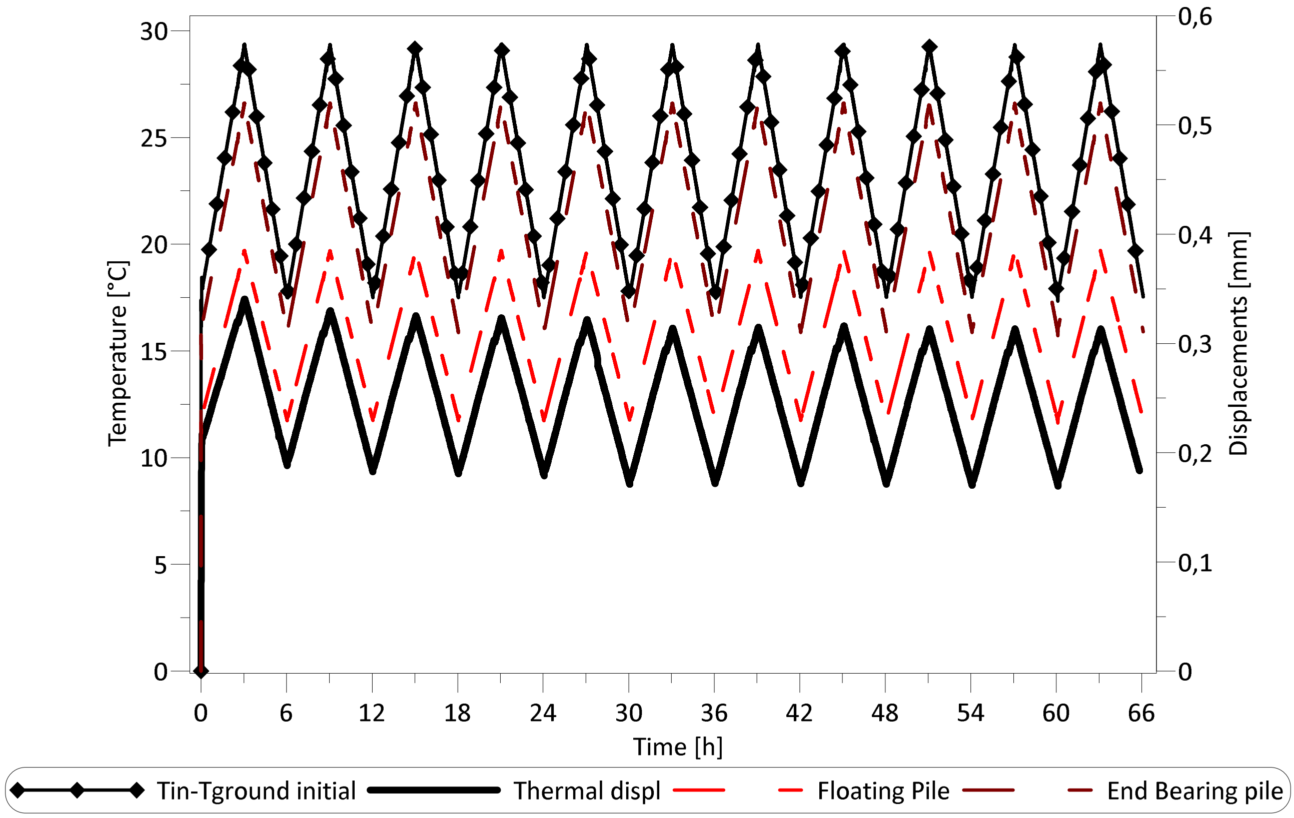

Figure 4-72: Pile's head thermal displacements (Thermal displ), Floating and End bearing Pile displacements (Floating Pile and End Bearing Pile) along with temperature variations (Tin-Tground initial) during the second step of test S3.

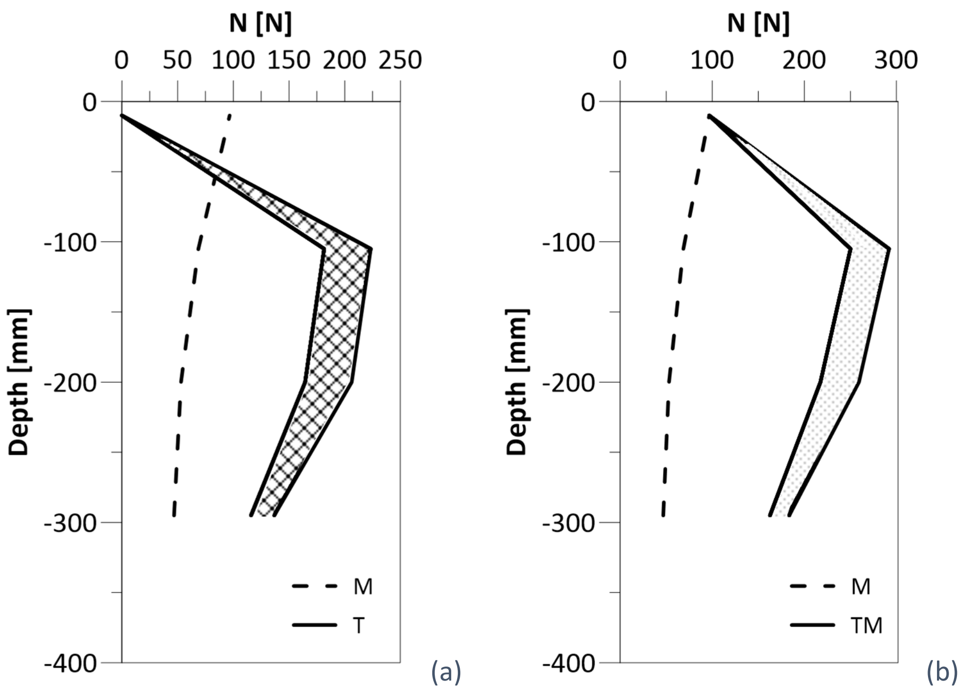

Figure 4-73: Axial Loading profile envelopes during test S3; (a) Thermal envelope(T) and purely mechanical profile (M) and (b) Thermomechanical envelope (TM) and purely mechanical profile (M).

Thermal and thermomechanical axial load profile envelope is plotted in Figure 4-73 (a) and Figure 4-73 (b), respectively. The upper and lower bounds of the thermal and thermomechanical profiles are plotted at the peak of heating. The mechanical load profile is also shown in Figure 4-73 (a) and Figure 4-73 (b) as clack dotted line (M). The thermal and thermomechanical loadings are compressive. Thermal loads combined to the mechanical loadings determines an increase of the axial load along the entire depth of measure.

At the peak of the first thermal cycle, the maximum thermal and thermomechanical load is 292 N and 223 N, respectively.

At the peak of the last thermal cycle and at the 105 mm of depth thermal and thermomechanical axial load is about 250 N and 182 N, respectively. The mobilised thermal and thermomechanical shaft friction envelopes are plotted in Figure 4-74 (a) and Figure 4-74 (b), respectively.

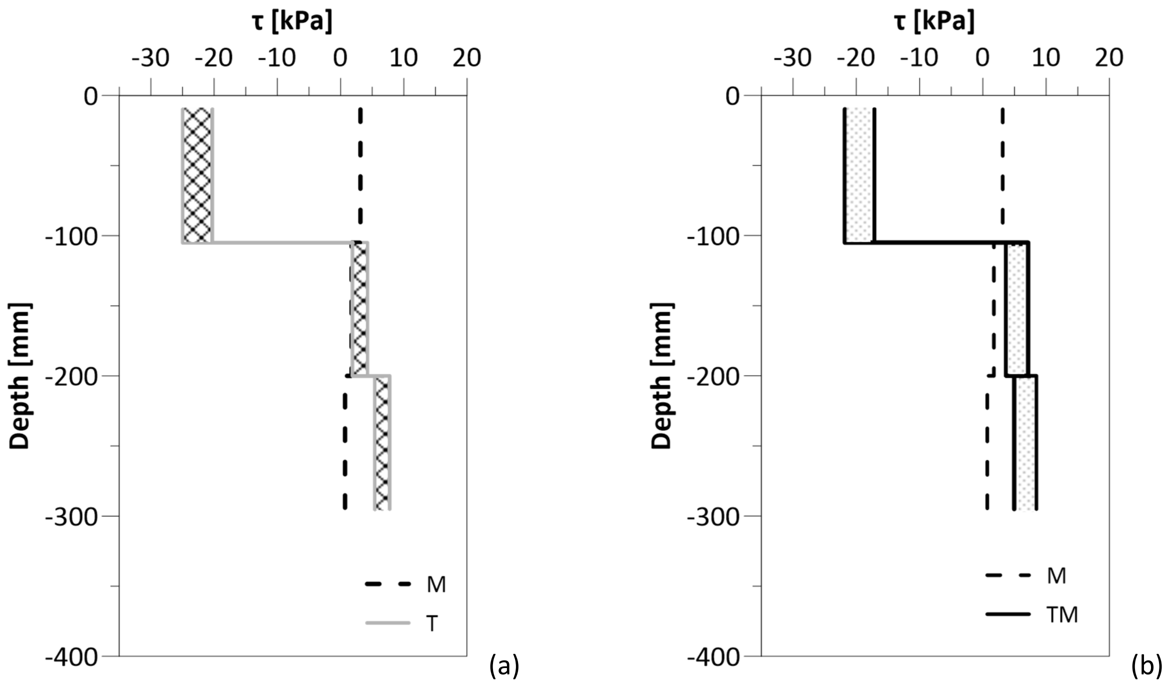

Figure 4-74: Envelope of mobilised shaft friction during the test S3; (a) thermal envelope (T) and purely mechanical profile (M) and (b) thermomechanical envelope (TM) and purely mechanical profile (M).

The maximum mobilization of shaft friction occurred at the first zone. The minimum thermal and thermomechanical mobilised friction is -25 kPa and -22 kPa, respectively. At 105 mm depth from pile's head the shaft friction is reversed, and the maximum thermal and thermomechanical stress is 4 kPa and 7 kPa. In the third zone the maximum thermal and thermomechanical shaft friction slightly differ and are about 8 kPa.

4.6.4.4 Simplified Thermo-mechanical Cyclic Test S4

During the first step of the test the pile's head settlement induced by the axial load of 144.89 N induced a pile's head settlement of -0.11 mm. The initial average soil temperature is about 18 °C. During the second step soil temperatures were measured by Tc2.Tc3 and Tc4. During the third step the temperature of soil was measured also by Tc5. Soil temperatures at different location are plotted along with the inlet and outlet water temperature and air temperature in Figure 4-75.

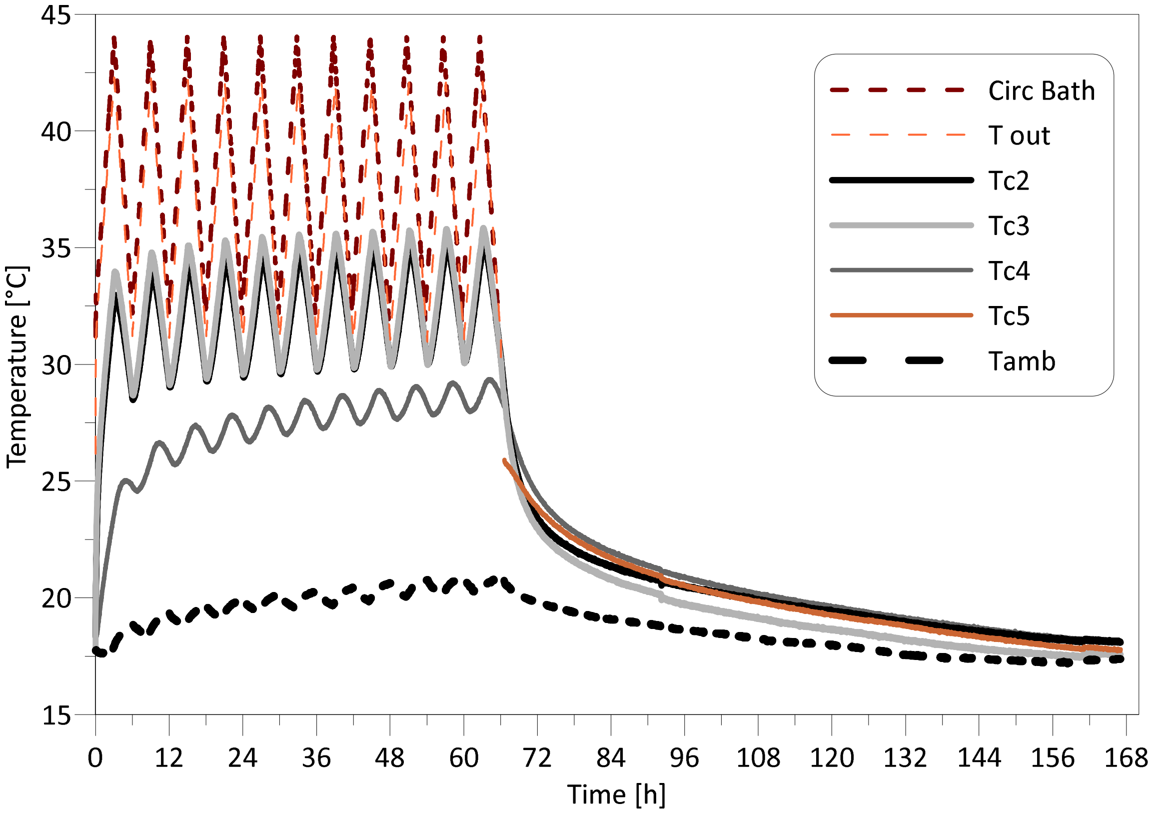

Figure 4-75: Temperature evolution during the cyclic thermo-mechanical heating test S4. Temperature of soil at soil pile interface (Tc2 and Tc3) and at 1D away from the pile (Tc4), outlet water temperature (Tout) and inlet water temperature (Circ Bath) during the first step and air temperature (T amb).

Soil temperatures during the test are reported also in Table 4-14. Soil and air ambient temperature measured during the recovery phase are reported in Table 4-15.

Table 4-14: Temperature of soil during the second step of test S4.

Time	Temperature Tc2	Temperature Tc3	Temperature Tc4
[h]	[°C]	[°C]	[°C]
3.03	32.73	33.84	23.58
6.03	28.53	28.69	24.74
9.04	33.76	34.64	25.91
12.04	29.09	29.14	26.04
15.04	34.11	34.99	26.76
18.04	29.37	29.41	26.64
21.04	34.26	35.19	27.28
24.04	29.57	29.63	27.08
27.04	34.4	35.26	27.57
30.05	29.66	29.71	27.41
33.05	34.51	35.42	27.88
36.05	29.79	29.77	27.67
39.05	34.65	35.46	28.1
42.06	29.9	29.9	27.92
45.06	34.72	35.53	28.35
48.07	30	29.95	28.07

51.07	34.8	35.64	28.53
54.07	30.11	30.06	28.24
57.07	34.89	35.66	28.67
60.08	30.21	30.09	28.44
63.08	34.95	35.68	28.82
66.08	30.29	30.18	28.58

Table 4-15: Temperature of soil and ambient air during the third step of test S4.

Time	Temperature Tc2	Temperature Tc3	Temperature Tc4	Temperature Tc5	Air Temperature
[h]	[°C]	[°C]	[°C]	[°C]	[°C]
75	22.55	22.17	23.46	23.09	19.579
80	21.75	21.28	22.49	22.25	19.27
85	21.25	20.7	21.88	21.59	19.056
90	20.87	20.25	21.4	21.08	18.866
95	20.55	19.82	20.91	20.61	18.675
100	20.29	19.5	20.63	20.26	18.509
105	20.07	19.29	20.34	19.96	18.343
110	19.85	18.99	20.08	19.71	18.176
115	19.6	18.78	19.85	19.44	18.057
120	19.42	18.61	19.61	19.27	17.986
125	19.23	18.47	19.41	19.03	17.843
130	19.04	18.28	19.21	18.9	17.653
135	18.82	18.1	19.03	18.68	17.486
140	18.67	17.91	18.85	18.5	17.439
145	18.54	17.81	18.68	18.32	17.368
150	18.38	17.64	18.46	18.11	17.296
155	18.26	17.59	18.36	17.99	17.249
160	18.13	17.49	18.2	17.83	17.225
165	18.13	17.59	18.16	17.76	17.368

At the end of the recovery phase as could be observed from Table 4-15 and Figure 4-75 thermal equilibrium between soil and ambient air is not completely reached. Soil temperature close to the pile's edged were larger than those observed a greater distance away from the pile.

Pile's head thermal and thermomechanical displacements during the test are plotted in Figure 4-76. The maximum thermal displacement it is observed during the first thermal cycle. The thermal and thermo-mechanical displacement is 0.31 mm and 0.20 mm, respectively. With increasing of thermal cycles, the pile's head heave decrease and reached 0.16 mm during the least thermal cycle.

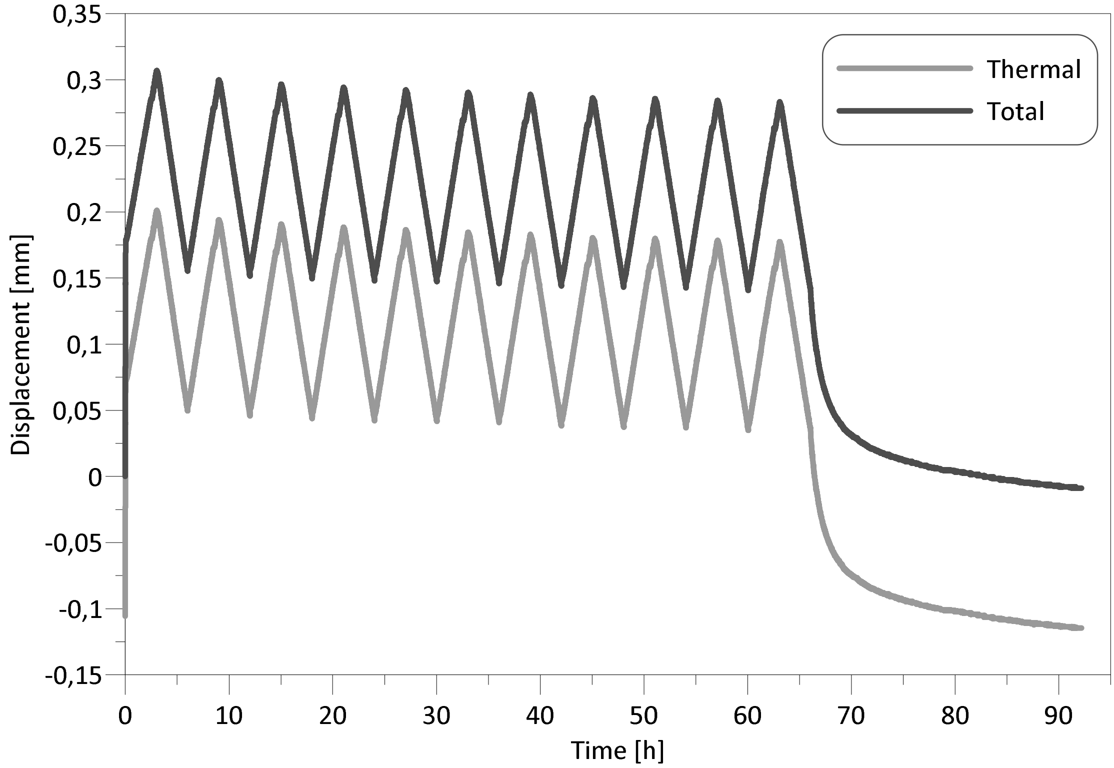

Figure 4-76:Pile's head thermal and Thermo-mechanical (Total) displacements measured during test S4.

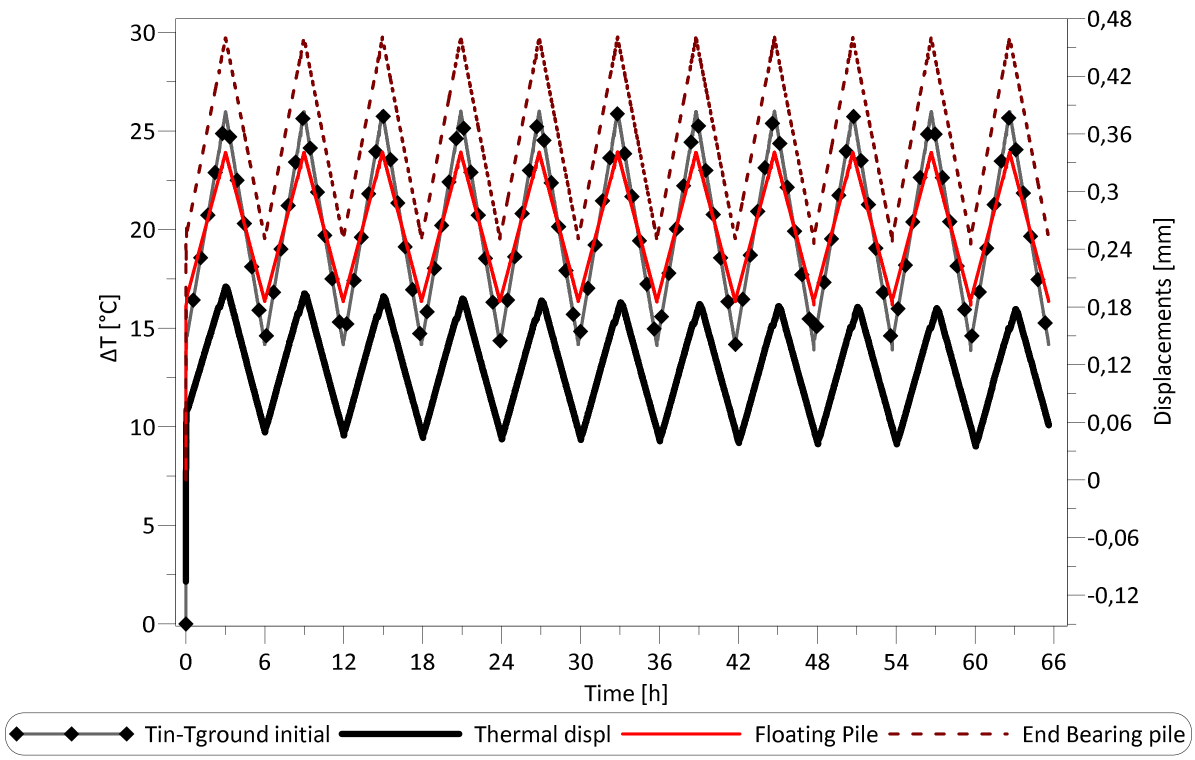

Figure 4-77: Pile's head thermal displacements (Thermal displ). Floating and End bearing Pile displacements (Floating Pile and End Bearing Pile) along with temperature variations (Tin-Tground initial) during the second step of test S4.

Thermal pile's displacement along with the end bearing and floating pile displacement and thermal variations versus elapsed time are plotted in Figure 4-76 where it can be observed that pile's thermal head displacement is lower than the displacement of the floating pile.

Axial thermal and thermomechanical profile envelope obtained considering the mid of each thermal cycle is plotted in Figure 4-78 (a) and Figure 4-78 (b), respectively. The maximum thermal load occurred above pile's mid depth (105 mm of depth from pile's head) during the first thermal cycles and then at 200 mm of depth. The maximum thermomechanical and thermal load observed at peak heating and 105 mm of depth is 347 N and 229 N. respectively. With the increasing number of thermal cycles, the thermomechanical and thermal load, at this depth, decreased to 305 N and 171 N, respectively. The thermomechanical and thermal load observed at the peak of the initial cycles and 200 mm of depth is 306 N and 207 N, respectively. At this depth (200 mm) an increasing trend it is observed with thermal and thermomechanical load of 337 N and 238 N, respectively. The increasing and decreasing of the axial load at pile's mid and 105 mm of depth were observed also during the other cyclic test even if the NP position was constant. The axial load evolution with increasing number of thermal cycles does not follow a precise trend but a downward movement of the NP depth could be identified. During the initial thermal cycles (until the fourth cycle), NP is located above pile's mid depth and then at pile's mid depth.

Thermal and thermomechanical shaft friction profile is plotted considering the upper and lower profiles occurring at the peak of each thermal cycle in Figure 4-79 (a) and Figure 4-79(b), respectively. The higher mobilised friction it is observed at the first zone of the pile. At this zone, the minimum thermal and thermomechanical mobilised shaft friction is -26 kPa and -23 kPa. In the second zone the maximum mobilised thermomechanical and thermal shaft friction is 4.5 KPa and 2.5 kPa, respectively. In the third zone the maximum thermomechanical and thermal shaft friction is 25.5 KPa and 22.5 KPa, respectively. The mobilised shaft friction in the second zone during the first fourth cycle is upward, and then it is downward because the NP position was moving downward during the test. As stated above, it was not possible to define a precise trend of thermal and thermomechanical shaft friction evolution with the increasing number of thermal cycles.

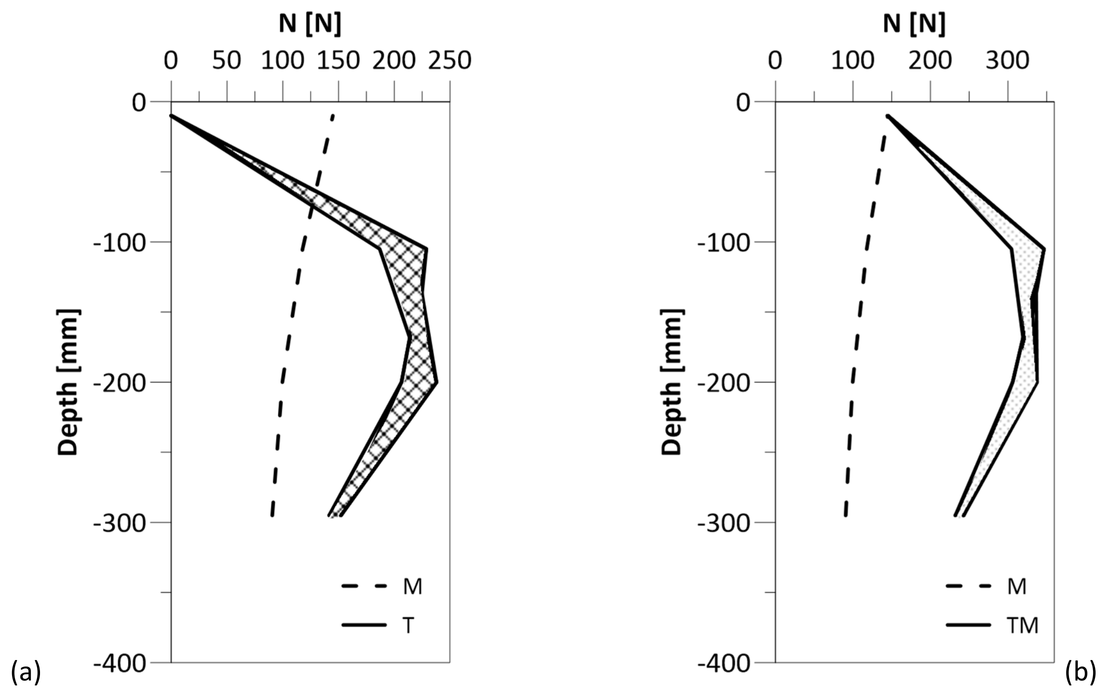

Figure 4-78: Axial Loading profile envelopes during test S4; (a) Thermal envelope(T) and purely mechanical profile (M) and (b) Thermomechanical envelope (TM) and purely mechanical profile (M).

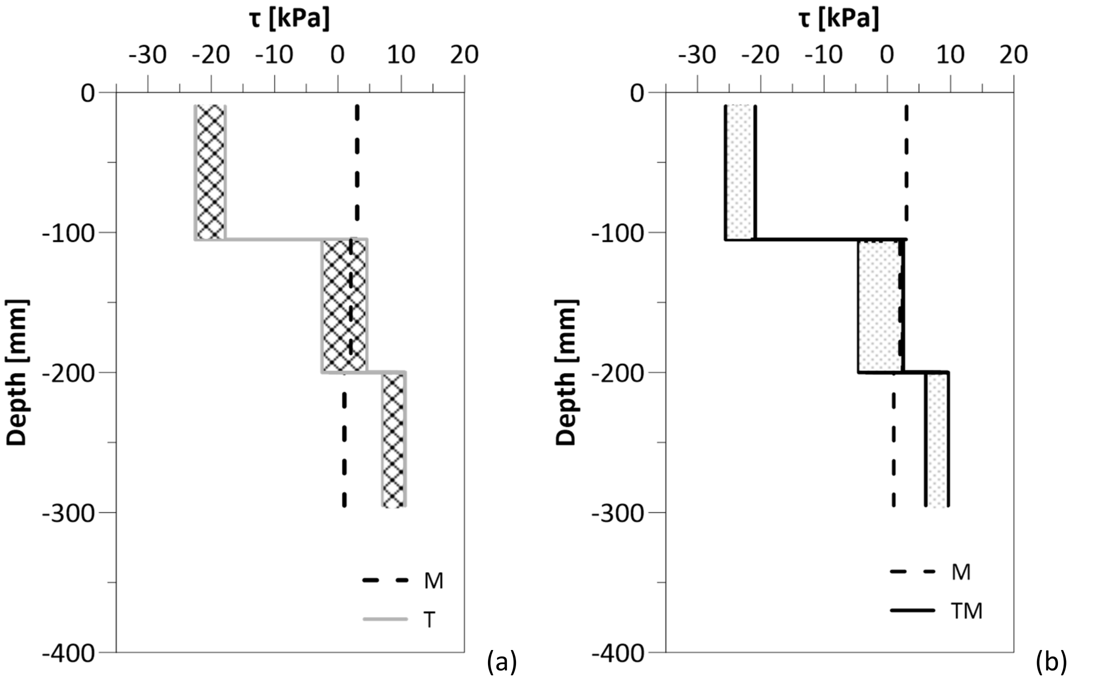

Figure 4-79: Envelope of mobilised shaft friction during the test S4; (a) thermal envelope (T) and purely mechanical profile (M) and (b) thermomechanical envelope (TM) and purely mechanical profile (M).

4.6.5 Observations and concluding remarks on Model B

In Model B the pile's head displacement measured during the mechanical load test are significantly smaller than those observed without loading at ground surface (Model A). This is caused by an increase of soil stiffness induced by the higher level of confining stress. Comparing the displacements between the two conditions (Model A and Model B) it is possible to estimate the increasing of soil stiffness that occurred in Model B. The effect of the increased soil stiffness on the thermomechanical interaction can be evaluated comparing the pile's head thermal displacements measured on Model B under the same level of thermal and mechanical loading to those measured on Model A. The pile's head displacement during the thermomechanical test at variable temperature (4.5.4) carried out on Model A is compared to the displacement during the first cycle of cyclic thermo-mechanical test on Model B in Figure 4-80. It should be highlighted that the differences between the two tests do not depend only on the different load condition at soil surface but also to the level of mechanical stress and applied thermal loading. With respect to the mechanical level of stress the tests are carried out at the same SF and only the thermal displacement is considered. The main differences in terms of applied load occurred with respect to the thermal loadings. The two tests are carried out at different soil initial temperature therefore even if the thermal history that had been applied matched different thermal variations occurred. To this aim the two cases are compared taking into account the average mobilised thermal expansion coefficient along the pile length until NP depth (α_{mob}). It is simply computed as the ratio of the thermal displacement to $y_{th.free}$ (free elongation of the pile, see 2.2) versus time. It is plotted in Figure 4-80 during the first cycle of the cyclic heating thermomechanical history On Model B and during the thermomechanical load test at variable temperature on Model A. In Model B the application of the load on ground surface determines an increasing of about 40% of soil secant stiffness at 50% of the ultimate pile's bearing capacity with respect to Model A. Comparing α_{mob} in Model A and Model B, Figure 4-80, greater mobilisation is observed in the former case. The increase of soil stiffness determines a decrease of α_{mob}. In this case the mobilised thermal expansion coefficient in Model B is about 15% smaller than α_{mob} in Model A.

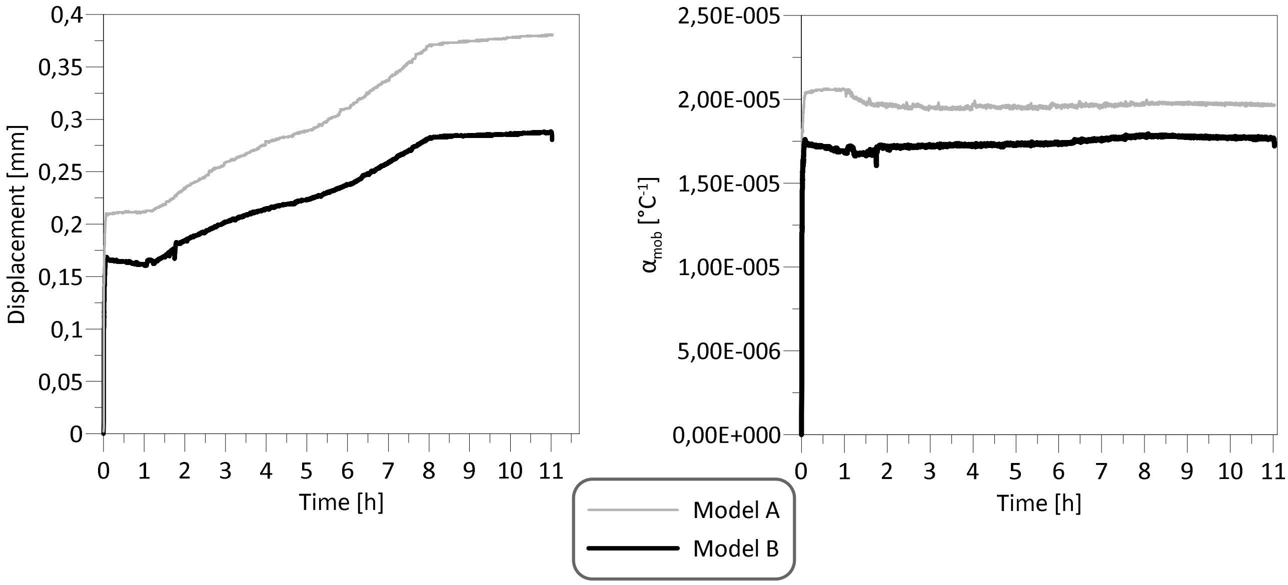

Figure 4-80: Pile's head thermal displacement and pile's mobilised thermal expansion coefficient (α_{mob}) versus time during the thermomechanical test at variable temperature on Model A and the first cycle of the cyclic thermomechanical test of heating on Model B.

DDRs for the thermomechanical cyclic histories of cooling and heating and tests S1, S2, S3 and S4 are plotted versus the number of thermal cycles in Figure 4-81. Heating and cooling modes are separated and the experimental results are plotted along with the data collected from previous studies (2.3).

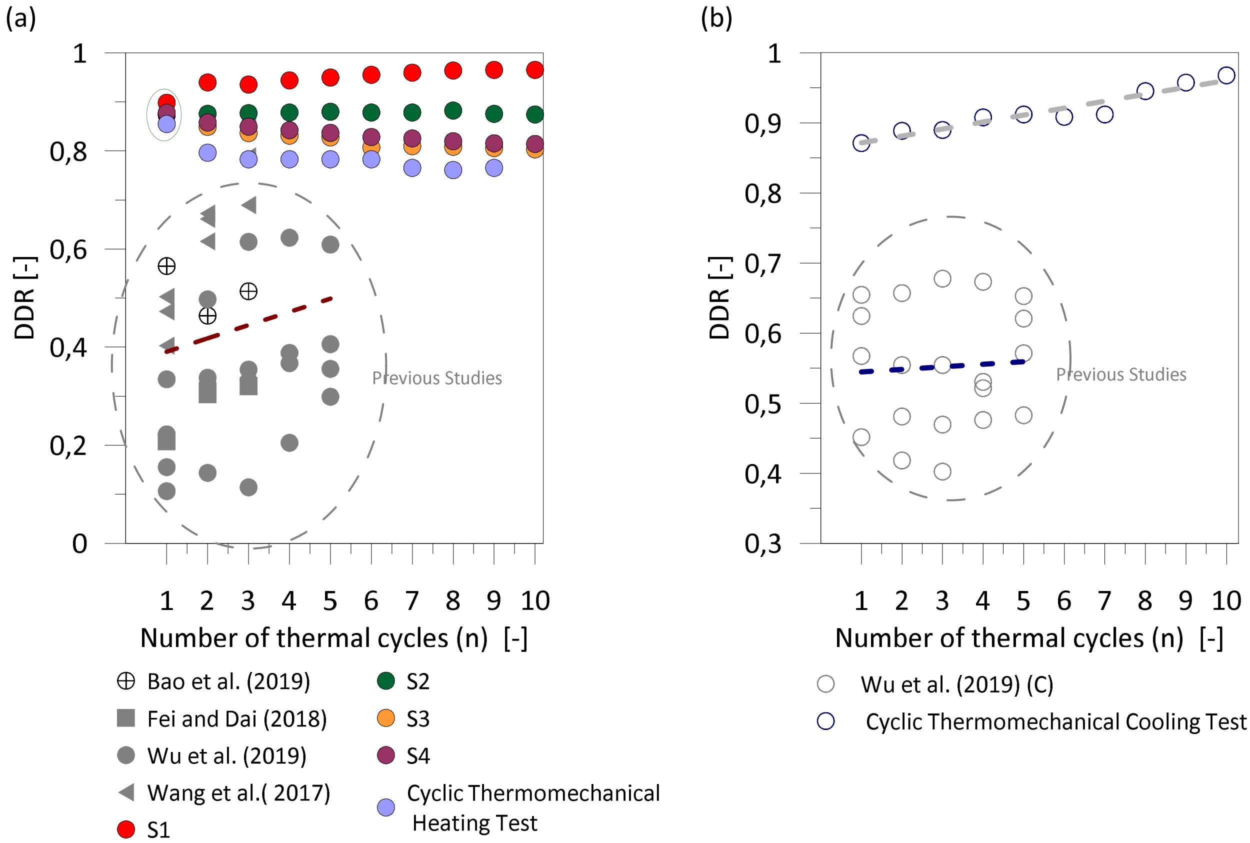

Figure 4-81:DDR versus number of thermal cycle (n) during heating (a) and cooling (b) modes.

From Figure 4-81 (a) different observations can be made about the relationship between the DDRs and numbers of thermal cycle. First of all, it could be observed that DDR computed at the peak of the first thermal cycle almost matches for each test. It should be highlighted that DDR is computed at different SFs and in the case of the cyclic thermal test different thermal loadings. Comparing DDR at the peak of the first thermal cycle of tests S1. S2. S3 and S4 a relationship between the SF and DDR is not founded. This result can be explained taking into account that the magnitude of the effects induced by thermal loading are larger than those induced by the mechanical loading. Considering the mobilised shaft friction. thermal loadings induced mobilised skin frictions that are larger of one order of magnitude with respect to those mobilised by the purely mechanical loading. A greater DDR and therefore a greater mobilised thermal expansion coefficient could be expected with increasing SF in the case of heating above the NP. The superposition of the effect induced by the thermal and mechanical loadings induces a smaller total skin friction with respect to those mobilised for purely thermal loadings. In this case this effect is very small and therefore a relationship is not observed during the first thermal cycle. From Figure 4-81 (a) and (b) a relationship between the DDR and number of thermal cycles is observed both in the case of cooling and heating episodes. In the former case. as observed from the results of Wu et al. (2019) with increasing number of thermal cycles the DDR increases. This is connected to a larger mobilisation of the skin friction with increasing of thermal cycles. Form Figure 4-81 (a) a different trend of DDR with increasing thermal cycles it is observed depending on the level of mechanical stress. For null mechanical loading (S1), DDR increases with increasing thermal loading. For lower level of stress e.g., SF=6 the DDR is almost constant with the increasing number of thermal cycles. For higher level of mechanical stress e.g., SF=3 and SF=2 DDR decreases with increasing thermal cycles. Therefore, in the case of heating a relationship between pile's head displacement and number of thermal cycles considering the level of mechanical stress is proposed. Thermal displacement at n thermal cycle $y_{th.n}$ is provided by Equation 4-15 and it is expressed in unit of length.

Equation 4-15: $y_{th.n} = \frac{a^{\eta}}{n} - 1$ [mm]

Where: η is a fitting parameter obtained from regression analysis that depends on the SF and n is the number of thermal cycles at which the variation of thermal displacement is considered. For null thermal loading $\eta = -0.008$ while for SF=2,3 and 6 it is 0.008,0.01 and 0.0006, respectively. The power law relationship calibrated on the experimental results is plotted in Figure 4-81 along with the maximum thermal displacement computed during each thermal cycles.

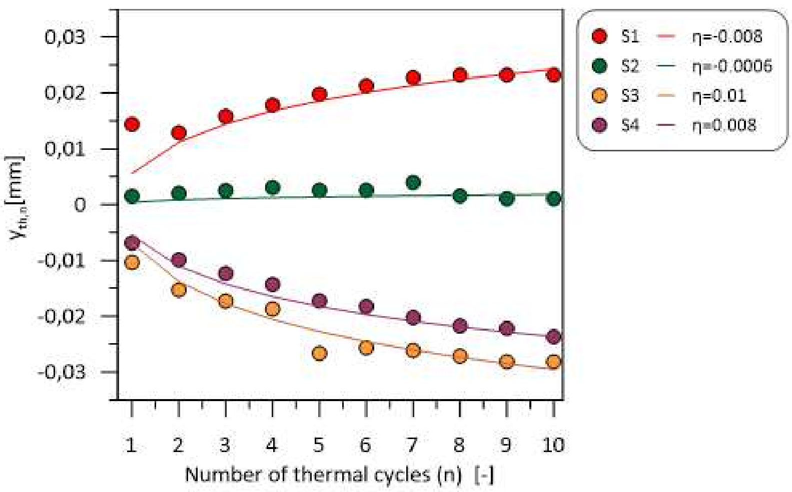

Figure 4-82: Thermal displacement $y_{th.n}$ with increasing number of thermal cycles, experimental relationship at different SF.

With respect to the thermal behavior the measurements provided by the temperature transducers confirmed that the heat was diffused radially from the pile to the surrounding soil in all the test performed. The thermal variations applied to the pile influences the temperature distribution inside the experimental box as summarised in Table 4-16.

Table 4-16: Cyclic Thermo-mechanical tests.

Cyclic thermal and thermo mechanical heating test	Steps									
	Mechanical				Thermal/Thermo-mechanical				Recovery	
	SF	Load [N]	Mechanical settlement [mm]	T av soil in [°C]	Time duration [h]	ΔT max [°C]	$N_{thermal\ max}$ [N]	$y_{thermal\ max}$ [mm]	Time duration [h]	T av soil end [°C]
S1	-	-	-	17.79	66	26.2	276	0.33	59.9	18.48
S2	6	48.17	-0.06	16.05	66	27.7	297	0.32	105	19.19
S3	3	96.68	-0.09	14.7	66	29.4	224	0.34	39	1.6
S4	2	144.89	-0.11	18.02	66	26.4	225	0.31	26	19.86

The thermal and thermomechanical axial force profiles and mobilised skin friction show the performance of SG capturing the mechanical behavior of model pile under thermal and thermomechanical tests. The maximum thermal axial load during each sinusoidal cyclic test is reported in Table 4-16. For test S3 and S4 the maximum thermal stress is probably measured between G2 and G3 therefore it is not completely captured from the SG.

References

ASTM Standards: D 3080 D3080M – 11 Standard Test Method for Direct Shear Test of Soils Under Consolidated Drained Conditions

ASTM Standards: D 4253 – 00 Standard test methods for maximum index density and unit weight of soils using a vibratory table.

ASTM Standards: D 4254 – 00 Standard test methods for minimum index density and unit weight of soils and calculation of relative density.

ASTM Standards D53334-14: Standard Test Method for Determination of Thermal Conductivity of soil and Soft Rock by Thermal Needle Probe Procedure

Baldi, G., Bellotti, R., Ghionna. V., Jamiolkowski, M., Pasqualini, E. 1986. Interpretation of CPT's and CPTU's. 2nd Part: Drained Penetration. Proceeding 4th International Geotechnical Seminar. Singapore. 143-156.

Berezantsev. V.G., Kristoforov. V., Golubkov. V. 1961. Load bearing capacity and deformation of pile foundations. Proceedings of the fifth International conference of Soil Mechanics and Foundation Engineering ,2, Paris, 11-15.

Bourne-Webb. P.J., Bodas Freitas, T.M., 2020. Thermally-activated piles and pile groups under monotonic and cyclic thermal loading–A review. Renew. Energy 147. 2572–2581. https://doi.org/10.1016/j.renene.2018.11.025

Brandl, H., 2006. Energy foundations and other thermo-active ground structures. Geotechnique 56, 81–122. https://doi.org/10.1680/geot.2006.56.2.81

Dias, A.S., Pirone. M., Urciuoli. G., 2018. Calibration of TDR probes for water content measurements in partially saturated pyroclastic slope. Proceeding UNSAT 2018.

Durgunoglhu, T., Mitchell, K, 1975. Static penetration resistance of soils: I-ANALYSIS. Proceedings. ASCE Specialty Conference on in-situ Measurement of Soil Parameters. Raleigh, 1.

Elzeiny, R., Suleiman, M.T., Xiao, S., Qamar, M.A., Al-Khawaja, M., 2020. Laboratory-Scale- Pull-Out Tests on a Geothermal Energy Pile in Dry Sand Subjected to Heating Cycles. Can, Geotech, J. submitted.

Faizal, M, Bouazza, A., Singh R.M., 2016. Heat transfer enhancement of geothermal energy piles. Renew.

Sustain. Energy Rev. 57. 16–33. https://doi.org/10.1016/j.rser.2015.12.065

Fioravante, V., 2002. On the shaft Friction modelling of Non displacement piles in sand. Soils Found. 42, 23–

Kalantidou, A., Tang. A.M.. Pereira. J.M.. Hassen. G.. 2012. Preliminary study on the mechanical behavior of heat exchanger pile in physical model. Geotechnique 62. 1047–1051. https://doi.org/10.1680/geot.11.T.013

Laloui. L., Sutman. M., 2020. Experimental investigation of energy piles: From laboratory to field testing. Geomech. Energy Environ. Article In Press. https://doi.org/10.1016/j.gete.2020.100214

Lancellotta R., 1983. Analisi di Affidabilità in Ingegneria Geotecnica. Atti dell'Istituto di Scienza delle Costruzioni. 625. Politecnico di Torino.

Ledieu, J., De Ridder, P., De Clerck, P., Dautrebande. S. 1986. A method of measuring soil moisture by time-domain reflectometry. Journal of Hydrology 88 .3-4.319-328.

Le Kouby, A., Canou. J., Dupla. J.C., 2004. Behavior of model piles subjected to cyclic axial loading. Cyclic Behavior of Soils and Liquefaction Phenomena. Triantafyllidis (ed). Taylor & Francis Group. London. 159-166.

Mayne, P.W., Coop. M.R., Springman. S., Huang. A.-B., Zornberg. J.. 2009. State-of-the-Art Paper (SOA-1): GeoMaterial Behavior and Testing. Proc. 17th Intl. Conf. Soil Mech. Geotech. Eng. 4. 2777–2872.

Nicotera, M.V., 2002. Resistenza a taglio delle pozzolane del napoletano: analisi statistica dei dati sperimentali. Rapporto interno. Università degli studi di Napoli Federico II.

Papa, R., Nicotera, M.V., 2012. Calibration of TDR probes to measure water content in pyroclastic soils. Unsaturated Soils: Research and Applications. 107-112.

Parkin, A.K. ,Lunne T. , 1982. Boundary Effects in the Laboratory Calibration of a Cone Penetrometer for Sand. Proceedings of the 2nd European Symposium on Penetration Testing. 2. 761–768.

Raucci, M.P., 2017. Comportamento di platee su pali in terreni sabbiosi. Università degli studi di Napoli Federico II.

Robertson, P. K., Campanella, G., 1983. Interpretation of cone penetration tests. Part I: Sand. Canadian Geotechnical Journal. https://doi org/ 10.1139/t83-078

Russo, G., 2013. Experimental investigations and analysis on different pile load testing procedures. Acta Geotech. 8. 17–31. https://doi.org/10.1007/s11440-012-0177-4

Vanapalli, S.K., Eigenbrod, K.D., Taylan, Z.N., Catana. C., Oh., W.T., Garven, E., 2011. A technique for estimating the shaft resistance of test piles in unsaturated soils. Unsaturated Soils - Proc. 5th Int. Conf. Unsaturated Soils 2. 1209–1215. https://doi.org/10.1201/b10526-188

Vanapalli, S.K., Fredlund D.G., Pufahl, D.E. and Clifton, A.W., 1996. Model for the prediction of shear strength with respect to soil suction. Canadian Geotechnical Journal. 33. 379-392.

Viggiani, C., Mandolini, A., Russo, G., 2012 Piles and pile foundations. Ed. Spon Press. Taylor & Francis. London.

Yang, W., Lu, P., Chen, Y., 2016. Laboratory investigations of the thermal performance of an energy pile with spiral coil ground heat exchanger. Energy Build. 128. 491–502. https://doi.org/10.1016/j.enbuild.2016.07.012

Yavari, N., Tang, A.M., Pereira, J.M., Hassen, G., 2014. Experimental study on the mechanical behavior of a heat exchanger pile using physical modelling. Acta Geotech, 9, 385–398. https://doi.org/10.1007/s11440-014-0310-7

5 In situ thermal tests

5.1 *Introduction*

A drilled EP constructed for research purposes was equipped to measure strains and temperatures along the shaft and displacements at the head. Thermal tests were performed by heating the pile to quantify the magnitude of the soil-pile thermo-mechanical interaction. The experimental site is detailed with the local stratigraphy, the pile characteristics and the layout of the tests. The sensors used as well as the data processing methods are also presented. Then, the thermomechanical responses of the pile during three different tests are analysed and compared. Thermal responses of soil and pile were also investigated; the performance of the system was evaluated through the measurements of the heat exchanger fluid temperatures.

5.2 *Test location, pile construction and layout of the test*

The experimental field is in Crispano, close to an industrial area, in North of Napoli. The subsoil is characterized by layered pyroclastic soils products of the Vesuvius and Phlegrean volcanoes. The grain size distribution for samples at different depths (5 m, 6.50 m,11 m and 12.50 m) is reported in Figure 5-1. The specific gravity obtained from samples until 5 m, 6.50 m, 11m and 12.50 m is 2.63 g/cm^3, 2.505 g/cm^3, 2.457 g/cm^3 and 2.467 g/cm^3, respectively.

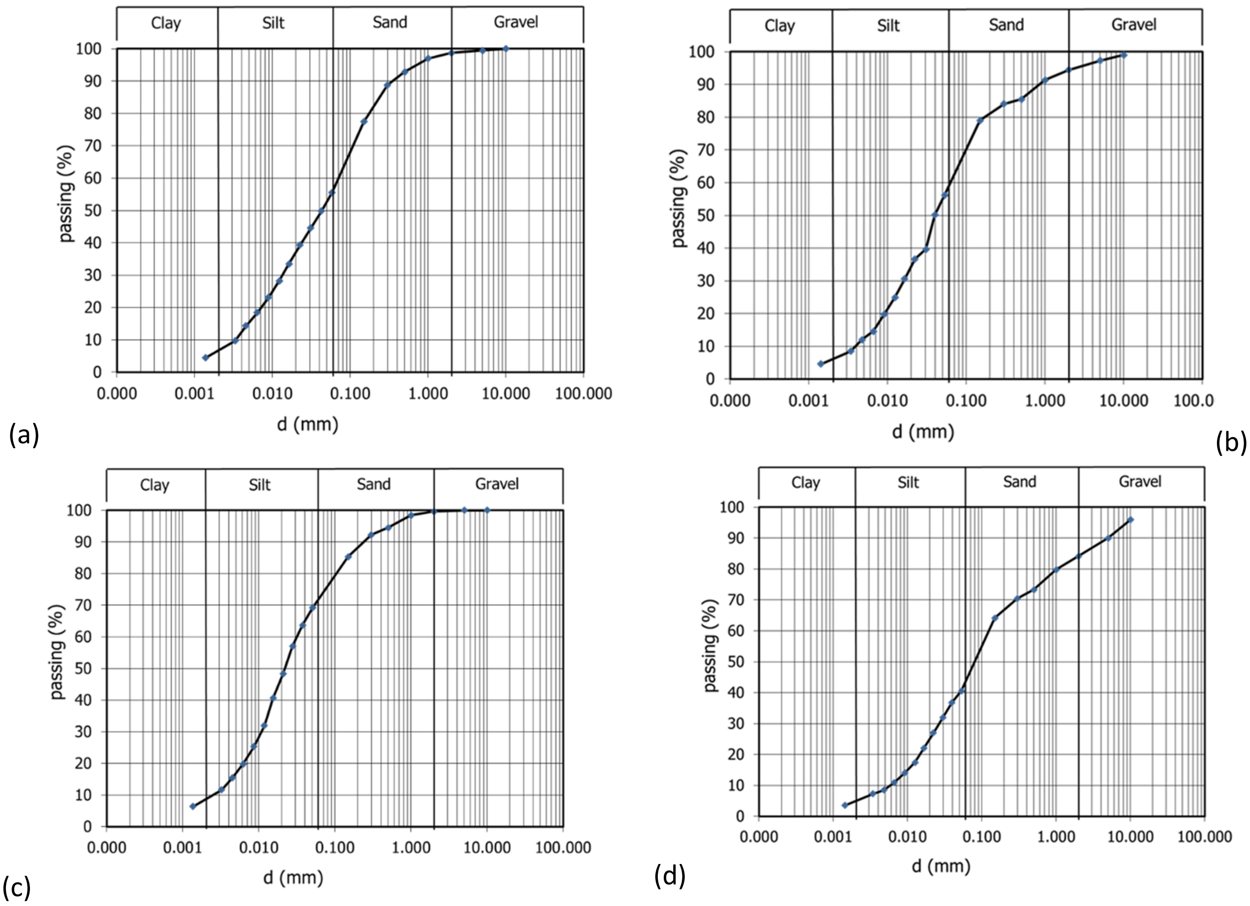

Figure 5-1: Grain size distributions of the soil between 4.70 m – 5 m (a). 6.30 m – 6.50 m (b). 10.80 m -11 m (c) and 12.40-12.50 m (d).

The soil profile is described through one borehole carried out with continuous coring and CPT tests. The cone resistance Qc versus depth is plotted in Figure 5-2.

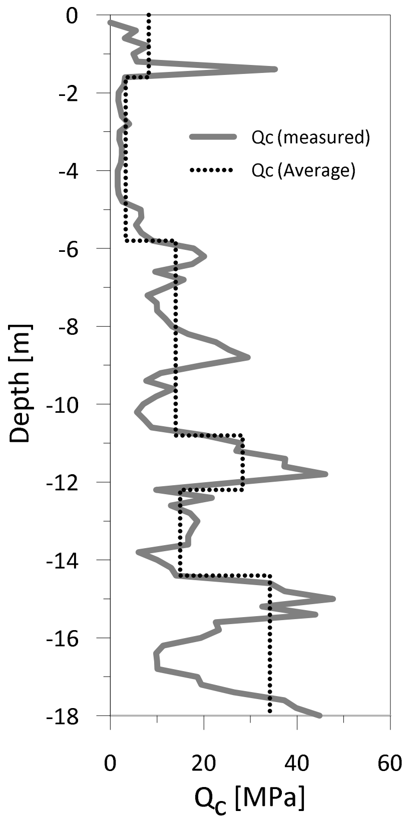

Figure 5-2: CPT results; measured and average cone tip resistances.

From both the borehole and the CPT soil layering was identified. The geotechnical subsoil model is characterised by six main layers. In the upper 1.80 m made ground is found. Between 1.80 m and 5.80 m pyroclastic silt and sand are located. From 5.80 m to 10.80 m alternating sandy silt and dark grey pyroclastic and cinerite materials with low cemented thickness are detected. The fourth layer, ranging between 10.80 to 12.20 m, is characterised by grey volcanic ashes (silt) and silty sand with a gravel fraction consisting in pumices. Between 12.20 m and 14.40 m the finer fraction of ashes prevails on the coarser fraction as it is confirmed by CPT. In the last layer between 14.40 m and 18 m alternating cemented yellow ashes and coarser silty sands are detected. The average cone resistance (Qc Average, Figure 5-2) along with Durgunoglu and Mitchell (1975) method provide the average shear strength angle for each soil layer. Young's modulus was computed by means of De Beer method (1965). Soil physical and mechanical properties are thus summarised in .

Table *5-1*.

Table 5-1:Physichal and mechanical properties of soil layers.

	layer depth [m]	n [-]	w[-]	ɣd [kN/m³]	ɣsat [kN/m³]	φ[°]	E[Mpa]
I	0-1.6	0.49	0.17	13.3	18.2	35	24
II	1.6-5.8	0.53	0.23	12.1	17.4	29	10
III	5.8-10.8	0.54	0.29	11.2	16.6	34	21
IV	10.8-12.2	0.46	0.22	13.2	17.8	35	43
V	12.2-14.4	0.47	0.23	12.9	17.5	31	30

VI	14.4-18	18	34	103

The installation of the pile requires the removal of soil, the installation of the reinforcement cage with the connected PC and sensors and finally the concrete pouring. A rotary drilling equipment was used for the excavation (Figure 5-3 (a)). The drilling tool is a coring bucket. The hole was excavated by the dry method because the soil was self-supporting. The concrete is simply poured via a tremie pipe into the hole without hitting against the walls.


(a)


(b)


(c)


(d)

Figure 5-3: Construction steps: (a) Drilling equipment, (b) excavation, (c) lowering reinforcement cage place (c), (d) concrete pouring.

The test pile is 12 m long and has a nominal diameter of 0.60 m. The concrete is a C25/30 class. The average uniaxial compressive strength of unreinforced cubic concrete samples (150 mm x 150 mm x 150 mm) tested in the laboratory was 35 MPa at 28 days with a modulus of elasticity of 30319 MPa (11.2.5- NTC18).

The reinforcing cage consists of 8 longitudinal rebars B450C class ,14 mm in diameter and 8 mm helical reinforcements with stirrups leg of 0.2 m, until a depth of 11.67 m. The equivalent Young’s modulus of the reinforced concrete is thus 31100 MPa.

The circulation pipes, 0.02 m in external diameter, were arranged in helical shape and attached to the helical reinforcement trough wire ties. The primary circuit was placed on the inside of the reinforcement cage to avoid damage during concreting. The nominal concrete cover to the edge of the pipes was 75 mm. The pitch of the primary circuit follows the one of the links throughout the length of the helical reinforcement reaching a total length of 90 m. To avoid any damage or contamination of the pipes assembly and fixing to the cage of the loop took place in a dedicate a space and pipes’ ends were closed through sealing caps to avoid material entering during any of the construction phases (Figure 5-4). Water pressure tests were carried out before and after concreting.

Figure 5-4: PC installation and configuration.

The instrumented EP was equipped with NTC thermometer's chain consisting of 4 thermistors placed at depth of 1.2 m (TP1), 4.5 m (TP2), 7.1 m (TP3) and 10. 15 m (TP4) along pile's shaft. The chain was attached to the reinforcement cage and each thermistor was placed between two subsequent pitches of the helical exchanger pipe (Figure 5-5).

Figure 5-5: NTC thermistor attached to the inside of the reinforcing cage close to primary circuit.

In the middle section of the pile a closed ends plastic pipe of 80 mm diameter was placed before concrete pouring as shown in Figure 5-6 (a). Before installation VWGS were fixed to a rope, tensioned by a weight at the bottom (Figure 5-6 (b)). The sealing cap placed in the upper section of the pipe was removed and VWGS were lowered into the hollow pipe. No-shrinkage cement grout was poured to fill the pipe ensuring full adhesion between the grout and the pipe (Figure 5-6 (c)). VWGs installation technique corresponded to those proposed by Russo (2004).

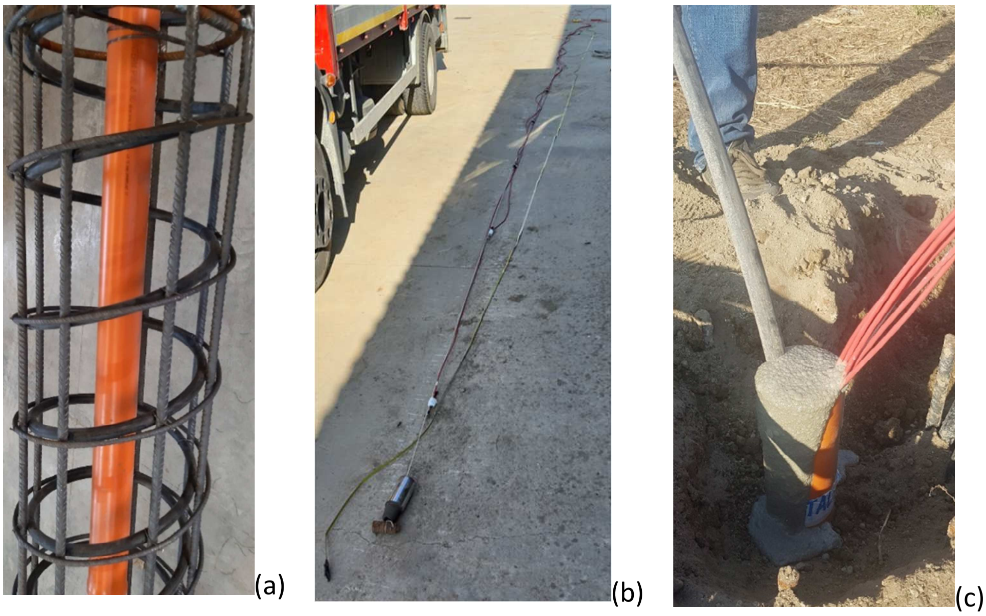

Figure 5-6: VWGs installation. closed ends plastic pipe (a). VWGS. rope and weight (b) and grout pouring (c).

As shown in Figure 5-7, the instrumented energy pile contained 8 VWGs of the type for embedding in concrete installed at eight depths of the pile (0.3 m (1), 1.8 m (2), 3.3 m (3), 4.8 m (4), 6.3 m (5), 7.8 m (6), 9.3 m (7) and 10.3 m (8)).

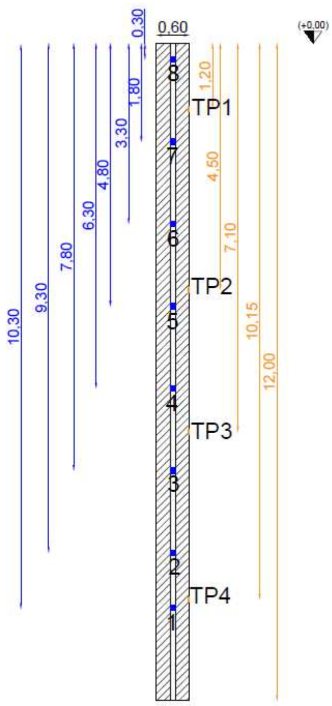

Figure 5-7: Test pile and sensors layout (annotations in m).

Pile's head settlements were measured using geodetic method through, electrical and mechanical, high precision geometric levelling. Displacements of pile head were deduced as change in the position of pile head, in relation to reference points, occurring at a specific time interval (5 minutes). The readouts were carried out on the levelling staff with an invar band showed in Figure 5-8(b). Digital level performs the readouts automatically via the analysis of the image of the invar bar coded rod (bar code scale was built). Two benchmarks sufficiently far away from the area of the test were adopted as fixed reference points both for optical and digital measurements.

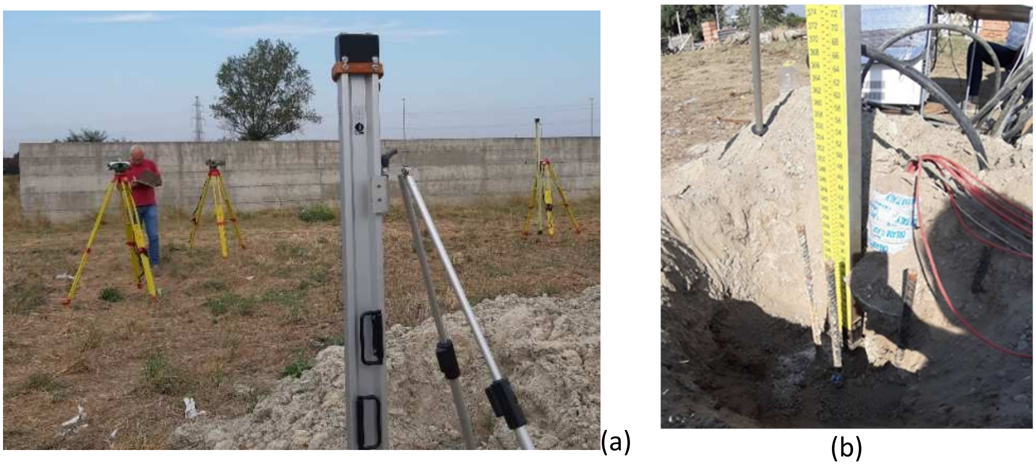

(a) (b)

Figure 5-8: Levelling system, tacheometers benchmarks and invar levelling staff placed on pile head (b).

The PC of the pile was connected to a heat circulating bath that allows both circulation and heating of the fluid. The inflow and outflow temperatures of the fluid are also measured. Inlet water temperature was measured inside the tank of the circulating bath. The outlet temperature of the water was measured through two additional thermocouples. Environmental temperature was also monitored during the tests to account for thermal interaction between the ambient air and the soil.

At 0.90 m from pile edge an observation borehole filled with cement mortar were equipped with NTC thermometer's chain. Four thermistors were placed along the chain at different depths from ground surface: 2 m (CNTC1), 5 m (CNTC 2), 8 m (CNTC3) and 11 m (CNTC4). The soil temperature measurements allow monitoring the temperature of the soil at 1.5 D from the pile and providing database of soil undisturbed temperature variations with depth. The layout of the test is reported in Figure 5-9.

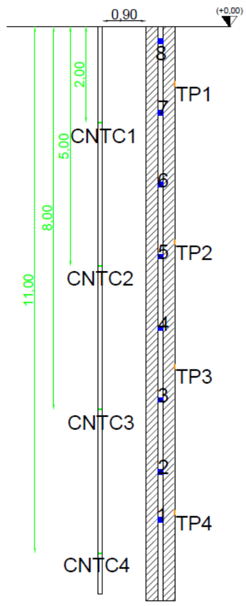

Figure 5-9: Layout of the test borehole and test pile (annotations in m).

During the tests described in the sections below, all the sensors remained operational throughout the in-situ test except CNTC 3 and the NTC of VWG 4.

5.3 *Vibrating wire Strain gauges (VWGs)*

Vibrating wire strain gauges (VWGs) consist in a hollow cylindrical body with the internal steel wire tensioned between the two ends. Outside, a resin cover protects the coils.

Figure 5-10:Embedded concrete VWG.

Height WSGs 0VK4200VC00 model were embedded in the pile to allow strains measurements along pile shaft. VWG transducer is composed by a taut wire clamped at its ends and tensioned so that it is free to vibrate at its natural frequency. The interpretation of VWGs measurements is based on the vibrating theory. The resonant frequency f of a wire under tension is given by Equation 5-1.

Equation 5-1 $: f = \frac{1}{2L_{wire}}\sqrt{f_{wire}/\nu_{wire}}$

Where L_{wire} is the wire length, f_{wire} is the wire tension and ν_{wire} is the wire linear density. The frequency of vibration varies with the wire tension.

The wire tension can be related to its strain ε though the Young's modulus (E_{wire}) and the cross section (A_{wire}) of the wire, according to Equation 5-2:

Equation 5-2: $f_{wire} = A_{wire}E_{wire}\,\varepsilon$

From Equation 5-1 and Equation 5-2, tensioned wire, when plucked. vibrates at a frequency that is proportional to the strain in the wire according to Equation 5-3.

Equation 5-3: $\mu\varepsilon = [(f^2 - f_0^2)\cdot 10^{-3}]\cdot G$

Where: $\mu\varepsilon$ is the deformation measure in micro-strains, f is the wire vibration frequency measured in Hertz, f_0 is the reference wire frequency measured in Hertz (reference base for subsequent measurements), G is the gauge factor that is written on the Compliance Certificate and depends on instrument's characteristics. For the embedment VWGs adopted Gauge factor G is 3.814. From Equation 5-3 elongations of the wire determine positive measurements while shortenings provide negative strains.

The experimental investigations were carried out applying to the pile thermal variations, therefore, thermal expansions or contractions of the wire must be accounted for. VWG internal thermistor allows the measure of the temperature of the wire. Any temperature increase induces expansion of the wire i.e., reduces its tension. The variations of the wire frequency when subjected to thermal changes is included in two extreme conditions: gauge mounted on unconstrained element free to expand or contract or gauge mounted on constrained element characterised by null thermal strains (Marshall and Hunter, 1980). If the gauge is mounted on unconstrained concrete element and temperature rise occurs, thermal strains correspond to elongations and are provided by Equation 5-4.

Equation 5-4: $\mu\varepsilon_{temperature\ induced\ (wire) free} = \Delta T\cdot(\alpha_s - \alpha_p)$

If the VWG is mounted on a constrained concrete element and temperature rise occurs thermal strains in the wire correspond to shortening and are provided by Equation 5-5.

Equation 5-5: $\mu\varepsilon_{temperature\ induced\ (wire)} = \Delta T \cdot \alpha_s$

Where: $\mu\varepsilon_{temperature\ induced\ (wire)}$ are thermal wire strains, α_s is the thermal expansion coefficient of the steel wire in °C^{-1}and α_p is the thermal expansion coefficient of concrete in °C^{-1}.

When thermal loads are applied to the pile thermal stresses and strains occur. Thermal stresses and strains are included in the range of free thermal expansion or contraction (DOF=1 and DSR=0) and fully constrained strains (DOF=0 and DSR=1) depending on the soil-pile thermo-mechanical interaction. Therefore, VWG could be mounted on unconstrained element (DOF=1) or fully constrained element (DOF=0) or partly constrained element (0<DOF<1) depending on the pile-soil interaction and the constraint action provided by the foundation system and upper structure. The investigation carried out involves a test pile that is free to expand or contract at the head. The pile is isolated and no structures that could restrain its movements are realised at its head, the state of constraint is only due to the ground friction and base compression. Therefore, strains measurements provided by the shallowest VWG *8*, are close to unrestrained condition (DOF=1). Therefore, from VWG 8, where shaft friction effects were minimal, the free thermal expansion coefficient of concrete can be estimated. Thermal strain measured by VWG *8*, corresponds to $\mu\varepsilon_{temperature\ induced\ (wire)}$free elongations of the wire and can be expressed by Equation 5-4. The convention used for strains is negative for elongations and positive for shortenings (opposite of those adopted in Equation 5-3). Tensile stresses are assumed to be negative while compressive stresses are assumed to be positive.

Thermal strains measured by the VWG 8 are reported versus temperature variations, during heating tests A and B (Figure 5-11). The slope of the trend lines 2 and 3 corresponds to the difference between the thermal expansion coefficients of the steel wire and the concrete ($\alpha_s - \alpha_c$).

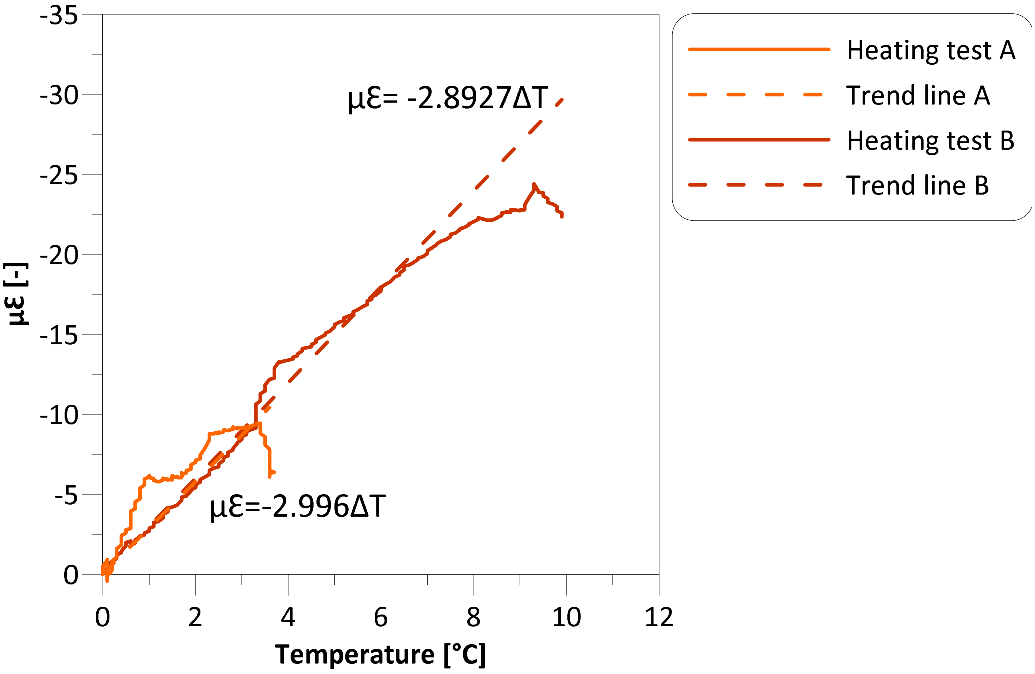

Figure 5-11:Determination of concrete pile thermal expansion coefficient from VWG 8, located at 0.3 m from pile's head.

Knowing that the thermal expansion of steel wire is $\alpha_s = 1.22 \cdot 10^{-5}\ °C^{-1}$ and considering the slope of the linear regressions in Figure 5-11, the coefficient of free thermal expansion of concrete is $9.5 \cdot 10^{-6}\ °C^{-1}$ (Equation 5-6).

Equation 5-6: $\alpha_p = \alpha_s - slope = 9.5 \cdot 10^{-6}\ °C^{-1}$

The coefficient of linear thermal expansion of concrete has been reported to range from 9 °C^{-1} to 14.5 °C^{-1} depending on the aggregate mineralogy of the concrete mix (Stewart and McCartney. 2014), therefore the coefficient computed is in the range of typical values.

Thermal strains of the pile in this section could be expressed as function of the free thermal expansion coefficient of concrete and thermal variations:

Equation 5-7: $\mu\varepsilon_{free} = \Delta T \cdot \alpha_p$

During the heating tests deeper VWGs (VWG 7, VWG 6, VWG 5, VWG 4, VWG 3, VWG 2, VWG 1) measurements of frequencies provide both elongations and shortenings. For thermal variations of reduced magnitudes, the steel wire expands, and elongations are measured. With the increasing of thermal variations, the wire starts to contract, and a decreasing of the elongation is recorded until a null strain is measured. Then, with the increasing of thermal variations shortening are recorded until and subsequently the end of heating test. This trend is recorded for VWG 7, VWG 6, VWG 5, VWG 4, VWG 3, VWG 2, VWG 1 during heating tests. For the sake of simplicity, the measurements provided by VWG 1 are reported in Figure 5-12 as an example. The strains measured by the wire and temperature variations obtained from the thermistor installed in the VWG are reported versus time in Figure 5-12. Three phases are identified, *E* (Elongations, blue rectangle), *SS* (Starting of Shortenings, pastel blue rectangle) and *S* (shortenings, red rectangle) (Figure 5-12). During the first phase, E, the wire is expanding. In this phase the measurements show that VWG is mounted on unconstrained pile. Then, in the second phase, SS, elongations of the wire decrease until reaching a null value. During the third phase, S, the wire is getting shorter because it is mounted on a partially constrained concrete pile.

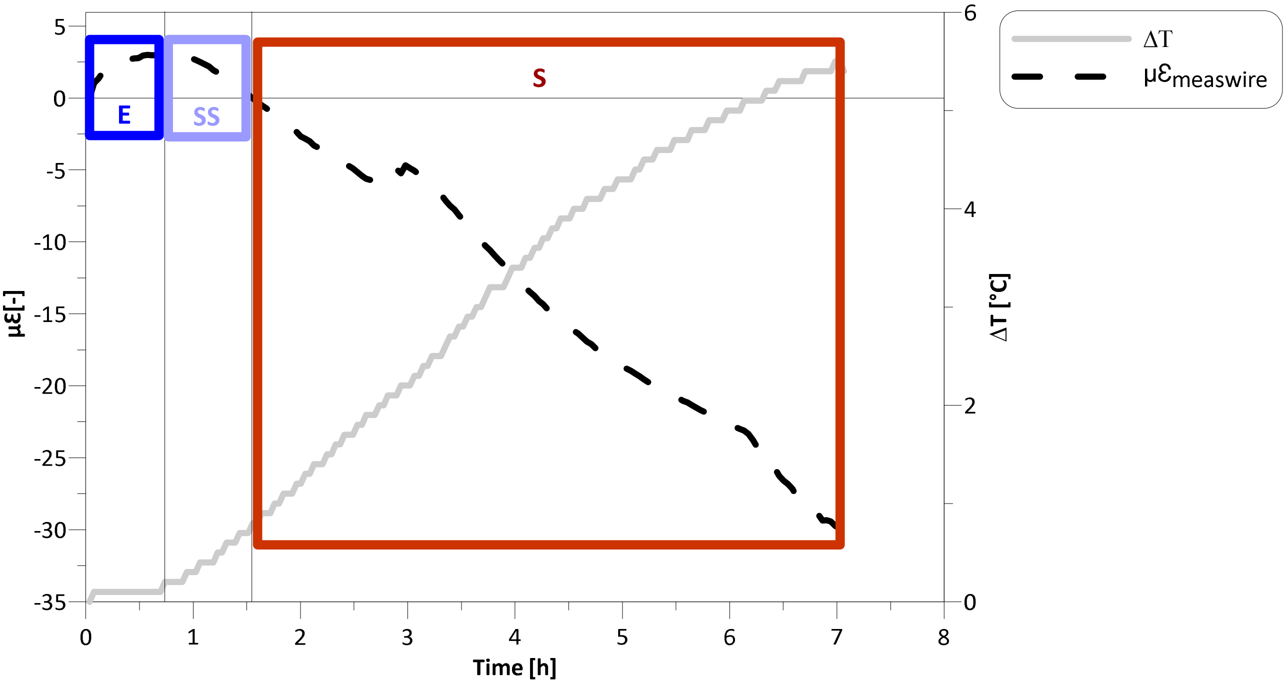

Figure 5-12: Strains recorded by VWG 1 during a heating test: Elongation phase (E). Starting of Shortenings phase (SS) and Shortening phase (S).

SS and S phases demonstrate that the free expansion of the pile is restrained by soil-pile thermo-mechanical interaction determining compression throughout the concrete element that is read by the VWG. During phase S, concrete's restrained strains are calculated by Equation 5-8.

Equation 5-8: $\mu\varepsilon_{\,restrained(pile)} = \mu\varepsilon_{\,temperature\ induced\ (wire)} + [\Delta T \cdot (\alpha_s - \alpha_p)]$

Where: $\mu\varepsilon_{\text{ pile restrained}}$ is the restrained strain of concrete induced by thermal loads and thermo-mechanical interaction, $\mu\varepsilon_{\text{wire}}$ is the strain measurement obtained from the wire resonant frequency variation according

Equation 5-3, ΔT is the temperature variation in °C, $\alpha_s = 1.22 \cdot 10^{-5}\,°C^{-1}$ and $\alpha_p = 9.5 \cdot 10^{-6}°C^{-1}$ are the thermal expansion coefficient of the steel wire and concrete pile, respectively.

Concrete unrestrained thermal strains $\mu\varepsilon_{th.o}$ are expressed by Equation 5-9.

Equation 5-9: $\mu\varepsilon_{th.o} = \mu\varepsilon_{temperature\ induced\ (wire)} + \alpha_s \Delta T$

5.4 *Soil temperature profile for the area of Napoli*

Soil temperature along the depth were monitored to the aim of providing data about soil temperature in the shallow and deep zone for the area of Napoli. The main investigation about soil temperatures in this area focused on the geothermal anomalies, as occurred for example in the Volcanic area of Phlegrean Field where the temperature gradient is very high. Furthermore, these studies typically explore temperatures at relatively large depth. At 100 m, for instance, the temperature is approximately 100 °C while at 3500 m the temperature reaches 350 °C (Aversa and Evangelista, 1993). These investigations are oriented mainly towards the use high enthalpy geothermal system. For low enthalpy geothermal systems i.e., vertical ground and closed-loop horizontal heat exchangers the temperature of the ground is a crucial parameter for correctly sizing the loops, whether the system is to be used for heating and/or cooling. Few data are available about soil temperature profile in Napoli particularly for the relatively shallow depths of about 10-20 m.

Temperatures at fifteen depths -11m, -10.30 m, -10.15 m, -9.30 m, -7.80 m, -7.10 m, -6.30 m, -5 m, -4.80 m, -4.50 m, -3.30 m, -2 m, -1.80 m, -1.20 m and -0.30 m from ground surface were recorded by thermistors installed in the test pile and in a close borehole. All temperatures measurements deal with undisturbed thermal conditions, i.e., when thermal tests were not carried out. From October 2020 to April 2021 temperature profiles are plotted in Figure 5-13. For each month, the soil temperature profile was computed as the average of all the temperature at each depth recorded during each day of the month at the same time of the day.

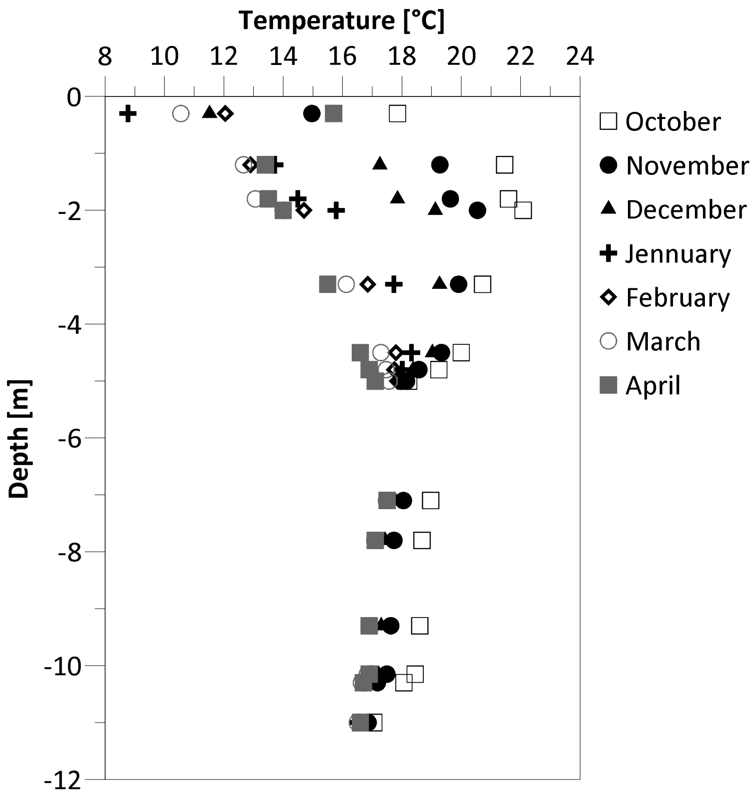

Figure 5-13: Monthly Soil temperature Profile during the seven months of monitoring.

Mean soil temperature displayed a decreasing trend with increasing soil depth in both Autumn and Winter.

As could be observed from the Figure 5-13 in the first 5 m soil temperatures are strongly influenced by the temperature air variations. From 5 m to 11 m the temperature changed in the narrow range 16.5 °C- 17.1 °C.

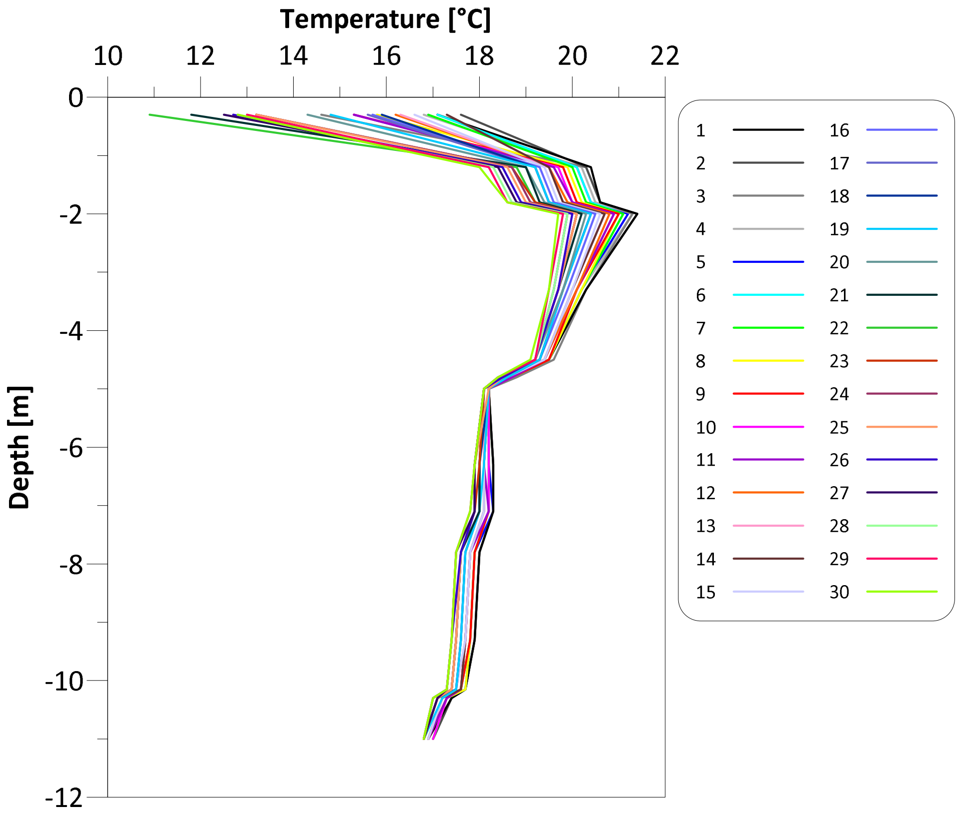

In Figure 5-14 for the month November 2020 daily temperature profile with depth are plotted with different colours. As observed from Figure 5-14 the greater influence of heat exchange phenomenon with the atmosphere is clear in the first 5 m of depth. Temperature fluctuation in the ground decreases in amplitude and increase in phase shift with depth as is clearly shown in Figure 5-15. The amplitude and phase changes can be used to derive the thermal diffusivity of the soil. On the basis of the temperature measurements and assuming temperature wave amplitude of 11.4 °C and an average external temperature of 17.4 °C, Equation 2-19 proposed by Tinti et al. (2014) is used to estimate 0.022 m^2/d of soil thermal diffusivity.

Extreme temperatures are given by the daily minimum and maximum temperatures, and these will be more dependent on the time period considered. These daily extremes may be considered when designing the heating pump system for peak load conditions.

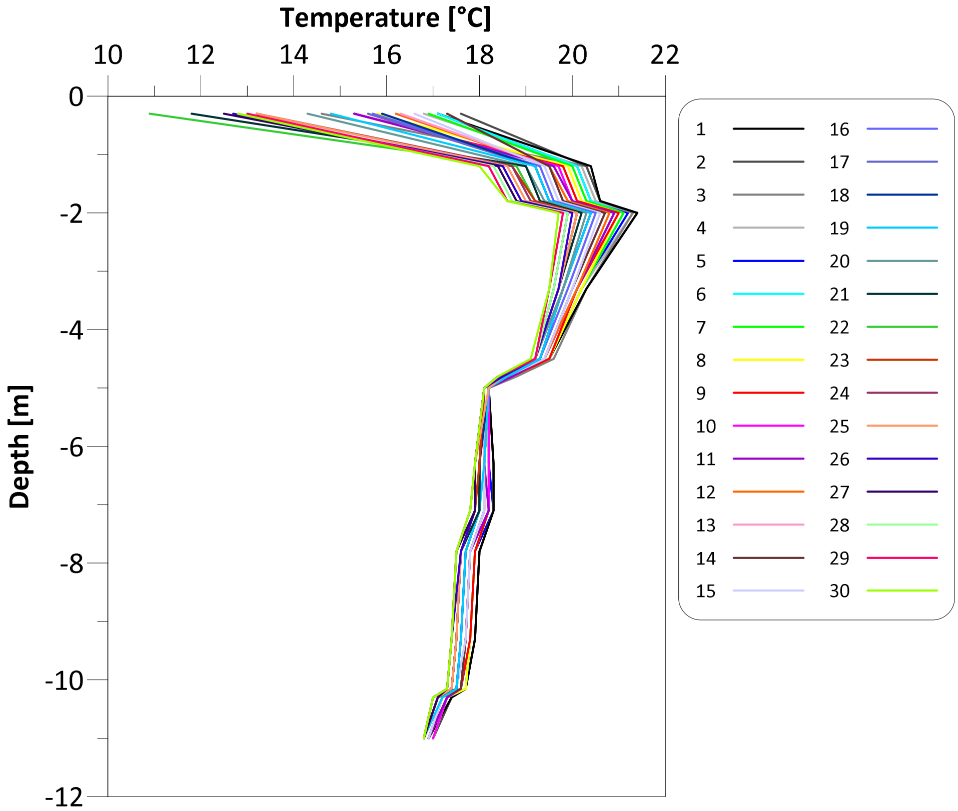

Figure 5-14: Daily soil temperature profile during the month of November 2020.

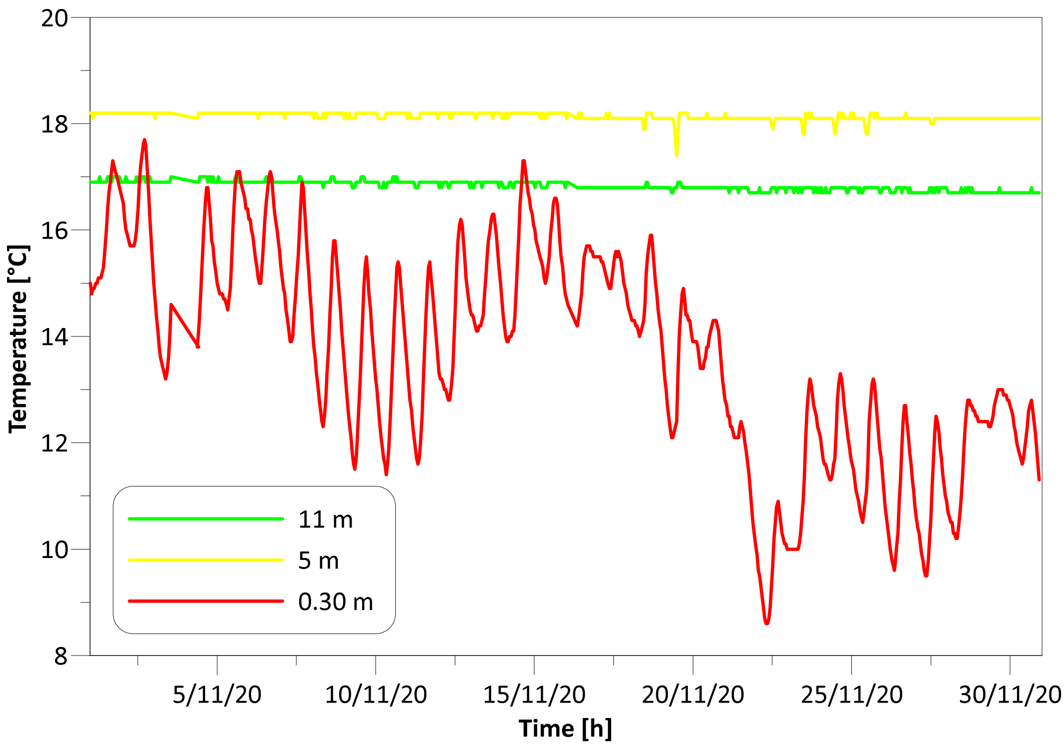

Figure 5-15: Temperature fluctuation in the ground at depths of 0.30 m, 5 m, and 11 m from ground surface.

An example of underground temperature profile and temperature fluctuations recorded for one day are reported in Figure 5-16 and Figure 5-17, respectively.

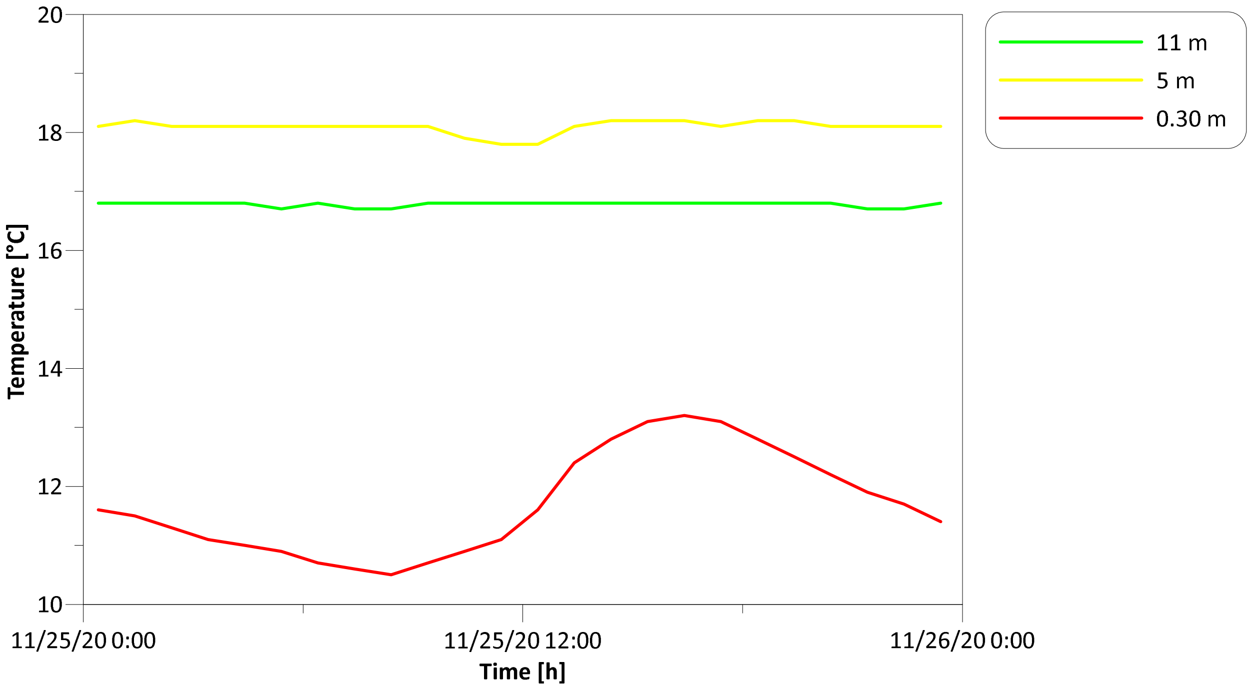

Figure 5-16: Temperature fluctuation in the ground at depths of 0.30m. 5 m and 11 m from ground surface during 25th November 2020.

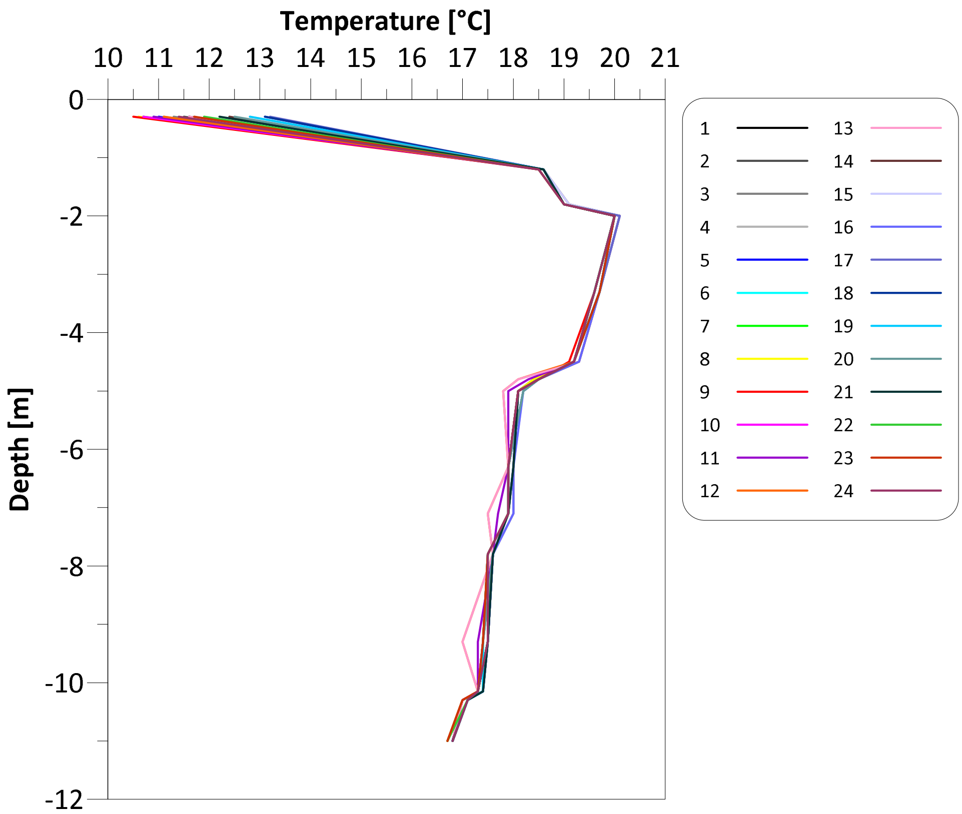

Figure 5-17: Hourly soil temperature profile during 25th November.

5.5 *Heating Thermal tests*

5.5.1 Experimental testing programme

Thermal tests were performed to investigate on short-term thermomechanical response of the pile-soil system under purely thermal loadings. Three heating tests are presented: Test C, Test B and Test A. All the tests are performed applying to the pile purely thermal loads by means of the PC and circulating bath. Heated water at a controlled inlet temperature and constant flow rate of 12.8 l/min circulating inside the exchanging pipes allowed the application of thermal loads. During tests B and C, the outlet temperature of water was monitored and TPTs were performed. The circulating pipes connecting the pile and the heating circulation bath were thermally insulated and characterised by above-ground length that was smaller than 1m. During the tests, pile's temperature, head displacements and thermal strains were monitored by means of TP and thermistors of the VWGs, precision levelling and VWGs, respectively (5.2). Prior to each heating tests, soil and pile temperatures were measured along with the reference resonant frequencies of the VWGs. The tests are characterised by different time duration. Each test consists of a thermal phase where the pile is heated and a thermal recovery phase where water circulation is stopped. Test B focused on the transient phenomena occurring when the circulation of heated water was stopped. Thermal tests A and C are characterised by longer heating phases and shorter recovering phases. After heating at least one hour of monitoring was performed during the rest phase. The effect of heating on pile-soil interaction were examined in terms of pile's head displacement, thermal deformations and axial loads.

5.5.2 Thermal test C

Inlet water temperature is plotted in Figure 5-18. The total time duration of the heating is about six hours during which the inlet temperature ranged between 26.6 °C and 30.9 °C, with an initial peak of 35.8 °C.

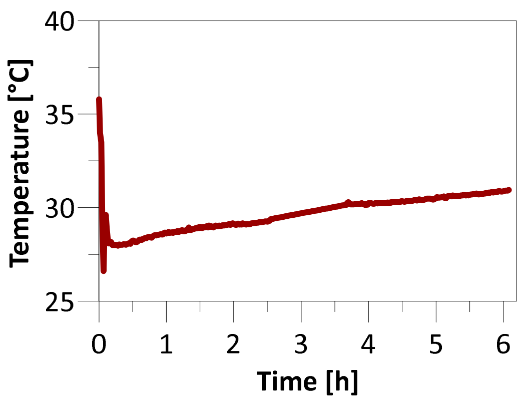

Figure 5-18: Inlet water temperature during thermal test C.

Before heating soil and pile initial temperature profiles are plotted in Figure 5-19. As clarified before, TP is close to the PC while VWG is in the middle of the pile section. The temperature profile measured 1.5 D away from the pile by the three NTCs, is named as *CNTC* (Figure 5-19).

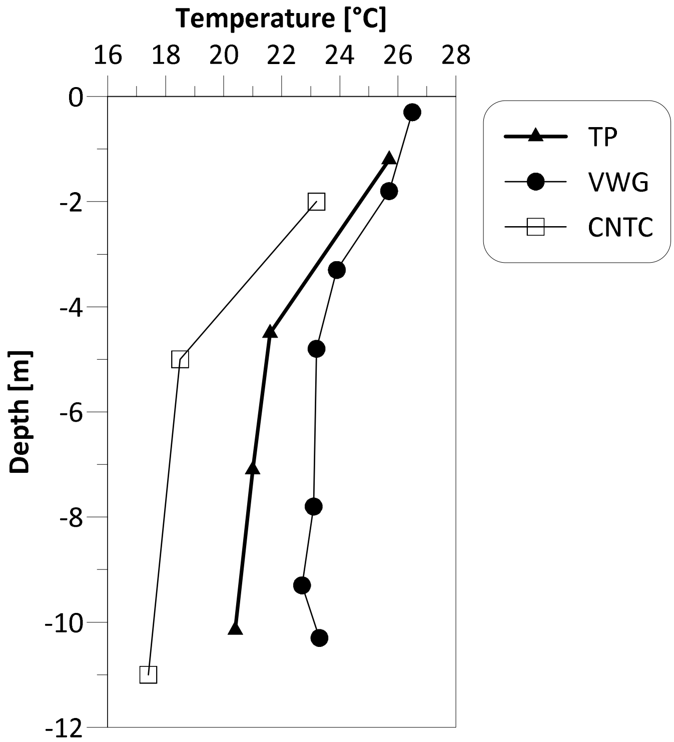

Figure 5-19: Temperature distribution along pile depth (TP and VWG) and soil depth (CNTC) before starting the heating test C.

As could be observed from in Figure 5-19 temperatures of the pile are greater than the soil ones. The pile temperature is still influenced by the thermal heating test (thermal test B) carried out the day before. After 20 hours from the end of test B, the radial heat flow in the concrete is still evident. The temperatures in the centre of the pile (VWG) are higher than those measured close to the pile's edges (TP).

The difference between the inlet and outlet water recorded during the heating along with the heat injected into the ground (Power) are plotted in Figure 5-20. The average temperature difference between inflow and return flow (ΔT_{in-out}) is about 3° C. According to Brandl (2006) a temperature difference of about 2°C is sufficient for economical operation of the energy system. The thermal performance of the test pile i.e., the heat power injected to the soil is computed according to Equation 4-7.

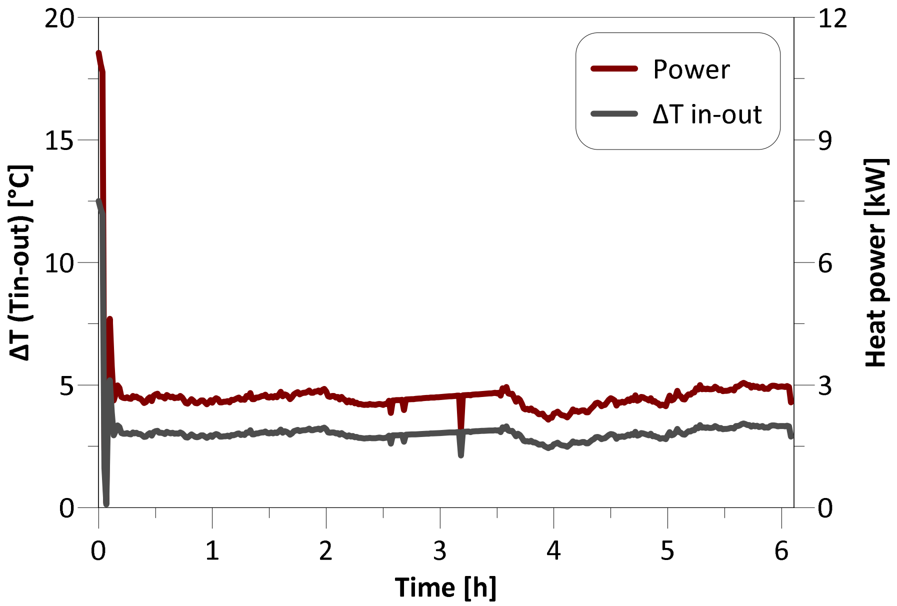

Figure 5-20: Difference in temperature between inlet and outlet water temperatures (ΔT) and heat injected into the ground (Power) during test C.

The average Power estimated during the test is about 2.7 kW that corresponds to specific heat injection rate per meter pile of 223 W/m.

The pile temperature changes in response to the heating are monitored during the heating and during the follow up of one hour of a rest phase (Figure 5-21). The evolution of the pile temperature at different depths was recorded both by the seven thermistors installed in the VWGs and four thermistors of the thermometer chain placed next to PC. In Figure 5-21 pile temperature changes are plotted along with Inlet and outer water temperature and air ambient temperature.

Temperature evolution of the pile are analysed both along pile's length and cross section. Starting from the variation of pile's temperature along the length the measures of the VWGs and thermistors are analysed separately.

As could be observed form the measures of the air ambient temperature the test was carried out during a warm summer's day. From the temperature measured at 0.3 m depth it is evident the thermal interaction between the pile and ambient air. The thermal interaction with the ambient air is an effective additional heating loading acting on the pile. As could be observed from the measures of the deeper VWGs, with increasing depths temperature decreases. It should be highlighted that the thermal boundary conditions of the test are different if compared to the case of an EP installed in the foundation below a superstructure (3.6.5).

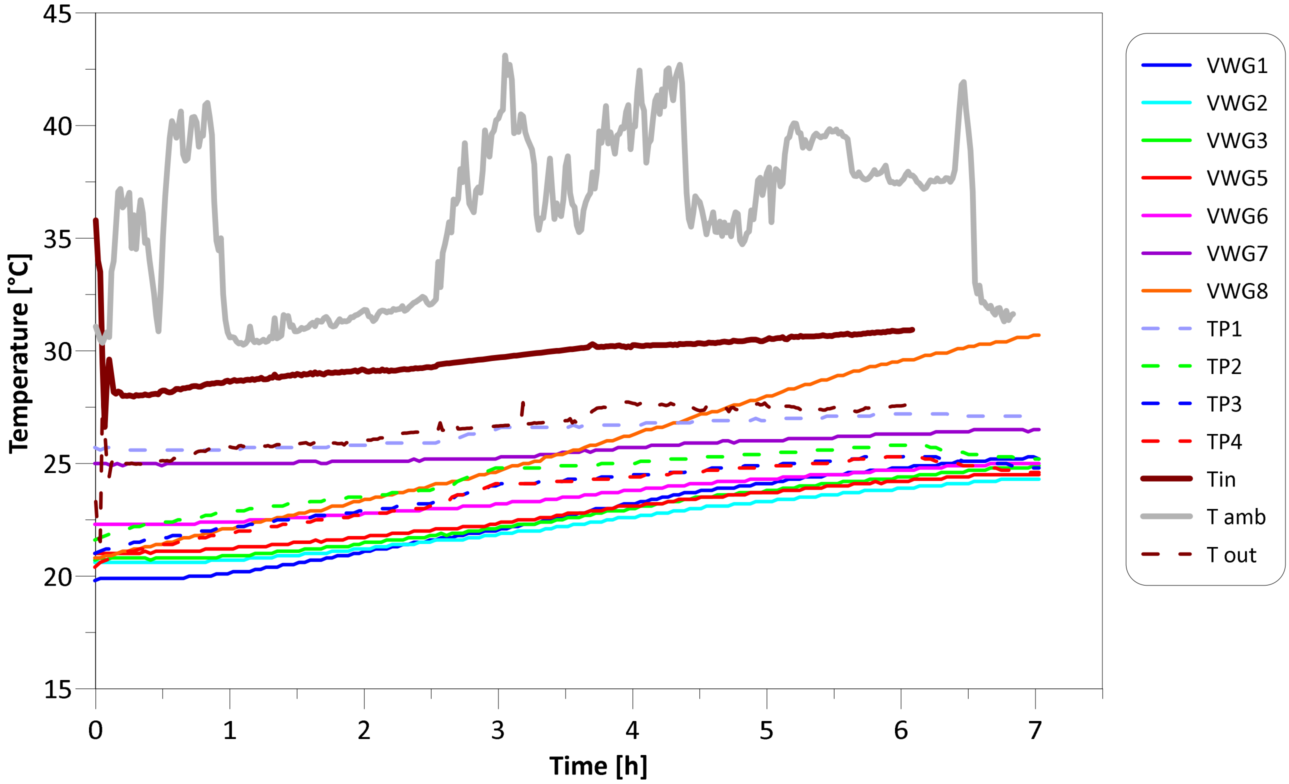

Figure 5-21:Temperature evolution in the pile at different depths and positions in the cross section (VWG and TP) along with inflow (Tin) and return flow (Tout) temperatures and ambient air temperature (Tamb).

At 0.30 m from pile head the highest temperature recorded is about 30.7 °C and temperature increase is recorded from the starting of the test. For deeper VWGs the rate of temperature increase starts after one hour from heating. The maximum temperature recorded at each depth at the end of the test are reported in Table 5-2.

Table 5-2: Maximum temperatures measured by the VWGs thermistors at the end of monitoring of thermal test C.

VWG	[m]	T [°C]
1	-10.3	25.3
2	-9.3	24.3
3	-7.8	24.9
5	-4.8	24.5
6	-3.3	25
7	-1.8	26.5
8	-0.3	30.7

The general trend that is observed is lower temperatures at larger depths.

Temperature evolution provided by the NTCs of the thermometric chain is characterised by a linear trend during all time duration of the test. Comparing temperature trend provided by NTCs and VWGs' thermistors some differences could be noticed. For NTCs temperature increase is recorded from the beginning of the test and the maximum temperature is measured when heating of the pile is still occurring. The maximum temperatures measured by thermistors placed next to the PC at different depths are reported in Table 5-3.

Table 5-3: Maximum temperatures measured by NTCs of the thermometric chain during thermal test C.

NTC	[m]	T [°C]

1	-1.2	27.2
2	-4.5	25.9
3	-7.1	25.4
4	-10.15	25.3

Temperature-time distribution recorded at different positions of the cross section but at similar depth respect to pile's head were compared to evaluate the evolution of heat transfer mechanism across pile radius. Sensors TP4 and VWG1 are placed at 10.15 m and 10.30 m, respectively. It could be assumed that they are located at the same depth with respect to pile head. Therefore, the difference in temperatures recorded at the two locations depends on the transient radial heat diffusion mechanism. Temperatures measured by the thermistor of VWG1 and thermistor 4 of the thermometric chain (TP4) are plotted in Figure 5-22 along with inlet and outlet water temperatures.

Additional three VWGs and NTCs located at similar depths were compared. In these cases, vertical distance between each thermistor of the VWG and NTC of the thermometric chain is at least twice time those occurring between VWG1 and TP4. The measures of TP2 and thermistor of VWG5 (0.3 m of vertical distance between the two sensors), TP 1 and VWG7 (0.6 m of vertical distance between the two sensors) and TP3 and VWG 3 (0.7 m of vertical distance) were also compared. Temperatures measured by the thermistor of VWG 5 and thermistor 2 of the thermometric chain (TP2) are plotted in Figure 5-23 along with inlet and outlet water temperature. Temperatures measured by the thermistor of VWG 7 and thermistor 1 (TP1) of the thermometric chain are plotted in Figure 5-24 along with inlet and outlet water temperature. Temperatures measured by the thermistor of VWG 3 and thermistor 3 (TP3) of the thermometric chain are plotted in Figure 5-25 along with inlet and outlet water temperature.

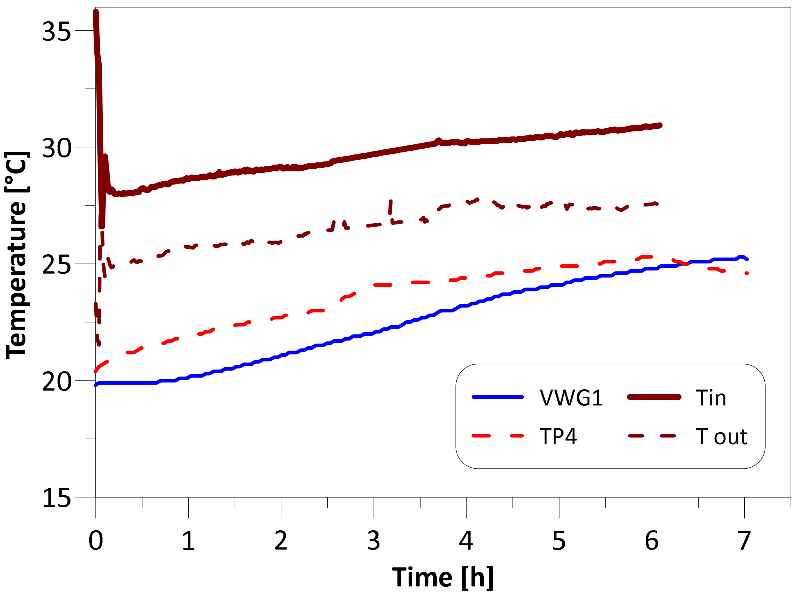

Figure 5-22: Evolution of heat transfer mechanism along pile's cross section. pile's temperature in the middle of pile at 10.30 m depth from pile head (VWG1). pile's temperature close to the heat exchanger tubes at 10.15 m depth from pile's head (TP4) and inflow and outflow water temperatures (Tin and Tout).

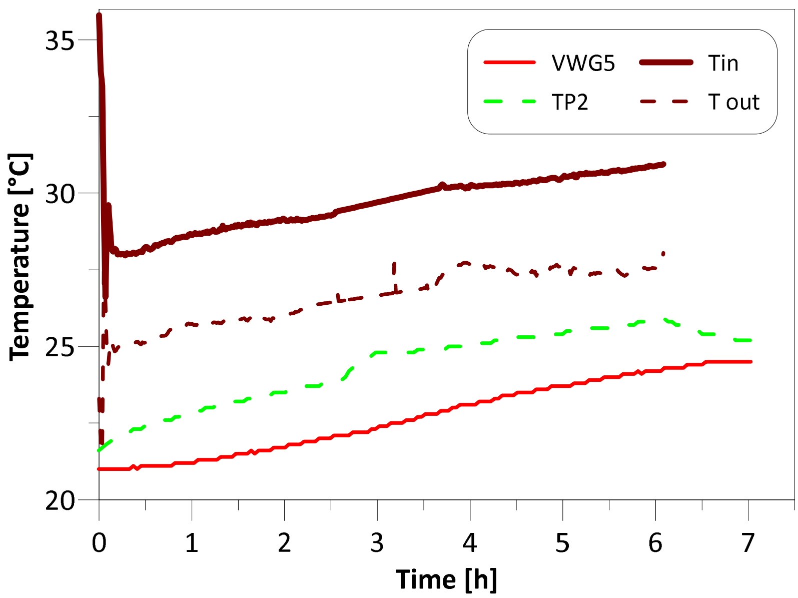

Figure 5-23: Evolution of heat transfer mechanism along pile's cross section. pile's temperature in the middle of pile at 4.80 m depth from pile head (VWG5). pile's temperature close to the heat exchanger tubes at 4.50 m depth from pile's head (TP2) and inflow and outflow water temperatures (Tin and Tout).

When the heating of the pile started, temperatures measured by the thermistor close to circulating pipes increased suddenly. When the heating of the pile was stopped, TP4 temperatures decreased immediately. In the case of thermistor of VWG 1 temperature started increasing after one hour from the end of heating. During the first three hours of the test, the temperature measured by TP4 is 2 °C greater than those at location of VWG1. With the evolution of pile heating, the heat transfer mechanism continued, and the temperatures measured at the two locations of cross section get closer and closer approaching to 0.4 °C at the end of heating. At the end of monitoring temperatures measured by the sensor close to the edge of pile and in the middle of the pile nearly matched. At the end of 6 hours of heating the heat transfer mechanism occurring in the cross section is still in a transient stage. These findings are confirmed also considering the comparisons between TP2 and VWG 5. TP1 and VWG7 and TP3 and VWG3 plotted in Figure 5-23, Figure 5-24 and Figure 5-25, respectively.

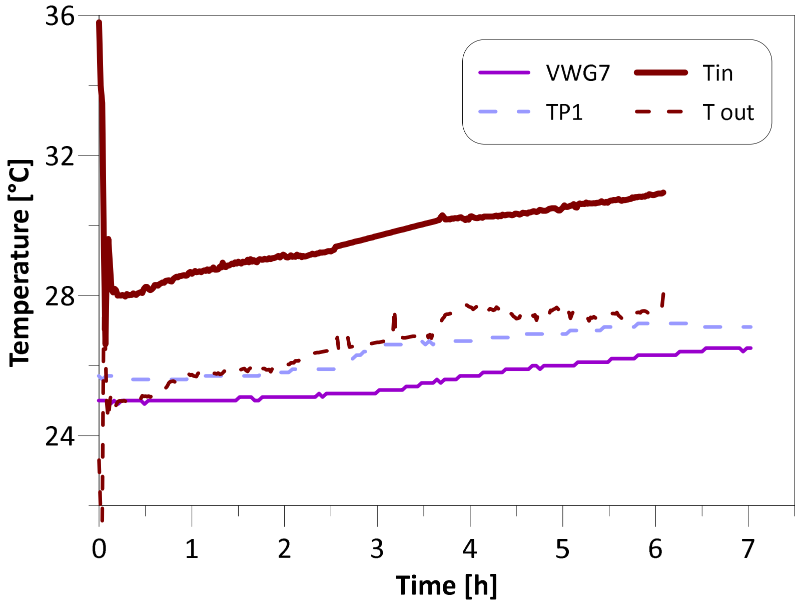

Figure 5-24: Evolution of heat transfer mechanism along pile's cross section. pile's temperature in the middle of pile at 1.80 m depth from pile head (VWG7). pile's temperature close to the heat exchanger tubes at 1.20 m depth from pile's head (TP1) and inflow and outflow water temperatures (Tin and Tout).

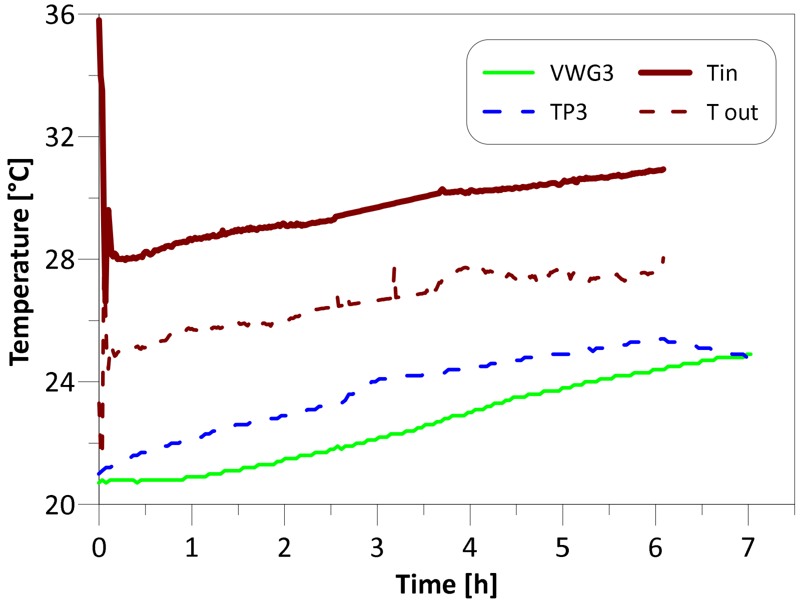

Figure 5-25: Evolution of heat transfer mechanism along pile's cross section. pile's temperature in the middle of pile at 7.80 m depth from pile head (VWG3), pile's temperature close to the PC at 7.10 m depth from pile's head (TP3) and inflow and outflow water temperatures (Tin and Tout).

Temperature evolution of the soil at 2 m. 5 m and 11 m of depth are plotted in Figure 5-26 along with inlet and outlet water temperature and air ambient temperature.

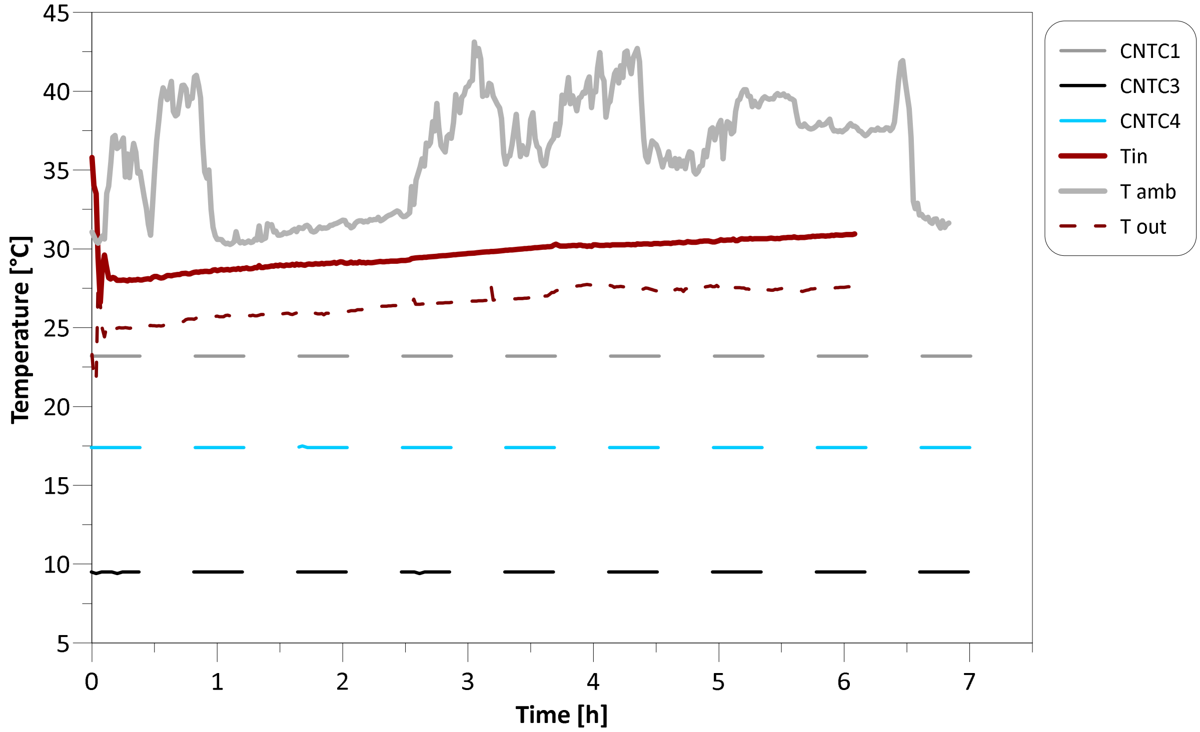

Figure 5-26: Temperature evolution in the soil at different depths (CNTC) along with inflow (Tin) and return flow (Tout) water temperatures and ambient air temperature (Tamb).

From the measures of soil temperature two main remarks can be made. The effects of short-term pile heating on soil undisturbed temperature and hourly variation of ambient air on soil temperature with depth are negligible. During the test, at each depth, soil temperature is nearly constant i.e., it is not influenced by the heating of the pile. The trend of soil temperature versus time shows that soil is not affected by hourly variation of ambient air.

The temperature and the variation in temperature at pile's middle section (△T) profiles are reported in Figure 5-27 (a) and Figure 5-27 (b), respectively. Different time instants were analysed: 3.8 h, 4.6 h and 5.6 h from the beginning of the heating test. For the same time instants thermal strain ($\varepsilon_{th.0}$) profiles are shown in Figure 5-27 (c). All the strains observed correspond to pile's elongation as expected. The thermal strains ($\varepsilon_{th.free}$) in the upper section are calculated by Equation 5-7 while $\varepsilon_{th.0}$ are calculated according to Equation 5-9.

At the same time instants DOF profiles are plotted in Figure 5-27 (d). The maximum DOF occurred in the upper section where the pile is free to expand i.e., $\varepsilon_{th.0} = \varepsilon_{th.free}$, With increasing depth DOFs decrease. Close to the pile toe DOF increases.

The DOF (Figure 5-27 d) decreases during the heating of the pile at each depth. Comparing DOF and $\varepsilon_{th.0}$ profiles opposite trends are observed with increasing time of heating. Even if thermal strains are increasing during the time evolution of the test the DOF is decreasing.

$\varepsilon_{th.0}$ can be expressed according to Equation 5-10.

Equation 5-10: $\varepsilon_{th.0} = \alpha_{mob} \cdot \Delta T$

Where α_{mob} is the mobilised thermal expansion coefficient that depends on the interaction between pile and soil, and it is smaller than free thermal expansion coefficient α_p(Equation 5-6) and ΔT is the temperature difference measured at the location of the gauge. Therefore, the DOF plotted in Figure 5-27 (d) can be expressed according to **Errore. L'origine riferimento non è stata trovata.**.

Equation 5-11: $DOF = \frac{\alpha_{mob} \cdot \Delta T}{\alpha_p \cdot \Delta T}$

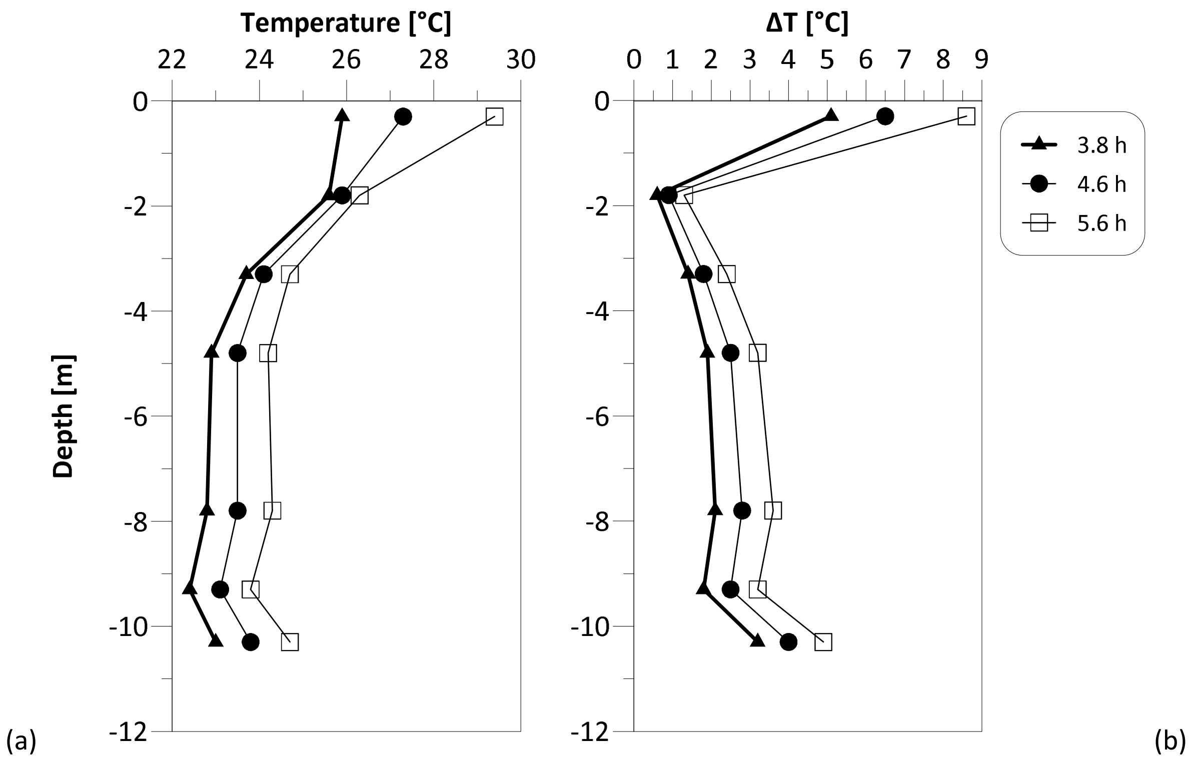

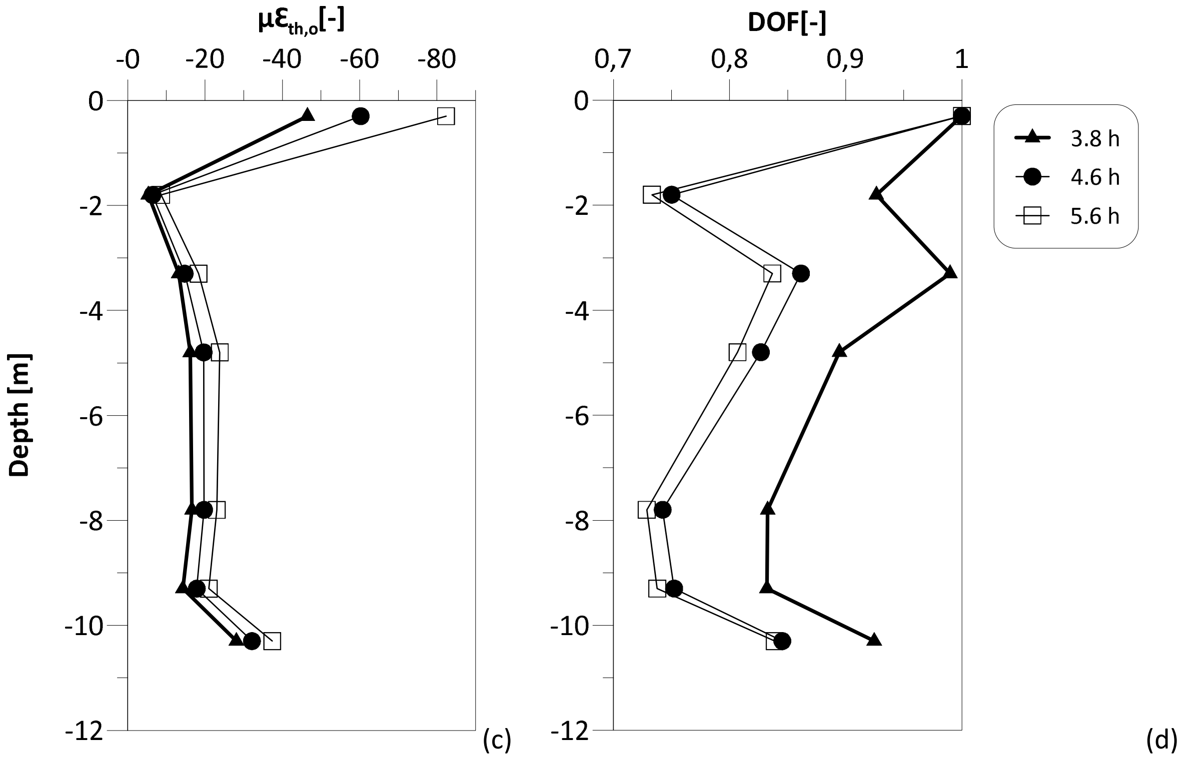

Figure 5-27: Pile's heating response during different time instants (3.8 hours. 4.6 hours and 5.6 hours) of C thermal test at pile's middle cross sectional; (a) Temperature. (b) Temperature difference △T. (c) Thermal strain and (d) DOF profiles.

Where α_{mob} is the mobilised thermal expansion coefficient that depends on the interaction between pile and soil, and it is smaller than free thermal expansion coefficient α_{p}(Equation 5-6) and $\Delta\mathrm{T}$ is the temperature difference measured at the location of the gauge. The increasing of thermal strains during the heating test depends on the increasing of △T even more than the decreasing of mobilised thermal expansion coefficient (Equation 5-10).

The thermal load profile versus pile's depth is reported in Figure 5-28(a) at 3.8 h, 4.6 h and 5.6 h, as for Figure 5-27. The thermal load at each depth is computed from the restrained thermal strain, Young's modulus and cross section of the pile. The restrained strains are evaluated according to Equation 5-8, and axial load induced by the temperature variations is computed according to Equation 5-12.

Equation 5-12: $N_i = \mu\varepsilon_{(restrained\ pile)\ i}\ E\ A$

Where $\mathrm{N}_{\mathrm{i}} \cdot 10^{-3}$ is the thermal load at VWG depth in kN, $\mu\varepsilon_{\mathrm{restrained\ i}}$ is the thermal restrained strain at VWG depth, $\mathrm{E} = 31100\ \mathrm{Mpa}$ is the Young's modulus of the reinforced concrete pile and $A = \pi r^2 = 282743.34\ mm^2$ is the pile's cross section, $\mu\varepsilon_{(restrained\ \mathrm{pile})\ i}$ can be also expressed according to Equation 5-13.

Equation 5-13: $\mu\varepsilon_{(restrained\ pile)\ i} = \varepsilon_{th.0\ i} - \varepsilon_{th.free\ i} = \Delta T \cdot (\alpha_p - \alpha_{mob})$

The difference between the free expansion coefficient and the mobilised thermal expansion coefficient is the restrained thermal expansion coefficient $\alpha_{restrained}$. The axial load N_i can be directly related to the temperature variation $\Delta\mathrm{T}$ and $\alpha_{restrained}$ according to Equation 5-14.

Equation 5-14: $N_i = (\Delta T \cdot \alpha_{restrained}) \cdot E\ A$

The maximum thermal load in Figure 5-28(a) is 98 kN and it is observed at 7.80 m depth and 5.6 h.

As showed in Figure 5-21 even if the circulation of heated water in the primary circuit is stopped the temperatures in pile's middle section are still increasing as well as the axial load.

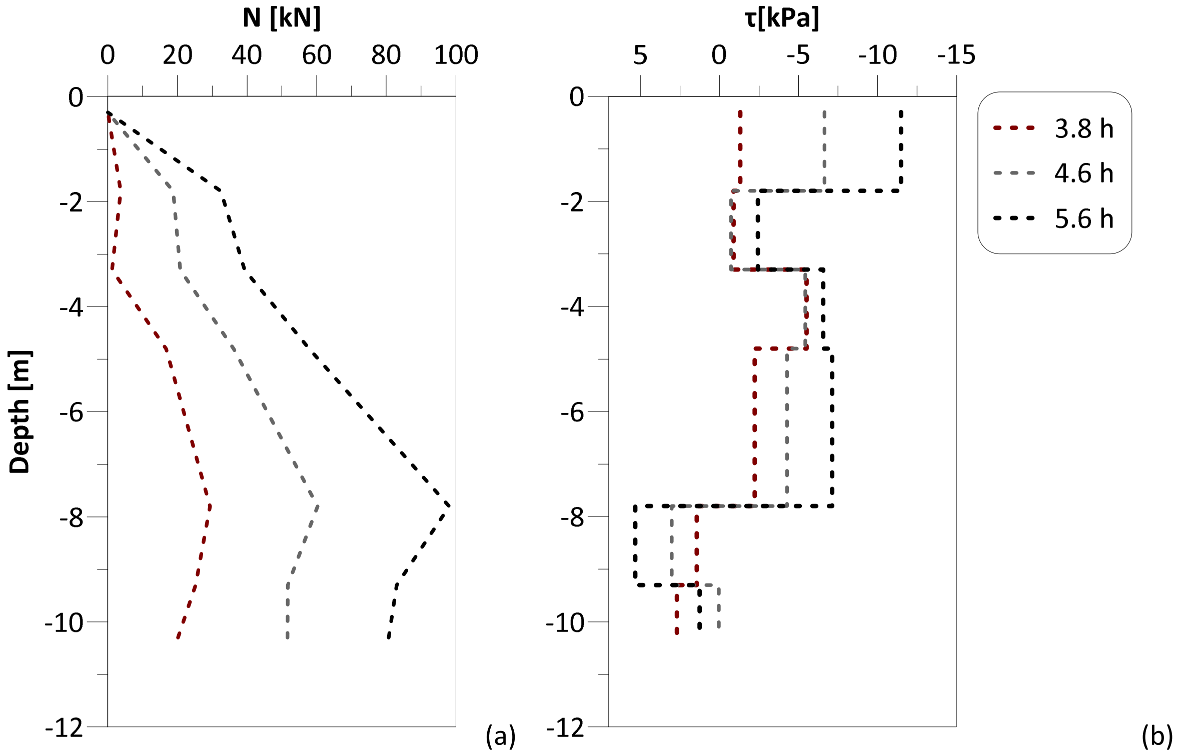

Figure 5-28: Pile's heating response during different time intervals of C thermal test (3.8 h. 4.6 h and 5.6 h). (a) thermal load along pile depth (b) Mobilized shaft resistance profile along pile depth.

At a depth of 7.80 m at the end of monitoring 143 KN of thermal load is measured for a temperature variation of 4.8 °C. The maximum measured thermal stress ($\sigma_{th.max}$) is 0.5 Mpa that is less than 2% of the characteristic cylindric resistance of the pile's concrete. $\sigma_{th.max}$ provides a DSR (Equation 2-2. section 2.2.2) of 0.41 considering that the $\sigma_{th.fixed}$ (maximum stress change computed in the hypothesis that the pile body is perfectly constrained) is about 1.2 MPa.

Mobilised shaft resistance was evaluated from the axial load reported in Figure 5-28(a). The pile was divided into six segments defined by two subsequent VWGs. In each segment the average mobilized shaft resistance is computed according to Equation 5-15.

Equation 5-15$: \tau_i = (Ni - N_{i+1})/(\pi d L_s)$

Where: τ_i is the average mobilized shaft friction in kPa referred to the i-th segment, Ni is the axial stress measured in the upper part of the segment in kN, N_{i+1} is the thermal load measured in the lower part of the segment in kN. The thermal mobilised skin friction profile is plotted in Figure 5-28 (b) at 3.8 h, 4.6 h and 5.6 h from the beginning of the test. The sign convection adopted for the shaft friction is that upwards shears are positive while downwards are negative. In the upper part of the pile the mobilised shaft frictions are downward in the opposite direction with respect to pile's elongation. At 7.80 m depth where the maximum axial load occurred the mobilised stresses are reversed i.e., upward. At increasing depth. the mobilised friction decreases. During the elapsed time. the mobilised friction in absolute value increases. The minimum thermal friction between 0.3 m and 1.80 m depth is -11kPa. As observed for the axial load the maximum shaft friction is mobilised when the circulation of heated water was stopped i.e., during the thermal recovery at the end of the test. At the end of monitoring the minimum shaft friction mobilised in the first pile's segment is about -20 kPa.

The Temperature difference profiles at pile's middle and edge sections are reported in Figure 5-29.

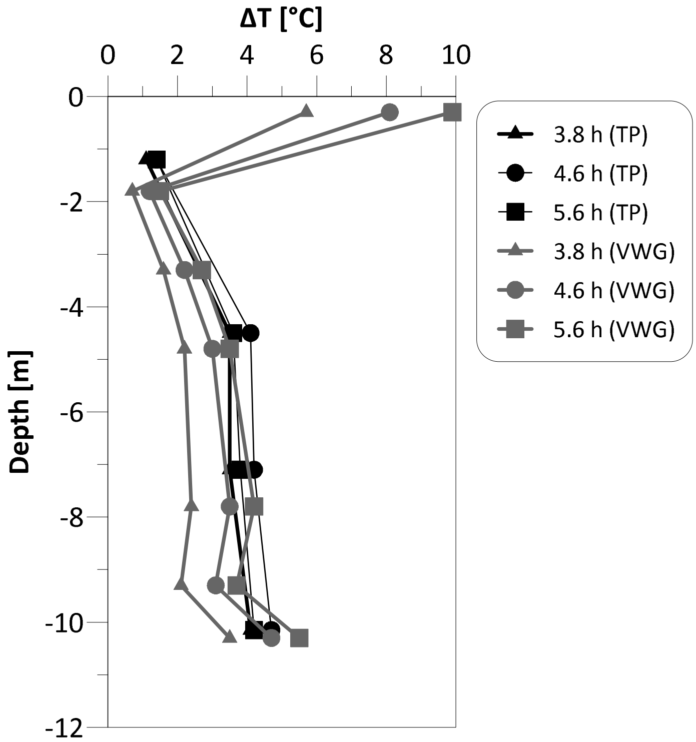

Figure 5-29: Difference in temperatures ΔT along pile depth in different positions of pile's cross section middle section (TP) and edge section (next to the primary circuit) (VWG) at different instant of time (4h. 6h and end of the test) of thermal test C.

Considering the same time interval, the temperature variation in the pile cross section is not uniform and varies along pile's diameter. ΔT obtained from the thermistor of the VWGs and NTCs of the thermometric chain are compared for similar depths. In order to evaluate the relative temperature difference at the cross -section during the heating test, measures obtained from TP4 and VWG1 (Figure 5-30), TP2 and VWG5 (Figure 5-31), TP 1 and VWG7 (Figure 5-32) and TP3 and VWG 3 (Figure 5-33) are compared. The temperature difference shows that the temperature was evenly distributed in the pile body after the pile was heated (Figure 5-30 to Figure 5-33). The relative difference in ΔT at two different positions in the cross sectional and approximately same depth (10.15m and 10.30 m) ranged between -1.3-1.5 °C (Figure 5-30). The relative difference in ΔT at 4.80 m (VGW 5) and 4.50 m (TP2) below the soil surface ranged between 0-1.9 °C (Figure 5-31). The relative difference in ΔT at the cross-section of the pile. at 1.20 m (TP1) and 1.80 m (VWG7) ranged between -0.1-0.6 °C (Figure 5-32).

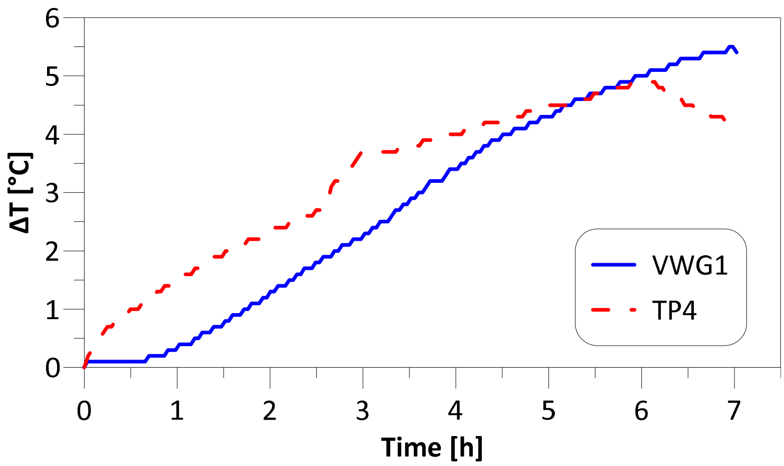

Figure 5-30: ΔTs in the middle of pile at 10.30 m depth from pile head (VWG1) and close to the heat exchanger tubes at 10.15 m depth from pile's head (TP4).

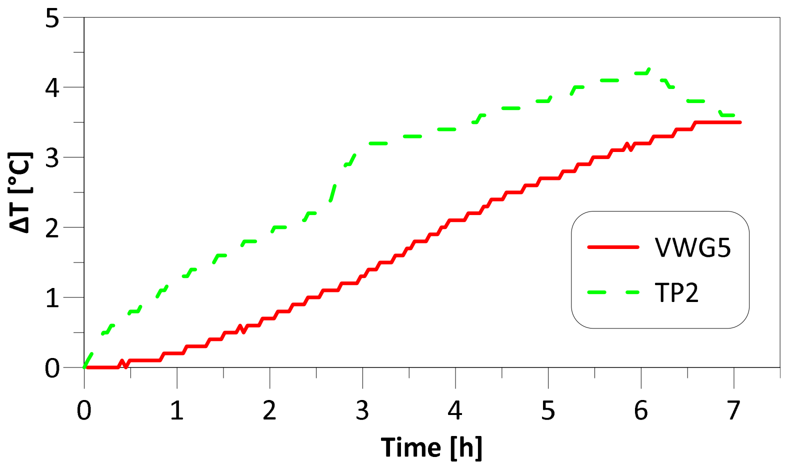

Figure 5-31: ∆Ts in the middle of pile at 4.80 m depth from pile head (VWG5) and close to the heat exchanger tubes at 4.50 m depth from pile's head (TP2).

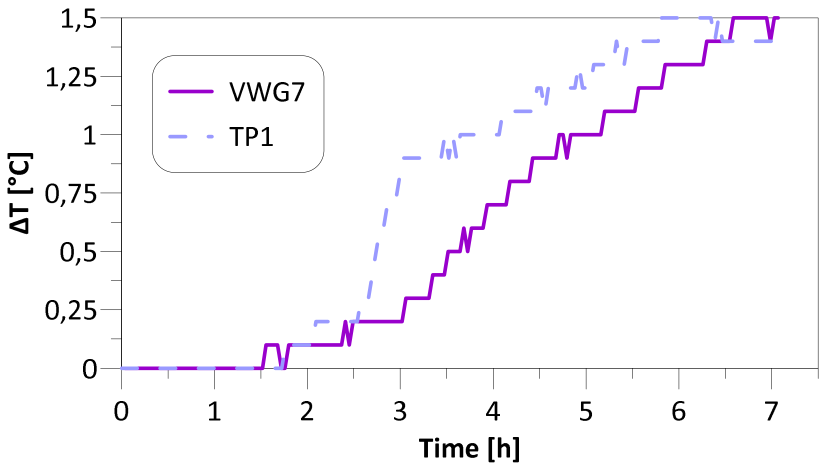

Figure 5-32: ∆Ts in the middle of pile at 1.80 m depth from pile head (VWG7) and close to the heat exchanger tubes at 1.20 m depth from pile's head (TP1).

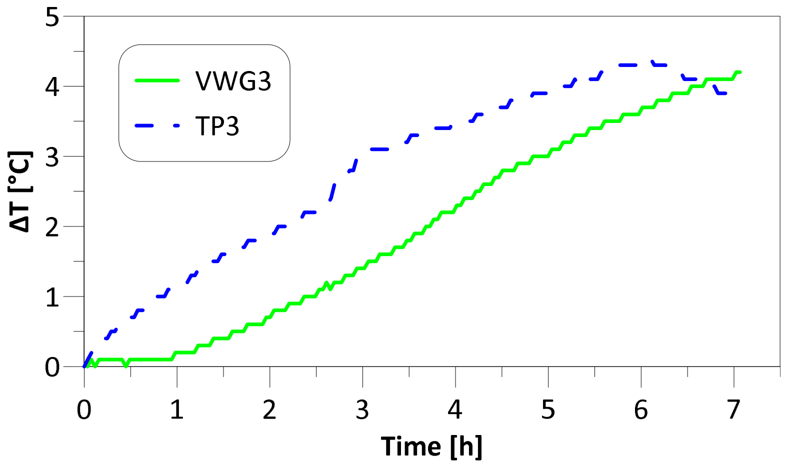

Figure 5-33: ∆Ts in the middle of pile at 7.80 m depth from pile head (VWG7) and close to the heat exchanger tubes at 7.10 m depth from pile's head (TP1).

The relative difference in ∆T at the two locations of the cross-section of the pile at 7.10 m and 7.80 m depth ranged between -0.4-1.6 °C (Figure 5-33). The distribution of the ΔTs determines different strain in the cross-section leading to a large stress difference within the pile body. This effect may have an influence on the work function of the EP when subjected to large loads (Bao et al., 2020).

During the test pile's head displacements is reported versus time in Figure 5-34 along with ambient air temperature, inlet, and outlet water temperatures.

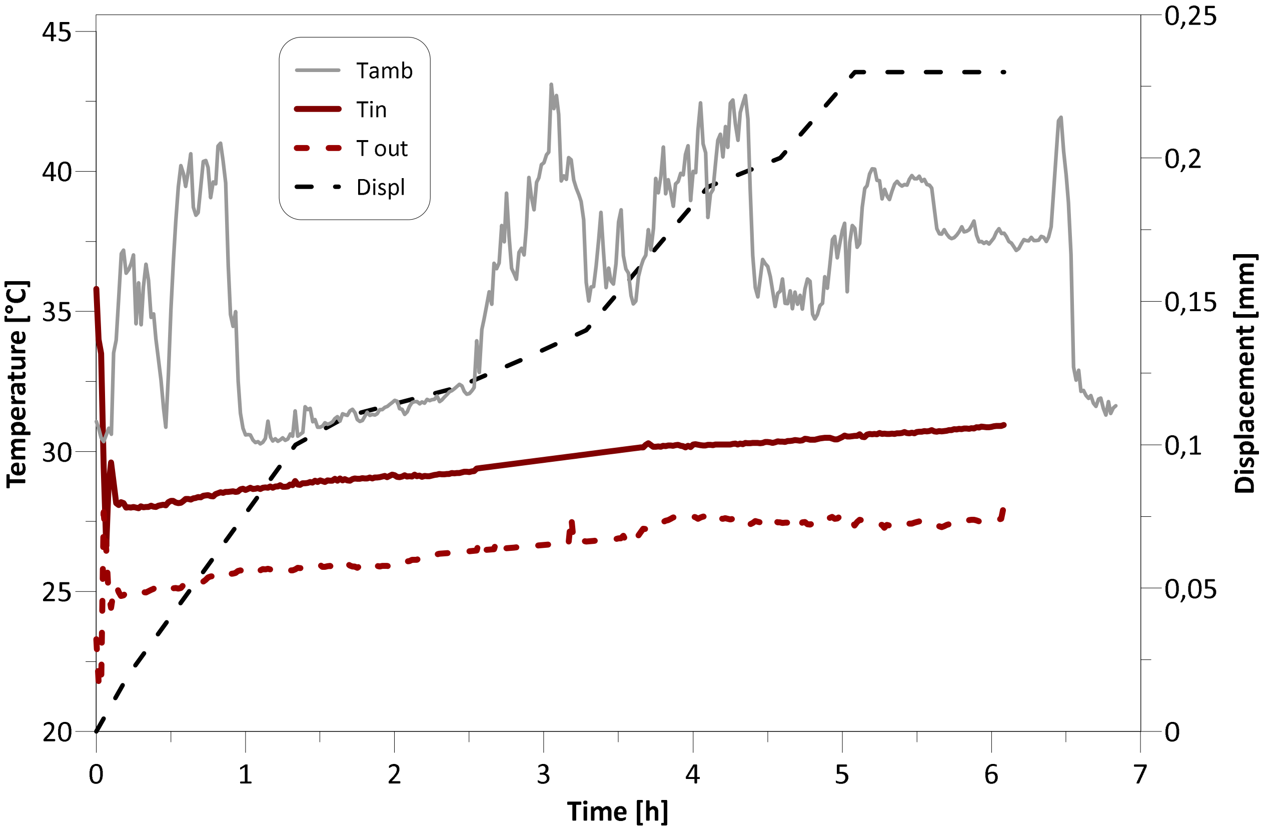

Figure 5-34: Average thermal displacements measured during the test (Displ) along with air ambient temperature. inlet and outlet water temperatures (Tin) and (Tout).

In response of heating, pile's displacements are upward in according to the expansion. The maximum displacement is 0.23 mm. According to the measurement of the VWGs the NP is located at 7.80 m depth. The maximum free expansion of the pile depends on L_{np}, α_p(Equation 5-6) and ΔT_{ave} . Temperature differences at different depths are reported in Table 5-4.

Table 5-4: Temperature difference computed from NTCs thermistors of VWGs at the time of maximum measured displacement.

VWG	[m]	ΔT [°C]
1	-10.3	5.3
2	-9.3	3.5
3	-7.8	4
5	-4.8	3.4
6	-3.3	2.6
7	-1.8	1.4
8	-0.3	8.6

Table 5-5: Difference in temperature computed from NTCs thermistors of thermometric chain at the time of maximum measured displacement.

TP	[m]	ΔT[°C]

1	-1.2	1.4
2	-4.5	3.8
3	-7.1	4.1
4	-10.15	4.5

To evaluate the DDR of the pile (2.2.2), $\Delta T_{ave} = 4\ °C$ and $L_{np} = 7.80\ \mathrm{m}$ were assumed. DDR obtained for this test is 0.78.

5.5.3 Thermal Test B

The thermal test B consists of a short heating phase of about 1.5 h and a longer thermal recovery phase of about 3.20 h. During the heating phase the inlet water temperature ranged between 25°C and 34 °C as shown in Figure 5-35.

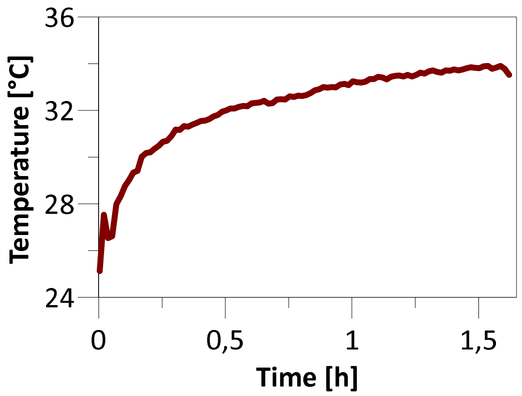

Figure 5-35: Inlet temperature of water during thermal test B.

The temperature profiles of pile and soil before starting the test are plotted in Figure 5-36.

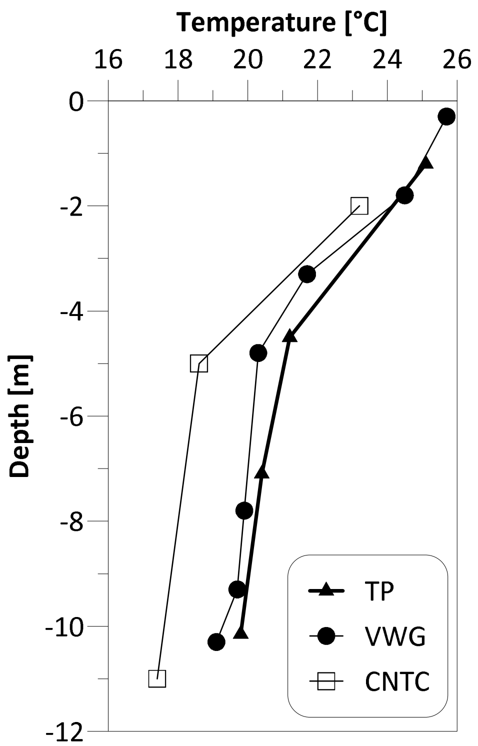

Figure 5-36: Temperature distribution along pile depth (TP and VWG) and soil depth (CNTC) before starting the heating test C.

Temperatures measured inside the pile at different locations of the cross section matched. Some differences in temperature profiles are observed between pile and soil below 4.80m – 5 m depth. The different temperature of pile and soil was probably induced by the heating tests carried out in the previous days as occurred during Test C (5.5.2).

The evolution of temperature difference ΔT (T in-out) and the heat injected into the ground is plotted in Figure 5-37.

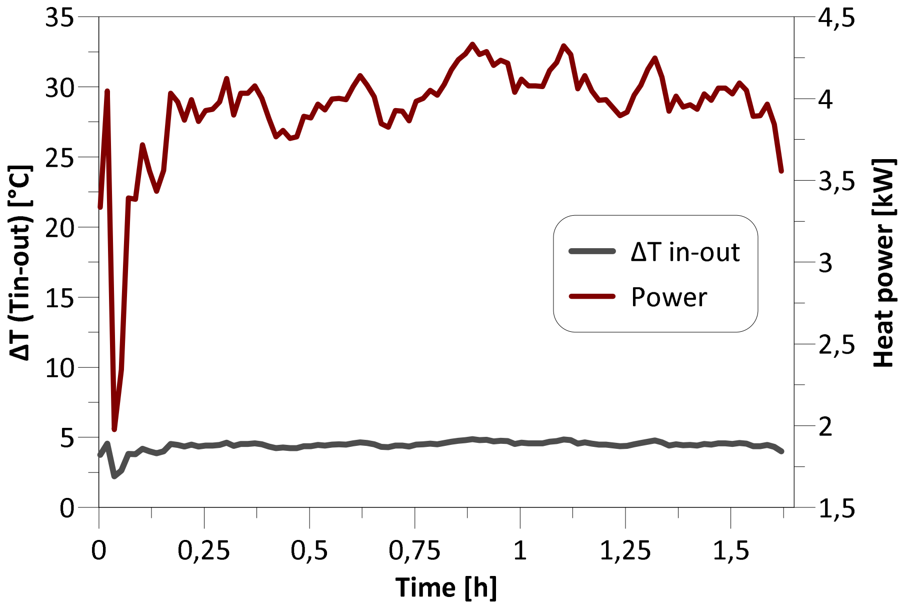

Figure 5-37: Difference in temperature between inlet and outlet water temperatures (ΔT) and heat injected into the ground (Power) during test B.

For the highest inlet temperatures, the difference in temperature reaches very high values more than 20 °C (Figure 5-37). The temperature difference between inflow and return flow temperature (ΔT, T in-out) ranges between 2.2 °C and 5 °C. The short-term thermal performance of the heat exchanger pile has revealed to be satisfactory also during this test. The average heat exchange rate is 4 kW. The average specific heat injection rate per pile meter is 330 W/m.

The pile temperature changes in response to temperature increase were reported during heating and subsequent recovery phase in Figure 5-38 along with Inlet and outer water temperature and air ambient temperature.

The thermistor of the VWG 8 is the strongly influenced by the ambient air temperature. At 0.30 m depth from ground surface thermal interaction with the environment is clear from the measurements. The ambient air temperature during the heating was about 35.5 °C with peak of 39 °C. Even if the heated water was circulated throughout the pile the highest temperatures are recorded at VWG8's depth. The increase of temperature in response of pile heating is immediately measured by the sensors placed next to the exchange circuit while at pile's middle section almost constant temperature are measured during the first hour (Figure 5-38).

Because of pile size and thermal properties of concrete only at the end of heating temperatures started increasing further at pile's middle section. After 3 hours from the end of pile heating, temperature measured in the middle section of the pile are still increasing.

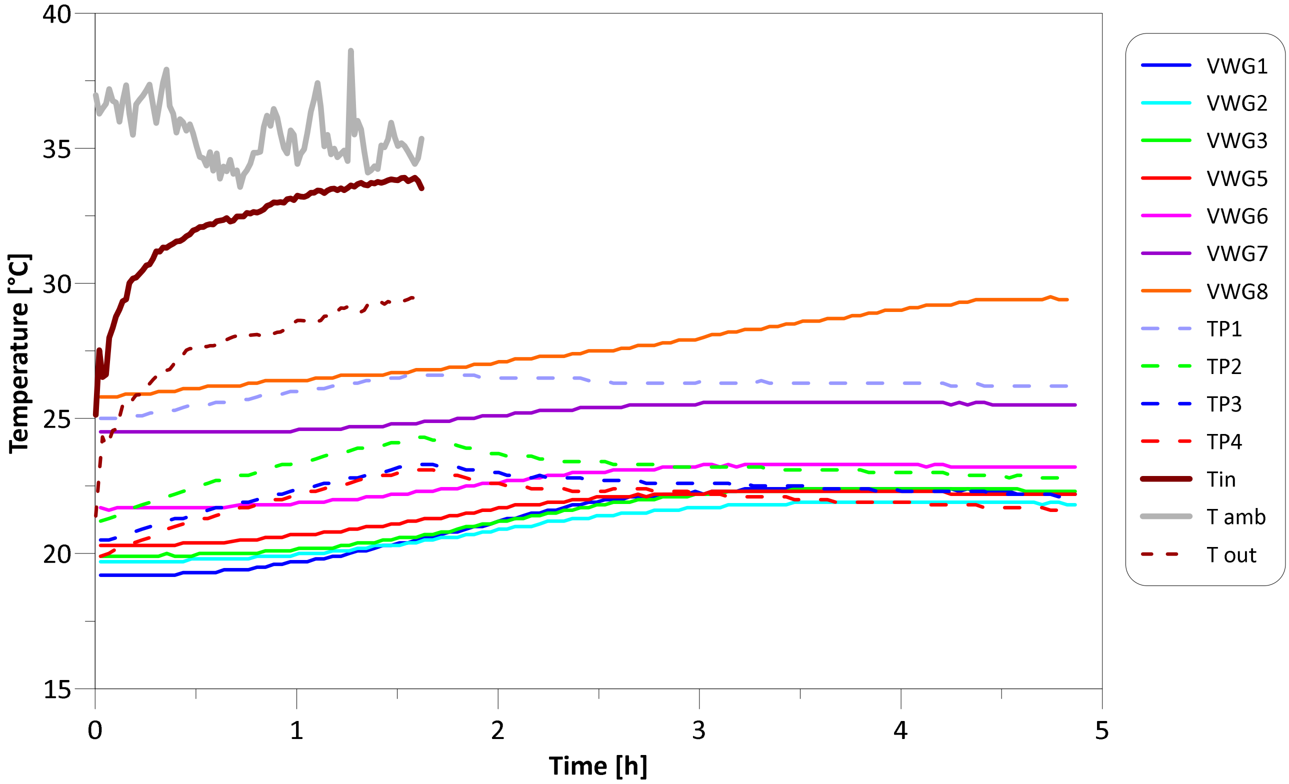

Figure 5-38: Temperature evolution in the pile at different depths and positions in the cross section (VWG and TP) along with inflow (Tin) and return flow (Tout) temperatures and ambient air temperature (Tamb).

Table 6-6 and Table 5-7 summarize temperature different trend observed in the two position of pile cross section.

Table 5-6: Temperatures measured by the VWGs thermistors at different time intervals (1 h. 2 h. 3 h and 4 h) during thermal test B.

		1 h	2 h	3 h	4 h
VWG	[m]	T [°C]	T [°C]	T [°C]	T [°C]
1	-10.3	19.7	21.3	22.2	22.4
2	-9.3	20	20.9	21.7	21.9
3	-7.8	20.2	21.2	22.2	22.4
5	-6.3	20.7	21.7	22.2	22.3
6	-3.3	21.9	22.7	23.3	23.3
7	-1.8	24.6	25.1	25.6	25.6
8	-0.3	26.4	27.1	28	29

Table 5-7: Temperatures measured by NTCs close to the primary circuit at different time intervals (1 h. 2 h. 3 h and 4 h) during thermal test B.

		1 h	2 h	3 h	4 h
NTC	[m]	T [°C]	T [°C]	T [°C]	T [°C]
1	-1.2	26	26.5	26.4	26.3
2	-4.5	23.4	23.6	23.2	23
3	-7.1	22.4	22.9	22.6	22.3
4	-10.15	22.2	22.5	22.2	21.9

Temperature evolution of the soil at 2 m, 5 m and 11 m of depth from pile head are plotted in Figure 5-39 along with inlet and outlet water temperature and air ambient temperature. From the measures of soil temperature. the observations of test C are still valid. The effects of short-term pile heating at 1.5 D away from the pile and hourly variation of ambient air are negligible on soil undisturbed temperature.

Temperatures of soil corresponded to those measured during heating test, 23.3 °C is the maximum temperature measured in the shallower sensor (CNTC 1). With increasing depth soil temperature decreases reaching 17.4 °C at depth of 11 m.

Temperature and temperature difference profiles at pile's middle section are reported in Figure 5-40 (a) and Figure 5-40 (b) after 2.6 h, 3.6 h and 4.9 h from the start of the test B.

During the heating phase, all the VWGs frequencies measures corresponded to the phases E and SS (Figure 5-12, 5.3). The S phase of VWGs frequencies measures occurred during the recovery phase. Therefore, the time instants have been chosen when the VWG measures are in the S phase i.e., after the end of heating.

It should be also highlighted that the end of heating does not correspond to the end of heating of the whole pile's cross sectional, as described above. The end of heating is connected to fact that heated water circulation was interrupted, but it does not mean that the pile temperature is not still increasing. At pile's middle section 3 hours later the circulating heated water was stopped temperature is still increasing.

As could be observed from Figure 5-40 (a) and Figure 5-40 (b), maximum temperatures and temperature differences occurred at the end of monitoring at all depths. The maximum temperature difference of 3.6 °C occurred at 0.30 m depth and decreases with increasing depth with except of 10.30 m. At this depth the temperature variation is about 3 °C.

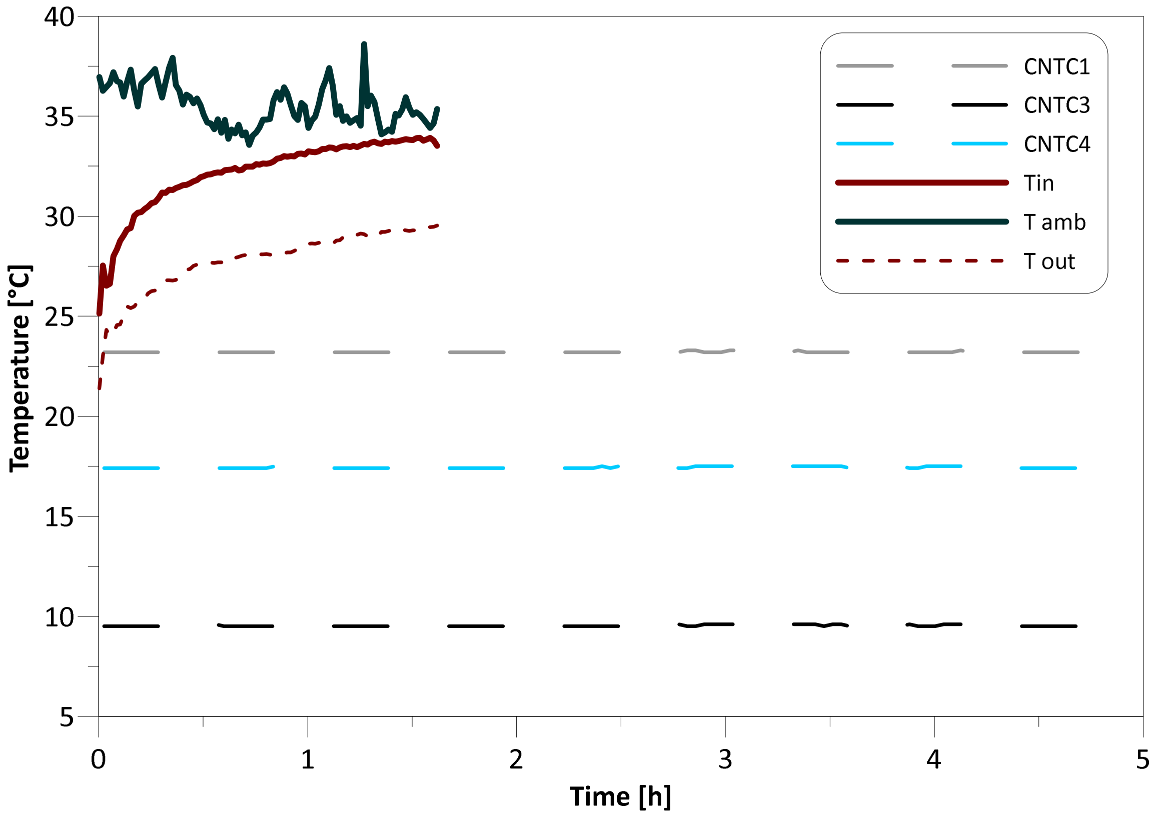

Figure 5-39: Soil temperature evolution at different depths (CNTC) along with inflow (Tin) and return flow (Tout) water temperatures and ambient air temperatures (Tamb).

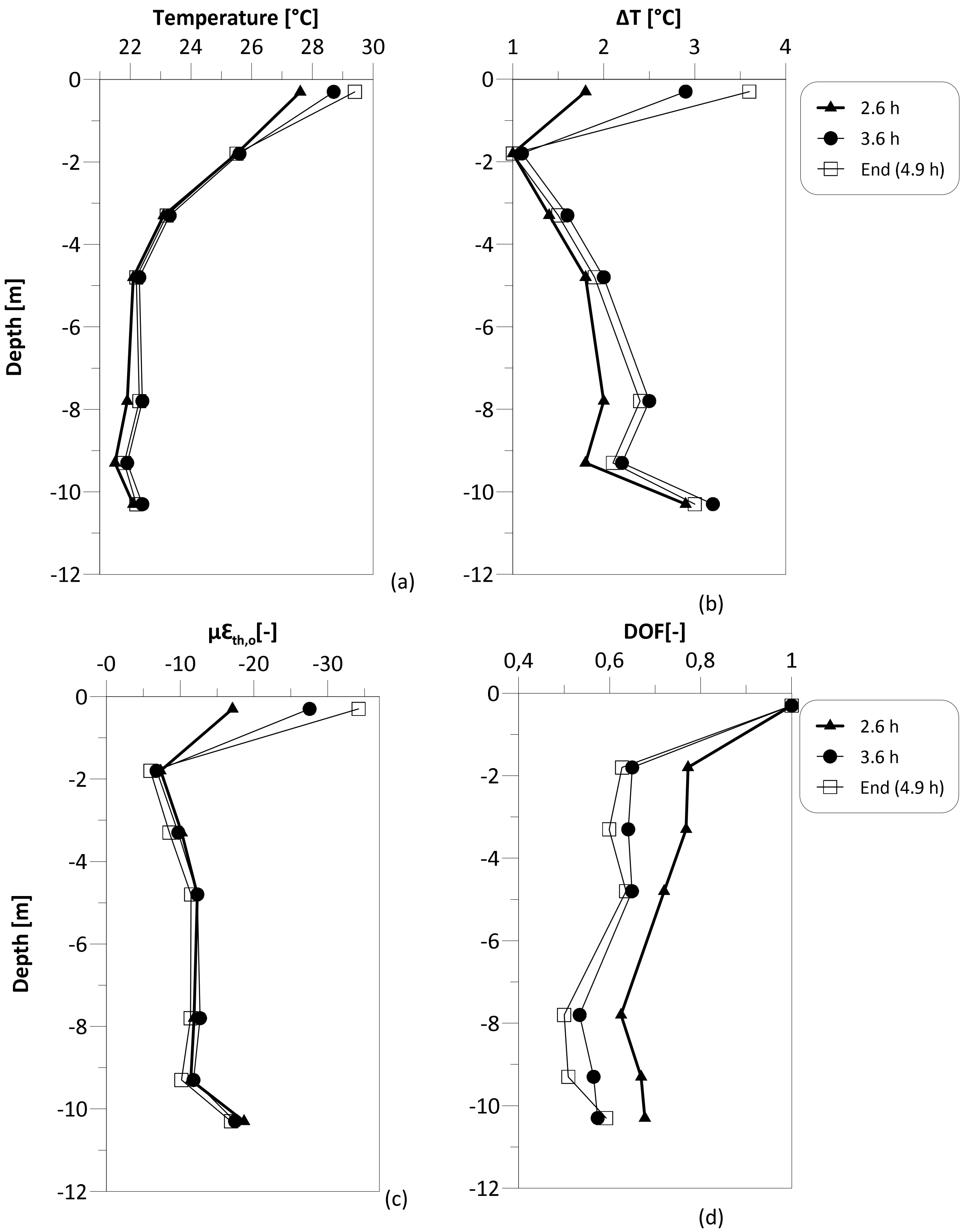

Figure 5-40: Pile's heating response during different time instants (2.6 hours. 3.6 hours and the end of monitoring) of B test at pile's middle cross sectional; (a) Temperature. (b) Temperature difference ΔT. (c) Thermal strain and (d) DOF profiles.

Thermal strains and DOF profiles are plotted in Figure 5-40 (c) and Figure 5-40 (d), respectively. All the thermal strains measured correspond to pile's elongation as expected during a heating test. At pile head maximum thermal strain occurred because the head is free to expand. Thermal strains decrease along pile's length. Concerning to strain's time evolution. the maximum thermal deformations occurred at the end of monitoring (more than 3 hours later the end of heating) at all depths. The DOF decreases with increasing time and depth (Figure 5-40 (d)) as observed during the heating of thermal test C. At the VWG1 location the DOF decreases at 2.6 h and 3.6 h while at 4.9 h i.e., at the end of monitoring a slight increase it is observed.

The thermal load and mobilised shaft friction average profiles are reported in Figure 5-41 (a) and Figure 5-41 (b), respectively. The maximum thermal load is 100 kN and occurred at 7.80 m depth and at the end of monitoring. During the test, the axial load increased at each depth. The maximum axial stress is 0.35 MPa for a temperature difference of 3 °C. The DSR is 0.4, and it is close to those computed during test C. The maximum mobilised shaft friction occurred in the upper part of the pile. The maximum friction in absolute value is about 11 kPa. During the recovery phase between 3.6 h and 4.9 h a slight decrease of mobilised skin friction is observed.

Pile's head thermal displacement versus time is plotted in Figure 5-42. Pile displacements are upwards with a maximum value reached after the end of heating as could be noticed from Figure 5-42. The maximum displacement is about 0.1 mm. DDR=0.76 is computed considering the average thermal variation $\Delta T_{ave} = 1.6\ °C$ and position of NP at 7.80 m depth.

The interpretation of results highlights the importance of monitoring of the recovery phase. The heat transfer evolution in pile cross section needed to be monitored also at the end of the heating phase. The maximum effects of heating in the middle of pile cross section occurred after a time interval that corresponded to two times the heating duration.

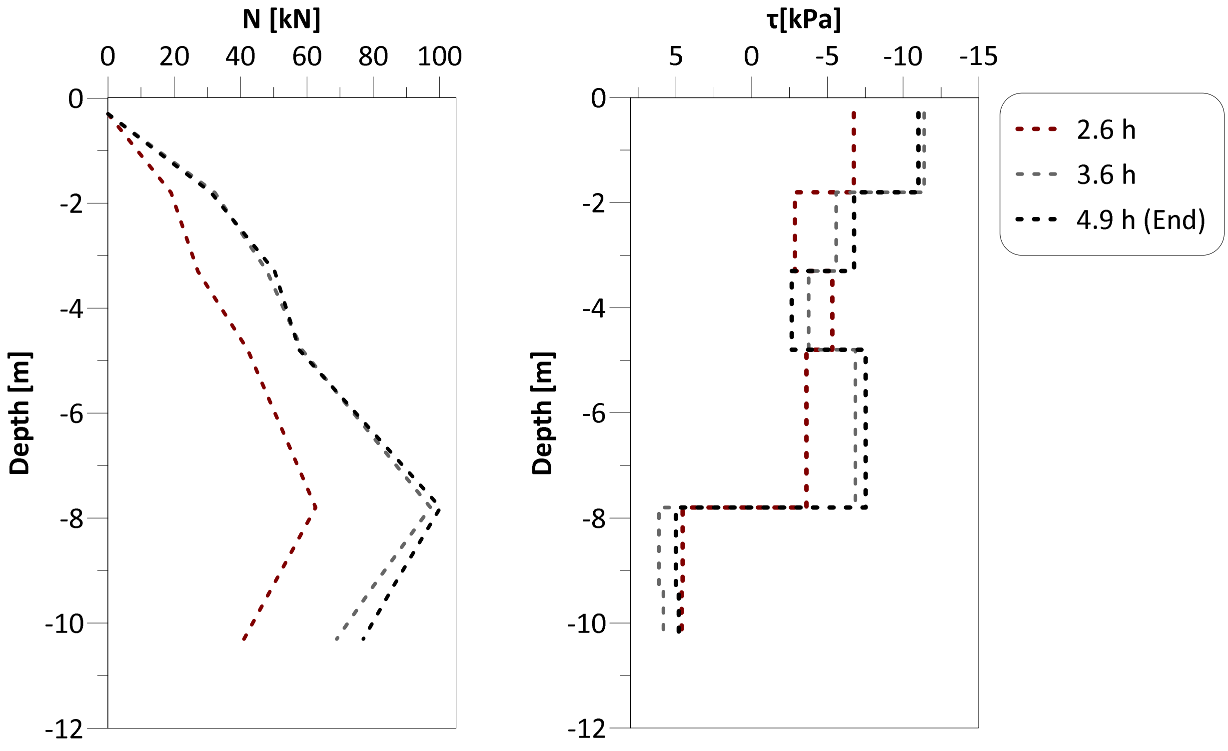

(a) (b)

Figure 5-41: Pile's heating response during different time intervals (2.6 hours. 3.6 hours and the end of monitoring) of B thermal test; (a) Average Thermal load and (b) Mobilized shaft resistance profiles.

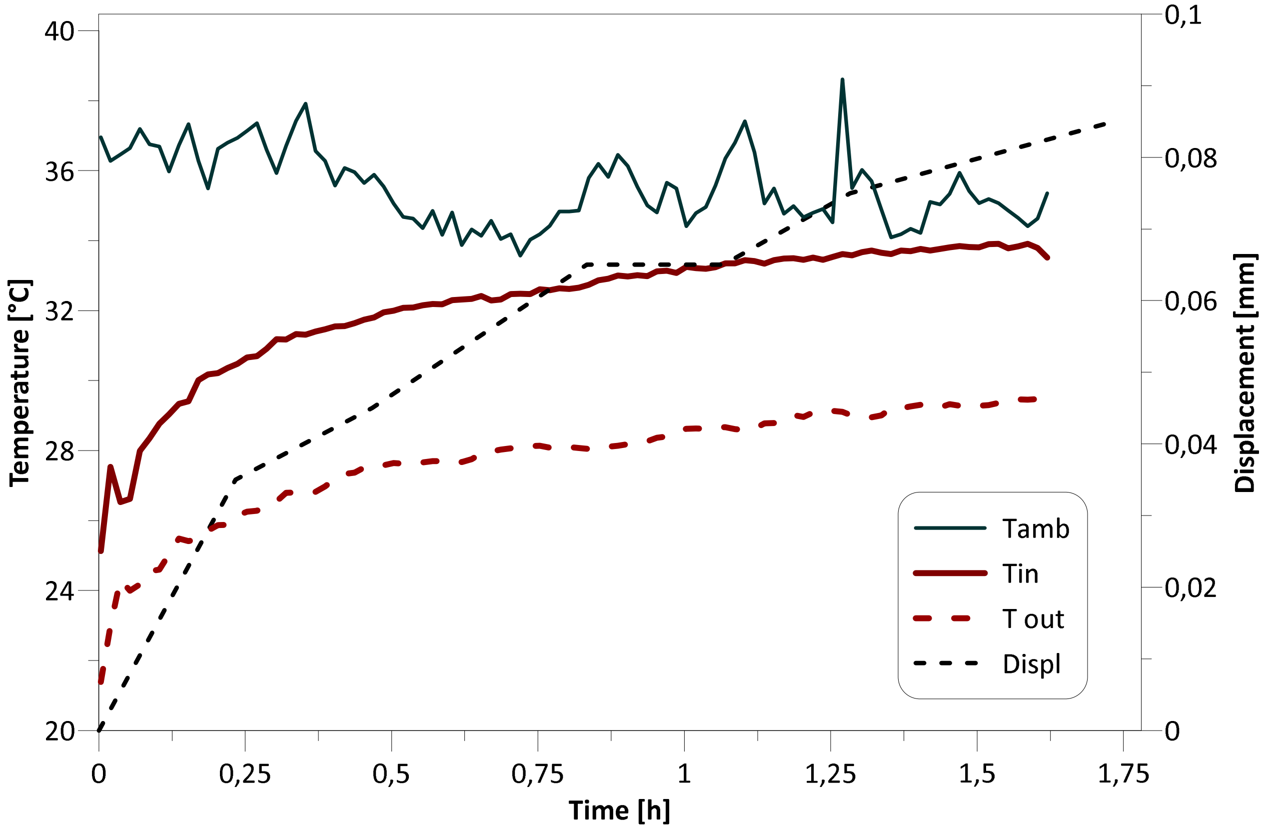

Figure 5-42: Average thermal displacements measured during the test (Displ) along with air ambient temperature (Tamb). inlet and outlet water temperatures (Tin) and (Tout).

5.5.4 Thermal Test A

Thermal test A was carried out heating the pile for about 5 hours. the temperature evolution of heated water entering the circulation pipes is reported in Figure 5-43. The inlet water temperature ranged between 26.5 °C and 35.1 °C. In the last 1.30 h of the test water temperature is almost constant between 34.7 °C -35.1 °C and throughout the test the temperature variations applied to the inlet water are always increasing. This thermal test is characterised by the longest heating. Thermal recovery was not monitored.

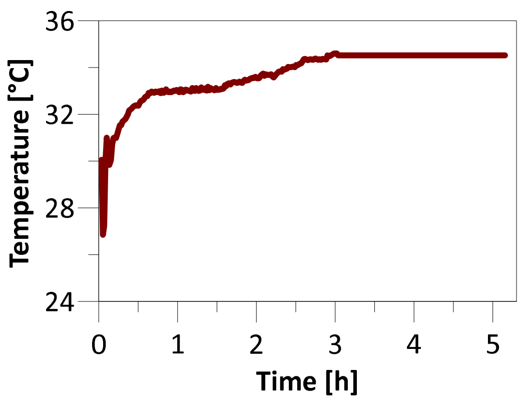

Figure 5-43: Inlet temperature of water during thermal test A.

Before starting the heating, pile and soil temperature are plotted in Figure 5-44. Pile and soil are characterised by thermal equilibrium, pile and soil temperatures matched.

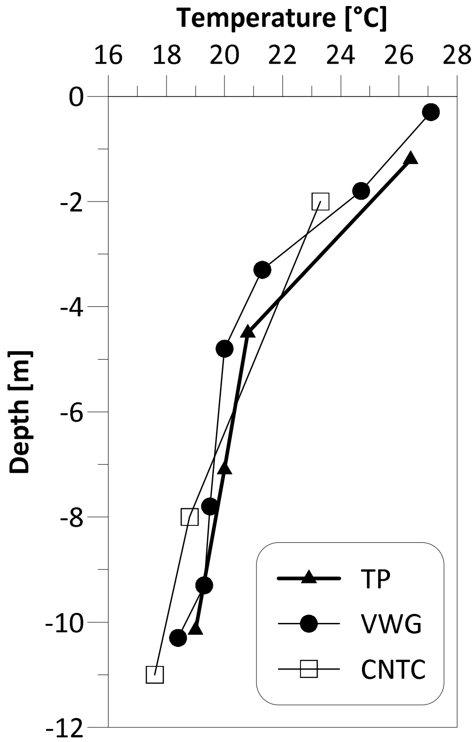

Figure 5-44: Temperature distribution along pile depth (TP and VWG) and soil depth (CNTC) before starting the heating test A.

Temperature differences between inlet and outlet water (T in-out) and the heat injected into the ground are plotted in Figure 5-45.

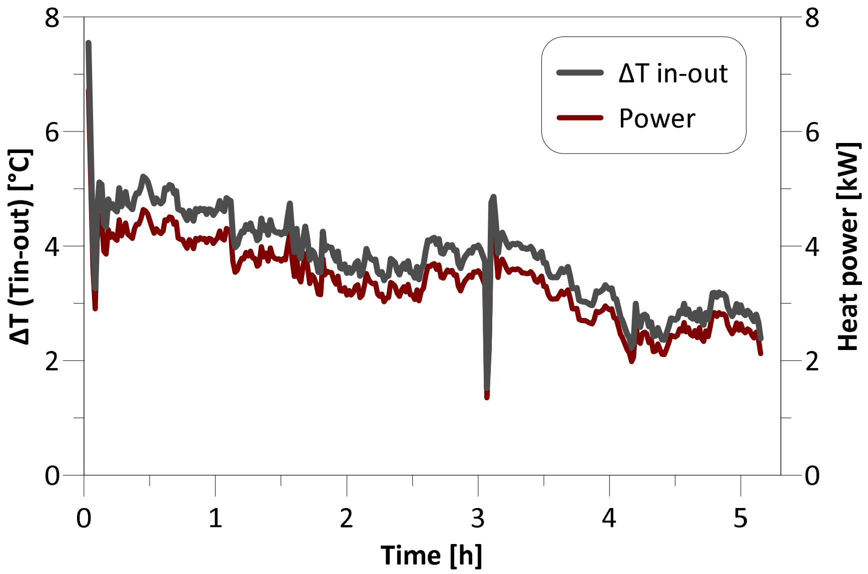

Figure 5-45: Difference in temperature between inlet and outlet water temperatures (ΔT) and heat injected into the ground (Power).

The temperature difference between inflow and return flow ranged between 1.50 °C and 7. 5 °C, with the highest value founded at the begging of the test. The average heating power injected into the ground is 3 kW while the specific heat injection rate per meter pile is about 280 W/m.

The pile temperature changes in response to the heating along with Inlet and outlet water temperatures are plotted in Figure 5-46. Even if air ambient temperatures were not recorded the test was carried out during a warm summer day. The shallowest VWG8 is characterised by the highest recorded temperatures because of the interaction with ambient air, at this depth the highest temperature recorded is about 31.3 °C. All temperatures measured by the thermistors of the VWGs are characterised by a first phase where temperatures were almost constant (first hour of heating) and a second phase where temperatures started to increase with a stronger rate. As observed in thermal tests B and C, the fact that the middle section of the pile needed time to response to heating depended on the radial heat transfer mechanism occurring in pile cross section and on pile thermal resistance.

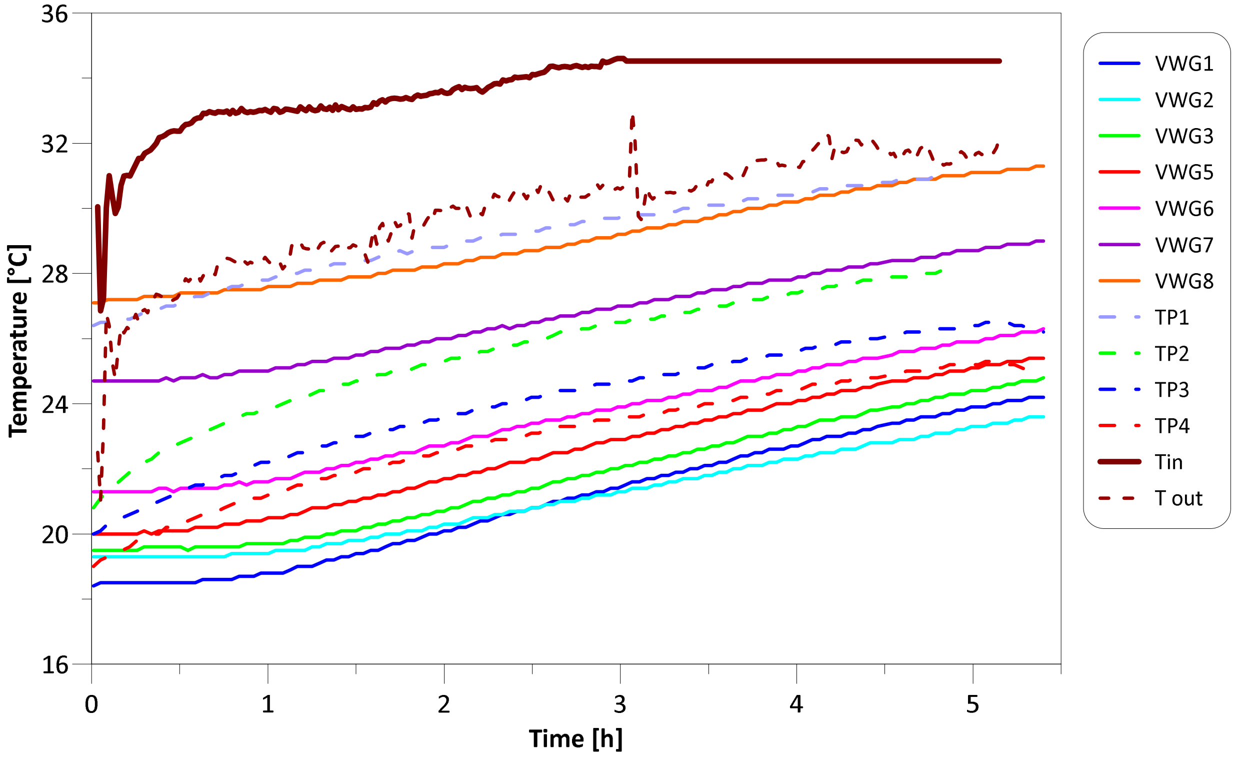

Figure 5-46:Temperature evolution in the pile at different depths and positions in the cross section (VWG and TP) along with inflow (Tin) and return flow (Tout) temperatures and ambient air temperature (Tamb).

The maximum temperature recorded at each depth at the end of the test are reported in Table 5-8 and Table 5-9.

Table 5-8: Maximum temperatures measured by the VWGs thermistors at the end of heating thermal test A.

VWG	[m]	T [°C]
1	-10.3	24.2
2	-9.3	23.6
3	-7.8	24.8
5	-4.8	25.4
6	-3.3	26.3
7	-1.8	29
8	-0.3	31.3

Table 5-9: Maximum temperatures measured by NTCs of the thermometric at the end of heating thermal test A.

NTC	[m]	T [°C]
1	-1.2	31.1
2	-4.5	28.3
3	-7.1	26.5
4	-10.15	25.3

Temperature-time distribution recorded by sensors placed in different positions of the cross section but at similar depths were compared to evaluate the evolution of heat transfer mechanism across pile radius. Comparisons between the measurements of TP4 and VWG1 and TP2 and VWG5 are reported in this section (Figure 5-47 and Figure 5-48, respectively).

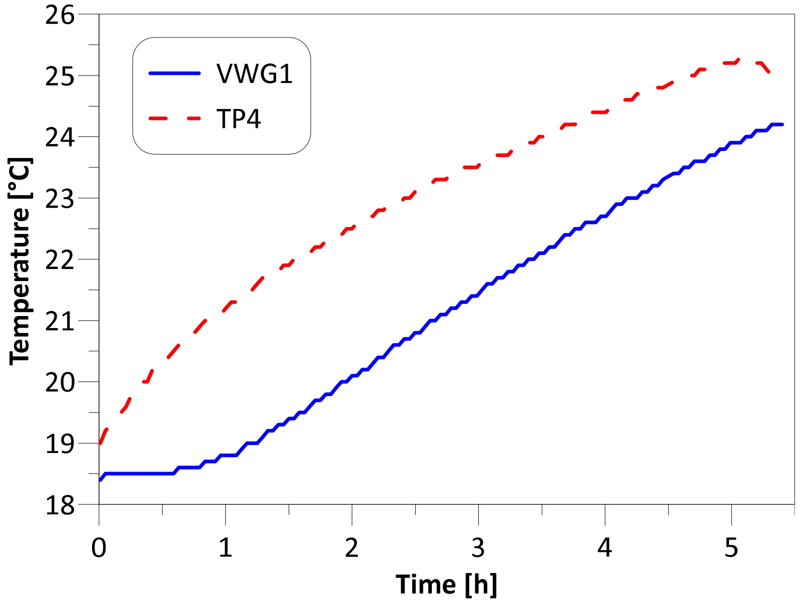

Figure 5-47: Evolution of heat transfer mechanism along pile's cross section. pile's temperature in the middle of pile at 10.30 m depth from pile head (VWG1). pile's temperature close to the heat exchanger tubes at 10.15 m depth from pile's head (TP4).

From Figure 5-47 it could be observed that at the beginning of the test the temperatures recorded in the two locations of pile's cross section started from values that differs of 0.5 °C, as observed for Test C. With the heating of the pile the initial difference in temperature of the two sensors increased reaching a peak of 2.4 °C. At the end of the heating the difference in temperature between the middle of the cross section and pile edge decreased to 1 °C. This decrease in temperature difference between VWG1 and TP4 is caused by the interruption of circulating.

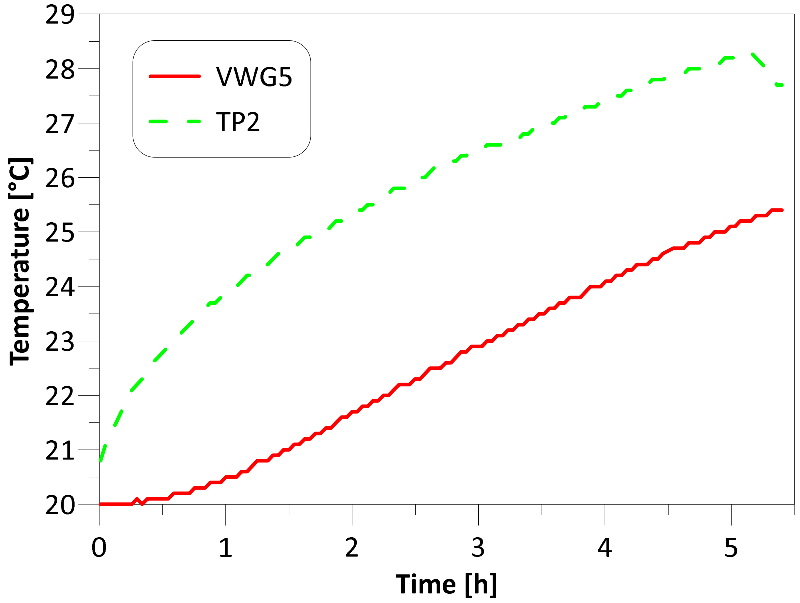

Figure 5-48: Evolution of heat transfer mechanism along pile's cross section. pile's temperature in the middle of pile at 4.80 m depth from pile head (VWG5). pile's temperature close to the heat exchanger tubes at 4.50 m depth from pile's head (TP2).

Temperature distribution in the cross section could be estimated also considering the comparison between the temperatures measured by TP2 and VWG 5. The temperatures recorded at the beginning of the test differed of about 1 °C. With the heating of the pile this difference was increased to 3.8 °C. Even if this difference in temperature is connected to slightly different position of VWG it provided a general view of the radial heat transfer mechanism. After 5 hours of heating the temperature of the middle of the pile did not reached the temperature measured close to the primary circuit. A longer monitoring time is needed to reach a uniform temperature distribution across pile's section.

Temperature evolution of the soil at 2 m, 5 m and 11 m of depth are plotted in Figure 5-49 along with inlet and outlet water temperatures. During the test, at each depth, soil temperatures followed a linear trend almost parallel to the abscissa axis. Measures of temperature with time demonstrated that soil temperature at 0.9 m from pile edge is not influenced by five hours of heating. As could be expected the maximum temperature is measured in the shallowest sensor (CNTC 1). With increasing depth temperature of soil decreased reaching 17.6 °C at 11 m depth.

Temperature and the temperature difference profiles with depth are reported in Figure 5-50(a) and Figure 5-50 (b) for the pile's middle section. Different time instants were analysed: 3.7 h, 4.5 h and 5.4 h. ∆T increased with depth, the maximum observed temperature difference is 5.8 °C at 10.30 m depth. The increase of difference in temperature is connected to the higher temperature recorded in the pile's upper part. Higher temperatures in the upper part of the pile determined lower temperature differences when the pile is heated. Therefore, at increasing depths, higher temperature differences are recorded.

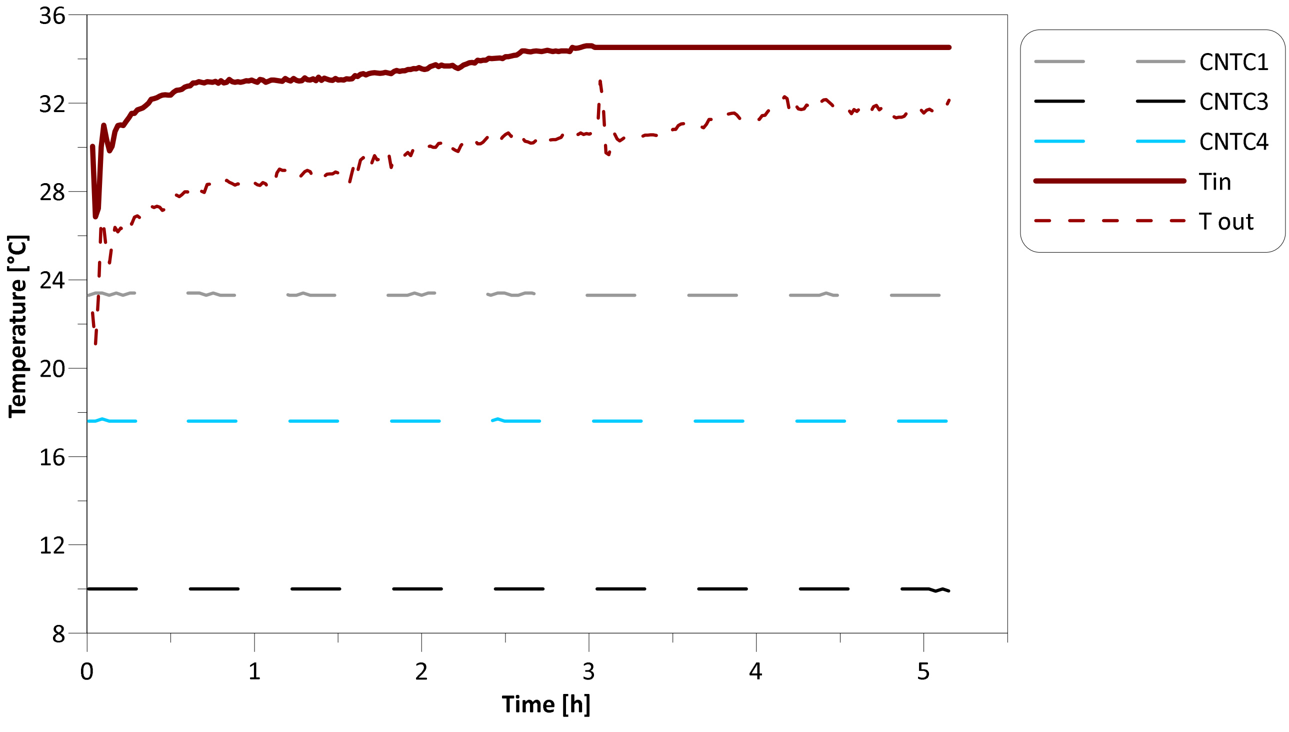

Figure 5-49: Temperature evolution in the soil at different depths (CNTC) along with inflow (Tin) and return flow (Tout) water temperatures.

Thermal strains are reported in Figure 5-50 (c). Thermal elongations are maximum at pile head and decreased with depth. The DOF profiles are reported in Figure 5-50 (d). The minimum DOF occurred at the deepest VWG. As observed during tests C and B with increasing depths the DOF decreased. With increasing elapsed time, the DOF decreased.

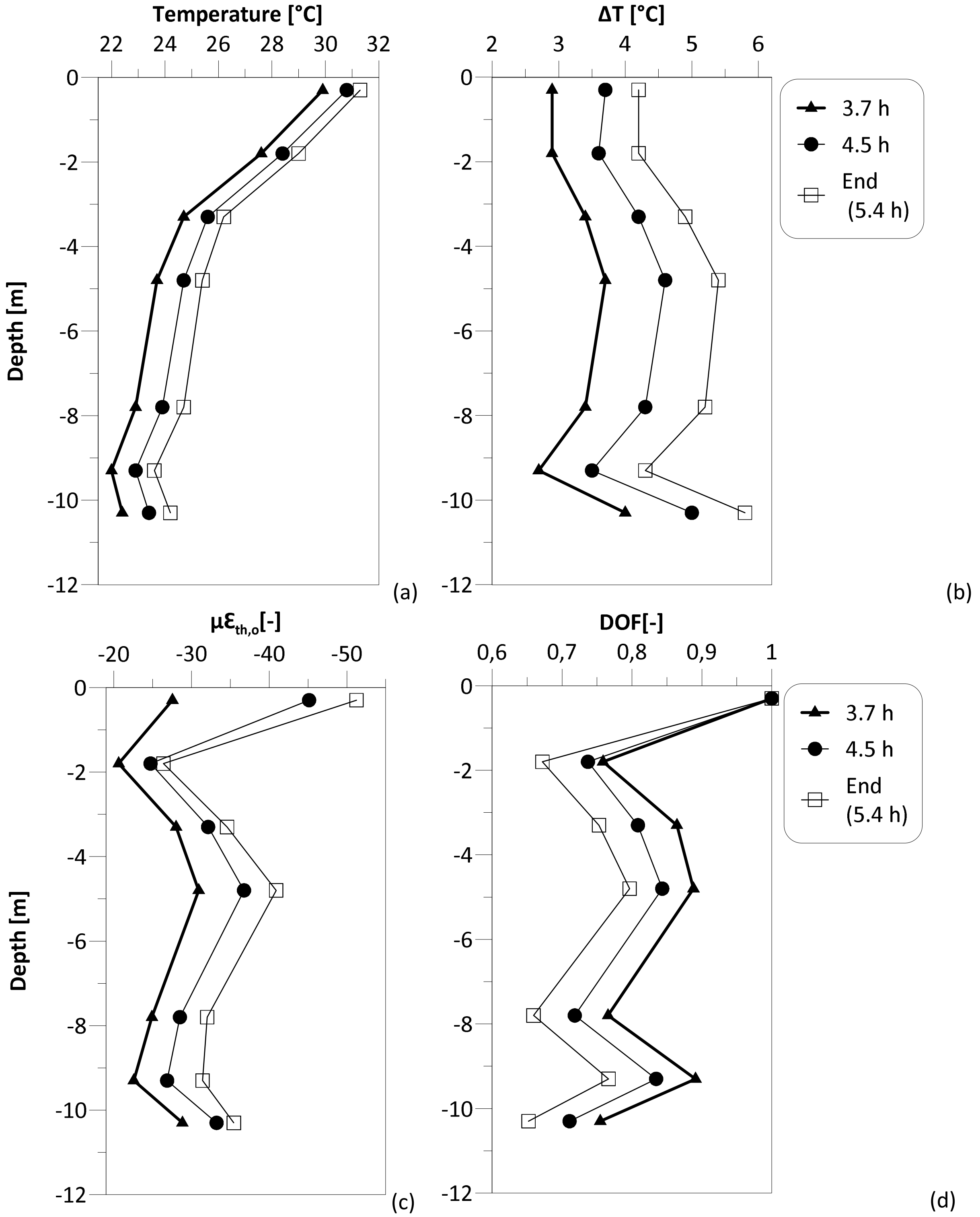

Figure 5-50: Pile's heating response during different time intervals (3 hours. 4 hours and end of monitoring) of A thermal test at pile's middle cross sectional; (a) Temperature. (b) Temperature difference △T. (c) Thermal strain and (d) DOF profiles.

The thermal load average profile and the average mobilised shaft resistance are plotted in Figure 5-51 (a) and Figure 5-51 (b), respectively. The average profiles have been obtained assuming that the NP is located at 7.80 m depth and assuming an average thermal load between 1.80 m and 7.80 m depth (Figure 5-51 (a)).

At the pile's head no thermal load occurred. The maximum thermal load of 152 KN is observed at 7.80 m for △T=5.2 °C. The maximum thermal stress, $\sigma_{th.max}$, is =0.54 MPa. $\sigma_{th.max}$ is smaller than 2% of the characteristic cylindric resistance of concrete. For △T=5.2 °C, DSR is 0.35.

The mobilization of shaft friction varies along pile length and during the test. The maximum mobilization of shaft friction occurred in the upper part of the pile, decreases along pile's depth and increases below the NP. As observed for the previous thermal test the NP is located at 7.80 m of depth. The maximum mobilised shaft friction in absolute value is 42 kPa.

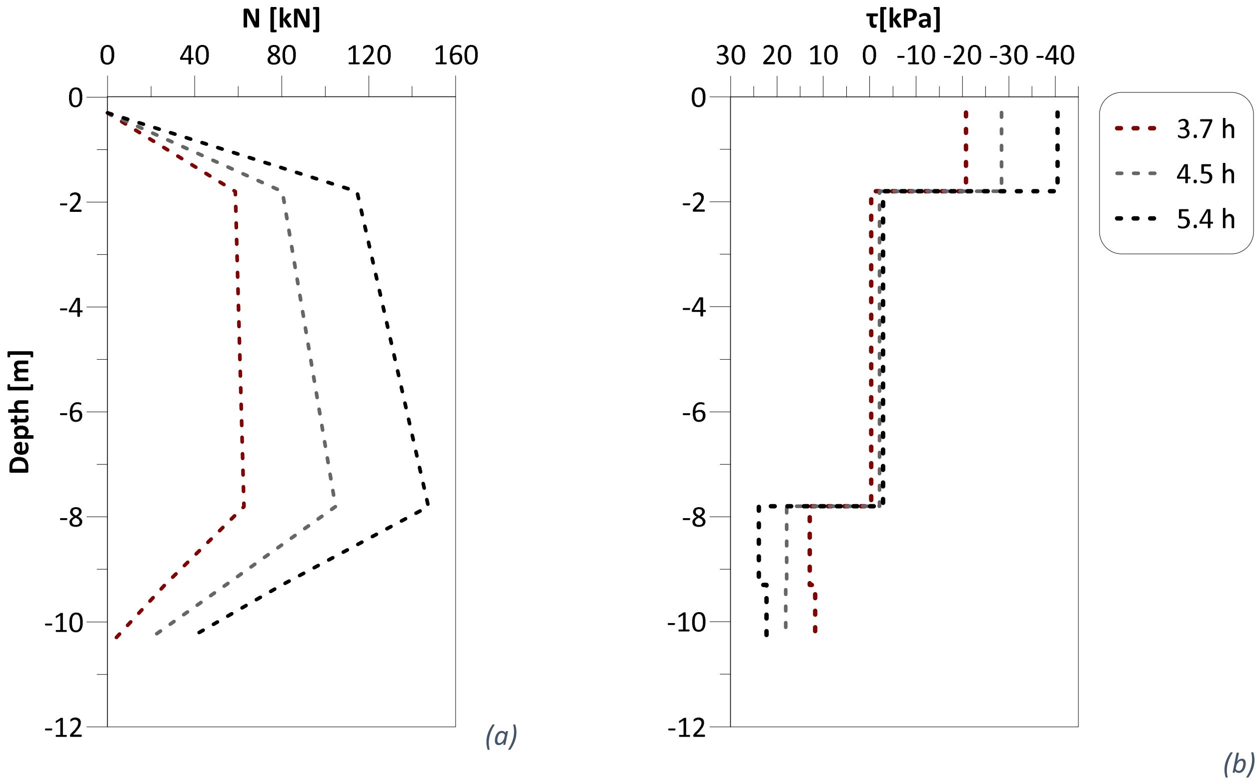

Figure 5-51: Pile's heating response during different time intervals of A thermal test (3.7 hours. 4.5 hours and the end of monitoring). (a) thermal load along pile depth (b) Mobilized shaft resistance profile along pile depth.

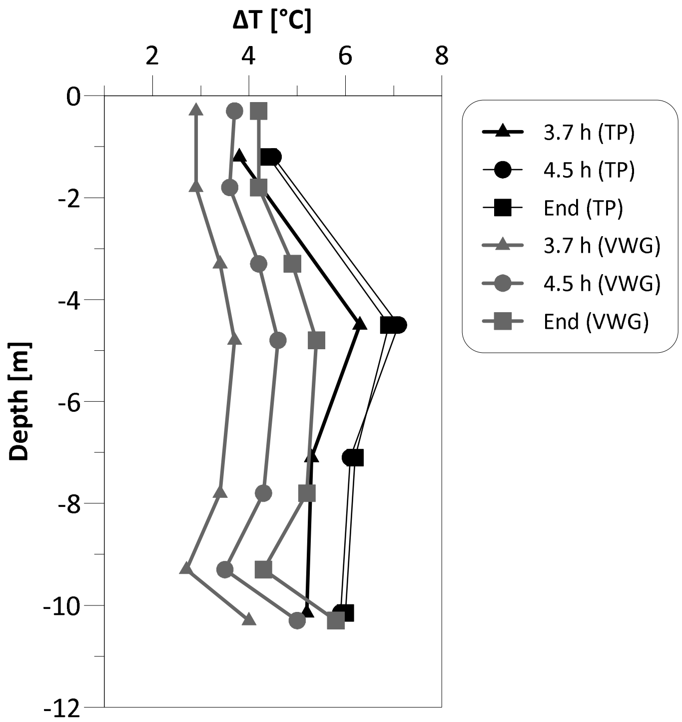

Figure 5-52: Difference in temperatures ΔT along pile depth in different positions of pile's cross section middle section (VWG) and close to the primary circuit (TP) at different instants of time (4h. 6h and end of the test) of thermal test C.

The temperature difference profiles for the middle section and close to the primary circuit are reported in Figure 5-52.

The average pile's head displacement is plotted in Figure 5-53 along with inlet and outlet water temperatures. Upwards displacements occurred as expected during the heating of the pile.The displacement trend follows the evolution of temperature increase. The maximum observed displacement ($y_{th,0}$) is 0.26 mm. If the NP is at 7.80 m depth and considering an average temperature variation of 4.7 °C along this length, the DDR is 0.75.

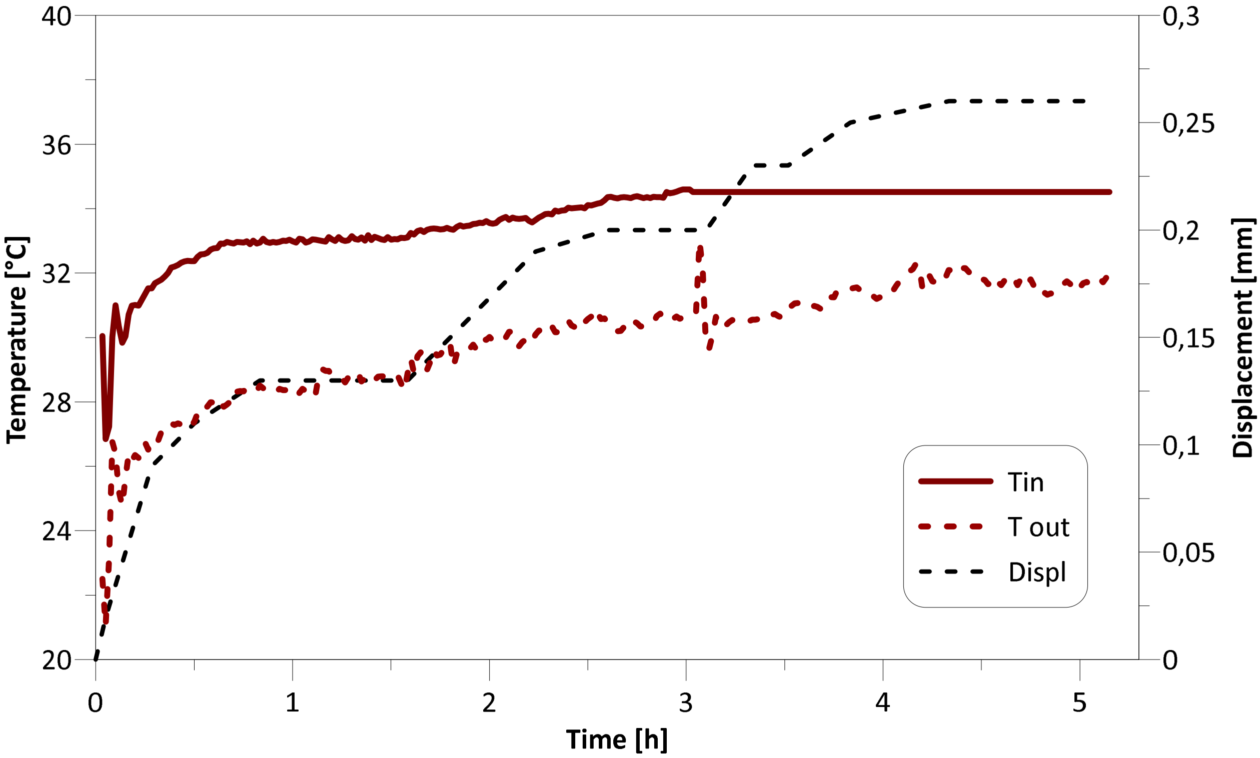

Figure 5-53: Average thermal displacements measured during the test (Displ) along with inlet (Tin) and outlet (Tout) water temperatures.

5.6 *Back analysis of thermal test A*

The Thermal test A described in 5.5.4 where the temperature profile of the pile corresponded to the undisturbed condition was chosen for FE back-analyses purposes by means of PLAXIS 2D. Pile and soil were discretized by means of an axisymmetric model. The soil layering corresponds to those reported in Table 5-1. i.e., six soil layers were considered (Figure 5-54). All the pyroclastic layers were modelled by the H-S constitutive model while the pile behavior was assumed as linear elastic. Rigid interface elements were adopted at the contact between the pile and the surrounding soil. The stiffness and thermal expansion coefficient of the pile corresponded to those reported in sections 5.2 and 5.3. respectively. The soil mechanical properties were defined from the results of the CPTs according to Table 5-1. The soil thermal conductivity and linear expansion coefficient were assumed as 0.5 W/m °C and 4x10^{-5} °C^{-1}. Fully coupled thermal analysis was carried out assigning thermal boundary conditions to the side and bottom of the domain. The thermal loading imposed as temperature time function corresponded to the inlet water temperature-time function (Figure 5-43) applied at the location of the helix circuit. following the procedure previously described in section 3.5. At the bottom of the model a constant temperature of 18 °C was assigned considering the initial soil (and pile) temperature profiles (Figure 5-44).

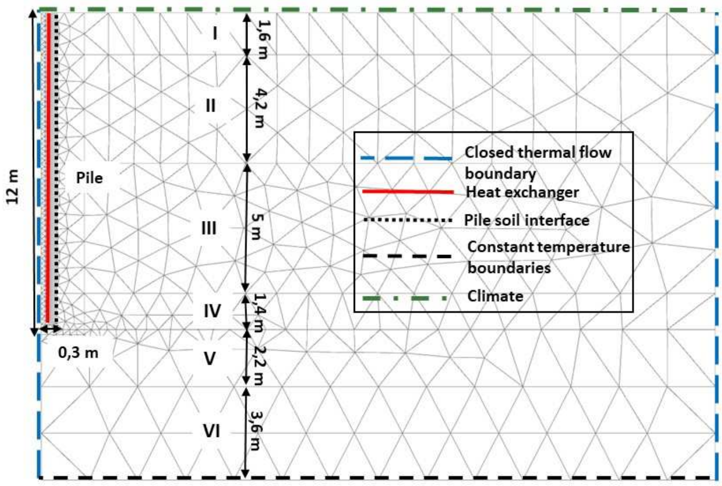

Figure 5-54:FE model adopted for the back analysis of test A.

Pile temperature profiles prior to starting the test and at the end of monitoring are compared to experimental profiles in Figure 5-55 (a). The initial temperatures measured in situ are assigned to the pile as temperature linear function with depth. At the end of monitoring the agreement between the results of the simulation and the experimental results seem rather satisfactory. The thermal properties of concrete were not measured in situ therefore, the back analysis was carried out calibrating the thermal conductivity of concrete. The pile is modelled as homogeneous polygon and an average thermal conductivity of 1 W/m °C.   This is confirmed by the axial load and thermal mobilised skin friction profiles Figure 5-55 (b) and Figure 5-55 (c), respectively.

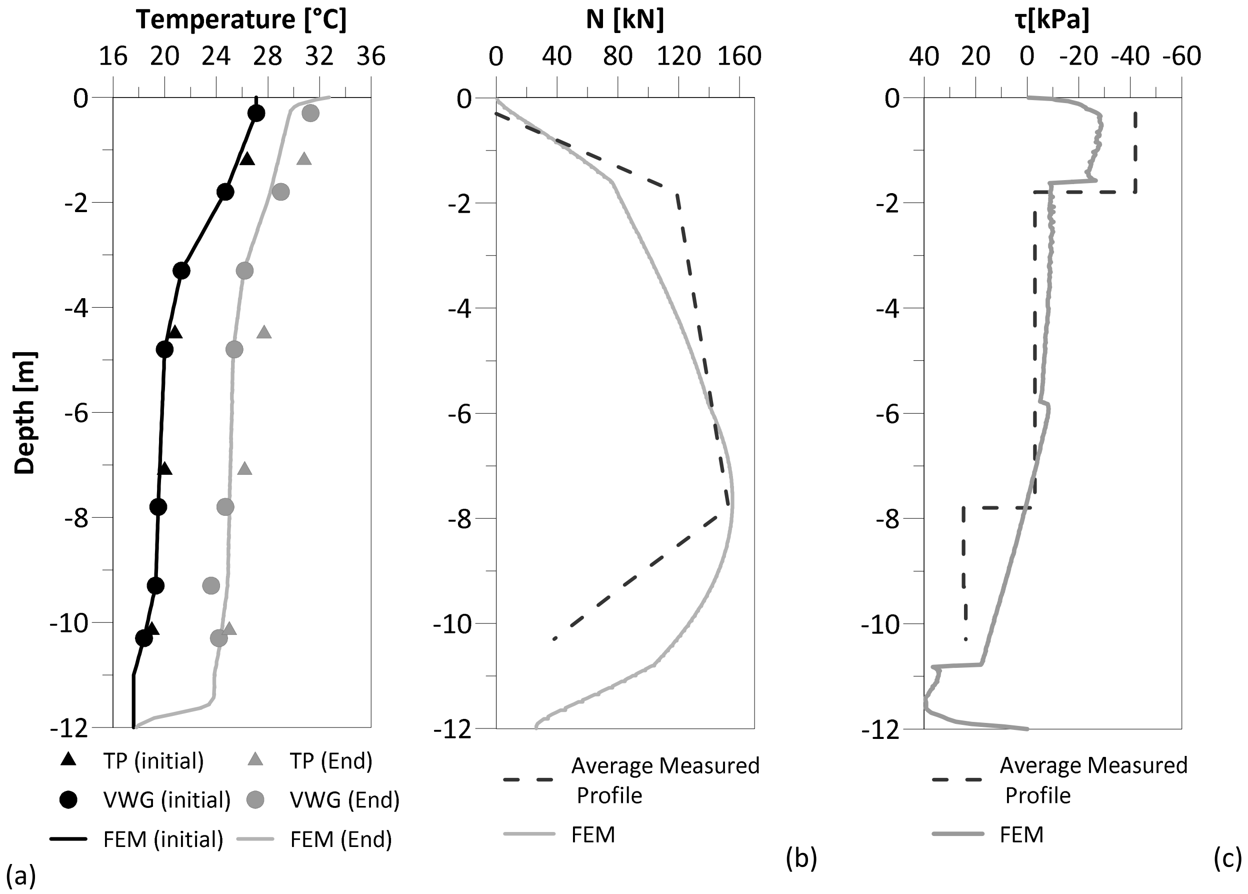

Figure 5-55:Comparison between experimental measurements and FEM results; (a) temperature profiles prior heating and at the end of monitoring. (b) axial load and (b) thermal mobilised skin friction maximum profiles.

The results of FE analysis provide NP depth that agrees to those obtained by the average axial load profile. The mobilised shaft friction provided by FEM is very close to those computed from the VWG measurements. Both axial load and mobilised skin friction with depth strongly depend on the degree of mobilisation of pile's thermal expansion. It is confirmed by the numerical results. The computed thermal profile is slightly different from those measured and it is constant with depth. When the temperature variation with depth is almost constant or characterised by small variation the shape of axial load profile is dictated by the surrounding soil properties i.e., soil stiffness variation with depth. While when the temperature variation profiles are strongly variable with depth the shape of the axial load is dictated by the temperature distribution.

5.7 *Concluding remarks and Observations*

Three short term purely thermal tests have been presented considering both the thermal performance of the pile and the effect of the thermal loadings on pile's response. In term of thermal performance. the average specific heat injection rate in W/m. the average inlet temperature $T_{in\ ave}$ in °C and time duration of the heating in hours are summarised in Table 5-10 for each thermal test.

Table 5-10: Thermal performance during the test

	$T_{in\ ave}$ [°C]	Time duration [h]	W/m
Test C	29.7	6.08	223
Test B	32.5	1.63	331
Test A	33.7	5.15	279

Test B is characterised by the shortest heating phase and therefore the best thermal performance i.e., highest specific heat injection rate was measured. This is of course a transient performance which would decrease with the operational time of the heating pump. During thermal tests C and A, that are characterised by similar time duration the highest thermal performance was monitored during Test A. This fact is obviously connected to the larger average inlet temperature $T_{in\ ave}$ as showed in Table 5-10. Again, here it is important to underline that the evaluations are on transient performance.

The specific heat injection rates are in agreement with those measured by Park et al. (2019) for in situ energy pile equipped with coil type exchangers at 200 mm of pitch. It should be remarked that the higher performance measured depends on the short time of measurement for longer tests smaller injection rate are expected.

The dimensionless ratios DDR and DSR computed during each test are reported in Table 5-11.

Table 5-11:DSR and DDR during the thermal tests

	DSR[-]	DDR [-]	ΔT_{av} [°C]	ΔT_{NP} [°C]
Test C	0.41	0.78	4	4.8
Test B	0.4	0.76	1.6	3
Test B	0.35	0.75	4.7	5.2

The dimensionless ratios DSR is computed taking into account the thermal variation ΔT_{NP} measured at the location of the maximum thermal stress i.e., NP depth. The DSR is computed for each test considering the average thermal variation ΔT_{ave} that allows taking into account for the temperature distribution both along pile's length and cross sectional.

As expected, both DSR and DDR computed for each thermal test are in substantial agreement not depending on the exact detail of the thermal history.

The temperature distributions over pile's cross section during heating at all pile's depths are characterised by a low range of variations that determine nonuniformly distributed thermal stress. The difference in magnitude of thermal stress is lower than 0.05 MPa as observed by Faizal et al. (2019). With respect to temperature distribution along pile's length different results are obtained from the tests. When the pile is heated for the first time (thermal test A) the temperature increase along the pile is almost uniform along the depth as showed in Figure 5-52. While during tests B and C higher difference are observed between the shallow and the deep pile's portion.

The DOF computed at the end of each test are plotted versus the dimensionless depth z/L and showed in Figure 5-56.

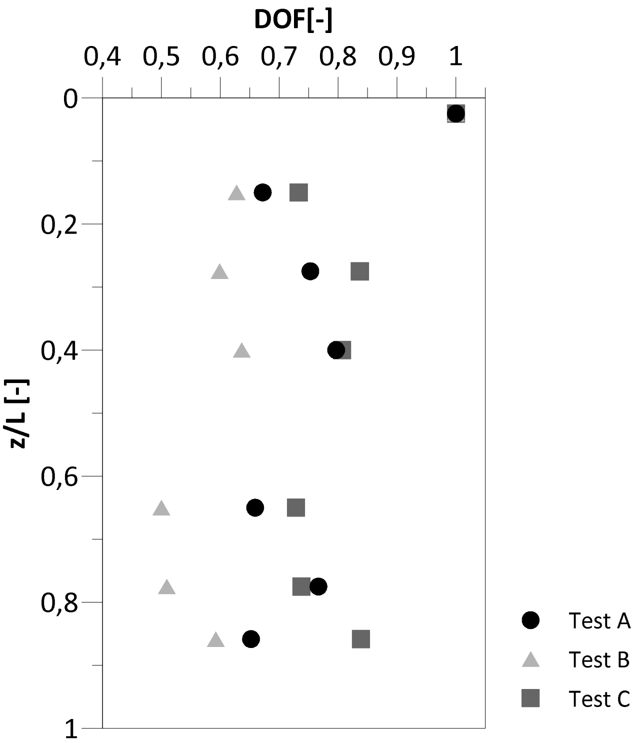

Figure 5-56: DOF versus dimensionless length for Tests A. B and C.

The minimum DOFs are observed for the test B that is characterised by the smaller heating phase and the longer recovery phase. The DOFs computed at the end of monitoring of Tests A and B are very similar in magnitude. During test C, at 0.86 dimensionless depth an increase of the DOF occurred. The measurement obtained by the VWG at this depth was corrected as observed in 5.5.2. As observed for DSR and DDR, DOF measured are in the range reported in section 2.2.2.

The mobilised shaft frictions during the test are reported in Table 5-12, Table 5-13 and

Table 5-14 for Tests A, B and C, respectively.

Table 5-12:Mobilised shaft resistance and skin resistance according to β Method during Test A.

[m]	τ mob [kPa]	τ βM [kPa]
1.8	-42	7
7.8	-3	31
9.3	25	37

10.3	24	41

Table 5-13: Mobilised shaft resistance and skin resistance according to β Method during Test B.

[m]	Ƭ mob [kPa]	Ƭ βM [kPa]
1.8	-11	7
3.3	-7	12
4.8	-3	17
7.8	-8	31
9.3	5	37
10.3	5	41

Table 5-14: Mobilised shaft resistance and skin resistance according to β Method during Test C.

[m]	Ƭ mob [kPa]	Ƭ βM [kPa]
1.8	-11	7
3.3	-2	14
4.8	-7	9
7.8	-7	31
9.3	5	37
10.3	1	41

The mobilised thermal friction reported in 5.5.4. 5.5.3 and 5.5.2 are computed from the average thermal load profile. As described the thermal load profile measures in case of test A and B are corrected considering an average thermal load profile. The average thermally induced shaft frictions are compared to the shaft resistance (Ƭ βM) computed according to well-known β method. The friction angle of the pile-soil interface corresponds to the friction angle of the soil reported in Table 5-1.

As already observed from the in-situ measurements reviewed in chapter 3. for the upper layers the mobilised shaft friction is often larger than the limiting values estimated via the β method. This finding is confirmed in this thermal experiment carried out on a bored pile in pyroclastic unsaturated soil.

Faizal et al. (2016) evaluated the effects of limited number of daily thermal cycles on the axial strains in energy piles embedded in sand. These experimental studies showed that the temperature along the depth of the foundation was relatively uniform and the thermal axial stresses had a trend similar to the change in pile temperature. This finding is confirmed by the experimental results of this study. When the pile's temperature distribution is almost uniformly distributed with depth the axial thermal load variation with depth is mainly governed by the restrained thermal expansion coefficient that varies with depth and time. When the temperature distribution along pile's length is not uniformly with length, as occurred in test C and test B. the axial thermal load profile is mainly governed by the temperature variation observed. As described in chapter 2, the temperature profiles of heated or cooled EPs are nearly constant with depth in some studies e.g., Bourne-webb et al. (2009) and Faizal et al. (2019) or variable with depth e.g., de Santiago et al. (2016). The higher variation with depth were observed during tests B and C where the pile was previously heated and then subjected to ambient air temperature variations and heating. During operational modes, the more likely conditions seem to be those observed during tests B and C where the pile's is subjected to heating. It should be also remarked that as numerically investigated in chapter 3 the thermal interaction with the upper structure may determines different temperature distribution and therefore different thermal response.

References

Aversa, S., Evangelista, A., 1993. Thermal expansion of Neapolitan Yellow Tuff. Rock Mech. Rock Eng. 26. 281–306. https://doi.org/10.1007/BF01027114

Bao, X., Li, Y., Feng, T., Cui, H., Chen, X., 2020. Investigation on thermo-mechanical behavior of reinforced concrete energy pile with large cross-section in saturated sandy soil by model experiments. Undergr. Sp. 5. 229–241. https://doi.org/10.1016/j.undsp.2019.03.009

Bourne-Webb, P.J., Amatya, B., Soga, K., Amis, T., Davidson, C., Payne, P., 2009. Energy pile test at lambeth college. London: Geotechnical and thermodynamic aspects of pile response to heat cycles. Geotechnique 59. 237–248. https://doi.org/10.1680/geot.2009.59.3.237

Brandl, H., 2006. Energy foundations and other thermo-active ground structures. Geotechnique 56. 81–122. https://doi.org/10.1680/geot.2006.56.2.81

Durgunoglhu, T., Mitchell, K., 1975. Static penetration resistance of soils: I-ANALYSIS. Proceedings. ASCE Specialty Conference on in-situ Measurement of Soil Parameters. Raleigh. 1.

De Santiago, C., De Santayana, F.P., Groot, M., De Urchueguía, J., Badenes, B., Magraner, T., Arcos, J.L., Martín, F., 2016. Thermo-mechanical behavior of a thermo-active precast pile. Eur, Geotherm. Congr, 2016 48, 41–54.

Faizal, M., Bouazza, A., McCartney, J.S., Haberfield, C., 2019. Axial and radial thermal responses of energy pile under six storey residential building. Can. Geotech. J. 56. 1019–1033. https://doi.org/10.1139/cgj-2018-0246

Faizal, M., Bouazza. A., Singh. R.M., 2016. An experimental investigation of the influence of intermittent and continuous operating modes on the thermal behavior of a full scale geothermal energy pile. Geomech. Energy Environ. 8. 8–29. https://doi.org/10.1016/j.gete.2016.08.001

MARSHALL, J.K., HUNTER, P., 1980. Effect of temperature on vibrating wire strain gauges, Strain 16, 37–44. https://doi.org/10.1111/j.1475-1305.1980.tb00313.x

Park, S., Lee, S., Lee, D., Ahn, D., Choi, H., 2019. Effect of thermal interference on energy piles considering various configurations of heat exchangers. Energy Build, 199, 381–401. https://doi.org/10.1016/j.enbuild.2019.07.008

Russo, G., 2004. Full-scale load tests on instrumented micropiles. Proc. Inst. Civ. Eng. Geotech. Eng. https://doi.org/10.1680/geng.2004.157.3.127

Stewart, M.A., McCartney, J.S., 2014. Centrifuge Modeling of Soil-Structure Interaction in Energy Foundations. J. Geotech. Geoenvironmental Eng. 140. 04013044. https://doi.org/10.1061/(asce)gt.1943-5606.0001061

Tinti, F., Barbaresi, A., Benni, S., Torreggiani, D., Bruno, R., Tassinari, P., 2014. Experimental analysis of shallow underground temperature for the assessment of energy efficiency potential of underground wine cellars. Energy Build. 80. 451–460. https://doi.org/10.1016/j.enbuild.2014.06.002

6 Conclusions

The aim of this PhD project was to investigate different aspects of pile-soil thermomechanical interaction by means of FE analyses, small scale and in situ tests.

In the chapter 1, the sustainable technology of heat exchangers piles is briefly described and an overview about the thermo mechanical pile-soil interaction is provided. Chapter 2 deals with literature review aimed to the description of the main thermal and mechanical phenomena occurring between Energy Piles (EPs) and the surrounding soil. The complex phenomenon of the heat exchange occurring in EPs and the thermal properties of all the components of EP system are described along with the mechanical behavior of soil under non isothermal conditions.

The main site investigations reported in the literature have been carefully scrutinised and a report has been done with the data collected from the studies. The data refers to piles with different technologies and in different subsoil conditions and on the overall they are still rather scanty to allow for separate analyses of the various factors. Being the focus of this research on the pile's foundation displacements, strains and stresses provided by the observations have been collected and summarized. Through the dimensionless parameters DOF (Degree Of Freedom), DSR (Dimensionless Stress Ratio), and DDR (Dimensionless Displacement Ratio) upper bounds values for stress and displacements are proposed, based on the experimental results. Differences in case of heating and cooling are detected and outlined. From the summarized data some preliminary suggestions for design of EPs can be offered. When estimating the maximum expected movement at the piled head in the case of cooling the pile can be considered as a free column while in the case of heating the movements are significantly restrained and the displacement on the average is about 40-50 % of the free column. In terms of stress under heating action the ideal scheme of perfectly fixed column may be a conservative but appropriate preliminary assumption. Under cooling action. the stress increase is indeed smaller because of the lower degree of constraint exerted by the soil and a conservative estimate can be obtained by considering the results of a perfectly fixed column divided by 2. With respect to the DOF the collected data show that the maximum values are reached at both the ends of the piles. It depends on the fact that the piles tested are generally single isolated pile. not belonging to a foundation system (i.e., the pile head is free to move) and the majority of the tested piles are of the drilled replacement type in rather homogeneous soil profiles. For such piles the response of the pile tip may be rather compressible and get high values of DOF.

The most well documented small-scale investigations have been also reported and the data summarised through the dimensionless previously introduced parameters DDR and DSR. The main aspects of the thermo mechanical interaction that need further investigations are also highlighted. Several studies reported DDR greater than unity and this is apparently not possible. However, some authors claim that it can be attributed to thermal effects in the surrounding soil (where the expansion thermal coefficient are larger than the ones associated to the pile material), or a likely cause may be issues and mistakes of the measurement system. Nevertheless, what is observed from in situ investigations is also confirmed by physical modelling under cooling the degree of constraint exerted by the surrounding soil is smaller than the comparable degree under heating actions. The cyclic behavior was investigated by a few studies under heating and cooling. The results showed a relationship between the level of head load mechanically applied and pile's head displacements with increasing thermal cycles that needed additional investigations.

Numerical investigations about pile-soil interaction have been largely used to back analyse experimental study, perform parametric analyses and provide long term predictions. What it is highlighted from the study of literature is that most of numerical studies do not consider real subsoil conditions and thermal loadings applied to the pile are rarely defined on the basis of a realistic energetic demand. Furthermore, many numerical studies predicted limited changes in internal stress and larger displacements, relative to those seen in field testing and it depends on modelled conditions that result in rather low soils' restraint action.

On the basis of the literature review chapter 3, chapter 4, chapter 5 and chapter 6 describe the investigations carried out in this research projected.

Chapter three is devoted to numerical studies carried out with the commercial FE program PLAXIS 2D. In the first part of the numerical studies, it was intended to back analyse two case-histories from literature referred to field scale test and one small scale test. Two different constitutive mechanical models were used to model the soil behavior assuming that for the range of temperature variations considered the behavior is thermo-elastic. The prediction by the hardening elastic-plastic H-S model matches the measured behavior much better than the elastic-perfectly plastic Mohr-Coulomb model. For each back analysed case a good consistency between experimental and numerical results was detected.

In the second part of numerical studies fully coupled short term simulations were performed. To this aim a well-documented case history of failure loading test on CFA pile installed in Napoli was considered. The subsoil geotechnical model was defined on the basis of the in situ investigations and results of the loading test through a best fitting procedure. The FE model was developed taking into account the measured shaft capacity of bored cast in situ piles embedded in sands. Several attempts to model the increase of horizontal stress responsible of the high measured shaft resistance. FE analyses are addressed to simply model the horizontal stress increase achieving a good agreement with the experimental results. On the basis of the observed mechanical behavior and the ultimate pile-soil measured capacity short term analyses were performed under operational condition. The results in terms of pile soil interaction can be summarised as follows.

- The maximum thermal displacement is about 53% and 49% of mechanical displacement during peak heating and cooling, respectively. The greater variation in the case of heating depends on the magnitude of thermal loadings.
- From the axial loads profiles the coupling of mechanical and thermal loadings determines 16% and 13% of variation with respect to the purely mechanical axial loading during heating and cooling, respectively.
- The magnitude of the residual thermal displacements at the end of heating and cooling are very small compared to the settlement induced by the mechanical loadings and could be considered as negligible as well as for the axial loading variations.

Then the effects of different parameters on pile thermomechanical response was investigated through a sensitivity analysis. The primary circuit configuration along with the restraint degree at pile's head are the parameters strongly influencing the response. The main conclusions about the sensitivity analyses are reported below.

- For the 100% of constraint at pile's head tensile stresses are observed during cooling episode. The amount of the maximum induced thermal stresses is about 30% of concrete Mean tensile strength
- For the 100% of constraint at pile's head maximum compressive stress is about 80% of concrete characteristic cylinder compressive strength.
- The degree of constraint determines a significant changing of thermo-mechanical loading along the entire pile length but does not compromise the structural integrity of the foundation.

- The recovery has no effect on the settlement of the pile. While the cooling before heating determines slightly greater pile's heaves.
- For daily thermal operation and with reference to isolated pile the boundary thermal conditions do not significantly affect the results of the pile-soil thermo-mechanical interaction.

The effects of the surface upper boundary conditions on the pile soil thermo mechanical interaction in short term condition is almost negligible but the superposition of the thermal interaction between the upper structure and pile should be deeply investigated. To address the investigation on thermo-mechanical response FE analyses are carried out considering thermal loadings defined on the heating and cooling demands of a building located in Napoli. To this aim dynamic energetic simulation are carried out by means of a dedicated software to define thermal loadings to be applied. Once thermal loadings are defined the geotechnical model employed for the short-term analyses were used to perform yearly fully coupled analyses. The effects of thermal loadings time scaling. upper thermal boundary conditions and head restraint were investigated.

Thermal loadings were applied with different time scansion function. The applications of hourly (HTV) and daily (DTV) scaling loadings determine different effects in terms of pile's response:

- DTV and HTV determine an additional displacement equal to about 40% and 50% of the mechanical displacement. respectively.
- The magnitude of both displacements and thermal loadings are however very similar from an engineering point of view and thus, considering also the much larger calculation efforts the need for hourly detailed function is at least questionable.

The upper thermal boundary conditions effects on the thermomechanical interaction for yearly simulations was investigated taking into accounts two extremes' conditions: outdoor air temperature and indoor air temperature applied as convective thermal boundary conditions at ground surface.

- Comparing the axial load profiles, during different phases. it is observed that the difference between the two simulated surface conditions is in the range of 10% to 15 %.
- The largest difference between the two thermal conditions occurs during the two recovery phases.
- From the results both in terms of axial loading and pile head displacement. the outdoor temperature variation assumed as surface boundary condition seems to be the most conservative design assumption. However, the possibility to design with the envelope describe by both conditions is a reasonable alternative.

With respect to the effects of the fully restrained pile head compared with free head pile it was observed that:

- During the peak of heating the load computed in the constrained case doubles the purely mechanical loading. Of course. this depends on the details of the subsoil layering analysed.
- At the end of the thermal cycle the thermomechanical loading at the head is about 60 % of the purely mechanical load. while at the end of the first cooling is about 30% of increment with respect to the purely mechanical load.
- The amount of additional stresses do not compromise the structural integrity of the foundation.

The effect of a stiffer subsoil layer at pile tip (tuff) was investigated comparing the thermo mechanical response occurring observed when the pile tip is socket (EBEP) and not (FEP) in a tuff layer. To this aim a new FE model consisting of layers of pyroclastic sands and an isolated hybrid pile equipped with spiral heat exchanger was developed. For the five layers of pyroclastic soil and pile H-S and linear elastic models were adopted. respectively. The hybrid pile execution was simulated by high levels of the horizontal stress fixed through the earth pressure coefficient at rest. The calibration of the soil parameters was carried out considering the load transfer curves and the load settlement relationship monitored during a failure loading test. Additional energetic simulations were performed considering the activities carried out and the occupancy density of mall common area. The new set of thermal loadings was coupled to mechanical service load during yearly fully coupled thermo mechanical analyses. The two piles kinds (EBEP and FEP) are compared both in terms of dimensionless displacements and axial loading.

- The thermo-mechanical settlement observed at the end of yearly operation corresponds to 0.06% and 0.10% of variation with respect to the mechanical initial settlement for EBEP and FEP, respectively.
- In the case of EBEP. the greater constraint effect induced by the tuff layer. induced additional loading in the lower part of the pile. In the case of the FEP the maximum changing of the axial loadings are observed in the upper part of the pile.
- From design perspective for the EBEP coupled thermo-mechanical loadings determine stronger effects on pile-soil interaction.
- These results confirm again that the behavior of pile subjected to thermo mechanical loading is very different to those occurring under conventional mechanical loadings. The induced stresses and displacements determined by thermal loadings lead to worst condition in the case of pile with socket depth.

The case of EBEP was considered to perform long term analyses i.e., 50 years of simulation. The main results of the simulations lead to the following conclusions.

- Pile's head displacement at the head passed to moving downward (under mechanical load), settlement, from heaves (under combined thermomechanical loadings).
- The accumulation of plastic displacements affects the long-term behavior at the end of the simulation a shakedown condition seems to be achieved.
- The axial load profile at different time instant during the long term operational was always lower than the mechanical load profile confirming the elongation trend of the pile. The trends can be partially explained by the hardening part of the model used for the sandy layers. The deviatoric hardening part of the constitutive model used for sand layers determines an increase of the shear stress along the pile shaft that induced a decrease of the axial loadings.
- For the climatic area considered in this study where pile's heating loading are predominant the observed behavior is characterised by a reduction of axial loadings and heaves of piles head providing a result that is slightly different to those obtained considering short-term simulation under simplified thermal loadings.
- The effects determined by the applications of thermal loadings on the single EP do not compromise the structural integrity of the pile. For serviceability related problems the displacement of the single pile can be considered as a starting point for the evaluation of the group's displacements.

In chapter 4 the design of physical model is described. An Aluminium model pile was equipped with heat exchangers and strains transducers. The small pile was embedded in pyroclastic soil pluviated to achieve a loose state. Different kinds of tests are carried out both with respect to the kinds of load applied to the pile and applied at ground surface. In the latter case two kinds of tests were performed. On Model A where the ground surface is free and on Model B where at surface dead weights are applied. The choice of performing these two different kinds of tests was dictated by the aim of working on a pile with different level of stress along the shaft inside the experimental box. In the case of Model A, thermal and thermomechanical tests were carried out. The pile-soil system resistance was estimated by means of load test to failure (purely mechanical) tests. Then purely thermal and one thermomechanical tests were performed.

- The results show different soil behavior under heating and cooling modes as observed from previous studies. All the tests presented provide measurements consistent with the relationship between the induced stress and displacement. DDRs are about 0.8 and 0.9 under heating and cooling modes, respectively. DSR are always lower than 0.10 with higher magnitudes in the case of heating.
- Thermal displacements measured during the thermomechanical test at the peak ($\Delta T \approx 25$ °C) is about 4 times the settlement induced by the operational mechanical load.
- The shear stress mobilised along pile's soil interface could seem very high considering an effective stress approach and neglecting the matrix suction. Taking into account the likely effect of the measured matrix suctions (i.e., TDR measurement were carried out in the box) the rather high skin friction is at least justifiable.

On Model B on load test to failure and two different kinds of cyclic thermomechanical tests are presented. Firstly, comparing the response under purely mechanical loading, it is observed an increase of the ultimate pile soil capacity with a significative reduction of the observed settlement. With respect to thermo mechanical tests a decrease of thermal displacements occurred on Model B with respects to Model A under the same applied thermal loadings. Cyclic thermo mechanical tests were performed in heating and cooling conditions considering thermal loadings derived from dynamic energy simulation described in chapter 3. One day of simulation was reproduced and repeated to investigate the cyclic response. In cooling mode under a level of stress that corresponds to those occurring in operational conditions a relationship between the observed settlement and pile head displacement is observed.

- Under cyclic thermo mechanical cooling with increasing number of thermal cycles pile's head settlement (in absolute value) increased. This result agrees on previous studies. The thermal settlement during the first and tenth thermal cycle increased about 30-40% and 50-60% with respect to the initial mechanical settlement. Tensile stress is observed at higher depth. The minimum tensile loading is about 70% of the axial load induced by mechanical loadings.
- In the case of heating different tests are performed under different levels of mechanical stresses. What is observed is that the trend of displacement with the number of cycles depend on the level of mechanical stress (SF). For null mechanical loadings applied at pile's head the pile's head displacement increased with the number of thermal cycles. At tenth cycle the displacement is about 10% higher than those measured during the first thermal cycle. For increasing level of mechanical stress an opposite trend. it is observed. Pile's head upward displacement during the last thermal cycle decreased about 10% with respect to the displacement measured during the first cycle.

On the basis of the experimental results the displacement increment can be described by a simple power law where the exponent depends on the SF. Further and deeper analysis of the observed results are opportune, and the cases are documented in a rather detailed way just for this future purpose.

In chapter five the layout and the results of short-term thermal tests at field scale are described. A drilled energy piles equipped with spiral heat exchangers fixed to the reinforcing cage was installed in the north area of Napoli. The pile was instrumented with vibrating strain gauges and temperature sensors to monitor both thermal strains and temperature. The soil undisturbed temperature was also monitored allowing both the measure of soil diffusivity and temperature and depth of the *Deep Zone*. Soil's temperature is about 18 °C while the depth of deep zone can be considered at 6 m from ground surface. The inlet and outlet temperature of water measures allowed also to test the energetic performance of the system (TPT). The performance measured was rather satisfactory demonstrating both the efficiency of the constructed spiral circuit and the potential performance of such system in the specific climatic area. Pile's head displacements and thermal strains are measured during purely thermal tests. The thermal strain, temperature and axial load profile allow different observations.

- The temperature distribution along the pile is not uniform with depth.
- Comparing the temperature measures at different locations in the cross-sectional maximum differences about 4 °C occurred. This determines different induced thermal strains and stresses along the cross sectional that can potentially contribute to deteriorate concrete. For the tests carried out the magnitude of this differential stresses is lower than 1% of characteristic cylinder compressive strength.
- The axial strain profiles followed the same trend of the temperature strain profile. When the temperature difference profiles with depth is more uniform the thermal strain variation with depth is justified on the mobilised thermal expansion coefficient variations with depth. The maximum compressive stresses occurring during heating do not exceed 10 % of concrete characteristic cylinder compressive strength.
- The axial loading along the pile increased with increasing temperature and the NP position does not varies during the tests and between different tests.
- The shaft friction evaluated from the axial load demonstrated again that the skin friction of drilled pile in sand could be underestimated with traditional methods.